Convergent-Beam Electron Diffraction III

by

Michiyoshi Tanaka
Masami Terauchi
Kenji Tsuda

Research Institute for
Scientific Measurements
Tohoku University

JEOL LTD.

Contents

Preface

My first motivation to have been concerned in convergent-beam electron diffraction (CBED) was to measure the absorption coefficient of barium titanate ($BaTiO_3$). For this purpose, I stayed at the laboratory of Professor K. Molière of Fritz-Haber-Institut der Max-Planck-Gesellschaft. There, I learned the CBED technique from Dr. G. Lehmpfuhl, who had already published pioneering papers in the field of modern CBED, and learned many theoretical aspects from Dr. K. Kambe, whose profound knowledge on diffraction physics impressed me grately. After coming back to Japan, I had to wait several years to begin CBED work because of financial and technical problems. JEOL microscopes in those days were equipped with a conventional objective lens, which was inconvenient for CBED work, and did not have a good enough vacuum. In the meantime, Dr. P. Goodman made a great contribution to the symmetry determination of crystals. Professor J. W. Steeds and his coworkers established a method to determine crystal point-groups. Owing to these developments, the importance of the CBED method rapidly gained recognition in the electron microscopy community. We purchased at length an electron microscope, converted for CBED use, the JEM-100CX. Since then, I have concentrated on CBED studies. The LaB_6 electron source of the microscope was replaced by a brighter one or a field-emission gun. Afterwards, an electron microscope, the JEM-2010 equipped with an imaging plate system, has been installed for both CBED and HREM use. These two electron microscopes, together with the JEM-2000FX, have helped create our achievements. It is happy for us that we have been able to make contributions in the field of electron microscopy and crystallography — the large angle technique, symmetry determination and lattice-defect identification.

I owe our achievements on CBED work firstly to the warm-hearted late Professor G. Honjo, the supervisor of my doctor thesis, who had made the effort to send me to Professor K. Molière. Secondly, I owe very much to Professor K. Molière for his generous hospitality during my whole stay in Berlin. Thirdly, my great thanks are due to Dr. G. Lehmpfuhl for his instruction in the CBED technique and collaboration in the work on barium titanate, and to Dr. K. Kambe for his theoretical advice and personal encouragement. I also thank Mrs. L. Schulz for her skillful and kind arrangements for my stay in Berlin.

The CBED method was established in the mid-1980's as an important technique in analytical electron microscopy and has now entered into the stage of application. We have already published two books on CBED and have received favorable reviews. After those publications, the method to determine the space groups of incommensurate crystals has been completed, the space groups of decagonal quasicrystals have been clarified and some of them have been discovered, and the methods to identify crystal lattice-defects have been polished up. In the present volume, we include these materials. We also deal with coherent CBED patterns (a recent topic), CBED patterns taken with a high-voltage electron microscope, crystal structure analysis which is our final goal, and other subjects. We provided some personal computer programs in the previous editions. Various good programs have become widespread in recent years in a very convenient form; therefore, we do not carry the programs in this edition. We have paid great attention to providing photographs that are as near perfect as possible. I hope these materials serve to allow readers to appreciate a glimpse of the beauty and exquisiteness of nature.

The data shown herein was obtained with the cooperation of successive graduate students of Physics Course, Tohoku University. They include Mr. T. Kaneyama (EM Group, JEOL Ltd.), Mr. A. Ishikawa (R&D Department, Nippon Precision Circuits Inc.), Mr. M. Saito (Hitachi Research Laboratory, Hitachi, Ltd.), Miss M. Takahashi (LSI Memory Division, NEC Corporation), Mr. A. Fujiwara (R&D Group, Oki Electric Industry Co., Ltd.), Mr. S. Yamada (Doctor Course of Physics, Tohoku Univ.), Miss M. Takizawa (Application & Research Center, JEOL Ltd.), Mr. O. Kamimura (Advanced Research Lab., Hitachi, Ltd.), Mr. K. Saitoh (Doctor Course of Physics, Tohoku Univ.), Mr. Y. Nishida (Master Course of Physics, Tohoku Univ.) and Miss N. Kanda (Master Course of Physics, Tohoku Univ.). The photographs included in this publication were taken with a JEOL electron microscope JEM-100CX equipped with a field emission gun (FEG), a JEM-2000FX, a JEM-2010 equipped with an imaging plate system, a JEM-2010F owned by JEOL Ltd. and a JEM-ARM1250 installed at the High Voltage Electron Microscope Laboratory of Tohoku University.

I express my cordial gratitude to the JEOL Ltd. staff, especially Mr. T. Eto (President), Mr. A. Fuse and Dr. Y. Harada for promoting and supporting this publication and to Mr. Y. Ishida and Mr. T. Honda for their devoted collaboration in instrumental development. I wish to thank Mr. F. Sato of our lab for his dedicated maintenance of the JEM-100CX-FEG, JEM-2000FX and JEM-2010, and for his highly skilled photography. Thanks are also due to Mr. E. Aoyagi of our university for his favorable arrangements to use the JEM-ARM1250. I am grateful to Miss M. Kita of our lab for her devoted typing of the manuscript.

Also, without the unstinted help of Mr. H. Matsuo and Mr. T. Handa of JEOL Ltd. in the compilation of the book, and of Mr. T. Takamatsu of JEOL Technoservice Co., Ltd. in the critical reading of the manuscript, this edition could never have been possible. It is my pleasure to pay a tribute also to Mr. T. Kondo of Kyoritsu Printing Co., Ltd. for the excellent printing of this book. Some of the photographs contained herein were reprinted from our papers with the publishers' kind permission.

This work was supported financially by the Grant-in-Aid for Scientific Research (No. 02402055), the Grant-in-Aid for Developmental Scientific Research (No. 01880014, No. 0554005) and the Grant-in-Aid for the Encouragement of Young Scientists (Terauchi: No. 03780053, No. 04740186, No. 05740193; Tsuda: No. 0523, No. 05740218), from the Ministry of Education, Science and Culture of Japan. Recently, I have been informed that my proposal to Grant-in-Aid for Specially Promoted Research for purchasing a new electron microscope equipped with an energy filter was accepted by the same Ministry (No. 06102003).

Sendai, Autumn 1994

Michiyoshi Tanaka

Introduction

When the accelerating voltage for the incident beam is lowered, higher-order Laue-zone (HOLZ) reflections with lower indices are excited. This enables us to obtain three-dimensional symmetries more easily than at higher accelerating voltages. If a low accelerating voltage and an ultrahigh vacuum specimen chamber are available in an electron microscope, convergent-beam electron diffraction (CBED) of the transmission type can be applied to studies of surface science. We already showed CBED patterns taken at an accelerating voltage of 20kV [1]. We have challenged to take CBED patterns at low accelerating voltages around 10kV.

Introduction of diperiodic plane figures by Buxton *et al.* [2] clarified that a fourfold rotoinversion or $\bar{4}$-axis can be observed in CBED patterns. The symmetry, however, has not ever been observed in a complete form, and thus not used for the point-group determination of materials because it requires four different crystal (or condenser aperture) settings. To complete the examination of the symmetries appearing in CBED patterns, a CBED symmetry 4_R due to the $\bar{4}$-axis has been examined by three methods which include the technique developed by Terauchi and Tanaka [3], [4].

The recording device for electrons is now changing from a traditional negative film to a slow-scan charge-coupled device (SSCCD) and to an imaging plate (IP) or, in other words, from an analogue device to a digital one. The new tools, each of which has a wide dynamic range and linear response in intensity recording, enable quantitative studies using the intensities of CBED patterns. Prior to quantitative studies, the devices are used effectively for the examination of symmetries of CBED patterns. Digital image-processing allows us to elucidate the symmetries of reflections with weak-intensity and monotonic-intensity distributions in a CBED disk — sometimes producing humorous patterns — and to make clear the CBED patterns by subtracting the background intensity. Effectiveness of the image processing is demonstrated for several examples. In a previous volume [4], the sensitivity of CBED patterns to the small breakdown of crystal symmetries was shown. In the present volume, the degree of real symmetries appearing in CBED patterns is expressed in a quantitative manner by digital processing of the patterns recorded on imaging plates. It is interesting to know what extent of deviation from the correct symmetry is permissive for visual examination.

It is fun to determine a space group from the symmetries of CBED patterns. We shall here introduce three examples which help readers become familiar with space-group determination by CBED. The first example is rutile (TiO_2), whose space group is well known. The second is the intermediate- and low-temperature phases of hexagonal $BaTiO_3$, whose space groups were determined reliably by CBED for the first time. The third is Sm_3Se_4, which is expected to have a different space group from the reported one.

The previous volume [4] included the CBED symmetries of incommensurate crystals. One-dimensional incommensurately modulated crystals can be regarded as four-dimensional crystals. We have clarified the theory interrelating the symmetries of CBED patterns and four-dimensional point-group symbols for incommensurately modulated crystals. The above theory is demonstrated using $Sr_2Nb_2O_7$ and $Bi_2Sr_2CaCu_2O_{8+\delta}$ with incommensurate modulations [5]. It is shown that approximate dynamical extinctions occur in incommensurate reflection disks [6]. In our treatment, the amplitude of the incommensurate modulation wave is assumed to be small. The study should be extended to composite crystals, which consist of two structures whose periods are of an incommensurate ratio.

In quasicrystals, the icosahedral phase was first discovered and became a target for intensive research. The phase can have two point groups, 235 and $m\bar{3}\bar{5}$, the latter having been found to date. Recent studies have been focused on the decagonal phase. We derived the point groups of decagonal and pentagonal systems, by analogy of hexagonal and trigonal point groups. We discovered decagonal quasicrystals which belong to two different point groups or to three different space groups. Among them, the decagonal phase with a space group of $P\bar{1}0m2$ is included, which is the first noncentrosymmetric space group in quasicrystals. The phase with $P\bar{1}0m2$ exhibits inversion domains accompanying an antiphase shift at the domain boundary. Further studies to discover other decagonal phases having different point and space groups are continuing.

Crystal-structure analysis is one of the development goals of the CBED technique. Its greatest advantage exists in making possible structure analysis from a crystal area about one nanometer or less in size, which X-ray and neutron diffraction can not achieve. In the structure analysis by X-rays and neutrons, positional

parameters are refined by measuring the intensities of many reflections, namely, more than five times the number of the parameters to be determined. Since electron diffraction requires no difficult correction like that of extinction, which is important in X-ray analysis, accurate intensity profiles can be obtained, which is suitable for fitting with the intensities calculated by the dynamical theory of electron diffraction. This matter probably decreases the number of reflections needed in obtaining the parameters with high accuracy. When the reflection intensities originated from a specific Bloch wave are used, the positional parameters of a definite atom can be selectively determined. As far as inorganic materials are concerned, it is hard to find substances whose structures are completely unknown. Secondary structures or deviations from the basic structures govern the physical properties useful in technology. Thus, it is important from the practical viewpoint to develop a CBED structure-refinement method similar to the Rietvelt method. In this volume, crystal-structure refinement of $SrTiO_3$ [7], which undergoes a typical second-order phase transformation, and CdS, which has a simple noncentrosymmetric structure, are demonstrated. Energy filtering is an indispensable technique for quantitative CBED studies. Since plasmon scattering and phonon scattering at small angles cause intraband and interband transitions, respectively, the former had been considered less harmful to diffraction patterns than the latter, until we demonstrated what clear patterns appeared when plasmon scattering was removed [8]. The effect of energy filtering is demonstrated for Si and FeS_2.

Crystal lattice-defects are sorted by their dimensions: point defects (0-dimension), dislocations (1-dimension), stacking faults and twin boundaries (2-dimension) and voids and clusters (3-dimension). From the viewpoint of the contrast theory of electron microscopy, it is convenient to sort them into defects causing phase shifts and those causing angular changes. A typical example of the former is a stacking fault and that of the latter is a twin boundary. Dislocations have been treated as an extension of the former. We have described the identification methods for stacking faults, dislocations and twin boundaries [4], [9]. The diffraction intensity I from a lattice defect is given as a function of position $\boldsymbol{r}$ and orientation θ or $I(\boldsymbol{r},\theta)$. The traditional electron-microscope method examines in most cases the intensity with respect to the distance from the defect, $I(\boldsymbol{r})$. Contrary, the conventional CBED method studies diffraction intensity changes at the defect with respect to the incident beam orientation, $I(\theta)$. These two methods give complementary information for lattice-defect identification. The large-angle CBED (LACBED) method [10], [1], however, provides intensity variation for both parameters, $I(\boldsymbol{r},\theta)$. Therefore, the LACBED method is quite an effective method to identify lattice defects. A procedure to determine the shift vector of the stacking fault [11] using LACBED is presented for TiO_2 and Si. The rocking curves obtained from the fault are interpreted by phase-amplitude diagrams calculated dynamically. In the case of Burgers vector determination, Niu, Wang and Lu [12] gave a more useful convention for determining the sign of $\boldsymbol{g}\cdot\boldsymbol{b}$ than we did [4], where $\boldsymbol{g}$ is a reflection vector and $\boldsymbol{b}$ is the Burgers vector of a dislocation. We give an exercise to determine the Burgers vector of a dislocation using their convention [9]. Wen, Wang and Lu [13] discovered a clever method to distinguish a screw and an edge dislocation using zone-axis LACBED patterns. A clear difference between the LACBED patterns produced by screw and edge dislocations is demonstrated for graphite and Si [9]. The LACBED method provides an accurate determination method for an angular difference at a twin boundary, which lies oblique to the incident beam [9]. Examples of the determination are shown for NiO and CoO. Based upon such developments since the last volume, the standard methods to identify the three types of lattice defects using LACBED are described efficiently. It should be noted, however, that the methods for stacking faults and twin boundaries hold for not-strongly dynamical situations. When strong dynamical effects occurring at excitation error $w<1$ are studied in detail and utilized, further information may be obtained. A method which corresponds to the weak-beam method should also be studied.

When an electron source with high brightness (*i.e.*, field-emission gun: FEG) is used, interference fringes are produced in the overlapping regions of CBED disks. An early observation of interference fringes in overlapping CBED disks was conducted by Dowell and Goodman [14] for a graphite double-crystal, using a tungsten filament as the electron source. Spence and Cowley [15] discussed in detail the interference effect from perfect single crystals appearing in overlapping CBED disks for both cases of scanning transmission

electron microscopy (STEM) and conventional transmission electron microscopy (CTEM). Cowley [16] observed the interference fringes in CBED patterns (shadow images) from $2TiO_2 \cdot 7Nb_2O_7$ with a lattice spacing of 1.05nm, using an HB5 scanning transmission electron microscope equipped with an FEG, though the fringes were distorted by the aberration of the probe forming lens. Lin and Cowley [17] analyzed the distorted figures to calibrate the operating parameters of the STEM instrument. Vine *et al.* [18] and Steeds *et al.* [19] observed the distortion-free interference fringes of 6H polytype SiC with a lattice spacing of 1.51nm in overlapping regions of CBED disks, by using an HF-2000 electron microscope equipped with an FEG. They showed that the fringes with a shift of a half period were due to the existence of a glide symmetry. They demonstrated that the phases of crystal structure factors can be determined from the relative positions of the fringes. Terauchi *et al.* [20] observed mirror and glide symmetries of $Sr_2Nb_2O_7$, $Sr_2Ta_2O_7$ and FeS_2, using the interference fringes. They observed interference fringes of FeS_2 with a lattice spacing of 0.27nm, using a JEM-2010F electron microscope equipped with an FEG. Recently, Tsuda *et al.* [21] succeeded in observing interference fringes of Si with a lattice spacing of 0.192nm, using the JEM-2010F. This implies that a beam smaller than the lattice spacing of 0.192nm was realized at the focused point of the incident beam. Application of the interference effect or coherent CBED to real crystals requires to obtain a lattice spacing of at least 0.2nm. A recent development of an electron microscope equipped with an FEG has made it possible to create a fine probe and obtain the fringes of such a spacing. It is a future problem how small a beam can be attained in an electron microscope. Electrical and mechanical stabilities of the microscope as well as the electron source, and the aberration of the objective prefield are important factors for solving this problem. We have succeeded in taking interference fringes of 1.3nm, using an LaB_6 emitter with the aid of imaging plates and digital image processing. The fringe features which can be kinematically interpreted appear only for thin crystalline specimens up to approximately 10nm. Interpretation of real fringes necessitates dynamical calculations, though the symmetries between the fringes in the different disks, which originate from crystal symmetries, are preserved. How the phases of the observed fringes vary with the specimen thickness is demonstrated, their quick changes with the thickness being noted. Various applications of coherent CBED are open to imperfect crystals.

The greatest advantage of high-voltage electron microscopes is to improve resolvable distances in electron microscope images mainly due to the decrease in the wavelength of electrons, though radiation damages become serious. Another advantage is to allow us to examine thick specimens. The accelerating voltage is an important parameter also for CBED, though three-dimensional information is apt to be lost at high accelerating voltages. CBED is a suitable method to observe the critical voltage [22], which is useful for studying ionic states of atoms. In fact, such studies have been continued using critical voltages for systematic reflections. The zone-axis critical voltage was studied by Steeds *et al.* [23], though it has not since been used for materials researches because of its insufficient sensitivity to the accelerating voltage. Systematic studies of the critical voltage for different crystal types and different crystal orientations should be performed. We demonstrate CBED patterns taken with a new high voltage electron microscope, the JEM-ARM1250, which is installed at the high voltage electron microscope laboratory of Tohoku Univ. These patterns show another different beautiful aspect of CBED patterns, not obtainable in those taken at lower accelerating voltages, to which we are accustomed. We have succeeded in taking CBED patterns at 1250kV, the highest accelerating voltage to date.

The "Miscellaneous" section contains the observation of magnetic domains, the determination of the lattice parameters and alloy compositions, and selected area CBED patterns. It should be noted that CBED provides a new method to observe magnetic domains. HOLZ lines are conveniently used for lattice parameter determination. As an example, determination of the compositions of Fe-Ni alloys using HOLZ lines is presented. Selected area CBED patterns vividly show one-to-one correspondence between the electron probe position on the image and the CBED pattern.

Original or monochrome CBED patterns are very enjoyable for our eyes. Color presentations will offer another way of enjoying the patterns.

Lastly, we introduce a book by Spence and Zuo [24], which is the best reference to learn extensive substances of the CBED method. A chapter of the

International Tables for Crystallography by Goodman [25] is important literature written by a true pioneer of CBED. A book chapter of Eades [26] provides a neat guide to CBED. A short handbook by Jackson [27] includes a CBED chapter, which carries simple but useful figures, equations and tables. A recent review on CBED [28] treats symmetry determination of three-dimensional and high-dimensional crystals and crystal structure determination.

References

[1] M. Tanaka and M. Terauchi: Convergent-Beam Electron Diffraction, JEOL-Maruzen, Tokyo, 1985.

[2] B. F. Buxton, J. A. Eades, J. W. Steeds and G. M. Rackham: *Phil. Trans. R. Soc. London*, **281** (1976) 171.

[3] M. Terauchi and M. Tanaka: *J. Electron Microsc.*, **34** (1985) 347.

[4] M. Tanaka, M. Terauchi and T. Kaneyama: Convergent-Beam Electron Diffraction II, JEOL-Maruzen, Tokyo, 1988.

[5] M. Terauchi and M. Tanaka: *Acta Cryst.*, **A49** (1993) 722.

[6] M. Terauchi, M. Takahashi and M. Tanaka: *Acta Cryst.*, **A50** (1994) 566.

[7] K. Tsuda and M. Tanaka: *Acta Cryst.*, **A51** (1995) 7.

[8] M. Tanaka and K. Tsuda: Proc. 25th Meeting of Microbeam Analysis Soc., San Jose, 1991, p.145.

[9] M. Tanaka, M. Terauchi and T. Kaneyama: *J. Electron Microsc.*, **40** (1991) 211.

[10] M. Tanaka, R. Saito, K. Ueno and Y. Harada: *J. Electron Microsc.*, **29** (1980) 408.

[11] M. Tanaka, S. Yamada and M. Terauchi: 5th Asia-Pacific Electron Microscopy Conference, Electron Microscopy I, World Scientific (1992) 154.

[12] F. Niu, R. Wang and G. Lu: *Acta Cryst.*, **A47** (1991) 36.

[13] J. Wen, R. Wang and G. Lu: *Acta Cryst.*, **A45** (1989) 422.

[14] W. C. T. Dowell and P. Goodman: *Phil. Mag.*, **28** (1973) 471.

[15] J. C. H. Spence and J. M. Cowley: *Optik*, **50** (1978) 129.

[16] J. M. Cowley: *Ultramicroscopy*, **4** (1979) 435.

[17] J. A. Lin and J. M. Cowley: *Ultramicroscopy*, **19** (1986) 31.

[18] W. J. Vine, R. Vincent, P. Spellward and J. W. Steeds: *Ultramicroscopy*, **41** (1992) 423.

[19] J. W. Steeds, R. Vincent, W. J. Vine, P. Spellward and D. Cherns: Hitachi Instrument News, **24** (1992) 3.

[20] M. Terauchi, K. Tsuda, O. Kamimura, M. Tanaka, T. Kaneyama and T. Honda: *Ultramicroscopy*, **54** (1994) 268.

[21] K. Tsuda, M. Terauchi, M. Tanaka, T. Kaneyama and T. Honda: *J. Electron Microsc.*, **43** (1994) 173 .

[22] F. Nagata and A. Fukuhara: *Jpn. J. Appl. Phys.*, **6** (1967) 1233.

[23] J. W. Steeds, P. M. Jones, G. M. Rackham and M. D. Shannon: Developments in Electron Microscopy and Analysis, Academic Press, New York, 1976, p.351.

[24] J. C. H. Spence and J. M. Zuo: Electron Microdiffraction, Plenum Press, 1992.

[25] P. Goodman: International Tables for Crystallography, Kluwer Academic Publishers, 1993, Chap. 2.5.2, p.290.

[26] A. Eades: Electron Diffraction Techniques, Vol. 1, ed. J. M. Cowley, Oxford Univ. Press, 1992, Chap. 7.

[27] A. G. Jackson: Handbook of Crystallography, Springer Verlag, 1991, Chap. 10.

[28] M. Tanaka: *Acta Cryst.*, **A50** (1994) 261.

Abbreviations of Technical Terms

CBED	Convergent-Beam Electron Diffraction
ZAP	Zone-Axis Pattern
WP	Whole Pattern
BP	Bright-Field Pattern
DP	Dark-Field Pattern
±DP	±G Dark-Field Pattern
ZOLZ	Zeroth Order Laue-Zone
H(F, S)OLZ	Higher (First, Second) Order Laue-Zone
GM Line	Gjønnes-Moodie Line = Dynamical Extinction Line
LACBED Pattern	Large-Angle CBED Pattern
SMB Pattern	Symmetrical Many-Beam Pattern
SA-CBED Pattern	Selected-Area CBED Pattern
CTEM	Conventional Transmission Electron Microscopy
STEM	Scanning Transmission Electron Microscopy
HREM	High-Resolution Electron Microscopy
SAMAG Mode	Selected Area Magnification Mode
SADIFF Mode	Selected Area Diffraction Mode
BF Image	Bright-Field Image
DF Image	Dark-Field Image
FEG	Field Emission Gun
CL	Condenser Lens
OL	Objective Lens
IL	Intermediate Lens
IP	Imaging Plate
SSCCD	Slow Scan Charge-Coupled Device
WS	Work Station
MEM	Maximum-Entropy Method
FWHM	Full Width at Half Maximum
CTB	Coherent Twin Boundary

Symmetry Determination

Low Accelerating Voltages

When the accelerating voltage is lowered, the probe current on a specimen decreases because the potential at the first accelerator in the accelerating tube lowers. In the normal use of a JEM-2010 microscope, electrons emitted from an LaB_6 cathode are accelerated serially by six accelerators, which are each supplied with a potential of one-sixth the total accelerating voltage. It is a question how to obtain a sufficient probe current on a specimen for the observation of CBED patterns at lower accelerating voltages.

In our microscope, two-stage acceleration is possible instead of usual six-stage acceleration when it is used at accelerating voltages below 50kV. That is, the potentials of the second and subsequent accelerators are set at the anode (ground) potential; electrons are accelerated at the first stage by a potential of half the total accelerating voltage. This technique allows easy observation of CBED patterns at lower accelerating voltages.

When the accelerating voltage is lowered, the background due to inelastically scattered electrons becomes serious. Use of the selected area (SA) aperture can eliminate inelastically scattered electrons to high angles. We have succeeded in taking CBED patterns of graphite at 8kV, which is the lowest accelerating voltage employed to date. It appears that CBED patterns can be obtained even at accelerating voltages lower than 8kV with our JEM-2010.

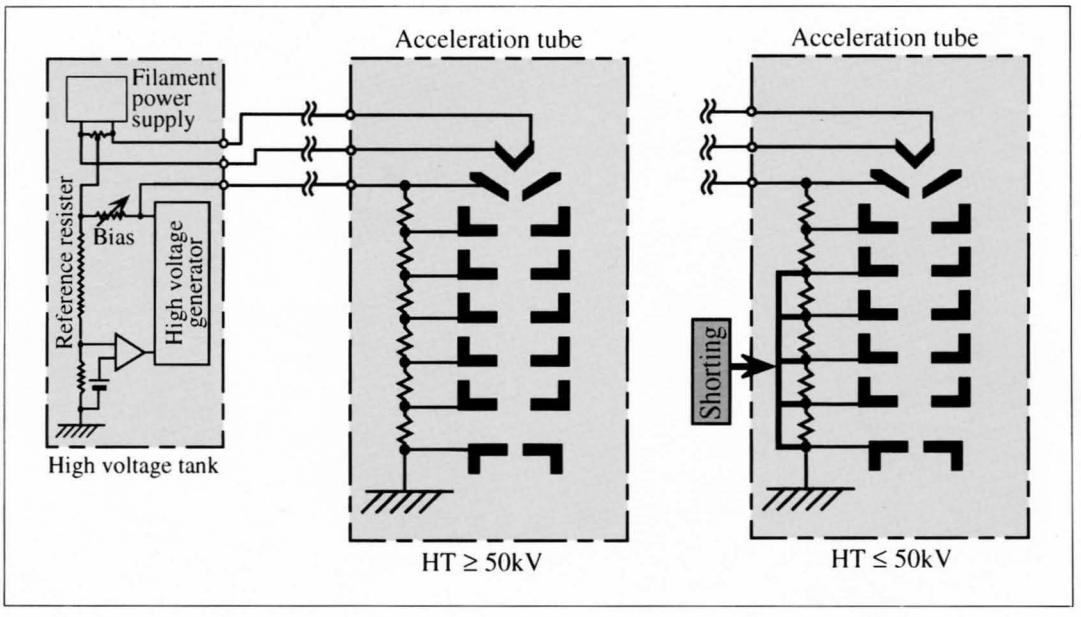

Graphite [0001]

20kV

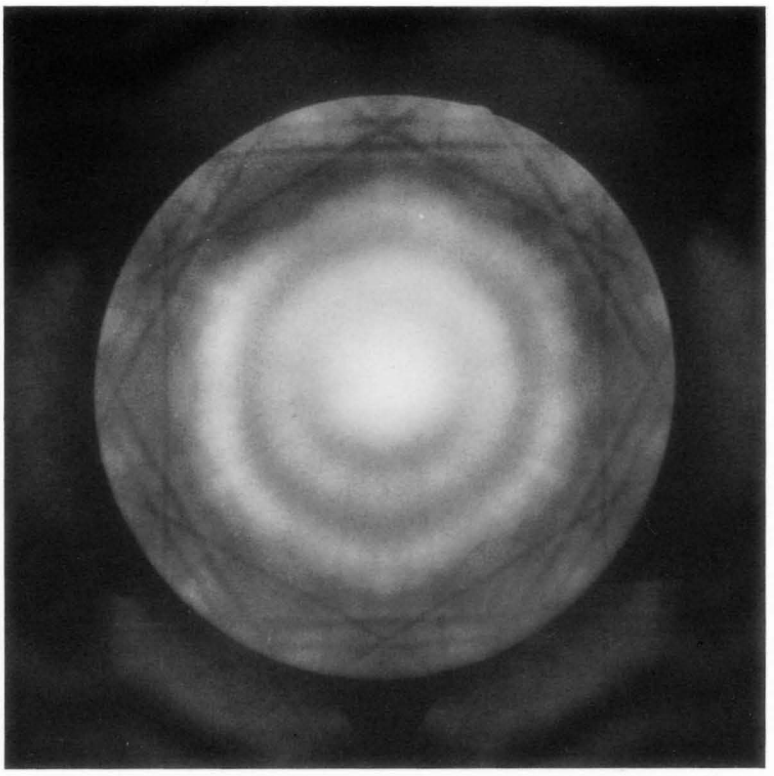

15kV

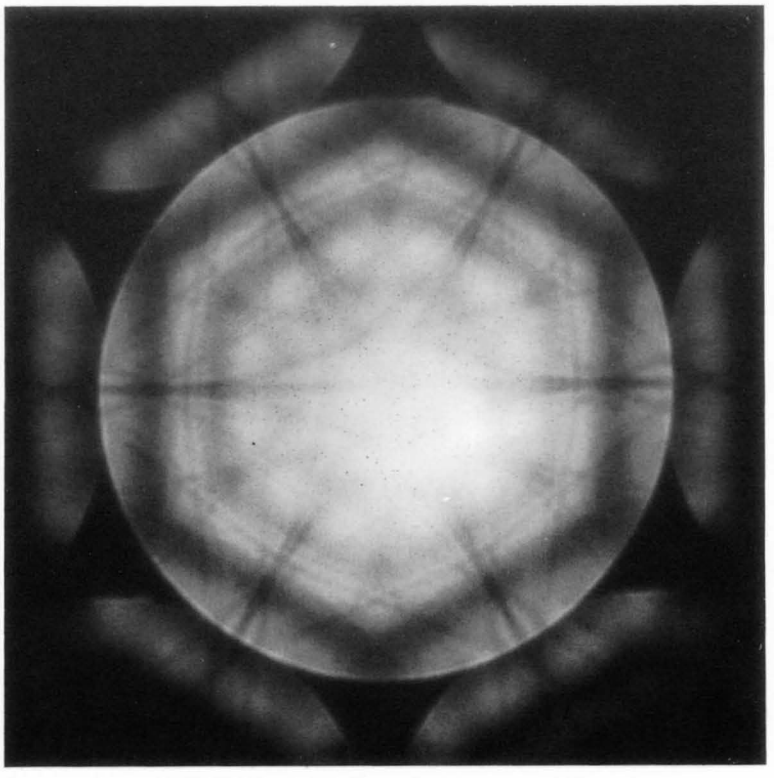

Graphite [0001]

10kV

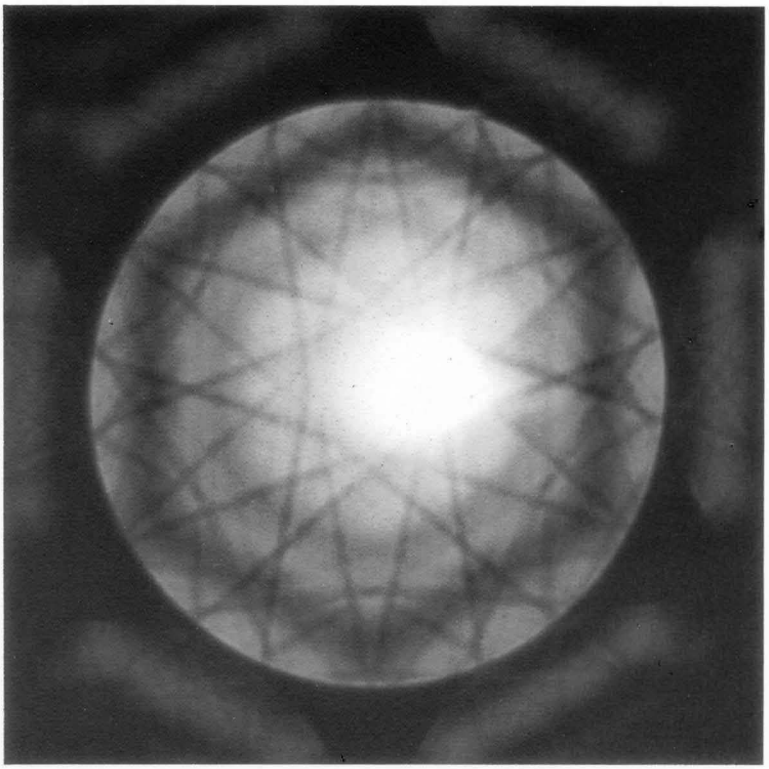

8kV

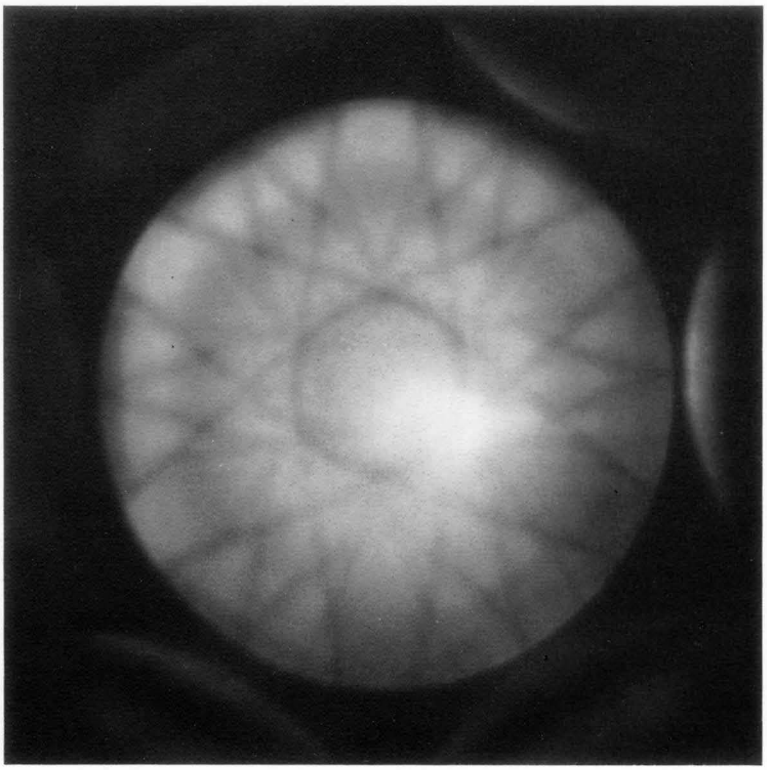

Fourfold Rotoinversion

A perfect crystalline specimen, which is parallel sided and extended infinitely in two dimensions, has ten point-group symmetry elements, *viz.*, one-, two-, three-, four- and six-fold rotation axes and a mirror plane, which are perpendicular to the specimen surface; an inversion center; a twofold rotation axis and a mirror plane, which are parallel to the surface; and a fourfold rotoinversion or $\bar{4}$-axis perpendicular to the surface. The symmetries of CBED patterns caused by the last four elements can be understood with the help of the reciprocity theorem. The CBED symmetry of the last symmetry element or the $\bar{4}$-axis is exhibited in three ways [a].

The symmetry element or the $\bar{4}$-axis is illustrated in Fig. (a). It is noted that the $\bar{4}$-axis contains a twofold rotation axis. The symmetry of a CBED pattern due to the axis is illustrated in Fig. (b). The cross at the center is the direction of the $\bar{4}$-axis. The four larger circles show the reflection disks in four different CBED patterns taken at the Bragg settings for the reflections. The center of each disk corresponds to the exact Bragg position of each reflection. The smaller circles in the disks are the marks to express the symmetry of the pattern. This symmetry is called 4_R. The operation 4_R is a combination of a rotation $2\pi/4$ of a smaller circle about the zone axis (+) and a rotation π about the exact Bragg position. A set of four reflection patterns can not be taken simultaneously with one exposure but with four exposures by the excitation of respective Bragg reflections. Hence, this pattern symmetry has not been used for the detection of the $\bar{4}$-axis because of experimental inconvenience.

1) A clever way of detecting the $\bar{4}$-axis is to use a zone-axis pattern taken at an electron incidence parallel to the $\bar{4}$-axis. The pattern of a bright-field (BF) disk shows a fourfold rotation symmetry, which is created by displacing the four diffraction disks in Fig. (b) onto the zone axis or the BF disk. The whole pattern, which is composed of the BF pattern and reflection patterns surrounding the BF disk, shows a twofold rotation symmetry because the $\bar{4}$-axis contains a twofold rotation axis. It should be noted that the twofold rotation symmetry does not appear until three-dimensional interaction takes place or higher-order Laue-zone reflections appear.

2) When we apply the symmetrical many-beam (SMB) method [b], symmetry 4_R can be observed in one CBED pattern, though the pattern obtained is a half of the pattern of Fig. (b). That is, Fig. (c) schematically shows the CBED symmetry due to the $\bar{4}$-axis appearing in a simultaneously excited four-beam pattern, which is obtained by tilting the incident beam from the zone axis to $\boldsymbol{g}/2$, $\boldsymbol{g}$ being the diffraction vector of reflection G. Thus, the centers of the DF disks G, F and F' are set at the exact Bragg positions. Between the two DF disks F and F' is seen the symmetry 4_R, which corresponds to a half of the pattern of Fig. (b).

3) When the technique invented by Terauchi and Tanaka [3], which is a kind of an LACBED technique, is applied to the $\bar{4}$-axis, the symmetry 4_R of Fig. (b) can be obtained on one film with one exposure. We demonstrate the CBED symmetry 4_R due to the $\bar{4}$-axis for ZnTe and GaAs, which belong to the space group $F\bar{4}3m$.

References

[a] M. Tanaka, M. Terauchi and F. Sato: *Ultramicroscopy*, **55** (1994) 241.

[b] M. Tanaka, R. Saito and H. Sekii: *Acta Cryst.*, **A39** (1983) 357.

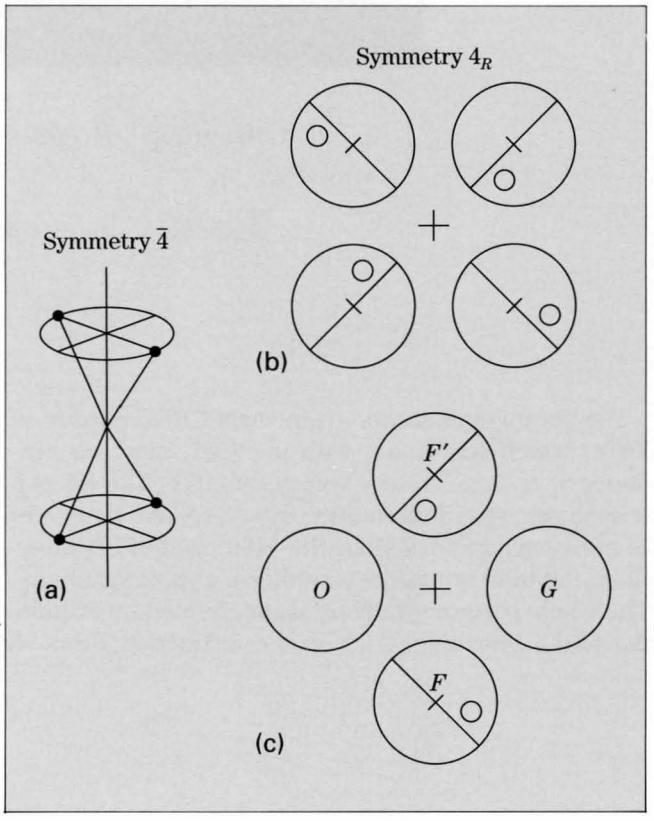

ZnTe

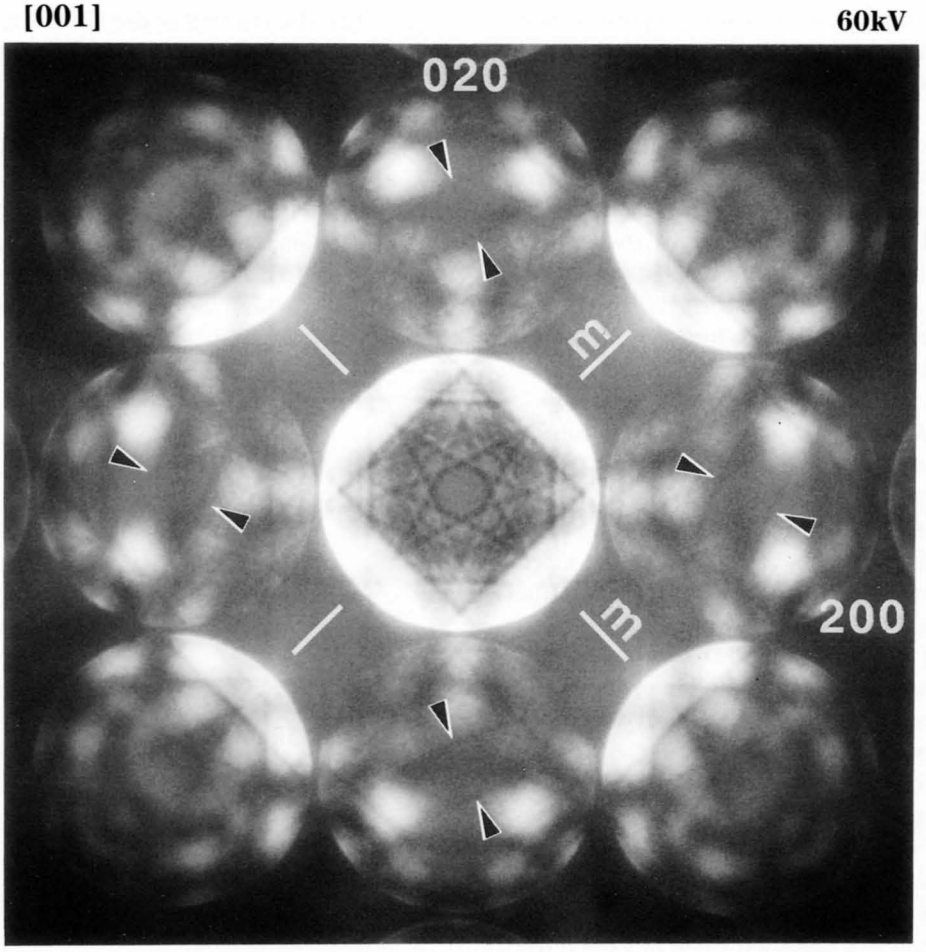

Diff. group	Bright-field pattern	Whole pattern
4_R	4	2
$4_R mm_R$	$4mm$	$2mm$

The photograph shows a zone-axis CBED pattern of ZnTe, which was taken with the [001] electron incidence at an accelerating voltage of 60kV. The BF pattern shows a fourfold rotation symmetry and two types of mirror symmetries along the <100> and <110> directions, the total symmetry resulting in a $4mm$ symmetry. The whole pattern symmetry is determined by examining HOLZ lines appearing in the diffraction disks. A close inspection reveals that the defect HOLZ lines in the 200 and equivalent disks, which are indicated by the arrowheads, form a $2mm$ symmetry. That the BF pattern has a fourfold rotation symmetry and the whole pattern a twofold rotation symmetry ascertains the existence of the $\bar{4}$-axis or the fourfold rotoinversion in ZnTe.

67kV

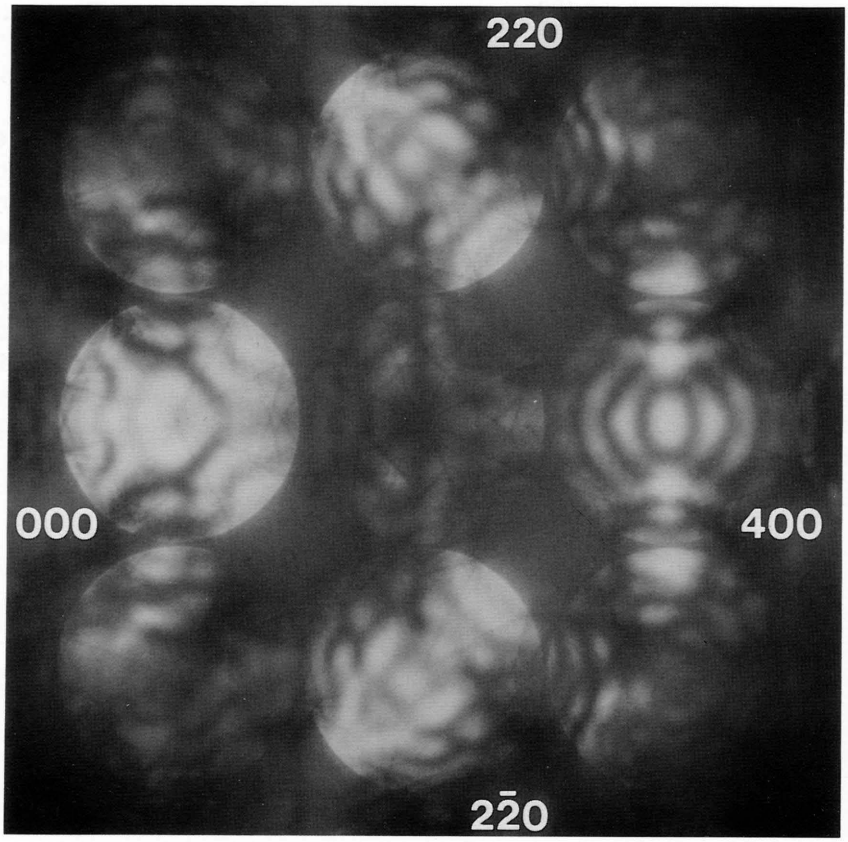

Diff. group	Dark-field pattern
4_R	4_R
$4_R mm_R$	4_R, $4_R m_v$

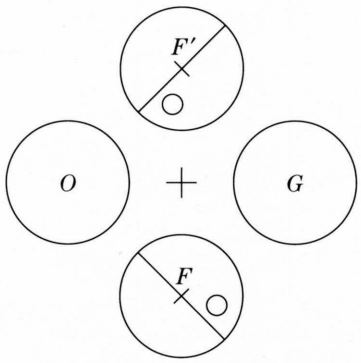

The photograph shows an SMB-CBED pattern of ZnTe, which was taken by exactly exciting the 220, 2$\bar{2}$0 and 400 reflections at an accelerating voltage of 67kV. The accelerating voltage was chosen so that the HOLZ lines are clearly seen in the DF disks. A 4_R symmetry is seen between the 220 and 2$\bar{2}$0 disks, showing the existence of a $\bar{4}$-axis. An m_2 symmetry [1] appears to exist in each of the two disks, and $4_R m_2$ symmetry, which does not exist theoretically, looks to exist between the two. It should be noted that the m_2 symmetry is a spurious symmetry described in the reference [4].

The method of Terauchi and Tanaka [3], [4] can take a CBED pattern from a specimen area about 100 nm in diameter with exact Bragg positions simultaneously kept at the centers of all DF disks.

The figure illustrates the ray diagram of the method. The incident-beam angle is made larger than that in the ordinary CBED method by removing the condenser aperture from the optical axis. The selector aperture is inserted in the optical axis. The excitation of the objective lens is increased so that the crossover point of the incident beam is imaged above the selector aperture. As a result, the back focal plane moves from plane A to a plane written as Diff. plane, but the two planes are so close to each other that they need not be distinguished. The intermediate lens remains focused on plane A. The specimen position is shifted from S to S′ with a specimen height control so that the exactly Bragg reflected beam crosses the optical axis at the selector aperture. The dotted line in the diffracted beam shows the direction of the exact Bragg angle. This implies that the exact Bragg position can be brought to the center of each diffraction disk.

The maximum nonoverlapping disk size on plane A is limited to the Bragg angle of the lowest-order reflection or one-half the angle obtained by the ordinary CBED method. Larger angular spreads can be obtained when CBED patterns are taken at a plane B. A disk size almost twice that at plane A is obtained. The selector aperture normally selects a specimen area, but in the present method, it selects both the illuminated specimen-area size and the angular size of the incident beam because a defocused image is formed on the selector aperture.

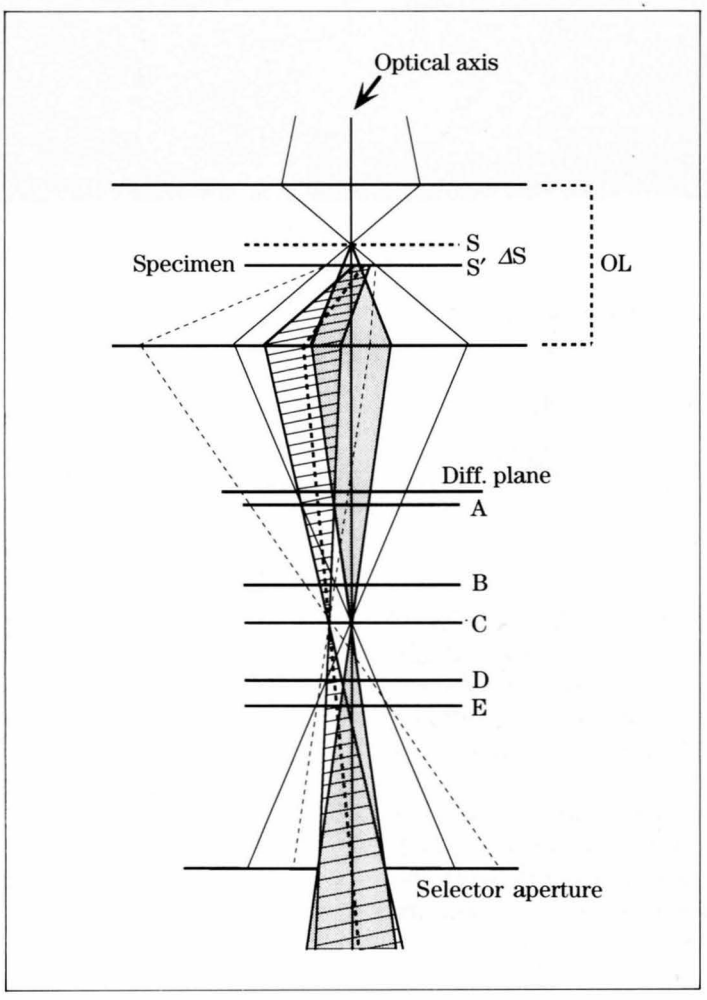

ZnTe [001] 60kV

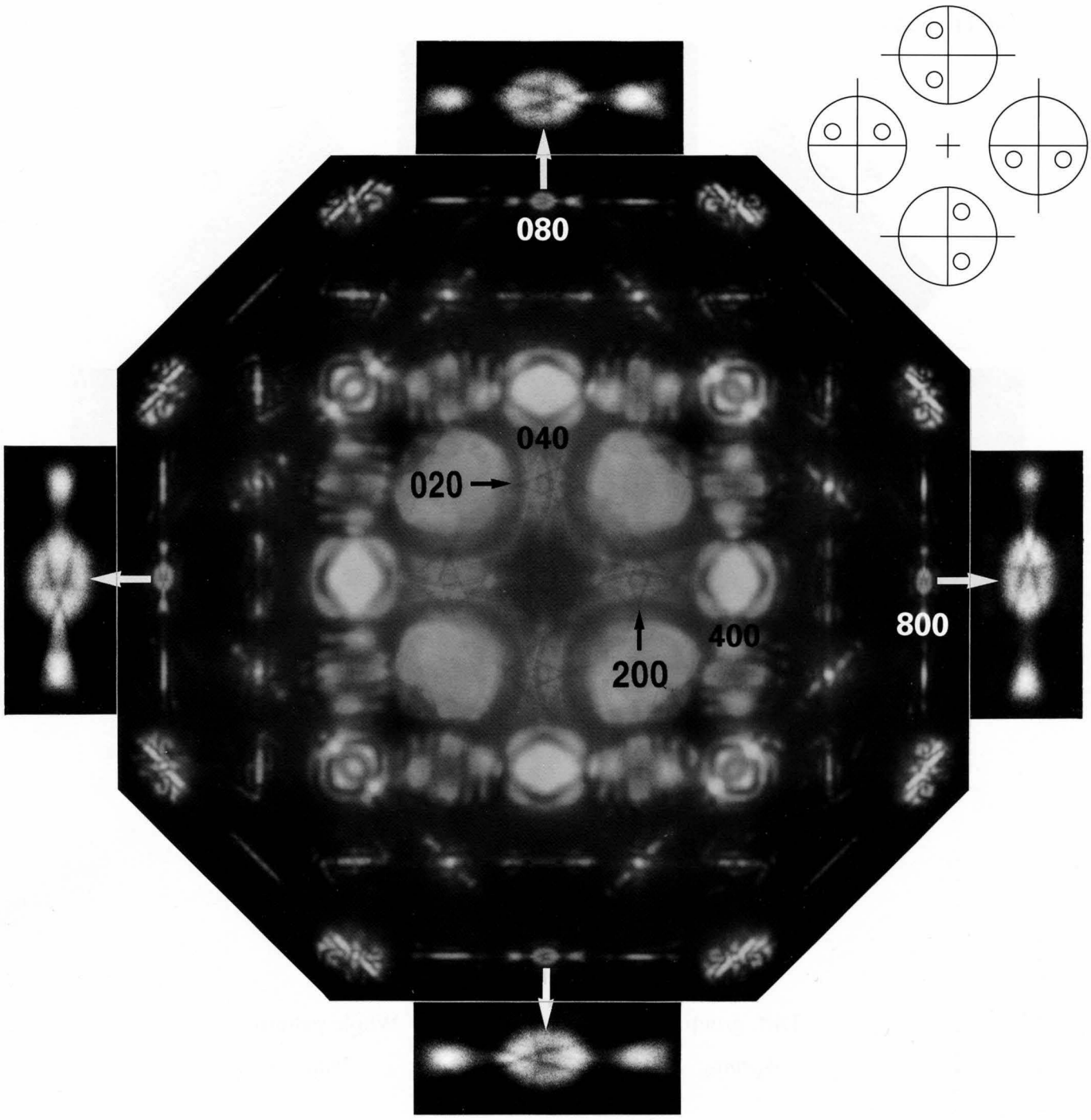

The photograph shows a CBED pattern taken with the [001] electron incidence at 60kV using the technique of Terauchi and Tanaka [3], by which the centers of all the diffraction disks are brought to the respective Bragg positions. The 200 and 800 reflections and their equivalents clearly show an m_2 symmetry [1] due to a horizontal twofold rotation axis parallel to the <100> axis. It is seen that the defect HOLZ lines shaped like scissors form a 4_R symmetry between the 800 and equivalent reflections, though the m_2 symmetry is superposed on it. The resultant symmetry is schematically shown in the figure. This symmetry is also seen for the curved doublet of HOLZ lines appearing between the 200 and equivalent reflections. The photograph provides a complete observation of the 4_R symmetry of Fig. (b) on page 15.

GaAs

[001] 60kV

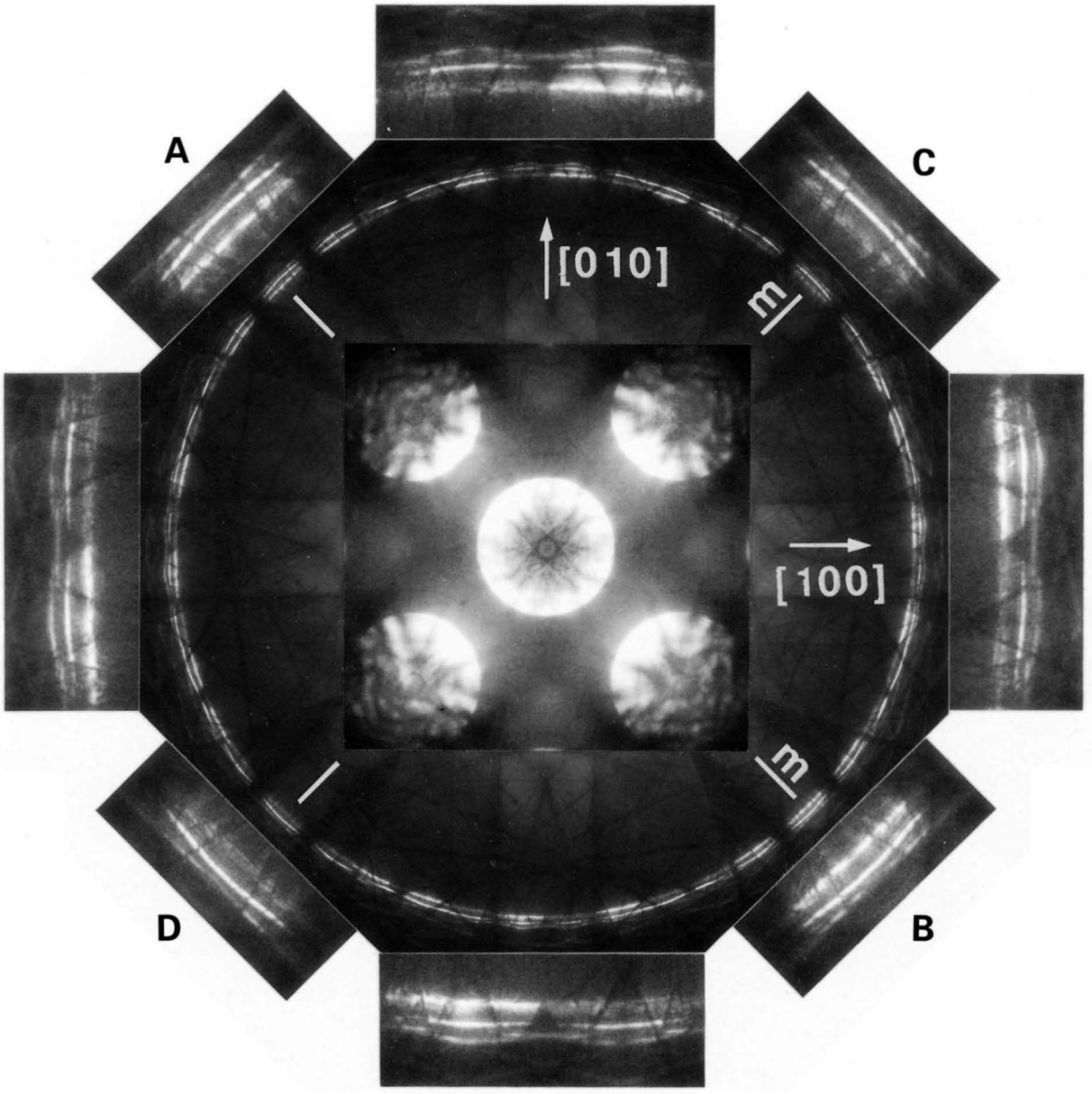

Diff. group	Bright-field pattern	Whole pattern
$4_R mm_R$	$4mm$	$2mm$

The photograph shows a [001] zone-axis CBED pattern of GaAs taken at an accelerating voltage of 60kV. The BF pattern shows a $4mm$ symmetry. The innermost intensity lines of two HOLZ reflections, A and B, have stronger intensities than those in the reflections C and D. Hence, the HOLZ reflections form a twofold rotation symmetry. This result shows the existence of a $\bar{4}$-axis in GaAs though two mirror symmetries about the <110> directions are added, the whole pattern symmetry being $2mm$. Another set of four insets in the [100] and [010] directions also shows a $2mm$ symmetry clearly. The selective observation of only symmetry 4_R is possible when the 420 and its equivalent reflections are used.

[001] **60kV**

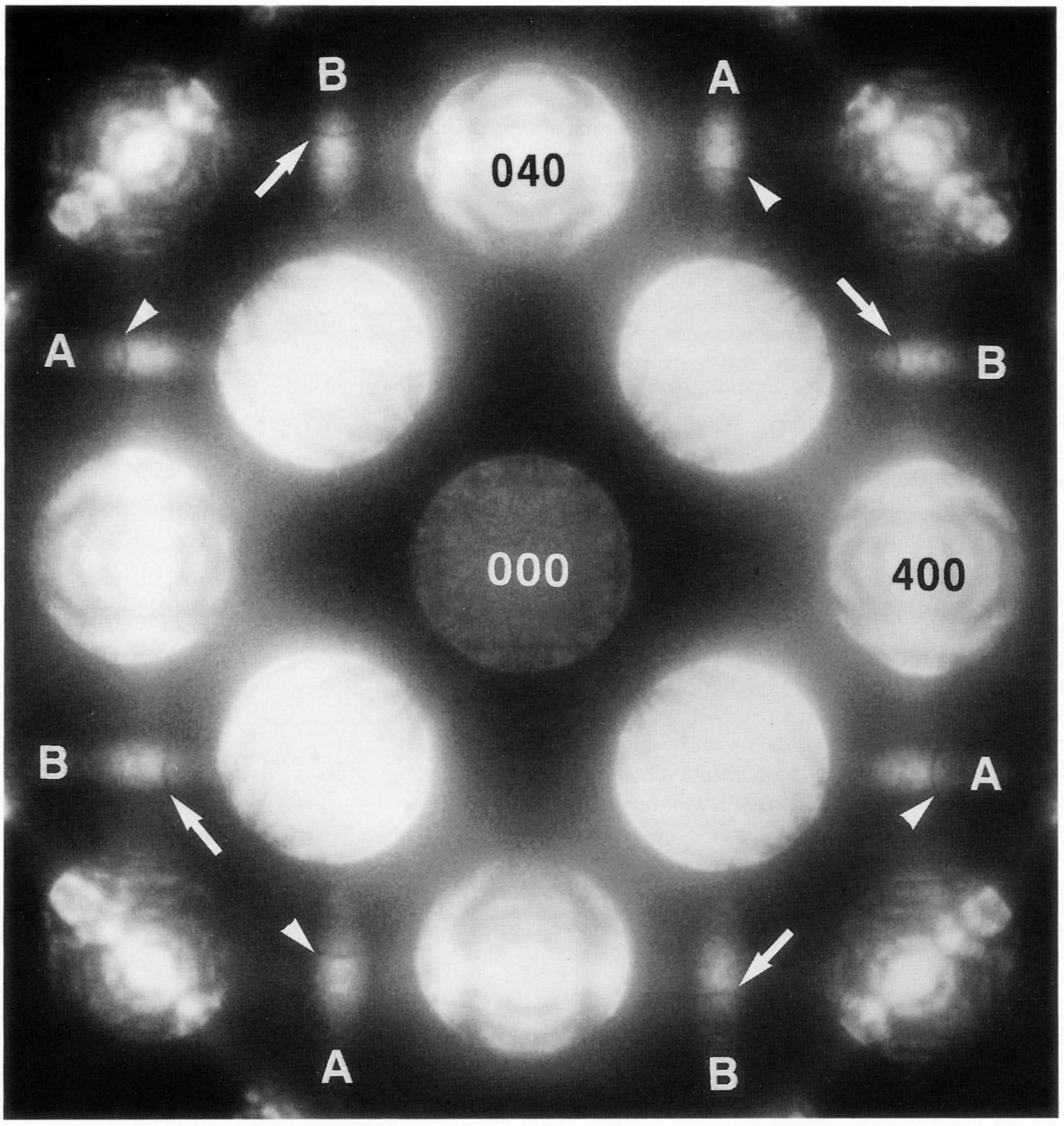

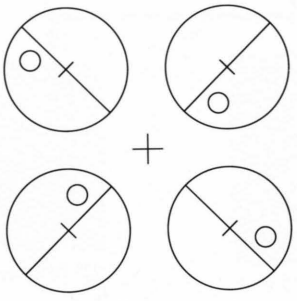

The photograph shows a CBED pattern taken with the [001] electron incidence at 60kV by the technique of Terauchi and Tanaka [3]. Two sets of 420 reflections, A and B, each consisting of four reflections, contain a fine defect line originating from HOLZ reflections. The defect lines in each set form a 4_R symmetry without the superposition of other symmetries.

Image Processing

CBED patterns have a wide dynamic range of intensities. When traditional films are used for recording them, their weak-intensity parts are below the level of background noise and strong-intensity parts exceed the saturation level of the film. The imaging plate (IP) has high sensitivity, wide dynamic range and linear response to the dose of incident electrons. Since recorded images on IPs are read out by a laser beam as digital data, image processing is easily carried out using a computer.

When CBED patterns are taken from a thick region, background intensity is high due to inelastically scattered electrons. The background intensity can be easily subtracted in a computer when the patterns are recorded on an IP. Therefore, clear symmetries can be recovered from a smeared pattern. When a pattern recorded on an IP is processed by a comb-shape function, then both weak- and strong-intensity parts are brought to a similar grayscale level. CBED patterns taken from thin specimen areas have a monotonic intensity distribution and do not show a clear symmetry. When such patterns are processed by a comb-shape function, the intensity difference can be enhanced and hidden symmetries are revealed. A high pass filter was applied to subtract a pattern formed by ZOLZ reflections and to elucidate HOLZ lines.

Symmetries of actual CBED patterns were quantitatively investigated by examining the difference between symmetry-related parts in the patterns. It is interesting to know the magnitude of the deviation from a perfect symmetry, which is negligible in the examination with the naked eye. The use of the imaging plate followed by image processing is effective in observing the symmetries of CBED patterns and examining CBED patterns quantitatively.

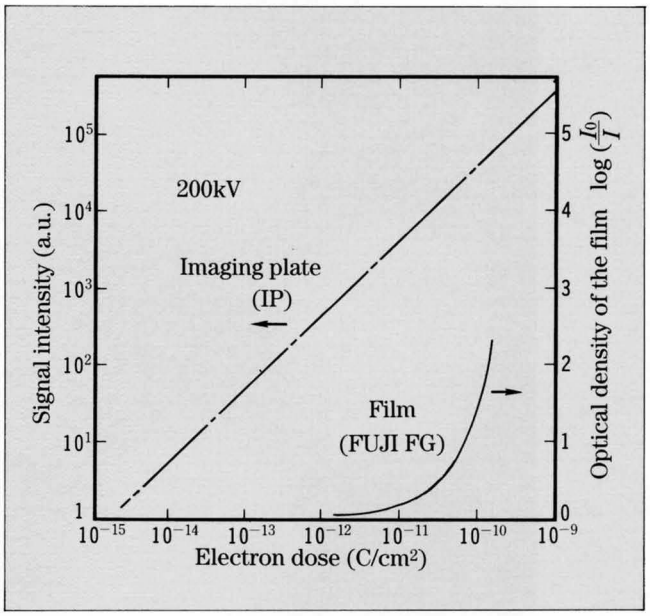

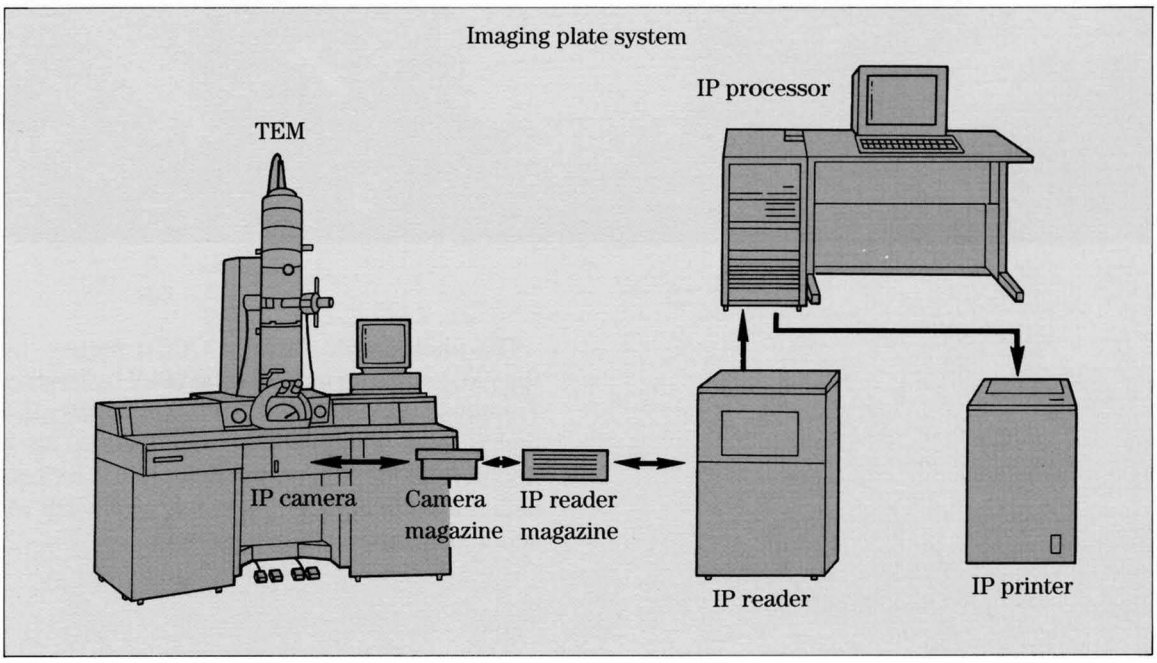

Subtraction of background

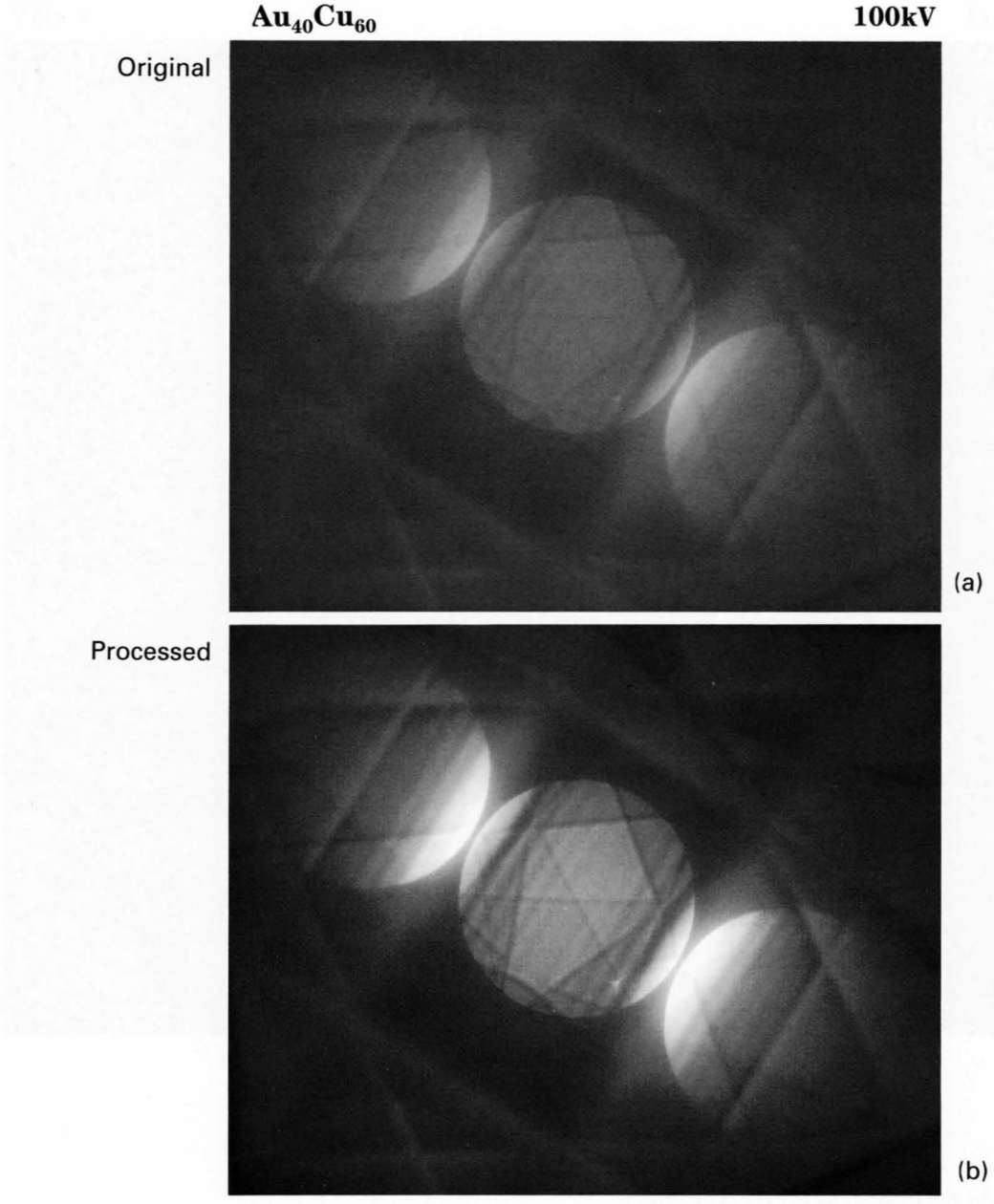

Photograph (a) shows an original CBED pattern recorded on an IP from a thick specimen area of $Au_{40}Cu_{60}$. Photograph (b) is a processed pattern, in which background intensity is subtracted by a processing function as shown in the attached figure.

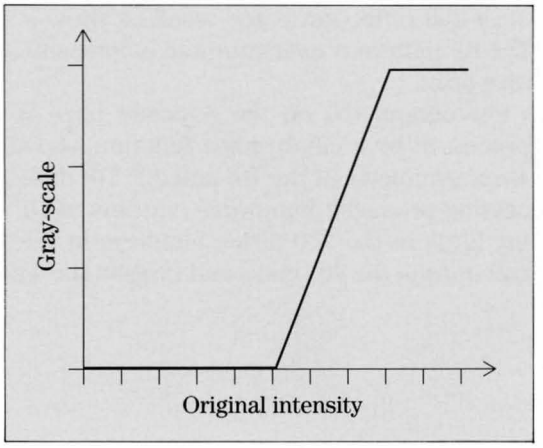

Comb-shaped filter

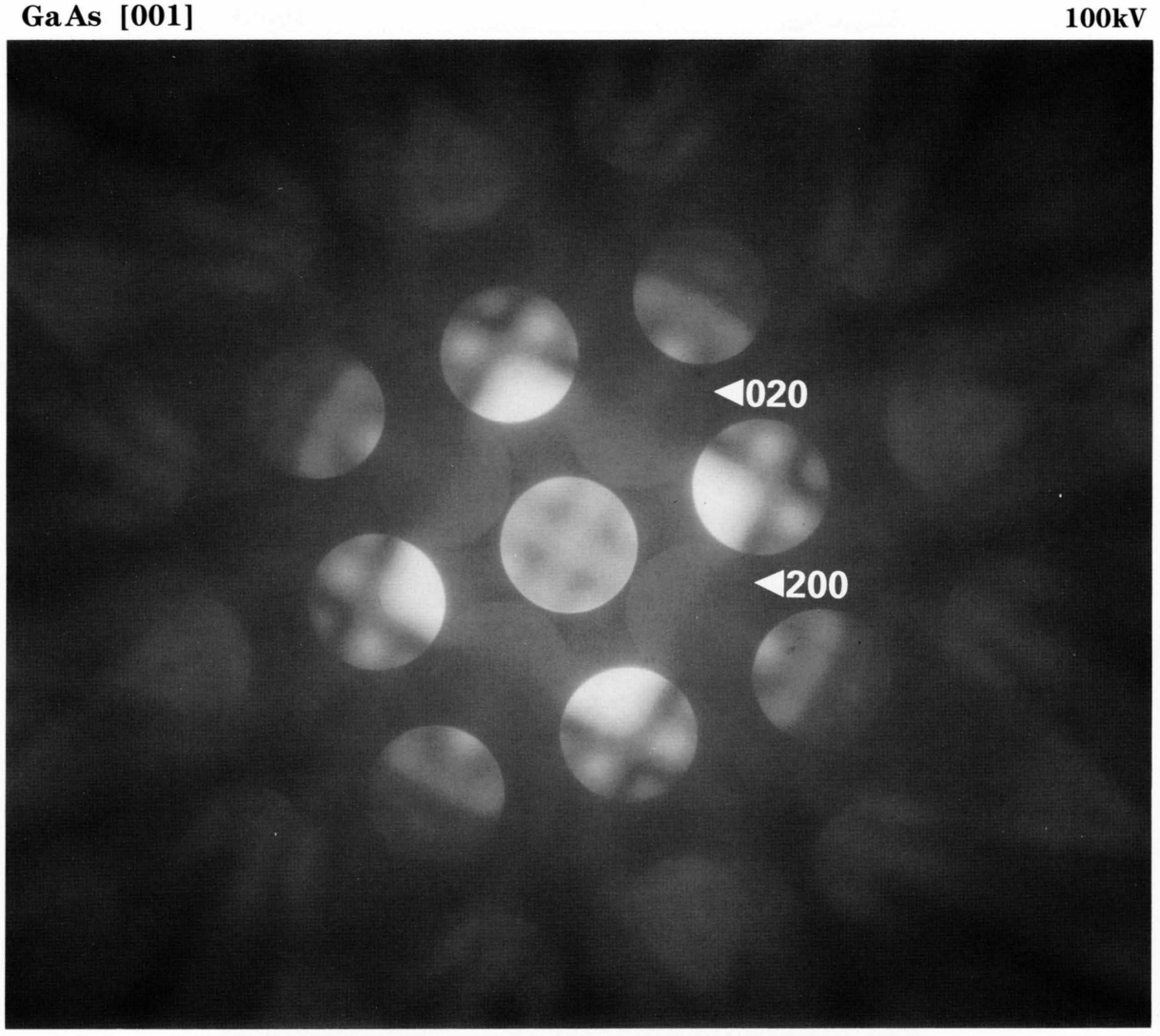

(a)

Photograph (a) shows a positive print of an original CBED pattern of GaAs recorded on an IP. The innermost 200 reflection is too weak to show a symmetry. The BF pattern is oversaturated in intensity on the positive print.

Photograph (b) on the opposite page is a pattern processed by a comb-shape function, showing a clear $4mm$ symmetry in the BF and 200 DF disks. This processing produced humorous patterns in DF disks: flying birds in the 200 disks, monkeys in the 220 disks, raccoons in the 400 disks and frogs in the 440 disks.

100kV

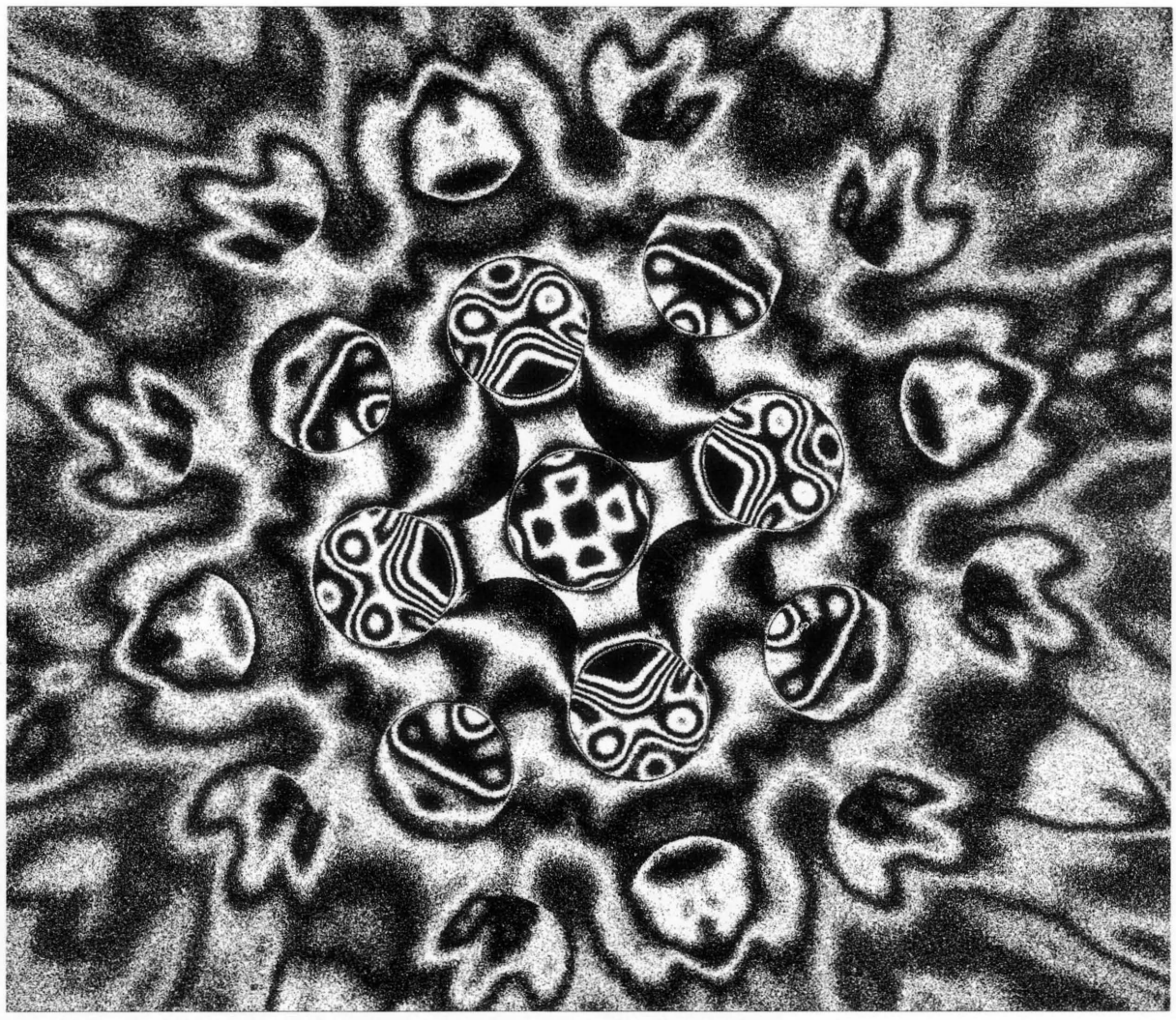

(b)

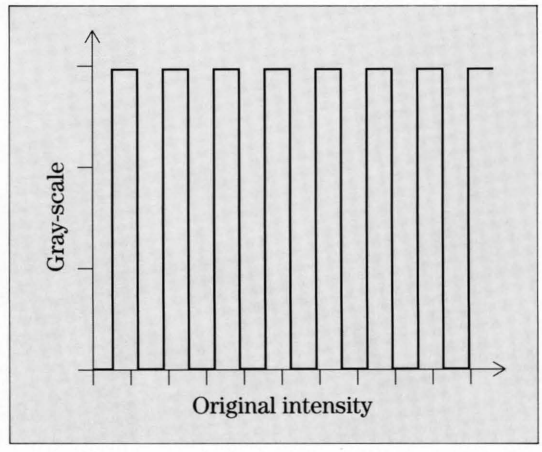

Nd_2CuO_4 [001] **100kV**

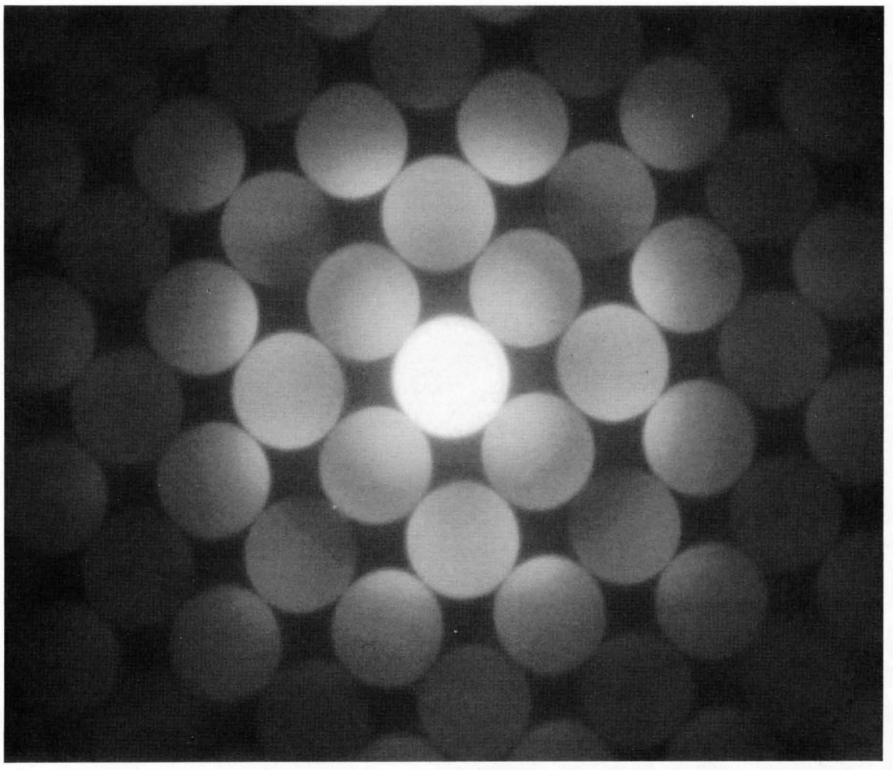

(a) Original

Pattern (a) is a positive print of an original CBED pattern of Nd_2CuO_4 recorded on an IP. Because of small specimen thickness, the intensity distribution shows monotonic changes over the entire area of each disk. Image processing by a comb-shape function elucidates a hidden symmetry $4mm$ (Pattern (b)).

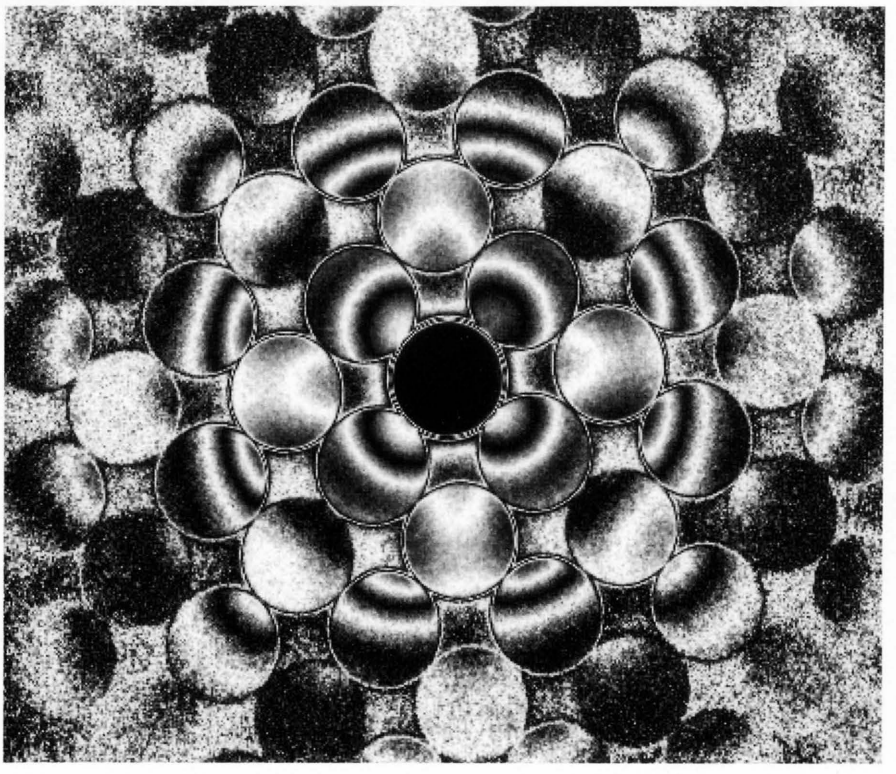

(b) Processed

Photograph (a) is an original CBED pattern of FeS_2 recorded on an IP, showing GM lines in the $00l$ (l=odd) reflections. Intensities are oversaturated in strong reflections on the positive print. A mirror symmetry is clearly seen in a processed pattern, Photo (b).

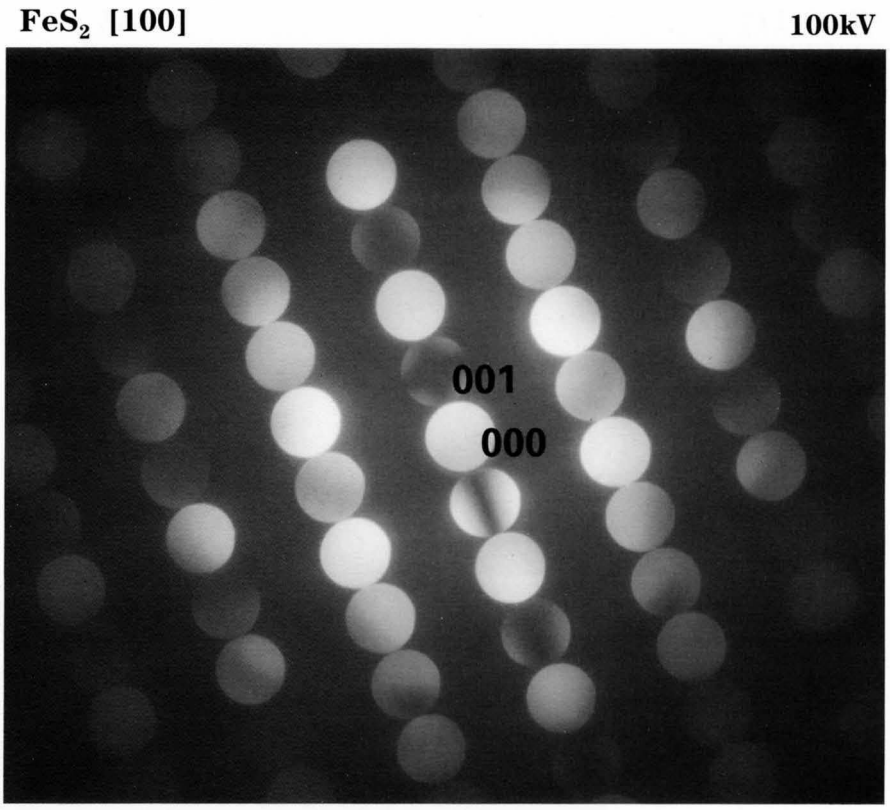

(a) Original

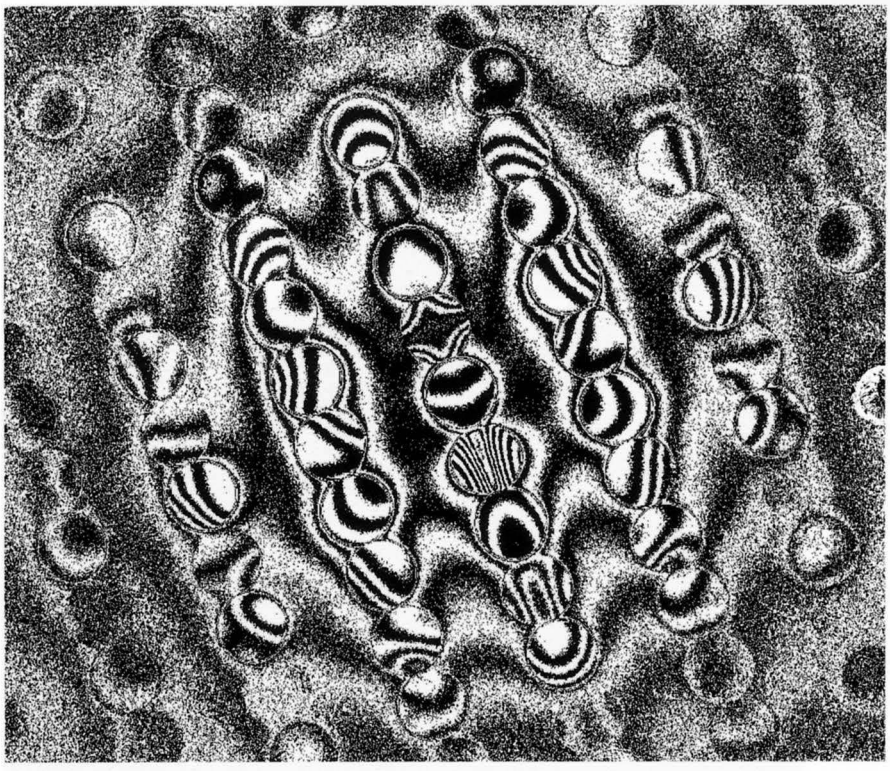

(b) Processed

Si [111] **100kV**

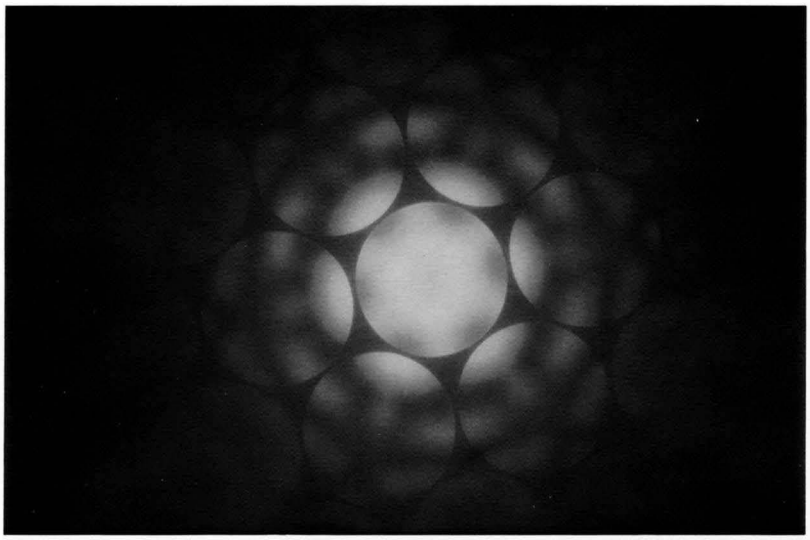

(a) Thin

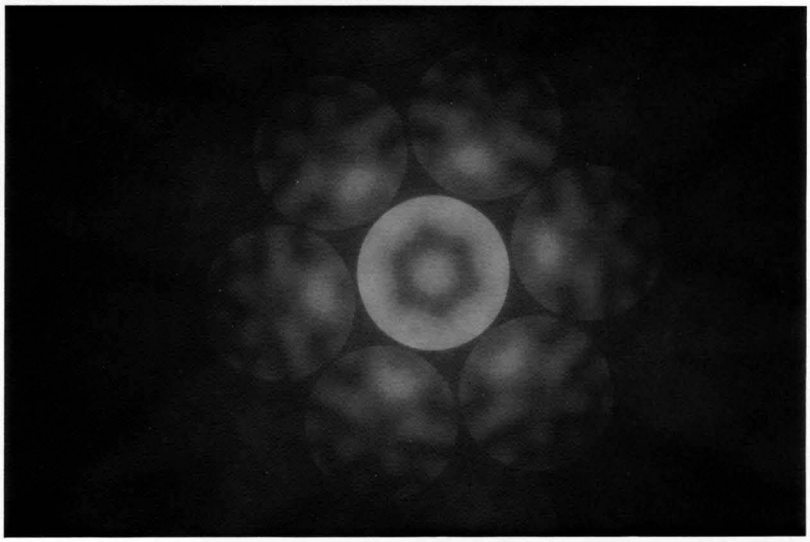

(b) Medium

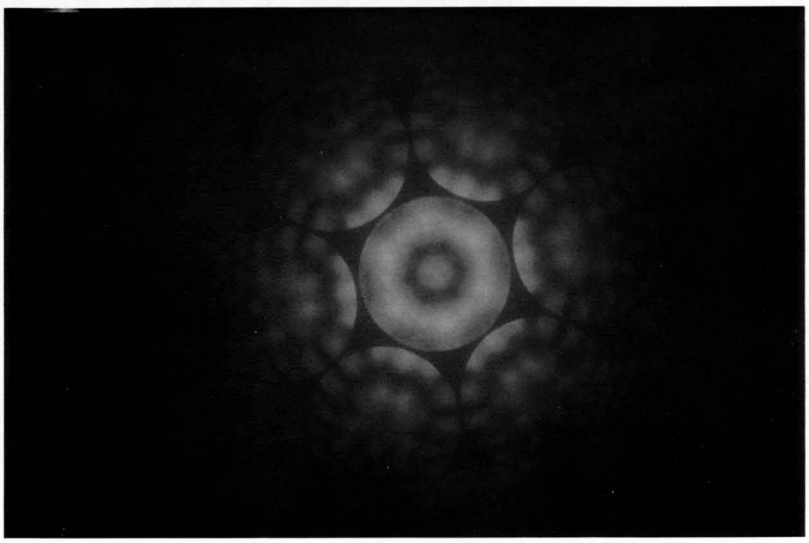

(c) Thick

The effect of image processing using a comb-shape function is demonstrated for three patterns with different specimen thicknesses, in Photos (a) to (f).

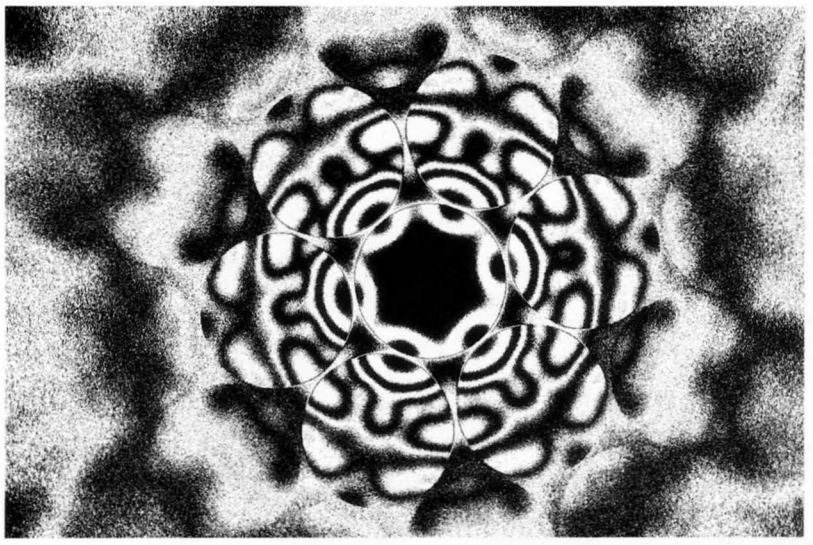

(d) Thin

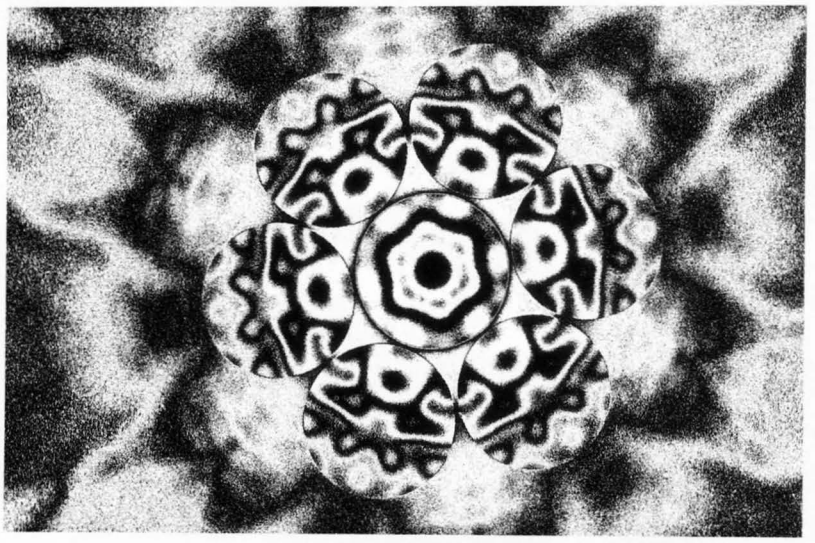

(e) Medium

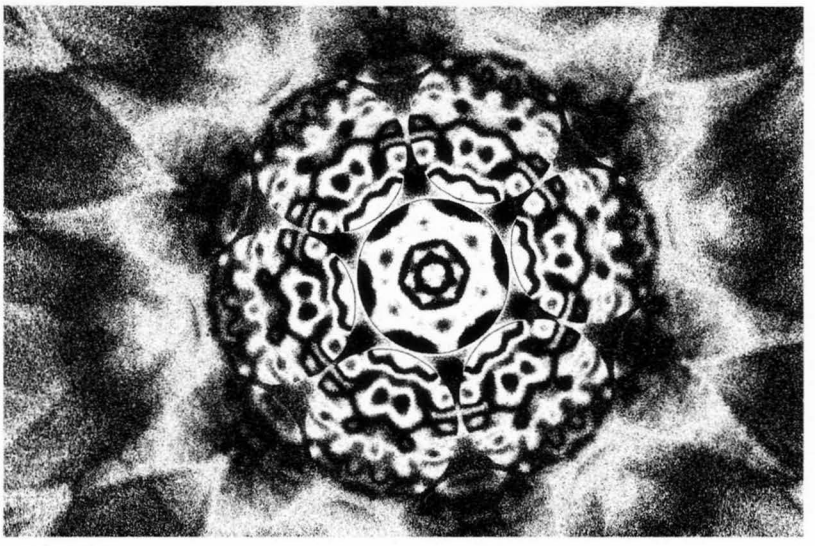

(f) Thick

Si [111] **100kV**

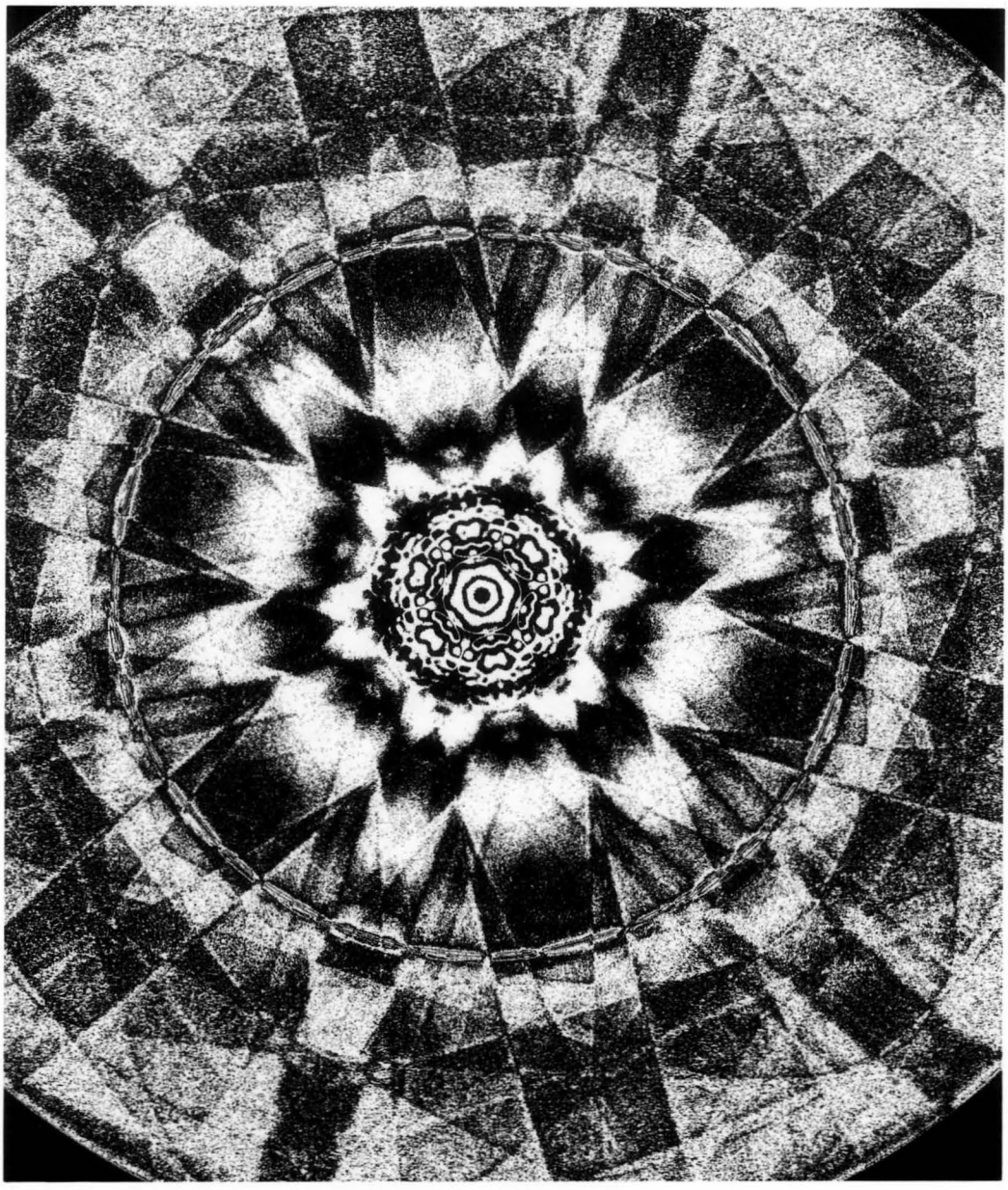

Image-processed CBED pattern of [111] Si by a comb-shape function.

TiO_2 [001] 100kV

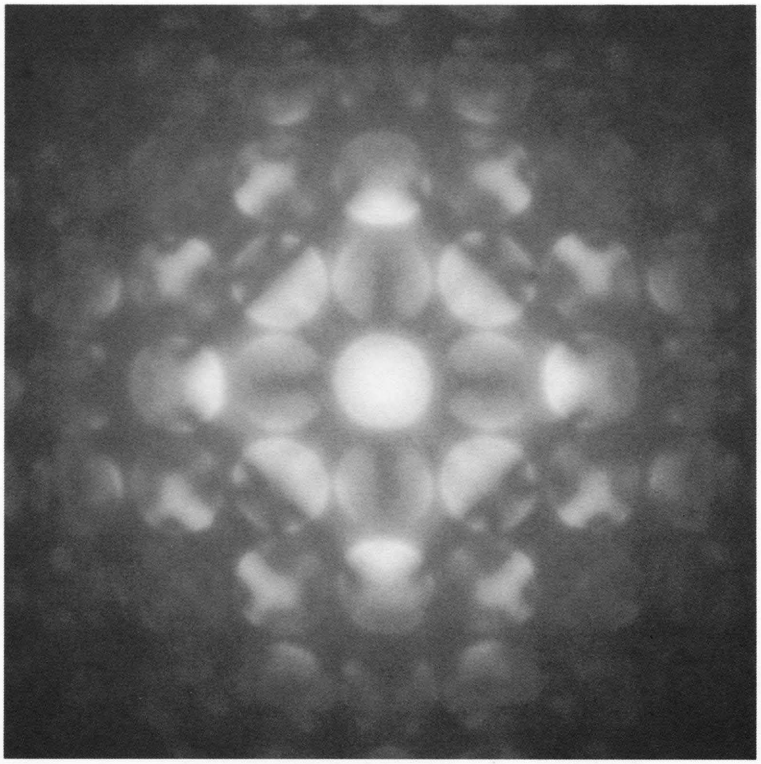

Original

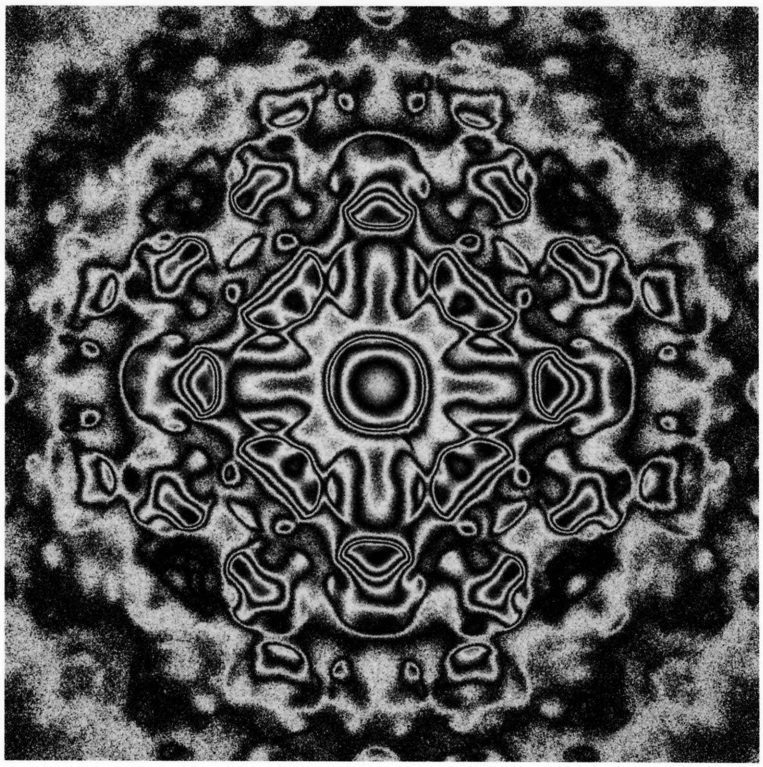

Processed

Graphite [0001] **100kV**

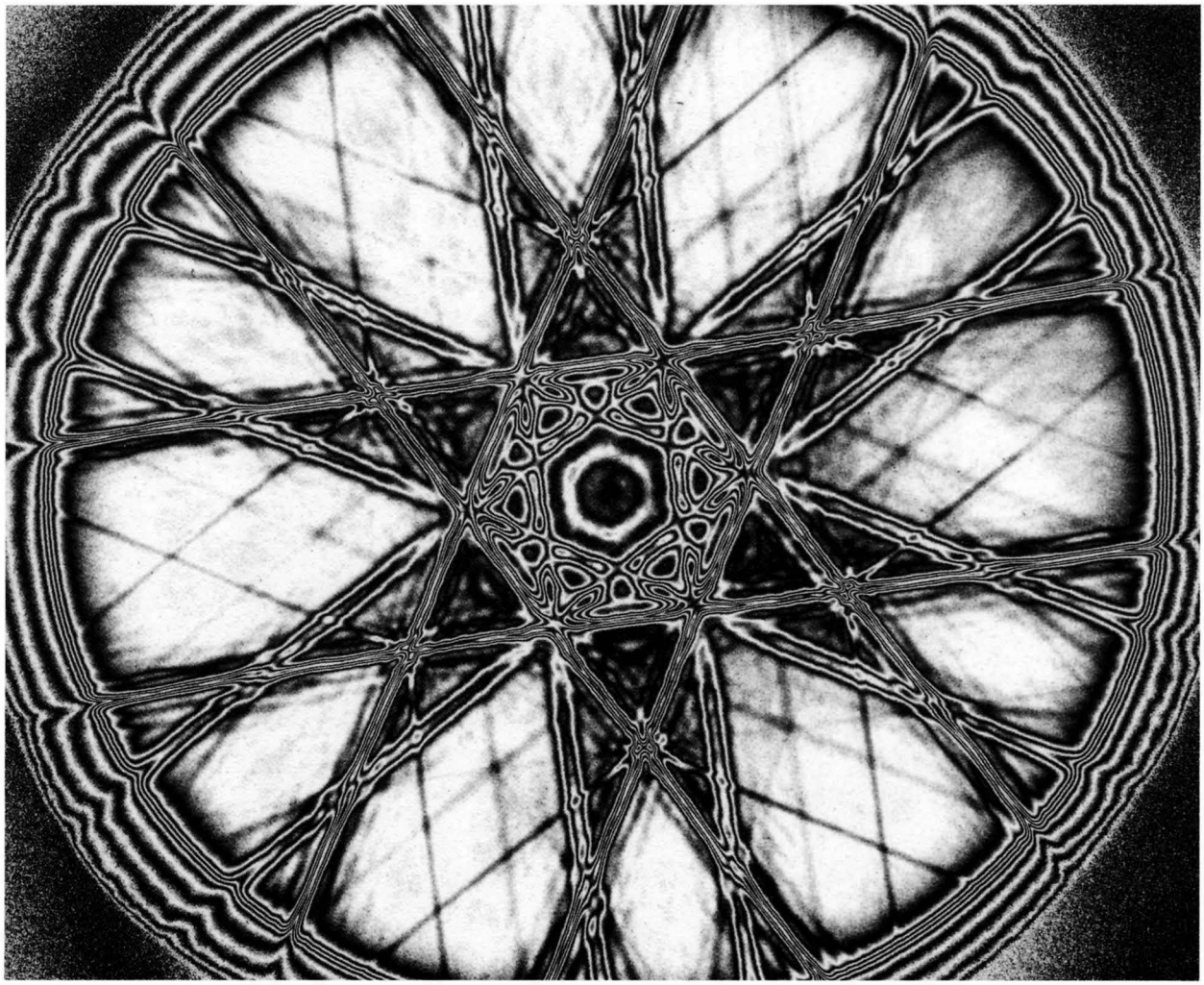

Image-processed LACBED pattern of graphite.

High-pass filtering

In a previous volume [1], analogue signal processing using a band-pass filter was applied to elucidating fine details of CBED patterns. In the following pages, examples of digital processing using a high-pass filter are shown. ZOLZ interaction produces broad or low-frequency CBED patterns but HOLZ reflections usually form fine lines. When a high-pass filter is applied to the patterns, broad ZOLZ patterns are removed but fine HOLZ lines remain. HOLZ lines are thus clearly seen without strong ZOLZ intensities though high-frequency components included in the ZOLZ pattern still remain.

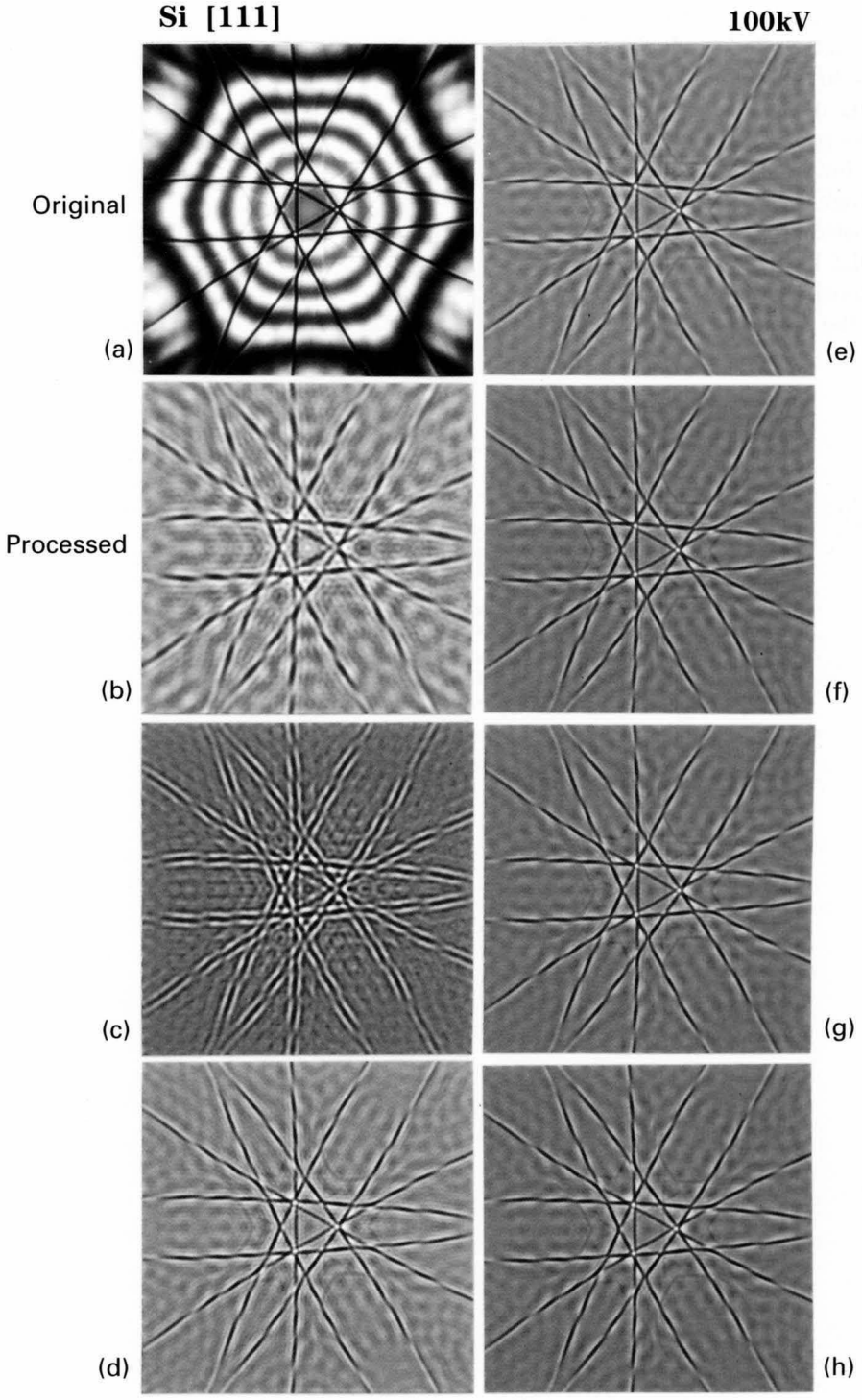

A series of zone-axis BF patterns of [111] Si. Photograph (a) is the original simulated pattern, exhibiting ZOLZ and HOLZ patterns. Photographs (b) to (h) are patterns processed by a high-pass filter at different cut-off frequencies. The broad ZOLZ pattern is completely removed. The cut-off frequency increases from (b) to (h). It is seen that the patterns of only higher frequencies remain in the arranged order from (b) to (h).

SiC [0001]

(a) Original (b) Processed **100kV**

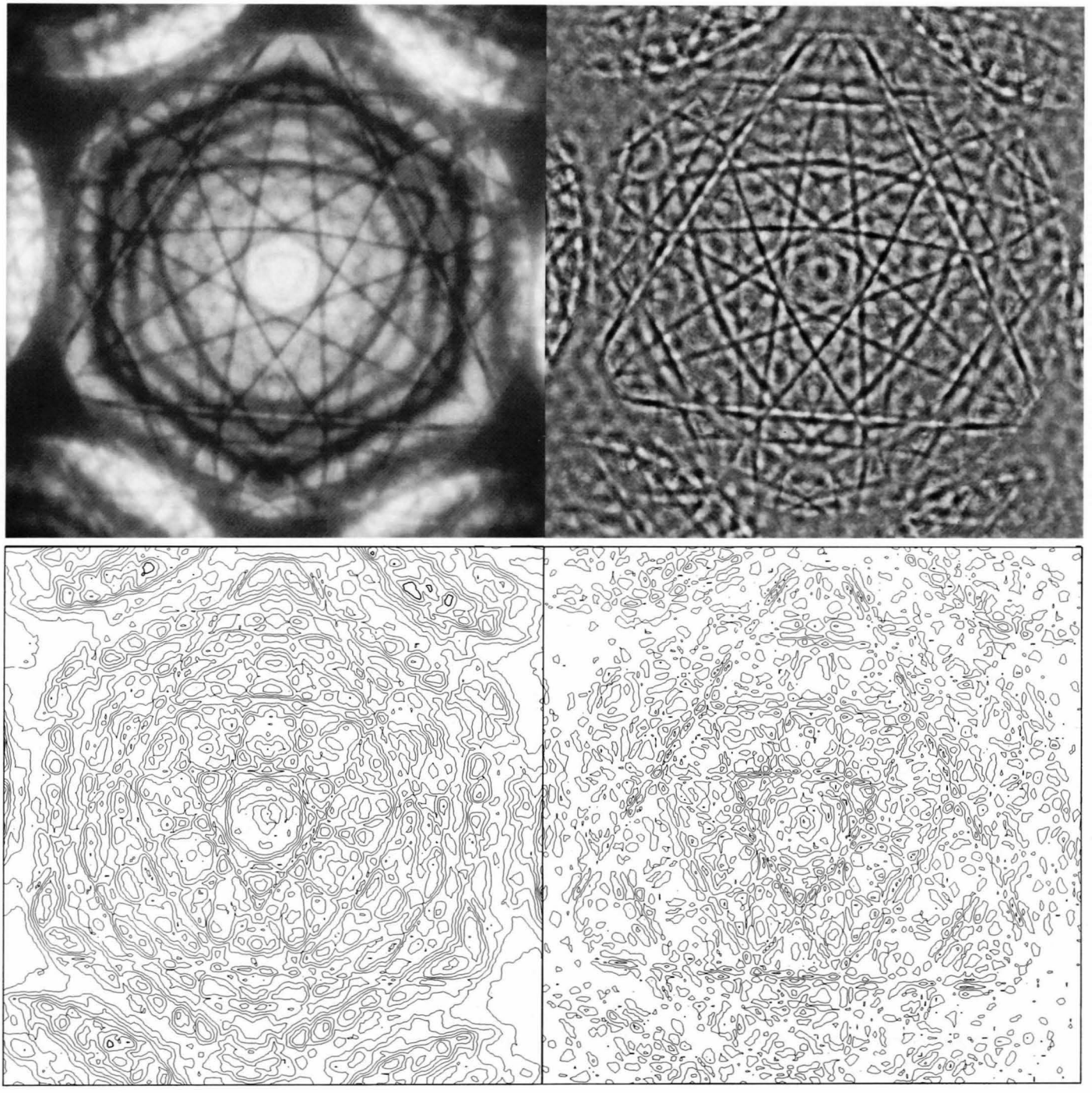

(c) Original (contour map) (d) Processed (contour map)

Comparison of zone-axis BF patterns of [0001] SiC without image processing (a) and with processing (b). Patterns (c) and (d) are contour map presentations of patterns (a) and (b), respectively.

FeS_2 [111]

(a) Original (b) Processed **100kV**

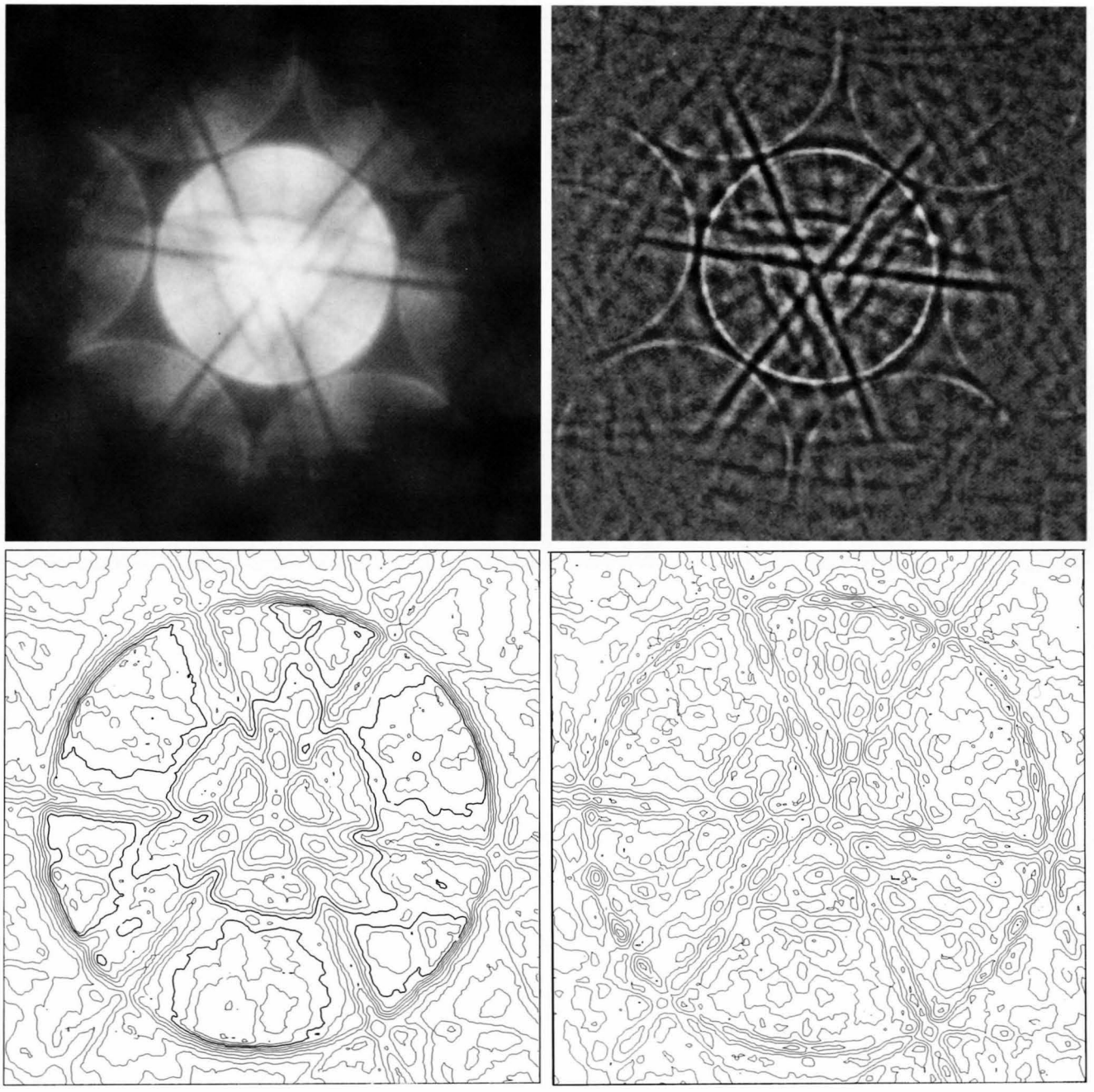

(c) Original (contour map) (d) Processed (contour map)

Comparison of zone-axis patterns of [111] FeS_2 without processing (a) and with processing (b). Patterns (c) and (d) are contour map presentations of the BF disks of patterns (a) and (b), respectively.

Evaluation of Symmetries

Symmetries of CBED patterns are evaluated quantitatively using *S*-factor for a fourfold rotation symmetry of a [100] zone-axis pattern of Si, a threefold rotation symmetry of a [111] zone-axis pattern of Si, and for a mirror symmetry of a [100] zone-axis pattern of Si. In advance of calculating *S*-factor, the axially symmetric background intensity, which is assumed expressed by a Lorentz function $b(r)$, is subtracted from the original pattern. *S*-factors, S_{total}, S_{BF} and S_{DF} are calculated for the entire pattern, BF pattern and DF pattern, respectively.

Real CBED patterns, which were considered to have a perfect symmetry by visual examination, showed a value of $S \approx 10\%$. The value may be attributed to the angular inhomogeneity of the incident beam intensity and to the thickness variation in the illuminated specimen area, the latter being a dominant contribution. *S*-value for the inhomogeneity of the incident beam and thickness variation are given on page 43.

$$S = \sqrt{\frac{\Sigma |I(x, y) - I(x', y')|^2}{\Sigma I(x, y)^2}}, \qquad \begin{pmatrix} x' \\ y' \end{pmatrix} = R(\theta) \begin{pmatrix} x \\ y \end{pmatrix}$$

$$b(r) = \frac{Hw^2}{r^2 + w^2}$$

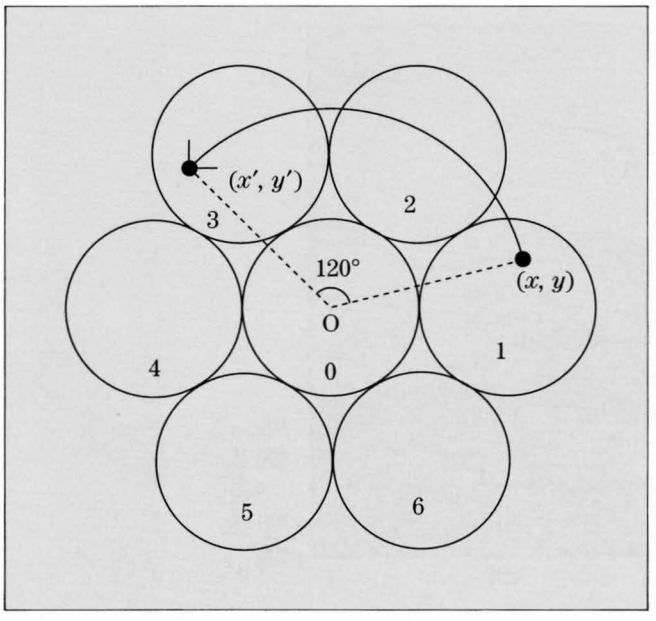

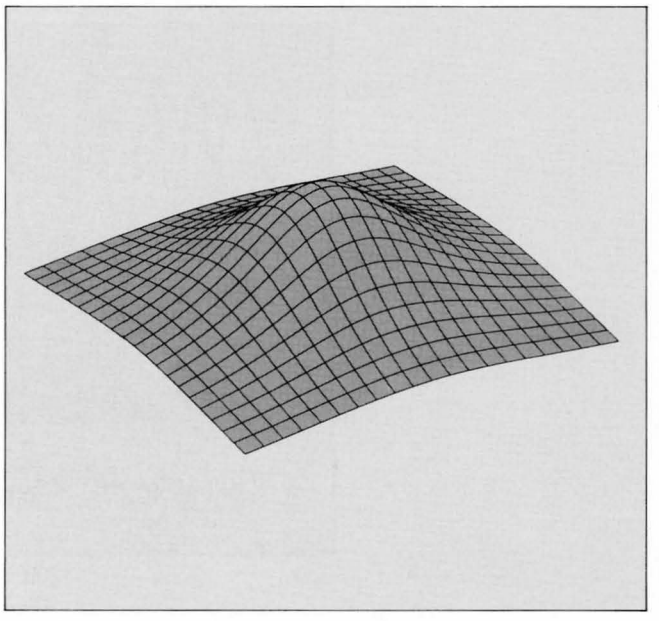

Background surface

Si [100] — fourfold rotation —

(a) Original (b) Difference pattern **100kV**

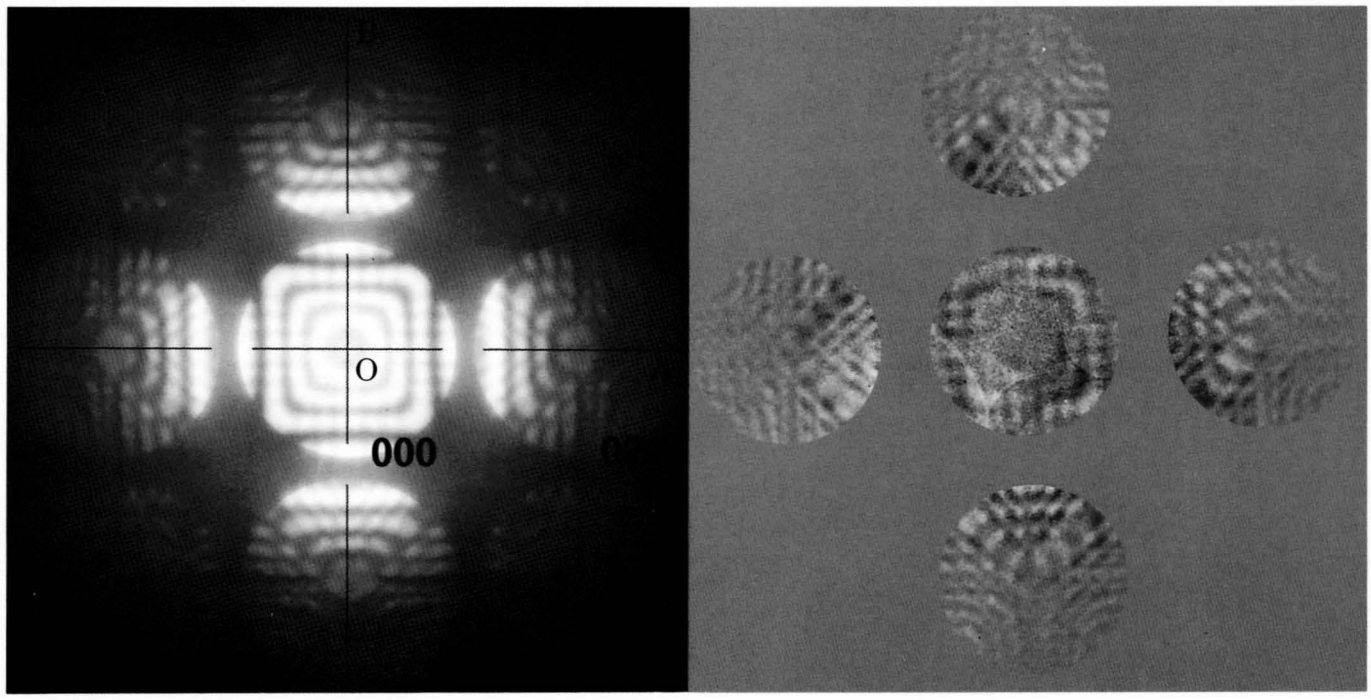

(a) Original pattern. (b) Difference pattern between the pattern (a) and the pattern rotated by 90° about the zone axis of the original pattern

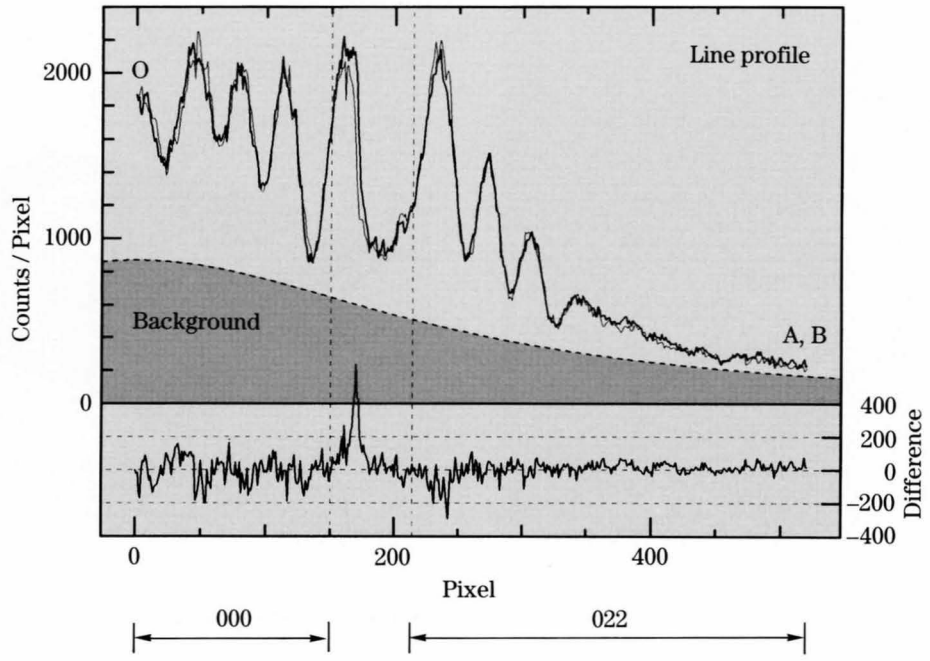

Thick and thin curves show line profiles along OA and OB in Photo (a).

$S_{total} = 10.1\%$, $S_{BF} = 7.6\%$, $S_{DF} = 12.4 \pm 0.5\%$

Si [111] — threefold rotation —

Original Difference pattern **100kV**

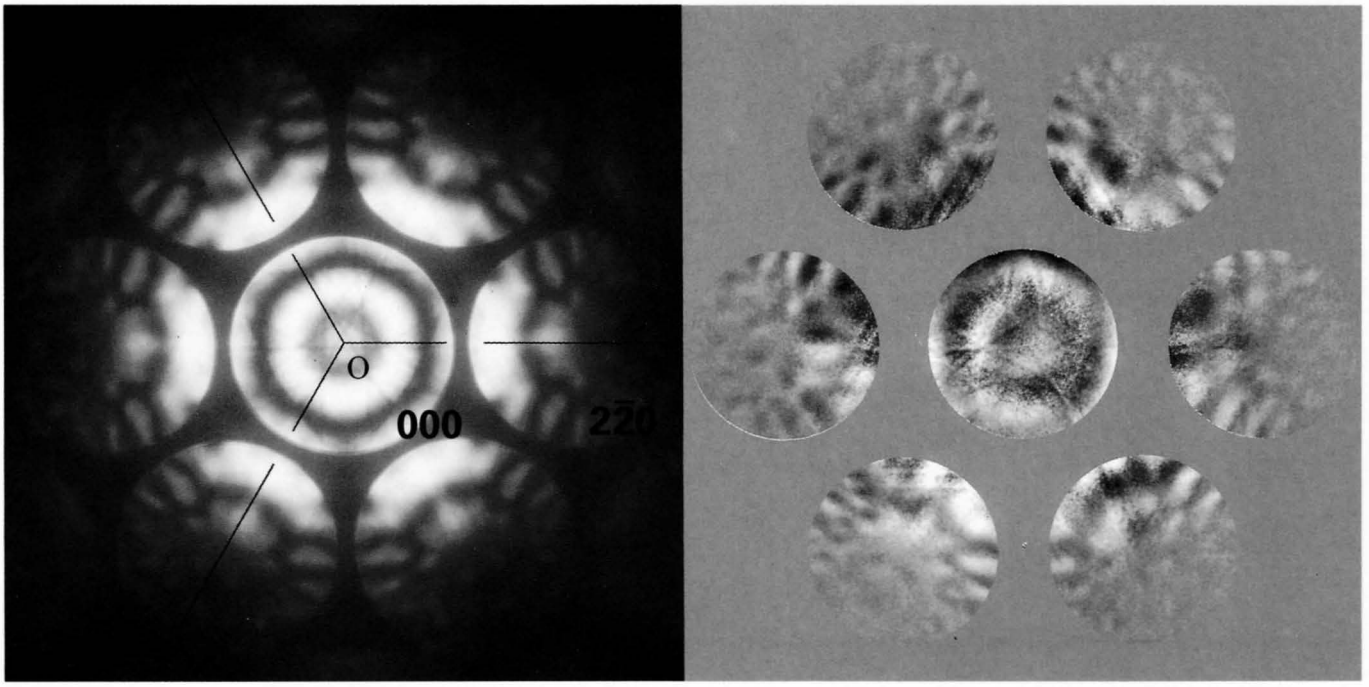

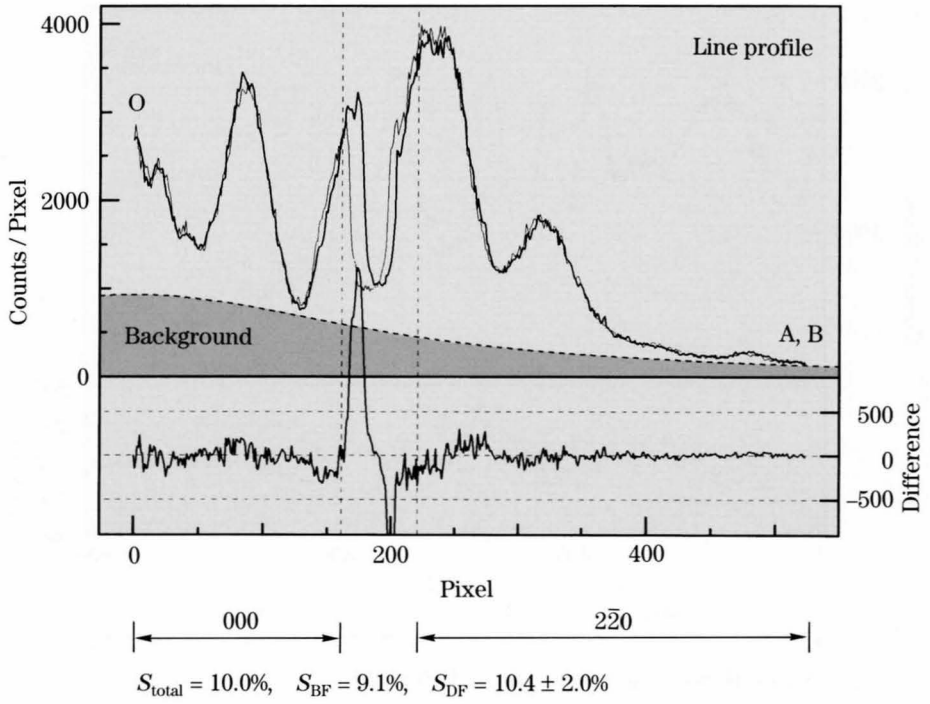

S_{total} = 10.0%, S_{BF} = 9.1%, S_{DF} = 10.4 ± 2.0%

Si [100] — mirror symmetry —

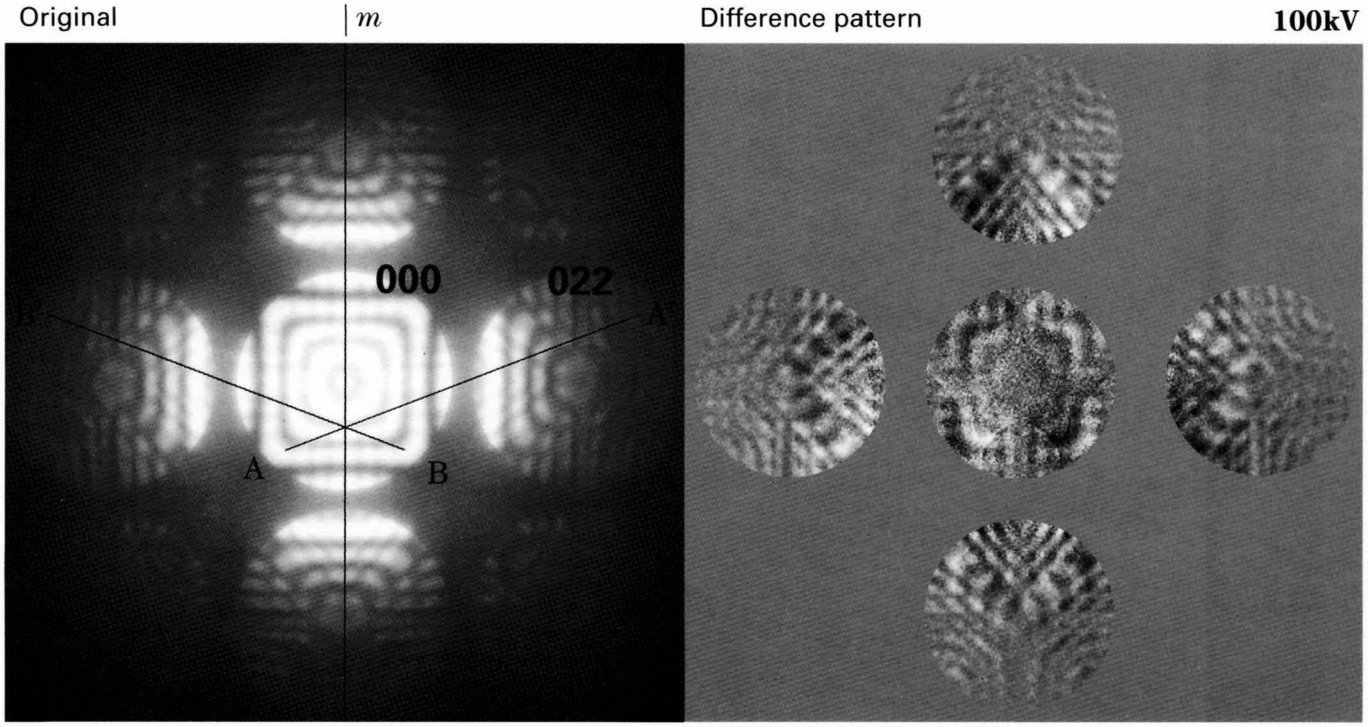

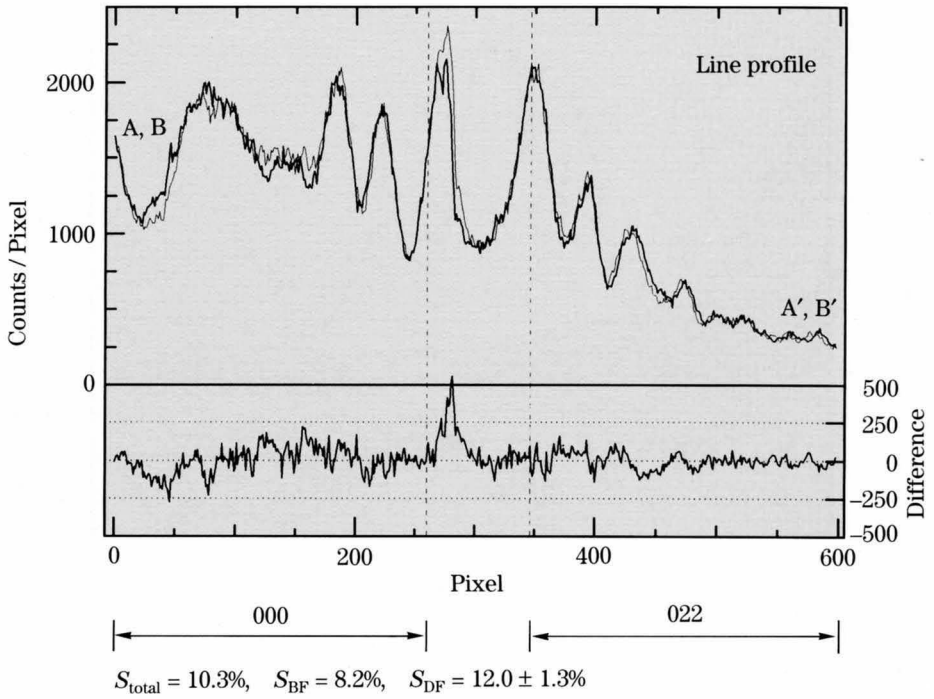

S_{total} = 10.3%, S_{BF} = 8.2%, S_{DF} = 12.0 ± 1.3%

The table summarizes values of *S*-factors investigated for three symmetries of three materials, which were judged to have a very good symmetry by visual examination. All the *S*-factor values are about 10%.

The figure shows changes of *S*-factor with the rotation angle for a fourfold rotation symmetry of [100] Si. It is seen that *S*-factor takes a minimum value of 10.1% at an exact rotation of 90°.

	Sym. op.	S_{total}(%)	S_{BF}(%)	S_{DF}(%)
Si[100]	4	10.1	7.6	12.4±0.5
	m	10.3	8.2	12.0±1.3
Si[111]	3	10.0	9.1	10.4±2.0
	m	9.5	8.2	10.0±1.5
FeS_2[111]	3	10.4	8.1	13.9±2.8
TiO_2[001]	4	9.9	5.1	9.6±3.1

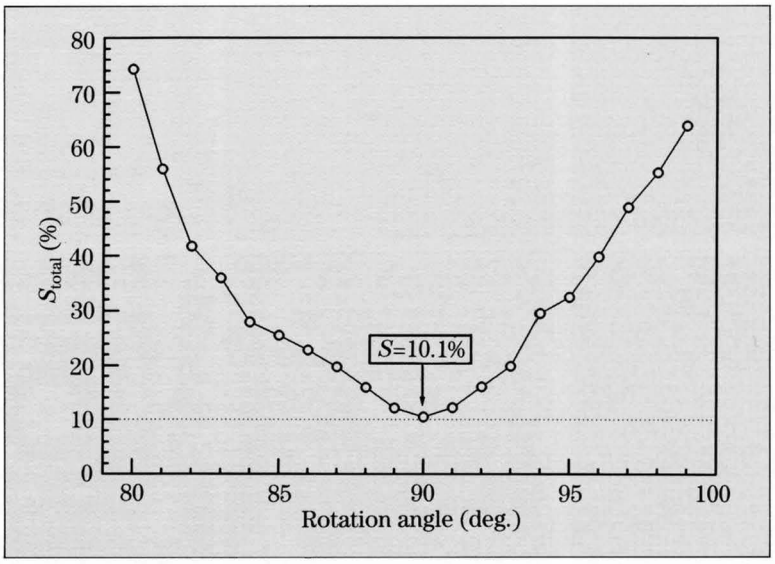

Thickness dependence of difference patterns

100kV

Si [100]

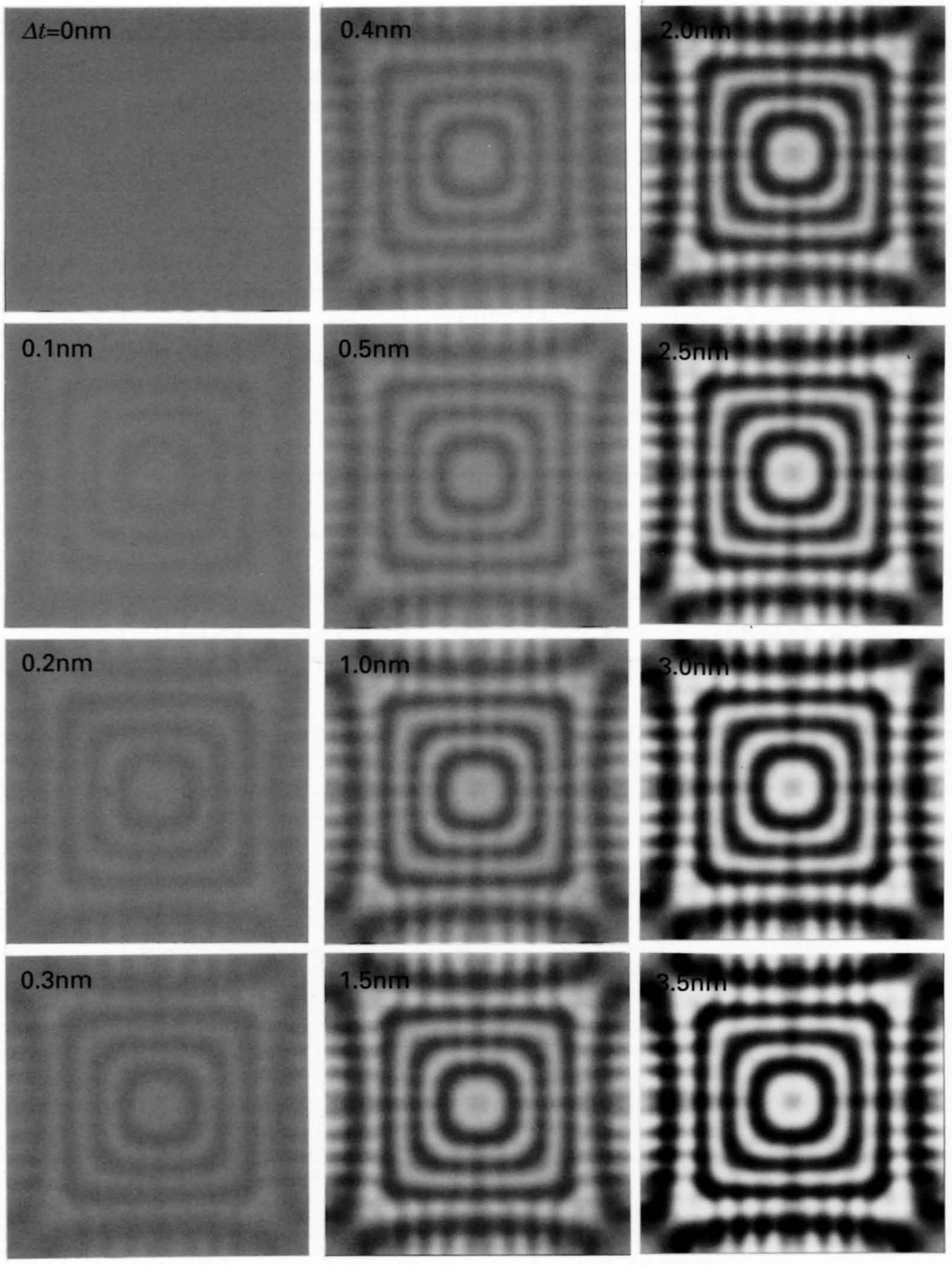

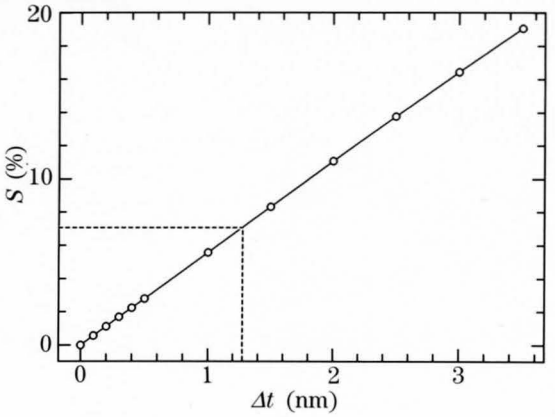

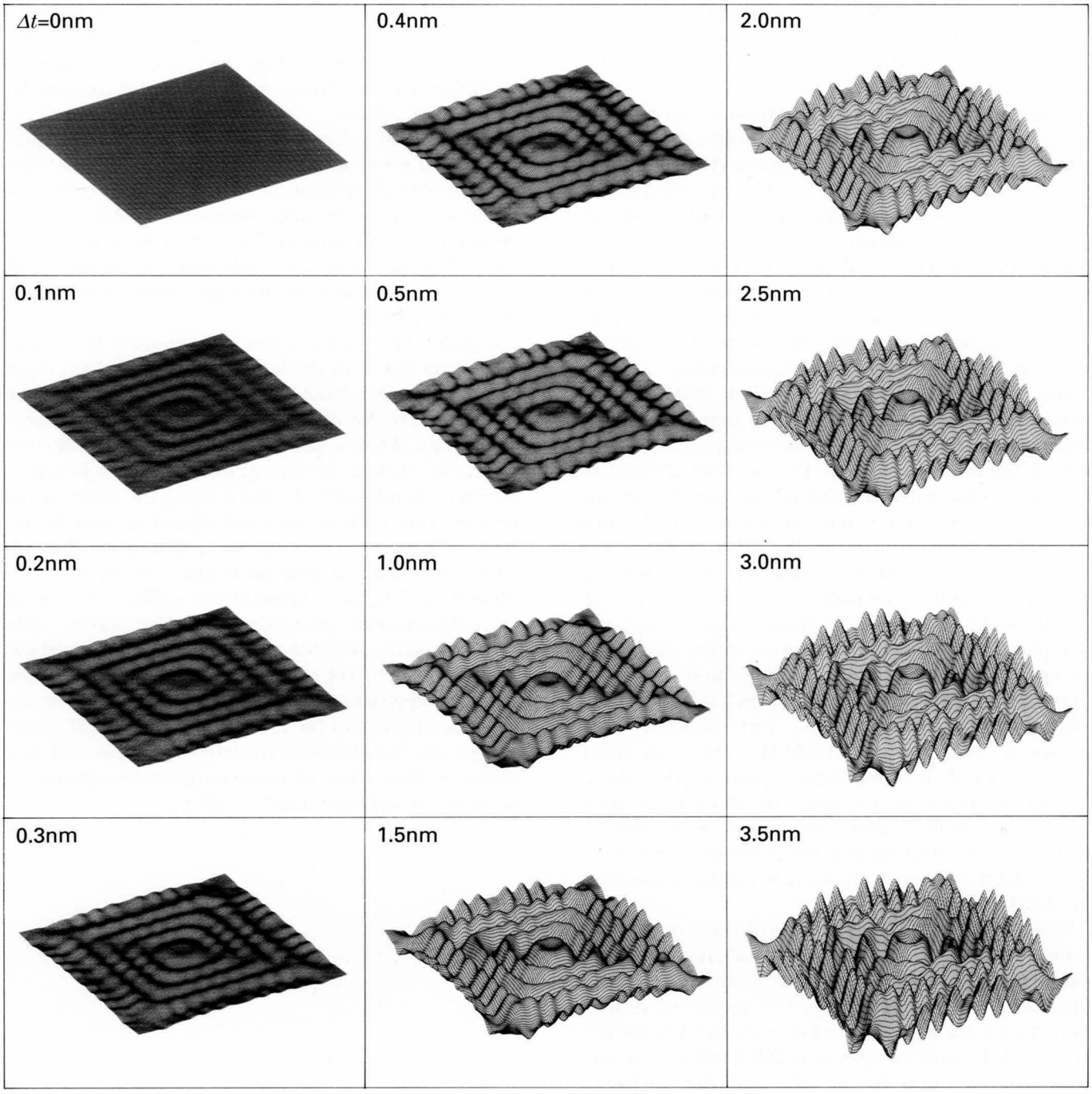

How S-factor changes with small changes of specimen thickness was investigated for a BF pattern of [100] Si calculated with a specimen thickness of 150 nm at an accelerating voltage of 100kV. Twelve BF patterns were calculated for different thicknesses of $150+\Delta t$ nm. Difference patterns between those patterns and the pattern with a thickness of 150 nm are shown in two ways on this page and on the opposite page.

The figure on the opposite page is a plot of the values of S-factor as a function of the increment of thickness Δt, showing a linear increase of the value of S-factor with increasing thickness.

A separate experiment revealed that the inhomogeneity of the incident beam intensity in a CBED disk accounted for about S=3%. The rest of S=10% observed or S=7% may be attributed to a thickness variation in the illuminated specimen area. The value of S=7% is seen to correspond to a thickness increment of about 1.3 nm.

Space-Group Determination

Procedure

A procedure of space-group determination is described here in a simple manner. A rigorous and precise description is given in a review paper by Tanaka [a], [28].

Four CBED patterns are taken from a thin parallel-sided crystalline specimen: a bright-field pattern (BP), whole pattern (WP), dark-field pattern (DP) and a pair (±G) of dark-field patterns (±DP). BP implies the bright-field pattern observed in a pattern taken with the electron incidence parallel to a zone axis (ZAP). WP implies the resultant of BP and all the diffraction patterns surrounding BP in the ZAP, or implies the ZAP itself. DP implies the dark-field pattern containing an exact Bragg position (angle). ±DP implies a pair of DPs whose reflection indices have opposite signs.

The diffraction group of a specimen is determined from the symmetries of the above four patterns by referring to Table (a) [1] in the following pages with the help of the illustration of the DP and ±DP symmetries on page 48. Table (a), in which all the possible symmetries are given to avoid confusion, is a modification of a table given by Buxton *et al.* [2]. When a diffraction group is identified, possible point groups are seen by referring to Table (b) on page 49, given by Buxton *et al.* [2]. In a lucky case, one point group is selected but usually plural point groups correspond to the diffraction group obtained. A different diffraction group is obtained by examining CBED symmetries at the second zone axis, and again its corresponding point groups are selected using Table (b). Then, one point group is identified by selecting a common point group among the point groups obtained at different zone axes. High-symmetry zone axes have to be chosen for point-group determination because low-symmetry zone axes exhibit only a small number of crystal symmetries in CBED patterns.

When HOLZ reflections are weak and only ZOLZ reflections are observed in a CBED pattern, the pattern exhibits only the symmetry elements of the specimen projected along the zone axis. Ten projection diffraction groups are given in the last column of Table (a). When CBED patterns show only ZOLZ reflections, projection diffraction groups are obtained. Hence, if a diffraction group is identified carelessly from CBED patterns in which only ZOLZ reflections are observed, wrong point groups are deduced. However, combined use of projection (two-dimensional) symmetries and HOLZ reflection (three-dimensional) symmetries often makes it easy to determine point groups.

In the course of point-group determination, orientations of symmetry elements and then those of the crystal axes are given on diffraction patterns. Based on the results, an integral index is given to reflection spots in each diffraction pattern. The systematic absence of reflections reveals the lattice type of a crystal (Table (c)). It should be noted that the reflections forbidden by lattice types are always absent even if dynamical diffraction takes place.

Conventional extinction rules (Table (d)) for glide planes and screw axes hold only in the approximation of kinematical diffraction. Kinematically forbidden reflections caused by these symmetry elements have a certain intensity owing to *Umweganregung* of dynamical diffraction; however, extinction of intensity still takes place in these reflections for certain directions of the incident beam.

A glide plane and a screw axis produce dynamical extinction line A in the kinematically forbidden disks through the interaction between ZOLZ reflections. Line A runs along the diffraction vector of the forbidden reflections. When a kinematically forbidden reflection is exactly excited, dynamical extinction line B is produced perpendicularly to line A along the exact Bragg position (line). These lines are named A_2- and B_2-GM lines. When *Umweganregung* paths pass through HOLZ reflections, a glide plane and a screw axis produce A_3 and B_3 lines, respectively, suffix 3 indicating three-dimensional interaction. GM line tables were given for all the possible crystal settings and for all the space groups [b], [1], [4]. Tables (e) [1] and (f) [4] show GM lines appearing in ZOLZ and HOLZ reflections for the space groups of the monoclinic system. 181 space groups can be identified by referring to the GM line tables. A flow chart of space-group determination is given on the opposite page.

References

[a] M. Tanaka: *J. Electron Microsc. Tech.*, **13** (1989) 27.

[b] M. Tanaka, H. Sekii and T. Nagasawa: *Acta Cryst.*, **A39** (1983) 825.

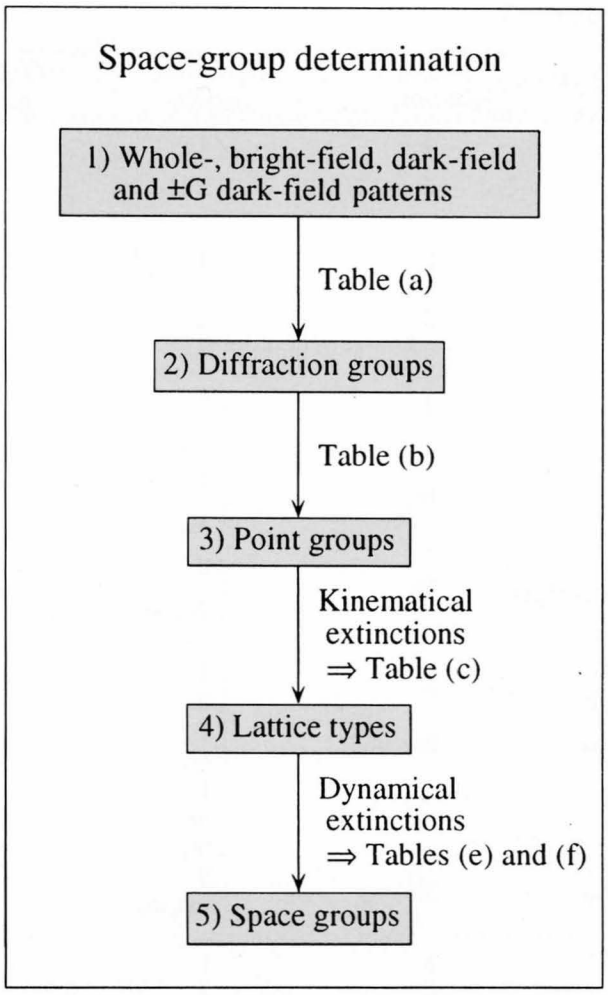

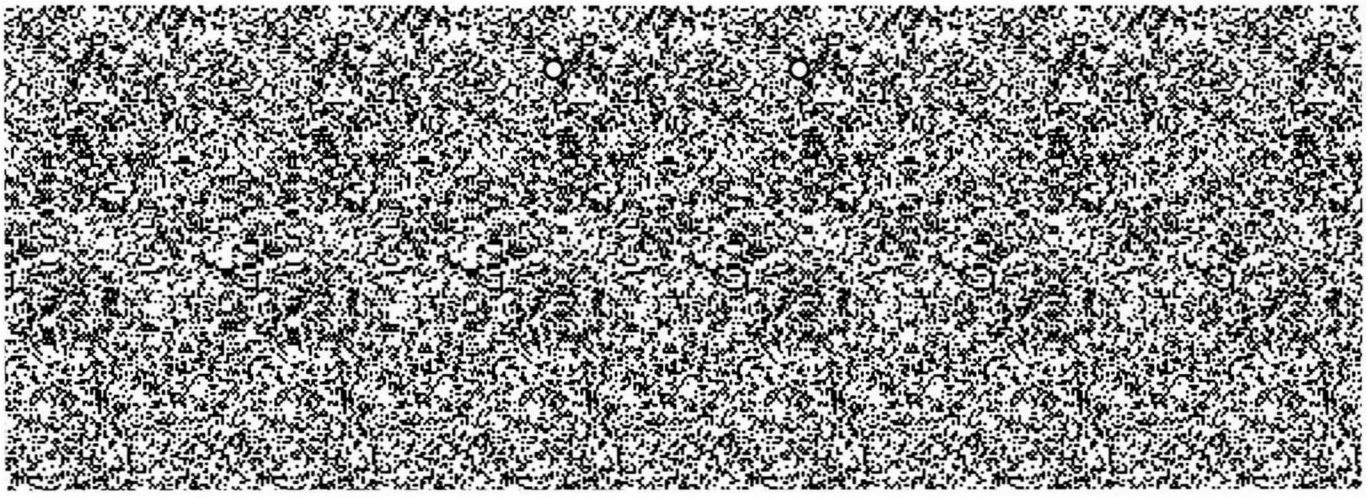

Random dot stereogram

CBED pattern symmetries of diffraction groups

Table (a) Symmetries of CBED patterns

Diffraction group	Bright-field pattern	Whole pattern	Dark-field pattern	±G dark-field patterns	Projection diffraction group
1	1	1	1	1	
1_R	2 (1_R)	1	$2=1_R$	1	1_R
2	2	2	1	2	
2_R	1	1	1	2_R	21_R
21_R	2	2	2	21_R	
m_R	m (m_2)	1	1 m_2	1 m_R 1	
m	m_v	m_v	1 m_v	1 m_v 1	$m1_R$
$m1_R$	$2mm$ $(m_v+m_2+(1_R))$	m_v	2 $2m_vm_2$	1 m_v1_R 1	
$2m_Rm_R$	$2mm$ $(2+m_2)$	2	1 m_2	2 $2m_R(m_2)$	
$2mm$	$2m_vm_{v'}$	$2m_vm_{v'}$	1 m_v	2 $2m_{v'}(m_v)$	
2_Rmm_R	m_v	m_v	1 m_2 m_v	2_R $2_Rm_{v'}(m_2)$ $2_Rm_R(m_v)$	$2mm1_R$
$2mm1_R$	$2m_vm_{v'}$	$2m_vm_{v'}$	2 $2m_vm_2$	21_R $21_Rm_{v'}(m_v)$	
4	4	4	1	2	
4_R	4	2	1	2	41_R
41_R	4	4	2	21_R	
$4m_Rm_R$	$4mm$ $(4+m_2)$	4	1 m_2	2 $2m_R(m_2)$	
$4mm$	$4m_vm_{v'}$	$4m_vm_{v'}$	1 m_v	2 $2m_{v'}(m_v)$	
4_Rmm_R	$4mm$ $(2m_vm_{v'}+m_2)$	$2m_vm_{v'}$	1 m_2 m_v	2 $2m_R(m_2)$ $2m_{v'}(m_v)$	$4mm1_R$
$4mm1_R$	$4m_vm_{v'}$	$4m_vm_{v'}$	2 $2m_vm_2$	21_R $21_Rm_{v'}(m_v)$	

Table (a) Continued

Diffraction group	Bright-field pattern	Whole pattern	Dark-field pattern	±G dark-field patterns	Projection diffraction group
3	3	3	1	1	31_R
31_R	6 $(3+1_R)$	3	2	1	
$3m_R$	$3m$ $(3+m_2)$	3	1 m_2	1 m_R 1	$3m1_R$
$3m$	$3m_v$	$3m_v$	1 m_v	1 m_v 1	
$3m1_R$	$6mm$ $(3m_v+m_2+(1_R))$	$3m_v$	2 $2m_vm_2$	1 m_v1_R 1	
6	6	6	1	2	61_R
6_R	3	3	1	2_R	
61_R	6	6	2	21_R	
$6m_Rm_R$	$6mm$ $(6+m_2)$	6	1 m_2	2 $2m_R(m_2)$	$6mm1_R$
$6mm$	$6m_vm_{v'}$	$6m_vm_{v'}$	1 m_v	2 $2m_{v'}(m_v)$	
6_Rmm_R	$3m_v$	$3m_v$	1 m_2 m_v	2_R $2_Rm_{v'}(m_2)$ $2_Rm_R(m_v)$	
$6mm1_R$	$6m_vm_{v'}$	$6m_vm_{v'}$	2 $2m_vm_2$	21_R $21_Rm_{v'}(m_v)$	

Illustration of dark-field pattern and ±G dark-field pattern symmetries

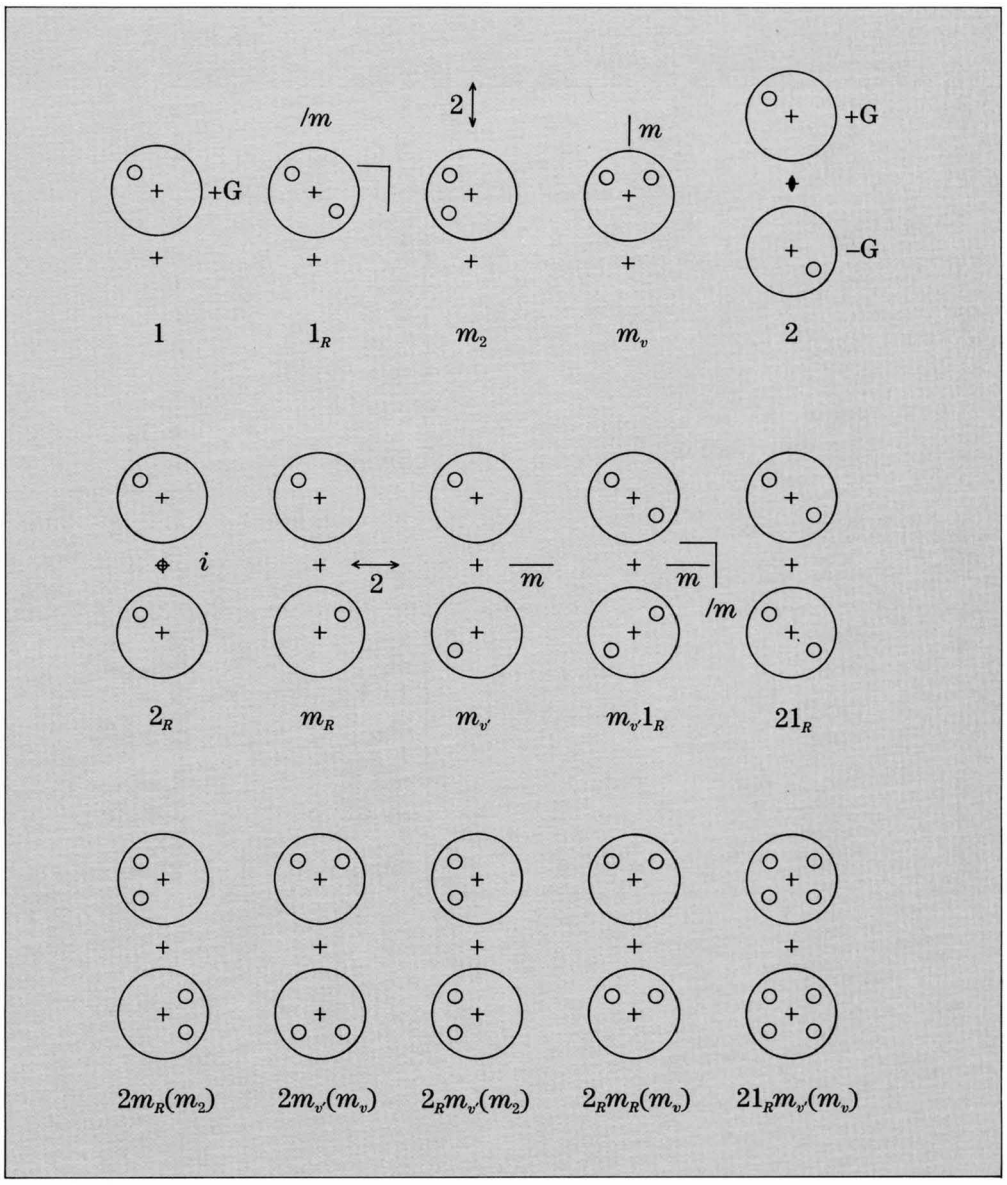

Point groups vs. diffraction groups

Table (b) Relation between diffraction groups and crystal point-groups

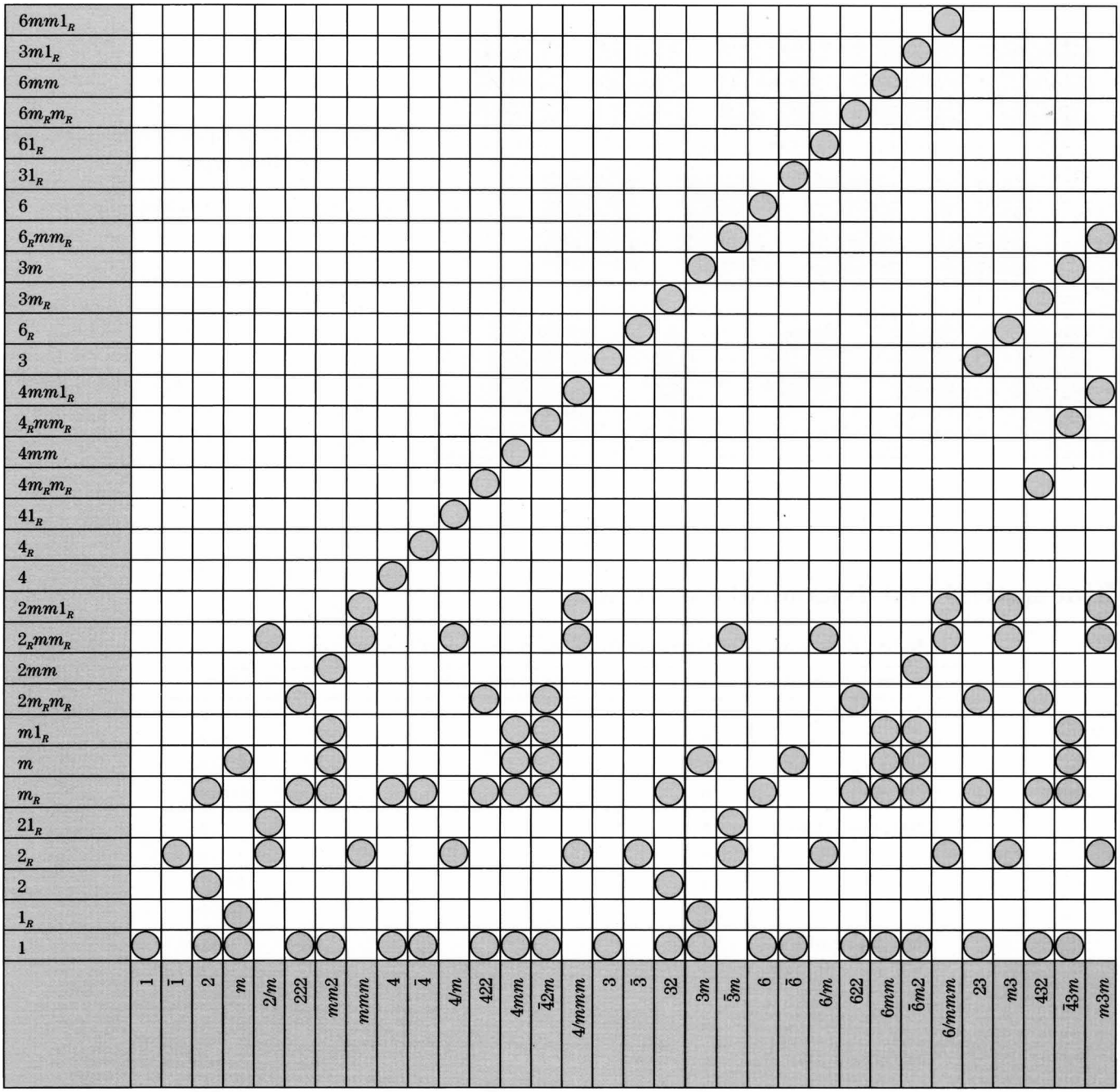

B.F. Buxton, J.A. Eades, J.W. Steeds and G.M. Rackham: *Phil. Trans. R. Soc. London*, **281** (1976) 171.
Courtesy of the Royal Society of London

Lattice types

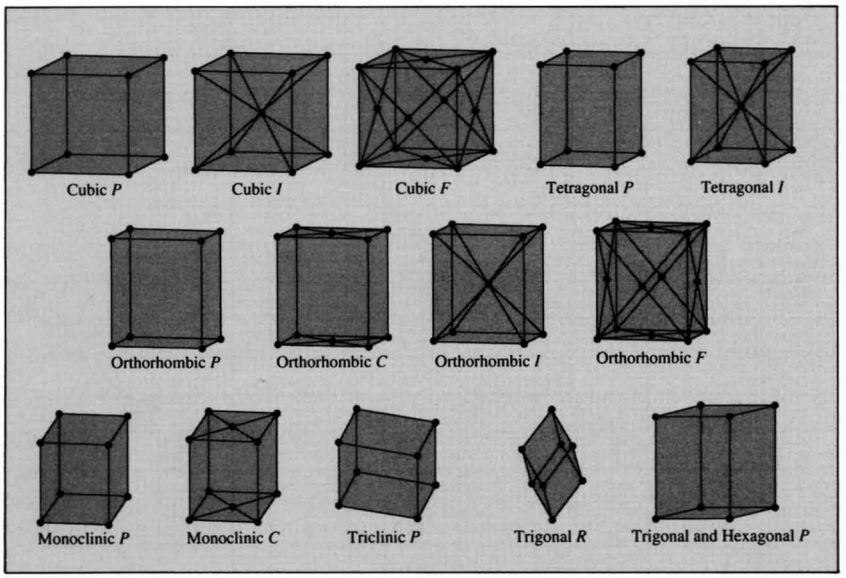

Table (c) Absence rules of reflections due to lattice types

Lattice type	Forbidden reflections
P	None
I	$h + k + l = 2n + 1$
C	$h + k = 2n + 1$
A	$k + l = 2n + 1$
B	$h + l = 2n + 1$
F	h, k, l mixed parity
R_{obv}	$-h + k + l = 3n + 1, 3n + 2$
R_{rev}	$h - k + l = 3n + 1, 3n + 2$

Kinematical and dynamical extinctions

Table (d) Kinematical extinctions for glide planes and screw axes

Symmetry elements		Set of reflections	Conditions
Glide plane // (001)	a	$hk0$	$h=2n$
	b		$k=2n$
	n		$h+k=2n$
	d		$h+k=4n$
Glide plane // (100)	b	$0kl$	$k=2n$
	c		$l=2n$
	n		$k+l=2n$
	d		$k+l=4n$
Glide plane // (010)	a	$h0l$	$h=2n$
	c		$l=2n$
	n		$h+l=2n$
	d		$h+l=4n$
Glide plane // (110)	c	hhl	$l=2n$
	n		$h+l=2n$
	d		$2h+l=4n$

Table (d) (continued)

Symmetry elements		Set of reflections	Conditions
Screw-axis $\parallel c$	$2_1, 4_2, 6_3$	$00l$	$l=2n$
	$3_1, 3_2, 6_2, 6_4$		$l=3n$
	$4_1, 4_3$		$l=4n$
	$6_1, 6_5$		$l=6n$
Screw-axis $\parallel a$	$2_1, 4_2$	$h00$	$h=2n$
	$4_1, 4_3$		$h=4n$
Screw-axis $\parallel b$	$2_1, 4_2$	$0k0$	$k=2n$
	$4_1, 4_3$		$k=4n$
Screw-axis $\parallel [110]$	2_1	$hh0$	$h=2n$

Details are referred to the International Tables for Crystallography A.

Dynamical extinctions (examples for the monoclinic system)

Table (e) GM lines in ZOLZ reflections

Incident beam direction / Space group	$[u0w]$	
3 $P2$		
4 $P2_1$	$0k0$ 2_1	A_2 B_2 B_3
5 $C2$		
6 Pm		
7 Pc	$h0l_o$ c	A_2 B_2 A_3
8 Cm		
9 Cc	h_e0l_o c	A_2 B_2 A_3

Incident beam direction / Space group	$[u0w]$	
10 $P2/m$		
11 $P2_1/m$	$0k0$ 2_1	A_2 B_2 B_3
12 $C2/m$		
13 $P2/c$	$h0l_o$ c	A_2 B_2 A_3
14 $P2_1/c$	$0k0$ 2_1 $h0l_o$ c	A_2 B_2 B_3 A_2 B_2 A_3
15 $C2/c$	h_e0l_o c	A_2 B_2 A_3

Table (f) GM lines in HOLZ reflections

Incident beam direction / Space group	$[u0w]$	
6 Pm		
7 Pc	$h0l_o$ c	A_h
8 Cm		
9 Cc	h_e0l_o c	A_h
10 $P2/m$		

Incident beam direction / Space group	$[u0w]$	
11 $P2_1/m$		
12 $C2/m$		
13 $P2/c$	$h0l_o$ c	A_h
14 $P2_1/c$	$h0l_o$ c	A_h
15 $C2/c$	h_e0l_o c	A_h

TiO_2 (Rutile)

The space group of rutile is well known to be $P4_2/mnm$. Determination of the space group, however, is rather sophisticated. Hence, it provides a good exercise for those who want to acquire experience in the CBED space-group determination method. Our lab uses this example for newcomers. The determination is carried out by assuming that the lattice parameters are known.

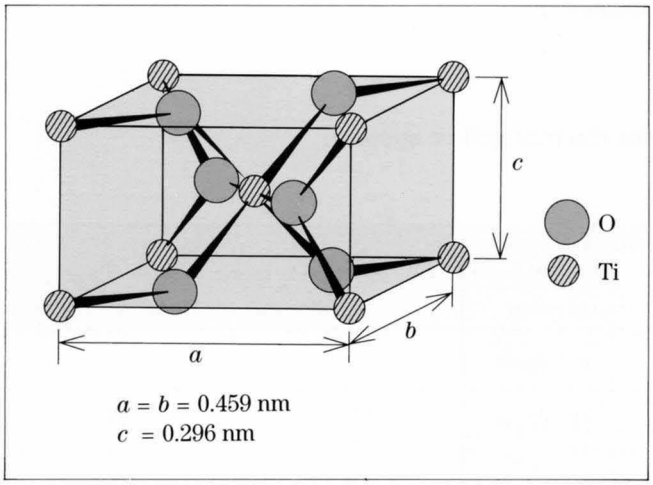

$a = b = 0.459$ nm
$c = 0.296$ nm

First incidence [001] **80kV**

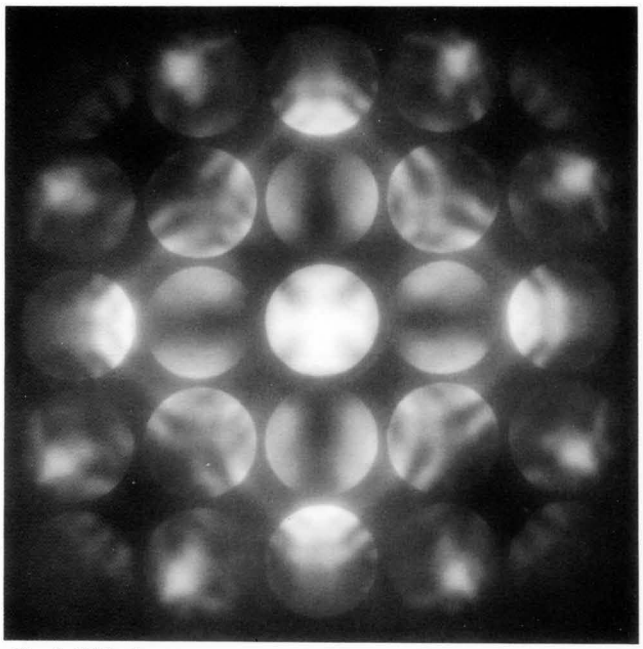

Proj. WP: $4mm$

Point group

1st incidence

Proj. WP : $4mm$

Proj. diff. group : $4mm1_R$

Possible diff. groups :

$4m_Rm_R$
$4mm$
4_Rmm_R
$4mm1_R$

Second incidence [101] 100kV

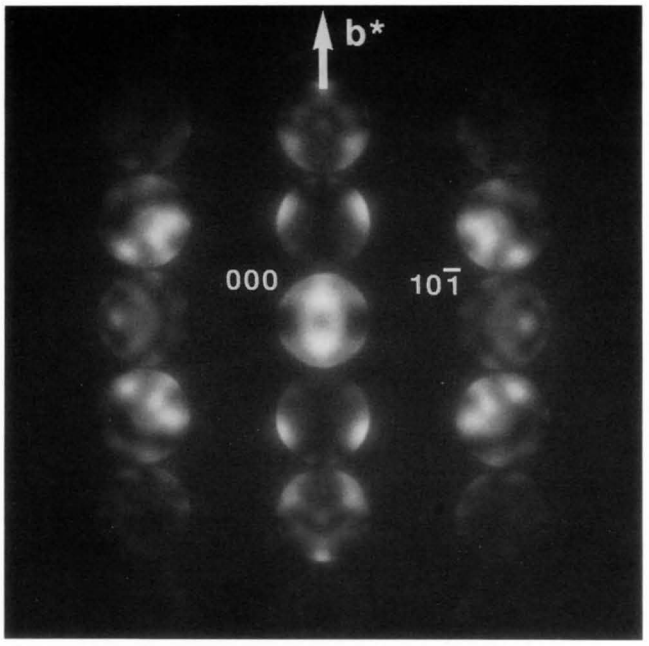

(a) Proj. BP, proj. WP: $2mm$

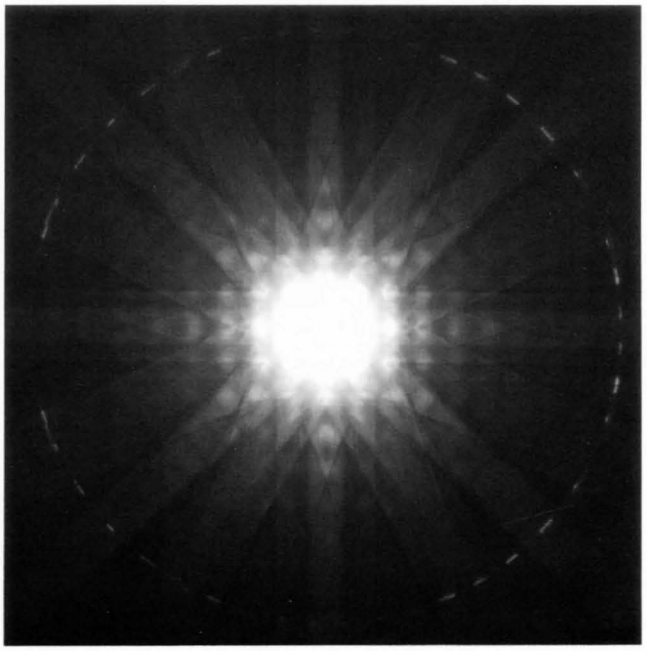

(b) WP: m

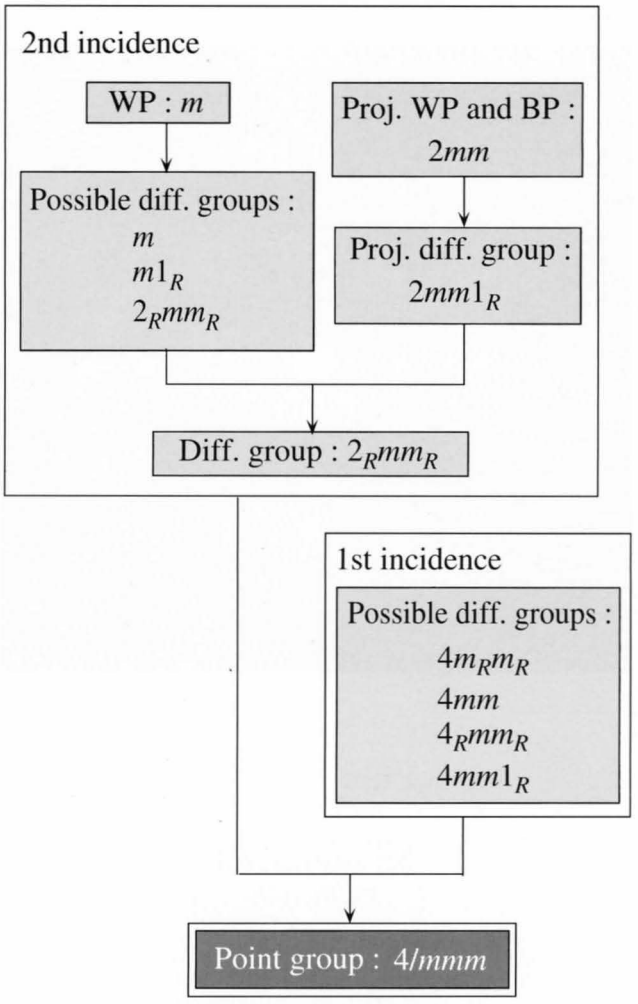

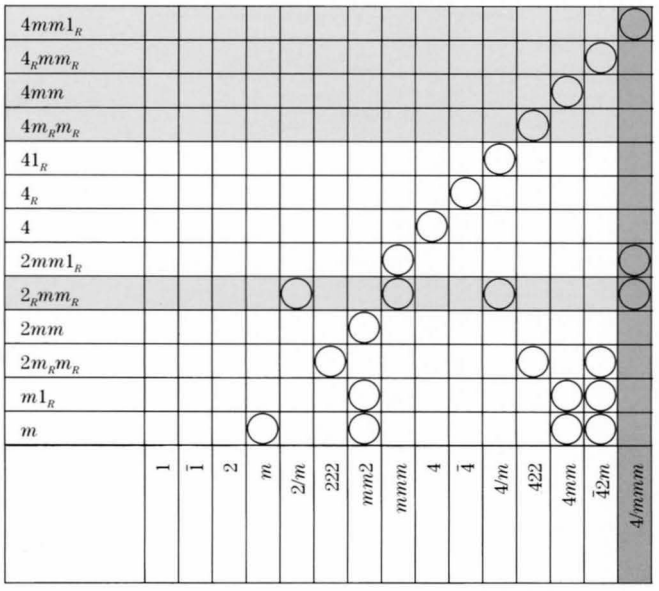

TiO_2

[001] **80kV**

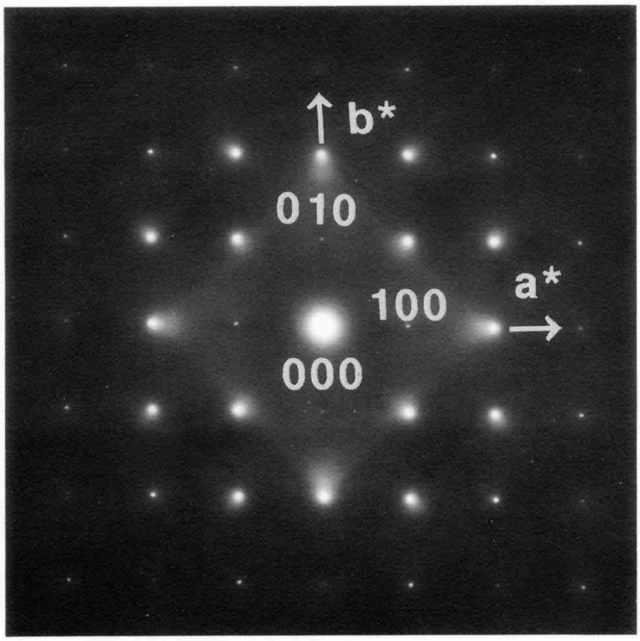

Lattice type

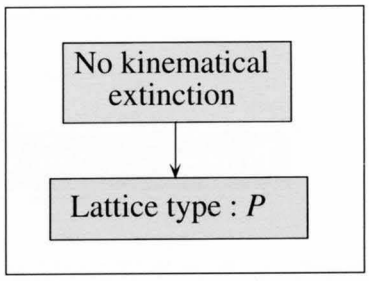

Space group

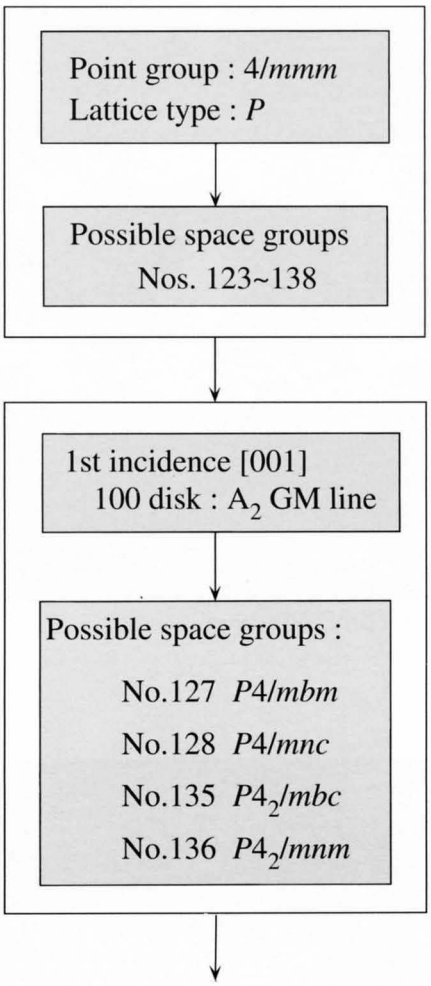

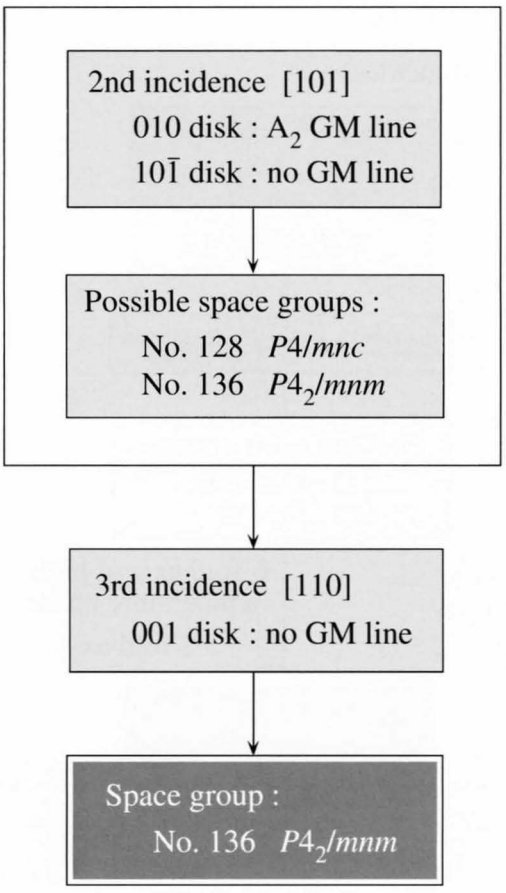

Third incidence [110] 100kV

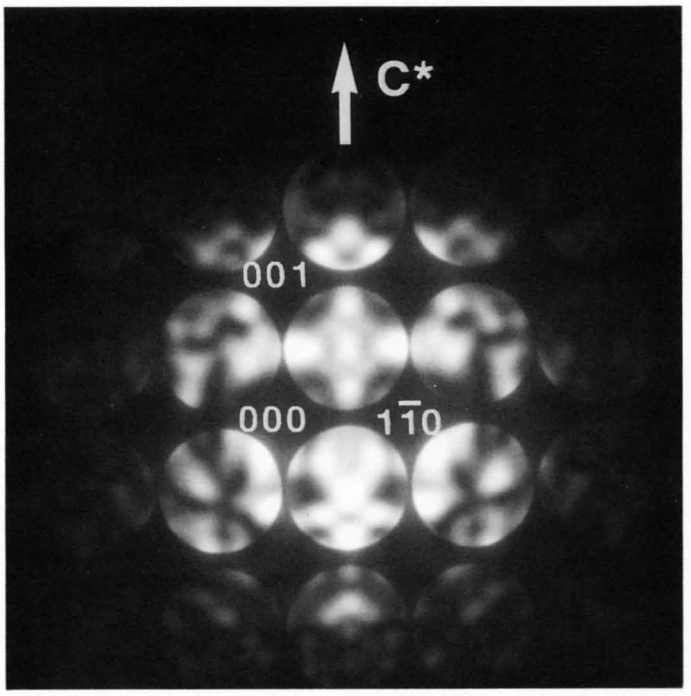

001 exact excitation

Incident beam direction / Space group		[100]		[001]		[110]		[$u0w$]*	
127	*P4/mbm* $P4/m2_1/b2/m$	$0k0$ 2_{12}	 B_3	$h00$ $a_2, 2_{11}$ $0k0$ $b_1, 2_{12}$	 A_2 B_2 A_3 B_3			h_o0l a $0k0$ 2_1	A_2 B_2 A_3 A_2 B_2 B_3
128	*P4/mnc* $P4/m2_1/n2/c$	$00l$ n_2 $0k0$ 2_{12}	 A_3 B_3	$h00$ $n_2, 2_{11}$ $0k0$ $n_1, 2_{12}$	 A_2 B_2 A_3 B_3	$00l$ c	 A_3	$h0l$ $h+l=2n+1$ n $0k0$ 2_1	 A_2 B_2 A_3 A_2 B_2 B_3
135	$P4_2/mbc$ $P4_2/m2_1/b2/c$	$0k0$ 2_{12}	 B_3	$h00$ $a_2, 2_{11}$ $0k0$ $b_1, 2_{12}$	 A_2 B_2 A_3 B_3	$00l$ c	 A_3	h_o0l a $0k0$ 2_1	 A_2 B_2 A_3 A_2 B_2 B_3
136	$P4_2/mnm$ $P4_2/m2_1/n2/m$	$00l$ n_2 $0k0$ 2_{12}	 A_3 B_3	$h00$ $n_2, 2_{11}$ $0k0$ $n_1, 2_{12}$	 A_2 B_2 A_3 B_3			$h0l$ $h+l=2n+1$ n $0k0$ 2_1	 A_2 B_2 A_3 A_2 B_2 B_3

*The symbol "*a*" in the column of [$u0w$] incidence is equivalent to the symbol "*b*" in the space groups of the first column.

Hexagonal $BaTiO_3$

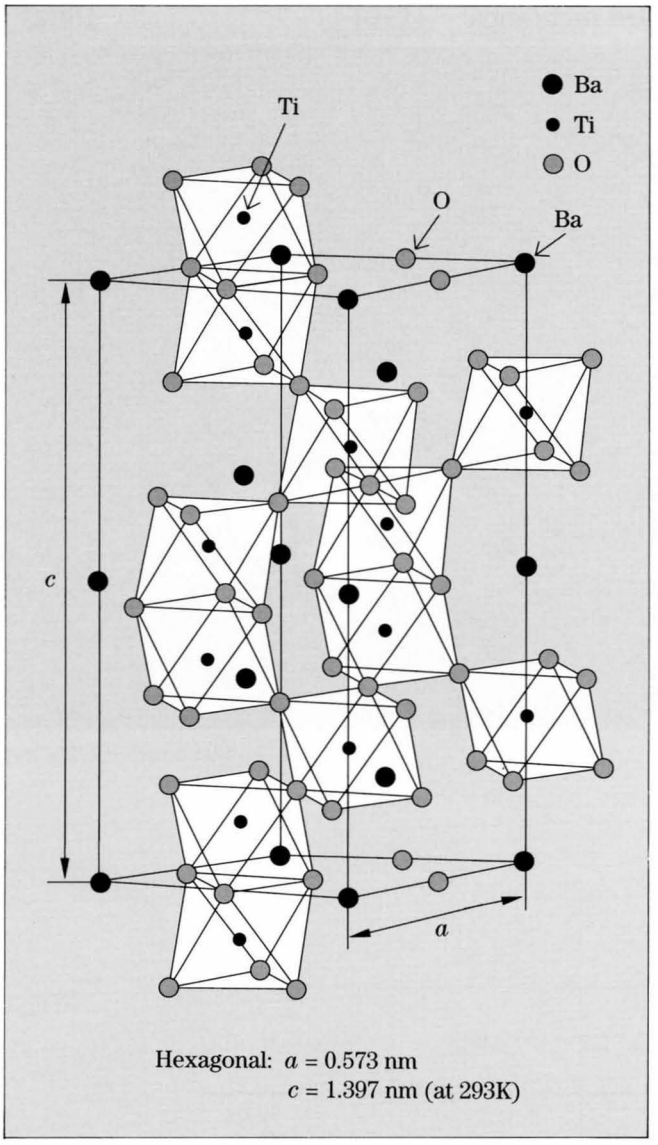

Hexagonal: a = 0.573 nm
c = 1.397 nm (at 293K)

Point group

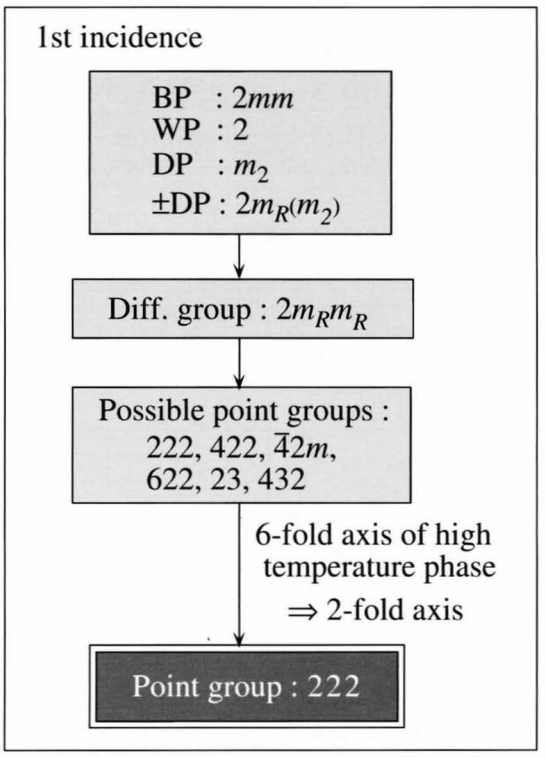

Hexagonal $BaTiO_3$ undergoes two phase transformations at 222K and 74K. The high temperature phase above 222K has a hexagonal space group $P6_3/mmc$ [a]. From an X-ray diffraction experiment, Yamamoto *et al.* [b] reported that the intermediate phase belongs to the space group $C222$. Akishige *et al.* [c] measured the lattice parameters as functions of temperature. The parameters are $a_o = a$ = 0.573 nm, $b_o = (a + b)/2$ = 0.989 nm, and $c_o = c$ = 1.394 nm at 100K, where a and c are the lattice parameters of the hexagonal phase. The low temperature phase below 74K is expected to have a point group $mm2$ or 2.

We intend to conduct crystal-structure determination of the intermediate phase. In advance of the determination, we identified the space groups of the intermediate and low temperature phases.

References

[a] H. T. Evans, Jr. and R. D. Burbank: *J. Chem. Phys.*, **16** (1948) 634.

[b] T. Yamamoto, Y. Akishige and E. Sawaguchi: *J. Phys. Soc. Jpn.*, **57** (1988) 3665.

[c] Y. Akishige, G. Oomi and E. Sawaguchi: *Solid State Commun.*, **65** (1988) 621.

Intermediate phase

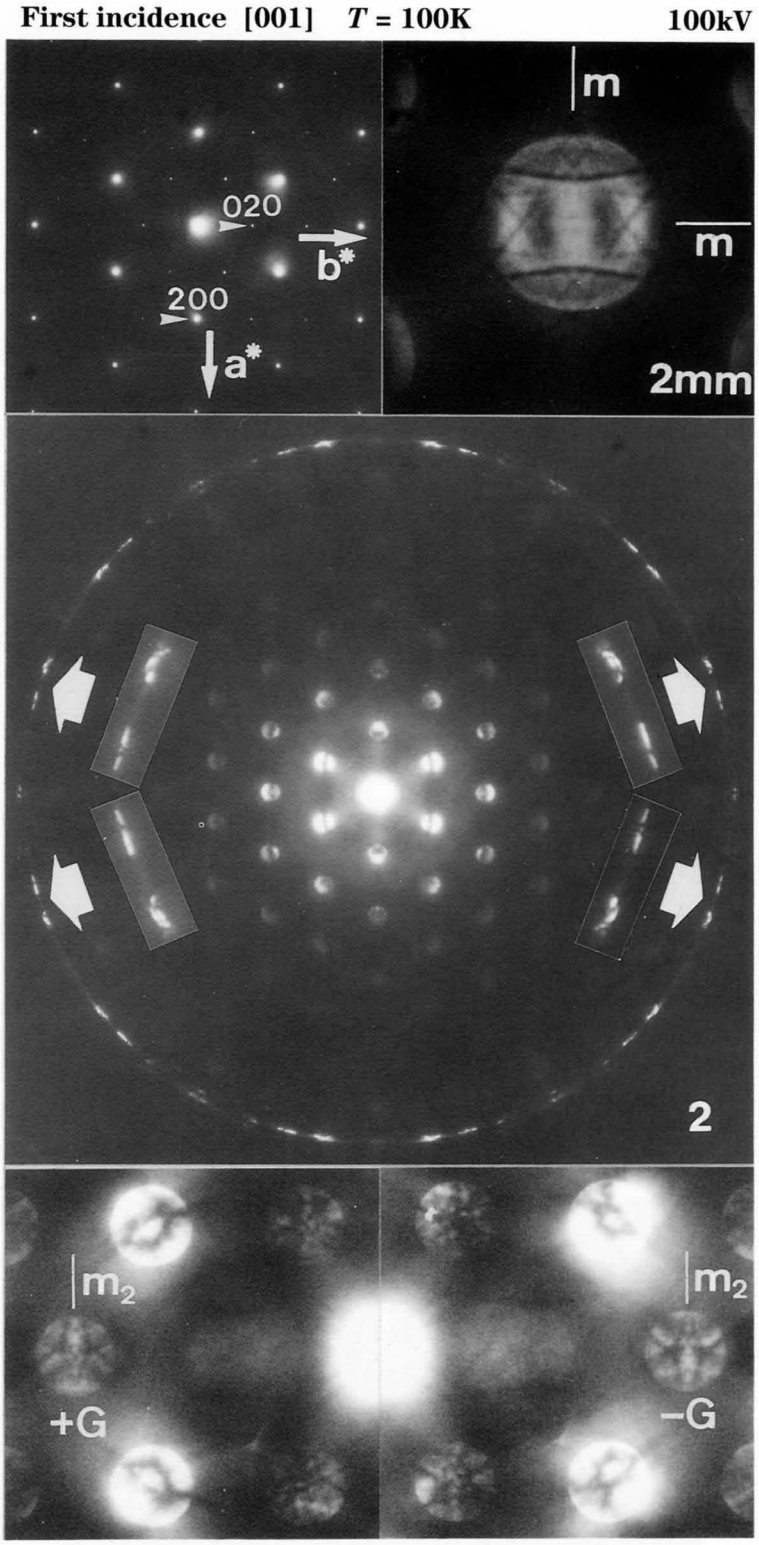

BP: $2mm$

WP: 2

DP: m_2
±DP: $2m_R(m_2)$

Hexagonal $BaTiO_3$ — intermediate phase —

Lattice type and space group

1st incidence [001]

Forbidden reflections :
$h\,k\,0$ ($h+k = 2n+1$)

Possible lattice types :
C and I

2nd incidence [010]

Forbidden reflections :
$h\,0\,l$ ($h = 2n+1$)

Lattice type : C

Point group :
222

Possible space groups :
No. 20 $C222_1$
No. 21 $C222$

First incidence [001]

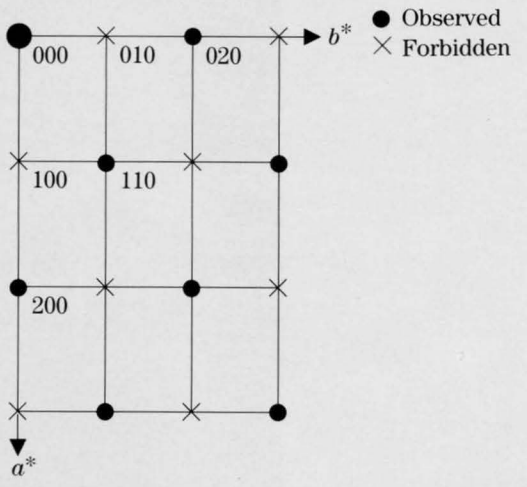

Second incidence [010]

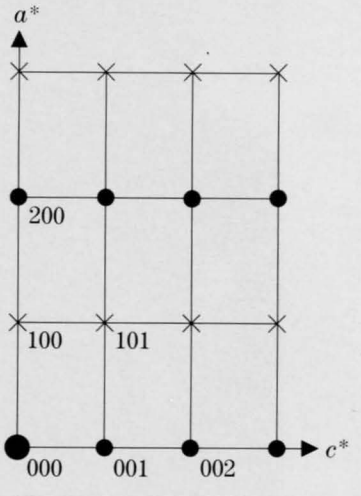

Second incidence [010] **80kV**

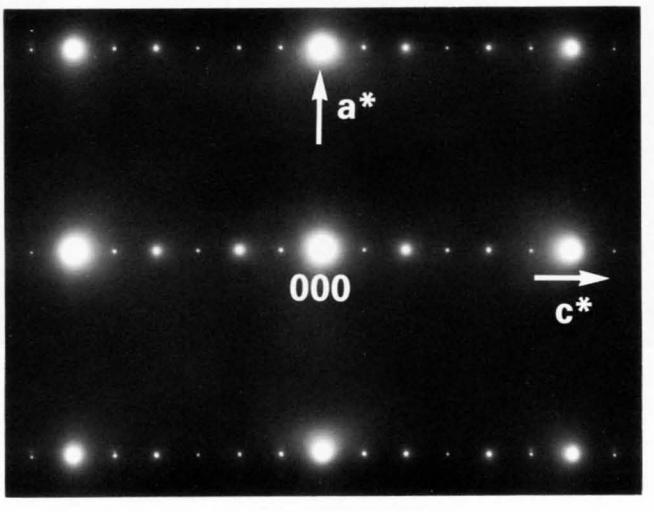

Second incidence [010] T = 100K **80kV**

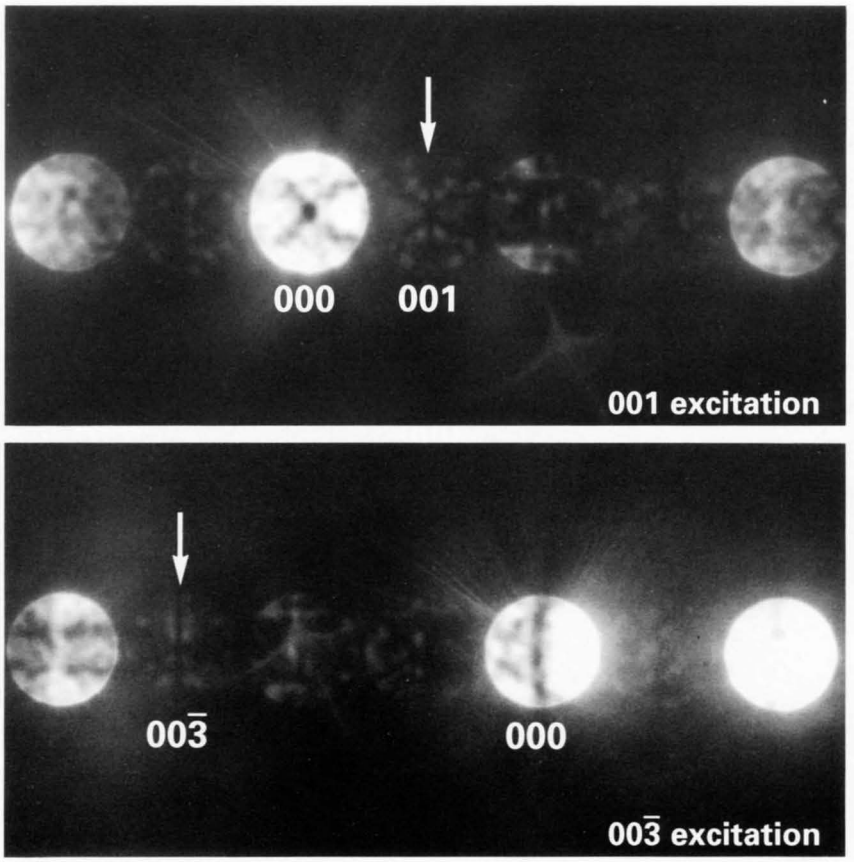

Incident beam direction / Space group	[100]		[010]		[001]	
20 $C222_1$	$00l$ 2_1	A_2 B_2 B_3	$00l$ 2_1	A_2 B_2 B_3		
21 $C222$						

2nd incidence [010]

0 0 l (l = odd) : B_3 GM lines

Space group :
No. 20 $C222_1$

Hexagonal $BaTiO_3$ — intermediate phase —

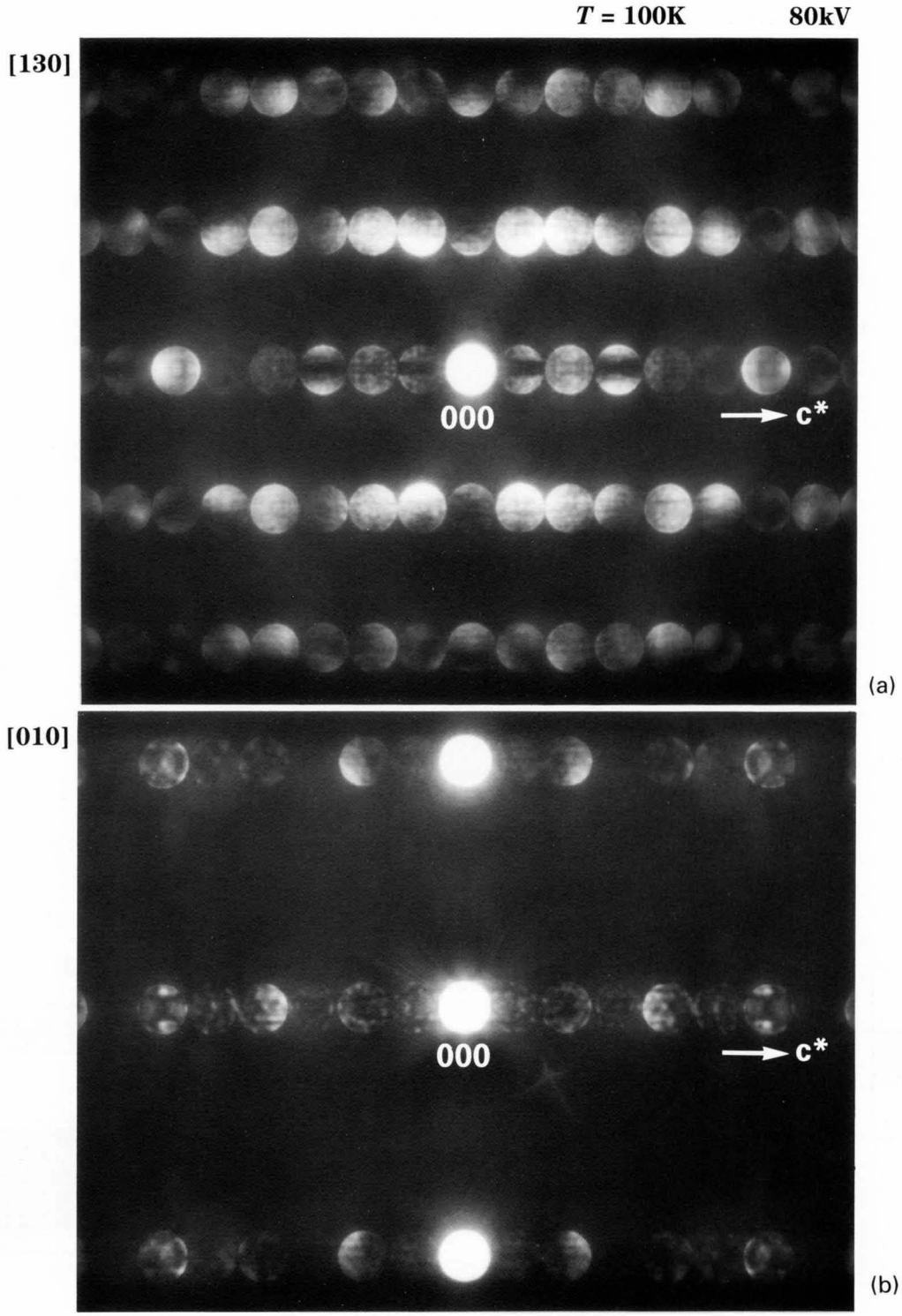

Photographs (a) and (b) show CBED patterns of the intermediate phase of hexagonal $BaTiO_3$ taken at the [130] and [010] incidences, respectively. (a) A_2 GM-lines due to a screw axis are seen because HOLZ lines are weak. (b) A_2 GM-lines are difficult to see because of a strong HOLZ reflection effect, A_3 GM-lines being absent.

Hexagonal $BaTiO_3$ — low temperature phase —

First incidence [001] T **= 22K** **100kV**

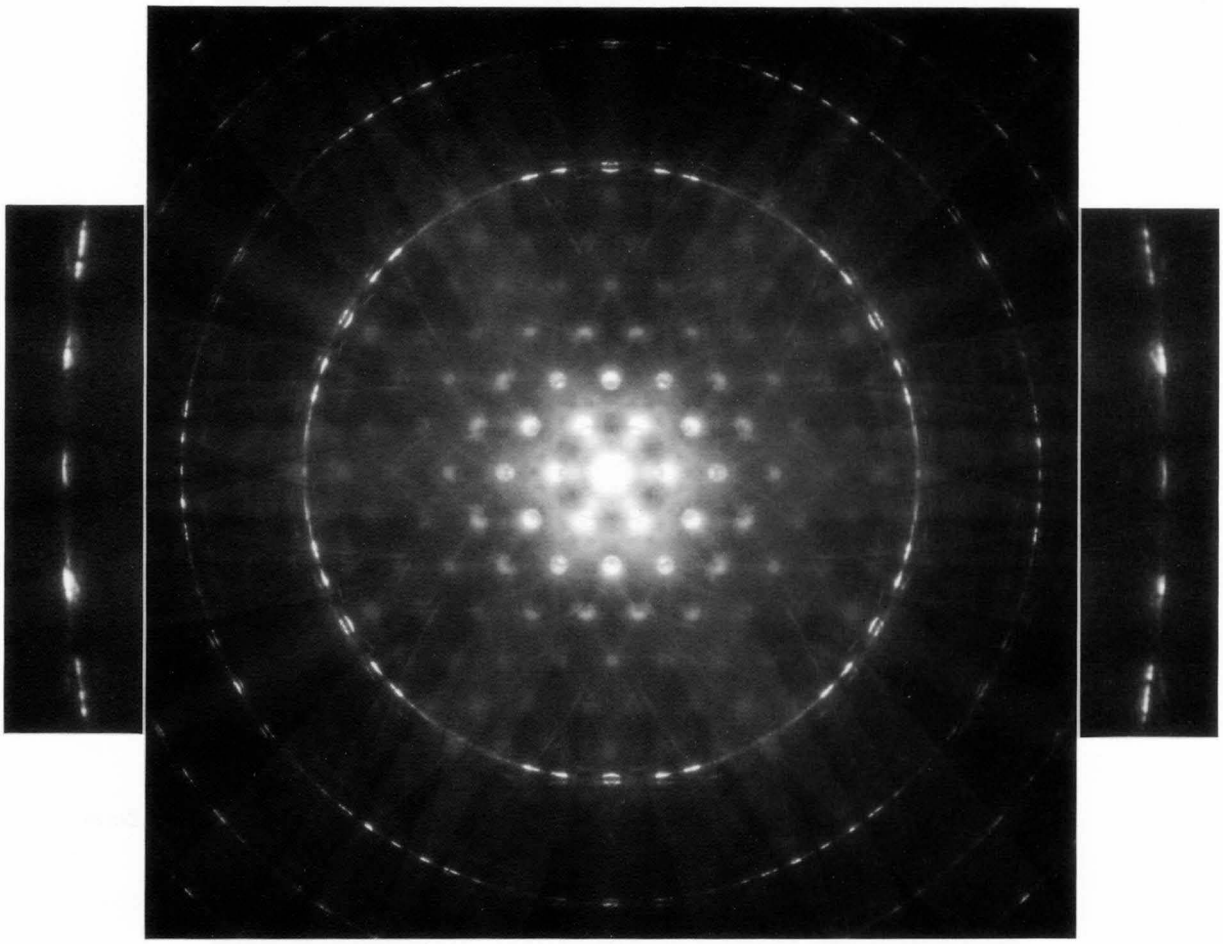

WP: 2

Point group

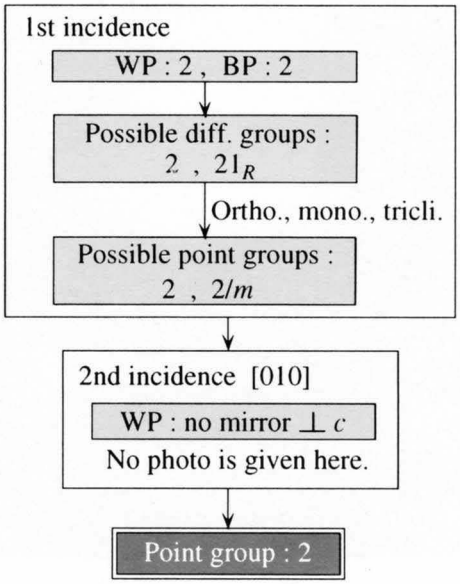

Hexagonal $BaTiO_3$

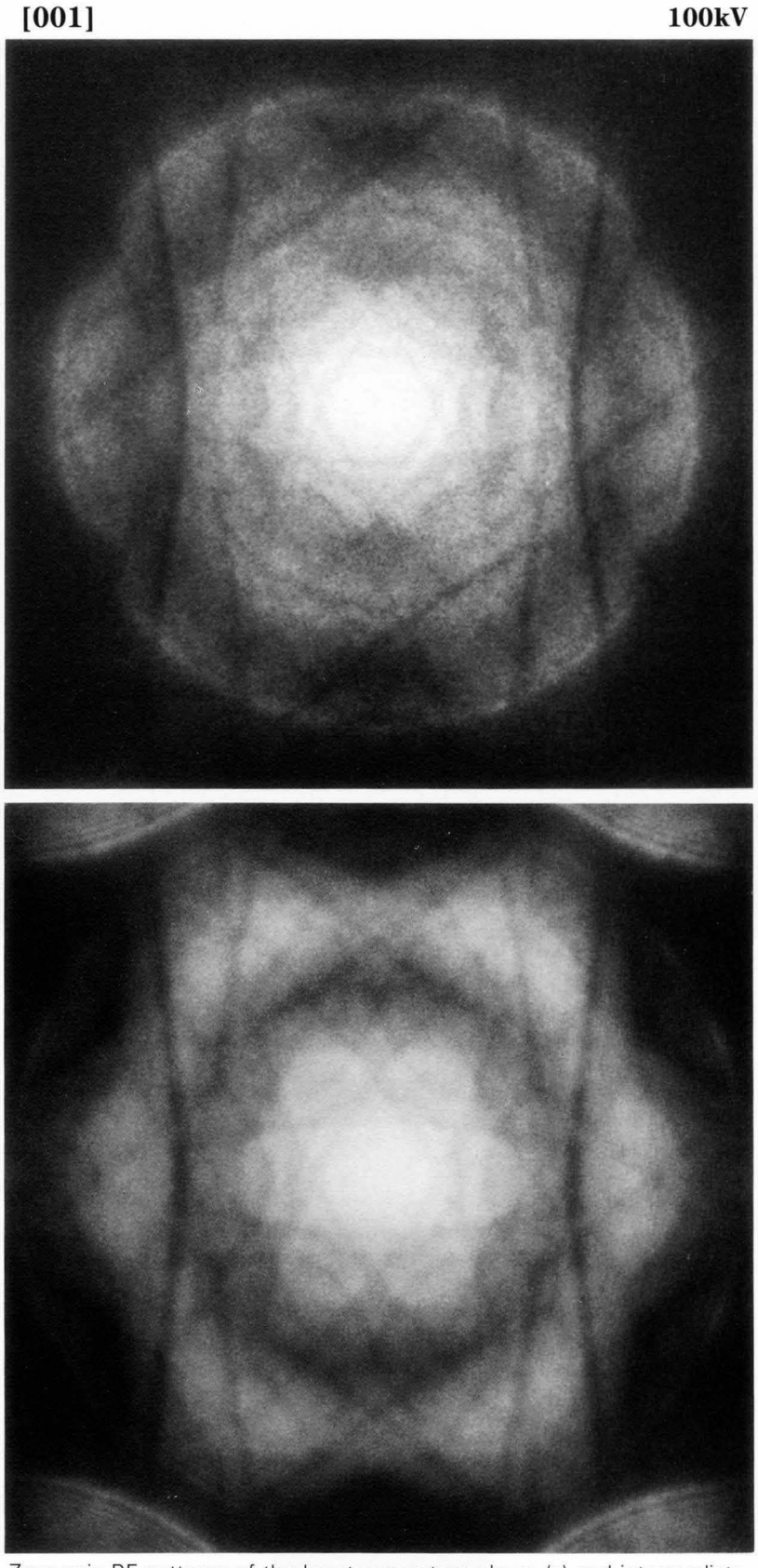

Zone-axis BF patterns of the low temperature phase (a) and intermediate phase (b) of hexagonal $BaTiO_3$, showing symmetries 2 and $2mm$, respectively.

Low temperature phase

Second incidence [010] T = 22K 100kV

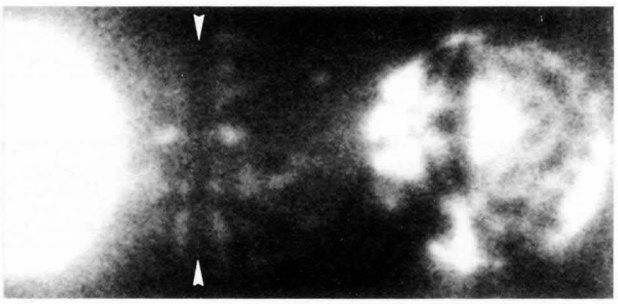

001 **002**

Incident beam direction / Space group	[uv0] (1st setting)	
3 $P2$		
4 $P2_1$	00l 2_1	A_2 B_2 B_3
5 $B2$		

Space group

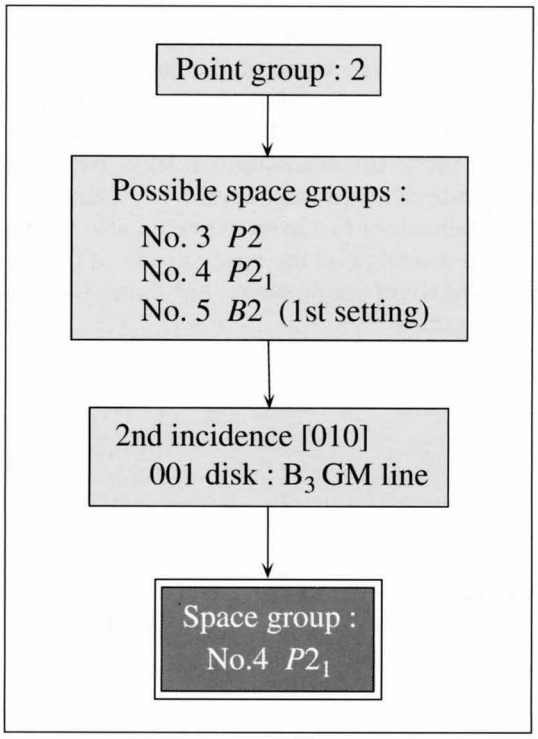

Sm_3Se_4

Sm_3Se_4 takes a Th_3P_4 type structure with the space group $I\bar{4}3d$ at high temperatures. From a measurement of dielectric constant, it has been expected to undergo a phase transformation at 305.5K. Sm_3X_4 (X = S, Se, Te) and Eu_3S_4 have structures of the same type and their valence electrons of metal atoms fluctuate in space and time between +2 and +3 [a]. Eu_3S_4 was found to undergo a phase transformation at 168K, resulting in an ordered state of electrons with the two valences. Thus, a similar behaviour has been expected also in Sm_3Se_4.

We have investigated the space group of the material at 100K and room temperature, but found no change in the space group.

Reference

[a] F. Holtzberg: *Phil. Mag.*, **B42** (1980) 491.

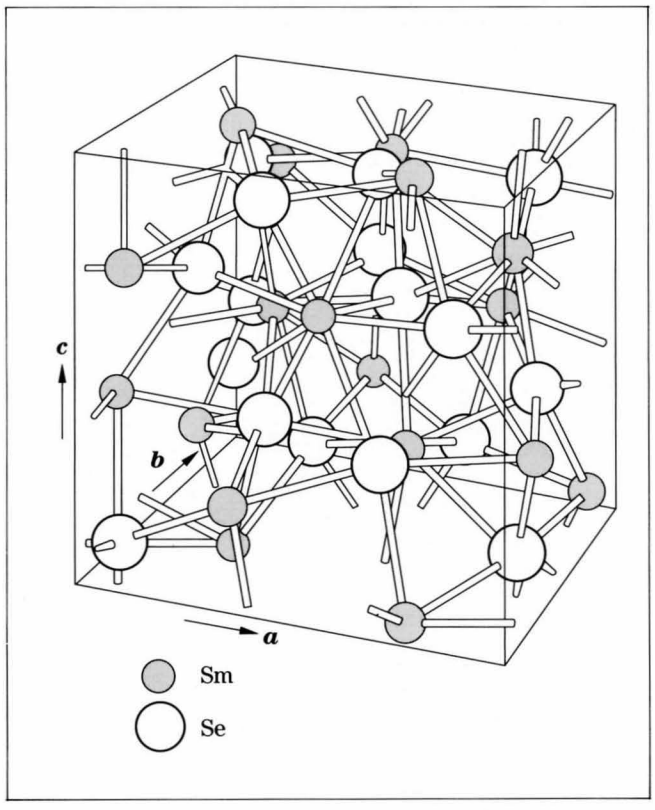

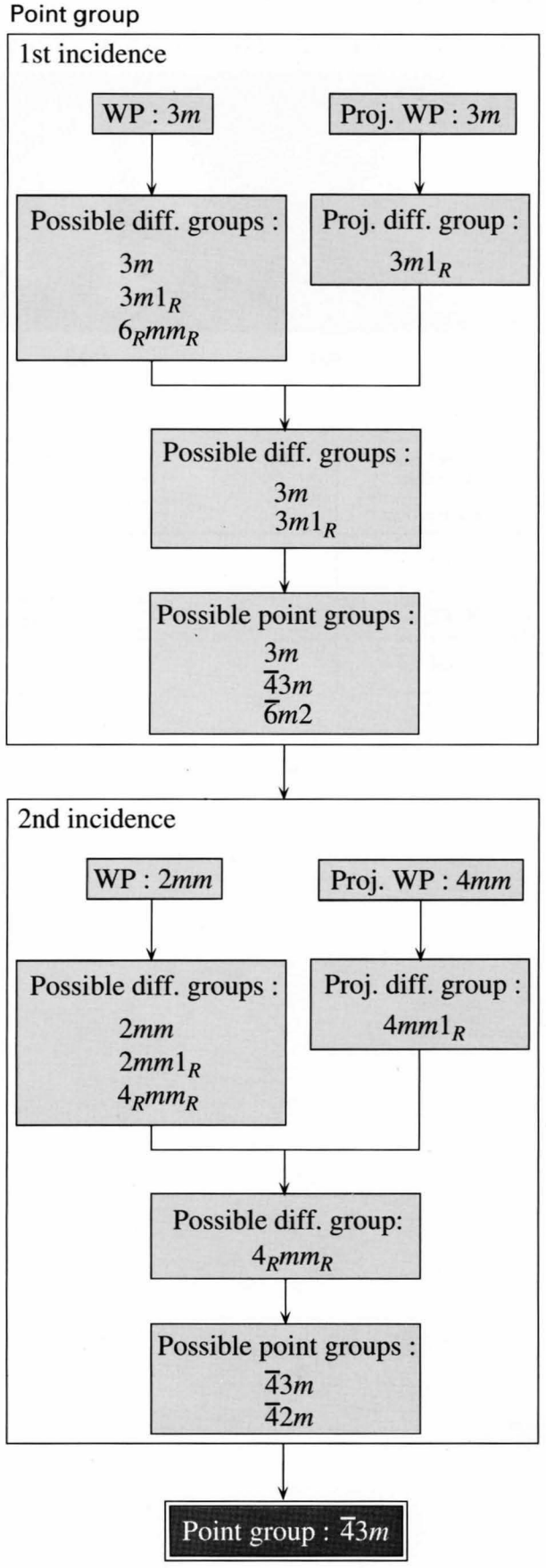

First incidence [111] T **= 100K** **80kV**

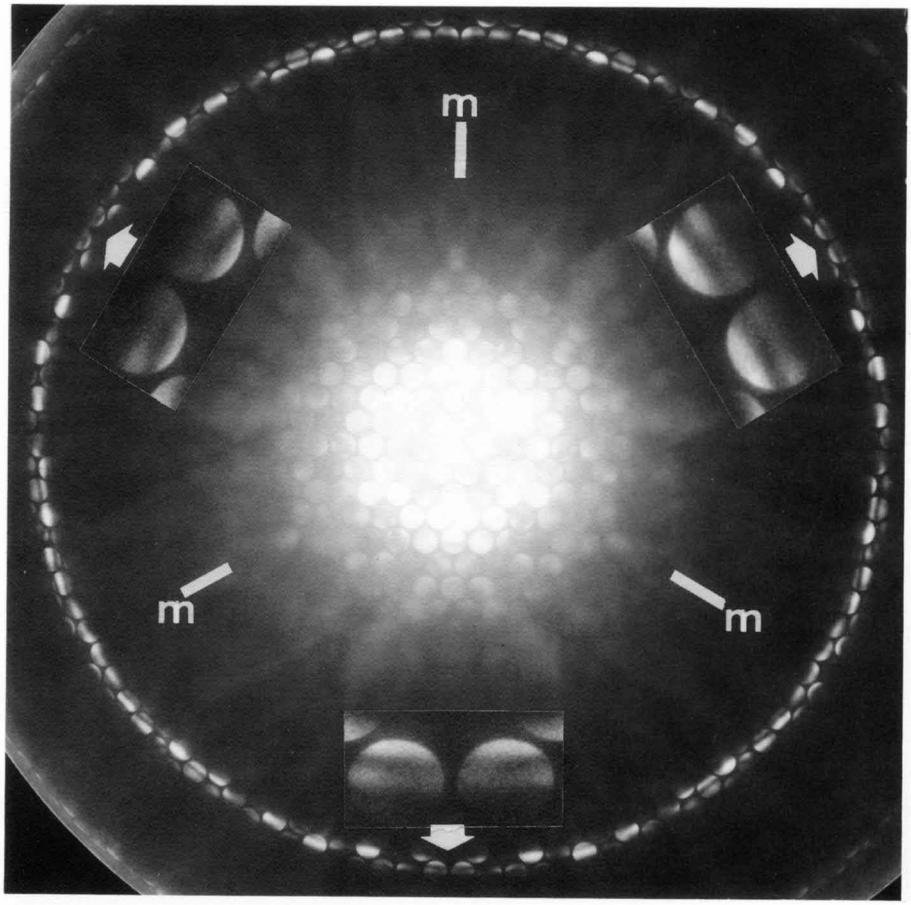

WP: $3m$

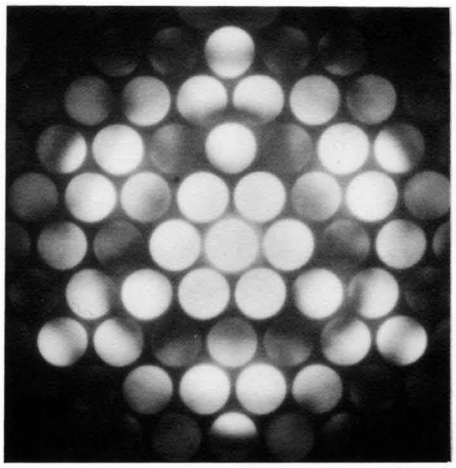

Proj. WP: $3m$

Point group

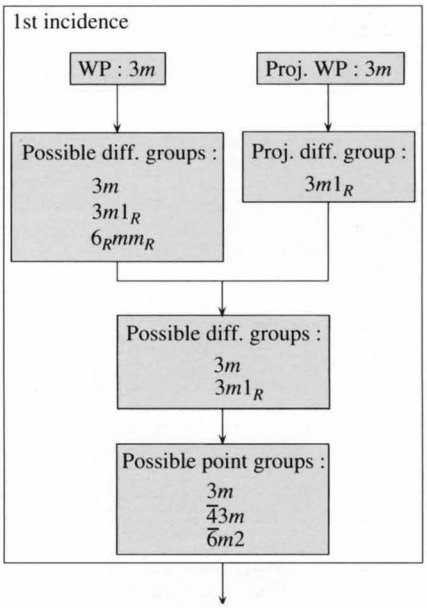

Sm_3Se_4

Second incidence [100] T = 100K **80kV**

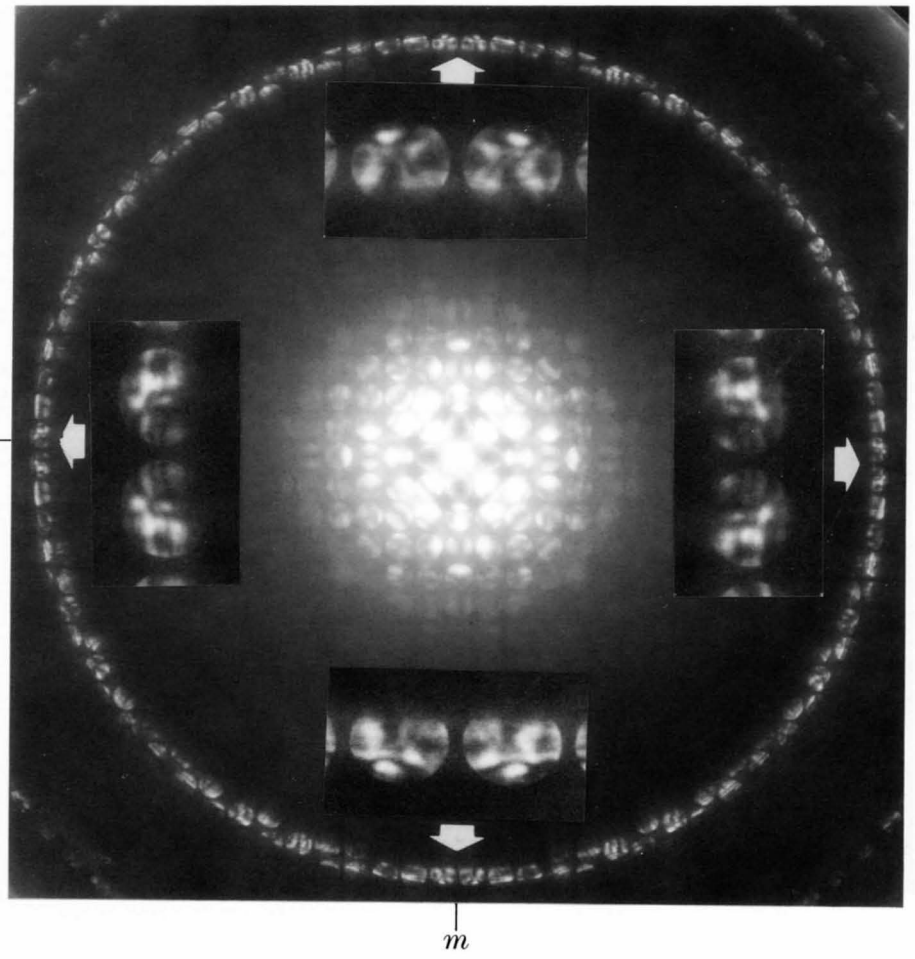

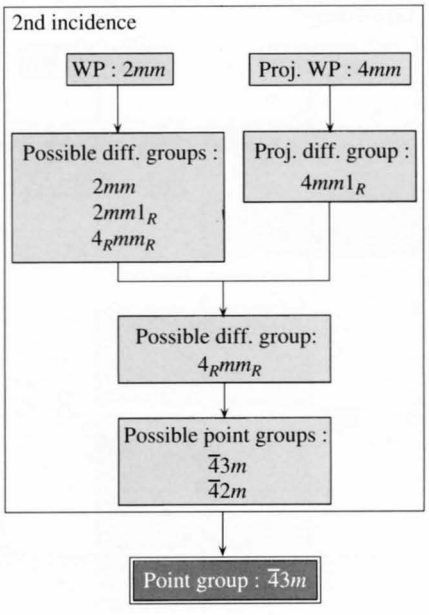

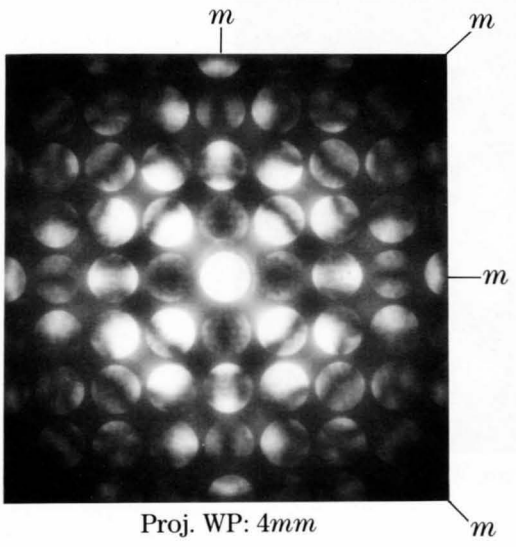

Proj. WP: 4*mm*

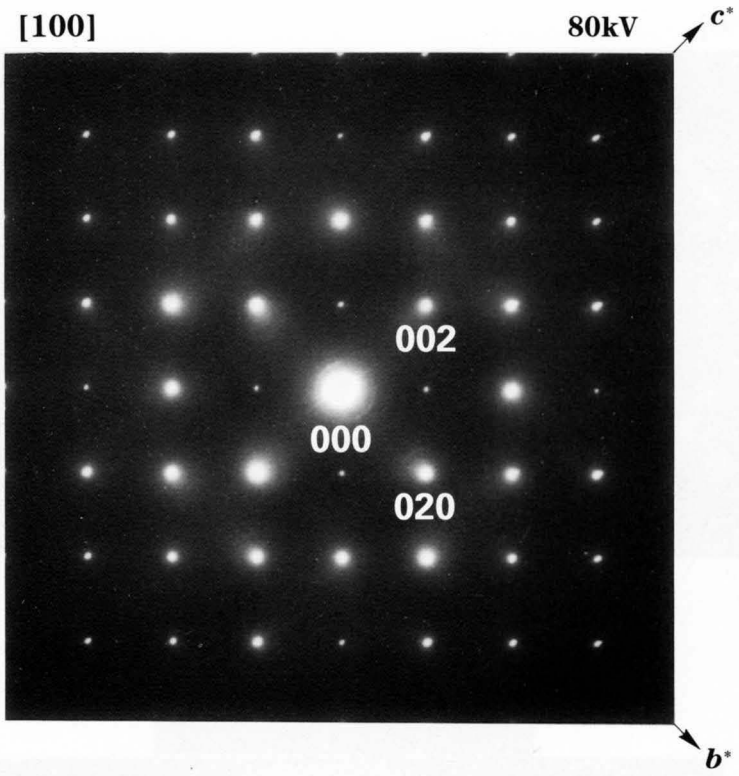

Lattice type

Forbidden reflections
0 *k l* (*k*+*l* = 2*n*+1)

Lattice type : *I*

Sm_3Se_4

[100] **100kV**

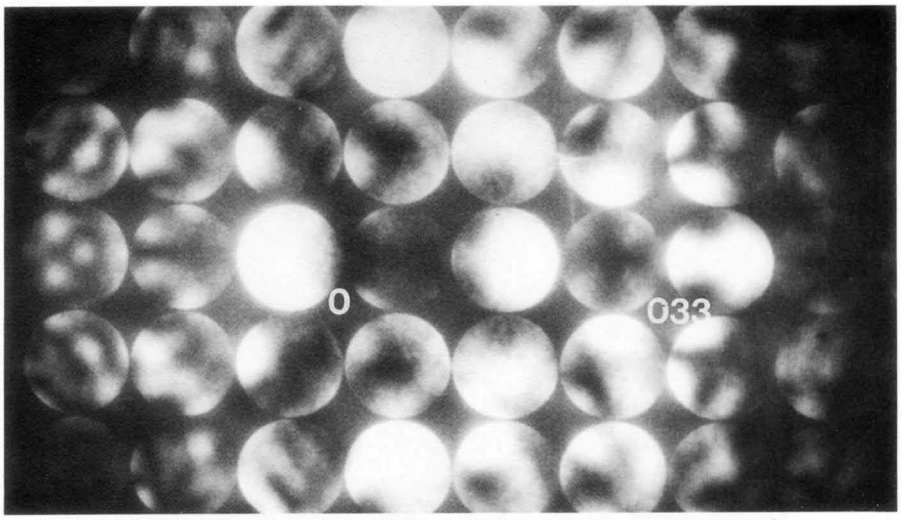

033 excitation

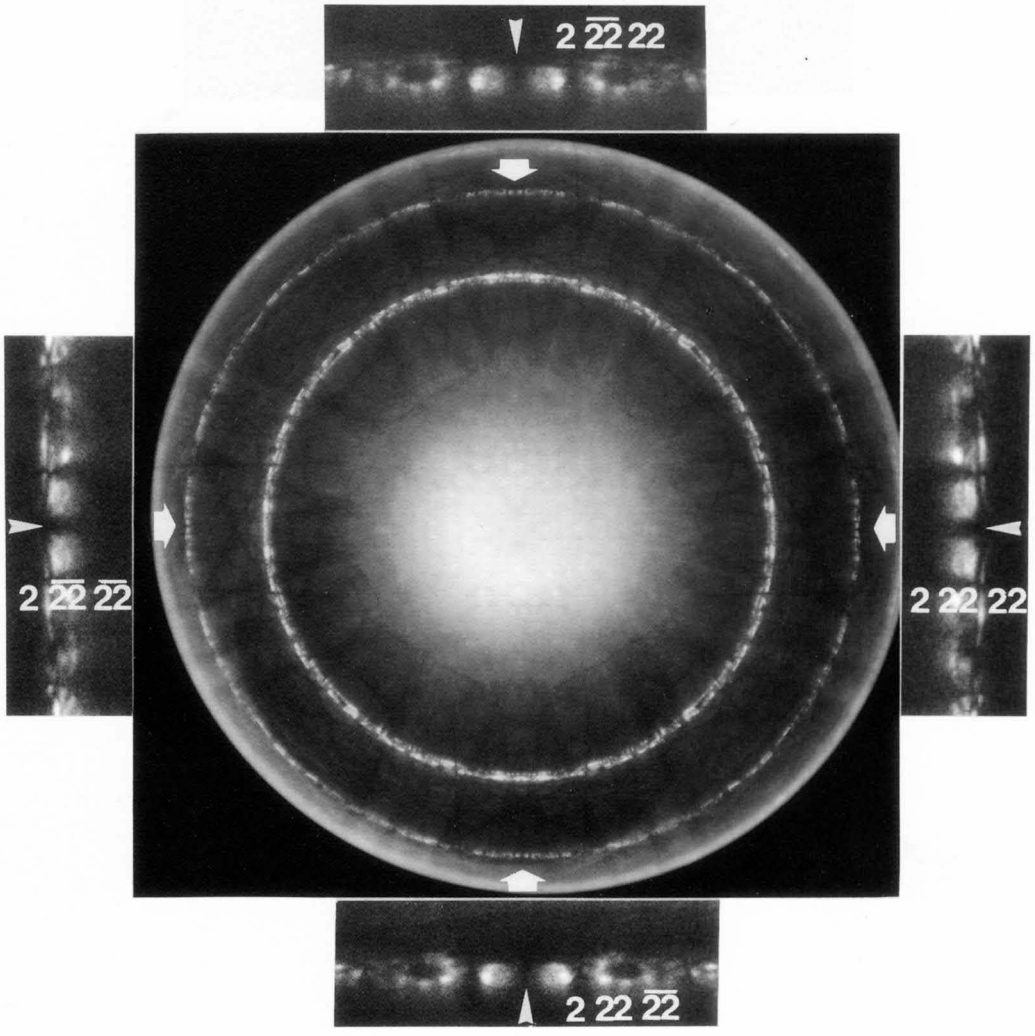

Space group

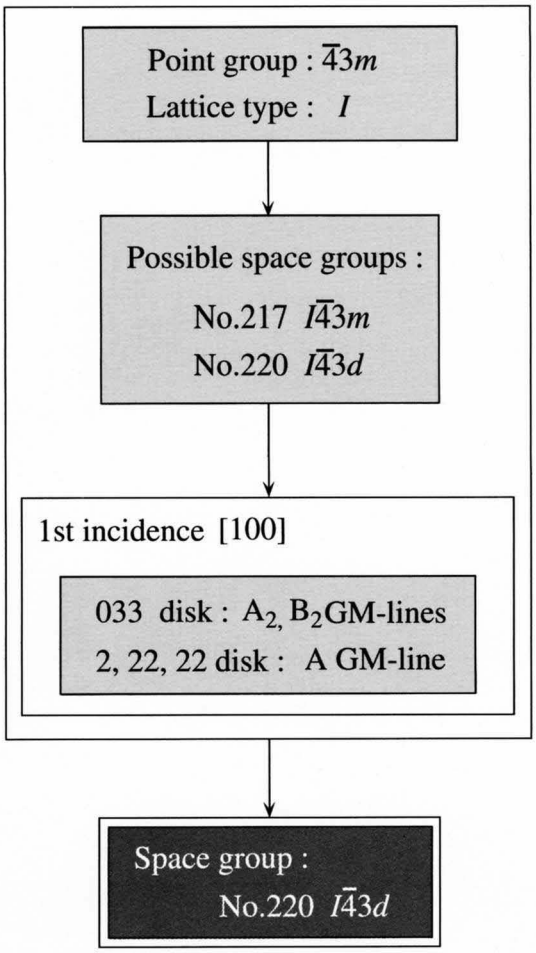

ZOLZ GM line table

Incident beam direction / Space group	[100] (cyclic)	
217 $I\bar{4}3m$		
220 $I\bar{4}3d$	$0kk$ $0\bar{k}k$ d	A_2 B_2 A_3

HOLZ GM line table

Incident beam direction / Space group	[100]	
217 $I\bar{4}3m$		
220 $I\bar{4}3d$	$h_e kk$ $h_e \bar{k}k$ $2k+h_e=4n+2$ d	A

Incommensurate Crystals

Theoretical Background

Displacively modulated crystals

The incommensurately modulated crystals do not have three-dimensional lattice periodicity, and their symmetries are not described by three-dimensional space groups.

The crystals, however, recover lattice periodicity in a space higher than three dimensions. de Wolff [a], [b] showed that one-dimensional displacively and substitutionally modulated crystals can be described as a three-dimensional section of a (3+1)-dimensional periodic crystal. The analysis of incommensurately modulated crystals using (3+1)-dimensional space groups has become familiar in the field of X-ray structure analysis.

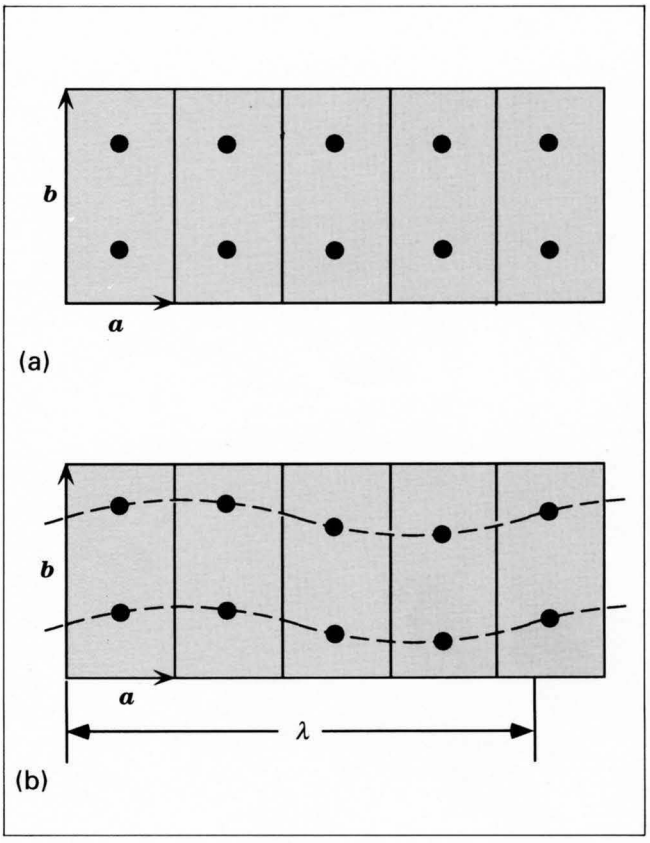

One-dimensional displacively modulated crystal:
(a) without modulation, (b) with modulation of wavelength λ.

References

[a] P. M. de Wolff : *Acta Cryst.*, **A30** (1974) 777.
[b] P. M. de Wolff : *Acta Cryst.*, **A33** (1977) 493.

Infinite crystals

Figures (a) and (b) illustrate (3+1)-dimensional descriptions of a crystal structure without modulation and a one-dimensional displacively modulated structure, respectively. The arrows labeled as $\boldsymbol{a}_1$~$\boldsymbol{a}_3$ and $\boldsymbol{a}_4$ indicate the (3+1)-dimensional crystal axes. The horizontal line labeled as $\boldsymbol{R}_3$ represents a three-dimensional space (real world). In the (3+1)-dimensional description, an atom is not located at a point as in a three-dimensional space but expressed by a string, which extends along the fourth direction $\boldsymbol{a}_4$ perpendicular to the three-dimensional space $\boldsymbol{R}_3$. The shaded parallelogram is a unit cell in the (3+1)-dimensional space. The unit cell contains two atom strings. The straight atom strings in Fig. (a) express a structure without any modulation. The wavy atom strings in Fig. (b), which are periodic along $\boldsymbol{a}_4$, represent a displacive modulation. The width of the atom strings indicates the spread of the atoms in $\boldsymbol{R}_3$. The atom positions of a modulated structure in $\boldsymbol{R}_3$ are given as a three-dimensional section of the atom strings in the (3+1)-dimensional space.

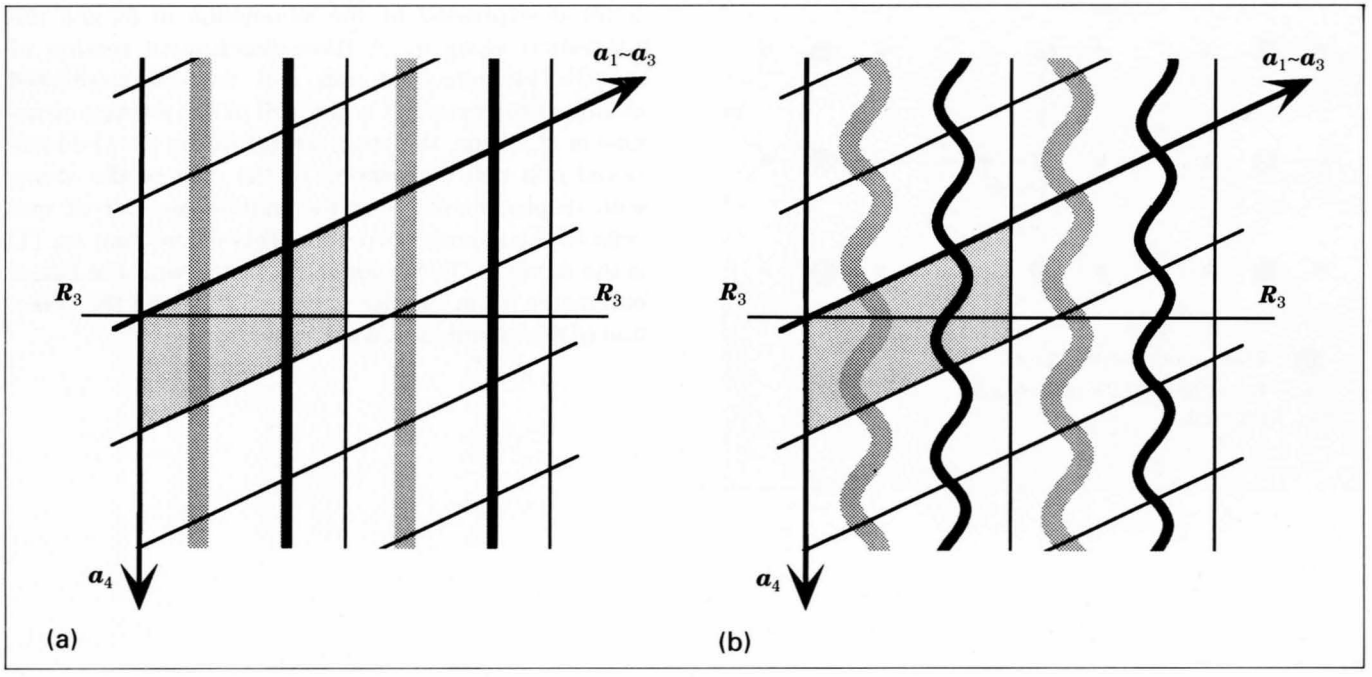

(3+1)-dimensional description of a one-dimensional displacively modulated crystal. Straight strings in (a) express no modulation in atom positions and the wavy strings in (b) represent a displacive modulation.

Diffraction pattern

The diffraction vector $\boldsymbol{G}$ is written as

$$\boldsymbol{G} = h_1\boldsymbol{a}^*+h_2\boldsymbol{b}^*+h_3\boldsymbol{c}^*+h_4\boldsymbol{k},$$

where a set of $h_1h_2h_3h_4$ is a (3+1)-dimensional reflection index, and $\boldsymbol{a}^*$, $\boldsymbol{b}^*$ and $\boldsymbol{c}^*$ are the reciprocal lattice vectors of the real lattice vectors $\boldsymbol{a}$, $\boldsymbol{b}$ and $\boldsymbol{c}$ of the average structure. The modulation wave vector $\boldsymbol{k}$ is written as

$$\boldsymbol{k} = k_1\boldsymbol{a}^*+k_2\boldsymbol{b}^*+k_3\boldsymbol{c}^*,$$

where one coefficient k_i (i = 1–3) is an irrational number and the others are rational. The figure schematically shows a diffraction pattern of a crystal with an incommensurate modulation wave vector $k_1\boldsymbol{a}^*$ ($k_2 = k_3 = 0$). The large black circles and the small ones respectively represent the fundamental and incommensurate reflections, only the first-order incommensurate reflections being shown.

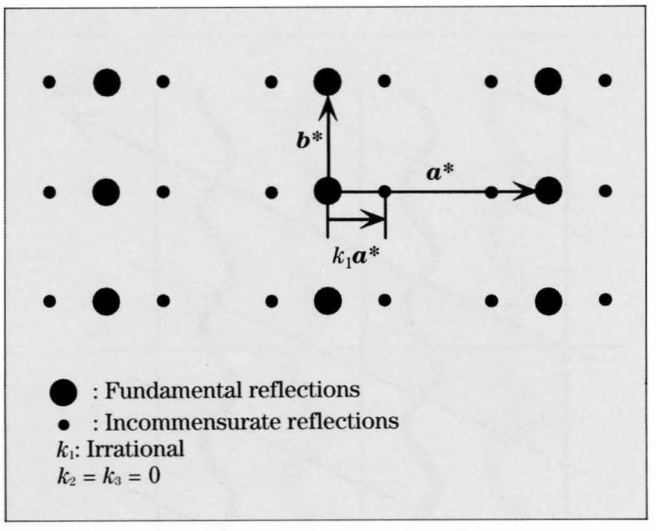

Structure factor

The structure factor $F(h_1h_2h_3h_4)$ for the (3+1)-dimensional crystal is given by de Wolff ([a] , [b] on page 72) as follows:

$$F(h_1h_2h_3h_4) = \sum_{\mu=1}^{N} f_\mu \exp 2\pi i\,(h_1\overline{x_1^\mu}+h_2\overline{x_2^\mu}+h_3\overline{x_3^\mu})$$

$$\times\int_0^1 \exp 2\pi i \left\{\sum_{i=1}^{3}(h_i+h_4k_i)u_i^\mu+h_4\overline{x_4^\mu}\right\}\mathrm{d}\overline{x_4^\mu}, \quad (1)$$

where

$$\overline{x_4^\mu} = (\overline{x_1^\mu}+n_1)k_1+(\overline{x_2^\mu}+n_2)k_2+(\overline{x_3^\mu}+n_3)k_3$$

The symbols f_μ and $\overline{x_i^\mu}$(i = 1–3) are respectively the atom form factor and the i-th component of the position of the μ-th atom in the unit cell of the average structure. The symbol u_i^μ is the i-th component of the displacement from the atom position of the μ-th atom. Since the atom in the (3+1)-dimensional space is continuous along $\boldsymbol{a}_4$ and discrete along $\boldsymbol{R}_3$, the structure factor is expressed by the summation in $\boldsymbol{R}_3$ and the integration along $\boldsymbol{a}_4$. A three-dimensional section of the (3+1)-dimensional unit cell gives a modulated atomic arrangement at a unit cell of the average structure in $\boldsymbol{R}_3$. Thus, the atom-strings in the (3+1)-dimensional unit cell correspond to the sum of the atoms with displacements over the infinite number of unit cells of the average structure. This means that eq. (1) is the structure factor for the unit cell with the lattice parameter of an infinite length in $\boldsymbol{R}_3$ along the direction of the modulation wave vector $\boldsymbol{k}$.

Finite crystals

CBED patterns are obtained from a finite area of a crystal. Hence, it is necessary to use the structure factor which takes account of the effect of the finite size, to discuss the symmetries of the CBED patterns obtained from the modulated structures [a]. A finite volume of a modulated structure in $\boldsymbol{R}_3$ corresponds to a finite number of the three-dimensional sections of the atom-strings in a (3+1)-dimensional unit cell, as indicated in the figure.

The structure factor for the finite volume is derived from eq. (1) by rewriting the integration over a unit length along $\boldsymbol{a}_4$ with the summation over a finite number of three-dimensional sections of the atom strings. Thus, the structure factor for the finite volume $F'(h_1h_2h_3h_4)$ is written as

$$F'(h_1h_2h_3h_4) = \sum_{\mu=1}^{N} f_\mu \exp 2\pi i\,(h_1\overline{x_1^\mu}+h_2\overline{x_2^\mu}+h_3\overline{x_3^\mu}) \times\left[\sum_{n_1}\sum_{n_2}\sum_{n_3}\exp 2\pi i\left\{\sum_{i=1}^{3}(h_i+h_4k_i)u_i^\mu+h_4\overline{x_4^\mu}\right\}\right], \quad (2)$$

where $N_1<n_1\leq N_1'$, $N_2<n_2\leq N_2'$, $N_3<n_3\leq N_3'$, and $N'=(N_1'-N_1)(N_2'-N_2)(N_3'-N_3)$ is the number of unit cells of the average structure included in the specimen volume from which CBED patterns are taken. The term in [ ] in eq.(2) expresses the effect of the finite volume on the diffraction intensity.

Reference

[a] M. Terauchi and M. Tanaka : *Acta Cryst.*, **A49** (1993) 722.

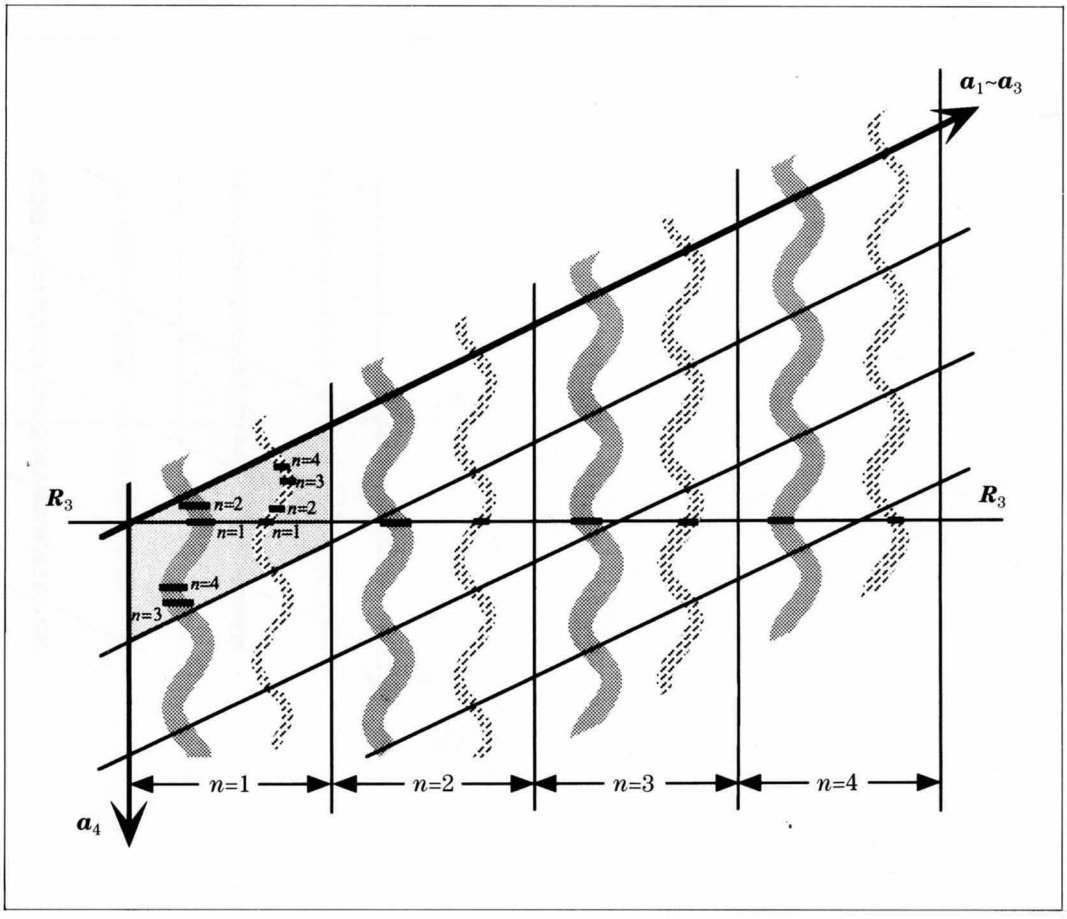

Substitutionally modulated crystals

The substitutional modulation arises from a periodic variation of the site occupation probability of atoms. This type of modulated structures is also described by the (3+1)-dimensional periodic structure. This type of modulation does not originate from the modulation of the atom displacement u_i^{μ} with x_4 as in the case of the displacive type, but is expressed by the modulation of the atom form factor f_{μ} in eq. (1) with x_4. The modulation is schematically shown in Fig.(a), and is expressed in the (3+1)-dimensional space by strings with density modulation (Fig.(b)), instead of wavy strings. The structure factor $F'(h_1h_2h_3h_4)$ for finite crystals with this type of modulation is written as

$$F'(h_1h_2h_3h_4) = \sum_{\mu=1}^{N} \exp 2\pi i\,(h_1x_1^{\mu}+h_2x_2^{\mu}+h_3x_3^{\mu}) \times\left\{\sum_{n_1}\sum_{n_2}\sum_{n_3} f_{\mu}(x_4^{\mu})\exp(2\pi i h_4 x_4^{\mu})\right\},$$

where $\quad x_4^{\mu} = \sum_i (x_i^{\mu}+n_i)k_i.$

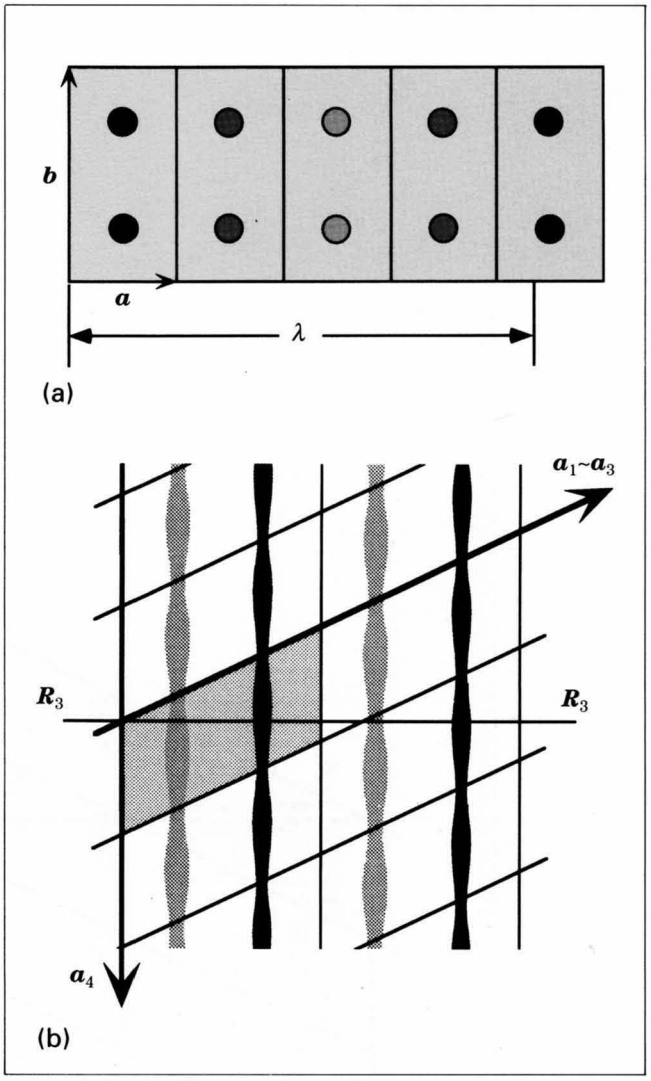

Figure (a) shows a (3+1)-dimensional representation of a displacively modulated crystal. The modulated structure in three dimensions is obtained by a three-dimensional section of the (3+1)-dimensional periodic structure. The diffraction pattern (Fig. (b)) of the modulated crystal is obtained by a projection of the Fourier transform of the (3+1)-dimensional periodic structure.

Reference

[a] K. N. Ishihara and A. Yamamoto : *Acta Cryst.*, **A44** (1988) 508.

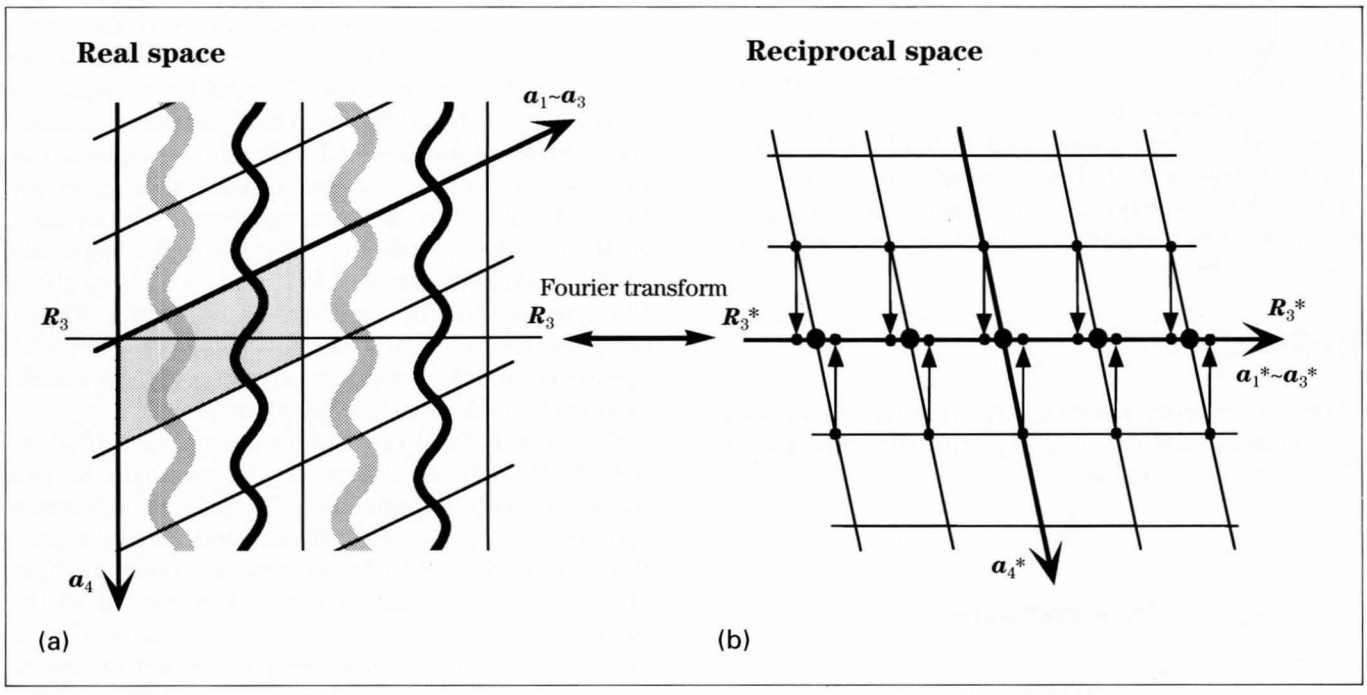

Point-Group Determination

$P^{P2/m}_{1\ \bar{1}}$

The symmetries of the CBED patterns can be determined by examination of the symmetries of the structure factor $F'(h_1h_2h_3h_4)$ or eq.(2). For simplicity, we assume that the modulation wave vector of a displacively modulated crystal is written as $\boldsymbol{k} = k_3\boldsymbol{c}^*$ and that the modulated structure belongs to the (3+1)-dimensional space group $P^{P2/m}_{1\ \bar{1}}$. This space group symbol indicates the following matters.

(i) The modulation wave vector $\boldsymbol{k}$ exists inside the first Brillouin zone for the average structure (P).

(ii) The average structure belongs to the space group $P2/m$, the twofold rotation axis being parallel to the c-axis.

(iii) The symmetry subsymbol 1, which is written beneath symmetry symbol 2 in the expression for the (3+1)-dimensional space group, indicates that the modulation wave vector $\boldsymbol{k}$ is transformed into itself by symmetry operation 2 of the average structure. The symmetry subsymbol $\bar{1}$, which is written beneath symmetry symbol m , indicates that the modulation wave vector $\boldsymbol{k}$ is transformed into $-\boldsymbol{k}$ by symmetry operation m.

The modulated structure has a twofold rotation axis, which is common to both average and modulated structures (subsymbol 1), but does not have a mirror symmetry, which is possessed by the average structure (subsymbol $\bar{1}$).

$P^{P\,2\,/m}_{1\ \bar{1}}$

For the twofold rotation axis (symbol 2) of this (3+1)-dimensional space group, the structure factor $F'(h_1h_2h_3h_4)$ is written as

$$
\begin{aligned}
&F'(h_1h_2h_3h_4)\\
&\quad=\sum_{\mu=1}^{N} f_\mu \exp 2\pi i\,(h_1\overline{x_1^\mu}+h_2\overline{x_2^\mu}+h_3\overline{x_3^\mu})\\
&\quad\times\Big[\sum_{n_3}\exp 2\pi i\left\{h_1u_1^\mu+h_2u_2^\mu+(h_3+h_4k_3)u_3^\mu+h_4\overline{x_4^\mu}\right\}\Big]\\
&\quad+\sum_{\mu=1}^{N} f_\mu \exp 2\pi i\,(-h_1\overline{x_1^\mu}-h_2\overline{x_2^\mu}+h_3\overline{x_3^\mu})\\
&\quad\times\Big[\sum_{n_3}\exp 2\pi i\left\{-h_1u_1^\mu-h_2u_2^\mu+(h_3+h_4k_3)u_3^\mu+h_4\overline{x_4^\mu}\right\}\Big],
\end{aligned}
\tag{4}
$$

where $\overline{x_4^\mu} = (\overline{x_3^\mu}+n_3)k_3$. The terms within [ ] in eq.(4) represent the effect of the finite volume on the diffraction intensity.

We consider the reflections $h_1h_2h_3h_4$ and $\bar{h}_1\bar{h}_2h_3h_4$, which are equivalent with respect to the twofold rotation axis of the average structure. It is clear from eq. (4) that the structure factor $F'(\bar{h}_1\bar{h}_2h_3h_4)$ is equal to $F'(h_1h_2h_3h_4)$. Hence, the intensities of the $h_1h_2h_3h_4$ and $\bar{h}_1\bar{h}_2h_3h_4$ reflections are equal. That is, not only the fundamental reflections (h_4=0) due to the average structure but also the reflections ($h_4\neq0$) due to the modulated structure (incommensurate reflections) show the twofold rotation symmetry about the c^*-axis.

$P^{P2/\,m}_{1\ \bar{1}}$

For the mirror plane (symbol m), the structure factor can be obtained in a similar manner to the case of the twofold rotation axis. It is seen that $F'(h_1h_2h_3h_4)$ is not equal to $F'(h_1h_2\bar{h}_3\bar{h}_4)$ for the incommensurate reflections $h_4 \neq 0$. Hence, the intensity of the $h_1h_2h_3h_4$ reflection is not equal to that of the $h_1h_2\bar{h}_3\bar{h}_4$ reflection.

For the fundamental reflections ($h_4 = 0$), the intensity of the $h_1h_2h_30$ reflection is equal to that of the $h_1h_2\bar{h}_30$ reflection because $F'(h_1h_2h_30)$ is equal to $F'(h_1h_2\bar{h}_30)$. It should be noted that this mirror symmetry m between fundamental reflections is expected to be destroyed by the dynamical diffraction effect between fundamental and incommensurate reflections. In most modulated structures, however, the amplitude of the modulation wave u_i^μ is not so large as to affect the symmetry of the fundamental reflections. Therefore, the fundamental reflections ought to show the symmetry of the average structure, while the incommensurate reflections lose this symmetry.

Equations (2) and (4) hold for any number of N', N_i and N_i' (i=1–3). A change of the numbers N_i and N_i'(i=1–3) with the number N' kept constant corresponds to a change of the illuminated specimen position, from which CBED patterns are taken without changing the illuminated volume. A change of all the numbers N', N_i and N_i' (i=1–3) corresponds to a change in both the illuminated volume and the specimen position. With these changes the magnitude of the structure factor changes, but the symmetry of the structure factor is unchanged. Even if the number N' is reduced to one, eqs. (2) and (4) still hold. This indicates that the symmetry of the incommensurately modulated structure ought to appear in principle even in a CBED pattern taken from one unit cell of the average structure.

In the substitutional modulation case, the atom form factor f_μ cannot be determined by one unit cell of the average structure but is determined by the average over a large number of unit cells. Thus, the symmetries of this type of modulated structure are not determined from one unit cell of the average structure, as in the case of the displacively modulated structure. Since CBED patterns, however, are taken usually from a specimen volume of ~10nm diameter × ~100nm thickness, the volume is large enough to obtain the average value of the occupation or the average atom form factor. Therefore, the CBED patterns taken with a usual electron probe exhibit (3+1)-dimensional symmetries also for substitutionally modulated crystals.

Wave vector transformation	Point-group symbol	Symmetry of incom. reflection
$\boldsymbol{k} \rightarrow \boldsymbol{k}$	1	Same symmetry as average structure
$\boldsymbol{k} \rightarrow -\boldsymbol{k}$	$\bar{1}$	No symmetry

General rules

The results obtained are summarized into the following rules:

Rule 1 : For symmetry subsymbol 1, both the fundamental and incommensurate reflections show the symmetries of the average structure.

Rule 2 : For symmetry subsymbol $\bar{1}$, the fundamental reflections practically show the symmetries of the average structure but the incommensurate reflections do not have any symmetry.

The rules imply that the symmetries of incommensurate reflections are determined by the point group of the average structure and the modulation wave vector $\boldsymbol{k}$. Observation of the symmetries of incommensurate reflections ascertains the point groups of modulated crystals but the point groups are identified without examination of the symmetries of the incommensurate reflections.

Remarks

Remark (a) : Even if the size and position of an illuminated specimen area are changed, the intensity distribution in the CBED pattern changes but the symmetry of the pattern does not.

Remark (b) : The symmetries of the modulated structures can appear in CBED patterns when more than one unit cell of the average structure is illuminated for the displacive modulation case and when a specimen volume enough to obtain the average atom form factor, namely, an area ~10nm in diameter, is illuminated for the substitutional modulation case.

To obtain the symmetries expected from the (3+1)-dimensional symmetry symbols, it is not necessary to take the CBED pattern from such a large specimen area whose diameter is larger than the approximate period of the modulated structure (the approximate least common multiple between the modulation wavelength and the unit cell length of the average structure).

$Sr_2Nb_2O_7$

Many materials of the $A_2B_2O_7$ family undergo phase transformations from the space group $Cmcm$ to $Cmc2_1$ and further to $P2_1$ with decreasing temperature. An incommensurate phase appears, for example, between the phase with $Cmc2_1$ and that with $P2_1$ in $La_2Ti_2O_7$ [a]. $Sr_2Nb_2O_7$ transforms at 488K from the phase with $Cmc2_1$ into the incommensurate phase with a modulation wave vector of $\boldsymbol{k} = (1/2-\delta)\boldsymbol{a}^*$ ($\delta = 0.009$–0.023) but does not transform into the phase with $P2_1$. The symmetry of the incommensurately modulated structure of $Sr_2Nb_2O_7$ is expressed by the (3+1)-dimensional space group $P^{Cmc2_1}_{\bar{1}s\bar{1}}$[b]. Thus, the (3+1)-dimensional point group of the structure is written as $\begin{smallmatrix} mm2 \\ \bar{1}\,1\,\bar{1} \end{smallmatrix}$. For the description of symbols, refer to page 84. The symbol implies the following. The modulation wave vector $\boldsymbol{k}$ is transformed to $-\boldsymbol{k}$ by a mirror symmetry operation perpendicular to the a-axis ($^m_{\bar{1}}$) and by a twofold rotation-symmetry operation along the c-axis ($^2_{\bar{1}}$). The wave vector is transformed into itself by a mirror symmetry perpendicular to the b-axis($^m_1$) .

$\begin{smallmatrix} m\,m\,2 \\ \bar{1}\;1\;\bar{1} \end{smallmatrix}$

The photograph shows a CBED pattern of the incommensurate phase of $Sr_2Nb_2O_7$ obtained with the [010] incidence at an accelerating voltage of 60kV. The reflections indicated by arrowheads are incommensurate reflections due to the modulation. Other reflections are fundamental reflections due to the average structure. The (3+1)-dimensional point-group symmetry ($^m_{\bar{1}}$) about the a-axis and the symmetry ($^2_{\bar{1}}$) about the c-axis are seen in this CBED pattern. When Rule 2 is considered, the symmetry ($^m_{\bar{1}}$) exhibits a mirror symmetry perpendicular to the a^*-axis between the fundamental reflections, but no mirror symmetry between the incommensurate reflections. The same symmetries are expected from symmetry ($^2_{\bar{1}}$) in the framework of the projected potential approximation. The photograph shows these symmetries exactly.

References

[a] M. Tanaka, H. Sekii and K. Ohi : *Jpn. J. Appl. Phys.*, **24** (1985) Suppl.24-2, 814.

[b] N. Yamamoto : *Kotaibutsuri*, **23** (1988) 547.

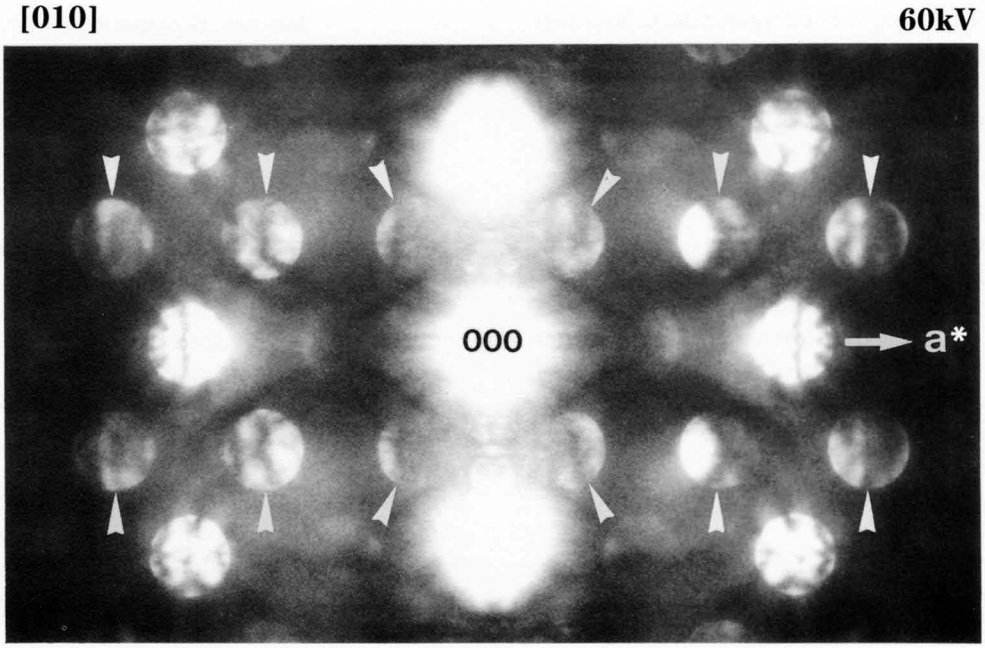

Photograph (a) shows a CBED pattern of the incommensurate phase obtained with the [201] incidence at an accelerating voltage of 60kV. The reflections in two rows indicated by arrowheads are the incommensurate reflections. The other reflections are fundamental ones. The (3+1)-dimensional point group symmetry about the b-axis ($^{m}_{1}$) is seen in this pattern. From Rule 1, the symmetry ($^{m}_{1}$) displays a mirror symmetry perpendicular to the b^*-axis not only between the fundamental reflections but also between the incommensurate reflections. Photograph (a) clearly shows the mirror symmetry between both kinds of reflections.

Photograph (b) shows a CBED pattern obtained at the same incidence as in Photo (a) but from a different specimen area with nearly the same specimen thickness. The pattern shows the same symmetry as in Photo (a) but the intensity distribution is different. This ascertains Remark (a).

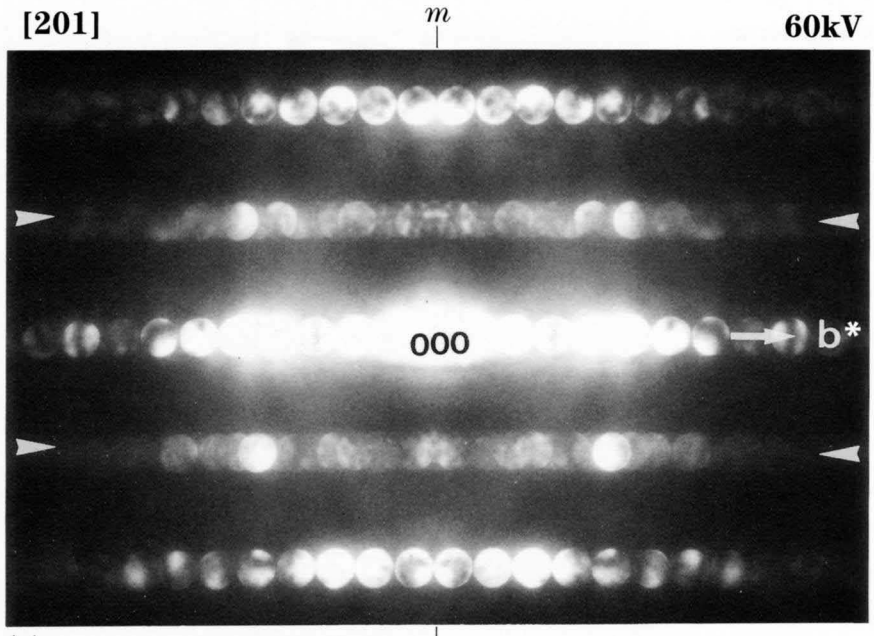

(a)

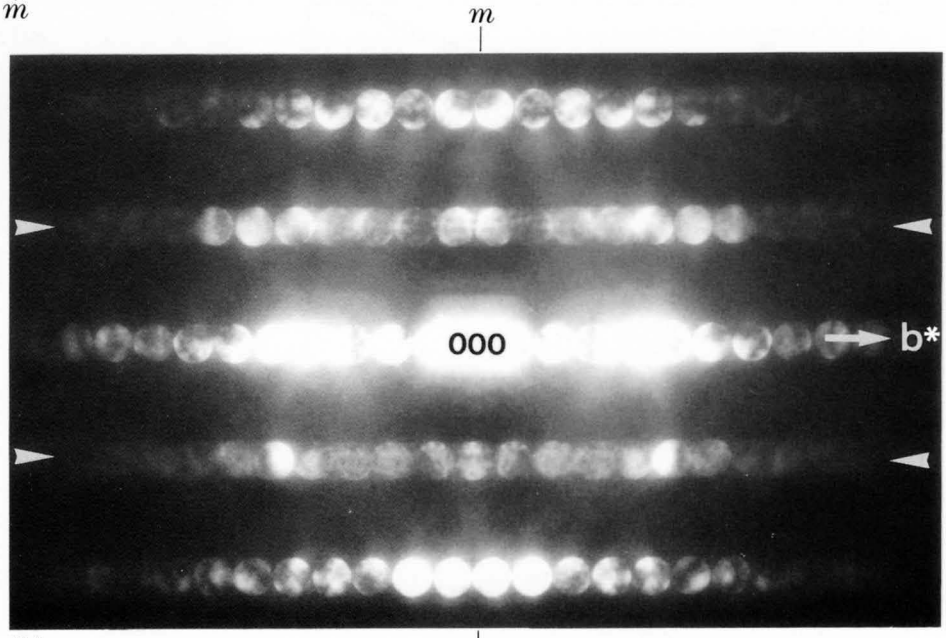

(b)

$Bi_2Sr_2CaCu_2O_{8+\delta}$

The oxide superconductor $Bi_2Sr_2CaCu_2O_{8+\delta}$ ($T_c \simeq 85$K) has an incommensurately modulated structure with a modulation wave vector of $\boldsymbol{k} = k_2\boldsymbol{b}^* + \boldsymbol{c}^*$ ($k_2 \approx 1/4.7$). The symmetry of the incommensurate structure of this material is expressed either by a (3+1)-dimensional space group $N^{Bbmb}_{1\bar{1}1}$ or N^{Bb2b}_{111} [a]. (The symbol N of the space groups indicates the lattice type whose modulation wave vector has a commensurate component $\boldsymbol{c}^*$.) Hence, the (3+1)-dimensional point group of the structure is written as $^{mmm}_{1\bar{1}1}$ or $^{m2m}_{111}$. The two possible (3+1)-dimensional point groups originate from an ambiguous determination of the space group of the average structure.

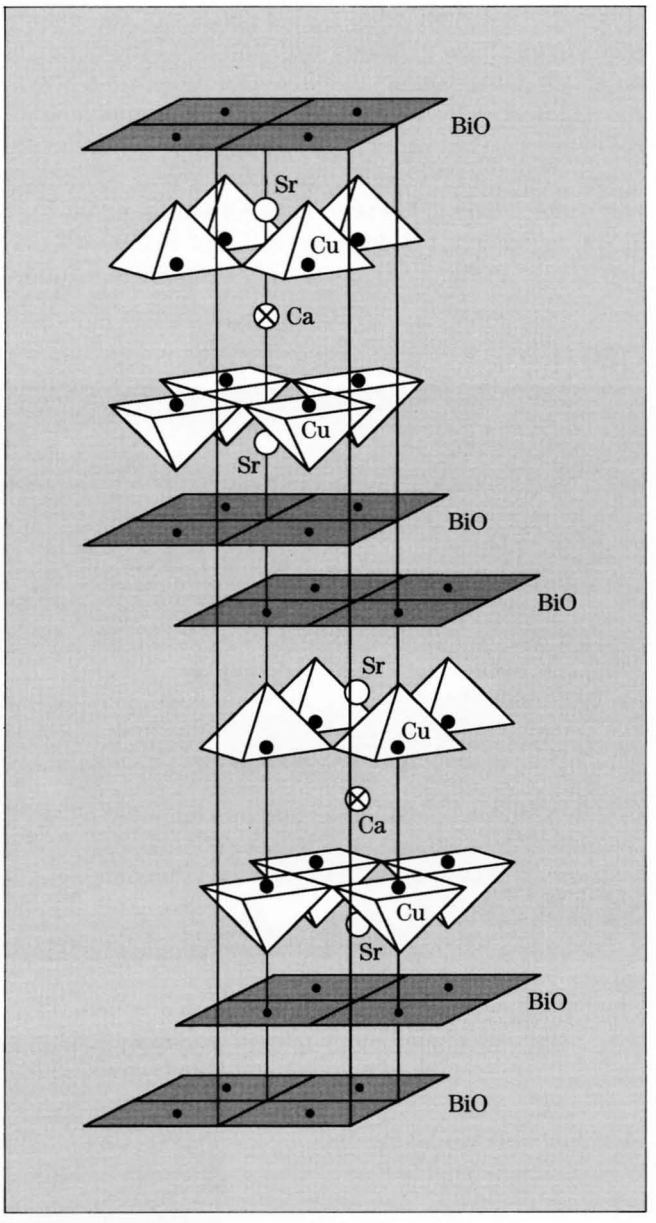

Average structure of $Bi_2Sr_2CaCu_2O_{8+\delta}$

Reference

[a] N. Yamamoto, Y. Hirotsu, Y. Nakamura and S. Nagakura : *Jpn. J. Appl. Phys.*, **28** (1989) L598.

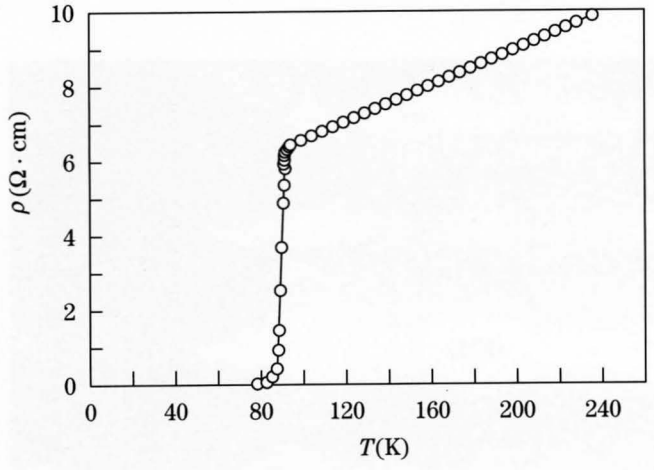

$\begin{smallmatrix} m & m & m \\ 1 & \bar{1} & 1 \end{smallmatrix}$ or $\begin{smallmatrix} m & 2 & m \\ 1 & 1 & 1 \end{smallmatrix}$

Photograph (a) shows a CBED pattern of the superconductor $Bi_2Sr_2CaCu_2O_{8+\delta}$ obtained with the [001] incidence at an accelerating voltage of 60kV. Diffraction disks of a large size were chosen for the ease of identification of the symmetry of fundamental reflections, where the fundamental and incommensurate reflection disks overlap. The intense diffraction disks are fundamental reflections. The intensities of incommensurate reflection disks are sufficiently weak to produce no effect on the symmetry of fundamental reflections. The fundamental reflections show a mirror symmetry perpendicular to the a^*-axis, but no mirror symmetry perpendicular to the b^*-axis. These symmetries revealed that the space group of the average structure is not *Bbmb* but *Bb*2*b*. Thus, the (3+1)-dimensional point and space groups are determined automatically as $^{m2m}_{111}$ and N^{Bb2b}_{111}, respectively, under the modulation wave vector $\boldsymbol{k} = k_2\boldsymbol{b}^* + \boldsymbol{c}^*$.

Photograph (b) shows a CBED pattern obtained at the same electron incidence as that in Photo (a) but with the disk size set to a smaller value than that for Photo (a), to identify the symmetry of the incommensurate reflections, several of them being indicated by arrowheads. These reflections show a mirror symmetry perpendicular to the a^*-axis, but no mirror symmetry perpendicular to the b^*-axis, as with the fundamental reflections. The symmetry of the incommensurate reflections has been ascertained to agree with those expected from (3+1)-dimensional point group symmetries about the *a*-axis ($^m_1$) and the *b*-axis ($^2_1$) (Rule 1). Therefore, these symmetries ascertain that the material belongs to the (3+1)-dimensional space group N^{Bb2b}_{111}.

[001] **60kV**

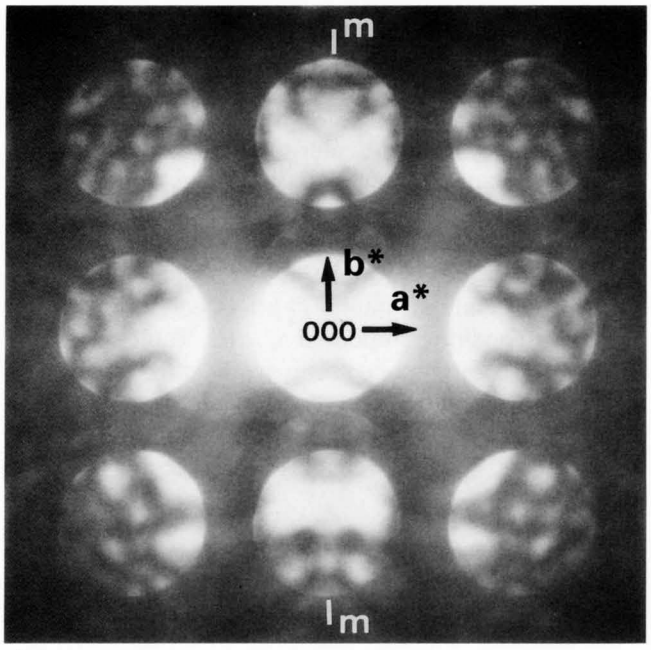

(a)

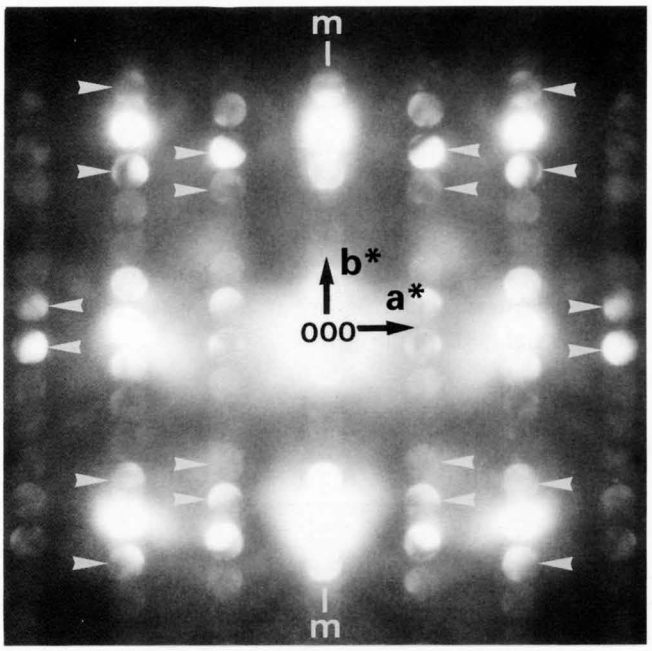

(b)

Space-Group Determination

Table shows the space-group symbols for modulated crystals. When a glide (screw) component τ_4 between modulation waves of two atom rows is 0, 1/2, ±1/3, ±1/4 or ±1/6, symbol 1, *s*, *t*, *q* or *h* is given, respectively. Such shifts can occur in the case of point-group symmetry 1 for modulations and do not for point-group symmetry $\bar{1}$. For example, the mirror plane $(^{m}_{1})$ and the glide plane $(^{m}_{s})$ perpendicular to the *a*-axis of a (3+1)-dimensional space group are illustrated schematically in Figs. (a) and (b). Figure (a) shows mirror symmetry $(^{m}_{1})$ between atom rows A and B with no glide component between these modulation waves ($\tau_4 = 0$). Figure (b) shows a glide symmetry $(^{m}_{s})$ between atom rows A and B with a glide component $\tau_4 = 1/2$. Tables of all the (3+1)-dimensional space group symbols for one-dimensional incommensurately modulated crystals were given by de Wolff, Janssen and Janner [a]. The structure factor $F(h_1h_2h_3h_4)$ (eq. (1)) is written for the glide plane $(^{m}_{s})$ perpendicular to the *b*-axis as

$$
\begin{aligned}
&F(h_1h_2h_3h_4)\\
&=\sum_{\mu=1}^{N} f_\mu \exp 2\pi i\,(h_1\overline{x_1^\mu}+h_2\overline{x_2^\mu}+h_3\overline{x_3^\mu})\\
&\times\int_0^1 \exp 2\pi i\left\{h_1u_1^\mu+h_2u_2^\mu+(h_3+h_4k_3)u_3^\mu+h_4\overline{x_4^\mu}\right\}\mathrm{d}\overline{x_4^\mu}\\
&+\exp(h_4\pi i)\sum_{\mu=1}^{N} f_\mu \exp 2\pi i\,(h_1\overline{x_1^\mu}-h_2\overline{x_2^\mu}+h_3\overline{x_3^\mu})\\
&\times\int_0^1 \exp 2\pi i\left\{h_1u_1^\mu-h_2u_2^\mu+(h_3+h_4k_3)u_3^\mu+h_4\overline{x_4^\mu}\right\}\mathrm{d}\overline{x_4^\mu}
\end{aligned}
\qquad (5)
$$

Thus, the following phase relations or eq.(6) between the two structure factors are obtained for the (3+1)-dimensional glide plane $(^{m}_{s})$.

$$
\begin{aligned}
F(h_1h_2h_3h_4) &= F(h_1\bar{h}_2h_3h_4) \quad \text{for } h_4 \text{ even},\\
F(h_1h_2h_3h_4) &= -F(h_1\bar{h}_2h_3h_4) \quad \text{for } h_4 \text{ odd}.
\end{aligned}
\qquad (6)
$$

These relations are analogous to the phase relations between the two structure factors for the three-dimensional glide planes. Dynamical extinction occurs for the screw axes and glide planes of the (3+1)-dimensional crystal with an infinite dimension along the direction of the incommensurate modulation wave vector $\boldsymbol{k}$. It was shown that approximate dynamical extinction occurs in the CBED patterns obtained from a finite specimen volume of the (3+1)-dimensional crystal [b].

Wave vector transformation	Point-group symbol	Space-group symbol
$\boldsymbol{k} \rightarrow \boldsymbol{k}$	1	1, *s* (1/2), *t* (±1/3), *q* (±1/4), *h* (±1/6)
$\boldsymbol{k} \rightarrow -\boldsymbol{k}$	$\bar{1}$	$\bar{1}$

References

[a] P. M. de Wolff, T. Janssen and A. Janner : *Acta Cryst.*, **A37** (1981) 625.

[b] M. Terauchi, M. Takahashi and M. Tanaka : *Acta Cryst.*, **A50** (1994) 566.

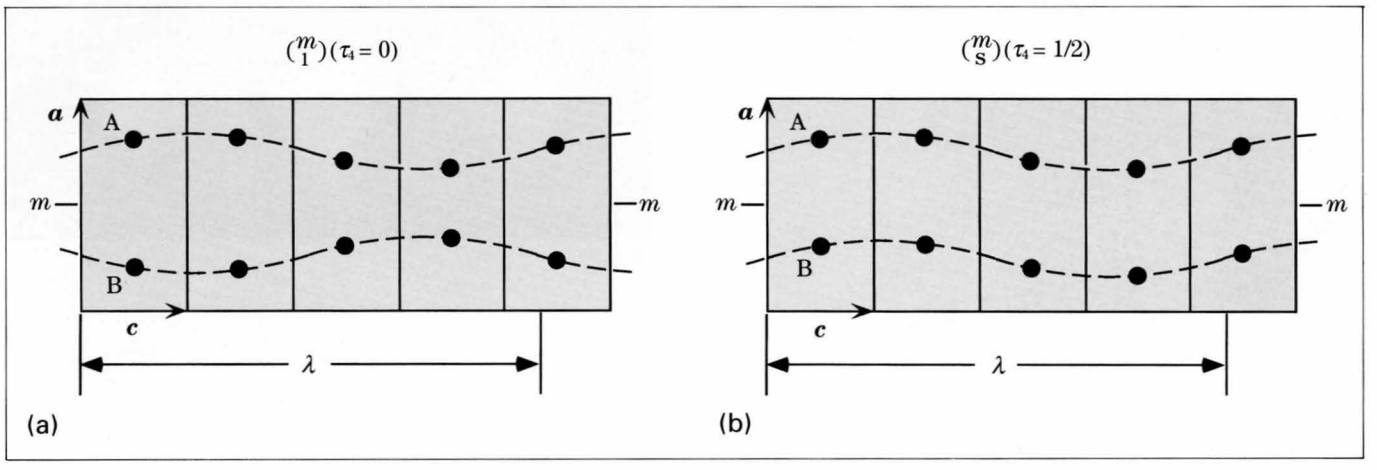

Figures (a) and (b) respectively illustrate a usual diffraction pattern and a CBED pattern expected from a modulated crystal with a (3+1)-dimensional space group $P^{P\bar{1}2mm}_{\bar{1}s\bar{1}}$ at the [100] incidence. The large and small dots in Fig. (a) indicate the fundamental reflections ($h_4 = 0$) and the incommensurate reflections ($h_4 \neq 0$), respectively. The $00h_3h_4$ (h_4 = odd) reflections denoted by the crosses are kinematically forbidden owing to the (3+1)-dimensional glide plane $(^{m}_{s})$ perpendicular to the b-axis. For simplicity, only the first- and second-order incommensurate reflections are drawn. *Umweganregung* paths "a", "b" and "c" in ZOLZ to a kinematically forbidden reflection are drawn in the figure. The two paths "a" and "b" are geometrically equivalent with respect to the line (m–m) perpendicular to the b^*-axis. Since every *Umweganregung* path to a kinematically forbidden reflection $00h_3h_4$ (h_4 = odd) contains an odd number of $F(0\ h_{2,i}\ h_{3,i}\ h_{4,i})$ with odd $h_{4,i}$, eq. (7) holds.

When the $00h_3h_4$ (h_4= odd) reflection is exactly excited, two paths "a" and "c" are symmetric with respect to the bisector (m'–m') of the diffraction vector of the reflection, and have the same excitation error. The waves passing through these paths have the same amplitude but different signs as shown by eq. (8).

$$\begin{aligned} &F(0\ h_{2,1}\ h_{3,1}\ h_{4,1})\,F(0\ h_{2,2}\ h_{3,2}\ h_{4,2})\cdots\cdots \\ &\qquad\qquad F(0\ h_{2,n}\ h_{3,n}\ h_{4,n}) \quad \text{for path "}a\text{"} \\ &= -F(0\ \overline{h_{2,1}}\ h_{3,1}\ h_{4,1})F(0\ \overline{h_{2,2}}\ h_{3,2}\ h_{4,2})\cdots\cdots \\ &\qquad\qquad F(0\ \overline{h_{2,n}}\ h_{3,n}\ h_{4,n}) \quad \text{for path "}b\text{"} \end{aligned} \tag{7}$$

$$\begin{aligned} &F(0\ h_{2,1}\ h_{3,1}\ h_{4,1})\,F(0\ h_{2,2}\ h_{3,2}\ h_{4,2})\cdots\cdots \\ &\qquad\qquad F(0\ h_{2,n}\ h_{3,n}\ h_{4,n}) \quad \text{for path "}a\text{"} \\ &= -F(0\ \overline{h_{2,n}}\ h_{3,n}\ h_{4,n})F(0\ \overline{h_{2,n\text{-}1}}\ h_{3,n\text{-}1}\ h_{4,n\text{-}1})\cdots\cdots \\ &\qquad\qquad F(0\ \overline{h_{2,1}}\ h_{3,1}\ h_{4,1}) \quad \text{for path "}c\text{"}, \end{aligned} \tag{8}$$

where $\sum_{i=1}^{n} h_{2,i} = 0$, $\sum_{i=1}^{n} h_{3,i} = h_3$, $\sum_{i=1}^{n} h_{4,i} = h_4$ (h_4 = odd).

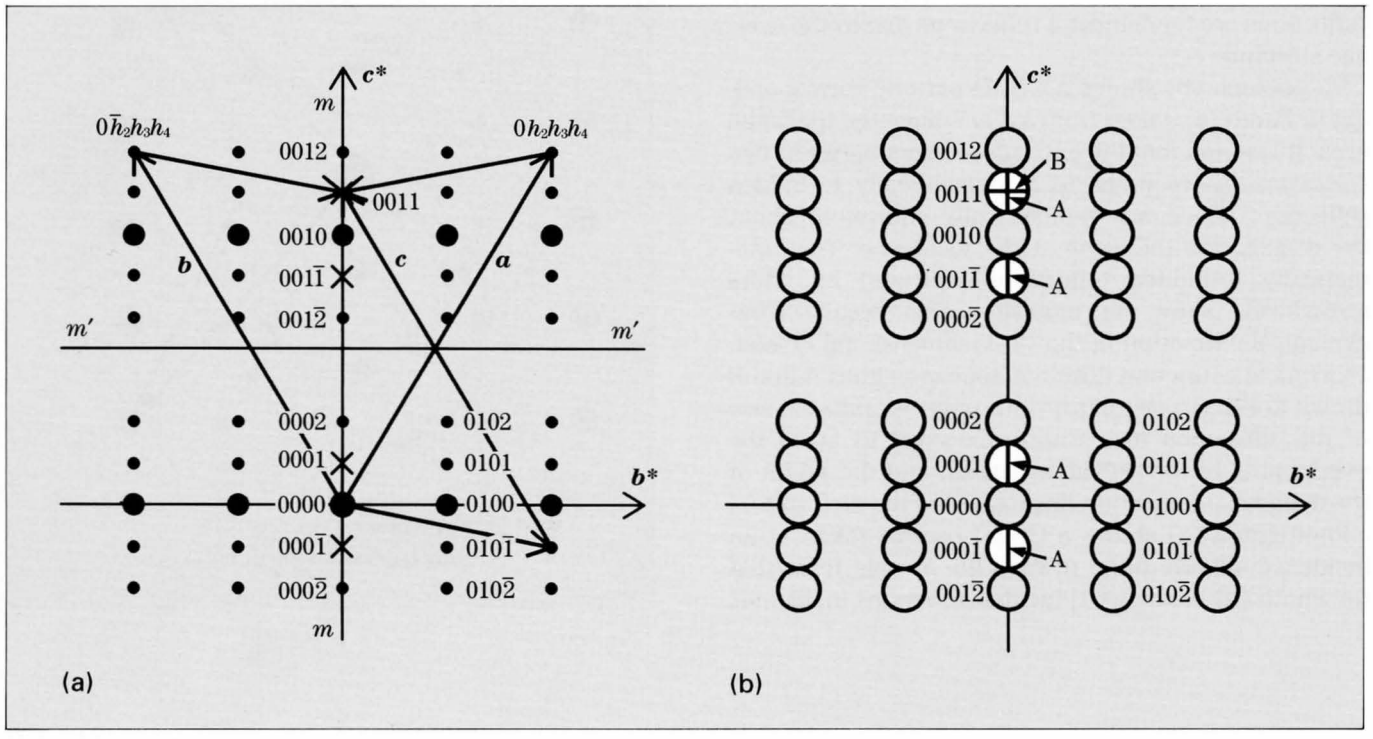

$Sr_2Nb_2O_7$

$P^{Cmc2_1}_{\bar{1}\,s\bar{1}}$

The symmetry of the incommensurately modulated structure of $Sr_2Nb_2O_7$ is expressed by the (3+1)-dimensional space group $P^{Cmc2_1}_{\bar{1}\,s\bar{1}}$ ([b] in page 80). The space group symbol implies that the modulated structure has (3+1)-dimensional glide planes ($^{c}_{s}$) perpendicular to the b-axis with a shift of $(\boldsymbol{c}+\boldsymbol{a}_4)/2$. Then, the reflections $h_1 0 h_3 h_4$ with $h_3+h_4 = 2n+1$ (n : integer) are kinematically forbidden. The figure illustrates a schematical diffraction pattern of $Sr_2Nb_2O_7$ at the [001] incidence. The large and small dots indicate the fundamental reflections ($h_4=0$) and the incommensurate reflections ($h_4\neq 0$), respectively. *Umweganregung* paths "a" and "b" in ZOLZ to the kinematically forbidden 0001 reflection are drawn in the figure.

Photograph (a) on the opposite page shows an electron diffraction pattern of the incommensurate phase of $Sr_2Nb_2O_7$ obtained with the [001] incidence at an accelerating voltage of 60kV. The incommensurate reflections in which dynamical extinction lines appear are restricted to those with the indices $h_{1,even}00h_{4,odd}$ because $h_3 = 0$ at this incidence and $h_1+h_2 = 2n$ due to the lattice type C of the average structure. The reflections in four columns indicated by black arrowheads are incommensurate reflections due to the modulation. The reflections 0001, $000\bar{1}$, $200\bar{1}$ and $\bar{2}001$ indicated by white arrowheads are kinematically forbidden but have intensities due to multiple diffraction. Other reflections are fundamental reflections due to the average structure.

Photograph (b) shows a CBED pattern corresponding to Photo (a), taken from a 3-nm-diameter specimen area. It is noted that the excitation errors between two *Umweganregung* paths to a kinematically forbidden reflection, which are geometrically equivalent about the a^*-axis, are the same at the incidence. The kinematically forbidden reflections indicated by white arrowheads show no intensity. This results from dynamical extinction in the (3+1)-dimensional crystal. Dynamical extinction does not appear as lines A and B drawn in Fig. (b) on the previous page because the size of the diffraction disk was made small to avoid the overlapping of the diffraction disks, and the width of the dynamical extinction line exceeded the disk size.

Photograph (c) shows a CBED pattern taken at an incidence slightly tilted toward the b^*-axis from that for Photo (b) or the [001] incidence. At this incidence, the excitation errors, which were equivalent between the pairs of *Umweganregung* paths in Photo (b), are not the same. Then, it is seen that the kinematically forbidden reflections indicated by white arrowheads have intensities due to an incomplete cancellation of the waves coming through the paths.

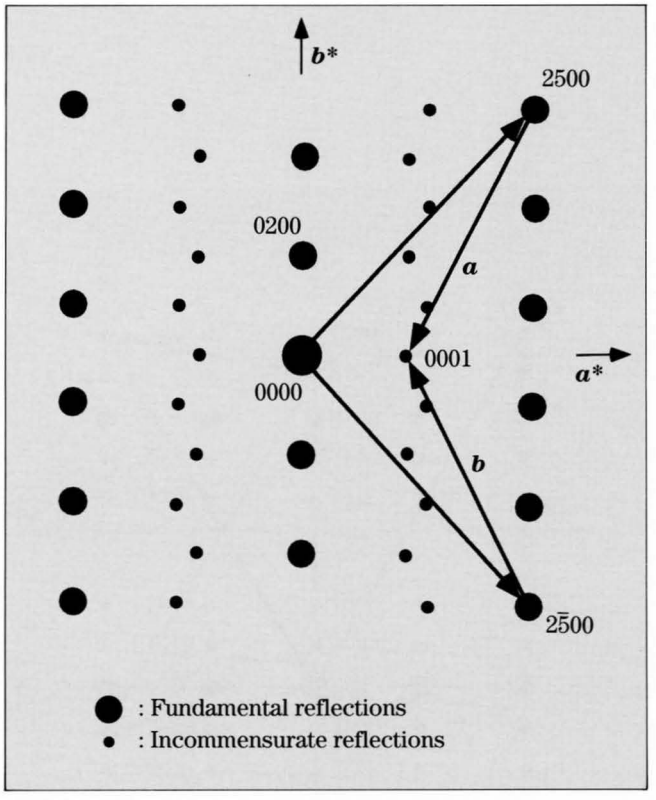

$Sr_2Nb_2O_7$

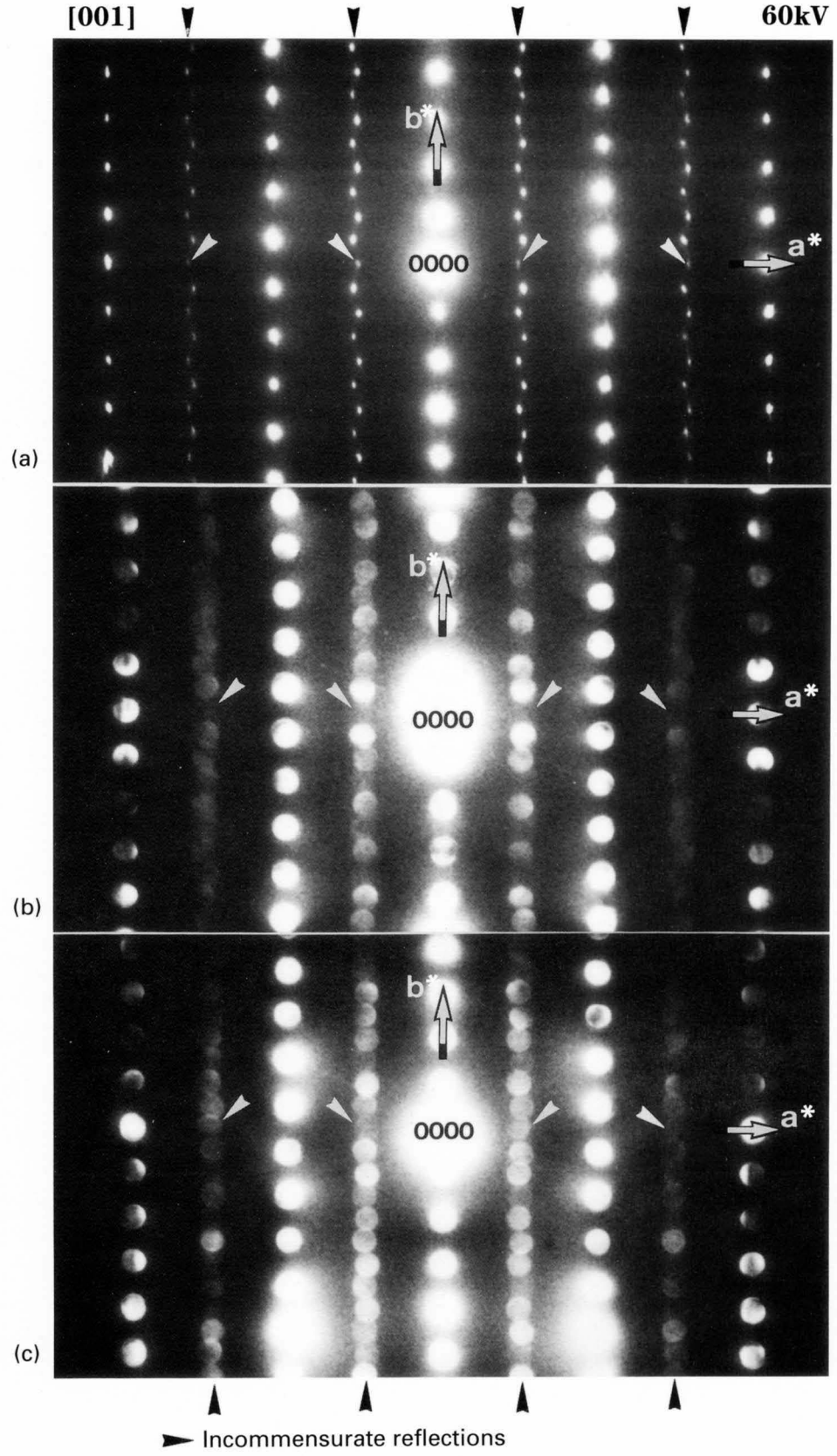
[001]
60kV
b*
0000
a*
(a)
b*
0000
a*
(b)
b*
0000
a*
(c)
Incommensurate reflections

Quasicrystals

Decagonal Phase

The decagonal quasicrystal is quasi-periodic in two dimensions and periodic in the third dimension parallel to a tenfold or a fivefold axis. The diffraction patterns of the quasicrystal are indexed by five indices.

A real decagonal quasicrystal was first discovered in an Al-Mn alloy by Bendersky [a]. Decagonal phases were subsequently found in binary alloys of Al-Fe, Al-Ru, Al-Pt and Al-Pd. These phases were thermodynamically metastable and had small quasicrystalline grains less than 10nm in diameter.

Thermodynamically stable decagonal phases were found afterwards in ternary alloys of $Al_{65}Cu_{15}Co_{20}$, $Al_{65}Cu_{20}Co_{15}$ and $Al_{70}Ni_{15}Co_{15}$. They were prepared by conventional solidification and subsequent annealing. Electron diffraction patterns of these alloys taken at an incidence along the decagonal axis showed only intense reflections and no weak reflections such as observed in Al-Cu-Fe stable icosahedral quasicrystals. The reflection spots were not sharp and had irregular shapes. Two point groups, $10/m$ and $10/mmm$, were proposed for the alloys but CBED patterns taken from the decagonal phases exhibited imperfect symmetries. Tsai *et al.* [b] produced metastable but good quality decagonal quasicrystals of a melt-quenched $Al_{70}Ni_{15}Fe_{15}$ alloy.

We present symmetry studies of melt-quenched quasicrystals of Al-Ni-Fe, Al-Cu-Co, Al-Co and Al-Ni-Rh alloys with good quality by quoting electron microscope images.

References

[a] L. Bendersky : *J. de Physique*, **47** (1986) C3-457.

[b] A. P. Tsai, A. Inoue and T. Masumoto : *Mater. Trans.* JIM., **30** (1989) 300.

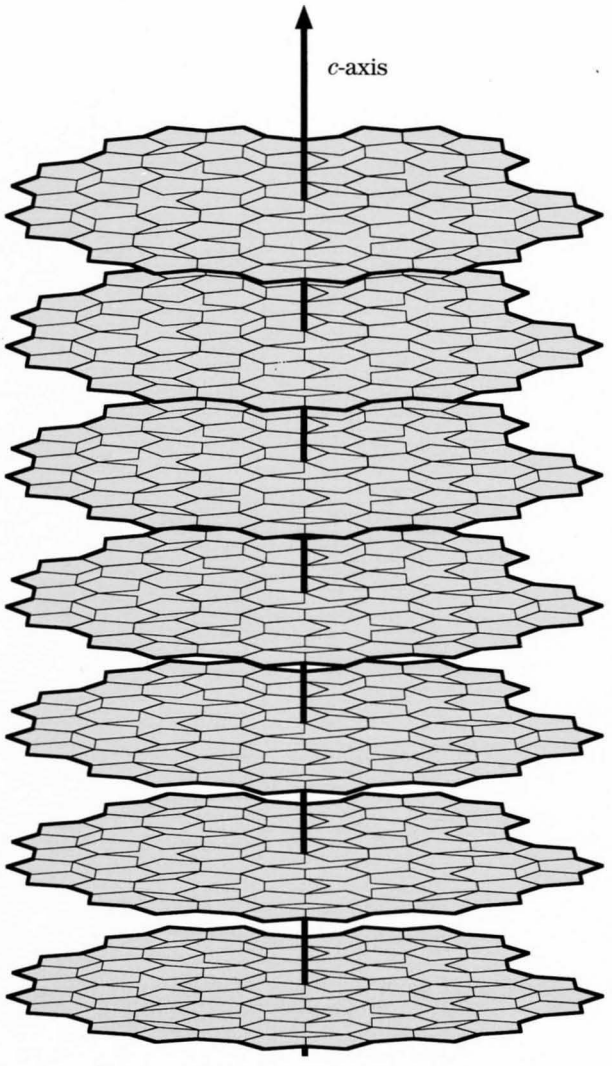

Illustration of a decagonal lattice. A stereoscopic image appears when viewed from the side of the book.

Section method — higher dimensional space —

Two-dimensional quasi-periodic structures can be described by a two-dimensional section of a four-dimensional crystal, in which "atoms" are periodically arranged in four dimensions, the method being called the section method. The two-dimensional section of the four-dimensional crystal provides a structure which we can actually observe. We call the two-dimensional section of the space the external space. The two-dimensional space perpendicular to the external space is called the internal space.

The unit vectors $\boldsymbol{d}_i$ (i = 1–4) of the quasi-periodic structure are expressed as $\boldsymbol{d}_i = \sum_j \mathrm{M}_{ij}\boldsymbol{a}_j$, where $\boldsymbol{a}_1$ and $\boldsymbol{a}_2$ are the base vectors in the external space, and $\boldsymbol{a}_3$ and $\boldsymbol{a}_4$ are those in the internal space. It is noted that the reciprocal lattice vectors of $\boldsymbol{d}_i$ are expressed as $\boldsymbol{d}_i^* = \sum_j ({}^t\mathrm{M}_{ij})^{-1}\boldsymbol{a}_j^*$ by the usual relation between the real and reciprocal lattices. When a decagonal "atomic domain" is given in the internal space as shown in Fig. (a), the pentagonal Penrose pattern shown in Fig. (b) is obtained.

$$\mathrm{M}_{ij} = \sqrt{(2/5)} \begin{pmatrix} c_1 - 1 & s_1 & c_2 - 1 & s_2 \\ c_2 - 1 & s_2 & c_4 - 1 & s_4 \\ c_3 - 1 & s_3 & c_1 - 1 & s_1 \\ c_4 - 1 & s_4 & c_3 - 1 & s_3 \end{pmatrix} \qquad ({}^t\mathrm{M}_{ij})^{-1} = \sqrt{(2/5)} \begin{pmatrix} c_1 & s_1 & c_2 & s_2 \\ c_2 & s_2 & c_4 & s_4 \\ c_3 & s_3 & c_1 & s_1 \\ c_4 & s_4 & c_3 & s_3 \end{pmatrix}$$

$$c_j = \cos(2j\pi/5),\ s_j = \sin(2j\pi/5)$$

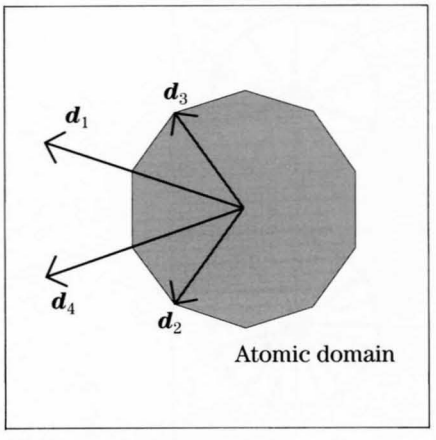

(a) Internal space

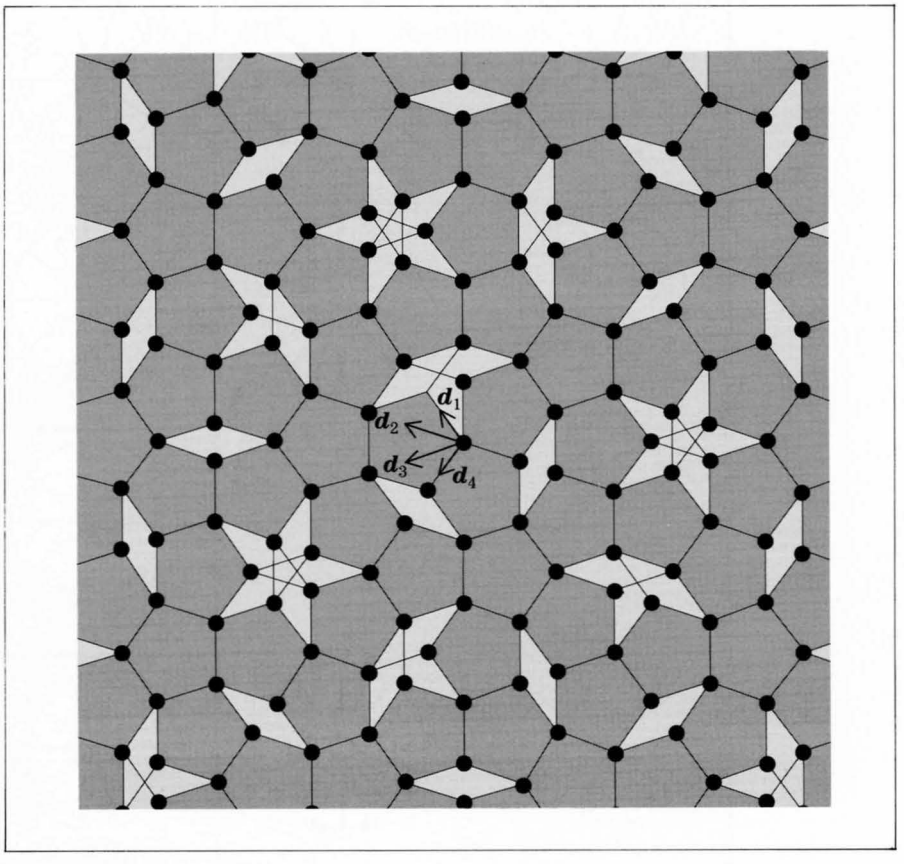

(b) External space

Pentagonal and decagonal point groups

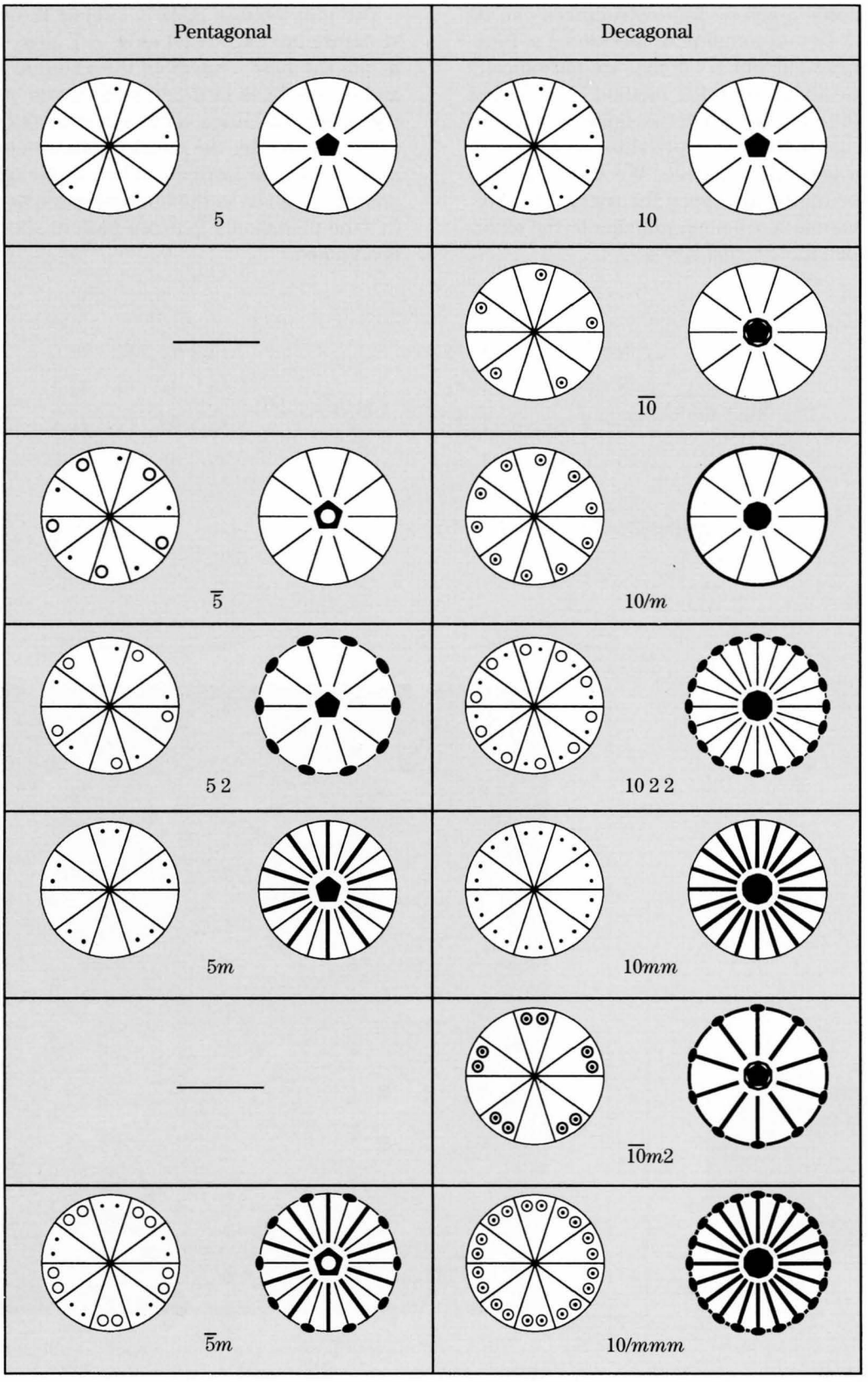

Pentagonal and decagonal point groups constructed by an analogy with trigonal and hexagonal point groups.

Al-Ni-Fe Alloys

A metastable alloy of $Al_{70}Ni_{15}Fe_{15}$ was found to be the first decagonal quasicrystal which can tolerate the symmetry examination using CBED. It is interesting to point out that the metastable quasicrystal has a higher quality or order of quasicrystallinity than do stable quasicrystals. Saito *et al.* [a] determined the space group of the alloy to be $P\bar{1}0m2$ (= $P5/mm2$). The alloy is the first quasicrystal which belongs to a noncentrosymmetric space group and has a fivefold axis.

Tsuda *et al.* [b] revealed that there exist inversion domains, at whose boundaries an antiphase shift of $c/2$ is accompanied, c being the lattice parameter in the fivefold axis. They found specific pentagonal atom clusters in high-resolution electron microscope images, and showed that all the clusters in a domain have the same sense polarity and those in the neighbouring domains have the opposite sense polarity.

Tanaka *et al.* [c] investigated the symmetry of the decagonal quasicrystals of $Al_{70}Ni_{10+x}Fe_{20-x}$ ($0 \leq x \leq 10$) and revealed that the alloys with $0 \leq x \leq 7$ belong to the noncentrosymmetric space group $P\bar{1}0m2$ and those with $7 < x \leq 10$ to the centrosymmetric space group $P10/mmm$. High-resolution electron microscope images detected the existence of the specific pentagonal clusters in all the alloys investigated. Dark-field microscopy disclosed that the change in space group at $x \approx 7.5$ takes place upon sudden decrease of the domain size or rapid mixing of the atom clusters with the positive and negative polarities.

References

[a] M. Saito, M. Tanaka, A. P. Tsai, A. Inoue and T. Masumoto : *Jpn. J. Appl. Phys.*, **31** (1992) L109.

[b] K. Tsuda, M. Saito, M. Terauchi, M. Tanaka, A. P. Tsai, A. Inoue and T. Masumoto : *Jpn. J. Appl. Phys.*, **32** (1993) 129.

[c] M. Tanaka, K. Tsuda, M. Terauchi, A. Fujiwara, A. P. Tsai, A. Inoue and T. Masumoto : *J. Non-Cryst. Solid*, **153 & 154** (1993) 98.

$Al_{70}Ni_{15}Fe_{15}$ — symmetry —

Photographs (a), (b) and (c) on the opposite page show conventional electron diffraction patterns taken from a 110-nm-diameter area of $Al_{70}Ni_{15}Fe_{15}$ at an incidence along the decagonal axis (c-axis) and at incidences A and B perpendicular to the c-axis, respectively (indicated in Photo (a)).

Photograph (a) shows a number of fine spots between strong reflections and the formation of a tenfold rotation symmetry. Reflections due to a lattice spacing of 2.6nm are seen in the innermost part of the pattern. The deviation of reflections from the correct symmetry positions due to phason strains and the irregularity of shapes of the reflection spots are smaller than those observed in a good quality icosahedral quasicrystal of $Al_{65}Cu_{20}Fe_{15}$.

Photograph (b) shows a regular periodicity in the c-direction with a period of 0.4nm. Quasiperiodic reflection arrays are seen in directions perpendicular to the c-axis. Diffuse streaks appear at positions corresponding to $0.8/n$ nm in the c-direction, where n represents an integer. The streaks are considered to be a section of diffuse intensity sheets. This indicates that there exist rodlike scattering objects, which extend in the c-direction with a periodicity of 0.8nm and have a small coherence length in the directions of quasiperiodicity.

Photograph (c) shows clear reflection spots on the diffuse streaks, appearing at positions corresponding to $0.8/n$ nm (n : integer) in the c-direction. Diffraction spot arrays at the positions X (n : even) are explained by the quasi-periodicity of the atomic arrangement. Those at the positions Y (n : odd) are not attributed to any periodicity or quasi-periodicity. The presence of the arrays at Y can be explained by structural modulations with wave number vectors $\boldsymbol{k}$ and $\boldsymbol{k}'$. A pair of reflection spots at Y appearing on both sides of an X is considered to be satellites connected by the wave vector $\boldsymbol{k}$ or $\boldsymbol{k}'$ with a fundamental reflection on the X. It should be noted that the modulated structures may not be simple ones because no two satellites which form a pair have the same intensity.

Photograph (d) shows a CBED pattern taken from a 3-nm-diameter area with an incidence parallel to the c-axis. The pattern clearly exhibits fivefold rotation and mirror symmetry, the total symmetry being expressed as $5m$. A slowly varying intensity distribution in the disks indicates that the pattern is not affected by the interaction with higher-order Laue zone (HOLZ) reflections, but is formed by interactions between zeroth-order Laue zone (ZOLZ) reflections. Thus, the projection approximation should be applied to the analysis of the pattern. Changes of the illuminated specimen area sometimes produced patterns related to each other by inversion of Photo (d), indicating the existence of inversion domains. By consulting the table of the pentagonal and decagonal point groups, the point groups which satisfy the observed symmetry $5m$ in the projection approximation are 52, $5m$ and $\bar{1}0m2$. The point group 52 is a possibility because the horizontal two-fold axis is equivalent to the vertical mirror plane in the projection approximation.

Photographs (e) and (f) were taken from 3-nm-diameter areas with incidences A and B, respectively. Mirror symmetry perpendicular to the c^*-axis is seen in Photo (e). Since this symmetry requires the existence of a twofold axis or mirror plane perpendicular to the c-axis, point groups 52 and $\bar{1}0m2$ remain as possibilities. Photograph (f) exhibits symmetry $2mm$. Mirror symmetry parallel to the c^*-axis requires the existence of a mirror plane parallel to the c-axis. Since the mirror plane does not exist in point group 52 but does exist in $\bar{1}0m2$, the point group of the alloy is determined to be $\bar{1}0m2$.

Since the reflections at the levels of $0.8/n$ nm (n : odd) in the c-direction are considered to be satellites, the periodicity of the fundamental structure in the c-direction is 0.4nm. It is seen that there is no extinction in the c-direction. Therefore, the space group of the decagonal phase is determined to be $P\bar{1}0m2$, though modulated structures coexist.

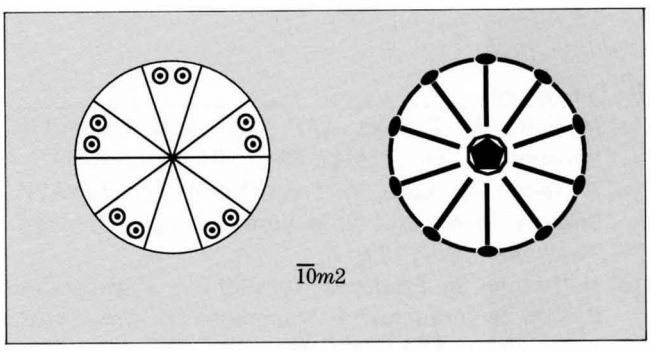

$Al_{70}Ni_{15}Fe_{15}$

60kV

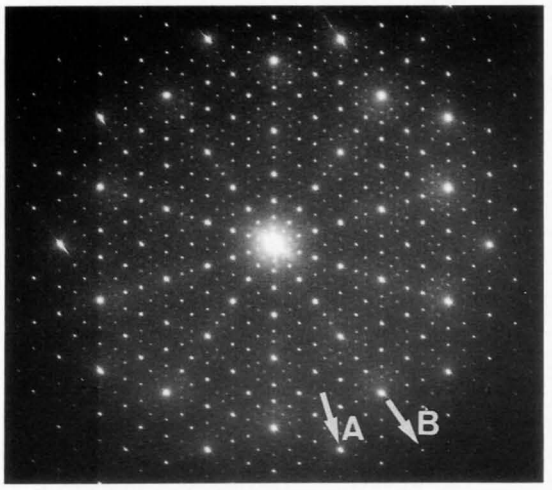

(a)

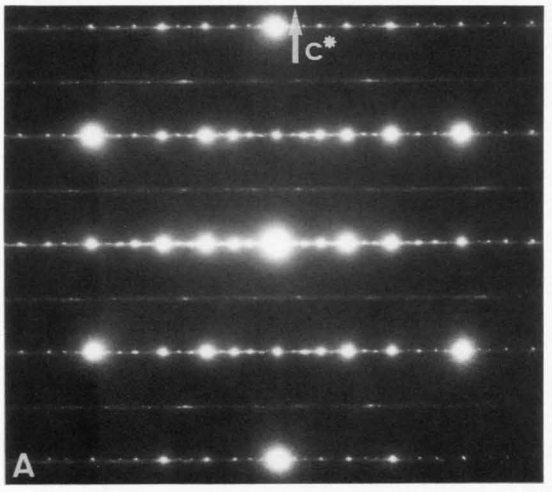

(b)

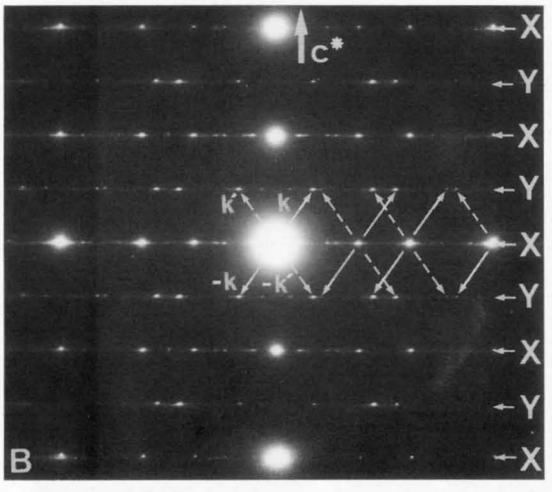

(c)

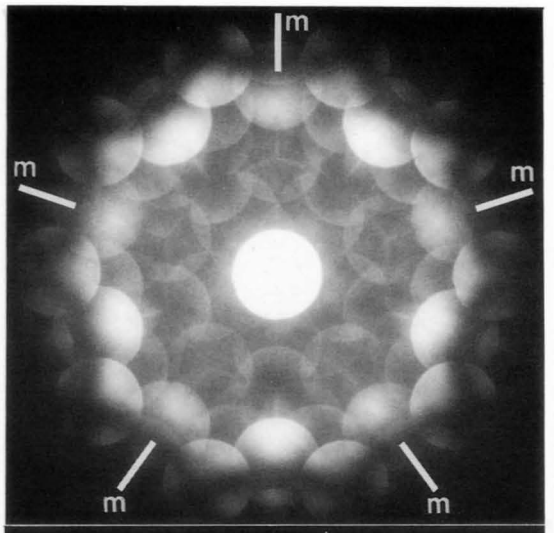

(d)

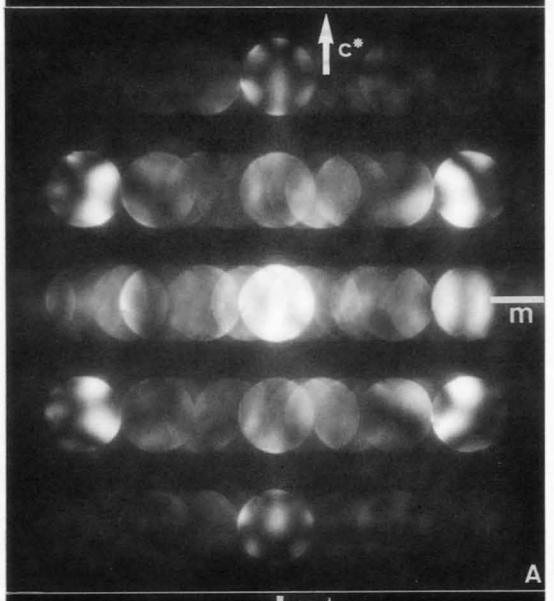

(e)

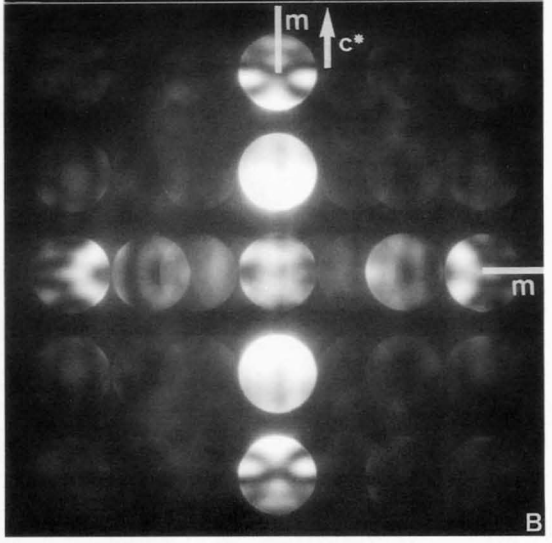

(f)

$Al_{70}Ni_{15}Fe_{15}$ — domain structure —

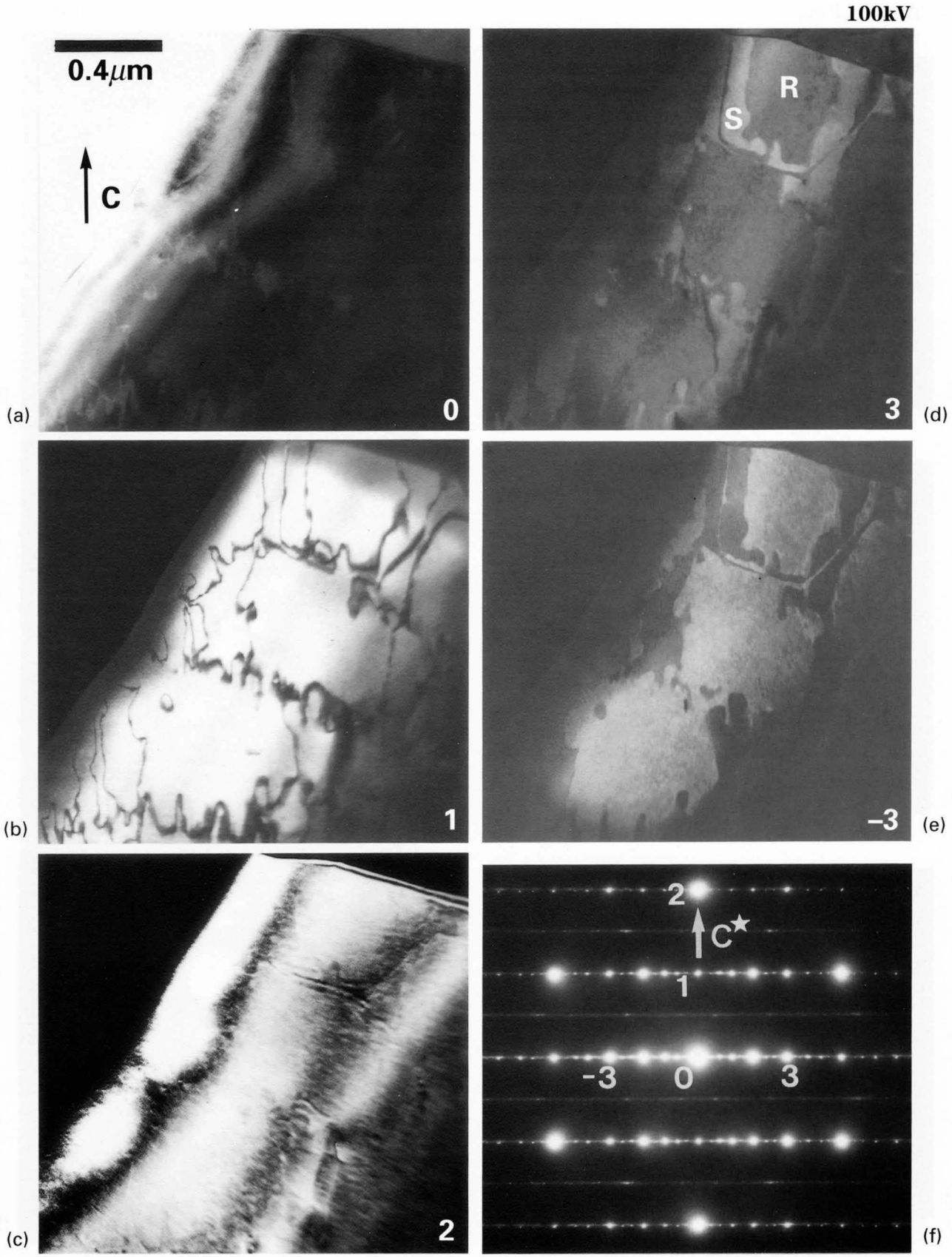

Photographs (a) to (e) on the opposite page are bright- and dark-field images due to reflections 0, 1, 2, 3 and –3 indicated in Photo (f), respectively. These images were taken by exciting those reflections by changing the electron incidence slightly from that in Photo (f).

The dark-field image due to reflection 1, Photo (b), shows irregular dark lines. The long straight segments of the lines run roughly parallel to the c-axis. It should be noted that the areas across the lines show no net contrast, indicating no bending between the areas. The dark lines disappear in the dark-field image of reflection 2, Photo (c). These results indicate that there exists an antiphase shift of $c/2$ (~0.2nm) at the dark lines. The antiphase shift corresponds to the lattice spacing of the second-order reflection of the c-planes. The size of the large domains is seen to be about 0.5μm square.

In the dark-field images due to reflections 3 and –3, Photos (d) and (e) respectively, the domains show net contrast. The contrast is reversed between Photos (d) and (e). That is, the dark domain R and the light one S in Photo (d) are, respectively, light and dark in Photo (e). This suggests that the domains R and S form inversion domains.

Photographs (g) and (h) show CBED patterns taken respectively from the domains R and S in Photo (d) at the same incidence as that in Photo (f). Although the symmetry is slightly imperfect, the CBED patterns exhibit a mirror symmetry perpendicular to the c^*-axis but no mirror symmetry parallel to the c^*-axis. The figures of the two reflection disks indicated by arrowheads are interchanged between Photos (g) and (h). The two CBED patterns are related to each other by inversion operation about the center of the bright-field disk and/or by mirror operation parallel to the c^*-axis.

These results indicate that the domains are inversion domains, which have the positive and the negative polarity, respectively. Close inspection of Photos (b), (d) and (e) ascertained that the boundaries of the inversion domains agree with the antiphase boundaries. Therefore, it became clear that the domains found in the $Al_{70}Ni_{15}Fe_{15}$ quasicrystal are inversion domains with an antiphase shift of $c/2$. It is noted that the polarity is perpendicular to the c-direction.

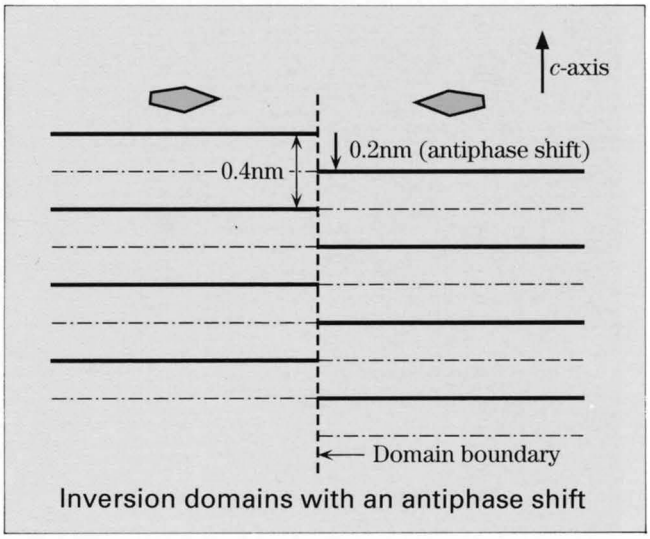

Inversion domains with an antiphase shift

60kV

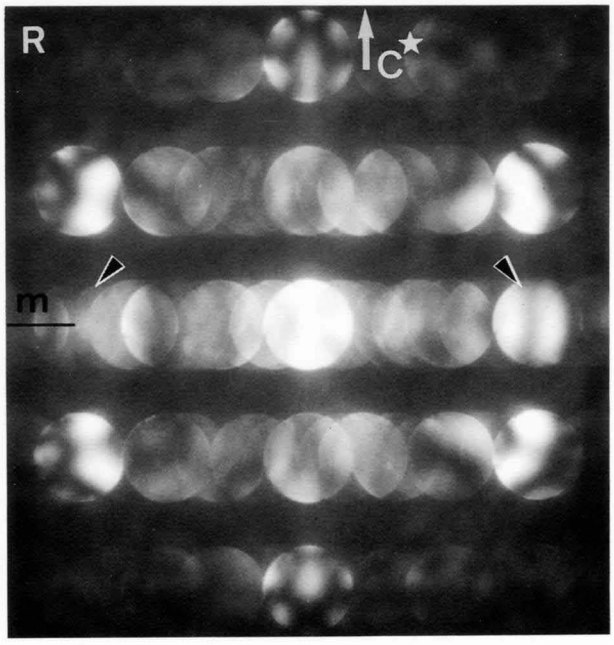

(g)

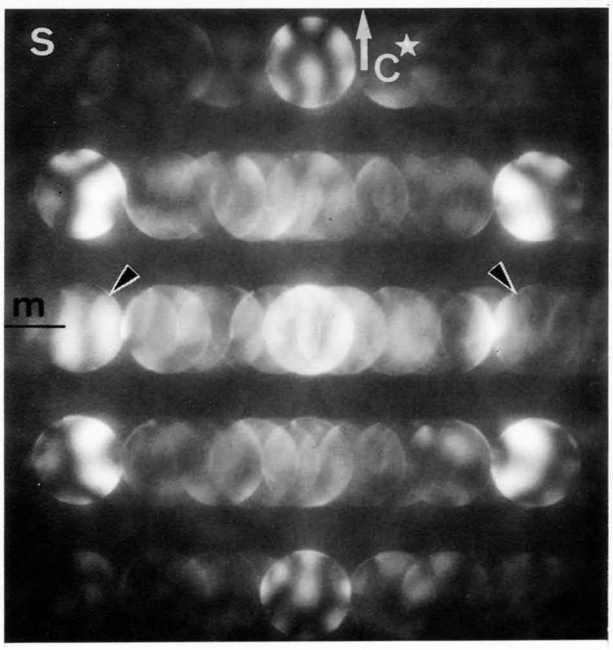

(h)

$Al_{70}Ni_{15}Fe_{15}$ — HREM image —

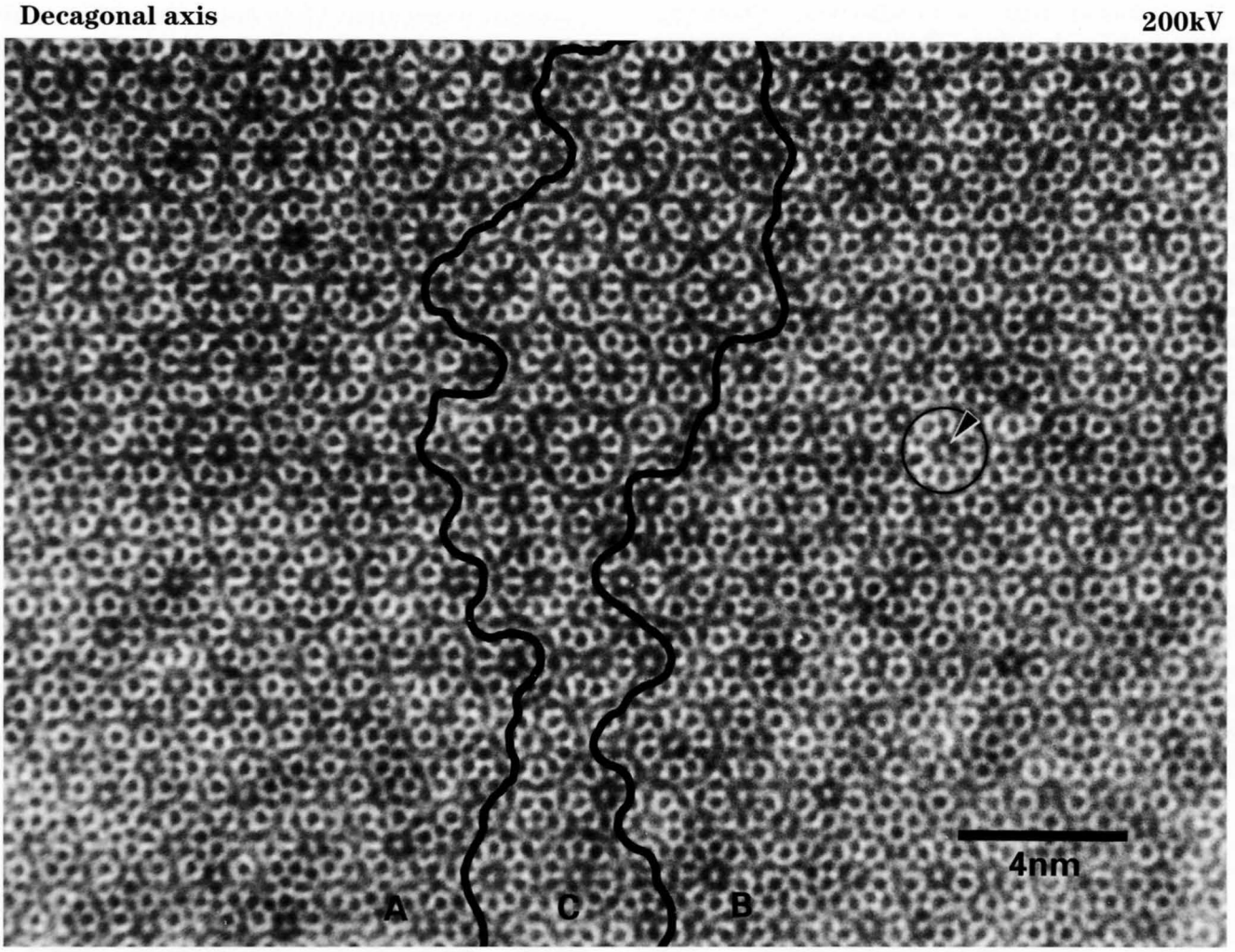

High-resolution image of $Al_{70}Ni_{15}Fe_{15}$ taken at an incidence parallel to the *c*-axis. The polarity of the pentagonal clusters is opposite between areas A and B. Area C is the overlapping region of domains A and B.

The photograph on the opposite page shows a high-resolution electron microscope (HREM) image taken at an incidence parallel to the *c*-axis. The image of a specific atom cluster with a diameter of about 2nm is clearly seen as encircled in black. The cluster is composed of a light dot at the center, a dark pentagon around it as indicated by an arrowhead, ten dark dots surrounding the pentagon separated by the light skeleton, and a dark ring around the skeleton. The distance between each two neighbouring dark dots is approximately 0.4nm.

The basic cluster is polar or noncentrosymmetric due to the existence of the dark pentagon. It should be noted that all the clusters in domain A have the same polarity and those in B the opposite one. CBED patterns taken from domains A and B showed the opposite polarity with the fivefold rotational symmetry. This ascertains that those domains are inversion domains. In the boundary region C, the clusters do not show a clear dark pentagon but a circular shape. This can be interpreted by the loss of clear polarity due to the overlapping of the domains A and B in the direction of the depth of the specimen.

$Al_{70}Ni_{15}Fe_{15}$

200kV

Decagonal axis

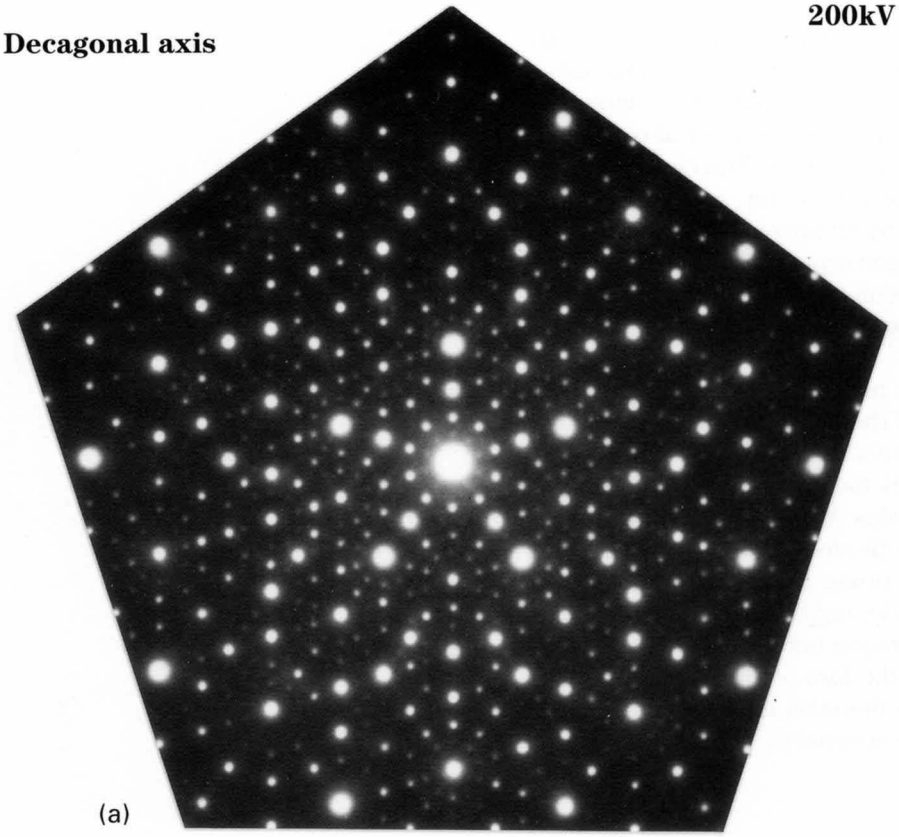

(a)

Single-domain

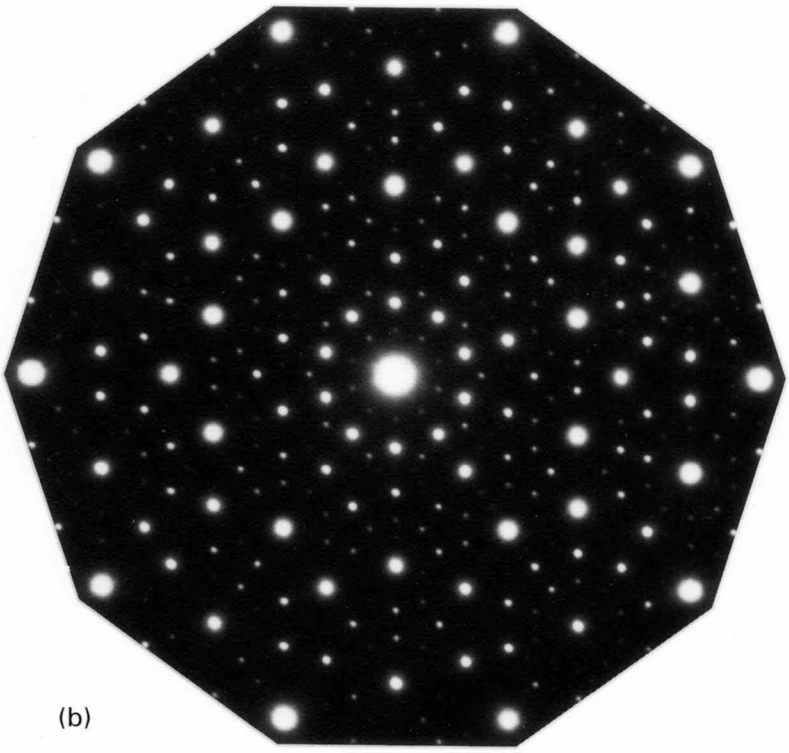

(b)

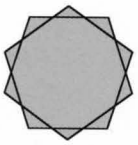

Multi-domains

Selected area diffraction patterns of $Al_{70}Ni_{15}Fe_{15}$ from a single domain (a) showing pentagonal symmetry and from multi-domains showing decagonal symmetry (b).

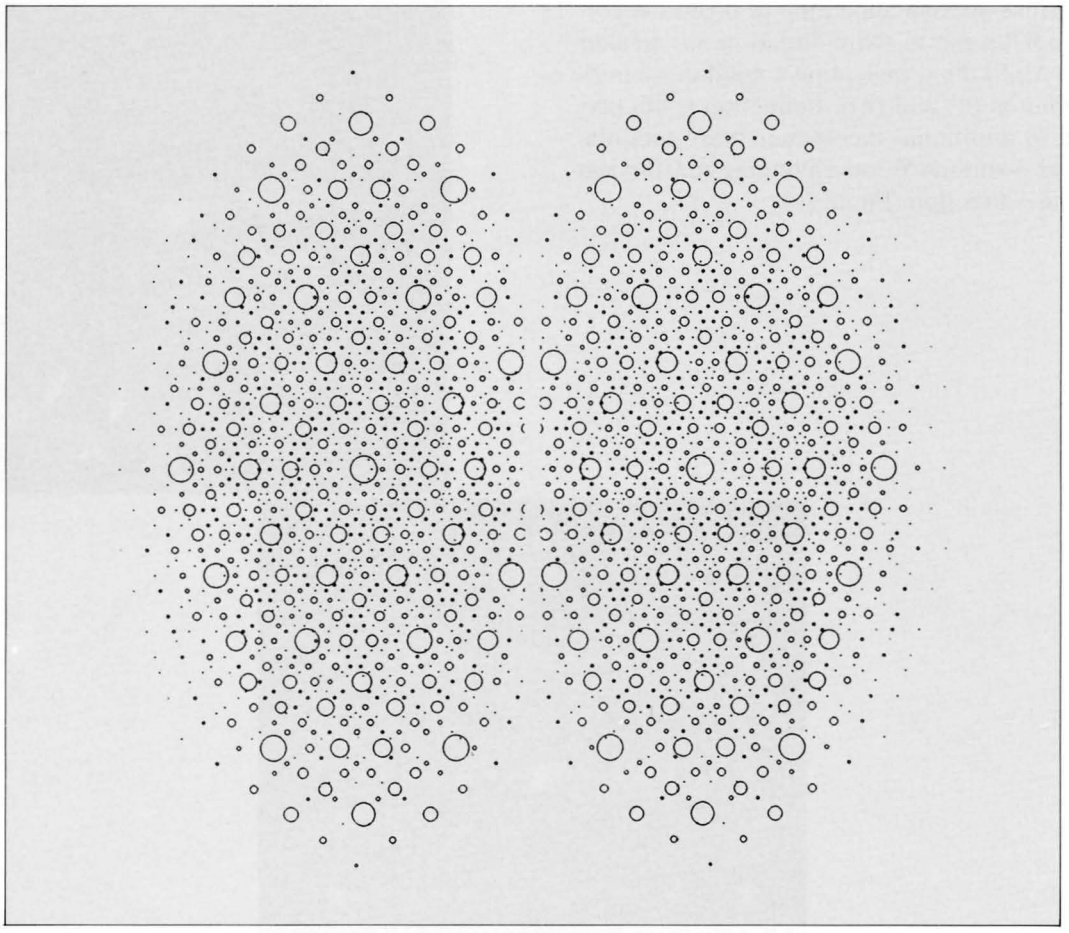

Stereogram of a schematic decagonal diffraction pattern.

$Al_{70}Ni_{20}Fe_{10}$ — symmetry —

Selected area diffraction patterns of $Al_{70}Ni_{20}Fe_{10}$ taken at incidences parallel to the c-axis show no pentagonal patterns but decagonal ones, as shown in Photo (a). Diffuse streaks appearing at positions corresponding to $0.8/n$ nm in the c-direction are weaker than those in $Al_{70}Ni_{15}Fe_{15}$, indicating a good quasi-periodic array (Photos (b) and (c)). Reflection spots presumably due to additional incommensurate modulations appear at positions Y corresponding to $0.8/n$ nm (n : odd) in the c-direction (Photo (c)).

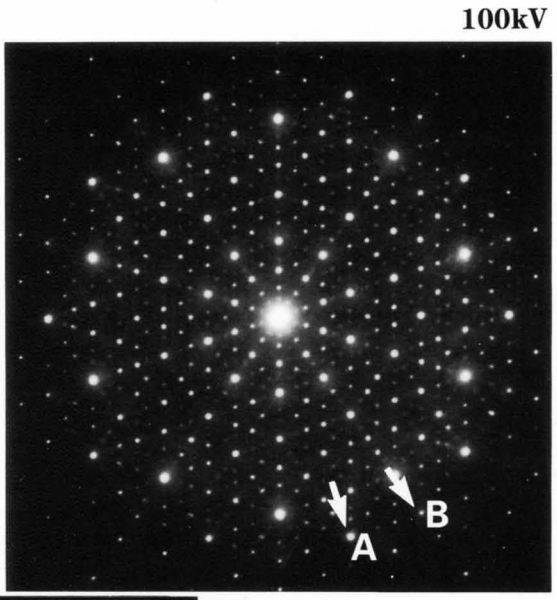

(a)

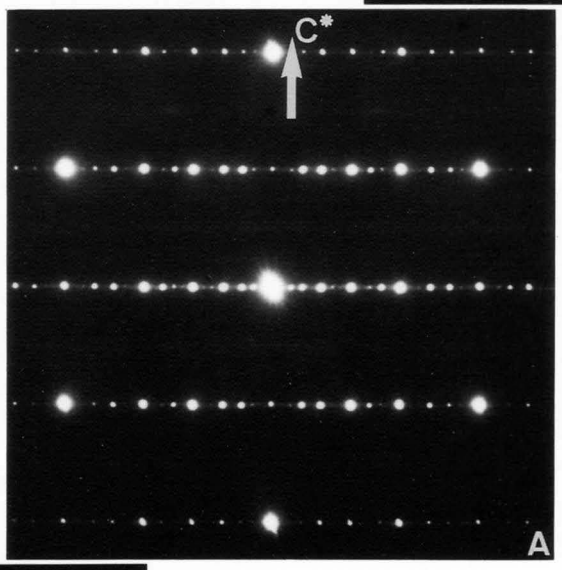

(b)

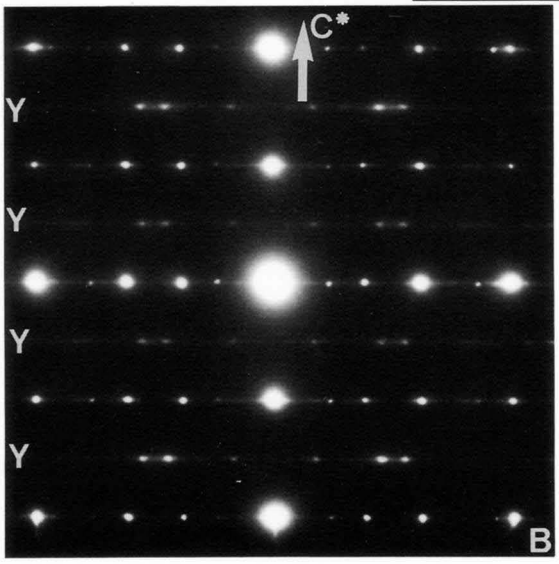

(c)

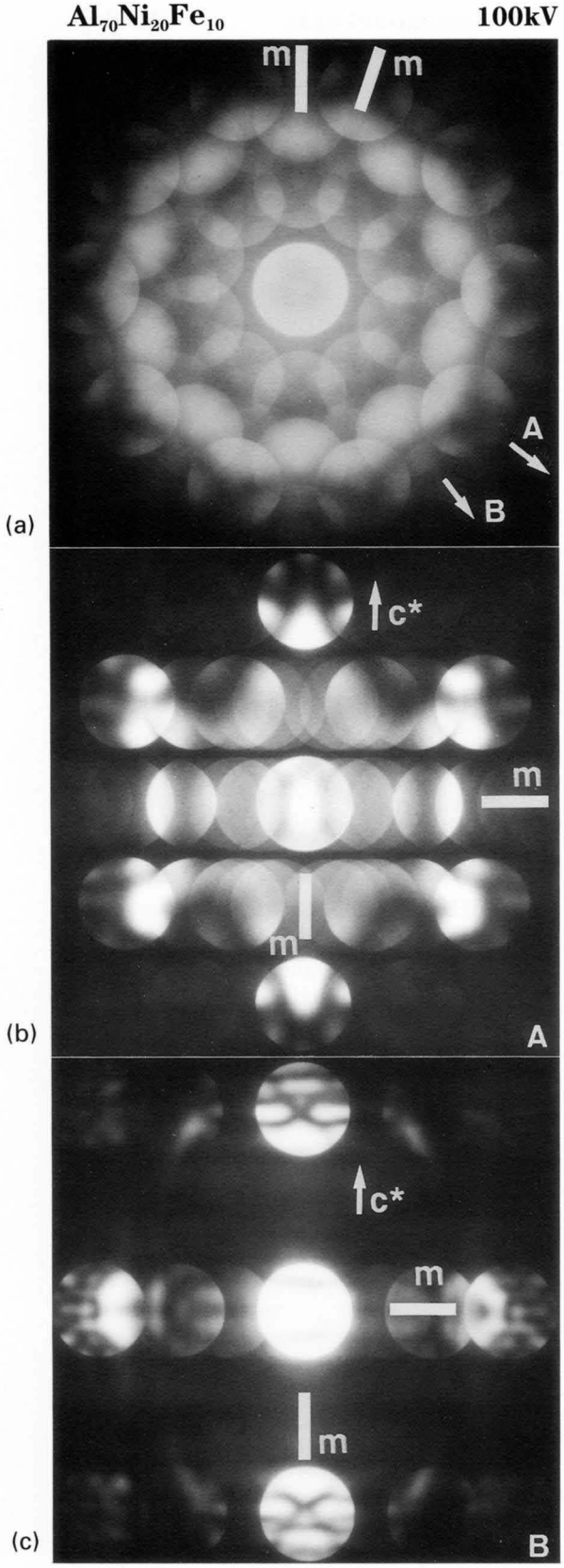

Photograph (a) shows a CBED pattern of an $Al_{70}Ni_{20}Fe_{10}$ alloy taken at an incidence parallel to the decagonal axis. The pattern exhibits tenfold rotation and mirror symmetry, the total symmetry being $10mm$. CBED patterns taken at incidences perpendicular to the c-axis show mirror symmetry perpendicular to the c^*-axis (Photos (b) and (c)). Since the symmetries of these patterns have to be considered by projection approximation, possible point groups are 10 2 2 and $10/mmm$. HOLZ reflections in Photo (d) shows $2mm$ symmetry, indicating the existence of mirror planes. These results indicate that the point group of the alloy is centrosymmetric $10/mmm$. Since no absence rule of the reflections was found in conventional diffraction patterns, the space group of the $Al_{70}Ni_{20}Fe_{10}$ alloy was determined to be $P10/mmm$.

As concerns the quality of CBED symmetry, this alloy is the best among all the quasicrystals of $P10/mmm$ which we have ever examined.

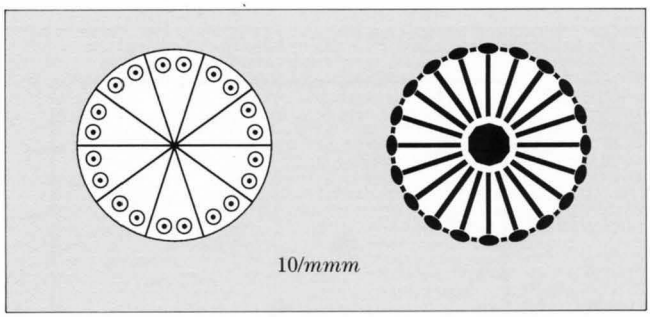

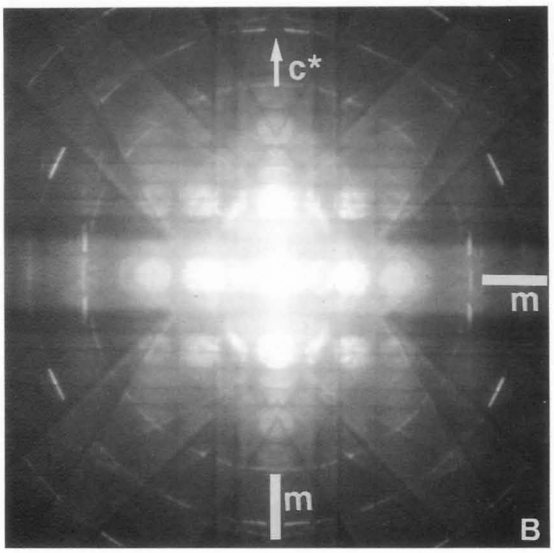

(d)

$Al_{70}Ni_{10+x}Fe_{20-x}$ — phase transformation —

Figure (a) shows the results of the space group determination for all the alloys $Al_{70}Ni_{10+x}Fe_{20-x}$ investigated. It is seen that the alloys in a range between $0 \leq x \leq 7$ belong to the noncentrosymmetric $P\bar{1}0m2$ and those between $7 < x \leq 10$ to the centrosymmetric $P10/mmm$. Therefore, these results show that a phase change occurs at around 17 at.% of Ni. It has been found for the first time that two different decagonal quasicrystal phases exist in one alloy system.

Recent examination shows that there may exist a long-term annealing effect. That is, a specimen of $Al_{70}Ni_{20}Fe_{10}$, whose space group had been determined as $P10/mmm$, was found to transform to have a space group $P10_5/mmc$ after the lapse of one year. The latter space group is obtained presumably by a more perfect mixing of the basic clusters with the positive and negative senses of polarity. If this is the case, the state of $Al_{70}Ni_{20}Fe_{10}$ with $P10/mmm$ may be an intermediate or transient state.

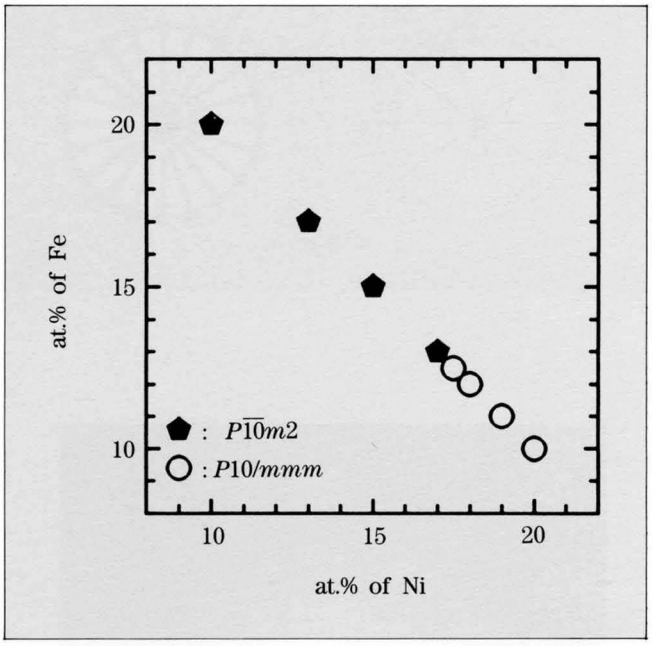

(a)

Changes in space groups of $Al_{70}Ni_{10+x}Fe_{20-x}$ with compositions of Ni and Fe.

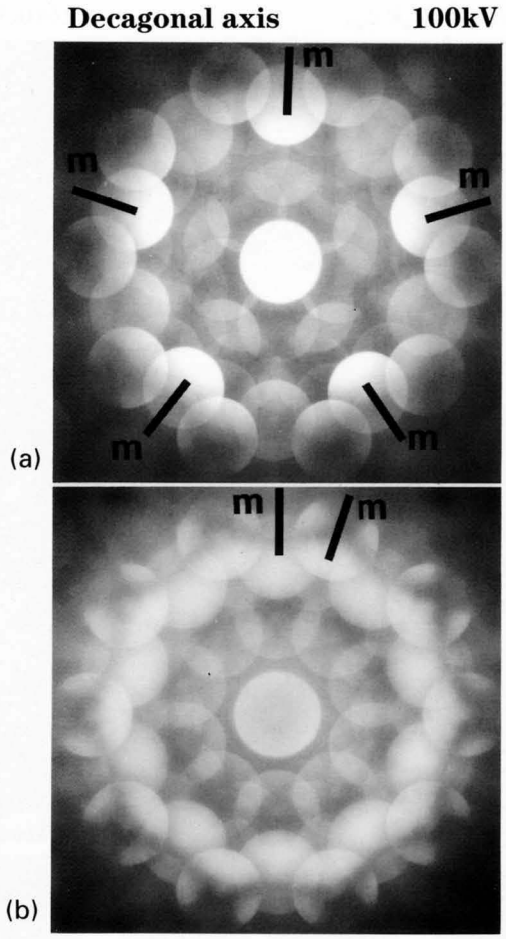

(a)

(b)

CBED patterns of decagonal quasicrystals $Al_{70}Ni_{13}Fe_{17}$ (a) and $Al_{70}Ni_{20}Fe_{10}$ (b) taken at incidences parallel to the decagonal axis. The pattern (a) shows fivefold rotation and mirror symmetry, $5m$ and the pattern (b) tenfold rotation and mirror symmetry, $10mm$.

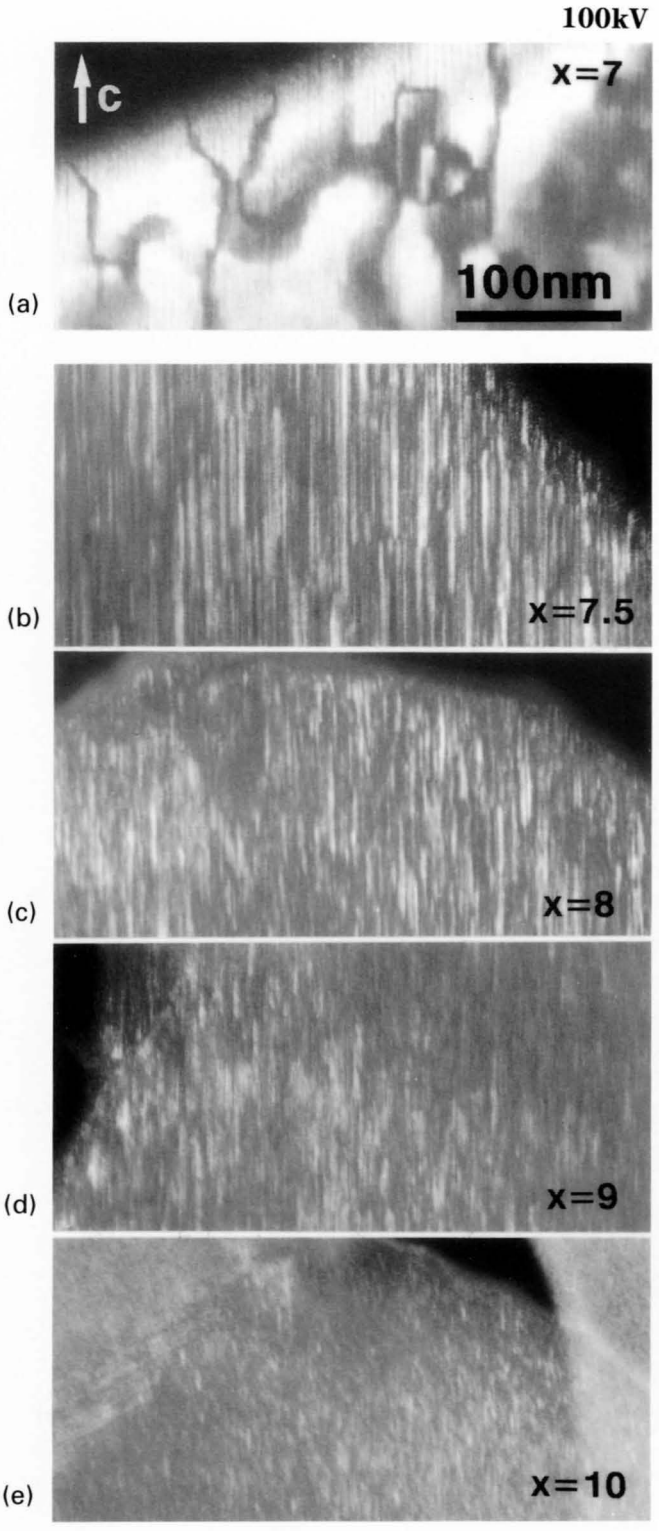

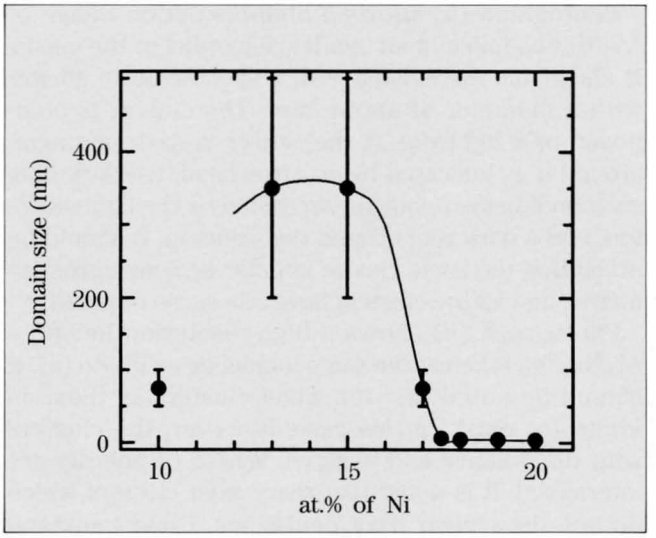

Changes in size of inversion domains with the composition of Ni. The size suddenly becomes very small when the Ni composition exceeds 17 at.%.

Photograph (a) shows a dark-field image taken from $Al_{70}Ni_{17}Fe_{13}$ at an incidence perpendicular to the *c*-axis with the first order reflection of the *c*-planes (0.4nm). The dark lines running nearly in the *c*-direction are inversion domain boundaries with the antiphase shift. The alloy is seen to have domains with a size of roughly 100nm.

Photographs (b) to (e) show dark-field images due to the same reflection, taken respectively from $Al_{70}Ni_{17.5}Fe_{12.5}$ (b), $Al_{70}Ni_{18}Fe_{12}$ (c), $Al_{70}Ni_{19}Fe_{11}$ (d) and $Al_{70}Ni_{20}Fe_{10}$ (e), their space group being centrosymmetric $P10/mmm$. A number of narrow black and/or white bands along the *c*-axis are seen due to inversion domain boundaries with the antiphase shift. One may expect that inversion domains disappear in the centrosymmetric phase. However, many small-sized inversion domains exist. The domain size of the alloys belonging to the noncentrosymmetric phase was a few hundred nm but that of the alloys belonging to the centrosymmetric phase was only a few nm. A rapid decrease of the size in the nanometer scale is seen with the increasing composition of Ni in Photos (b) to (e).

Figure shows a plot of the inversion domain size that changes with the composition of Ni, where the size suddenly becomes very small when the Ni composition exceeds 17 at. %.

Photograph (a) shows a high-resolution image of $Al_{70}Ni_{15}Fe_{15}$ taken at an incidence parallel to the *c*-axis. It elucidates the existence of a specific atom cluster with a diameter of about 2nm. The cluster is composed of a light dot at the center, a dark pentagon around it as indicated by an arrowhead, ten dark dots surrounding the pentagon separated by the light skeleton, and a dark ring around the skeleton. It should be noted that the basic cluster is polar or noncentrosymmetric, and all the clusters have one sense of polarity.

Photograph (b) shows a high-resolution image of $Al_{70}Ni_{20}Fe_{10}$ taken at the same incidence as Photo (a). It should be noted that the same clusters as those in Photo (a) exist. In this case, however, the clusters with the positive and negative senses of polarity are intermixed. It is noted that there exist clusters which do not show clear dark pentagons. Clear pentagon images should disappear if the clusters with one sense are on top of the clusters with the other sense.

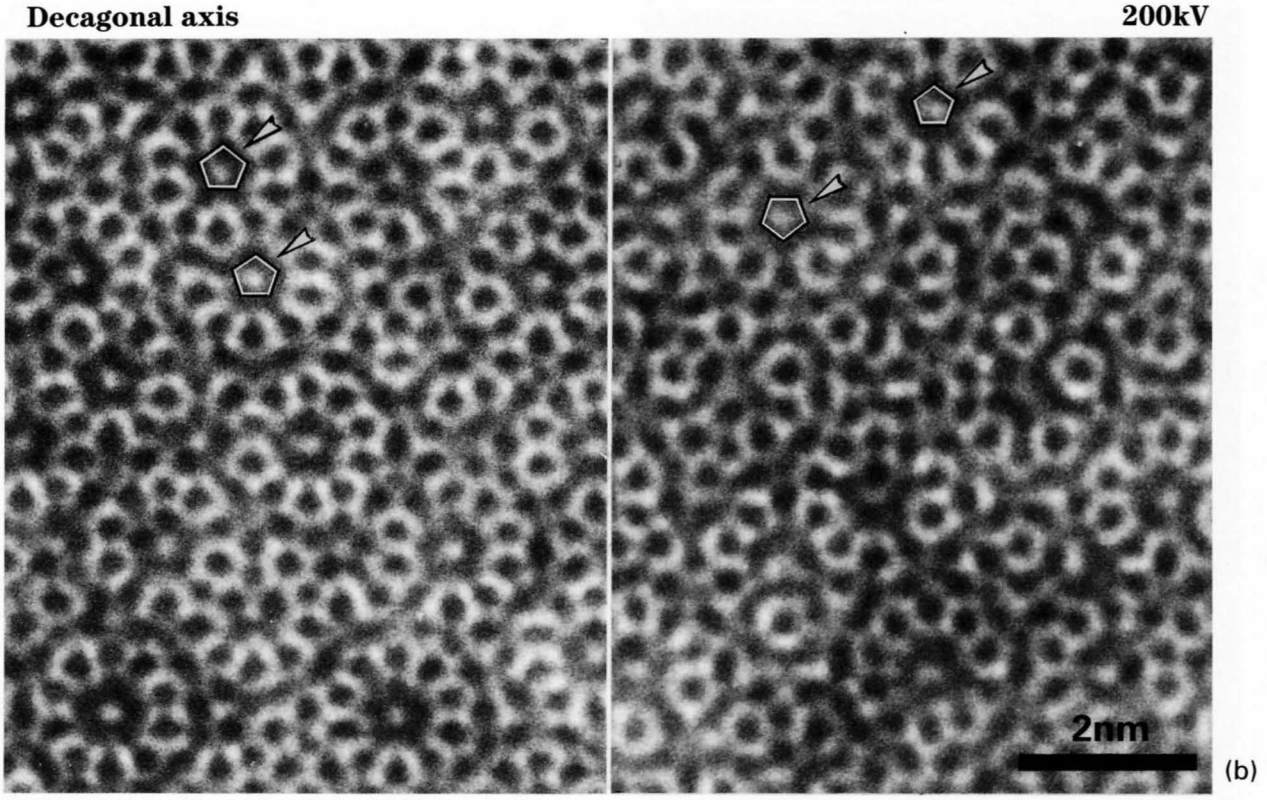

High-resolution images of the noncentrosymmetric decagonal quasicrystal $Al_{70}Ni_{15}Fe_{15}$ (a) and the centrosymmetric decagonal quasicrystal $Al_{70}Ni_{20}Fe_{10}$ (b).

Al-Cu-Co and Al-Co Alloys

Decagonal quasicrystals of melt-quenched $Al_{70}Cu_xCo_{30-x}$ (x=2, 4, 6, 8, 10 and 12), $Al_{65}Cu_xCo_{35-x}$ (x=15 and 20) and $Al_{73}Co_{27}$ were investigated by CBED and transmission electron microscopy [a], [b]. It was found that all the alloys belong to the noncentrosymmetric space group $P\bar{1}0m2$. $Al_{73}Co_{27}$ is the first noncentrosymmetric binary quasicrystal.

Figure shows the electron-atom ratio (e/a) of $Al_{70}Cu_xCo_{30-x}$ and $Al_{65}Cu_xCo_{35-x}$ as a function of composition (at.%) of Cu. Tsai *et al.* [c] proposed a value of e/a=1.75 for the formation of stable decagonal quasicrystals on slow cooling. The alloys $Al_{70}Cu_xCo_{30-x}$ with a value of $e/a \approx 1.75$, $Al_{70}Cu_4Co_{26}$ (e/a=1.70), $Al_{70}Cu_6Co_{24}$ (e/a=1.75) and $Al_{70}Cu_8Co_{22}$ (e/a=1.80), show a good quasicrystalline order. $Al_{73}Co_{27}$ with e/a=1.73 also shows a good quasicrystalline order. For the $Al_{65}Cu_xCo_{35-x}$ system, however, $Al_{65}Cu_{15}Co_{20}$ with e/a=1.76 does not form a good quasicrystalline order.

Dark-field microscopy revealed the existence of inversion domains with an antiphase shift of $c/2$ at the domain boundaries. These results are analogous to those for the melt-quenched alloy $Al_{70}Ni_{15}Fe_{15}$. However, structural phase transformation as a function of the transition metal composition, as observed for the Al-Ni-Fe system, does not occur in the present system, and two types of pentagonal atom cluster images were observed in high-resolution electron microscope images.

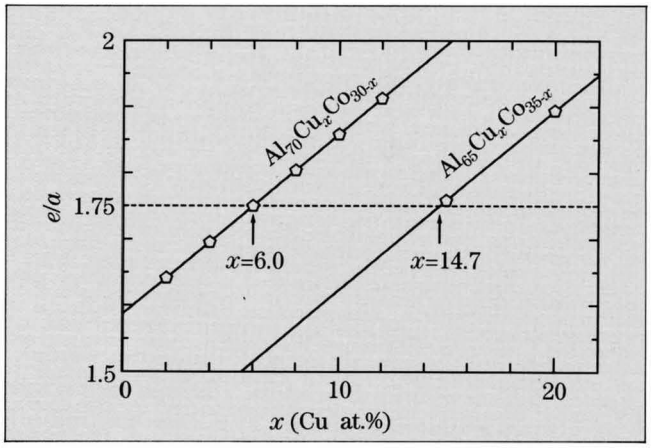

Electron-atom ratio e/a of $Al_{70}Cu_xCo_{30-x}$ and $Al_{65}Cu_xCo_{35-x}$. It is noted that the alloys with $e/a \approx 1.75$ show a good quasicrystalline order for the $Al_{70}Cu_xCo_{30-x}$ system.

References

[a] K. Saitoh, K. Tsuda, M. Tanaka, A. P. Tsai, A. Inoue and T. Masumoto: *Mat. Sci. and Eng.*, **A181/A182** (1994) 805.

[b] K. Tsuda, M. Saito, K. Saitoh, M. Terauchi, M. Tanaka, A. P. Tsai, A. Inoue and T. Masumoto: *Materials Science Forum*, **150-151** (1994) 255.

[c] A. P. Tsai, A. Inoue and T. Masumoto: *Mater. Trans. Jpn. Inst. Met.*, **30** (1989) 463.

$Al_{70}Cu_4Co_{26}$ — symmetry —

Three sets of photographs, (a) to (c), (d) to (f) and (g) to (i) show CBED patterns of $Al_{70}Cu_4Co_{26}$ taken from an area 10nm in diameter with three different incidences. The fact that even thick specimen areas give good symmetry in each set indicates the alloy to have a good quasicrystalline order. By the same procedure as used for $Al_{70}Ni_{15}Fe_{15}$, the space group of $Al_{70}Cu_4Co_{26}$ was determined to be $P\bar{1}0m2$, which is the same as that of $Al_{70}Ni_{15}Fe_{15}$.

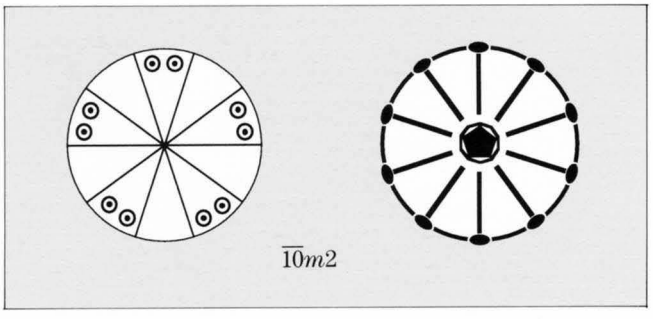

100kV

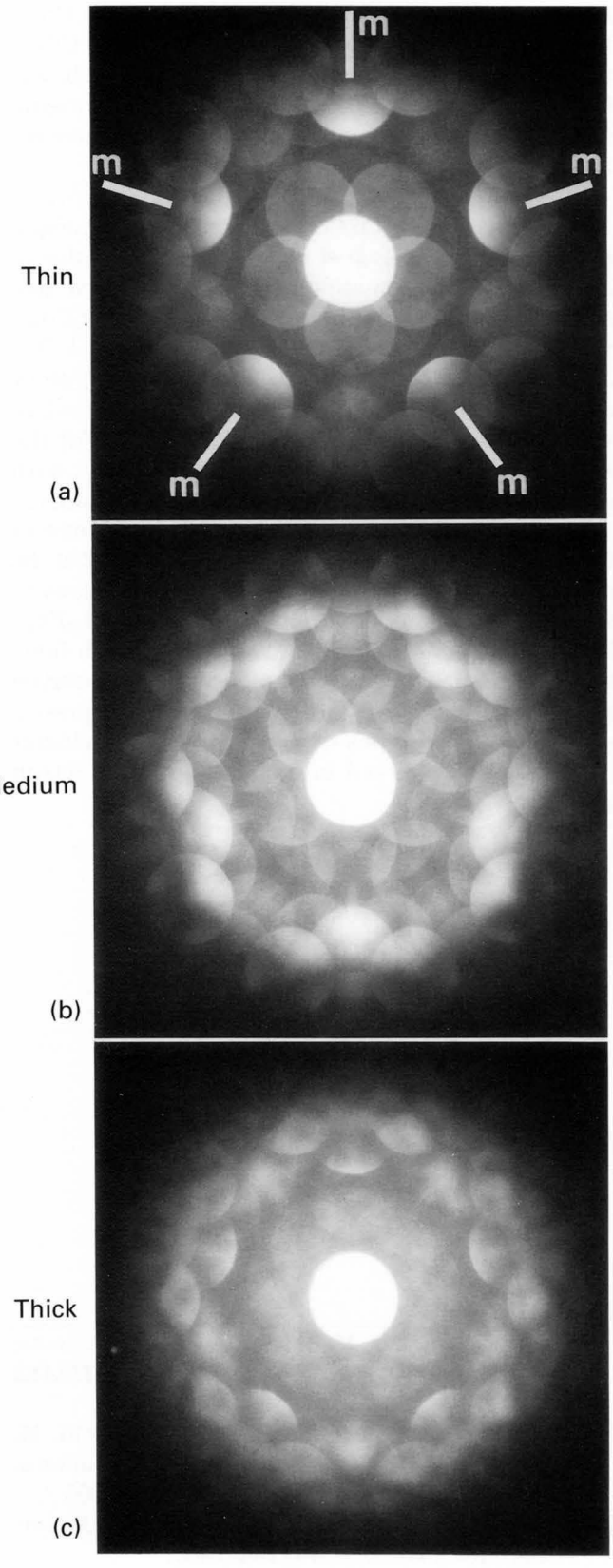

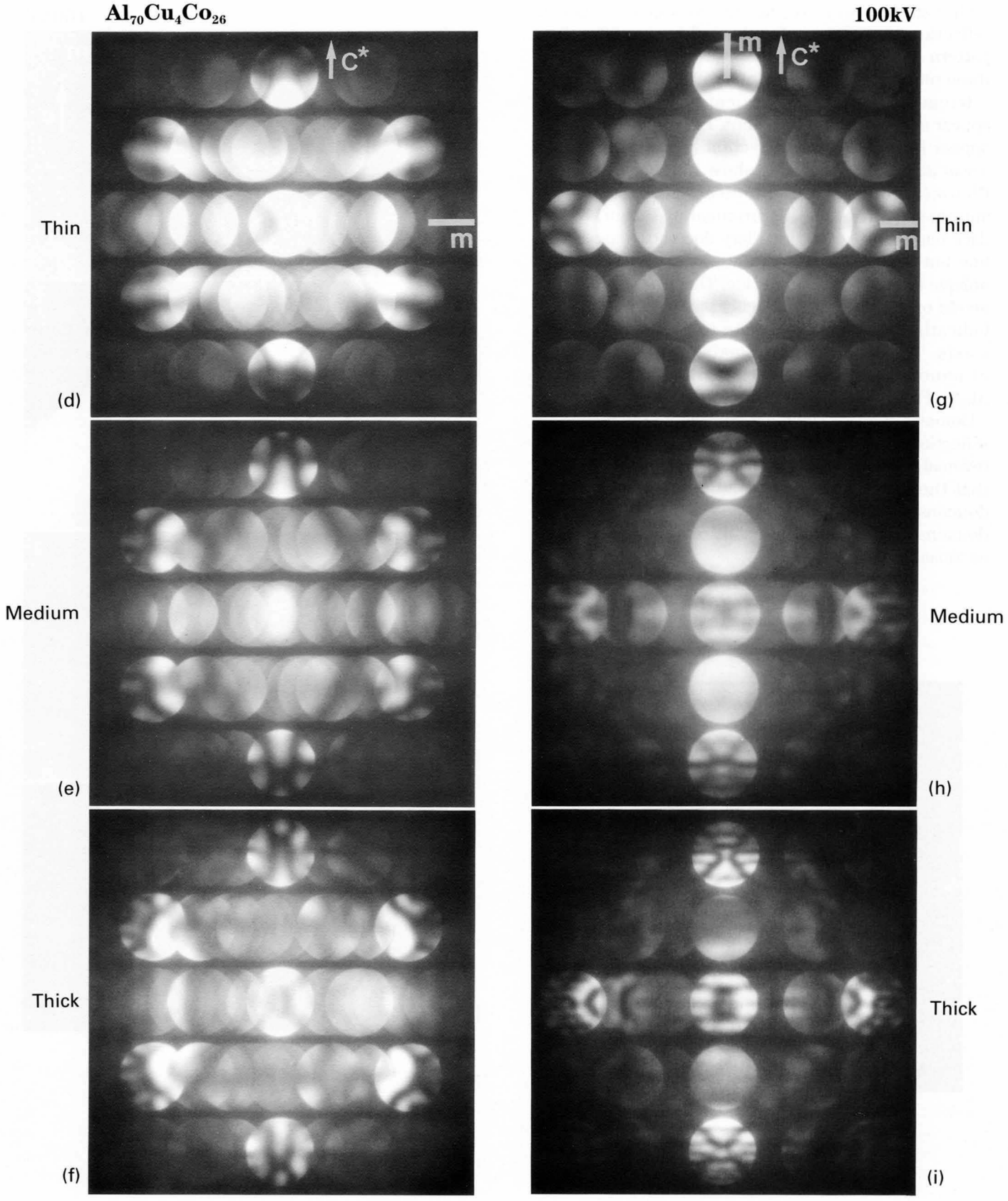
$Al_{70}Cu_4Co_{26}$
100kV
c*
m
c*
m
Thin
Thin
(d)
(g)
Medium
Medium
(e)
(h)
Thick
Thick
(f)
(i)

$Al_{70}Cu_4Co_{26}$ — domain structure —

Photographs (a) to (d) are the dark-field images of reflections 1, 2, 3 and –3 indicated in the diffraction pattern below. These images were taken by exciting these reflections at a systematic reflection condition.

Irregular dark bands indicated by arrowheads appear in the image of reflection 1 (Photo (a)) but disappear in the image of reflection 2 (Photo (b)). The areas adjoining the bands show no net contrast in Photo (a). These results indicate that there is an antiphase shift of $c/2$ (approximately 0.2nm) at the dark bands. Since the boundary does not appear as a line but a broad band, the antiphase boundaries lie oblique to the specimen surface. The long straight segments of the bands run roughly parallel to the c-axis, indicating the boundary plane to be parallel to the c-axis. The sizes of the domains are several tens of nanometers, which are smaller than those of $Al_{70}Ni_{15}Fe_{15}$.

Domains R and S show net contrast in the images of reflections 3 and –3 (Photos (c) and (d)) and contrast reversal between the two images. These results imply that the domains are inversion domains. Thus the domains of $Al_{70}Cu_4Co_{26}$ were revealed to be inversion domains with an antiphase shift of $c/2$, *i.e.*, the same as those found in $Al_{70}Ni_{15}Fe_{15}$.

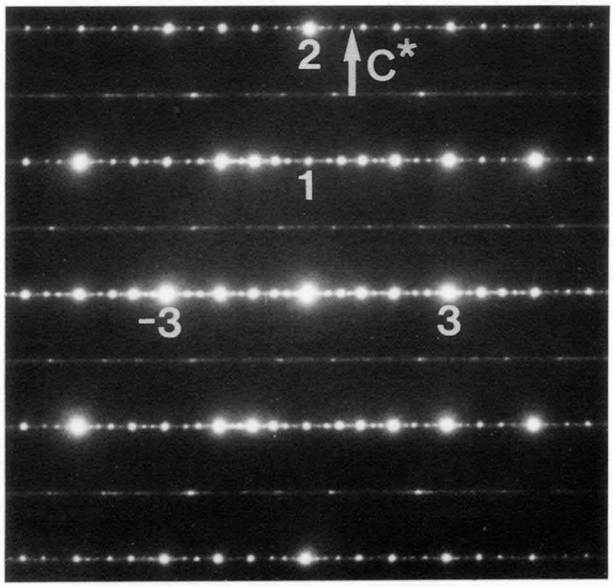

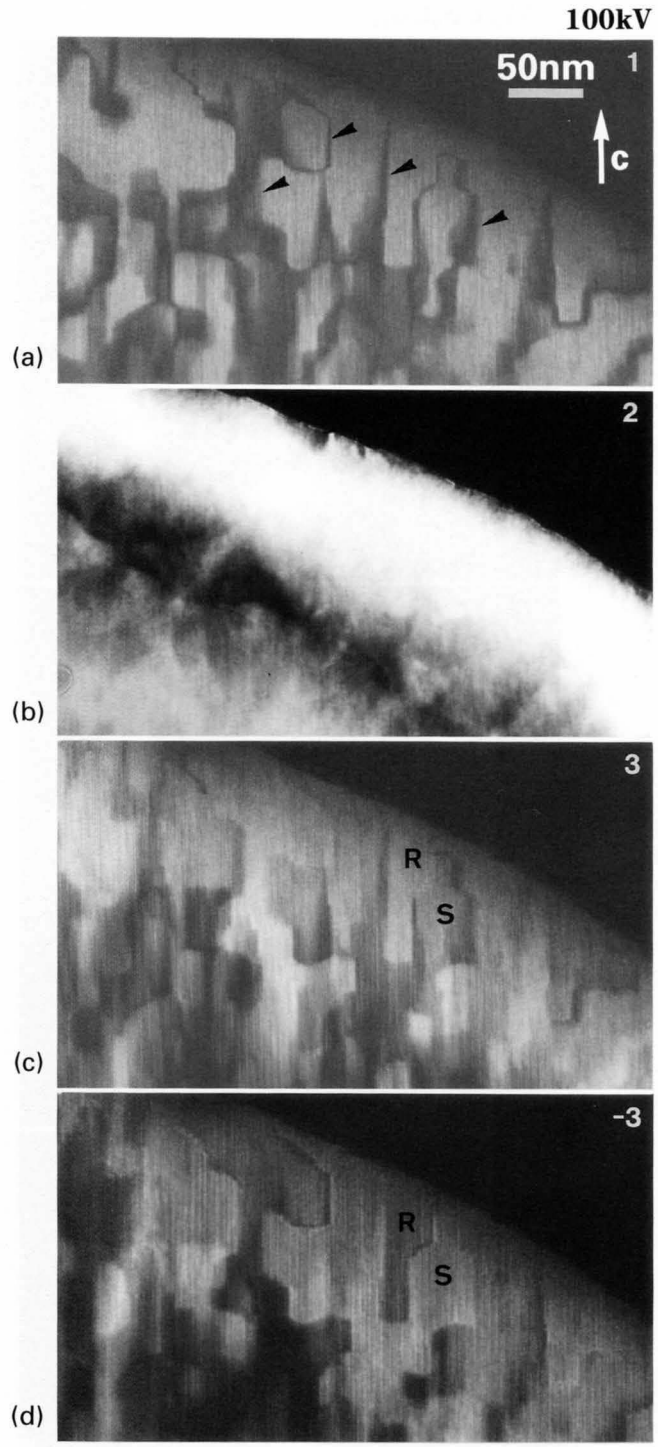

Photograph shows a high-resolution electron microscope (HREM) image of $Al_{70}Cu_4Co_{26}$ taken at an incidence parallel to the *c*-axis. Two types of specific atom cluster images with a diameter of about 2nm are seen (designated by α and β). These two basic clusters are polar or noncentrosymmetric.

The cluster of type α is composed of a light dot at the center, a dark pentagon around it, ten dark dots separated by a light skeleton surrounding the pentagon and a dark ring around the skeleton. The cluster of type β, which exhibits more conspicuous fivefold symmetry than the cluster of type α, is composed of a light dot at the center, a dark pentagon around it, and five dark dots separated by a light skeleton surrounding the dark pentagon. It should be noted that most clusters are of type β and clusters of type α are less in the present alloy.

All the clusters in domain A have one polarity, but those in domain C have the opposite polarity. In region B, domains A and C overlap in the direction of specimen thickness and the clusters do not show a clear pentagonal shape.

Decagonal axis **200kV**

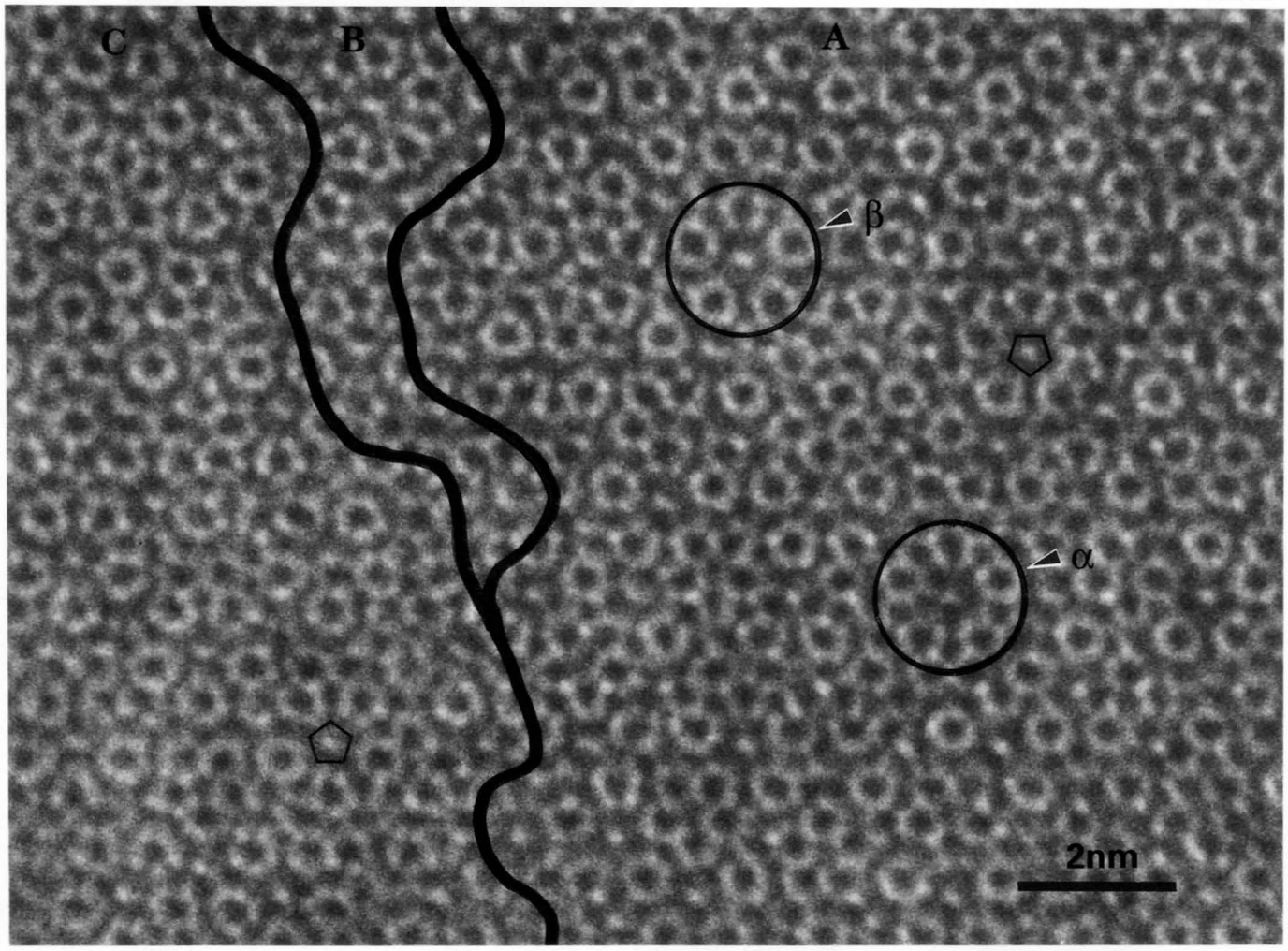

High-resolution electron micrograph of $Al_{70}Cu_4Co_{26}$ taken at an incidence parallel to the *c*-axis. Two types of pentagonal clusters, types α and β, are seen.

$Al_{73}Co_{27}$

The three CBED patterns of $Al_{73}Co_{27}$ show the same symmetries as those of $Al_{70}Cu_4Co_{26}$ taken with the corresponding incidences. The space group of $Al_{73}Co_{27}$ is $P\bar{1}0m2$. This alloy is the first noncentrosymmetric binary quasicrystal.

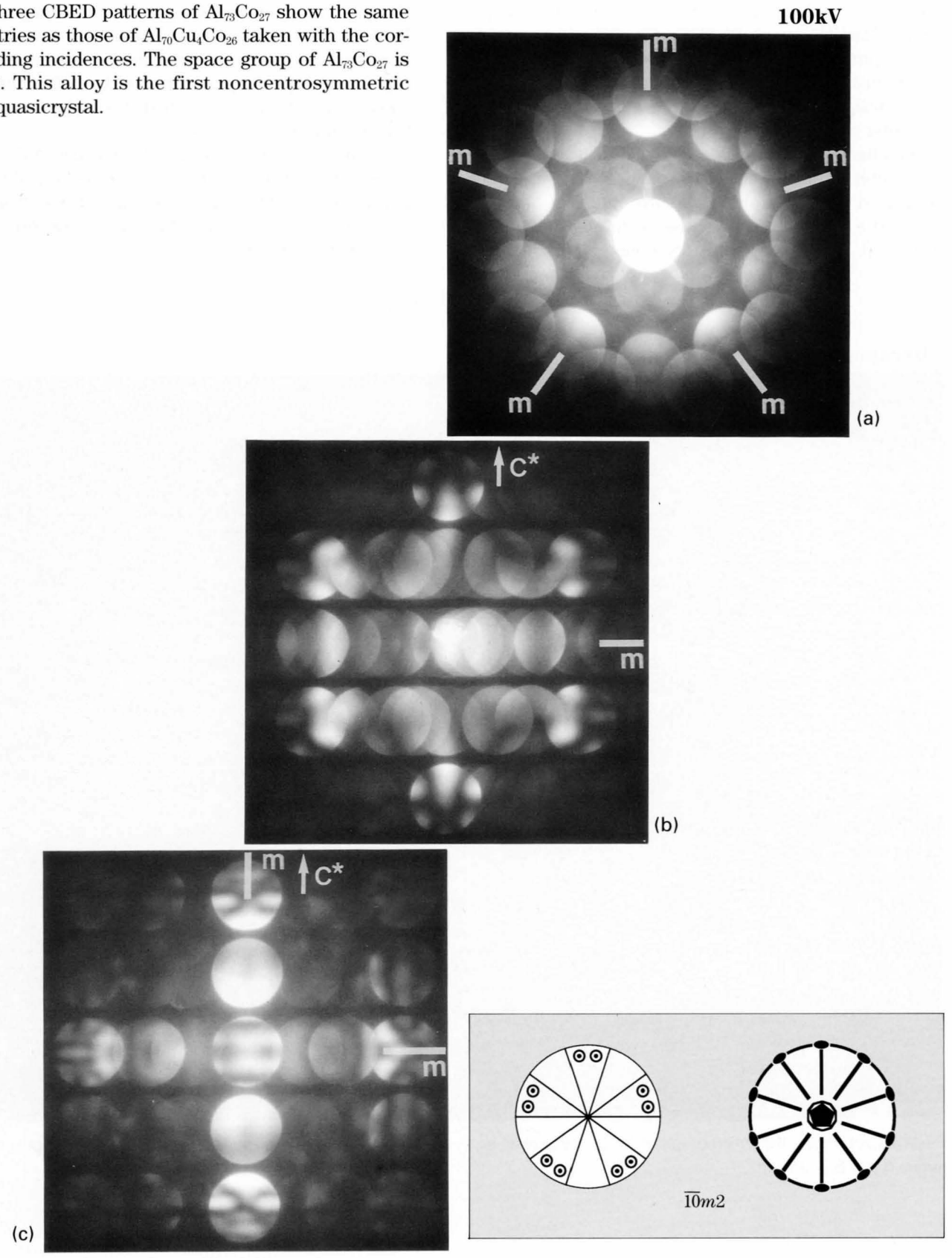

Al-Ni-Rh Alloys

$Al_{70}Ni_{20}Rh_{10}$ — symmetry —

Decagonal quasicrystals of melt-quenched $Al_{70}Ni_{20}Rh_{10}$ were examined by CBED and HREM.

A CBED pattern (a) exhibits a tenfold rotation and mirror symmetry, the total symmetry being $10mm$. CBED patterns (b) and (c) taken at incidences A and B perpendicular to the c-axis showed mirror symmetries perpendicular and parallel to the c^*-axis. Possible point groups are 10 2 2 and $10/mmm$ under projection approximation. HOLZ reflections seen in the outer part of Photo (c), which is not shown here, exhibited $2mm$ symmetry. Thus, the point group was revealed to be $10/mmm$.

Photograph (d) on the next page was taken by tilting slightly the incident beam to the c^*-direction from incidence A. Dynamical extinction (arrowheads) is seen in the odd order reflections along the c^*-axis. This indicates the existence of a 10_5 screw axis and a c-glide plane. Any other absence rule of the reflections was not observed, implying the lattice type to be primitive. As a result, the space group of $Al_{70}Ni_{20}Rh_{10}$ was determined to be $P10_5/mmc$.

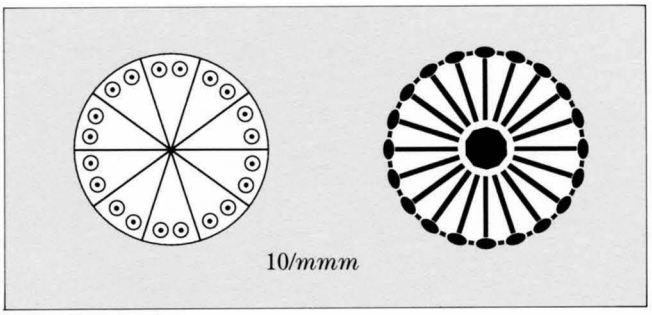

100kV

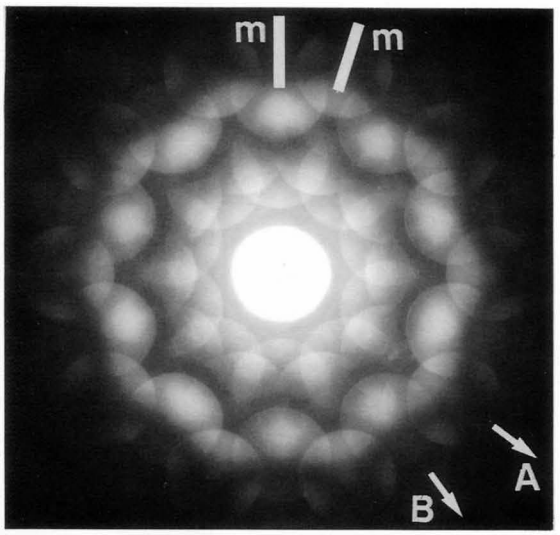

(a)

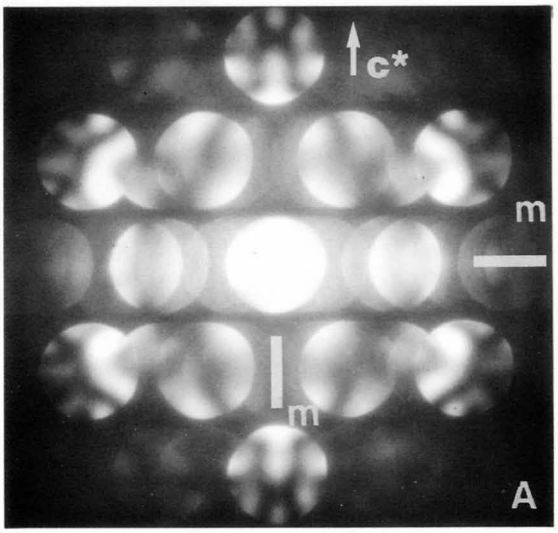

(b)

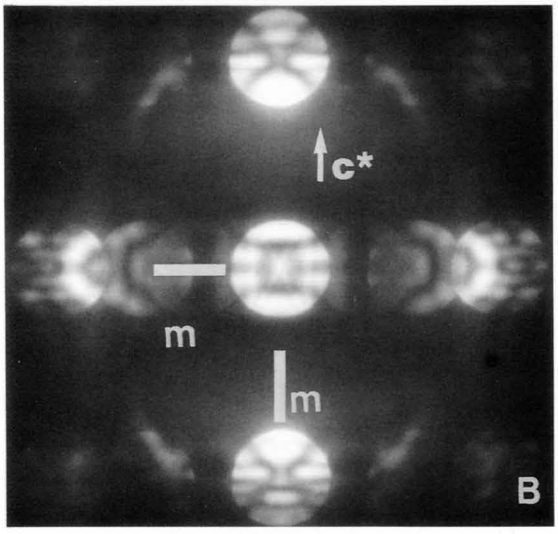

(c)

$Al_{70}Ni_{20}Rh_{10}$ 100kV

$P10_5/mmc$

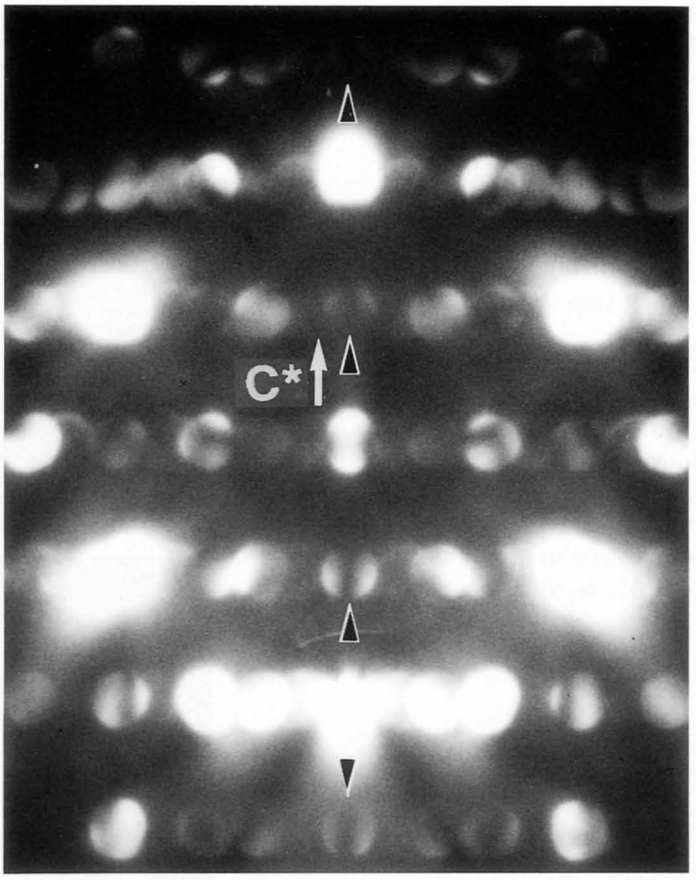

(d)

$Al_{70}Ni_{20}Rh_{10}$ — HREM image —

The photograph shows a HREM image taken at an incidence parallel to the *c*-axis. Specific atom clusters with a diameter of about 2nm are seen. They looks similar to those of $Al_{70}Ni_{15}Fe_{15}$ but are nonpolar and of almost tenfold symmetry. It should be noted that the nonpolar image can be formed by a superposition of two polar atom clusters in neighbouring two layers along the *c*-axis, which are related by a 10_5 screw axis.

Decagonal axis

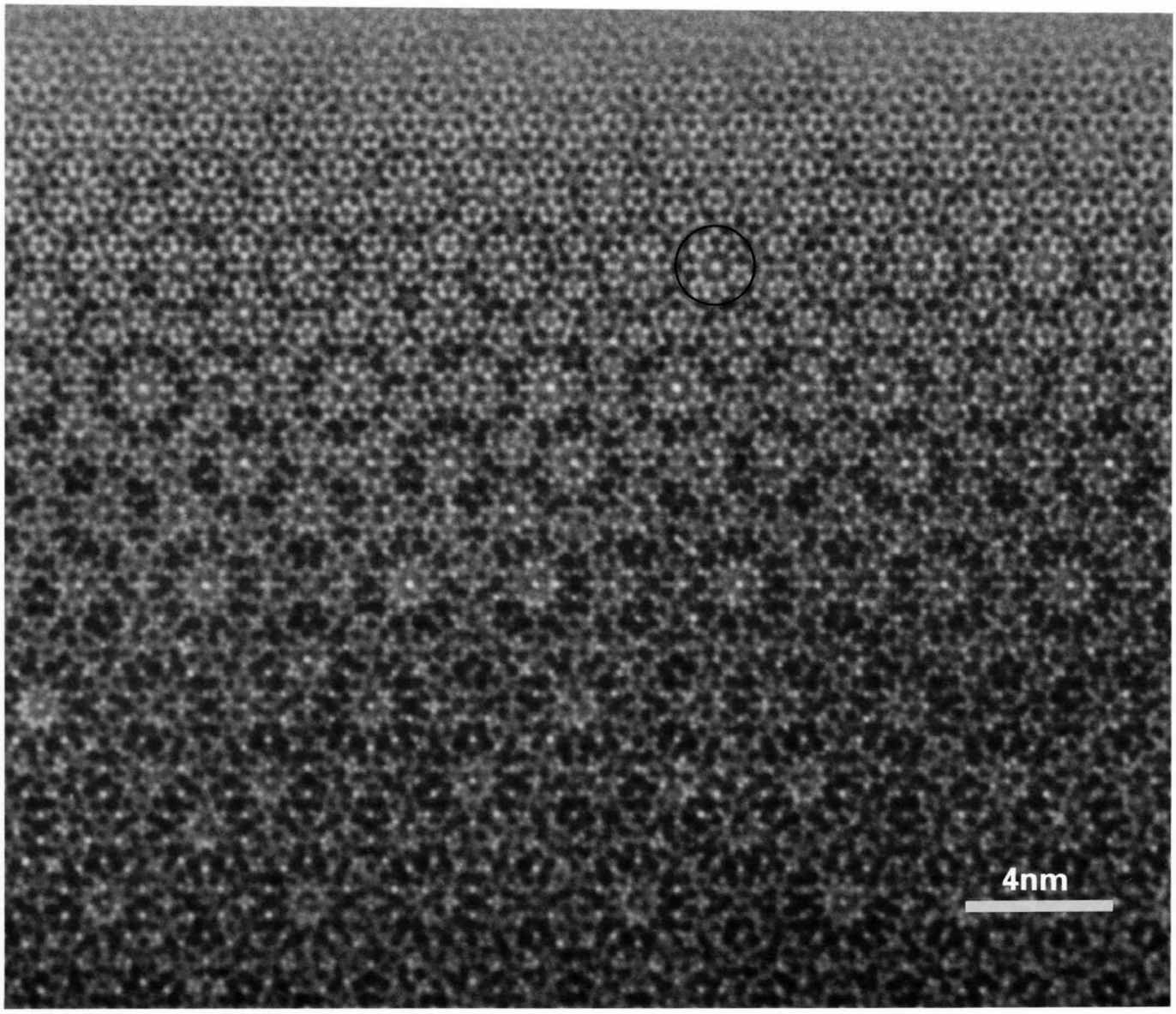

High-resolution image of $Al_{70}Ni_{20}Rh_{10}$ taken at an incidence parallel to the *c*-axis. Not pentagonal but decagonal specific clusters are noted.

Structure Analysis

Characteristics of CBED Structure Analysis

CBED is entering a stage of quantitative studies, among which crystal structure analysis is the most important one. The CBED method has the following advantages compared with the X-ray and neutron diffraction methods with respect to crystal structure analysis.

Firstly, the CBED method enables us to obtain diffraction patterns from a small specimen area about one nanometer in diameter. The area illuminated with the incident electron beam is small enough to expect that a crystal is perfect and has a constant thickness and no bending. Consequently, CBED patterns can be directly compared with calculated ones based on the dynamical theory of electron diffraction. The method can be applied not only to the determination of perfect crystal structures but also to that of local crystal structures which change with the specimen position. This is contrasted with the fact that X-ray and neutron diffraction analyses determine the structural parameters averaged over a large specimen volume which consists of mosaic crystals and includes many domains and lattice defects.

Secondly, CBED intensities possess information on the phases of crystal structure factors because of strong dynamical diffraction effects. This fact shows a great difference from X-ray and neutron diffraction analyses, in which the intensities can be explained by the kinematical diffraction theory and information on the phases of crystal structure factors is lost. Therefore, CBED can determine atom positions without encountering the phase problem with which X-ray structure analysis is confronted.

In X-ray analysis, corrections of intensity data especially for extinction and absorption are important while such corrections are not necessary in the case of CBED. Hence, raw intensity data on CBED patterns are of good quality to compare directly with theoretical intensities when the patterns are taken from thin specimens. However, one important thing to be done for accurate structure determination is the subtraction of inelastically scattered electrons. On the opposite page, a comparison between structure analysis by X-rays and that by CBED is given.

We should not forget to emphasize that recent technical developments have enabled the structure analysis by the CBED method. The first is new recording tools for electrons – an imaging plate (IP) and a slow scan CCD camera, which have taken the place of negative films. They have high sensitivity, a wide dynamic range and a linear response for electron doses. The second is energy filtering techniques to eliminate inelastically scattered electrons, using energy filters of the sector-type and the omega-type. A commercial filter of the former type is available from Gatan Inc., and a commercial electron microscope equipped with the latter type filter from Zeiss Co., Ltd. Those filters are indispensable for the structure analysis with high precision. The third is high-speed computers for laboratory use or work stations (WS). Many-beam dynamical calculations using more than one hundred beams are necessary for obtaining accurate CBED intensities. The calculations are carried out for a large number of points with different excitation errors, and further repeated by changing structural parameters to obtain their final values, using the nonlinear least square method. Without use of a recent work station, the structure analysis by CBED is impossible.

Vincent *et al.* [a] first applied the CBED method to the determination of the atom positions of AuGeAs. They estimated the experimental intensities of the HOLZ reflections recorded on negative films, using their eyes. They determined the positional parameters by fitting the experimental intensities with the theoretical ones calculated under a quasi-kinematical approximation. Vincent & Exelby [b] applied the same method to the structure determination of a metastable Al-Ge phase. Tanaka & Tsuda [c], [d] refined the structural parameters (the rotation angle of the oxygen octahedron and the Debye-Waller factor) of the low-temperature phase of $SrTiO_3$, which is known to undergo a typical second-order phase transformation, on the basis of the dynamical theory of electron diffraction.

Recently, the automatic matching of experimental and theoretical CBED patterns has been challenged by minimizing the R factor by the steepest-descent method (Marthinsen, Høier & Bakken [e]), the simplex method (Zuo & Spence [f]), the quasi-Newton method (Bird & Saunders [g]) and by the Marquadt method (Tsuda & Tanaka [7]). Bird & Saunders [h], [i] studied the sensitivity and accuracy of CBED pattern matching and tested an *ab-initio* determination method for the structure factors on the [110] axis of GaP, using simulated patterns as ideal experimental data.

We think that a method to refine crystal structural parameters is important for materials science. The procedure of our method for structure refinement is briefly described. A refinement of the structural parameters of $SrTiO_3$ is demonstrated together with a description of their Bloch states. Another example of CdS is briefly described and the effect of energy filtering is demonstrated.

References

[a] R. Vincent, D. M. Bird and J. W. Steeds: *Philos. Mag.*, **A50** (1984) 745 and *ibid* 765.

[b] R. Vincent and D. R. Exelby: Proc. XIIth International Congress on Electron Microscopy, Seattle, eds. L. D. Peachy and D. B. Williams, San Francisco press, Vol. 2, 1990, p.524.

[c] M. Tanaka and K. Tsuda: Proc. XIIth International Congress on Electron Microscopy, Seattle, eds. L. D. Peachy and D. B. Williams, San Francisco press, Vol. 2, 1990, p. 518.

[d] M. Tanaka and K. Tsuda: Proc. 26th Meeting of Micro-beam Analysis Soc., San Jose, ed. D. G. Howitt, San Francisco press, 1991, p. 145.

[e] K. Marthinsen, R. Høier and L. N. Bakken: Proc. XIIth International Congress on Electron Microscopy, Seattle, eds. L. D. Peachy and D. B. Williams, San Francisco press, Vol. 2, 1990, p. 492.

[f] J. M. Zuo and J. C. H. Spence: *Ultramicroscopy*, **35** (1991) 185.

[g] D. M. Bird and M. Saunders: Proc. 26th Meeting of Micro-beam Analysis Soc., San Jose, ed. D. G. Howitt, San Francisco press, 1991, p. 153.

[h] D. M. Bird and M. Saunders: *Ultramicroscopy*, **45** (1992) 241.

[i] D. M. Bird and M. Saunders: *Acta Cryst.*, **A48** (1992) 555.

Comparison

	Electron diffraction	X-ray diffraction
Scattering length	Large ($\sim 10^4$) (dynamical)	Small (1) (kinematical)
Lenses	Usable	Not usable
Specimens	Small specimens (local structure)	Large crystals (average structure)
Influence of twins and defects	No (perfect crystal, single-domain)	Yes (mosaic crystal, multi-domains)
Important corrections of intensity data	Background due to inelastic scattering	Absorption and extinction
Phase information on structure factors	Obtainable (dynamical)	Not obtainable (kinematical)

Use of HOLZ reflections

HOLZ reflections are used for structure analysis by CBED. Generally, the intensities of HOLZ reflections with large reciprocal lattice vectors $\boldsymbol{g}$ are more sensitive to the displacements of atoms than those of ZOLZ reflections. This can be understood from the fact that the crystal structure factor F_g includes the phase factor $\exp(-2\pi i \boldsymbol{g}\cdot\boldsymbol{r})$. For a reflection with a large $\boldsymbol{g}$, the phase factor varies greatly with small changes of atomic coordinate $\boldsymbol{r}$. Thus, small displacements of atoms can be sensitively detected using HOLZ reflection intensities.

HOLZ reflections have two-dimensional intensity distributions, which are explained in terms of dispersion surfaces of Bloch waves. The best way for structure analysis is to use all the two-dimensional data. We, however, use them as one-dimensional line profiles to reduce the computing time of dynamical intensities, since the intensities of HOLZ reflections are almost uniform to a limited extent in the azimuthal direction when a CBED pattern is taken from a thin specimen area. It is possible to use integrated intensities as fitting data instead of line profiles.

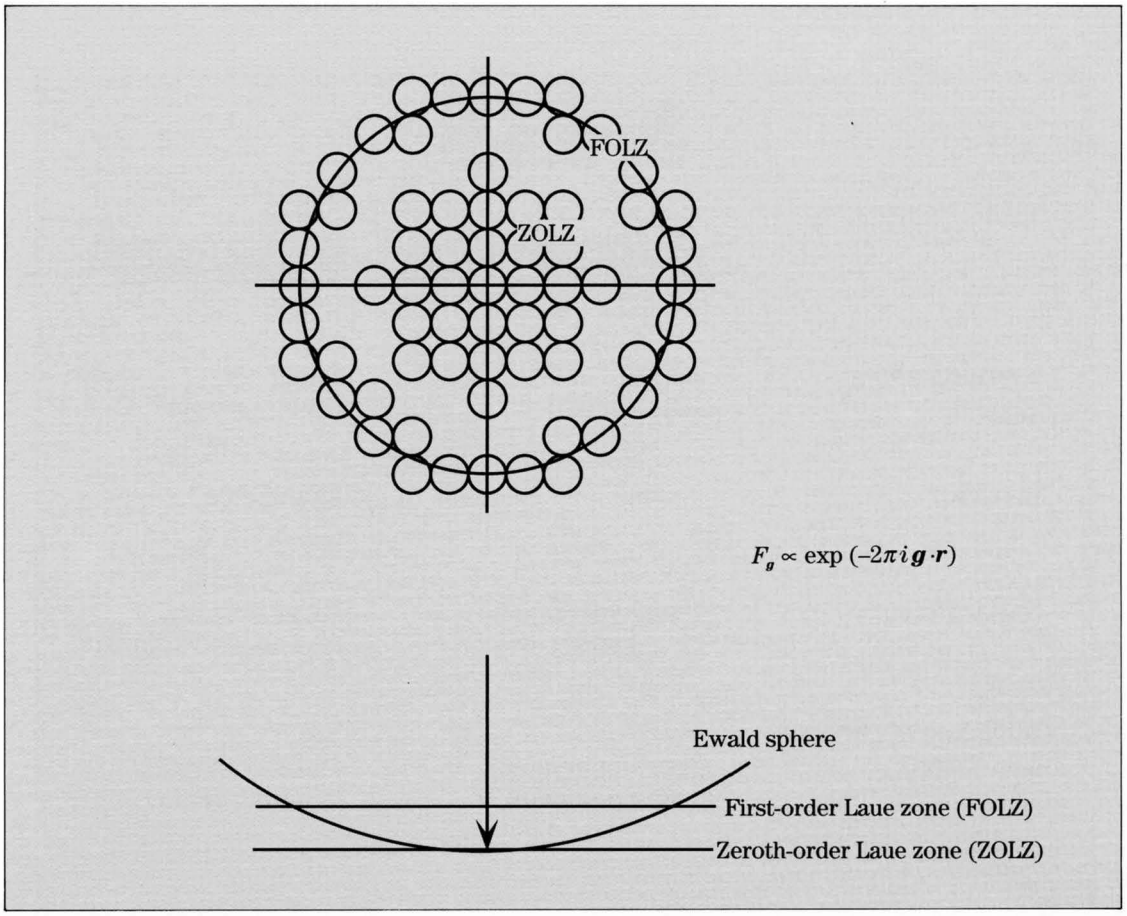

Crystal structure factor includes the phase factor $\exp(-2\pi i \boldsymbol{g}\cdot\boldsymbol{r})$.
The phase factor varies greatly with small changes of $\boldsymbol{r}$ for a large $\boldsymbol{g}$.

Analysis Procedure

In advance of analysis, the space group, the lattice parameters and the tentative positional parameters of atoms of a crystal are assumed to be known, and the accelerating voltage of the incident electrons is separately determined using a HOLZ line pattern of a standard specimen like Si. The analysis procedure is as follows:

(i) CBED patterns are taken from the crystal, using IPs in an electron microscope. A thin area of the specimen has to be chosen to reduce inelastically scattered intensities. We do not use an energy filter at present. If the expected atomic displacements are known in advance, an electron incidence that makes CBED patterns sensitive to the displacements should be selected.

(ii) The intensities of the CBED patterns are read out from the IPs in an IP-reader and are transferred to a work station as digital images.

(iii) The distortion of the patterns due to the lens aberrations of the electron microscope is numerically corrected on the work station. The line profiles of HOLZ reflections which run along the radial directions through the centers of the disks are taken from the CBED patterns. Background intensities are subtracted from the line profiles in a certain approximation.

(iv) The thickness of the specimen is determined by comparing a ZOLZ pattern with those simulated at different thicknesses. Since the patterns are not so sensitive to the structural details, the dynamical simulations are carried out using the structural parameters initially assumed.

(v) The structural parameters are refined by a nonlinear least square method [a] so as to minimize the residual sum of squares S between the experimental HOLZ line profiles and calculated ones. Intensity calculations are carried out by the Bloch wave dynamical theory of electron diffraction with the aid of a generalized Bethe approximation [b]. The analysis procedure is summarized in the following two pages.

References

[a] R. Fletcher: A Modified Marquardt Subroutine for Nonlinear Least Squares, *Harwell Report*, AERE-R (1971) 6799.

[b] M. Ichikawa and K. Hayakawa: *J. Phys. Soc. Jpn.*, **42** (1977) 1957.

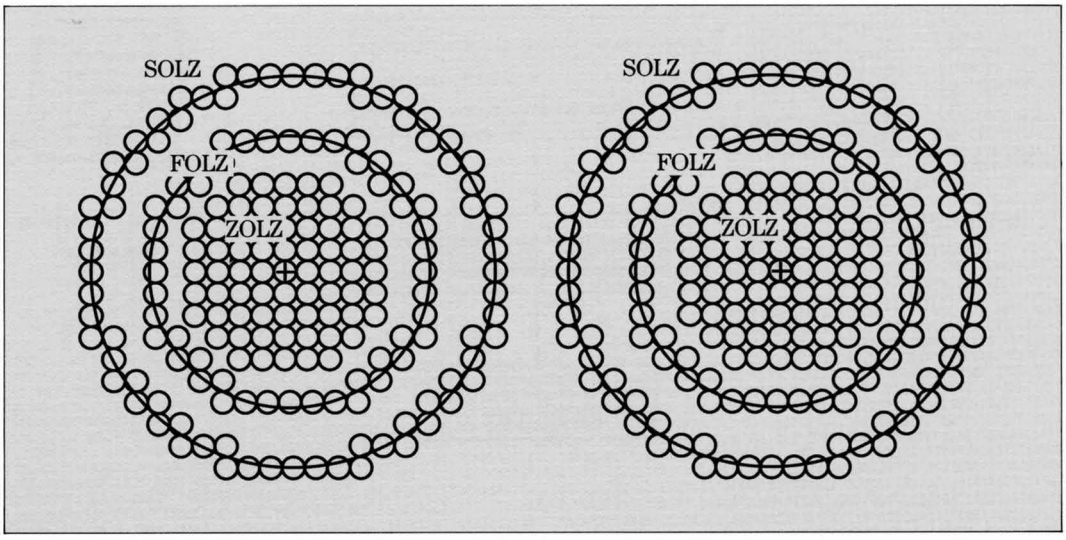

Stereogram of schematic zone-axis CBED pattern.

Experiments

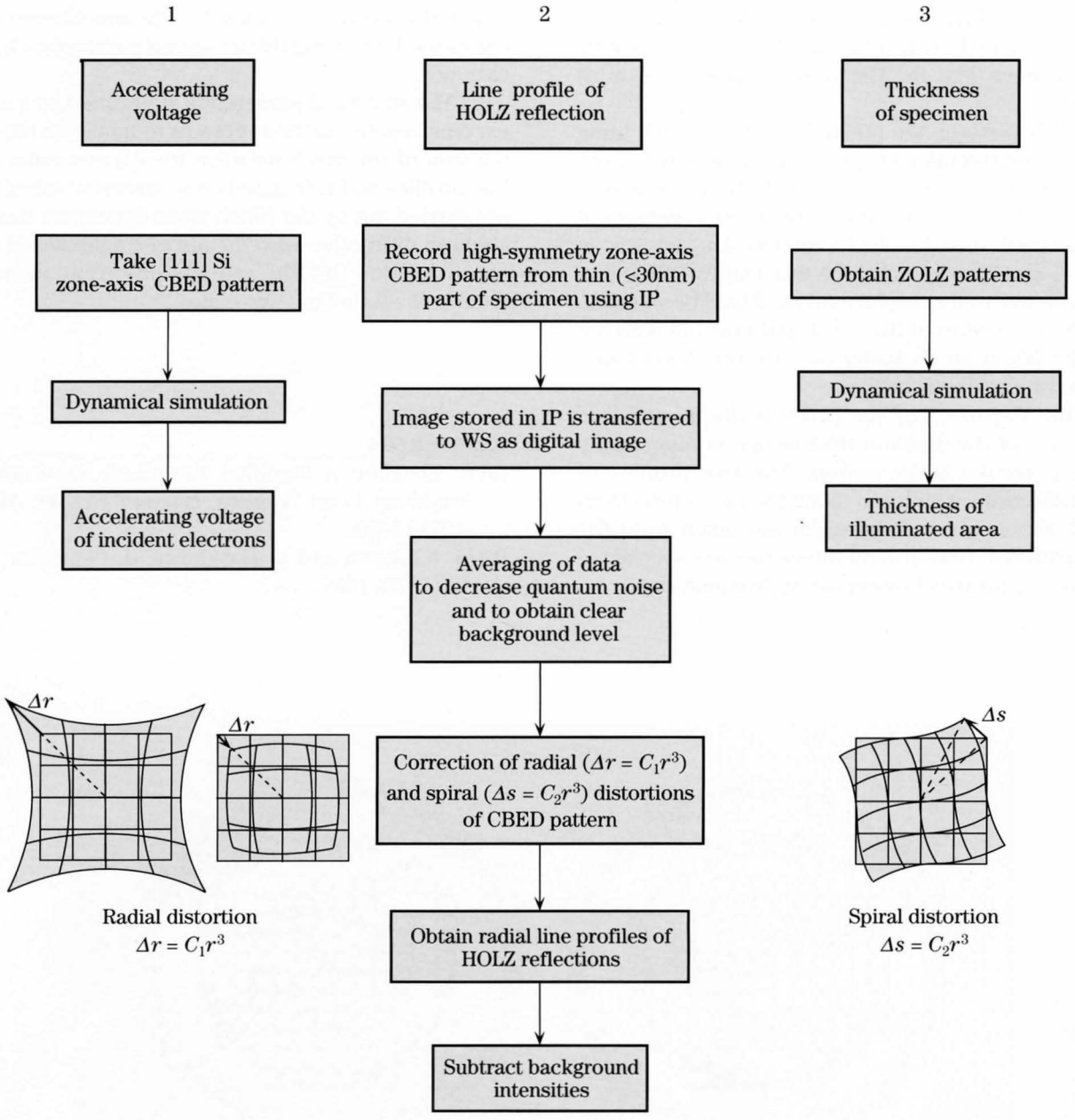

Calculations

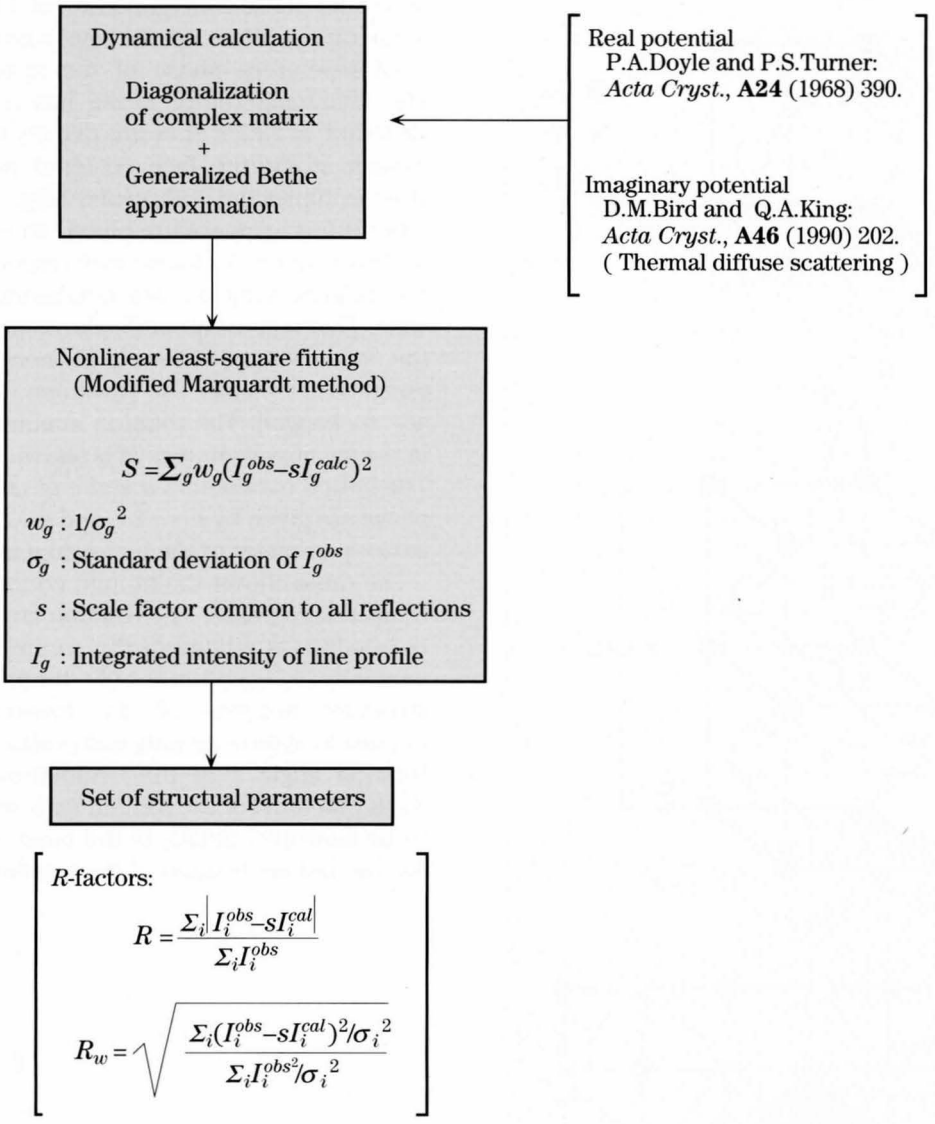

To attain better accuracy for the present method, 1) two-dimensional fittings of the intensity distributions of HOLZ reflections are necessary instead of one-dimensional fitting of the line profiles, 2) energy filtering to remove plasmon-loss electrons is required (see a later part of this chapter), 3) the installation of image-forming lenses with small distortion is necessary, and 4) the number of fitting parameters, which is limited to a small number at present to reduce the calculation time, should be increased. It is noted that an increase of the calculation time with the number of the parameters should be compensated, for example, by a perturbation method [a], [b] to calculate Jacobian matrices.

The maximum entropy method (MEM) is worth applying to obtaining crystal-potential distribution from CBED patterns without determining Debye-Waller factors — ambiguous parameters due to anisotropy, anharmonicity, etc.

References

[a] D. M. Bird: *Acta Cryst.*, **A46** (1990) 208.
[b] J. M. Zuo: *Acta Cryst.*, **A47** (1991) 87.

$SrTiO_3$

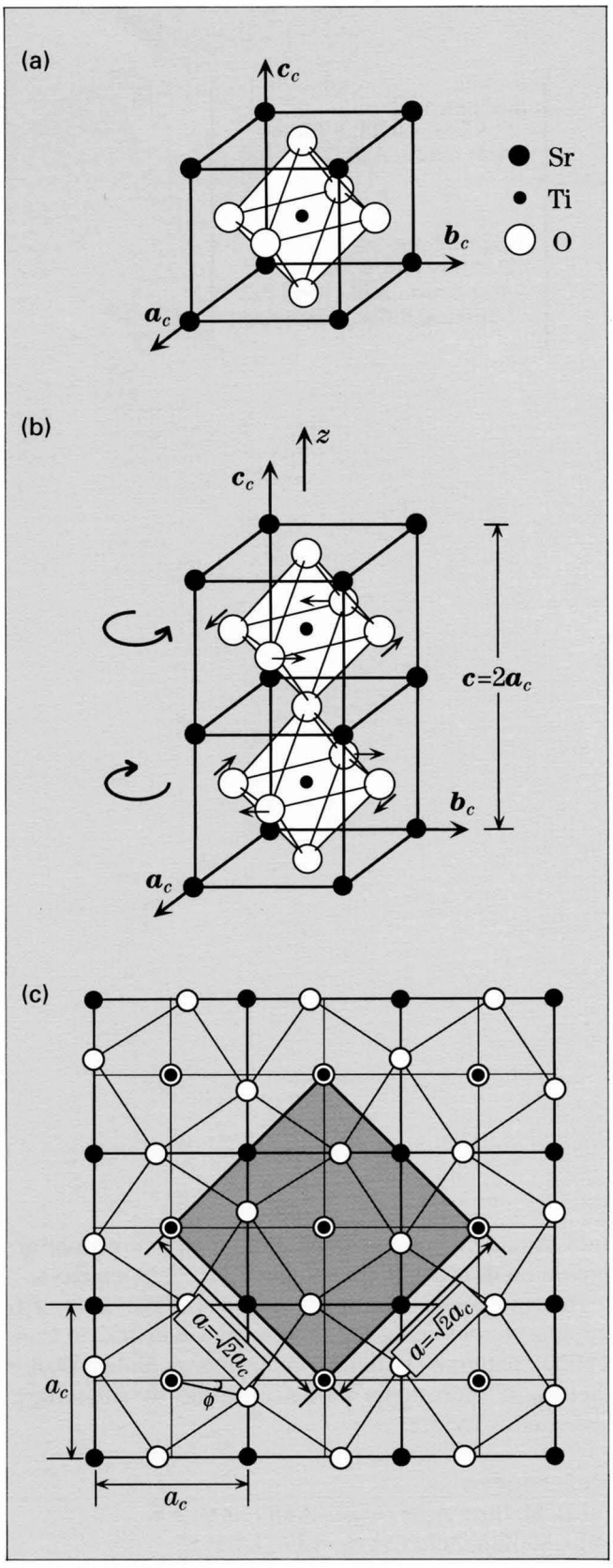

We have applied the present method to the low-temperature phase of $SrTiO_3$. $SrTiO_3$ undergoes a second-order phase transformation at 105K from the high-temperature phase of the space-group $Pm3m$ to the low-temperature phase of the space-group $I4/mcm$. The high-temperature phase has a cubic perovskite structure, in which Sr atoms occupy the lattice corners, oxygen atoms the face centered positions and a Ti atom occupies the body center (Fig. (a)).

In the low-temperature phase, an oxygen octahedron slightly rotates clockwise with respect to the z-axis and the neighbouring oxygen octahedra rotate anticlockwise. This type of atom displacements is described by the condensation of the R_{25}-phonon mode of the high-temperature phase. The positions of Sr and Ti atoms are unchanged. The rotation manner of the octahedra in the successive unit cells is shown in Fig. (b) and (c). The lattice parameters a and c of the low-temperature phase are given by $a \sim \sqrt{2}a_c$ and $c \sim 2a_c$, where a_c is the lattice parameter of the high-temperature phase.

The table shows the atomic coordinates of the low-temperature phase. The rotation angle ϕ of the oxygen octahedron is related to the parameter x for the O(2) atoms by the equation $x = (1 - \tan\phi) / 4$. Therefore, the structure analysis of the low-temperature phase implies to determine only one positional parameter, the rotation angle ϕ of the octahedron and the Debye-Waller factor B of the oxygen ions, where B is assumed to be isotropic. $SrTiO_3$ is the most suitable substance for the first application of the present method.

Atom	Wyckoff position	x	y	z
Sr	4*b*	0	1/2	1/4
Ti	4*c*	0	0	0
O(1)	4*a*	0	0	1/4
O(2)	8*h*	x	1/2+x	0

$SrTiO_3$ [001] T = 87K

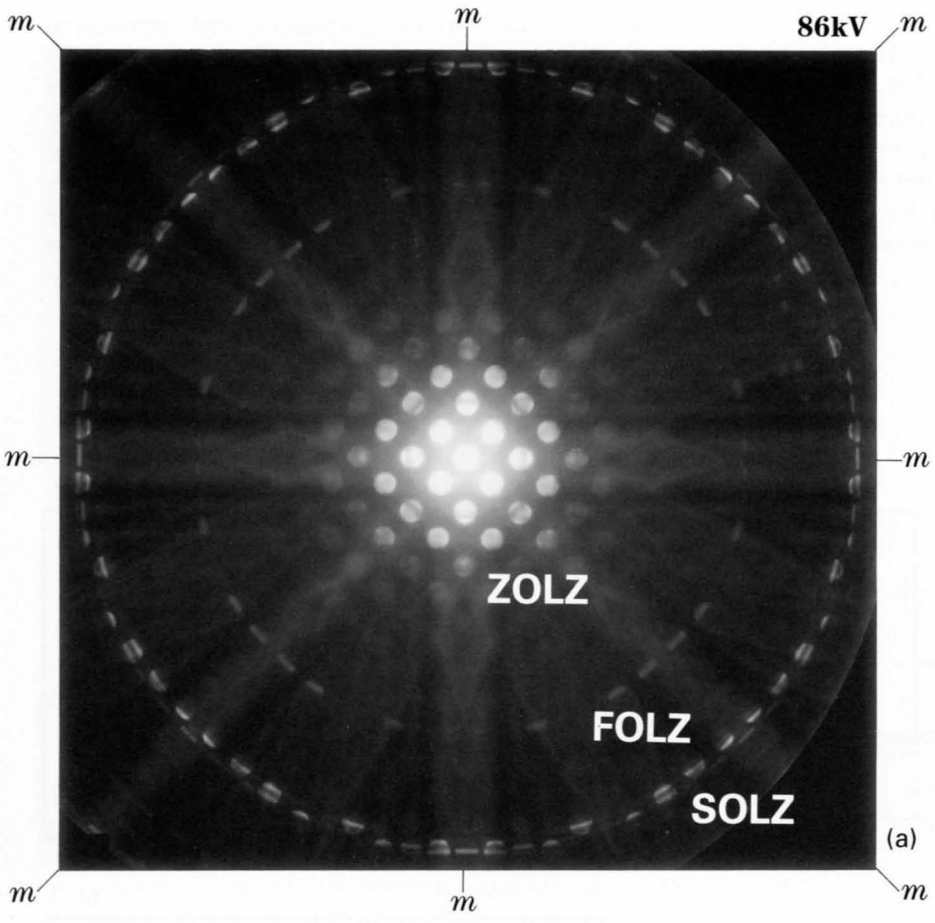

(a)

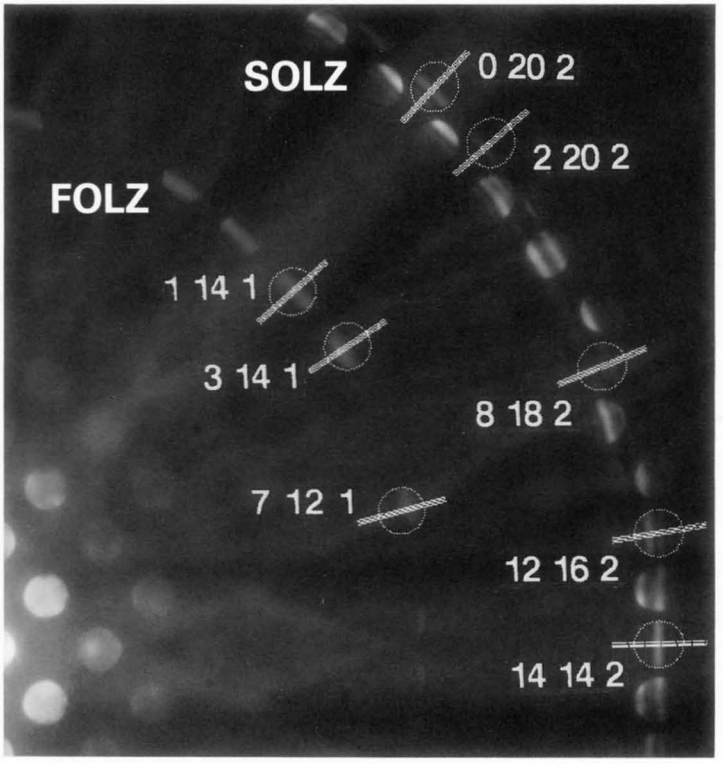

(b)

Photograph (a) shows a CBED pattern of the low-temperature phase of $SrTiO_3$ taken with the [001] incidence at 87K from a 3-nm-diameter area in one domain. The electron microscope used was a JEM-100CX equipped with a field emission gun (FEG).

The first-order Laue zone (FOLZ) reflections are superlattice reflections appearing only in the low-temperature phase, where the lattice parameter c is twice that in the high-temperature phase. The intensities of the reflections are governed by the value of the rotation angle of the oxygen octahedron.

The second-order Laue zone (SOLZ) reflections were the FOLZ reflections in the high-temperature phase. Only O(2) oxygens contribute to the h k 2 (h, k = even) reflections, but all the atoms to the h k 2 (h, k = odd) reflections. The CBED pattern exhibited a fourfold rotation and two types of mirror symmetries, the total symmetry being $4mm$. Hence, the reflections within one eighth sector are symmetry independent.

Photograph (b) shows a quarter sector of Photo (a). After performing distortion correction and averaging of the CBED pattern (see page 122), three FOLZ reflections and five SOLZ reflections with even values of h and k indicated in Photo (b) were used for the analysis, all of these reflections being unaffected by Sr, Ti and O(1) atoms but only by O(2) atoms.

Background subtraction

Background intensities are subtracted from the original line profiles (see page 122). Figure (a) shows a line profile of the 1 14 1 reflection. The subtraction of a linear form background, using the intensities at both ends of the line profile, resulted in the profile of Fig. (b). Positional parameters of $SrTiO_3$ are determined by fitting the intensities of line profiles and the integrated intensities of HOLZ reflections with theoretical ones calculated by full dynamical treatment.

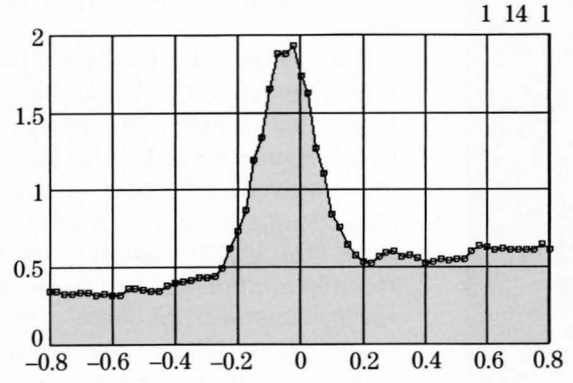

(a) Original

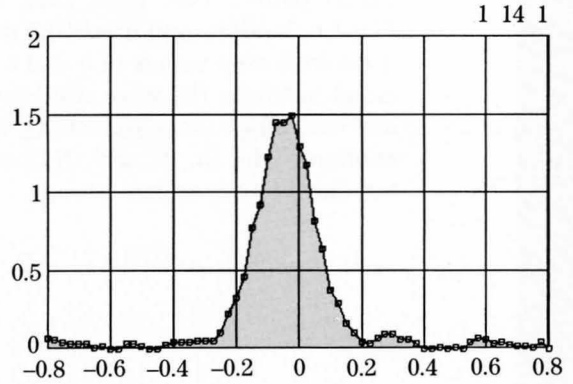

(b) Background subtracted

Sensitivity of HOLZ reflections to ϕ and B

Figures (c) and (d) show sensitivity-test simulations of the 7 12 1 reflection to the rotation angle ϕ of the oxygen octahedron and the Debye-Waller factor B of the oxygen, respectively. Considerable intensity changes are seen to occur with small changes in ϕ and B, ensuring accurate determination of these parameters. It should be noted that the profiles do not change in peak positions but in intensities. This indicates that the parameters can be determined by using the integrated intensities as well as the line profiles.

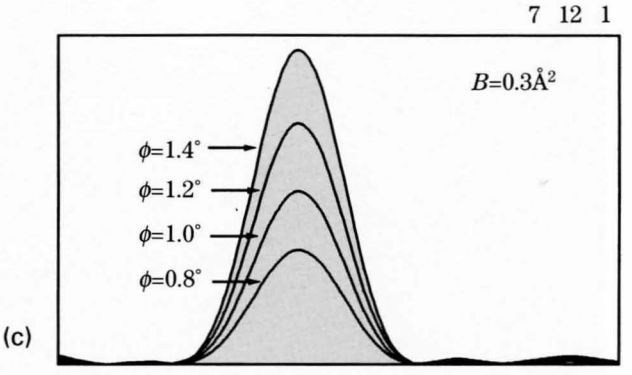

(c)

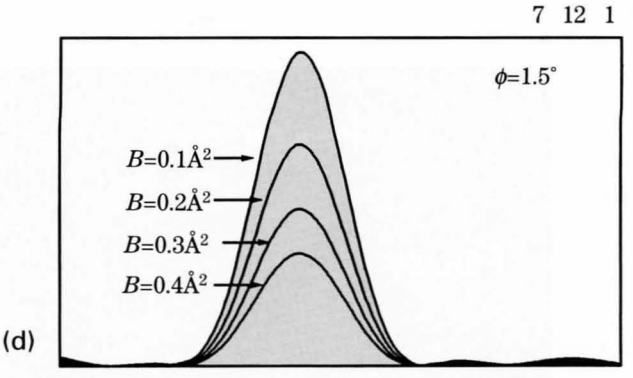

(d)

Determination of specimen thickness

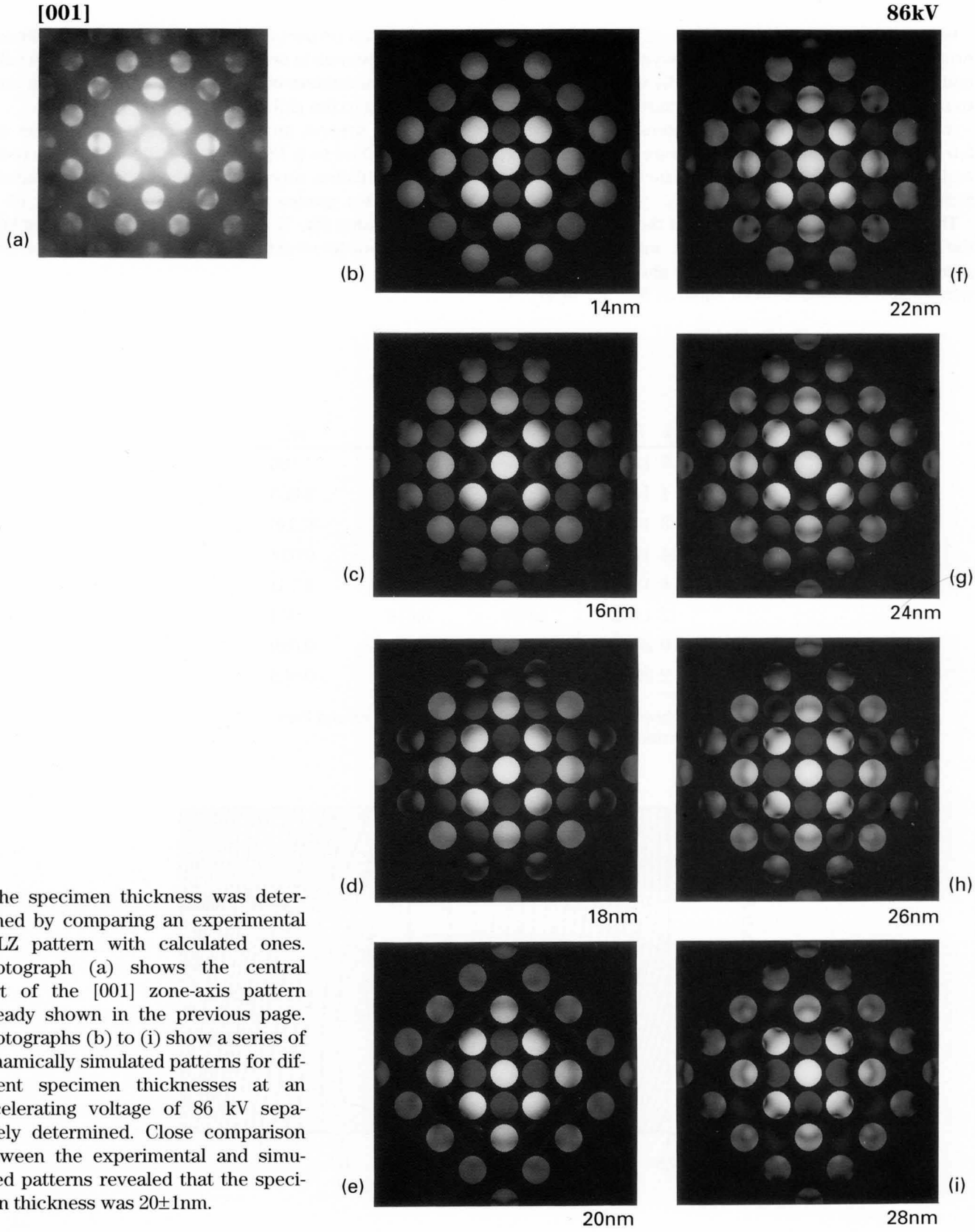

The specimen thickness was determined by comparing an experimental ZOLZ pattern with calculated ones. Photograph (a) shows the central part of the [001] zone-axis pattern already shown in the previous page. Photographs (b) to (i) show a series of dynamically simulated patterns for different specimen thicknesses at an accelerating voltage of 86 kV separately determined. Close comparison between the experimental and simulated patterns revealed that the specimen thickness was 20±1nm.

Results

Case I: integrated intensity

Using the integrated intensities of the HOLZ line profiles, the rotation angle of the oxygen octahedron ϕ and the Debye-Waller factor B(O(2)) were determined to minimize the residual sum of squares $S = \sum_g w_g (I_g^{obs} - sI_g^{calc})^2$ between experimental intensities and calculated ones. The values obtained were $\phi = 1.12 \pm 0.04°$ and B(O(2)) = 0.35 ± 0.06Å^2 with R-factor values of R = 8.2% and R_w = 5.3%.

The table gives the final results of the fitting between the experimental and calculated intensities, which show good agreement. The figure shows the contour map of the residual sum of squares $S = \sum_g w_g (I_g^{obs} - sI_g^{calc})^2$ with respect to the parameters ϕ and B. Since no local minimum is seen, it is ascertained that the values of the parameters obtained are the true solution corresponding to the global minimum of S.

In the present analysis, the fitting parameters used were limited to ϕ, B(O(2)) and scale factor s, to reduce the calculation time. The method will be extended to add lattice parameters, Debye-Waller factors of the other atoms (Sr, Ti and O(1)), the specimen thickness and low-order structure factors as fitting parameters.

h k l	obs.	cal.	res.
7 12 1	3.675	2.489	1.186
1 14 1	4.627	4.563	0.063
3 14 1	5.494	5.734	−0.240
14 14 2	8.518	8.501	0.017
8 18 2	1.675	2.405	−0.731
12 16 2	2.964	3.018	−0.054
0 20 2	4.458	4.429	0.029
2 20 2	1.000	1.353	−0.353

Observed intensities, calculated intensities and their residuals.

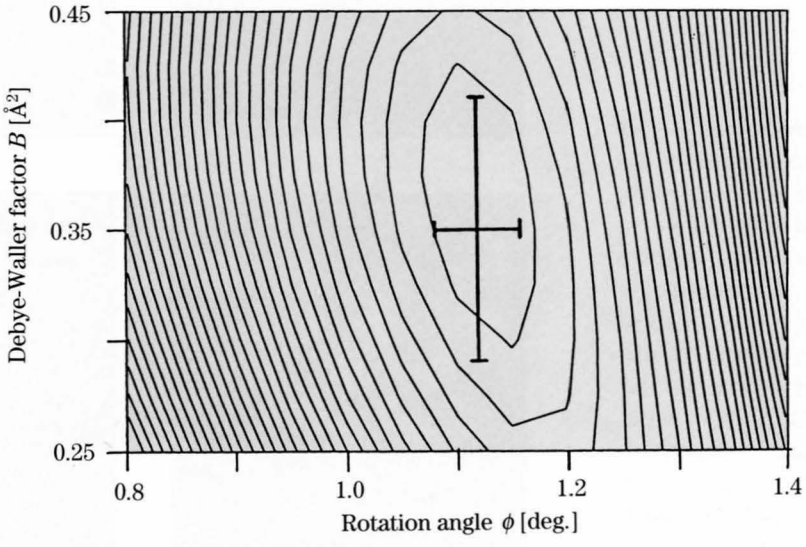

Case II: line profiles

Using the HOLZ line profiles, ϕ and B(O(2)) were determined so as to minimize S. The values refined were $\phi = 1.14 \pm 0.01^{\circ}$ and $B(O(2)) = 0.37 \pm 0.01 Å^2$. This result agrees with that obtained for the integrated intensities, within error.

Calculated intensities are seen to agree well with experimental ones. However, the remaining small discrepancies give not good R-factors, $R = 31.6\%$ and $R_w = 41.6\%$. One of the reasons for the large R and R_w factors compared with those for the integrated intensity (case I) is a uniform shift of the line profiles with respect to the calculated ones because of a distortion of the CBED pattern due to the aberration of the image forming lenses.

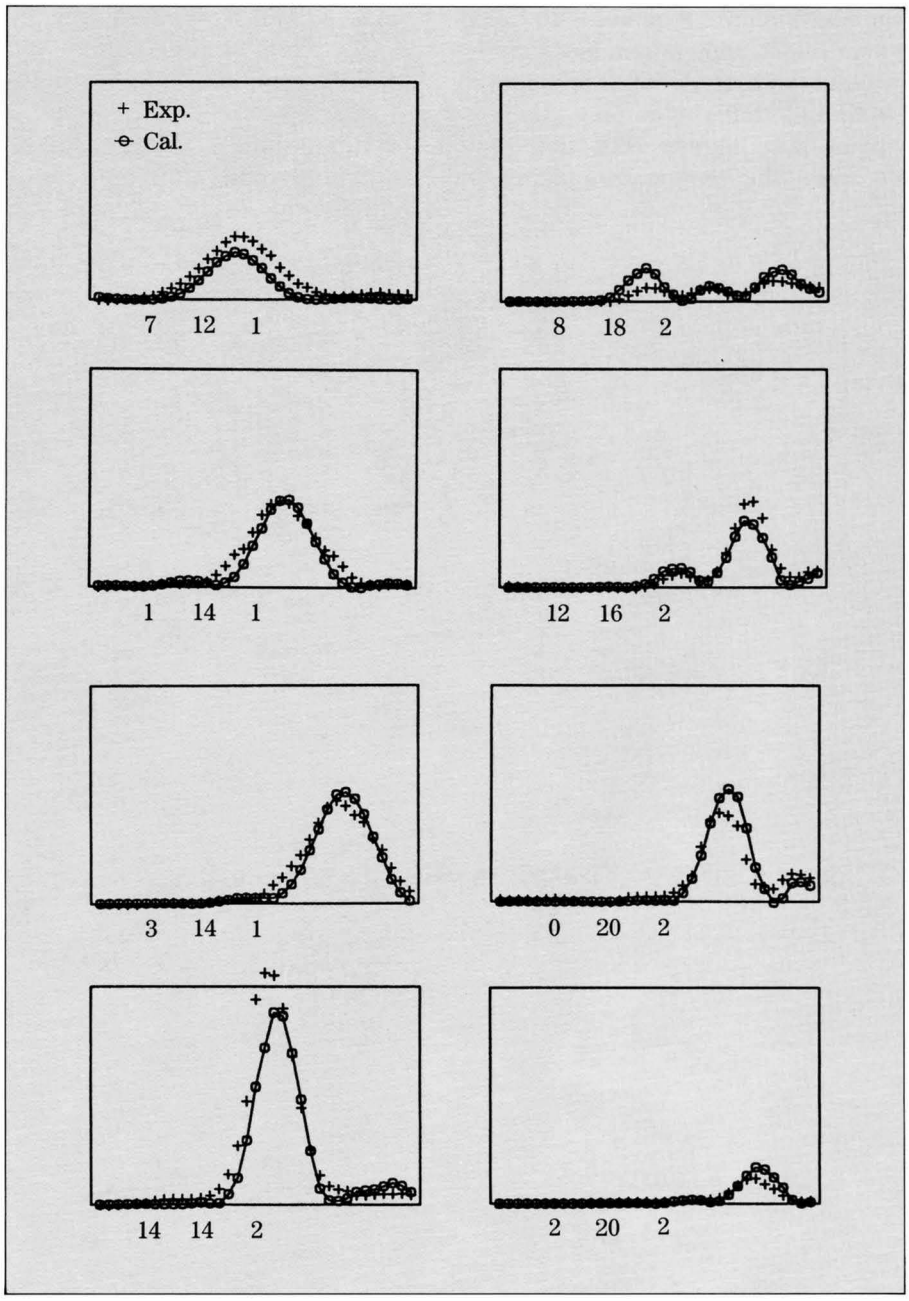

Comparison

By electron spin resonance experiments, Unoki and Sakudo [a] and Müller *et al.* [b] measured the rotation angle ϕ of the oxygen octahedron as a function of temperature over the temperature range from 4 to 105K. The former obtained $1.4 \pm 0.1^\circ$ as the value of ϕ and the latter 1.25°, both at 78K. Shirane and Yamada [c] determined ϕ to be a similar value of $1.37 \pm 0.35^\circ$ with a little low precision at 78K by neutron diffraction. Fujishita *et al.* [d] determined ϕ to be $1.6 \pm 0.1^\circ$ at 77K by X-ray diffraction.

The figure shows the above results together with the present one. The present result, shown by a black circle, is in good agreement with those of Unoki and Sakudo ($\phi = 1.3^\circ$ at 87K) and Müller *et al.* ($\phi = 1.1^\circ$ at 87K). The present result also agrees with that of Shirane and Yamada when the temperature dependence obtained by Unoki and Sakudo and Müller *et al.* is assumed. The value by Fujishita *et al.* is a little larger than the other results reported and may be a little different from ours even if the temperature difference is taken into account.

References

[a] H. Unoki and T. Sakudo: *J. Phys. Soc. Jpn.*, **23** (1967) 546.

[b] K. A. Müller, W. Berlinger and F. Waldner: *Phys. Rev. Lett.*, **21** (1968) 814.

[c] Y. Shirane and Y. Yamada: *Phys. Rev.*, **177** (1969) 858.

[d] H. Fujishita, Y. Shiozaki and E. Sawaguchi: *J. Phys. Soc. Jpn.*, **46** (1979) 581.

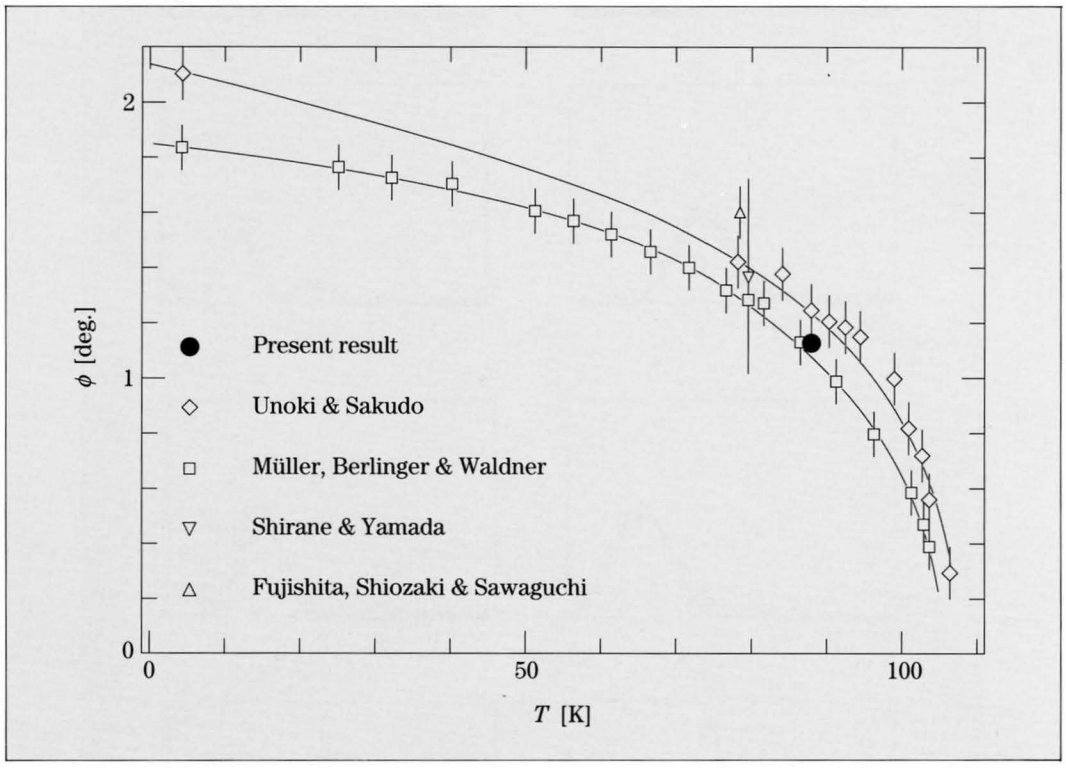

Bloch states

Intensity profiles of HOLZ reflections are interpreted in terms of Bloch waves. Bloch waves of wave vector $\boldsymbol{k}_0^{(j)}$ are obtained by solving Schrödinger's wave equation in a periodic potential $V(\boldsymbol{r})$. The wave vectors or the eigenvalues $\boldsymbol{k}_0^{(j)}$ obtained by continuously changing the incident beam direction form "*dispersion surfaces*", whose sections are called "*branches*" 1, 2 ... in the order of the magnitude of $\boldsymbol{k}_0^{(j)}$.

Figure (a) shows the branches around the [001] incidence or the section of the dispersion surfaces in the plane formed by the [001] vector and the reciprocal lattice vector of the 5 19 2 reflection. The line profile of the 5 19 2 reflection corresponding to the section is shown in Fig. (b). For simplicity, the eigenvalues were calculated using only one HOLZ reflection 5 19 2 and 109 ZOLZ reflections. The branch originating from the HOLZ reflection is clearly distinguished from the other branches formed by ZOLZ reflections because the HOLZ branch crosses skew to the ZOLZ branches, which are almost parallel to $\boldsymbol{k}_{xy}$.

The HOLZ and ZOLZ branches interact at their intersections and give rise to intensity peaks in the line profile of the HOLZ reflection. Thus, each peak appearing in the HOLZ line profile can be assigned to a ZOLZ branch. It should be, however, noted that only well-excited branches cause peaks in a HOLZ line profile. The peaks of the line profile in Fig. (b) are assigned to those from branches 1, 2, 3 and 9. The present analysis of $SrTiO_3$ has used the HOLZ reflections to which only O(2) atoms contribute. In these reflections, the intensity peaks originate from branches 3 and 9. It is seen in the following pages that the Bloch waves of these branches localize on the O(2) atoms. Therefore, the HOLZ reflections are sensitive to the displacement of the O(2) atoms and their Debye-Waller factor. Since the index of the reflection shown in Fig. (b) is $h\ k\ 2$ (h, k=odd), not only the contributions from the O(2) atoms but also those from the Sr, Ti and O(1) atoms (branches 1 and 2) are seen.

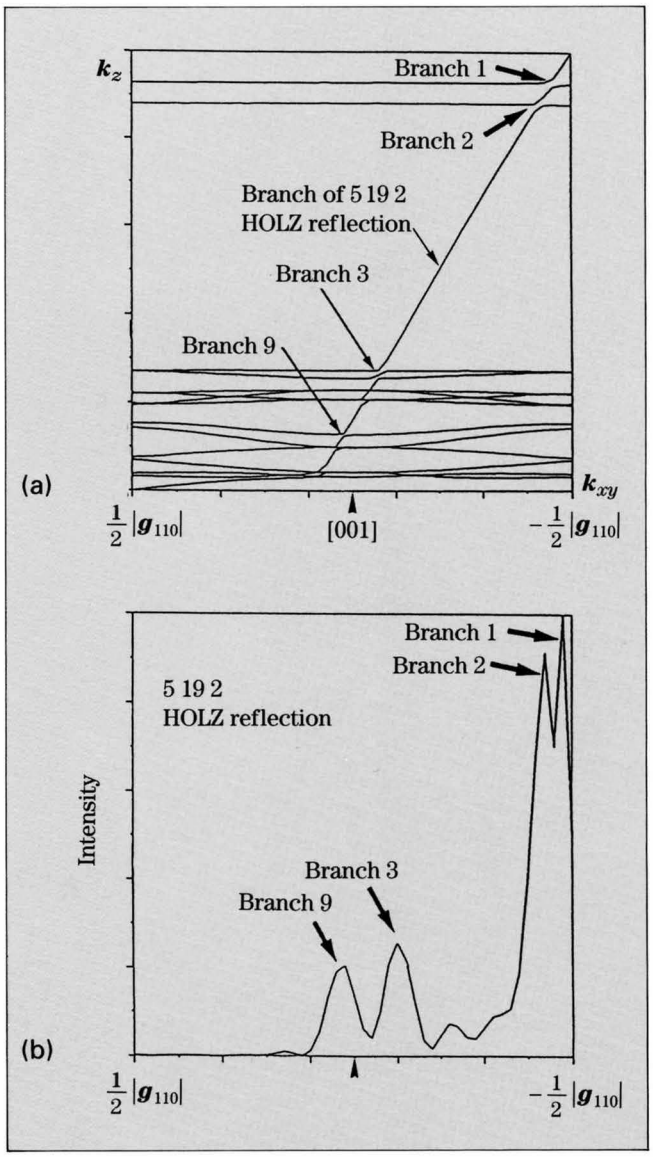

$SrTiO_3$ consists of Sr-atom rows, Ti and O(1)-atom rows and O(2)-atom rows when viewed along the [001] direction as shown in Fig. (a) on the opposite page. Figures (b) to (u) in the following pages show stereograms of the electron-density distributions of the Bloch waves corresponding to branches 1 to 20, which were calculated using 109 ZOLZ beams for the [001] electron incidence at an accelerating voltage of 86kV.

The electron density is concentrated on the rows of Ti and O(1) atoms for branch 1 (Fig. (b)), on the rows of Sr atoms for branch 2 (Fig. (c)) and on the rows of O(2) atoms for branches 3 and 4 (Figs. (d) and (e)). Branches 3 and 4 correspond to a bonding state and an anti-bonding state between O(2) atoms, respectively. The wave functions at the neighbouring O(2) atoms have the same sign in branch 3 but the opposite sign in branch 4.

The electron-density distributions of the Bloch waves resemble the two-dimensional atomic states localizing on the rows of particular atoms because the formulation of the dynamical theory is similar to the two-dimensional band theory of solid state physics.

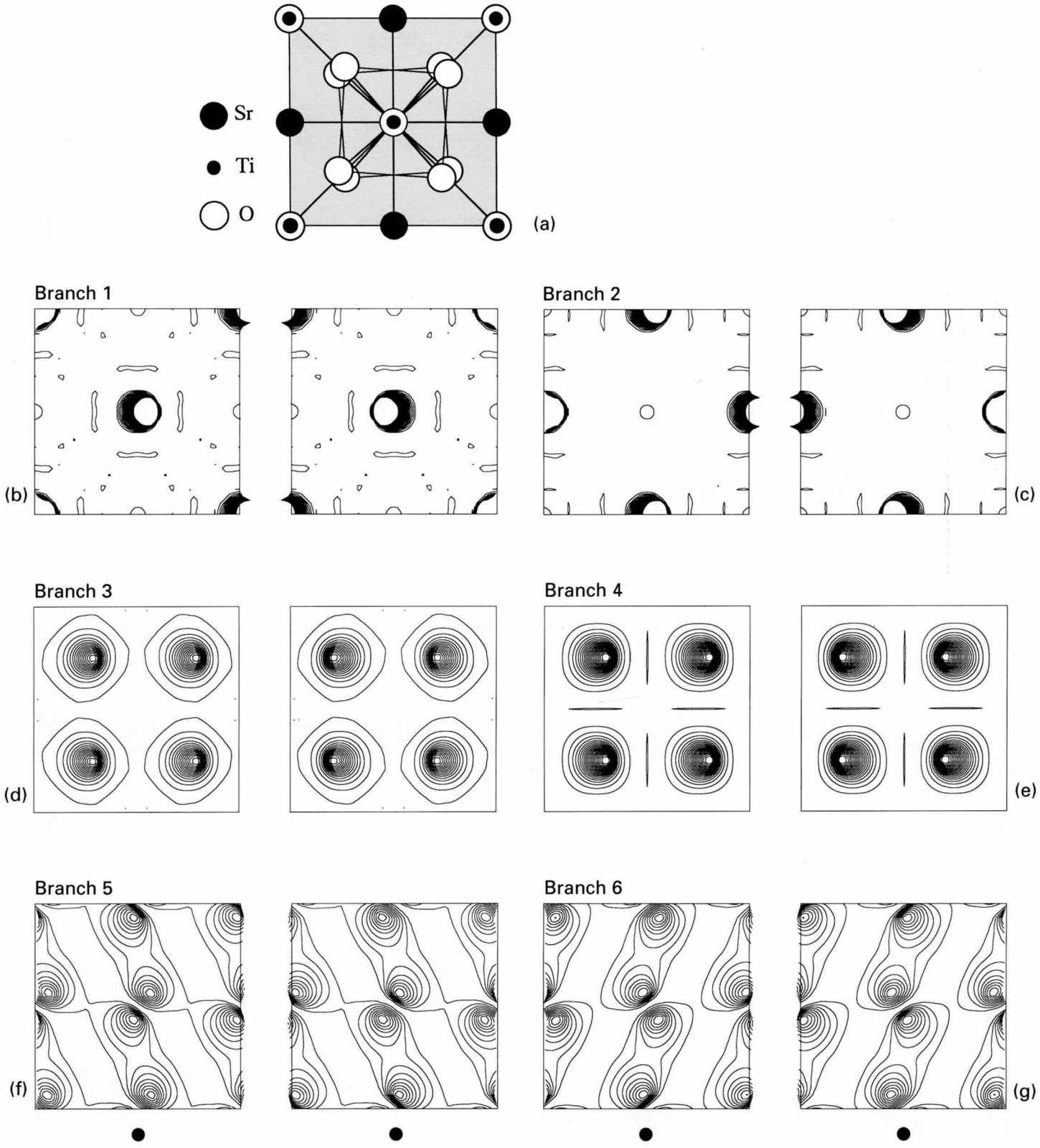
Sr
Ti
O
(a)
Branch 1
Branch 2
(b)
(c)
Branch 3
Branch 4
(d)
(e)
Branch 5
Branch 6
(f)
(g)

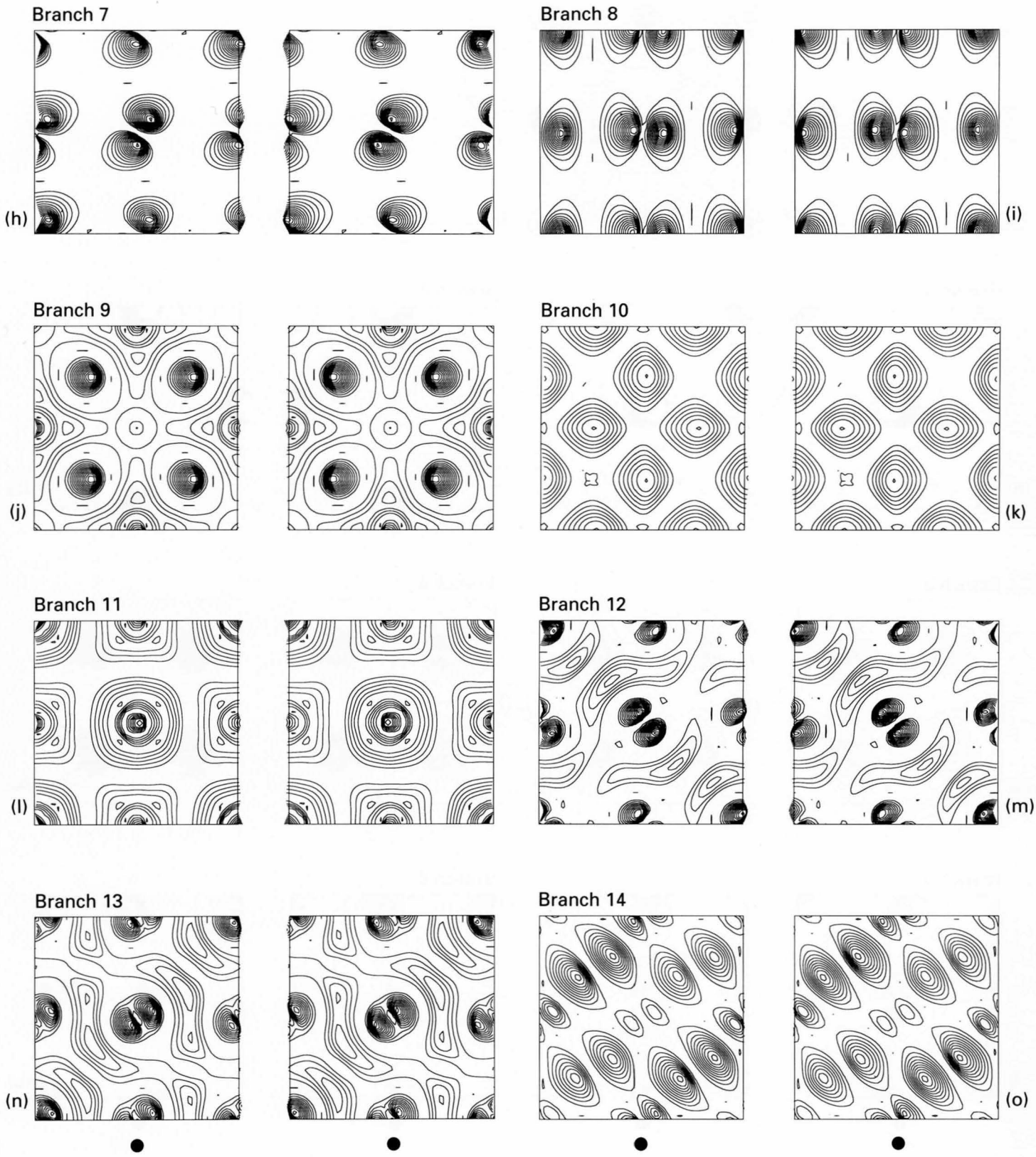
Branch 7
Branch 8
(h)
(i)
Branch 9
Branch 10
(j)
(k)
Branch 11
Branch 12
(l)
(m)
Branch 13
Branch 14
(n)
(o)

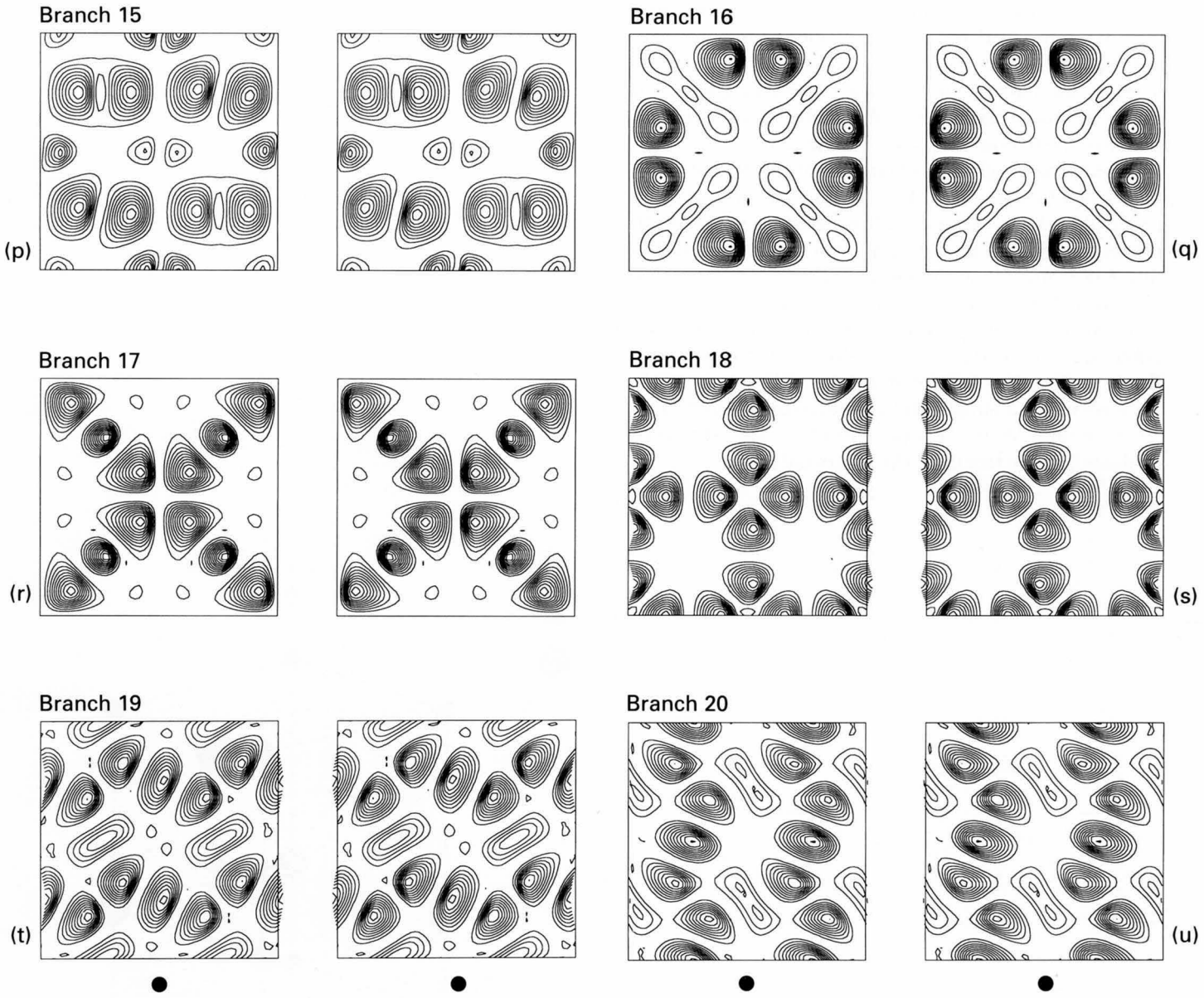

Stereograms of Bloch waves.

CdS

Hexagonal cadmium sulfide (CdS) is of the wurtzite type structure and belongs to a noncentrosymmetric space group of $P6_3mc$. The structure is shown schematically in the figure. The distance between adjacent Cd and S atoms, u, and Debye-Waller factors B(Cd) and B(S) are the parameters to be determined.

The nearest-neighbour environment of each atom in the ideal wurtzite structure is tetrahedral with u = 3/8 (=0.375) and $c/a = (8/3)^{1/2}$. If the structure is not ideal, nearest-neighbour atoms may form distorted tetrahedra. A deviation from the ideal value of c/a is accompanied by a change in u. Stevenson *et al.* [a] performed an X-ray structure analysis and determined by assuming cubic anharmonicity that the value of u is 0.37715(8). We have investigated the structure of hexagonal CdS because it has a simple and noncentrosymmetric crystal structure. A preliminary result of the structure analysis is given briefly in the following pages.

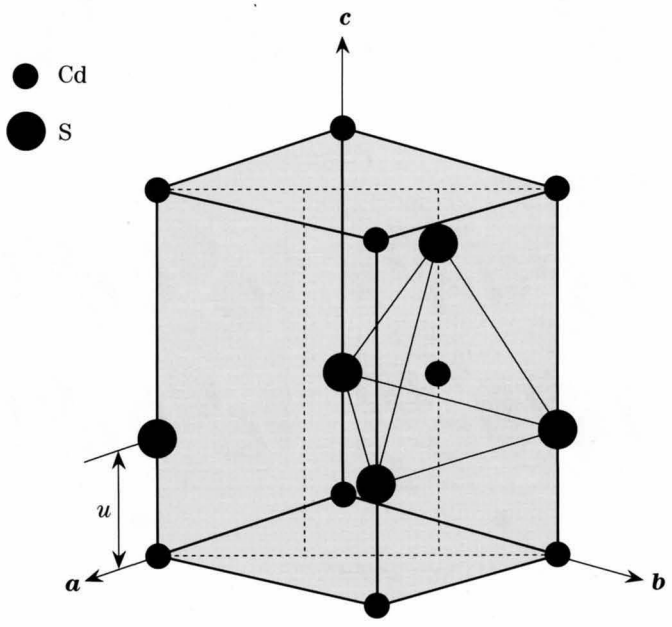

$a = 0.4136$ nm
$c = 0.6716$ nm

Cd: $(0, 0, 0)$, $(\frac{1}{3}, \frac{2}{3}, \frac{1}{2})$

S: $(0, 0, u)$, $(\frac{1}{3}, \frac{2}{3}, \frac{1}{2} + u)$

Reference

[a] A. W. Stevenson, M. Milanko and Z. Barnea: *Acta Cryst.*, **B40** (1984) 521.

CdS

[10$\bar{1}$0] T = 100K 86kV

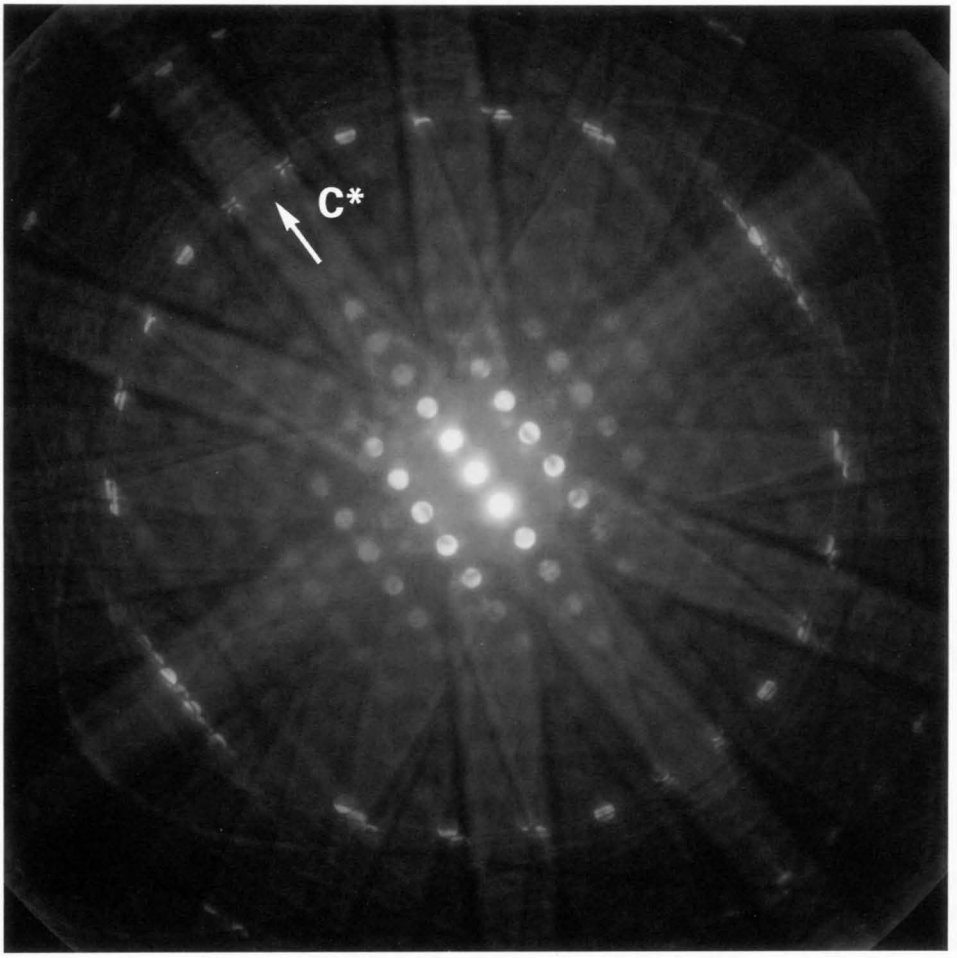

A [10$\bar{1}$0] CBED pattern taken at a temperature of 100K and an accelerating voltage of 86kV with the JEM-100CX-FEG. Since the pattern has only one mirror symmetry, only the reflections on one side of the pattern separated by the c^*-axis are symmetry independent. The specimen thickness was determined to be 32.5±1nm.

Results

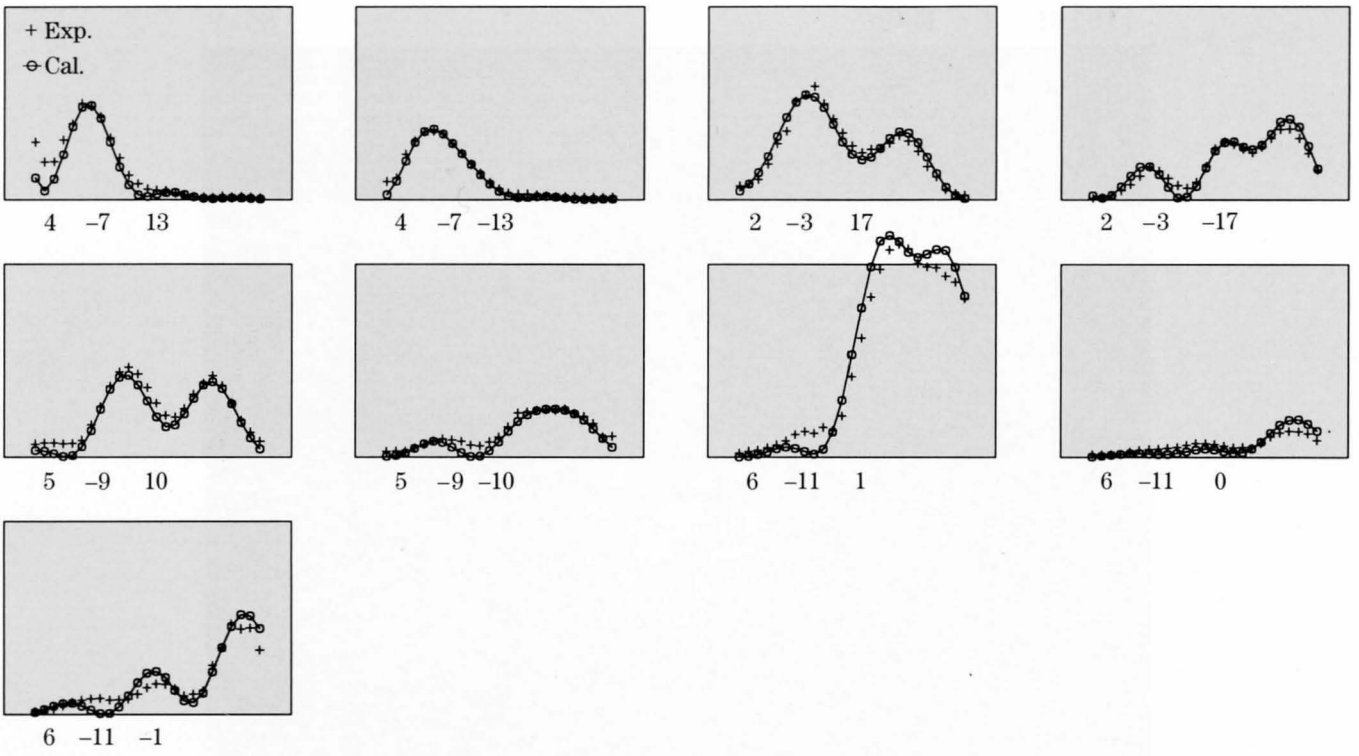

Figures show experimental line profiles (+) of nine HOLZ reflections and calculated ones (⊖). The latters were calculated by applying the many-beam dynamical theory with 61 ZOLZ and 21 HOLZ reflections, in which the generalized Bethe approximation was applied to 28 ZOLZ reflections. It is seen that the calculated profiles roughly reproduced the experimental profiles. The values of the parameters determined were $u = 0.3776(2)$, $B(\mathrm{Cd}) = 0.47(1)\text{Å}^2$ and $B(\mathrm{S}) = 0.47(1)\text{Å}^2$ with $R = 16.1\%$ and $R_w = 24.3\%$. The value of u shows good agreement with the reported value given on the page 136, though anharmonicity of Debye-Waller factors was not taken into account in the present study.

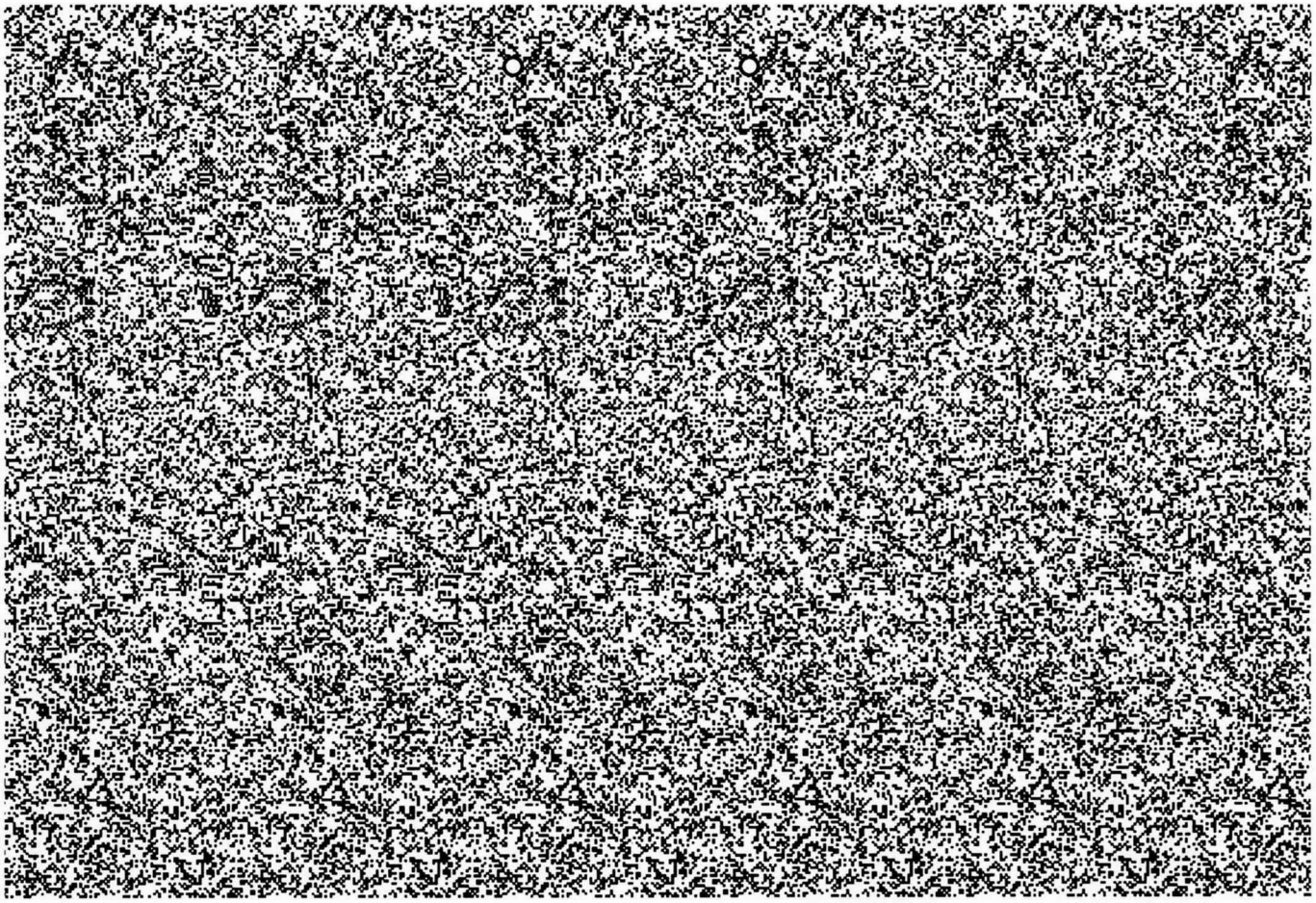

Random dot stereogram

Energy Filtering

The effect of energy filtering is demonstrated. There are three types of inelastic scattering processes due to phonon, plasmon and one-electron excitations [a]. The excitation energy is less than 0.1eV for phonons, 10-50eV for plasmons and ranges from a few eV to several thousand eV for one-electron excitations. The cross section of one-electron excitations is small compared with the other two excitations. The total cross section of phonon excitations is the largest but the differential cross section is small because the scattering due to phonon excitations covers a very large angle. On the other hand, plasmon scattering is concentrated to a small angle.

Phonon scattering causes interband transitions but plasmon scattering causes intraband transitions. Interband transitions change the symmetry of Bloch waves but intraband transitions preserve the symmetry. Hence, phonon scattering was considered harmful for quantitative analysis of diffraction patterns and microscope images. However, this was not correct because electrons which suffered phonon scattering form monotonic background in diffraction patterns except Kikuchi lines and Kikuchi bands.

The worst inelastic scattering was found to be due to plasmon excitations because electrons which suffered plasmon scattering form a similar but blurred pattern on the pattern produced by elastically scattered electrons. To remove electrons which suffered plasmon scattering is very effective for obtaining intensities which can be compared with those calculated by the dynamical theory dealing with elastic scattering. Plasmon excitations are observed in metals and semiconductors, but not always clear in insulators. However, even in insulators, the removal of inelastically scattered electrons due to valence-electron excitations is still effective for elucidating the CBED patterns formed by elastically scattered electrons.

We have tried to subtract electrons which suffered plasmon scattering from CBED patterns, using an electron microscope equipped with an energy filtering system as shown in the figure. A CBED pattern is produced on the viewing screen. A small portion of the pattern passes through the entrance aperture of a sector type spectrometer. An energy spectrum is formed on the energy selecting slit, by which the acceptance energy width is determined. The energy filtered electrons are detected by a photomultiplyer, converted to electric signals and sent to a CRT. The CBED pattern on the screen is scanned using scanning coils located just below the objective lens. The electric signals obtained are displayed on the CRT synchronously with scanning, then an energy filtered CBED pattern is formed. The instrument used a serial detection system for energy filtering. More efficient two-dimensional detection systems are available at present.

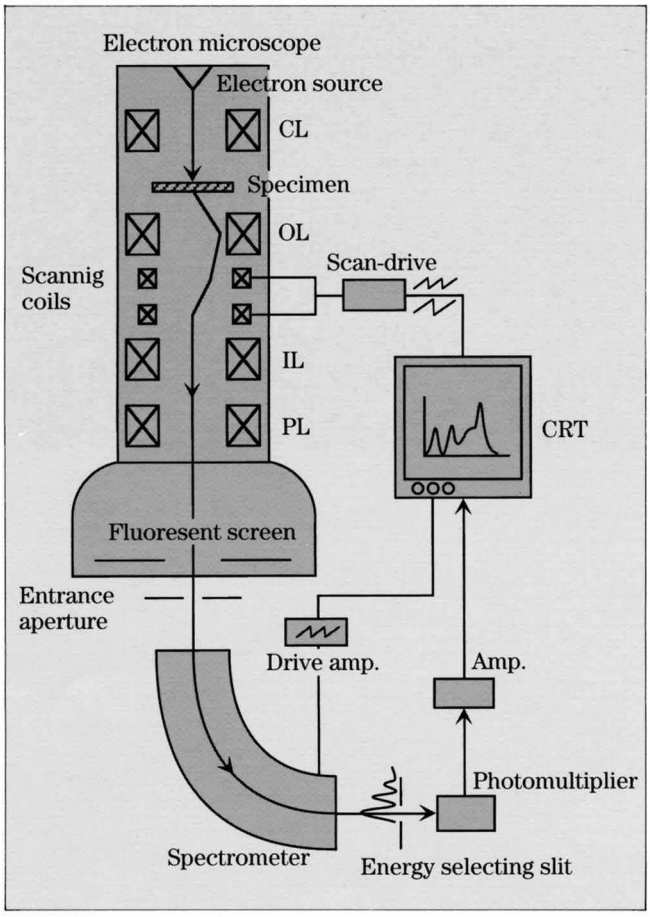

Energy filtering system

Reference

[a] *e.g.* L. Reimer: Transmission Electron Microscopy (2nd ed.), Springer-Verlag, 1989, chap. 5.

Si

ZOLZ patterns

(a) Unfiltered **[111]** **100kV** (b) Zero loss

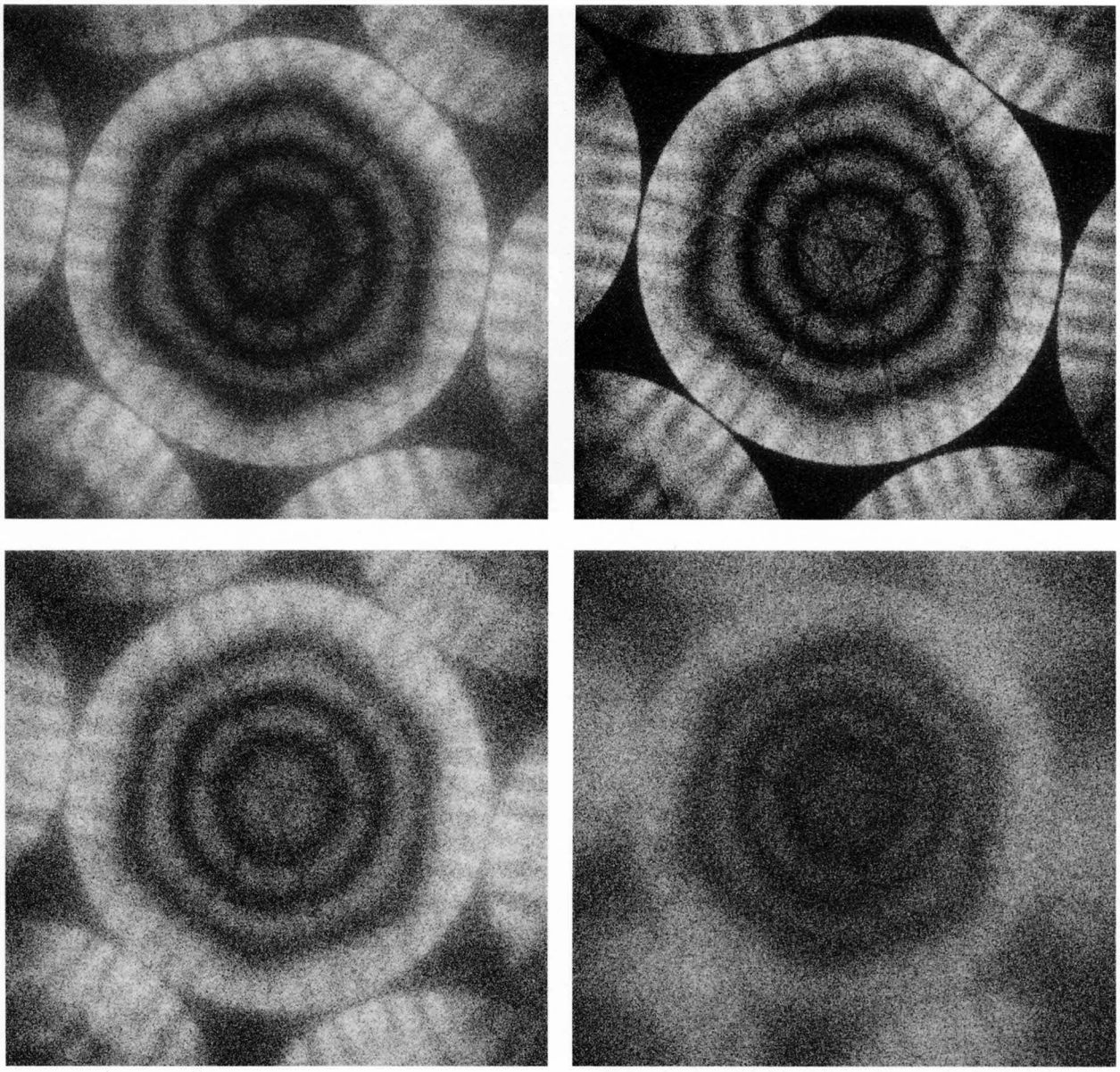

(c) 1st plasmon loss (d) 2nd plasmon loss

Photograph (a) shows an unfiltered [111] zone-axis CBED pattern taken at 100 kV. The figure shows an energy spectrum of the pattern. Photograph (b) is a filtered pattern taken with an acceptance energy width of 14 eV (the first peak in the figure), which we call a zero-loss pattern for simplicity. Clearness of the pattern is noted when plasmon scattering is cut off. Photograph (c) is a pattern formed by the 1st plasmon-loss electrons (the second peak in the figure). The pattern is similar to the zero-loss pattern but is blurred. Photograph (d) shows a more blurred pattern produced by the 2nd plasmon-loss electrons (the third peak in the figure). The exposure time was 512 sec. for each photograph.

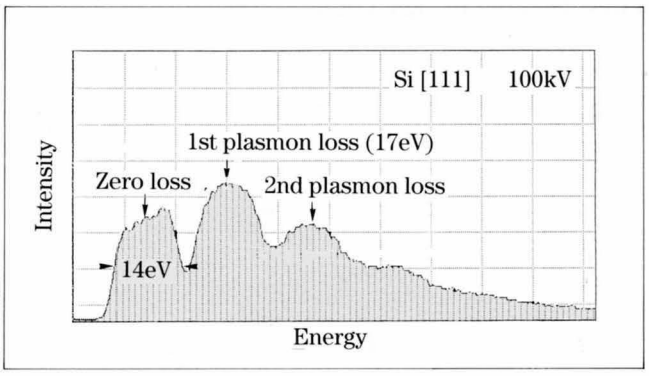

Energy spectrum

Si — two-beam condition —

100kV

(a) Unfiltered

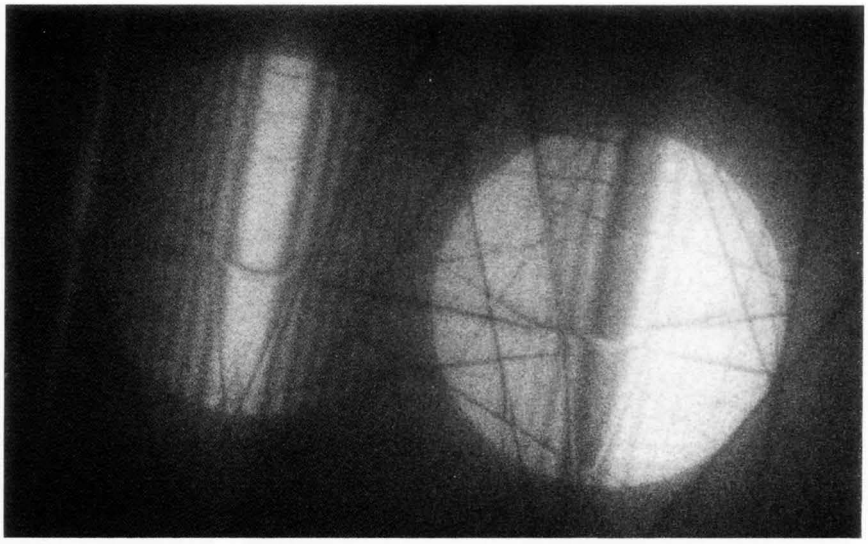

$2\bar{2}0$ **000**

The differential cross section $d\sigma/d\Omega$ of a plasmon loss is proportional to $1/(\theta^2+\theta_E^2)$, where the characteristic angle $\theta_E = \Delta E/E$, E and ΔE being the energies of incident electrons and of the plasmon loss, respectively. The cross section decreases as a function of θ^{-2} and becomes the half-maximum at $\theta = \theta_E$. A typical value of θ_E is 2×10^{-4} rad. for E = 100kV and ΔE = 20eV. Intensity valleys of the rocking curves formed by elastically scattered electrons are filled with intensity robes formed by plasmon-loss electrons with an FWHM of $2\theta_E$, resulting in a blurred pattern.

Photographs (a) to (d) show a similar example to that on the previous page, which were taken at a two-beam condition. The figure shows the energy spectrum for Photo (a). We can see again that the subtraction of plasmon-loss electrons produces a clear pattern. It should be noted that the use of an acceptance energy-width smaller than the width of the zero-loss peak does not improve the clearness of the pattern but deteriorates the noise to signal ratio.

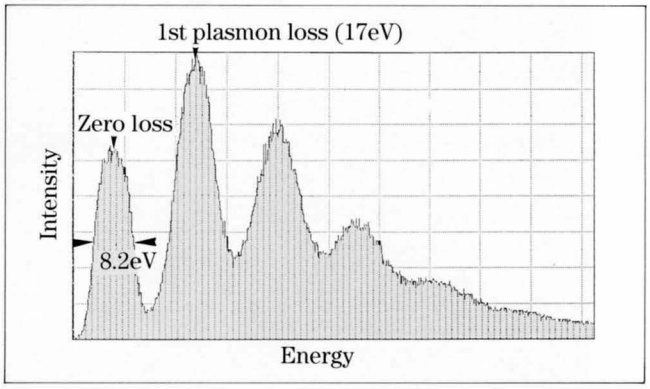

(b) Zero loss

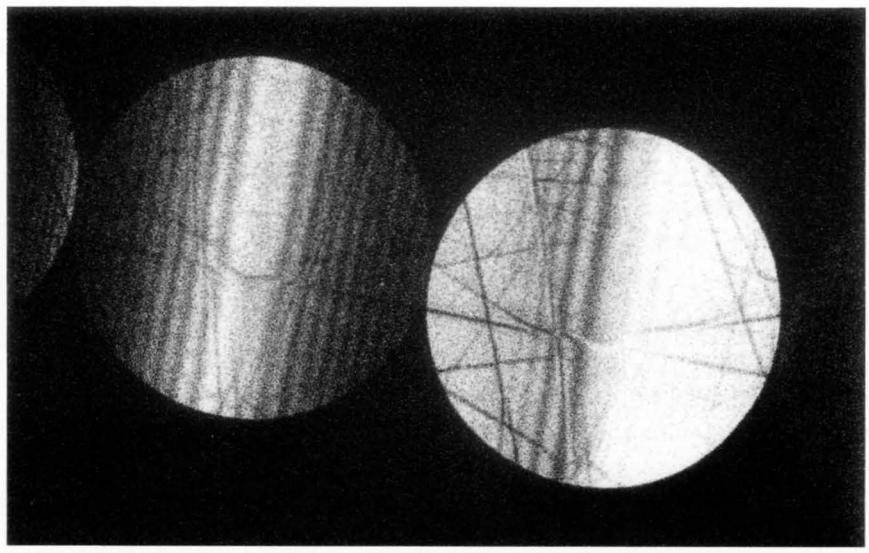

(c) 1st plasmon loss

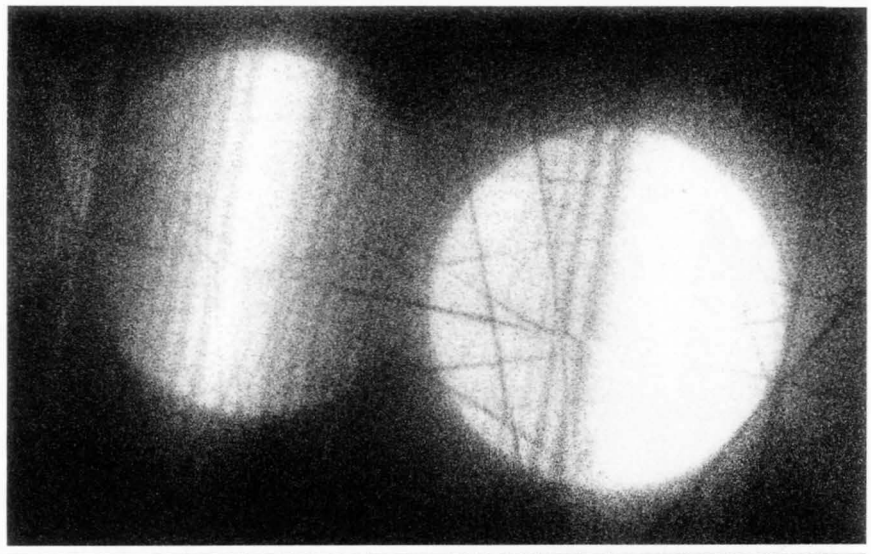

(d) 2nd plasmon loss

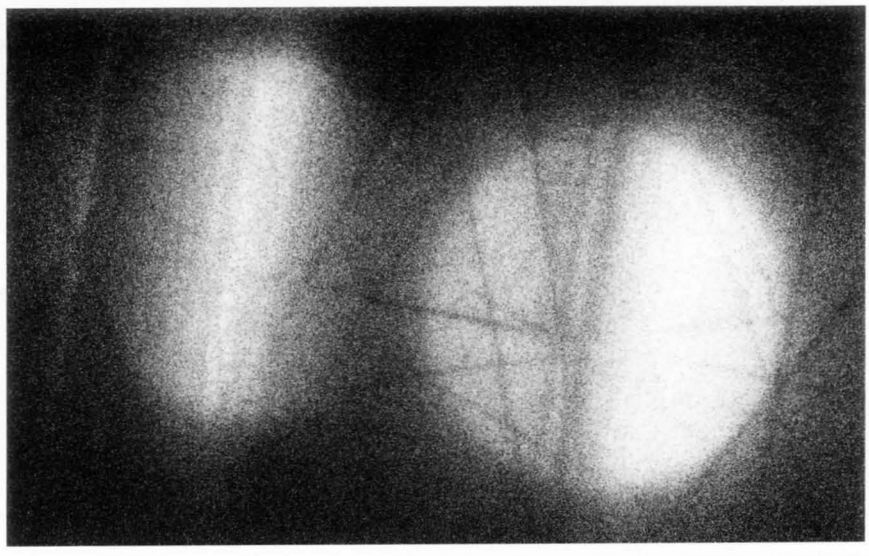

Acceptance energy width 8.2eV

Si — two-beam condition —

Figures (a) to (i) show thickness dependence of the effect of plasmon-loss electrons for line profiles of the transmitted beam and the 220 reflection of Si. Figures (a) to (c) give a data set for a specimen thickness of 52nm: (a) an unfiltered line profile together with a line profile due to the 1st and 2nd plasmon-loss electrons (lightly shaded area), (b) a zero-loss line profile, and (c) an energy spectrum. Figures (d) to (f) and (g) to (i) are two data sets for specimen thicknesses of 144nm and 325nm, respectively. As the thickness increases, the ratio of plasmon-loss intensities to zero-loss intensity increases. It is quite clear how the plasmon losses prevent quantitative fitting of the experimental data with data calculated by the theory dealing with elastic scattering only.

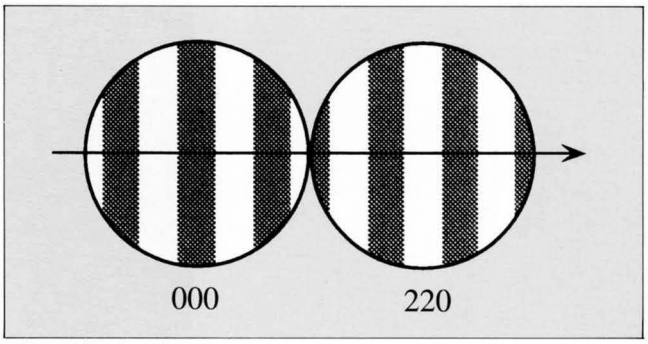

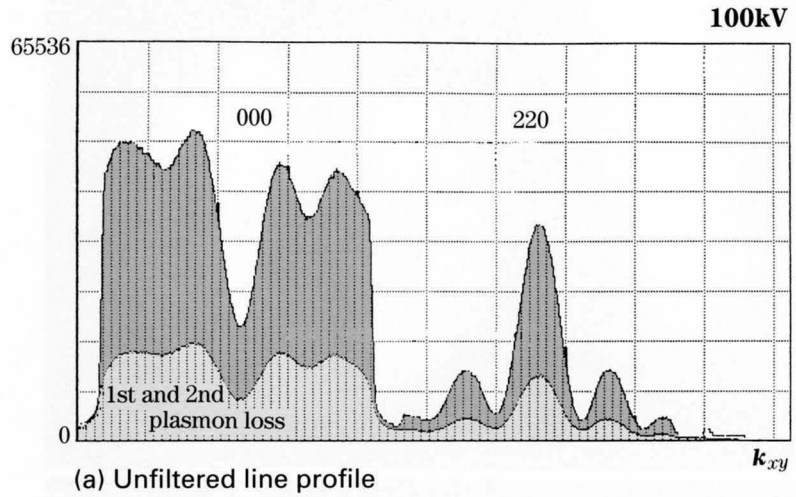

(a) Unfiltered line profile

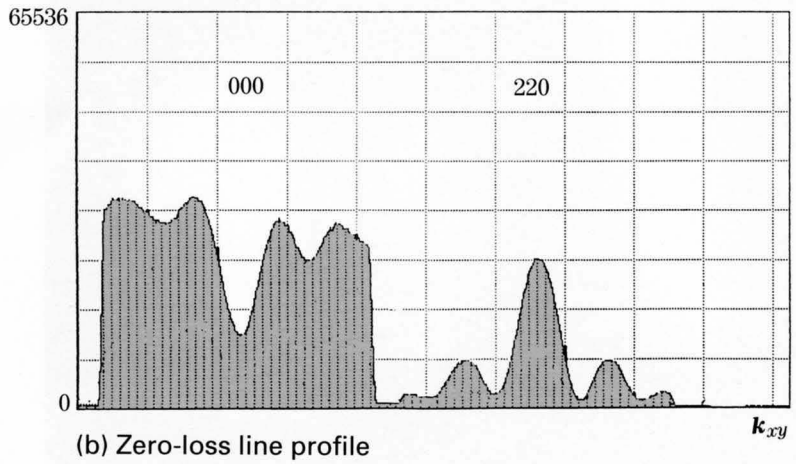

(b) Zero-loss line profile

Specimen thickness 52nm

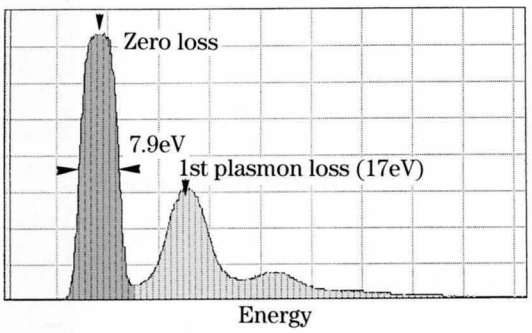

(c) Energy spectrum

Acceptance energy width 7.9eV

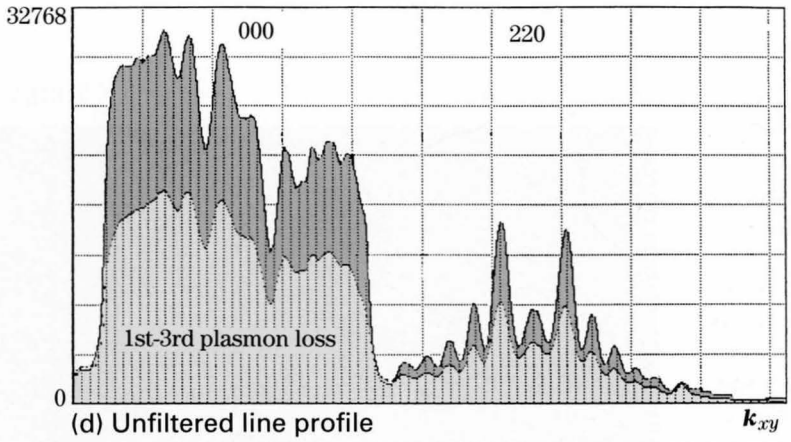

(d) Unfiltered line profile

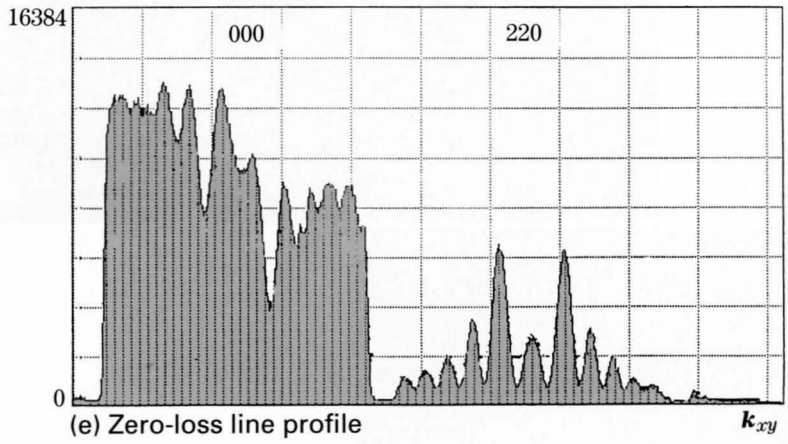

(e) Zero-loss line profile

Specimen thickness 144nm

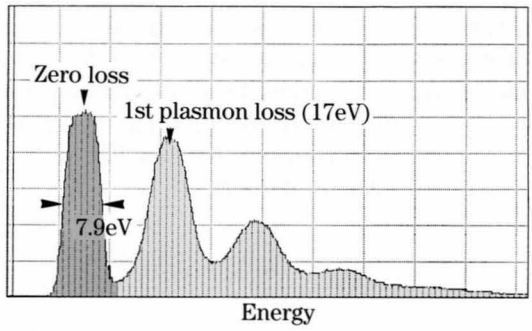

(f) Energy spectrum

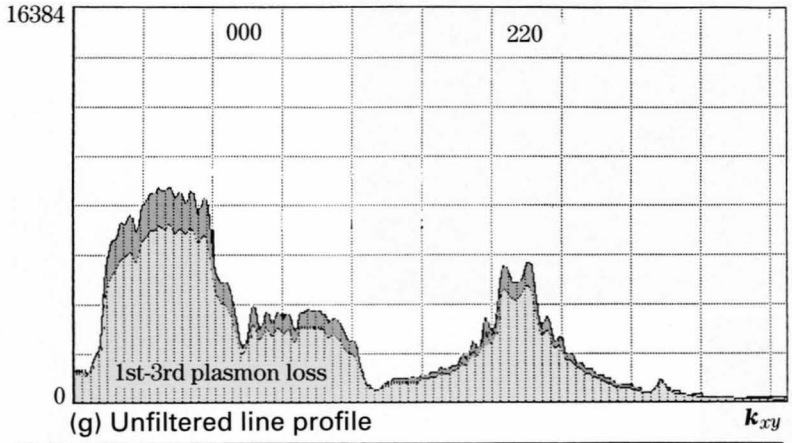

(g) Unfiltered line profile

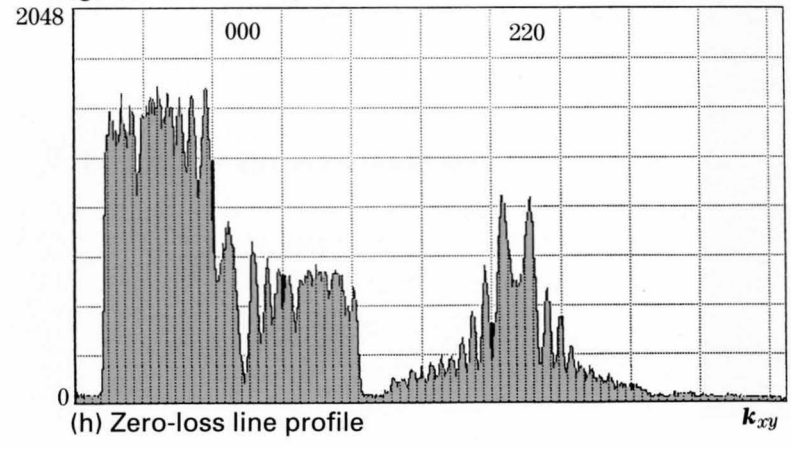

(h) Zero-loss line profile

Specimen thickness 325nm

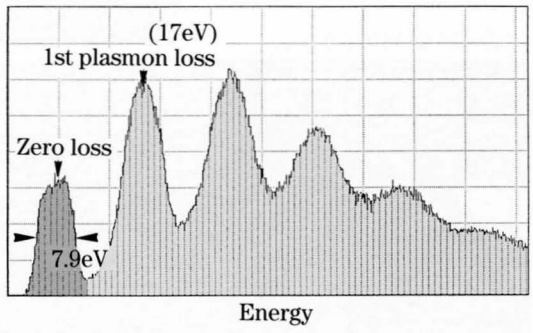

(i) Energy spectrum

Si — HOLZ reflections —

Shown here are HOLZ reflection patterns of [111] Si formed by unfiltered electrons (a), zero-loss electrons (b) and by the 1st plasmon-loss electrons (c). Intensities due to plasmon-loss electrons indicated by arrows are seen between the CBED disks in Photos (a) and (c), while no intensity is seen in Photo (b).

Figure (a) on the opposite page shows a line profile of the $9\bar{9}1$ reflection due to unfiltered electrons (solid line) together with that due to the 1st and 2nd plasmon-loss electrons (lightly shaded area). Figure (b) is a line profile due to zero-loss electrons. Figure (c) shows an energy spectrum of the reflection.

(a) Unfiltered **[111] 100kV**

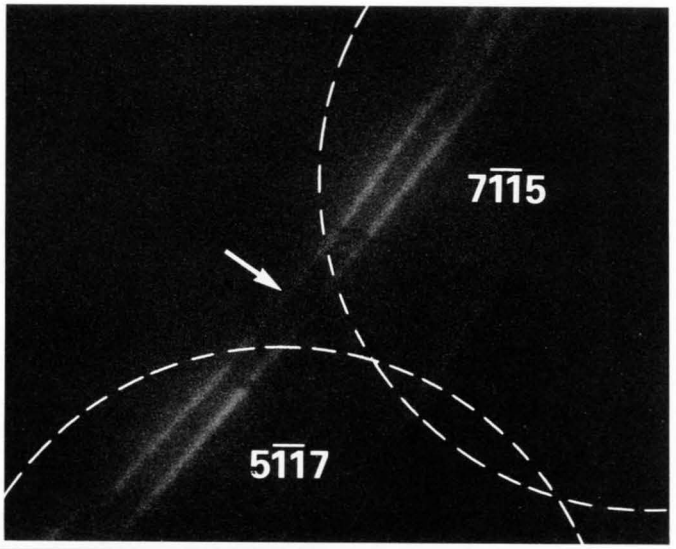

(b) Zero loss

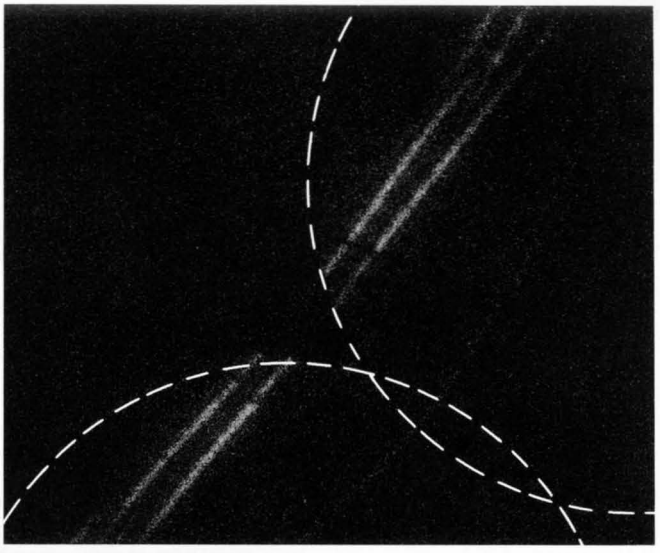

(c) 1st plasmon loss

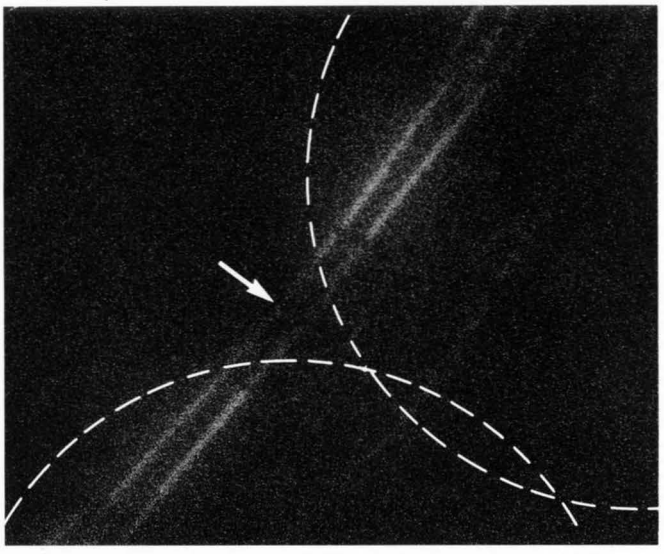

Acceptance energy width 14eV

HOLZ line profiles

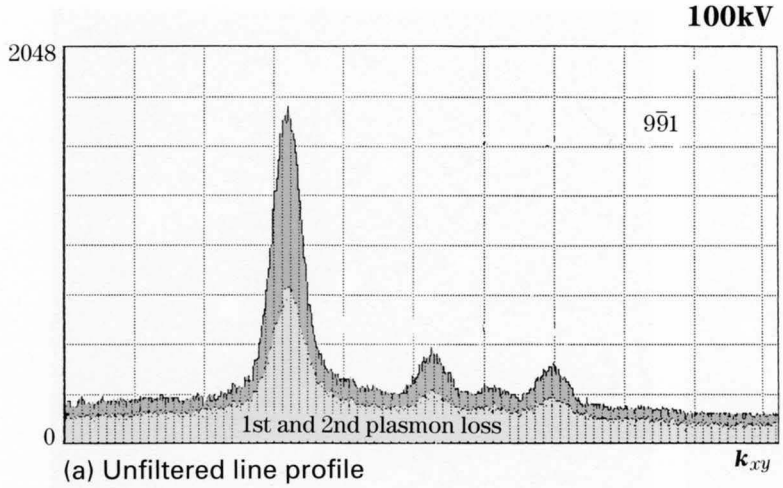

(a) Unfiltered line profile

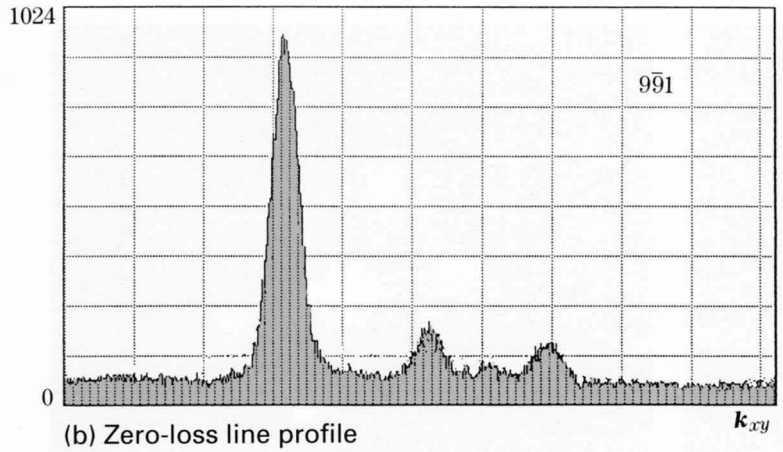

(b) Zero-loss line profile

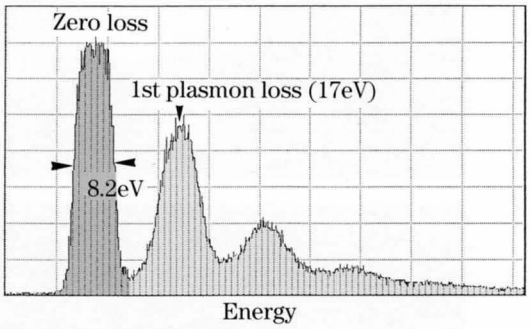

(c) Energy spectrum

Acceptance energy width 8.2eV

Si — small convergence angle (ZOLZ) —

(a) Unfiltered **[111] 100kV**

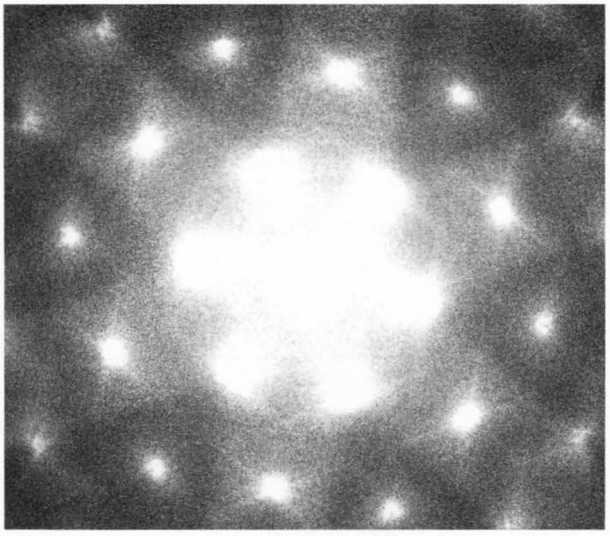

(b) Zero loss

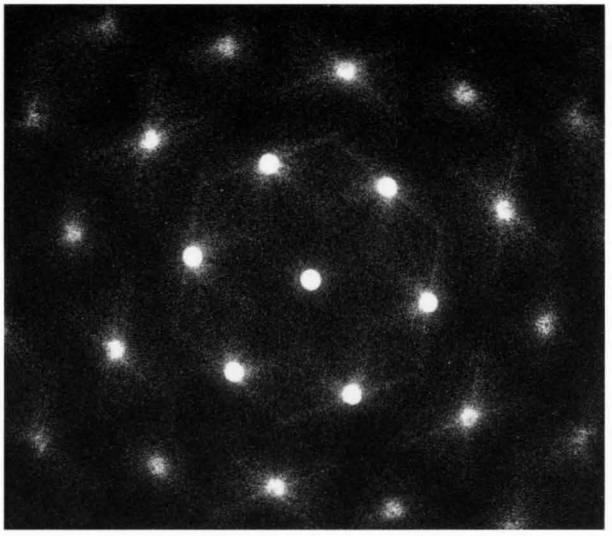

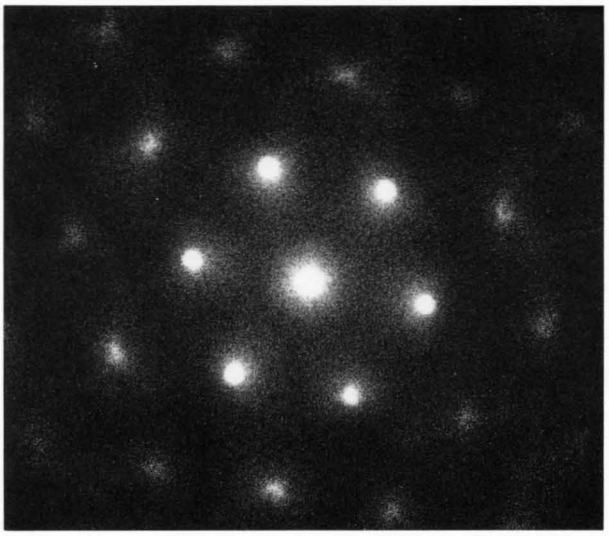

(c) 1st plasmon loss

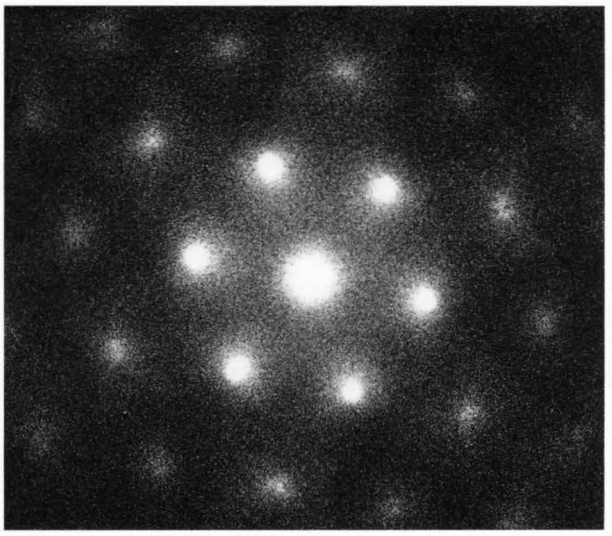

(d) 2nd plasmon loss

Acceptance energy width 8.5eV

Shown on the opposite page is a set of CBED patterns of [111] Si taken at a small convergence angle with unfiltered electrons (a), zero-loss electrons (b), the 1st plasmon-loss electrons (c) and the 2nd plasmon-loss electrons (d). In pattern (b), as the background intensity due to the plasmon-loss electrons is removed almost perfectly, all the diffraction disks are sharply seen and streaks projecting from the disks due to phonon scattering are also clearly observed.

Si — small convergence angle (HOLZ) —

[111] 100kV

(a) Unfiltered

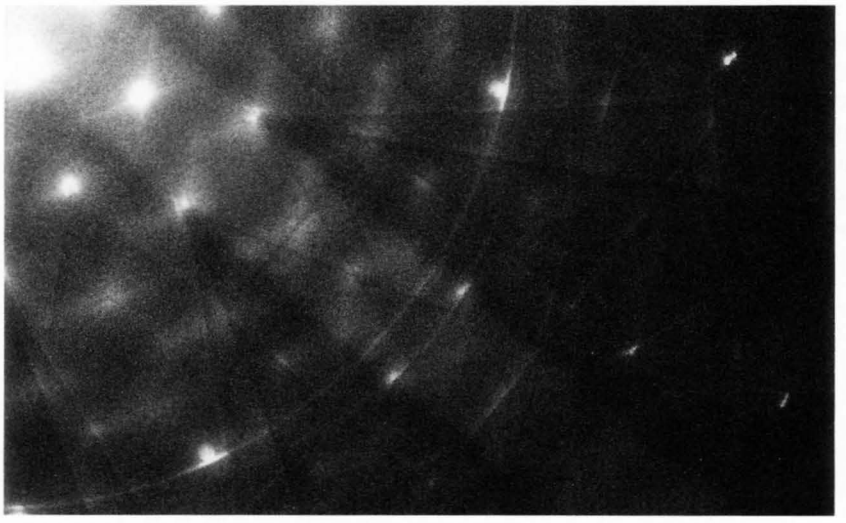

Shown on this page and the next page is a set of HOLZ reflection patterns of [111] Si taken at a small convergence angle with unfiltered electrons (a), zero-loss electrons (b), the 1st plasmon-loss electrons (c) and the 2nd plasmon-loss electrons (d). In pattern (b) with zero-loss electrons, Kikuchi lines and Kikuchi bands due to phonon scattering are still seen, but an intensity ring passing through the HOLZ disks, which originated from plasmon-loss electrons, was removed.

(b) Zero loss

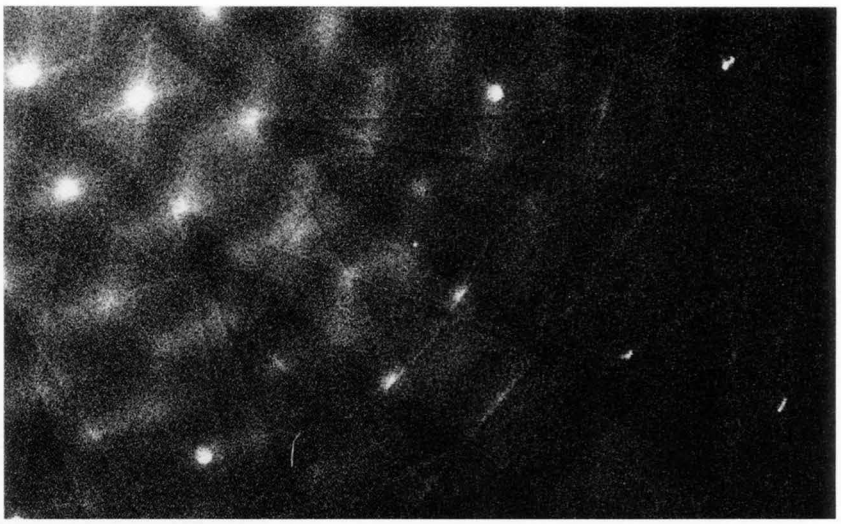

(c) 1st plasmon loss

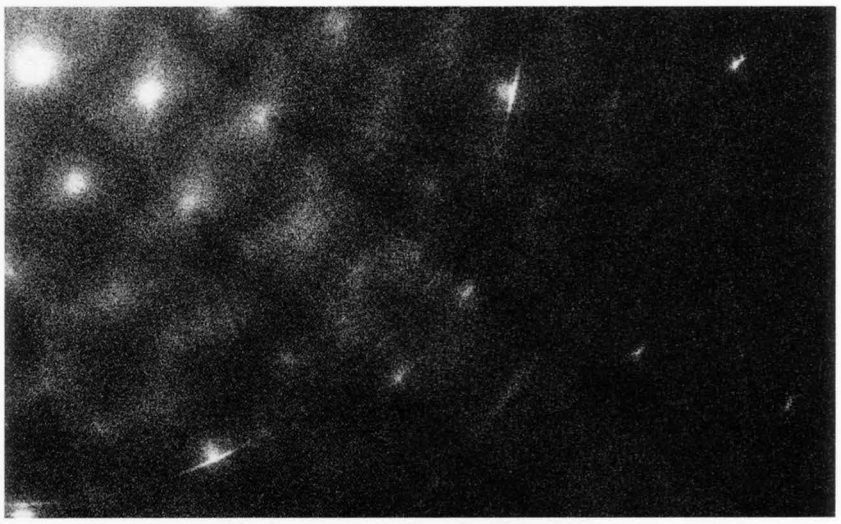

(d) 2nd plasmon loss

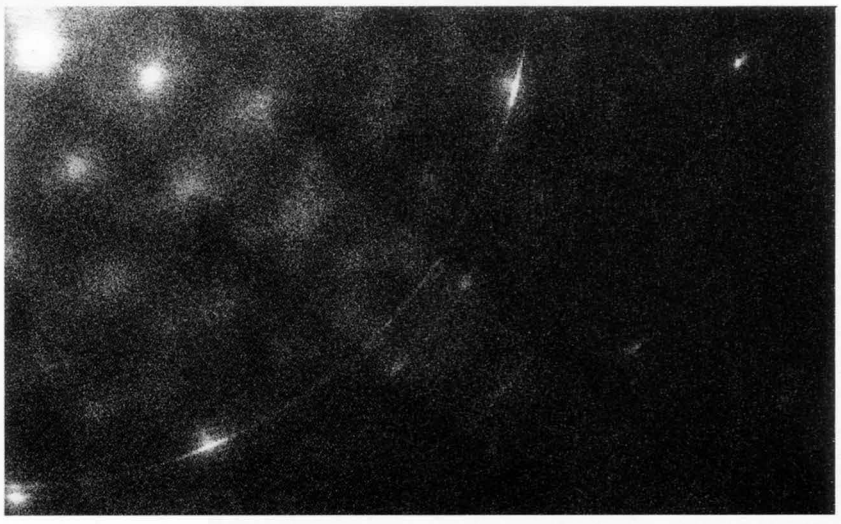

Acceptance energy width 8.5eV

FeS_2

[100] **100kV**

(a) Unfiltered

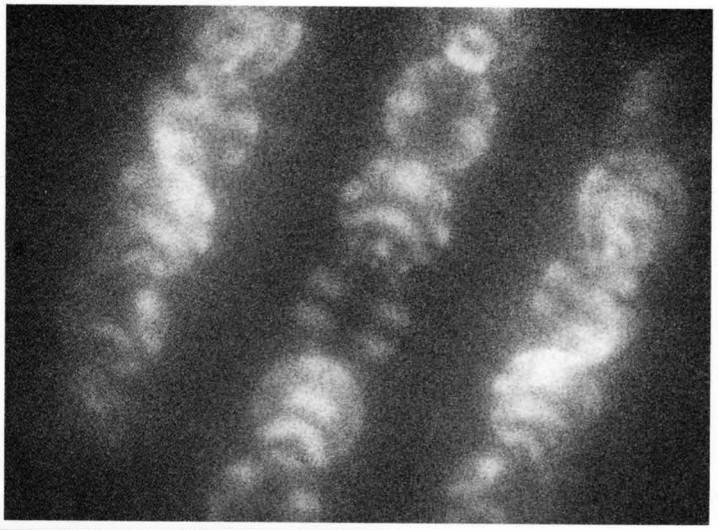

Acceptance energy width 7.8eV

(b) Zero loss

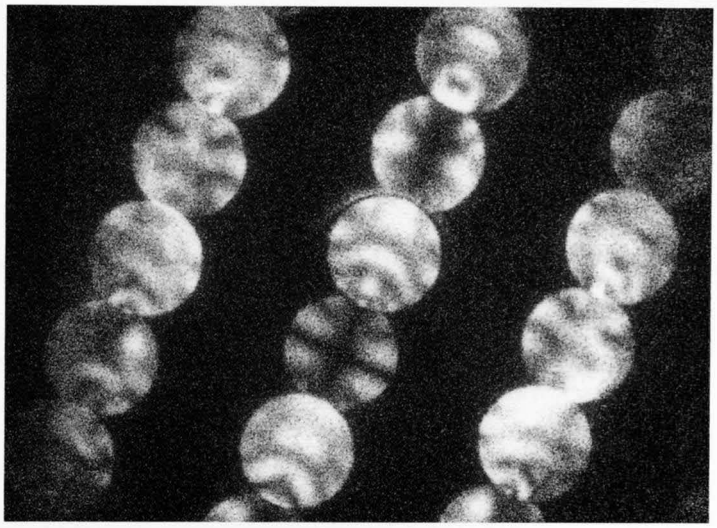

(c) 1st plasmon loss

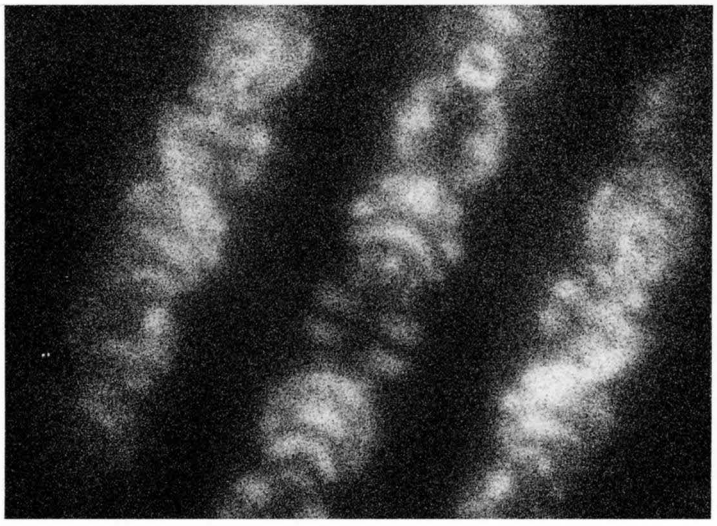

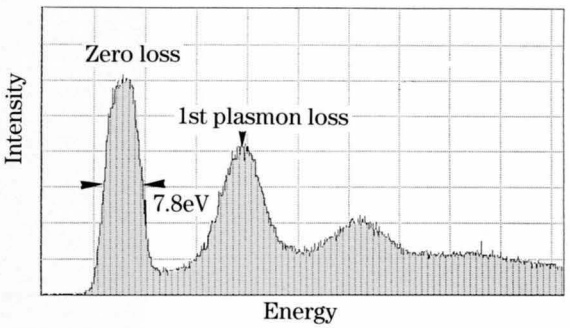

(d) Energy spectrum

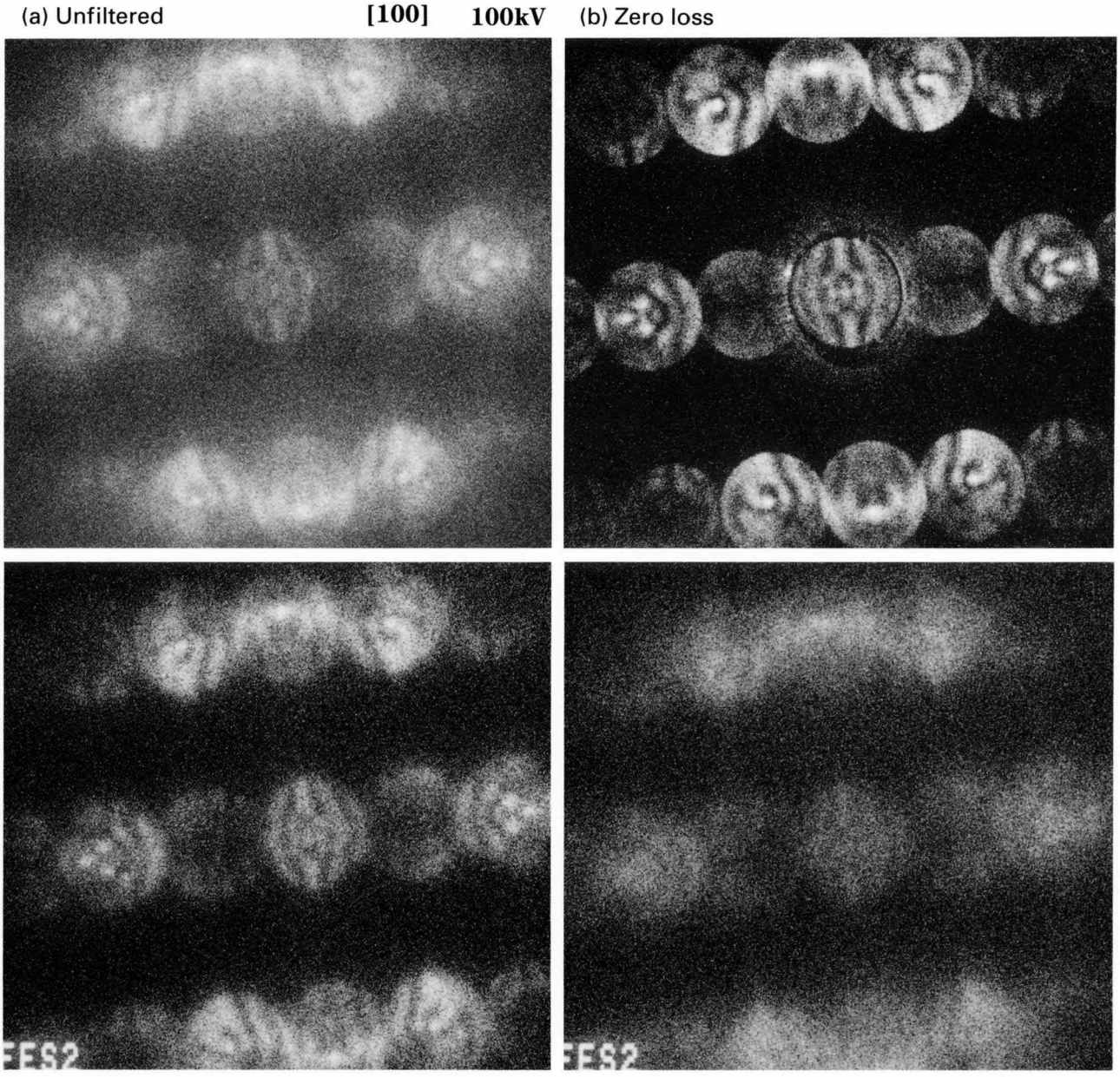
(a) Unfiltered
[100] 100kV
(b) Zero loss
(c) 1st plasmon loss
(d) 2nd plasmon loss

Lattice Defects

Stacking Faults

Many reflections appear simultaneously in one CBED pattern. Rocking curves of the reflection lines obtained from a specimen area containing a stacking fault show profiles characteristic of the values of phase shifts caused by the displacement at the fault. These facts enable the unambiguous determination of the displacement vector $\boldsymbol{R}$ without knowing the sense of tilt of the fault [4], [9]. It is emphasized that the CBED method can easily determine whether the fault is intrinsic or extrinsic without such complication as occurs in the electron-microscope-image method. A better method [11], which uses defocus CBED patterns, than the previous CBED method [4], [9] for the determination of the displacement vector is described.

When a defocused electron beam illuminates an area across a stacking fault, a reflection line across the fault shows a continuous change of the rocking curve such as illustrated in the figure. The bird's-eye views of the calculated rocking curves of a reflection line for different phase shifts are shown in the figures on pages 158 and 159.

The photograph on the opposite page shows a defocus CBED pattern obtained from an area containing a stacking fault of Si. An electron micrograph of the fault is attached as an inset. The $1\bar{3}5$ and $5\bar{5}1$ reflections exhibit a specific change in the rocking curve according to the phase shift $\alpha = 2\pi \boldsymbol{g}\cdot\boldsymbol{R}$ at the fault, where $\boldsymbol{g}$ is the reflection vector. The $\bar{6}60$ reflection is not affected by the fault because of $\alpha = 0$.

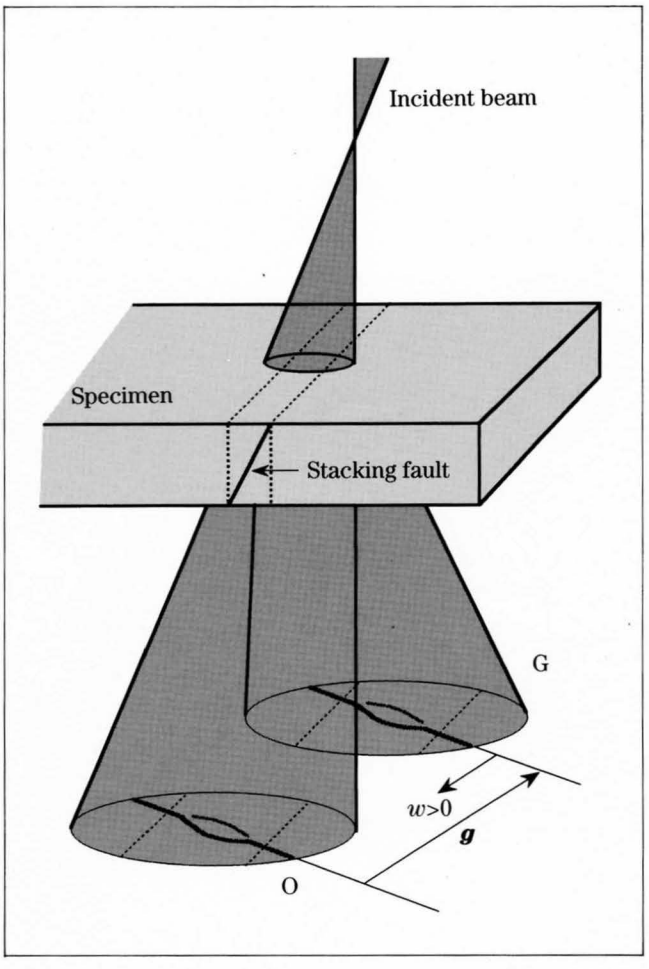

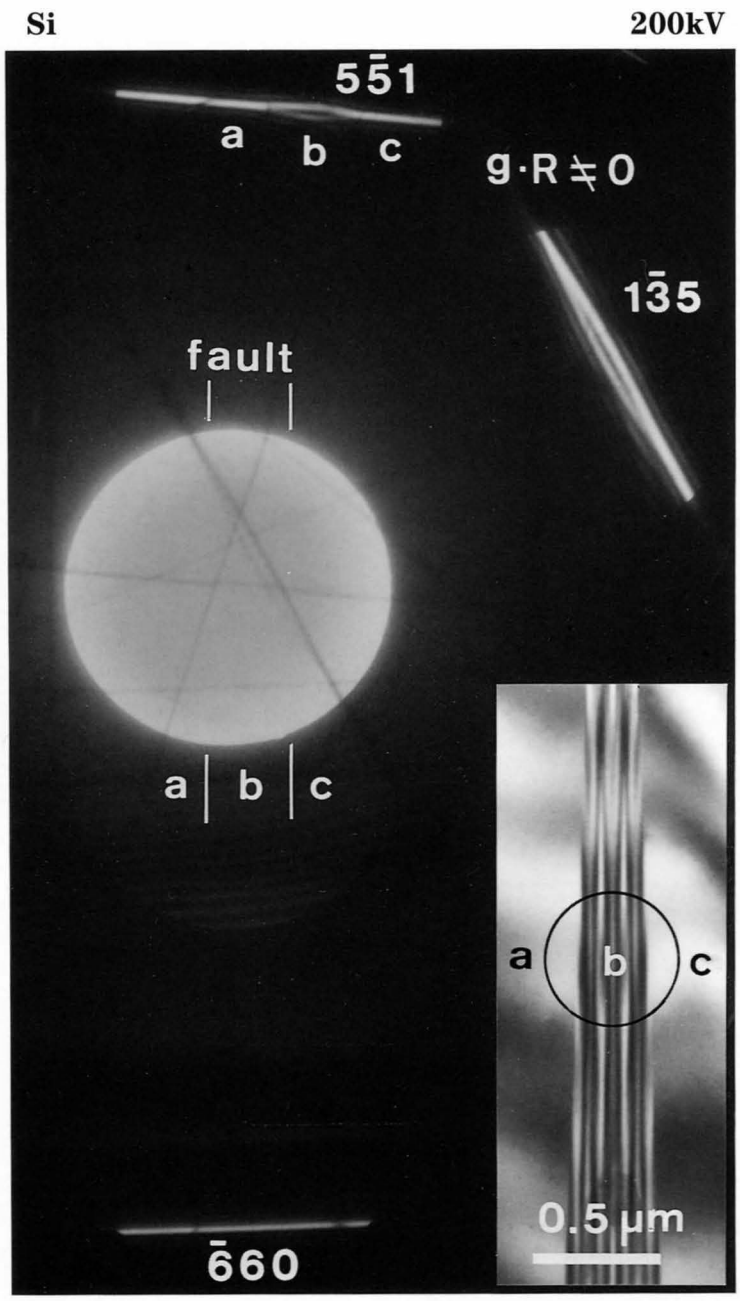

Defocus CBED pattern from a stacking fault of Si.

LACBED and defocus CBED patterns of stacking faults

LACBED pattern of a stacking fault

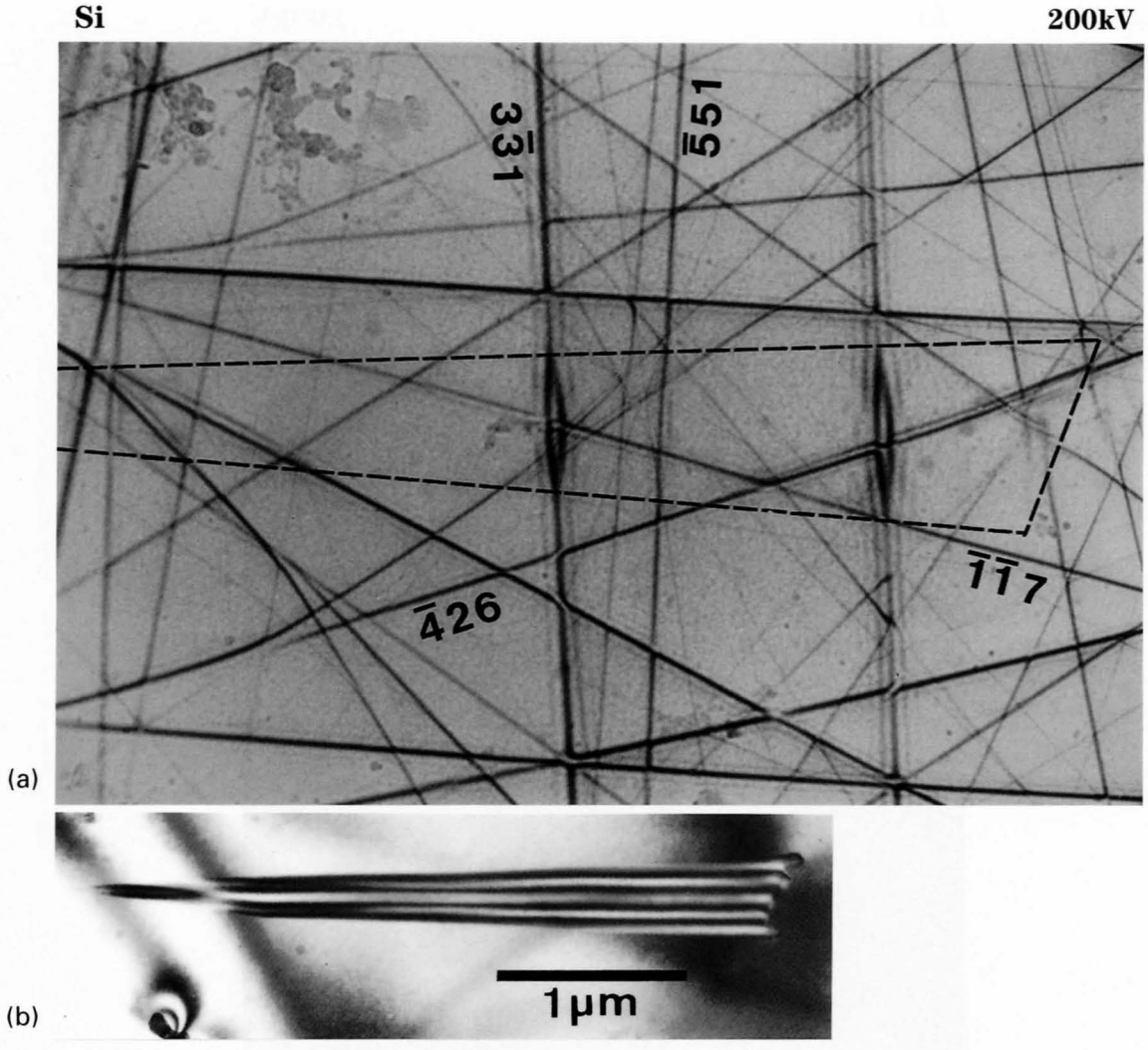

Photograph (a) shows an LACBED pattern of a stacking fault in Si, whose image is given in Photo (b). The faulted area was identified as indicated by the dotted lines. A number of reflection lines show split rocking curves at the fault. That is, information on both the real and reciprocal spaces is obtained from the LACBED pattern.

The figure shows a bird's-eye view of the rocking curve of a reflection line across a stacking fault lying oblique to the specimen surface calculated for $\alpha = 2\pi \boldsymbol{g}\cdot\boldsymbol{R} = +(2/3)\,\pi$ and $t/\xi_g = 1/4.25$.

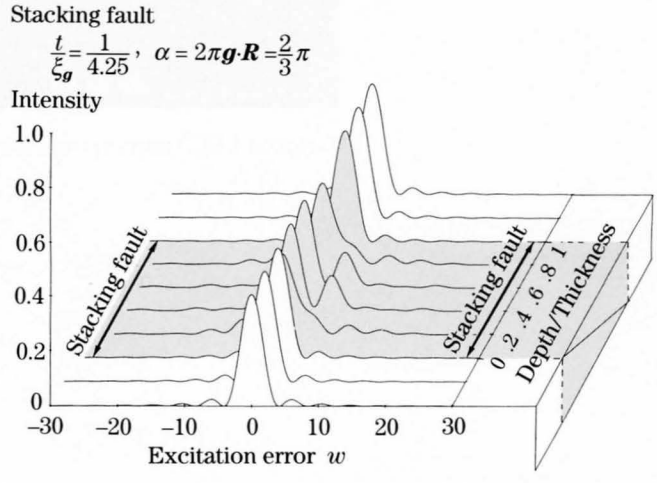

Defocus CBED patterns of stacking faults

TiO_2 **160kV**

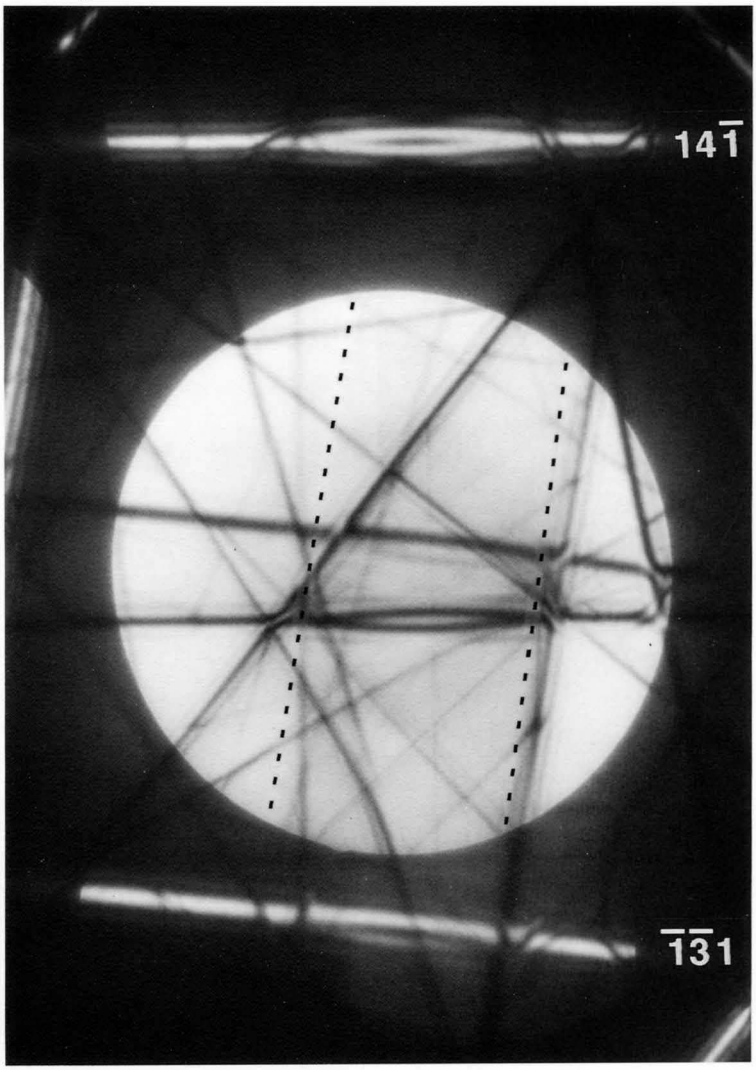

The photograph shows a defocus CBED pattern of a stacking fault in TiO_2 (rutile). The illuminated specimen area is about 150nm in diameter. The area bounded by the dotted lines corresponds to the area containing the fault. The rocking curve of the $14\bar{1}$ reflection is symmetric with respect to the original Bragg position, which is characteristic of the fault with a phase shift of $\alpha = \pi$. This is the first observation of the reflection line for a phase shift of π. The $\bar{1}\bar{3}1$ reflection shows the rocking curve for $\alpha \simeq -(2/3)\pi$.

The figure shows a bird's-eye view of the rocking curve of a reflection line from a stacking fault oblique to the specimen surface calculated for $\alpha = \pi$ and $t/\xi_g = 1/4.25$.

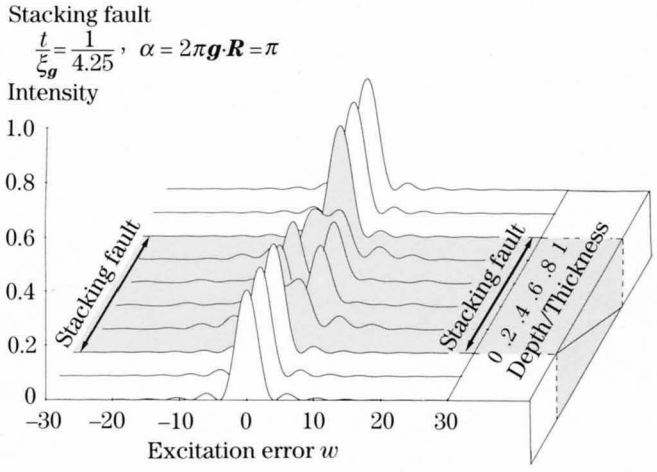

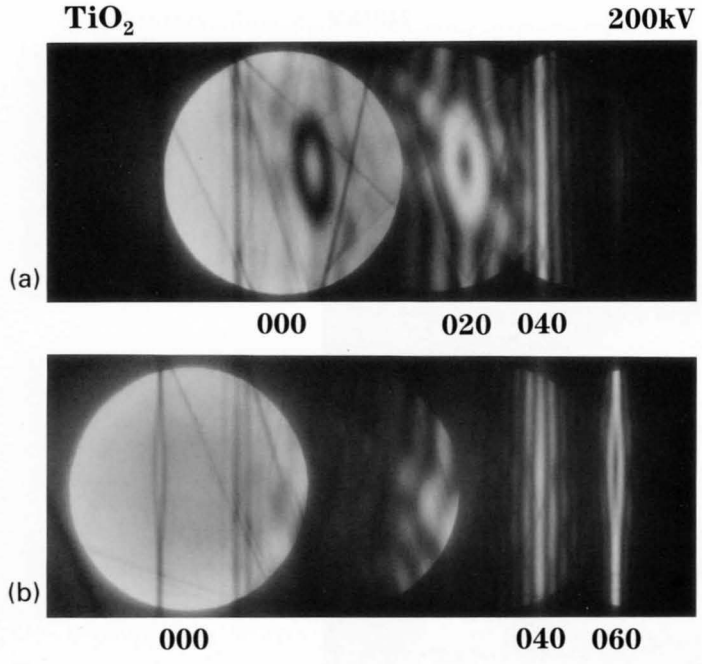

Photographs (a) and (b) show defocus CBED patterns from a stacking fault in TiO_2. Alternate changes of the profiles of reflection lines is seen in the 020, 040 and 060 reflections. That is, the 020 reflection shows a profile for $\alpha = \pi$, the 040 that for $\alpha = 0$ or 2π, and the 060 again shows the profile for $\alpha = \pi$.

Photographs (c) and (d) show a defocus and an in-focus CBED pattern from another stacking fault in TiO_2. The 020, 040 and 060 reflections exhibit profiles for $\alpha = (1/3)\pi$, $(2/3)\pi$ and π, respectively.

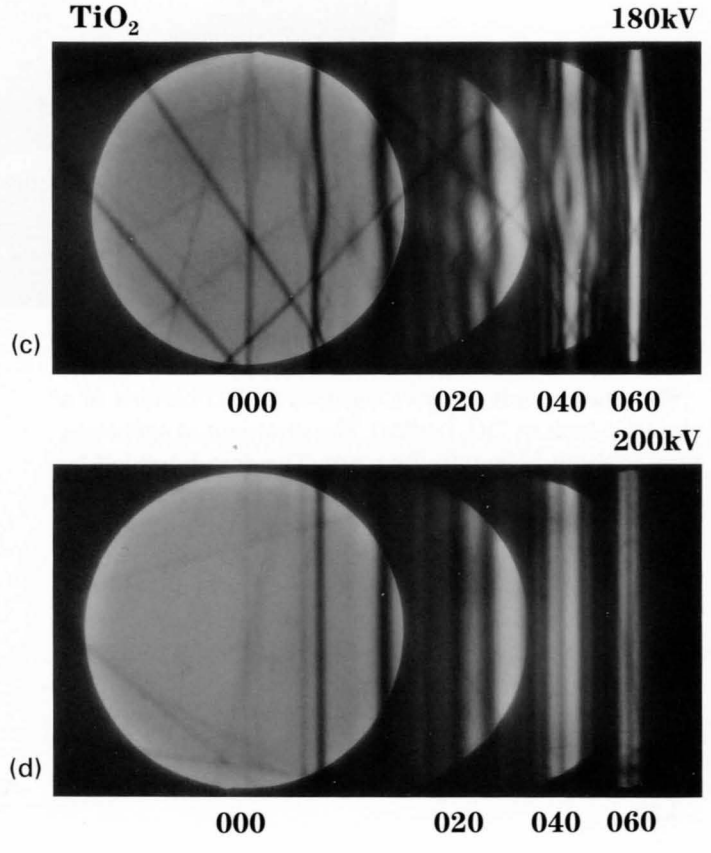

LACBED patterns of a stacking fault

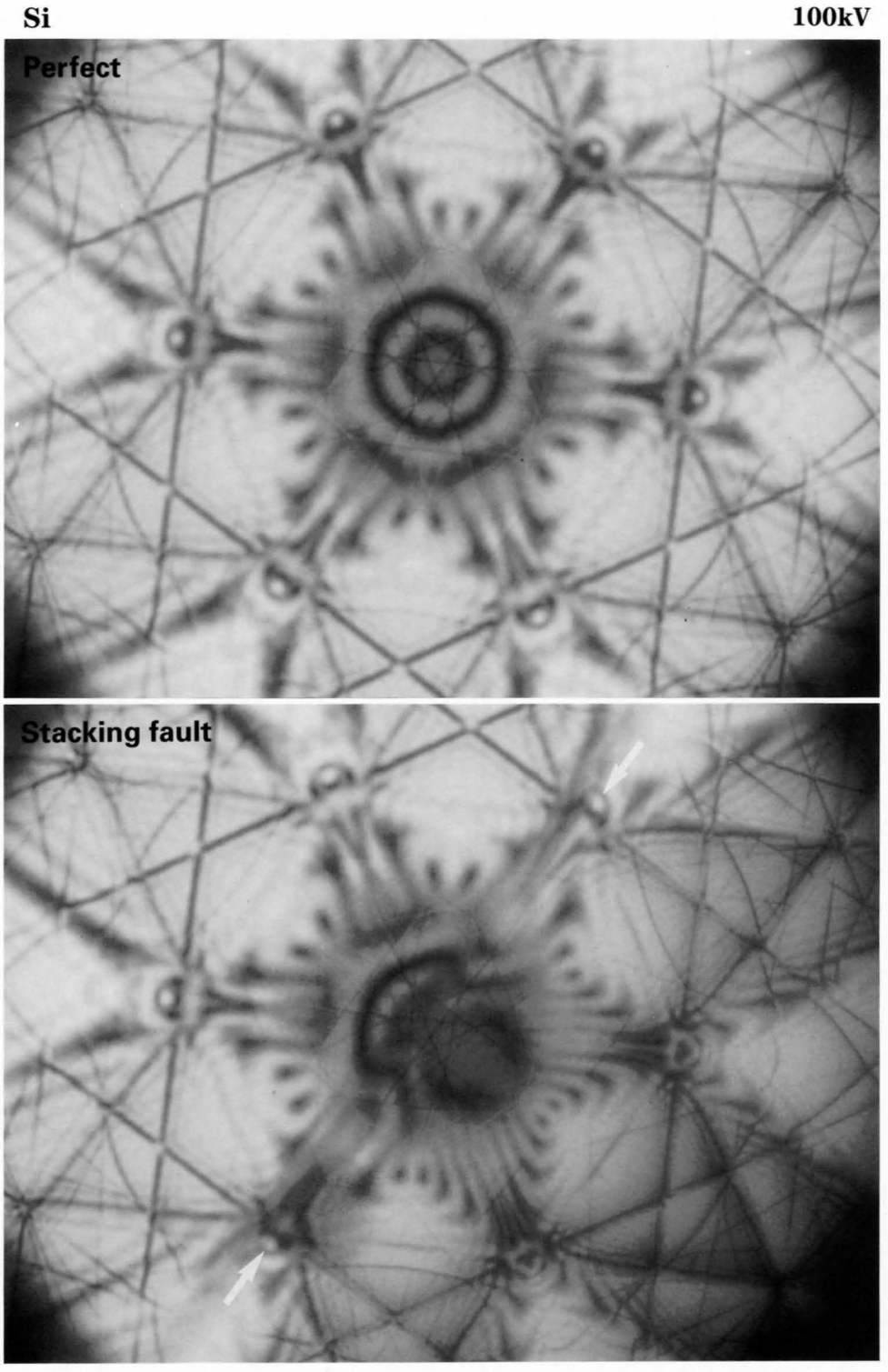

LACBED patterns of Si recorded on IPs at the [111] electron incidence from a perfect specimen area (a), showing a $3m$ symmetry, and from an area containing a stacking fault (b), in which two mirror symmetries are destroyed and only one mirror symmetry survives. Arrows in Fig. (b) indicate the stacking fault.

Determination of the shift vector of a stacking fault

Dynamical calculations of intensity profiles of a stacking fault

The figure shows rocking curves of reflection intensities calculated dynamically for different phase shifts of $\alpha = 2\pi \boldsymbol{g} \cdot \boldsymbol{R}$, where the ratio between the specimen thickness t and the extinction distance ξ_g, t/ξ_g was assumed as 1/2 and the depth of the fault as $t/2$.

The intensity I_g is symmetric about the excitation error $w = 0$ for $\alpha = 0$. As α ($\alpha > 0$) increases, the intensity becomes asymmetric; the first subsidiary maximum at $w > 0$ becomes greater and the one at $w < 0$ smaller. It should be noted that both the principal peak and the subsidiary peak shift a little in the negative direction of w. For $\alpha = \pi$, the two peaks have the same intensity and are again symmetric about $w = 0$. For negative values of α, the behavior of the peaks is reversed to that for positive α.

The intensity behavior for different α at $w = 0$ and $t/\xi_g = 1/2$ is simply interpreted. For $\alpha = 0$, the diffracted waves at the upper and lower halves of the specimen are added constructively to produce an intensity maximum. For $\alpha = \pi$, the diffracted wave at the second half of the specimen is of antiphase to the wave at the first half, causing an intensity minimum by destructive interference. For intermediate phases, the cancellation is imperfect. Thus, intensities smaller than that for $\alpha = 0$ but larger than that for $\alpha = \pi$ are produced.

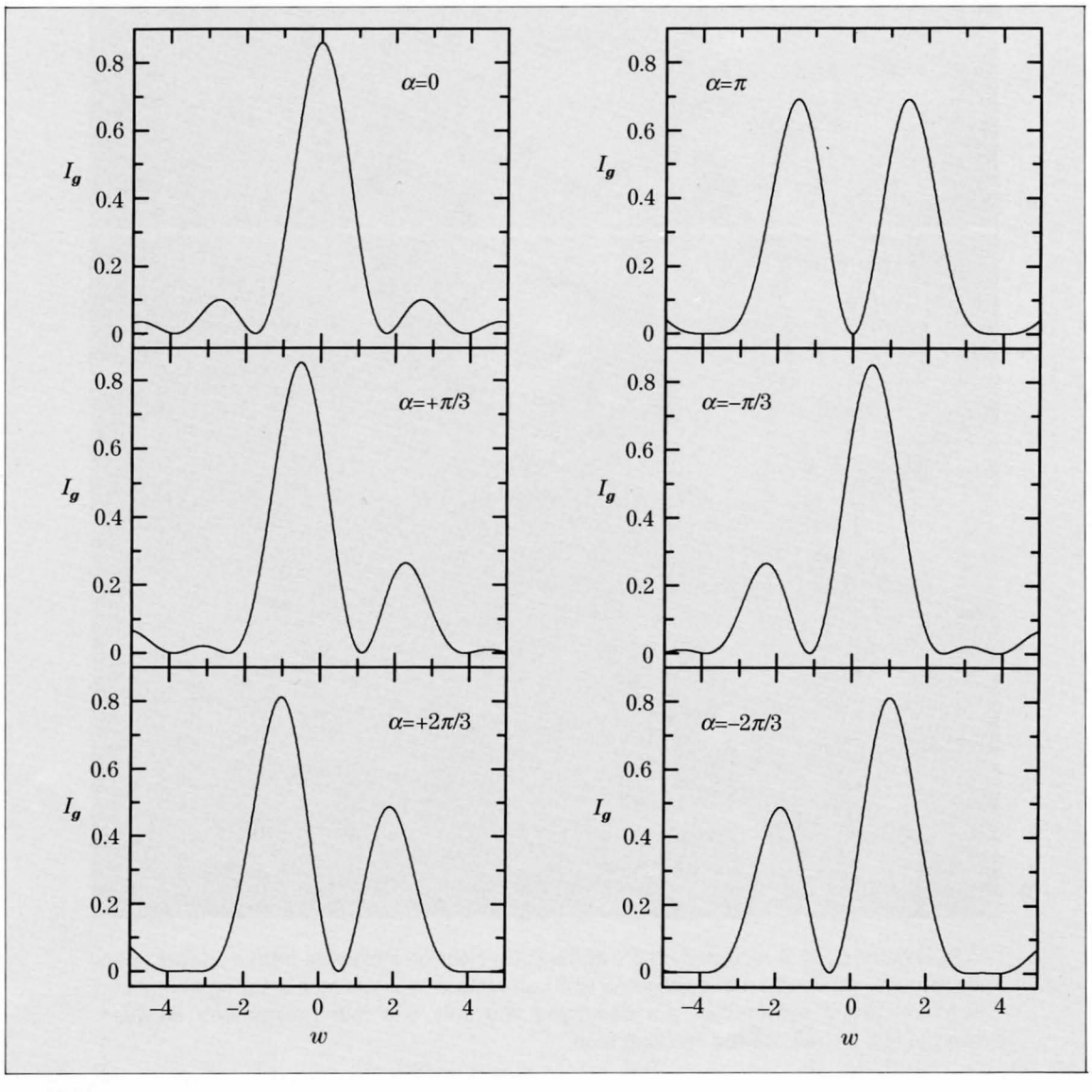

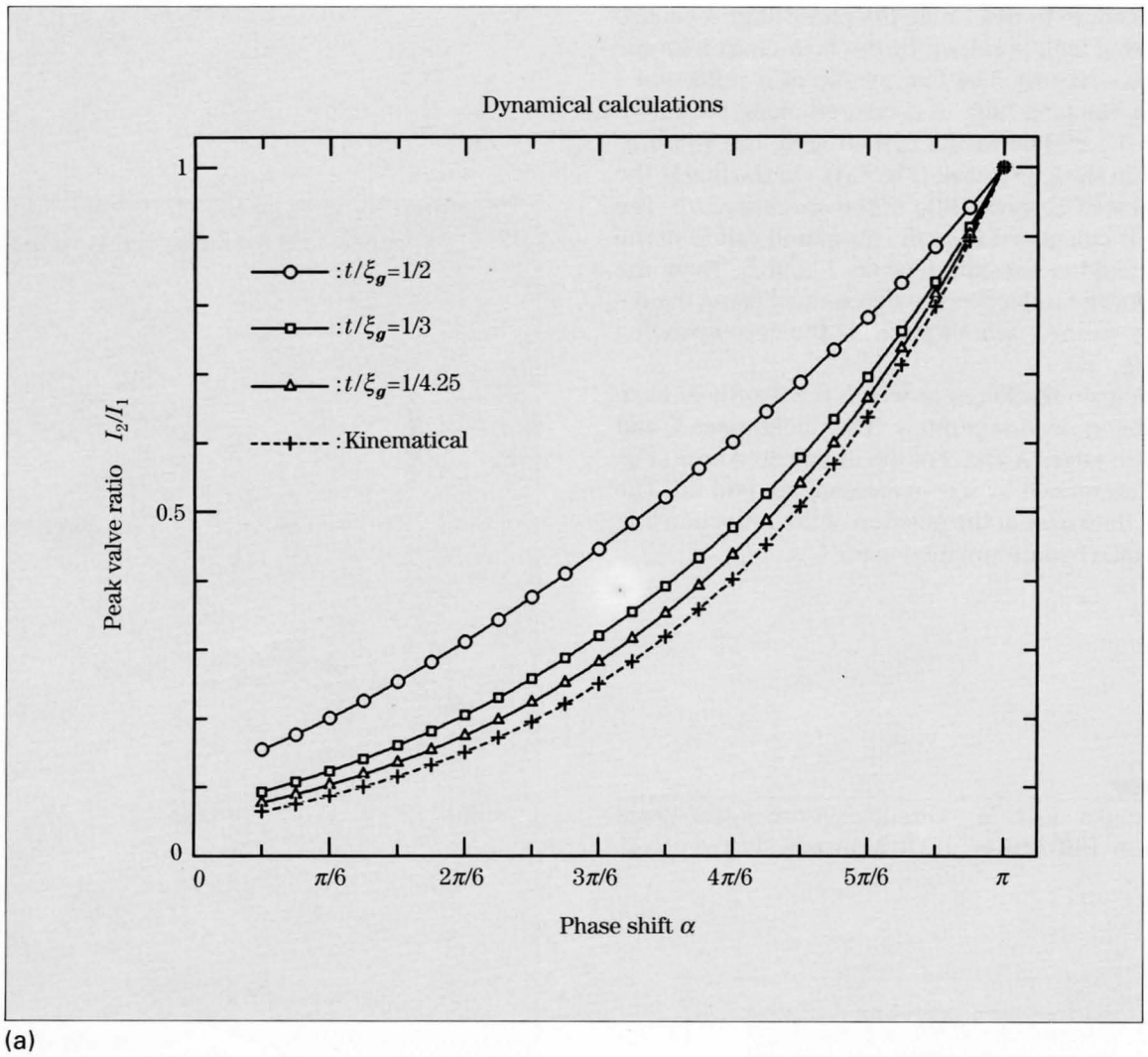

(a)

Figure (a) shows the peak value ratio I_2/I_1 as a function of the phase shift α. Monotonic increase of I_2/I_1 with increasing α is noted, though the curves of I_2/I_1 are different for different values of t/ξ_g. When t/ξ_g decreases, the curves approach the curve calculated under the kinematical approximation of the dynamical theory of electron diffraction. These curves make it possible to determine the phase shift α from the measured intensity ratio I_2/I_1. It should be noted that the ratios between the integrated intensities show very similar curves to those of Fig. (a).

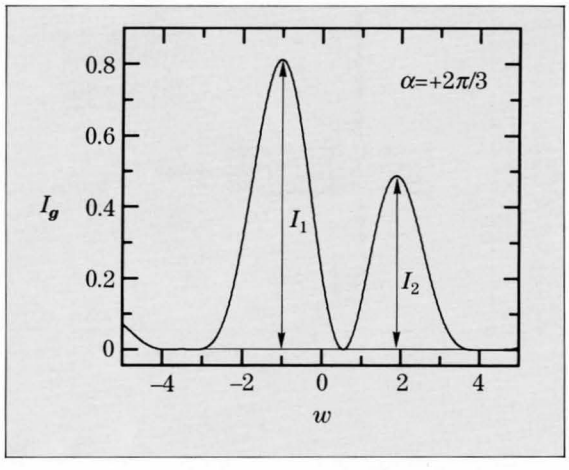

(b)

Determination of phase shift α

The procedure to determine the phase shift α caused by a stacking fault is shown by the flow chart with the help of illustrations. The line profile of a reflection i crossing a stacking fault is measured along the line L drawn in the middle of the faulted area, the width of which is l in the CBED disk (Fig. (a)). On the line L, the fault is located in the middle of the specimen, $t/2$. The ratio I_2/I_1 is calculated from the measured values of the principal and the subsidiary peaks I_1 and I_2. Then, the phase α_i for the reflection i is determined using the α_i–I_2/I_1 curve on the previous page for the corresponding value of t/ξ_g.

The specimen thickness at which the profile is measured is determined separately. The thicknesses t_A and t_B at the two edges A and B of the illuminated area (Fig. (b)) are determined by a conventional method [a]. The specimen thickness at the position of the reflection line is determined by interpolation using t_A and t_B.

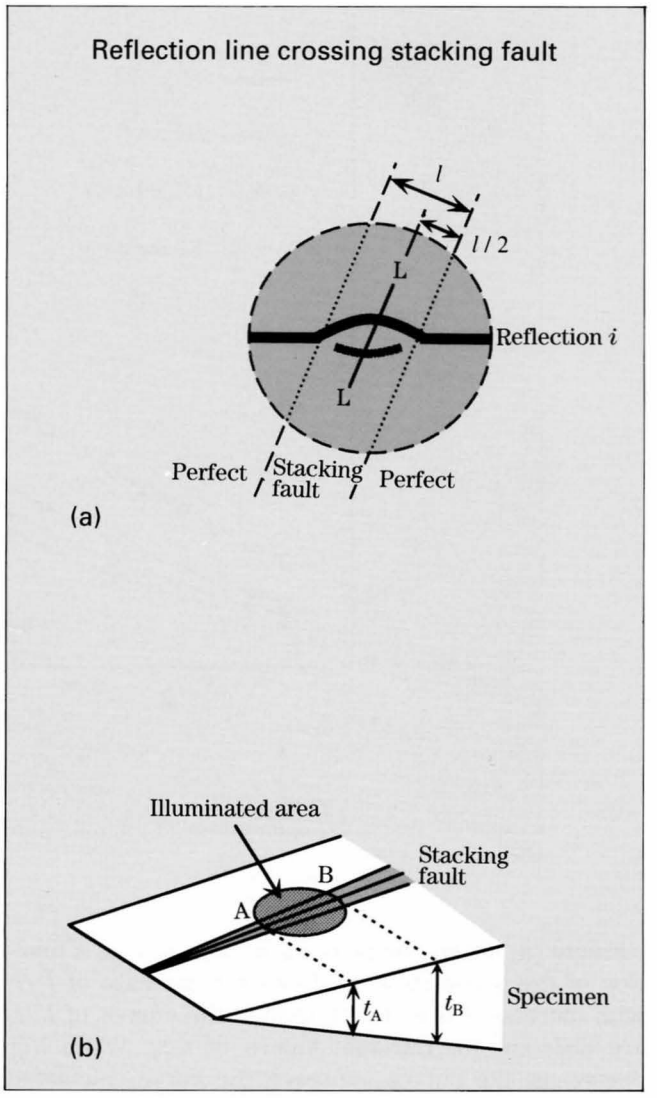

Reference

[a] M. Tanaka and M. Terauchi: Convergent-Beam Electron Diffraction, JEOL-Maruzen, Tokyo, 1985, p.38.

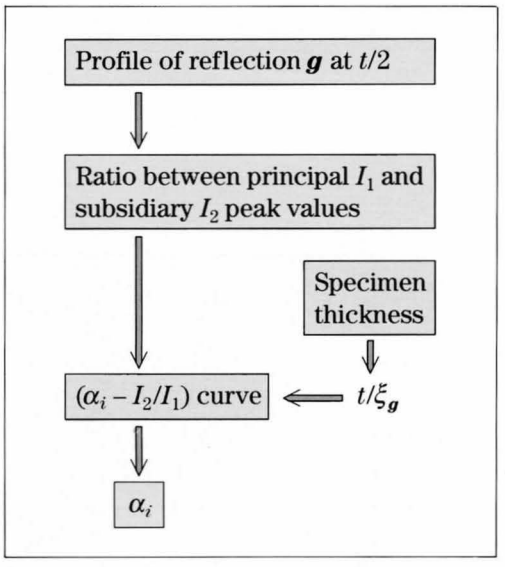

Determination of shift vector $\boldsymbol{R}$

The phase shift α is expressed as follows.

$$\alpha_i = 2\pi \boldsymbol{g}_i \cdot \boldsymbol{R} = \alpha_i' + 2\pi n_i, \tag{1}$$

where the suffix i specifies the reflection index, α_i' takes a value between $-\pi$ and π, n_i is an integer, $\boldsymbol{g}_i$ is (h_i, k_i, l_i), and $\boldsymbol{R}$ is $'(u, v, w)$. For three linearly independent reflections, eq. (1) is rewritten as

$$\begin{aligned} 2\pi\, \boldsymbol{g}_1 \cdot \boldsymbol{R} &= \alpha_1' + 2\pi n_1 \\ 2\pi\, \boldsymbol{g}_2 \cdot \boldsymbol{R} &= \alpha_2' + 2\pi n_2 \\ 2\pi\, \boldsymbol{g}_3 \cdot \boldsymbol{R} &= \alpha_3' + 2\pi n_3. \end{aligned} \tag{2}$$

When we define G, A and N as follow

$$G = \begin{pmatrix} \boldsymbol{g}_1 \\ \boldsymbol{g}_2 \\ \boldsymbol{g}_3 \end{pmatrix}, \quad A = \begin{pmatrix} \alpha_1'/2\pi \\ \alpha_2'/2\pi \\ \alpha_3'/2\pi \end{pmatrix} \text{ and } \quad N = \begin{pmatrix} n_1 \\ n_2 \\ n_3 \end{pmatrix}, \tag{3}$$

then, eq. (2) is rewritten as

$$G\boldsymbol{R} = A + N. \tag{4}$$

By multiplying G^{-1} from the left, we obtain

$$\boldsymbol{R} = G^{-1} A + G^{-1} N. \tag{5}$$

To determine $\boldsymbol{R}$, we have to know both the values of A and N. The values of the three components of A are determined by an experiment using the α_i–I_2/I_1 curves, but those of N can not be found from the experiment. This fact indicates that $\boldsymbol{R}$ cannot be determined by a set of three linearly independent reflections. However, from the translational symmetry of crystals, the components of $\boldsymbol{R}$ are limited to values in the ranges of $-1/2<u\leq 1/2$, $-1/2<v\leq 1/2$, and $-1/2<w\leq 1/2$. Application of the conditions enables us to obtain possible values of n_i or possible displacement vectors $\boldsymbol{R}$. We calculate the value of $2\pi \boldsymbol{g}_i \cdot \boldsymbol{R}$ for the 4th reflection and, if necessary, for the 5th, and compare the value with the experimental one. The displacement vector $\boldsymbol{R}$ is determined unambiguously by selecting the vector whose calculated phase shifts are compatible with the experimental values.

TiO_2

160kV

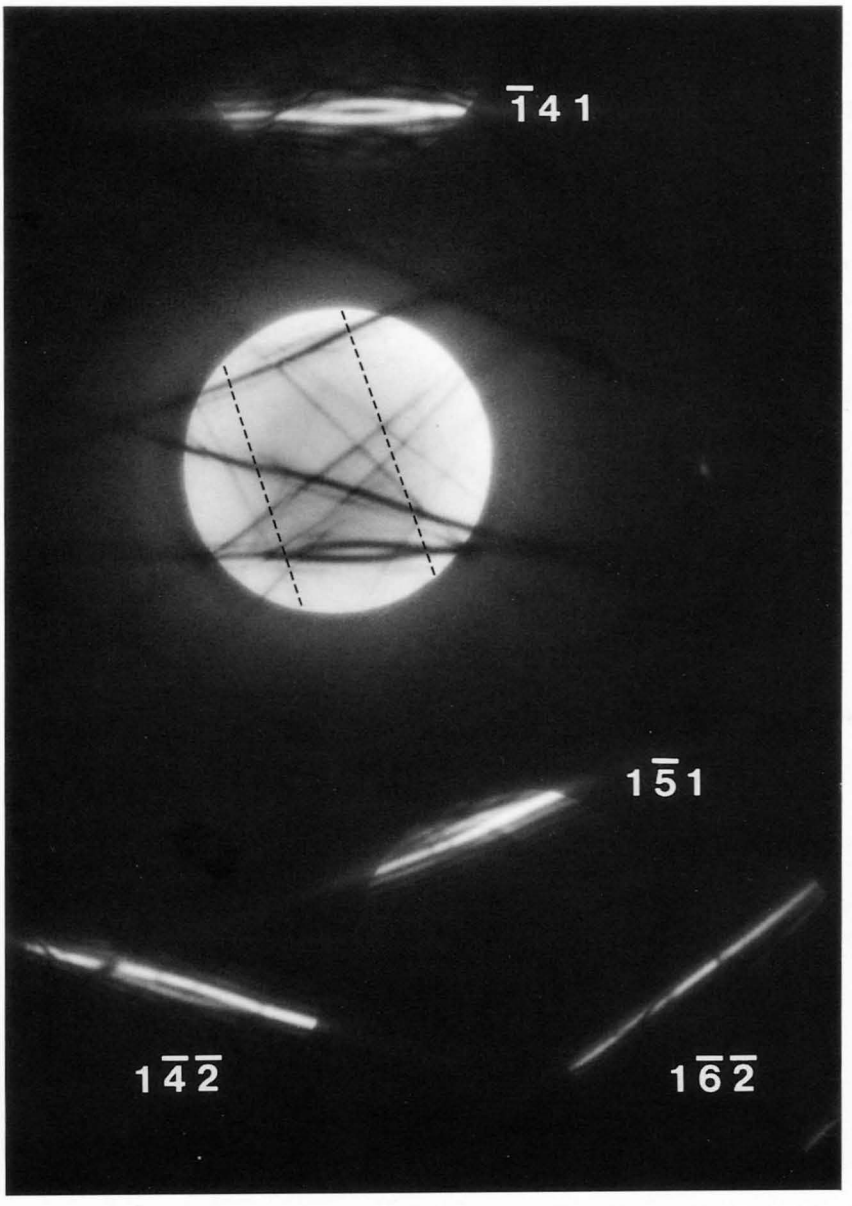

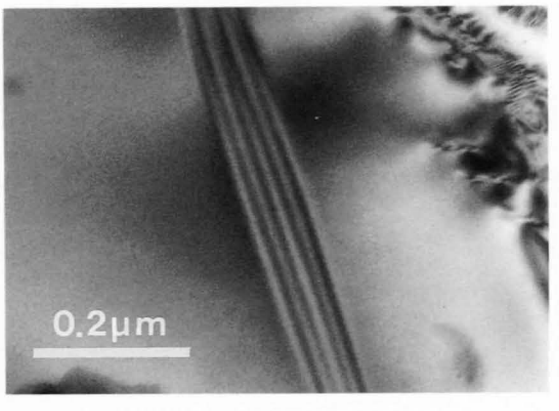

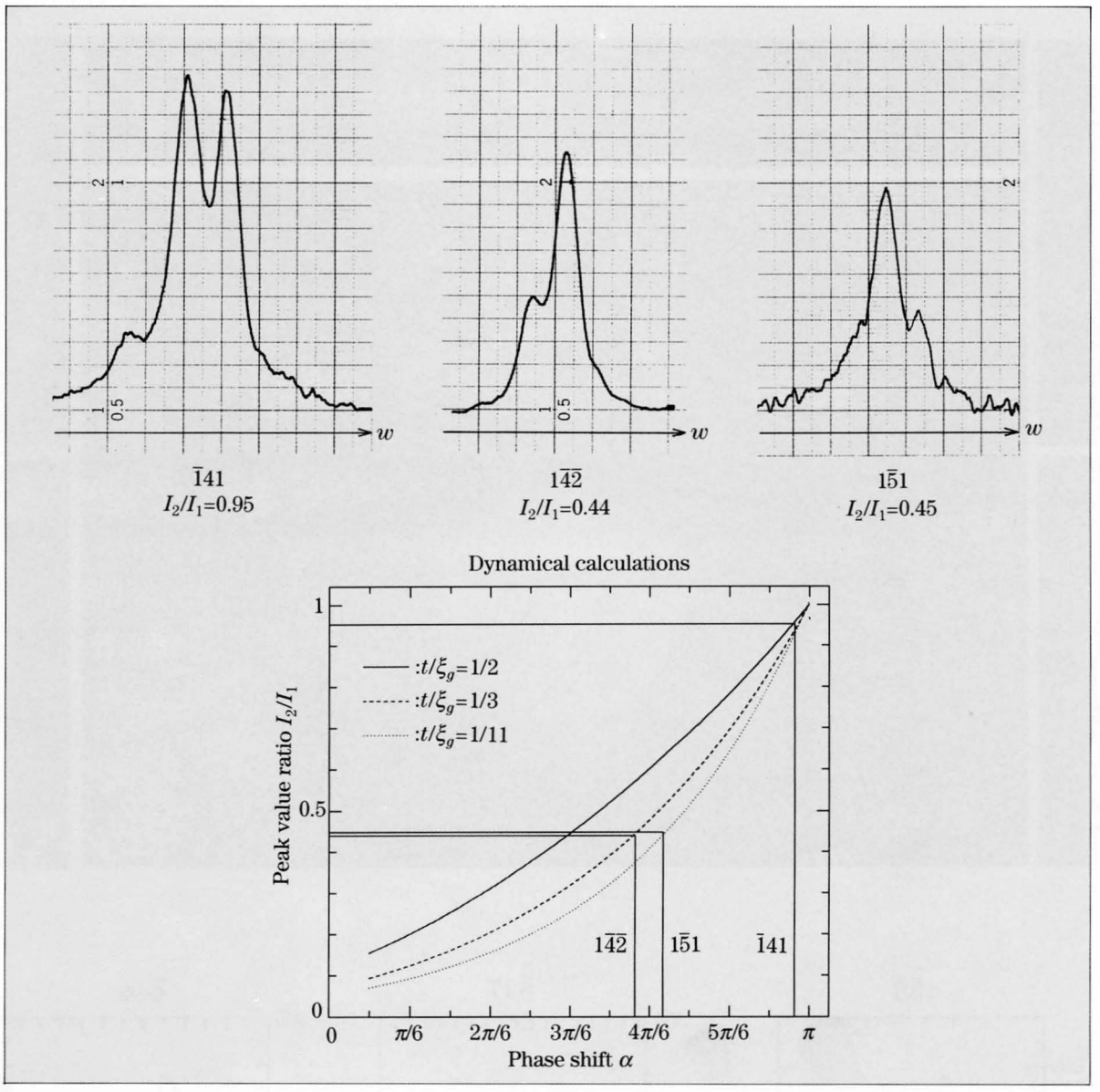

Displacement-vector determination was carried out for a stacking fault of rutile (TiO_2). The photograph on the opposite page shows a defocus CBED pattern taken from an area containing a stacking fault at an accelerating voltage of 160kV.

The intensity ratios I_2/I_1 of the four reflections $1\bar{6}\bar{2}$, $\bar{1}41$, $1\bar{4}\bar{2}$ and $1\bar{5}1$ were measured respectively to be —, 0.95, 0.44 and 0.45. The specimen thickness was evaluated to be about 100nm. The values of t/ξ_g for these reflections were determined as 1/7, 1/2, 1/3 and 1/11, respectively. The phase shifts α for these reflections were determined by using the corresponding α_i-I_2/I_1 curves to be 0, $+0.97\pi$, -0.64π and $+0.69\pi$, respectively. Using the $1\bar{6}\bar{2}$, $\bar{1}41$, and $1\bar{4}\bar{2}$ reflections, two possible displacement vectors were evaluated as $\boldsymbol{R}_1$=1/6 [$\overline{1.9}$ $\overline{1.0}$ $\overline{0.86}$] and $\boldsymbol{R}_2$=1/6 [$\overline{1.9}$ 2.0 $\overline{0.86}$]. For the 4th reflection of index $1\bar{5}1$, $\boldsymbol{R}_1$ and $\boldsymbol{R}_2$ give phase shifts $2\pi\boldsymbol{g}_4\cdot\boldsymbol{R}$ of $+0.73\pi$ and -2.23π. Since the experimental value of $2\pi\boldsymbol{g}_4\cdot\boldsymbol{R}$ is $+0.69\pi$, $\boldsymbol{R}_1$ is determined to be the correct displacement vector. When we assume that u, v and w take simple integers, $\boldsymbol{R}$ becomes 1/6 [$\bar{2}\,\bar{1}\,\bar{1}$], which agrees with the reported displacement vector [a].

The above example clearly shows that the present method is successful in determining the displacement vector of the stacking fault. It should be noted that the accuracy of the method is limited at present by the effect of inelastically scattered background.

Reference

[a] J. Van Landuyt: *Phys. Stat. Sol.*, **16** (1966) 585.

Si

200kV

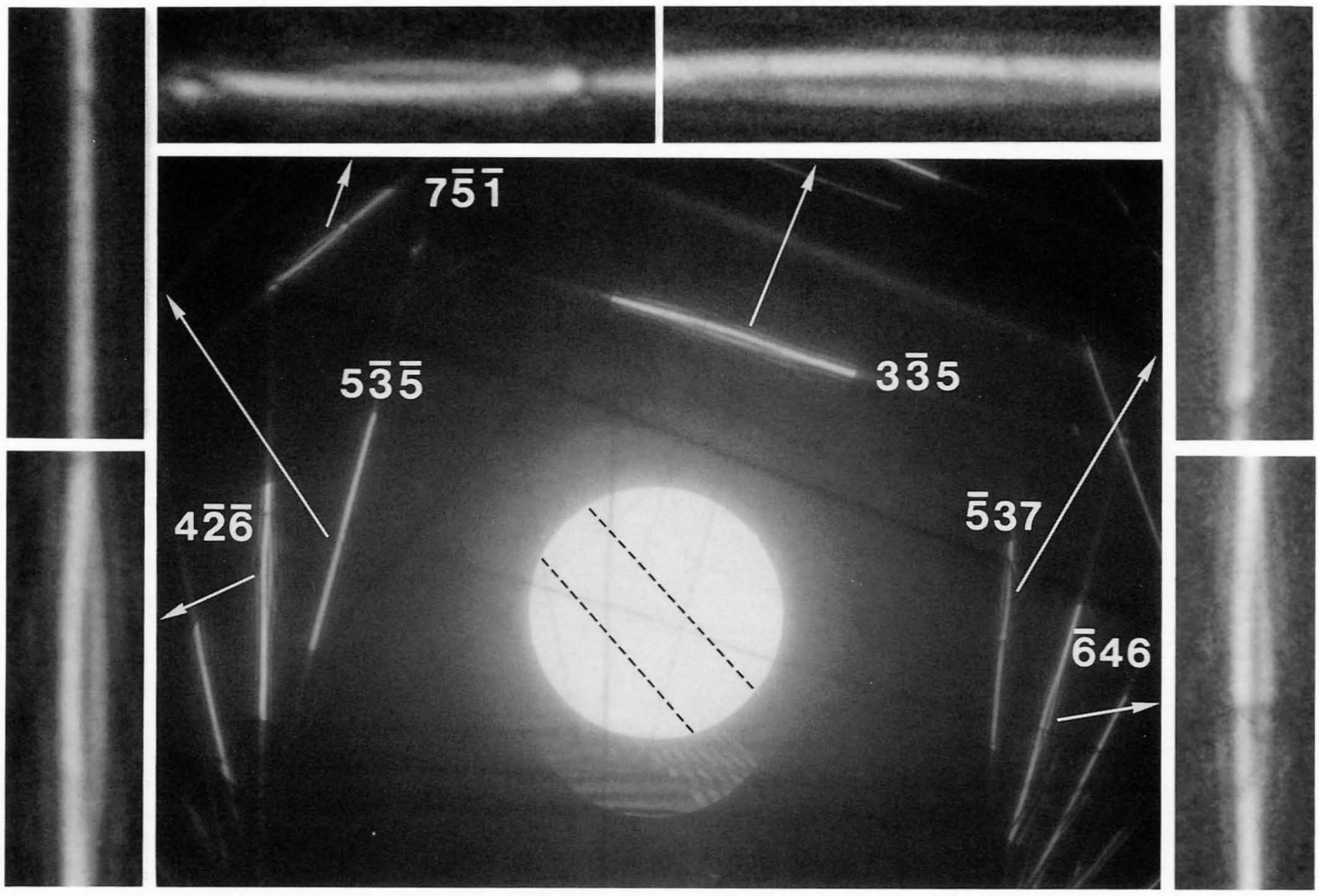
7$\bar{5}\bar{1}$
5$\bar{3}\bar{5}$
3$\bar{3}$5
4$\bar{2}\bar{6}$
$\bar{5}$37
$\bar{6}$46

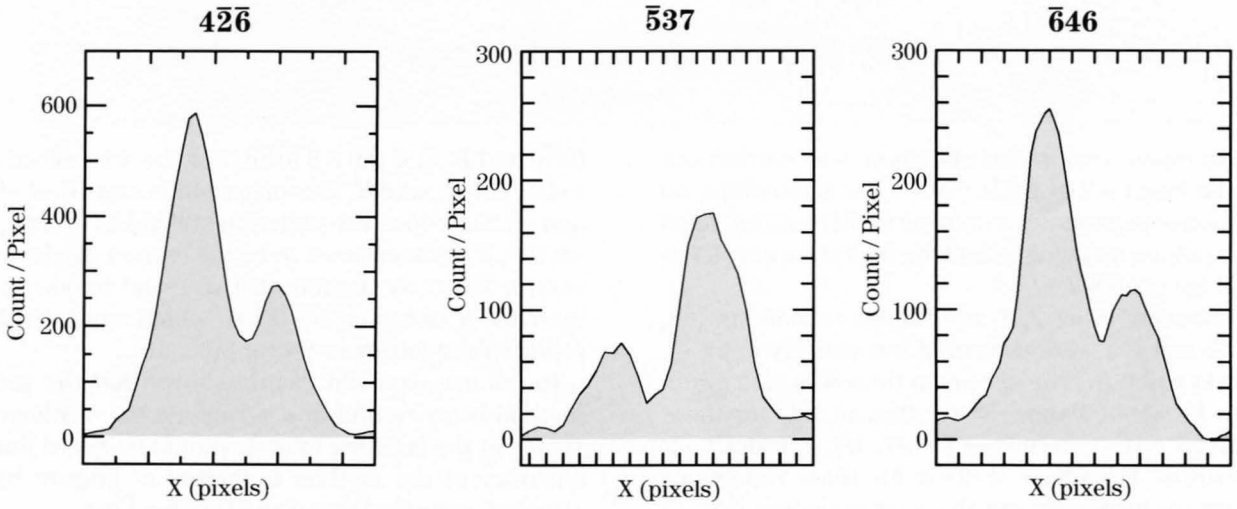
4$\bar{2}\bar{6}$
Count / Pixel
600
400
200
0
X (pixels)
$\bar{5}$37
Count / Pixel
300
200
100
0
X (pixels)
$\bar{6}$46
Count / Pixel
300
200
100
0
X (pixels)

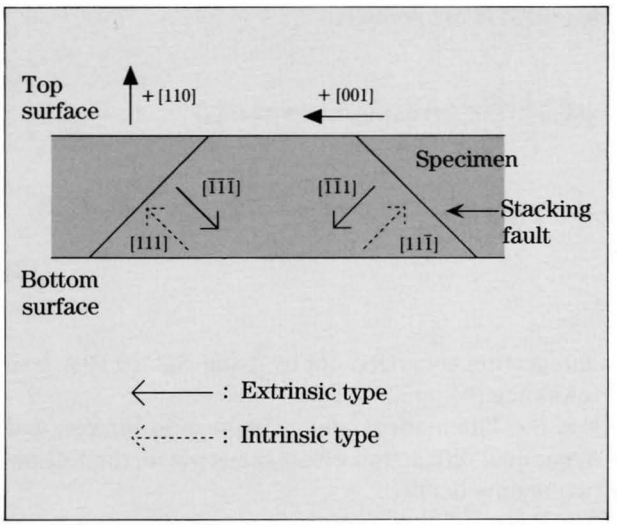

(a)

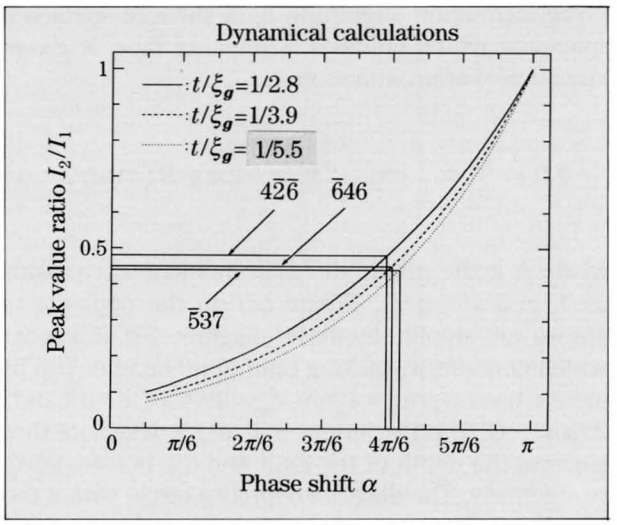

(b)

The photograph on the opposite page is a defocus CBED pattern of Si. The signs of the reflection indices were determined by assuming the senses of the [110] and [100] directions as shown in Fig. (a).

The shift vector $\boldsymbol{R}$ was determined using the 4$\bar{2}\bar{6}$, $\bar{5}$37, $\bar{6}$46 and 5$\bar{3}\bar{5}$ reflections, line profiles of the former three reflections being shown beneath the photo. The thicknesses t at the reflection lines were determined by the interpolation method described previously. Using the α_i–I_2/I_1 curves (Fig. (b)) for the values of t/ξ_g, the phase shifts α of the 4$\bar{2}\bar{6}$, $\bar{6}$46 and $\bar{5}$37 reflections were evaluated from the measured values of I_2/I_1. The 5$\bar{3}\bar{5}$ reflection was not affected by the fault. Four possible shift vectors $\boldsymbol{R}$ were obtained by solving eq. (5) with the help of translational symmetry condition. It was found that any other reflections could not select one shift vector. Readers can ascertain this fact for the 5$\bar{3}\bar{5}$ reflection for example. The crystal lattice was assumed tacitly to be face-centered cubic. As a result, these four vectors are equivalent by adding or subtracting a translational vector 1/2 <110>.

Only one shift vector $\boldsymbol{R}$ = 1/3 [$\bar{1}\bar{1}\bar{1}$] was obtained when a primitive lattice or a primitive rhombohedral lattice was used instead of a face-centered cubic lattice. The result implies that the fault is of the extrinsic type. It is known that stacking faults of the extrinsic type are produced usually in Si.

Determination of α

$\boldsymbol{g}$	ξ_g(nm)	t/ξ_g	I_2/I_1	α
4$\bar{2}\bar{6}$	374.3	1/2.8	0.48	$+2\pi/3-0.04\pi/3$
$\bar{6}$46	532.3	1/3.9	0.45	$-2\pi/3$
$\bar{5}$37	717.6	1/5.5	0.44	$+2\pi/3+0.06\pi/3$
5$\bar{3}\bar{5}$	549.9	1/3.8	—	0

$$\boldsymbol{R} = G^{-1}A + G^{-1}N$$

$$\boldsymbol{R} = \begin{pmatrix} u \\ v \\ w \end{pmatrix} = \begin{pmatrix} 4 & \bar{2} & \bar{6} \\ \bar{6} & 4 & 6 \\ \bar{5} & 3 & 7 \end{pmatrix}^{-1} \begin{pmatrix} 0.327 \\ -0.333 \\ 0.343 \end{pmatrix} \begin{pmatrix} 4 & \bar{2} & \bar{6} \\ \bar{6} & 4 & 6 \\ \bar{5} & 3 & 7 \end{pmatrix}^{-1} \begin{pmatrix} n_1 \\ n_2 \\ n_3 \end{pmatrix}$$

$$= \begin{pmatrix} 2.18 \\ 2.18 \\ 0.673 \end{pmatrix} + 1/4 \begin{pmatrix} 10 & \bar{4} & 12 \\ 12 & \bar{2} & 12 \\ 2 & \bar{2} & 4 \end{pmatrix} \begin{pmatrix} n_1 \\ n_2 \\ n_3 \end{pmatrix}$$

Translational symmetry condition

$$-1/2 < 2.18 + (10n_1 - 4n_2 + 12n_3)/4 \leq 1/2$$
$$-1/2 < 2.18 + (12n_1 - 2n_2 + 12n_3)/4 \leq 1/2$$
$$-1/2 < 0.673 + (2n_1 - 2n_2 + 4n_3)/4 \leq 1/2$$

⇓

n_1	n_2	n_3
−3	4	3
0	−1	−1
1	−1	−2
2	−2	−3

⇓

$\boldsymbol{R}_1$ = 1/6 [$\overline{1.9}$ 1.1 1.0]
$\boldsymbol{R}_2$ = 1/6 [1.1 $\overline{1.9}$ 1.0]
$\boldsymbol{R}_3$ = 1/6 [$\overline{1.9}$ $\overline{1.9}$ $\overline{2.0}$]
$\boldsymbol{R}_4$ = 1/6 [1.1 1.1 $\overline{2.0}$]

⇒

1/6 [$\bar{2}$ 1 1]
1/6 [1 $\bar{2}$ 1]
1/6 [$\bar{2}$ $\bar{2}$ $\bar{2}$]
1/6 [1 1 $\bar{2}$]

Amplitude-phase diagram

The diffraction amplitude ϕ_g at the exit surface of a specimen which contains a stacking fault is given by kinematical approximation as

$$\phi_g(t)=\frac{\pi i}{\xi_g}\phi_o\int_0^t \exp(-2\pi isz-2\pi i\boldsymbol{g}\cdot\boldsymbol{R}(z))\,dz, \qquad (6)$$

where ϕ_o is the amplitude of the incident wave assumed as 1, and $s = w/\xi_g$. Figure (a) on the opposite page shows an amplitude-phase diagram for a specimen which contains a stacking fault in its middle. The parameters used were t = 10nm, ξ_g = 200nm, w = 15 and $\alpha = 2\pi\boldsymbol{g}\cdot\boldsymbol{R} = (2/3)\pi$. The letters O, P and R designate the top surface, the depth of the fault and the bottom surface, respectively. The diagram depicts a circle with a radius of $1/(2\pi s)$. The locus of the diagram suddenly changes its direction by $(2/3)\pi$ at the fault and finishes at R. The resultant amplitude is given by the segment OR.

According to Howie and Whelan [a], [b], the amplitudes of the transmission ϕ_o and diffraction ϕ_g waves are given for dynamical diffraction cases by

$$\frac{d\phi_o(z)}{dz}=\frac{\pi i}{\xi_o}\phi_o(z)+\frac{\pi i}{\xi_g}\phi_g(z)\exp(2\pi isz+2\pi i\boldsymbol{g}\cdot\boldsymbol{R}(z)) \qquad (7)$$

$$\frac{d\phi_g(z)}{dz}=\frac{\pi i}{\xi_o}\phi_g(z)+\frac{\pi i}{\xi_g}\phi_o(z)\exp(-2\pi isz-2\pi i\boldsymbol{g}\cdot\boldsymbol{R}(z)), \qquad (8)$$

where ξ_o is the extinction distance for forward scattering. The amplitude of the diffraction wave ϕ_g is expressed by

$$\phi_g(t)=\int_0^t\left[\frac{\pi i}{\xi_o}\phi_g(z)+\frac{\pi i}{\xi_g}\phi_o(z)\exp(-2\pi isz-2\pi i\boldsymbol{g}\cdot\boldsymbol{R}(z))\right]dz. \qquad (9)$$

We use the expressions of 10.10 a, b in the book of Hirsch *et al.* [b] for ϕ_o and ϕ_g. It should be noted, however, that the phase factors omitted there must be correctly taken into account. That is, ϕ_o and ϕ_g must be replaced by

$$\phi_o(z)\rightarrow\phi_o(z)\exp(\pi isz+\pi iz/\xi_o) \qquad (10)$$

$$\phi_g(z)\rightarrow\phi_g(z)\exp(-\pi isz+\pi iz/\xi_o). \qquad (11)$$

Thus, eq. (9) is rewritten as

$$\phi_g(t)=\int_0^t\left[\frac{\pi i}{\xi_o}\phi_g(z)\exp(-\pi isz+\pi iz/\xi_o)+\frac{\pi i}{\xi_g}\phi_o(z)\exp(-\pi isz+\pi iz/\xi_o-2\pi i\boldsymbol{g}\cdot\boldsymbol{R}(z))\right]dz. \qquad (12)$$

The integration is carried out by using eqs. 10.10 a, b of the reference [b].

When the kinematical approximation is broken and the dynamical diffraction effect takes place, the following two results occur:

1) The locus of the amplitude-phase diagram is no longer circular.
2) The discrete change in the locus at the fault is not the same as the phase shift $\alpha = 2\pi\boldsymbol{g}\cdot\boldsymbol{R}$.

The result 1) is caused by the fact that ϕ_o and ϕ_g change with thickness while ϕ_o is constant for the kinematical approximation. The result 2) is caused by the presence of the first term in eq. (9) while this term does not exist in the case of kinematical approximation (eq. (6)). These results are seen in Fig. (b), which shows a non-circular locus and a phase jump different from $\alpha = (2/3)\pi$ at the fault (P).

References

[a] A. Howie and M.J. Whelan: *Proc. Roy. Soc.*, **A263** (1961) 217.

[b] P.B. Hirsch *et al.*: Electron Microscopy of Thin Crystals, 2nd ed., Krieger, Florida, 1977.

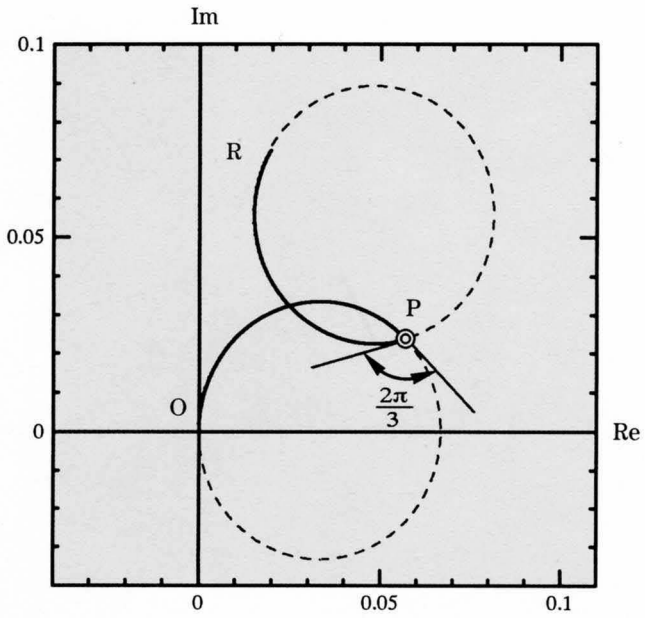

$t = 10\text{nm}$

$\xi_g = 200\text{nm}$

$w = 15$

$\alpha = \frac{2}{3}\pi$

(a)

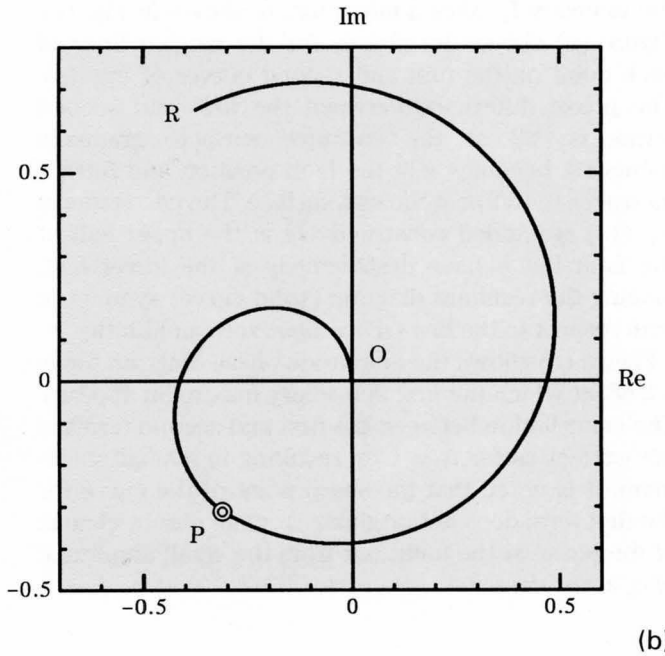

$t = 50\text{nm}$

$\xi_o = 20\text{nm}$

$\xi_g = 100\text{nm}$

$w = 2$

$\alpha = \frac{2}{3}\pi$

(b)

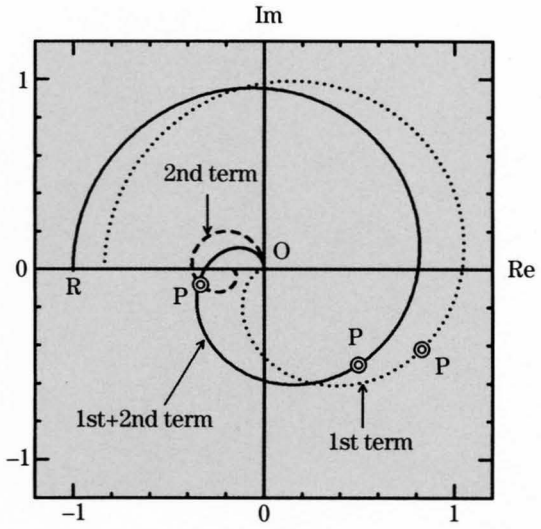

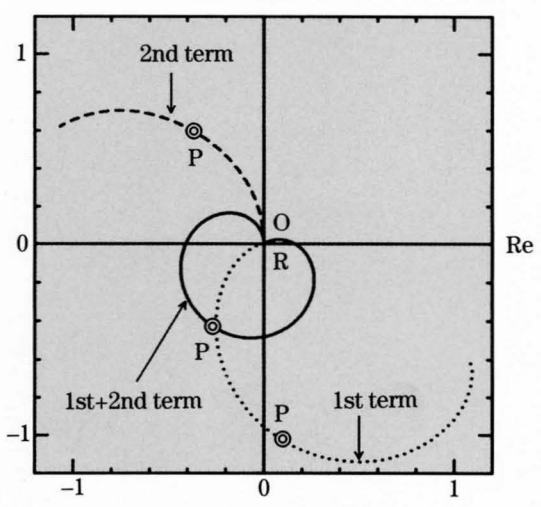

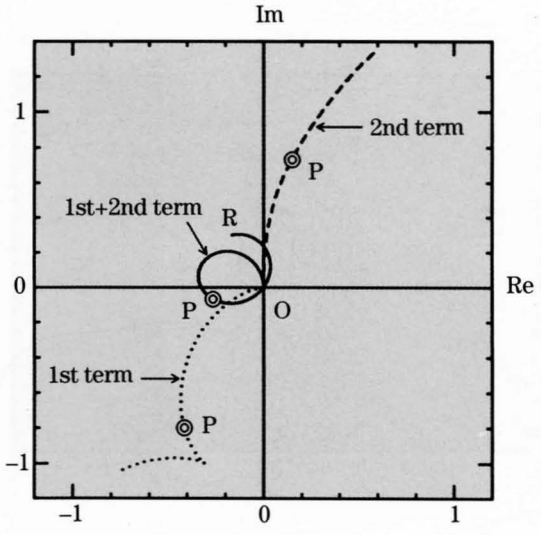

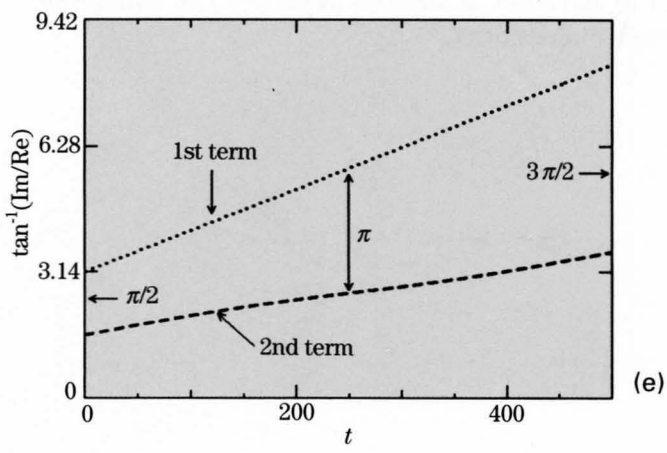

The figures show amplitude-phase diagrams for a specimen containing a stacking fault calculated by the two beam dynamical theory. The diagram starts from the top surface O, passes the fault at P and reaches the bottom surface R. The segment OR provides the resultant amplitude.

Phase shift $\alpha = \pi$

Figure (a) shows a rocking curve for $\alpha = \pi$. Figure (b) depicts an amplitude-phase diagram for $w = 0$. The resultant amplitude is symmetric about the line passing through O and P. The phase difference between the first and second terms at the upper half of the specimen stay at the same value of $\pi/2$. The second term undergoes a phase shift of π at the fault P, resulting in a phase difference of $(3/2)\pi$ between the two terms (Fig. (d)).

Figure (c) shows the amplitude-phase diagram for $w = 1.45$, at which the intensity I_g takes a maximum value. The second term shows a phase shift of π at the fault. The first and second terms are added destructively at the upper half of the specimen, but rather constructively at the lower half. As a result, the resultant curve at the lower half becomes large in amplitude and small in curvature. When the value of w deviates from 1.45, the constructive interference of the two terms in the lower half is not so effective as for $w = 1.45$, producing smaller intensities I_g.

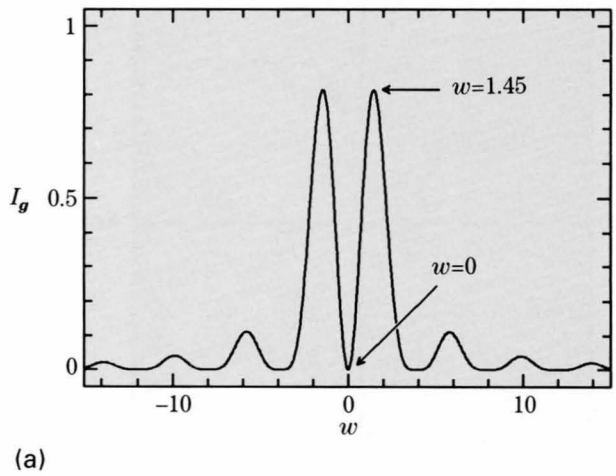

(a)

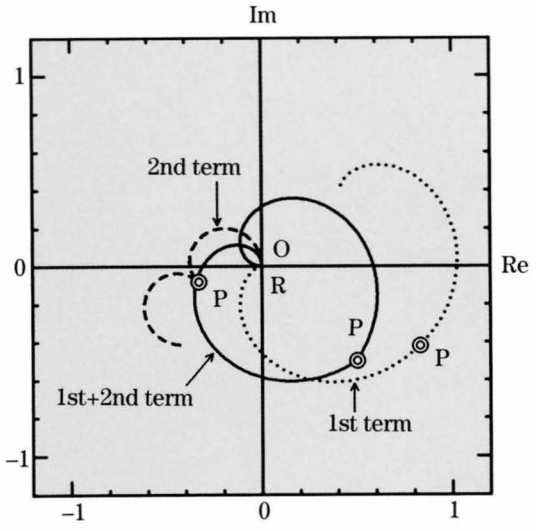
Im
w=0
1
0
−1
Re
2nd term
O
R
P
P
P
1st+2nd term
1st term
−1
0
1
(b)

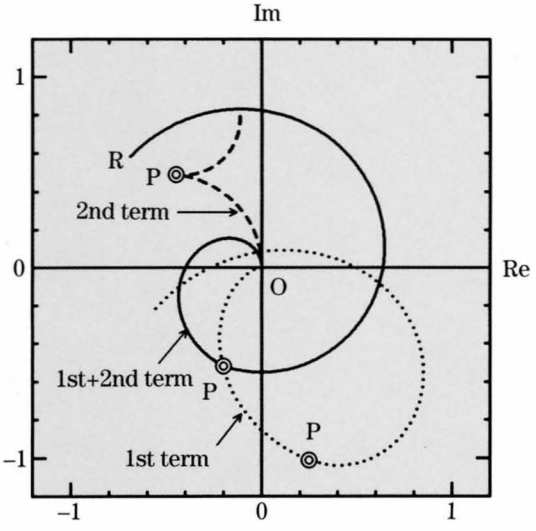
Im
w=1.45
1
0
−1
Re
R
P
2nd term
O
1st+2nd term
P
P
1st term
−1
0
1
(c)

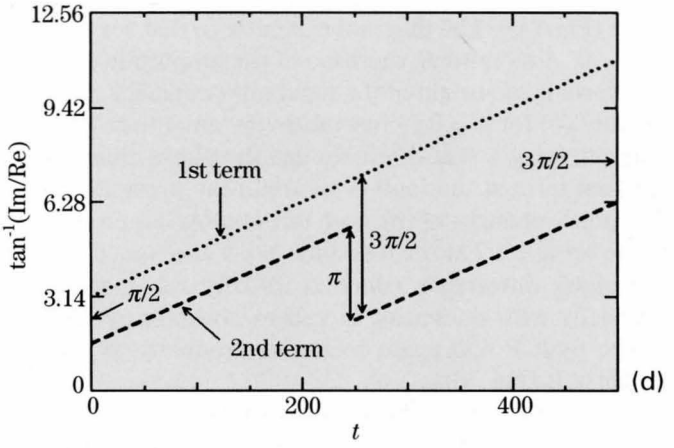
12.56
9.42
6.28
3.14
0
tan⁻¹(Im/Re)
1st term
3π/2
3π/2
π
π/2
2nd term
0
200
400
t
(d)

Phase shift $\alpha=2\pi/3$

Figure (b) shows the amplitude-phase diagram for w = –0.99, at which the intensity I_g takes the principal maximum (Fig. (a)). The diagram is similar to that for w = 0 at α = 0. A monotonic increase of the amplitude of the first term is the origin of the maximum intensity.

Figure (c) for w = 0.54 resembles the amplitude-phase diagram for w = 0 at $\alpha = \pi$, though the phase change in the first term at the fault is $(2/3)\pi$ in the present case. The phase changes of the both terms show a mixture of those for w = 1.7 at α = 0 and for w = 0 at $\alpha = \pi$. That is, the phase difference, which is initially $\pi/2$, increases gradually with thickness, increases abruptly by $(2/3)\pi$ at the fault P and again increases gradually to reach $(3/2)\pi$ at R (Fig. (e)).

Figure (d) for w = 1.86 is similar to the diagram for w = 1.45 at $\alpha = \pi$. A similar interpretation for the latter diagram holds for the present case.

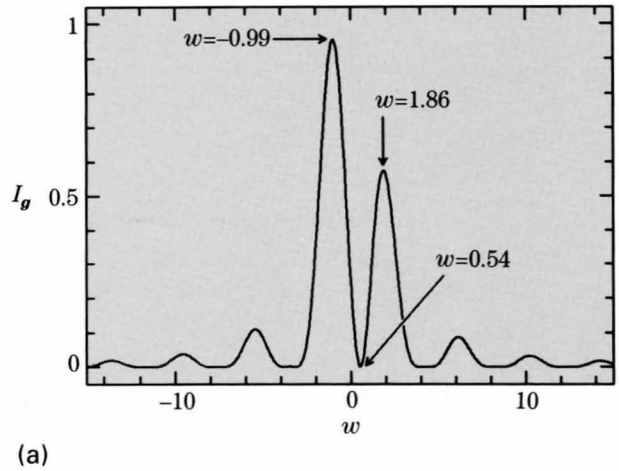

(a)

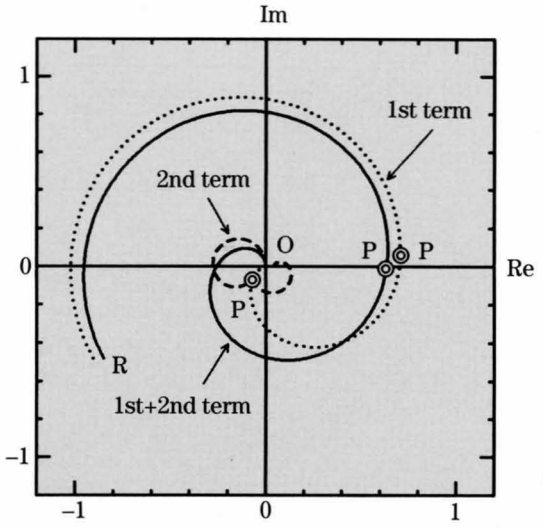

w=−0.99

(b)

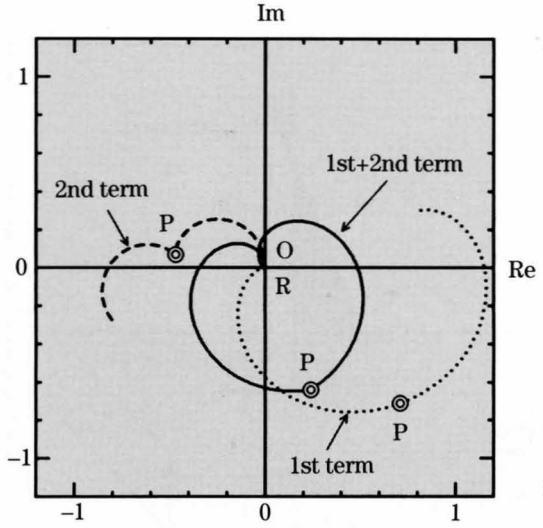

w=0.54

(c)

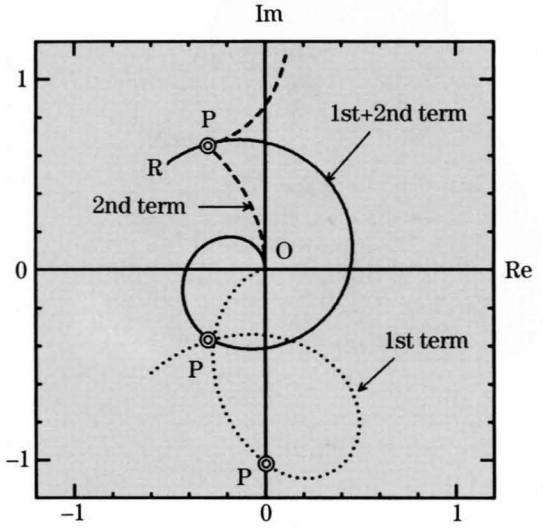

w=1.86

(d)

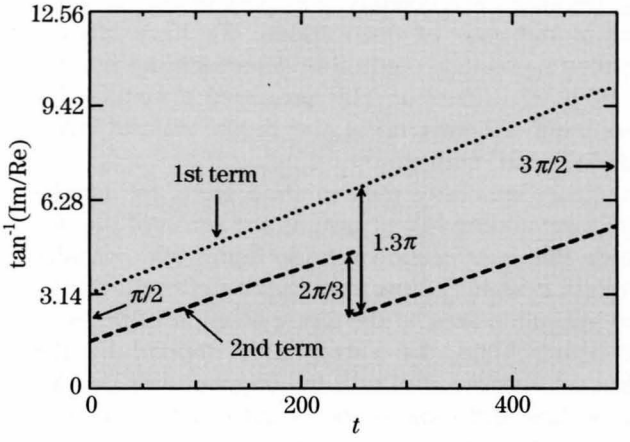

(e)

Dislocations

Defocus illumination allows observing the whole strained area and identifying the Burgers vector of a dislocation. The LACBED pattern gives the intensity profile of a reflection as a function of the distance x from a dislocation and of the excitation error w. The method given by Cherns and Preston [a] uses information obtained not only at $\boldsymbol{g}\cdot\boldsymbol{b} = 0$ but also at $\boldsymbol{g}\cdot\boldsymbol{b} = n$ ($n \neq 0$) for the determination of the Burgers vector $\boldsymbol{b}$, while information obtained at $\boldsymbol{g}\cdot\boldsymbol{b} \neq 0$ has been discarded in the traditional electron-microscope-image method except in a few reports.

The LACBED pattern shows n nodes at the crossing region between a dislocation line and a reflection line when $\boldsymbol{g}\cdot\boldsymbol{b} = n$. When the relative sign of $\boldsymbol{g}\cdot\boldsymbol{b}$ is correctly determined, the Burgers vector is identified using three linearly independent reflections. It should be noted that these three reflections are sufficient to determine the Burgers vector in contrast to the case of stacking faults because the ambiguity of a phase of $2n\pi$ does not occur in the case of dislocations. We have already described a practical method to determine the relative sign of n [4]. Niu *et al.* [12] proposed a method for determining the sign using the finish to start/right-handed (FS/RH) convention.

The figure illustrates their method. Here, we use the FS/RH convention. Let us assume the sense of the dislocation line $\boldsymbol{u}$ as is shown in the figure. We consider the vector $\boldsymbol{c}$, which points from the center of the illuminated specimen area to the focus position of the incident beam. Thus, the vector $\boldsymbol{v}$ is defined by the equation $\boldsymbol{v} = \boldsymbol{u}\times\boldsymbol{c}$. Let us take the origin of $\boldsymbol{v}$ on the dislocation line and look at the positive side of $\boldsymbol{v}$ with respect to the dislocation line. If the sense of the bend of a reflection line at the positive side of $\boldsymbol{v}$ is the same as the sense of the reflection vector $\boldsymbol{g}$ as shown in the figure, the sign of $n = \boldsymbol{g}\cdot\boldsymbol{b}$ is negative and vice versa. In this figure, n is determined to be –1. If we use the SF/RH convention, then the sign becomes opposite.

The type of a dislocation can be precisely identified from the Burgers vector determined and the orientation of the dislocation line. Wen *et al.* [13], however, reported that the type of a dislocation can be easily determined by examining zone-axis LACBED patterns. Several examples of such patterns are given in the present volume.

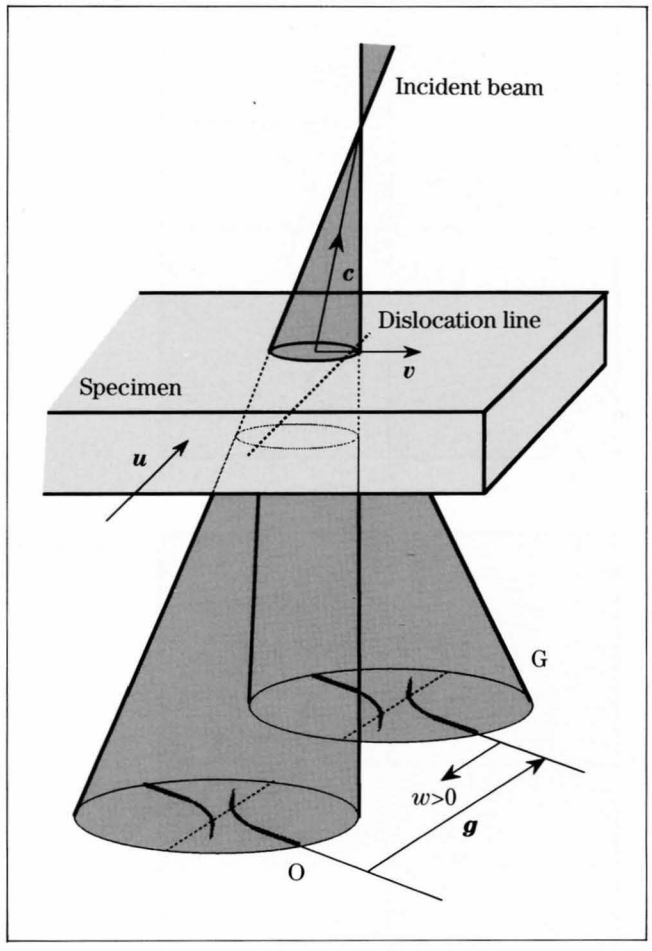

Reference

[a] D. Cherns and A.R. Preston: Proc. XI Int. Congr. on Electron Microsc., Kyoto, 1986. p.721.

Silicon

Burgers vector determination

200kV

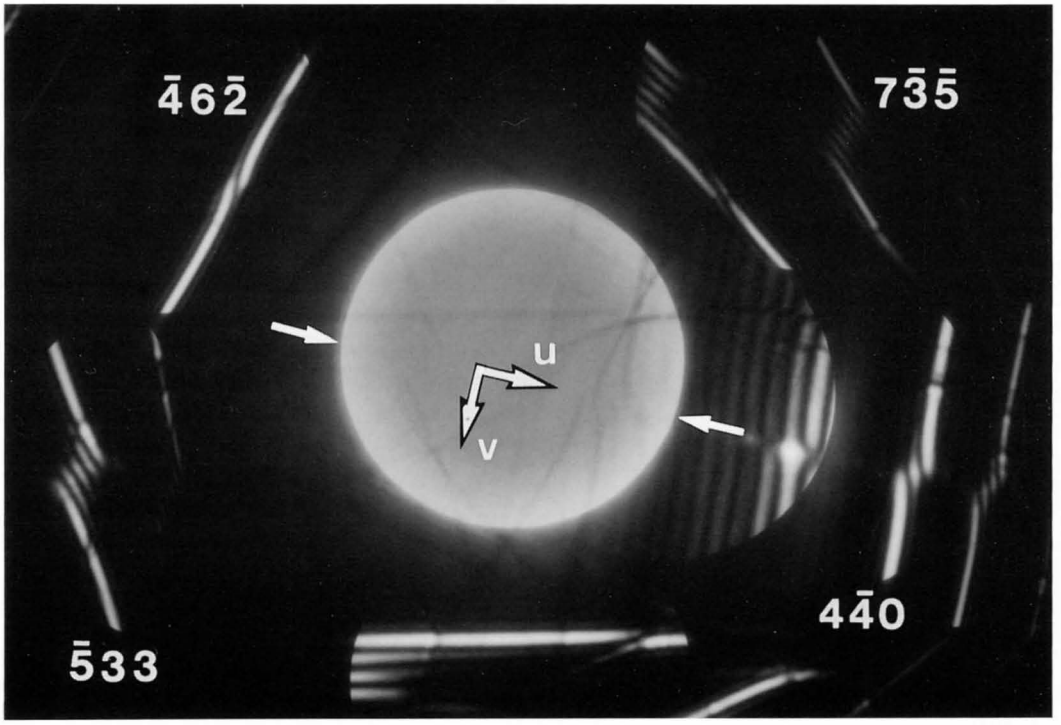

$$\begin{aligned} 4u - 4v &= +2 \\ -5u + 3v + 3w &= -4 \\ -4u + 6v - 2w &= -1 \end{aligned}$$

For Burgers vector determination, it is not necessary to set a crystal at a particular zone axis, but at an orientation so that three linearly independent reflections are excited.

Photograph shows a defocus CBED pattern of Si taken from an area containing a dislocation at such a setting. The position of the dislocation line is indicated by the arrows. Let us write the Burgers vector $\boldsymbol{b} = [uvw]$. The $4\bar{4}0$, $\bar{5}33$ and $\bar{4}6\bar{2}$ reflections give values of $n = +2$, -4 and -1, respectively. By solving the linear system of equations, the Burgers vector was determined to be $\boldsymbol{b} = (1/2)[10\bar{1}]$. From the Burgers vector obtained, the $7\bar{3}\bar{5}$ reflection is expected to have a value $n = \boldsymbol{g}\cdot\boldsymbol{b} = (1/2)(7+5) = +6$. It is seen that the $7\bar{3}\bar{5}$ reflection in the photo shows six nodes as predicted.

The dislocation of Si was assumed to be a perfect dislocation because of a small separation between the two extended partial dislocations. The effect of the dissociation can be examined using a reflection satisfying $\boldsymbol{g}\cdot\boldsymbol{b} = 0$ [4].

LACBED patterns

Figures (a) and (b) show schematical LACBED patterns from an edge dislocation and a screw dislocation, respectively [13]. Owing to the characteristic lattice distortion caused by the two types of dislocations, the LACBED patterns show compression or elongation for the edge type and shear deformation for the screw type.

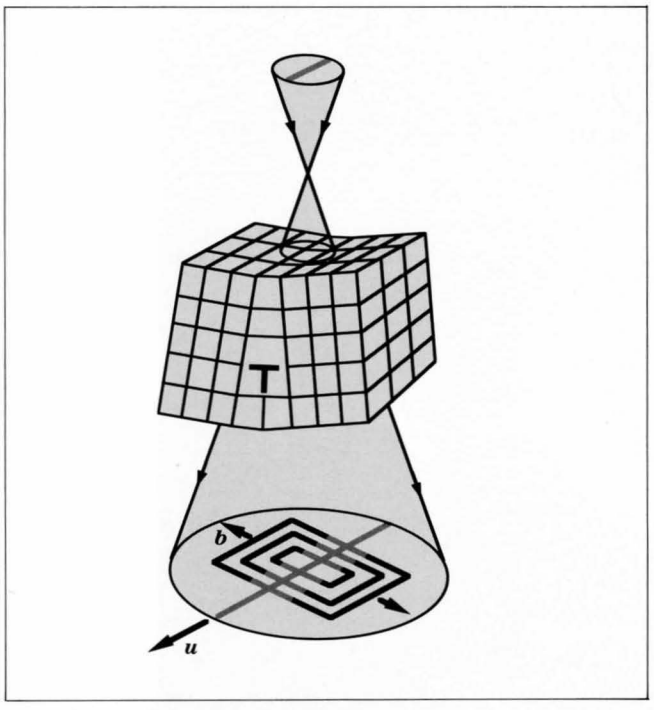

(a) Edge dislocation

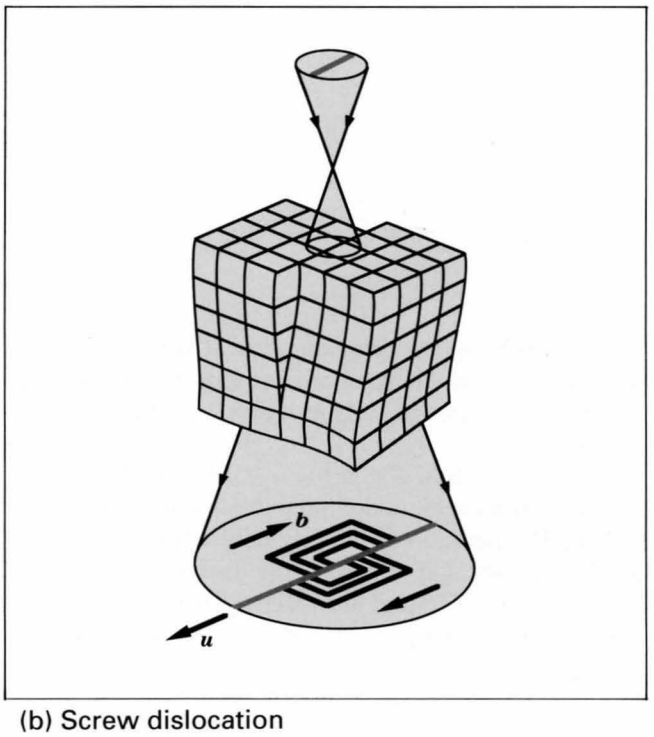

(b) Screw dislocation

Si [111]

Edge dislocation **180kV**

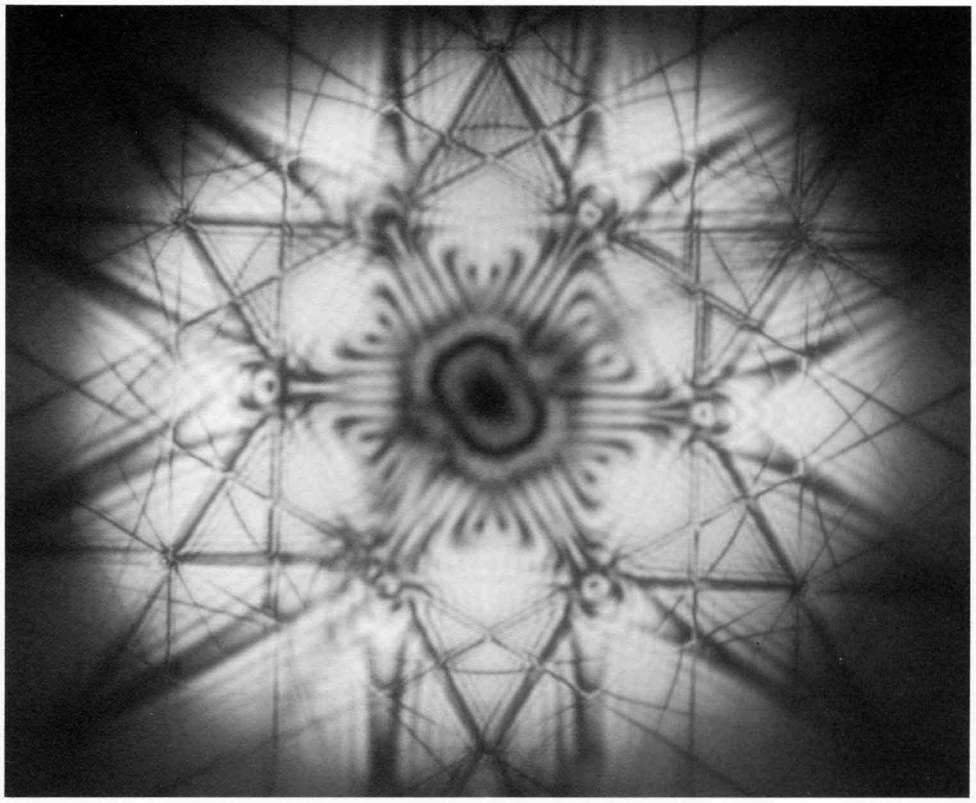

Screw dislocation

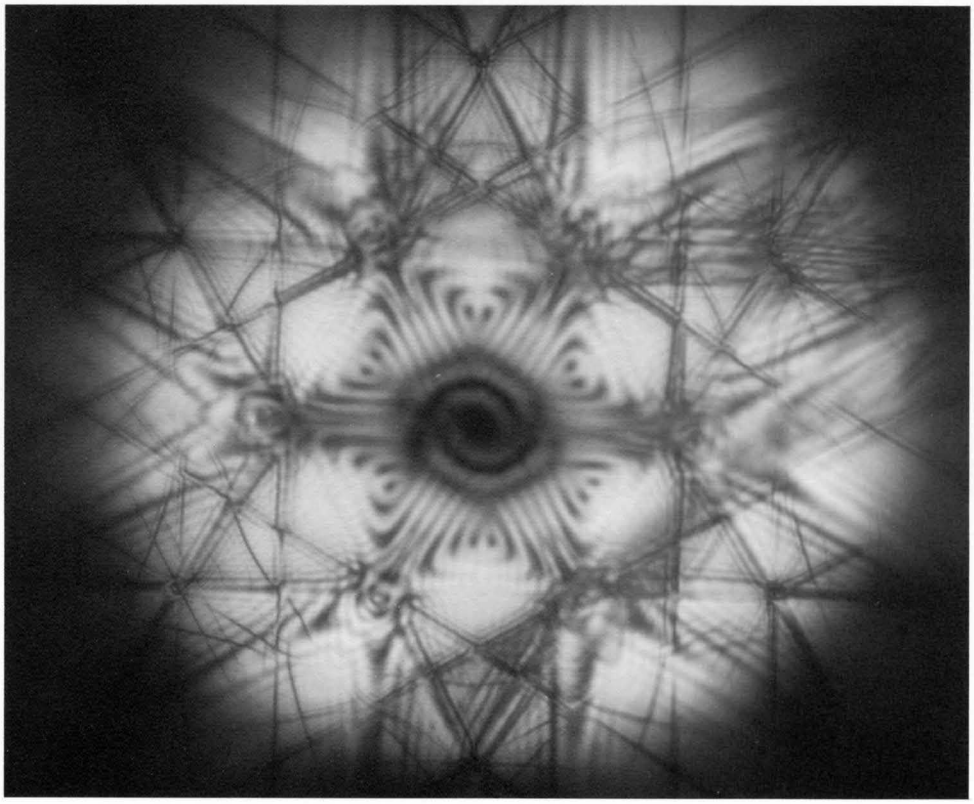

Si [111]

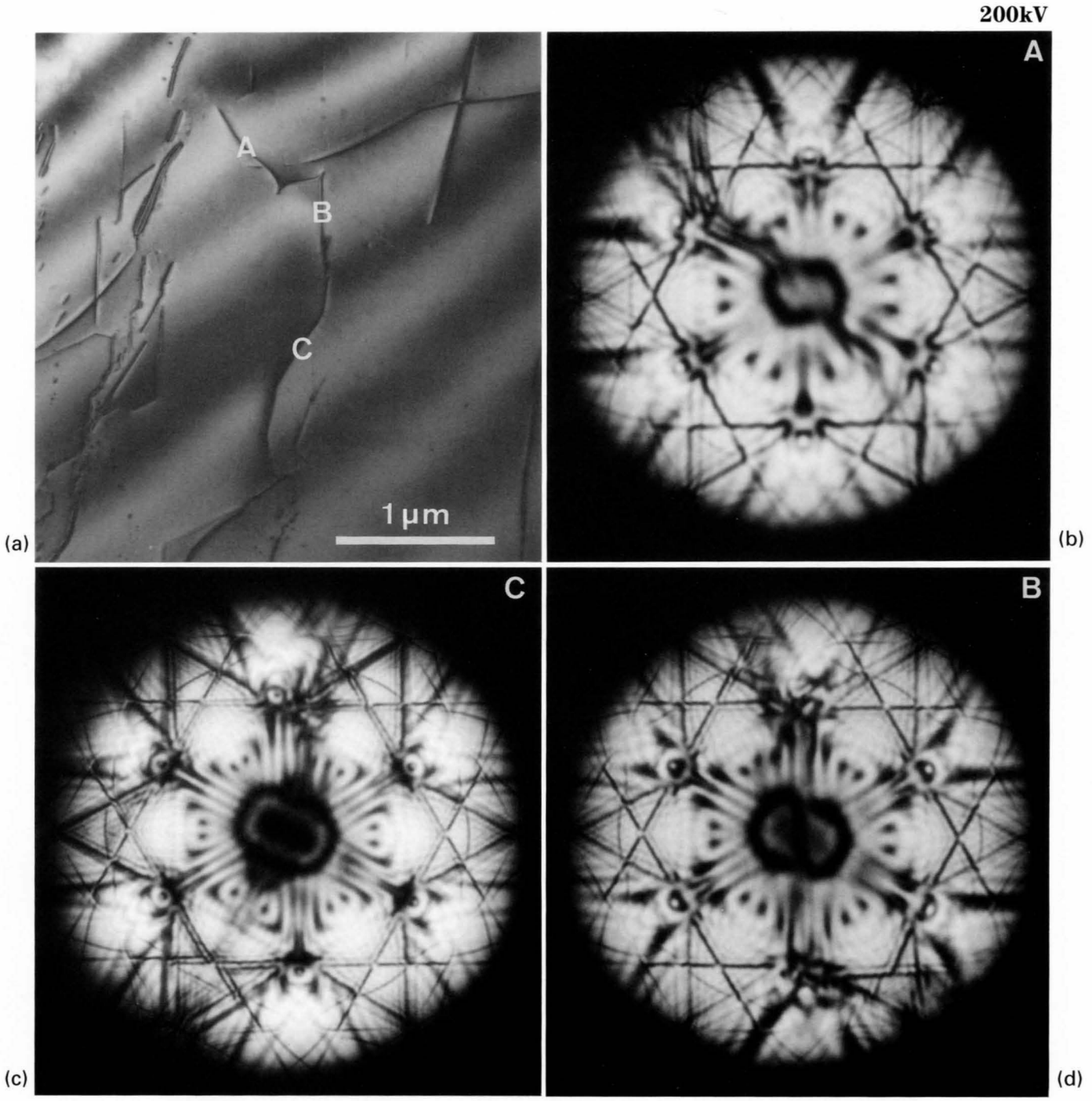

LACBED patterns (b), (c) and (d) taken respectively from dislocations A, C and B in Photo (a) ; Pattern (b) is of the pure screw type, (c) pure edge type and (d) mixed type.

Graphite

Graphite [0001]

200kV

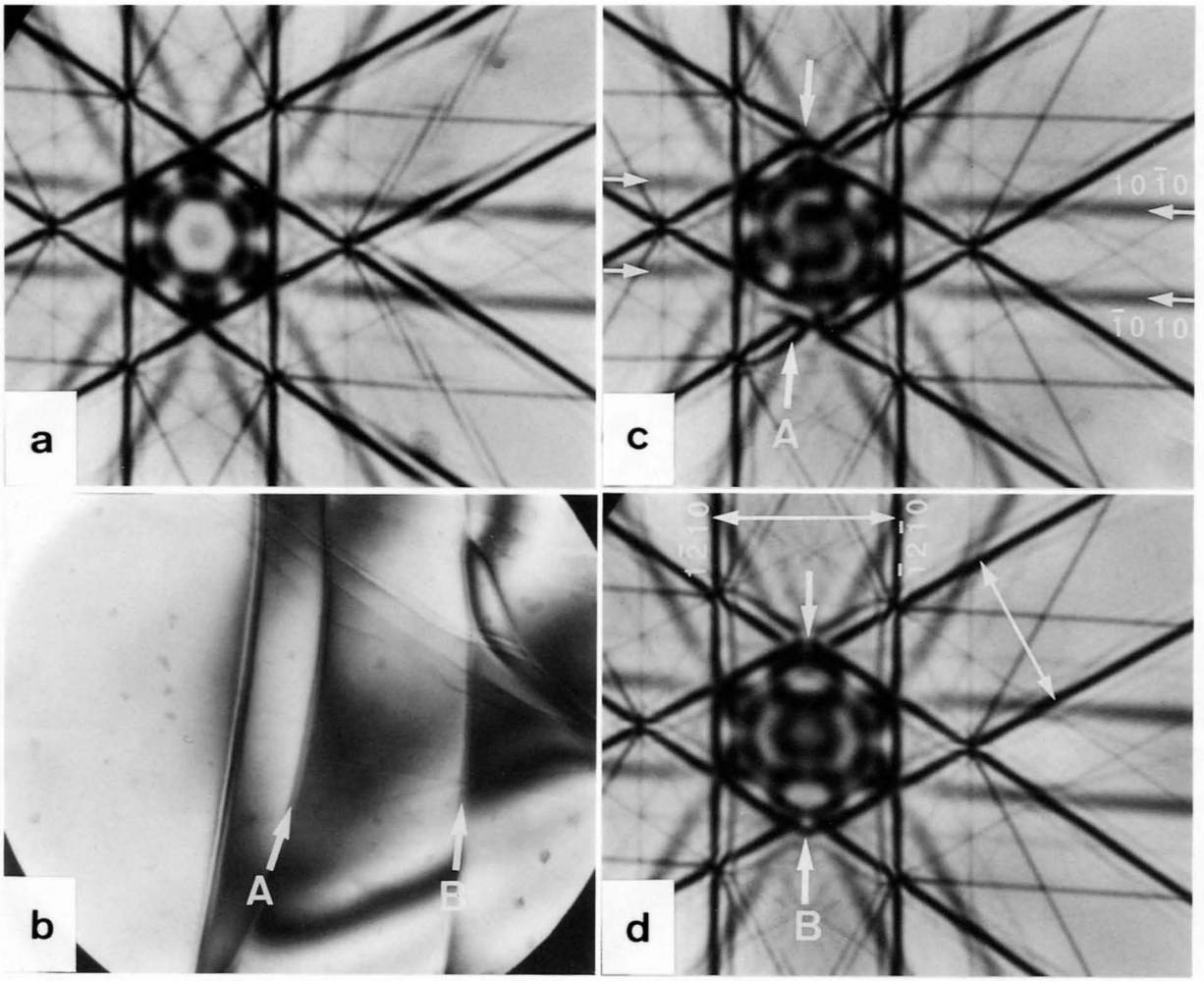

Photograph (a) is an LACBED pattern of graphite taken by setting a perfect area between dislocations A and B of Photo (b) to satisfy the [0001] zone-axis incidence. Photographs (c) and (d) are LACBED patterns taken by setting respectively dislocation lines A and B to satisfy the zone-axis incidence. Photograph (a) shows a hexagonal pattern about the [0001] zone axis, though it is slightly deformed due to a bend of the specimen.

Photograph (c) shows a shear deformation of the hexagon at dislocation A. A pair of $10\bar{1}0$ and $\bar{1}010$ lines indicated by the arrows also shows a vertical shift at the dislocation. These results indicate that the dislocation is of the screw type.

Photograph (d) shows that two halves of the hexagon recede horizontally from each other at dislocation B or the hexagon elongates horizontally. The distance between the $1\bar{2}10$ and $\bar{1}2\bar{1}0$ lines running vertically is larger than those between other equivalent pairs. These two facts indicate the dislocation to be of the edge type.

Graphite [0001]

160kV

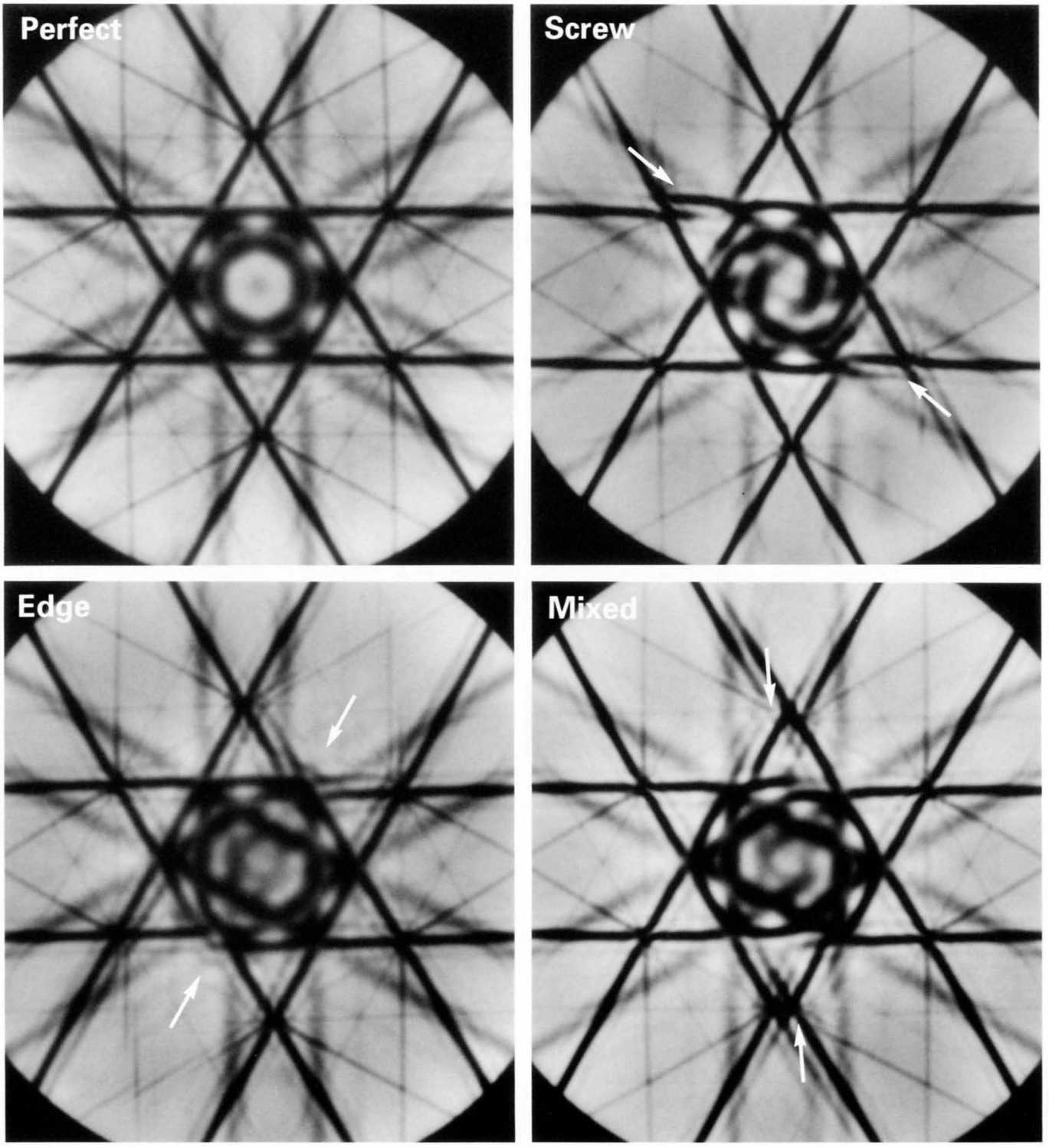

Graphite [0001] — edge dislocation —

160kV

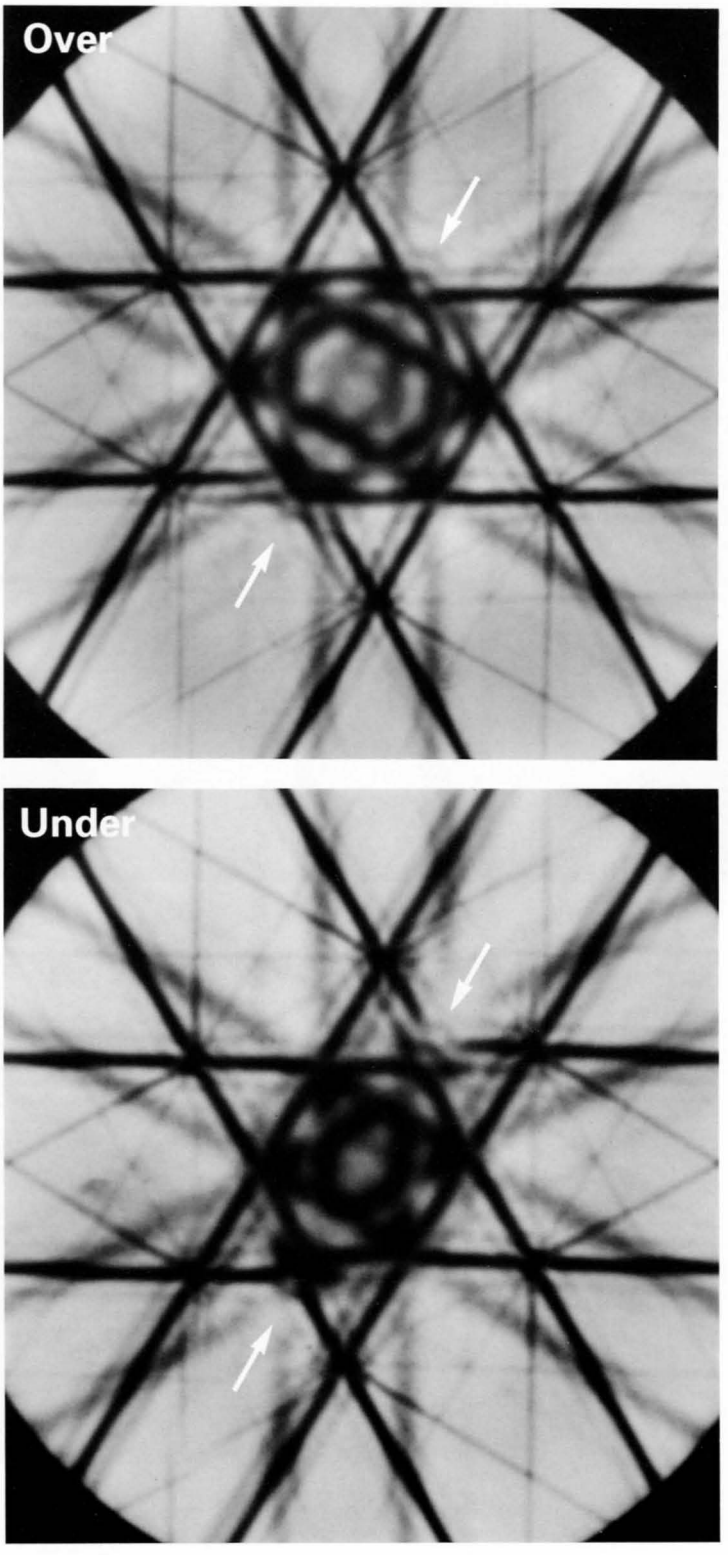

Photographs (a) and (b) were taken from an edge dislocation at an over focus (a) and an under focus (b). It is noted that the hexagonal pattern is elongated in Photo (a) but compressed in Photo (b).

Graphite [0001] — dislocation network —

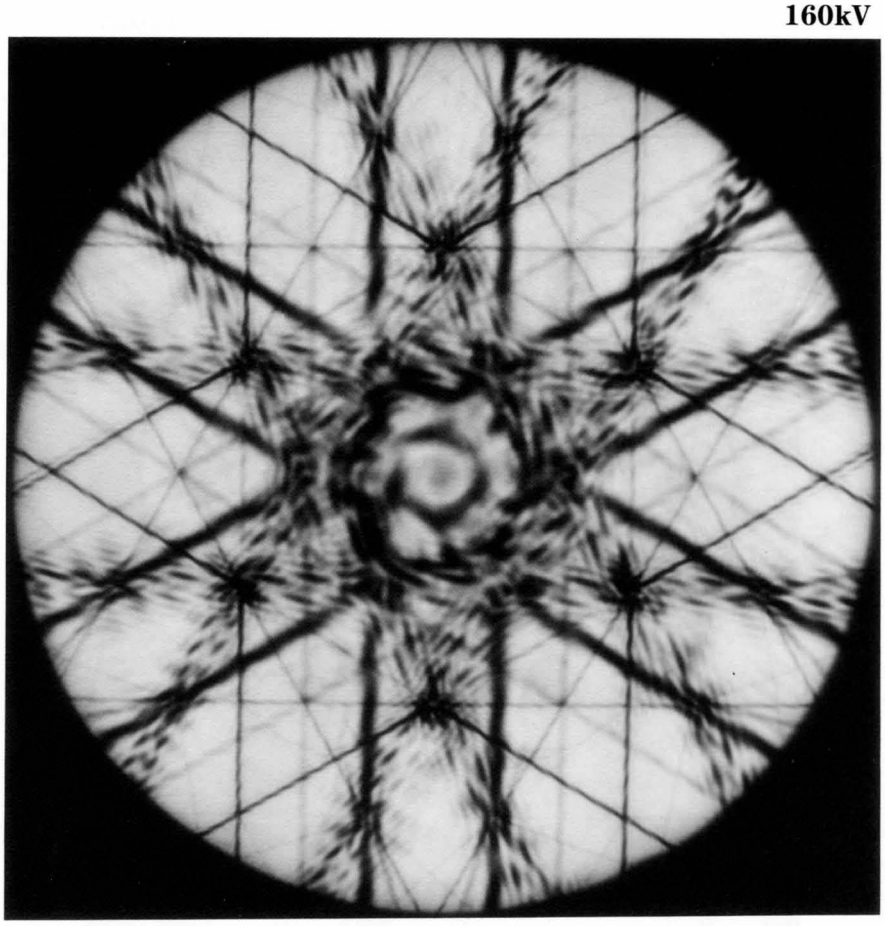

LACBED pattern (a) of a dislocation network of graphite (b).

Graphite (edge dislocation) — specimen orientation change —

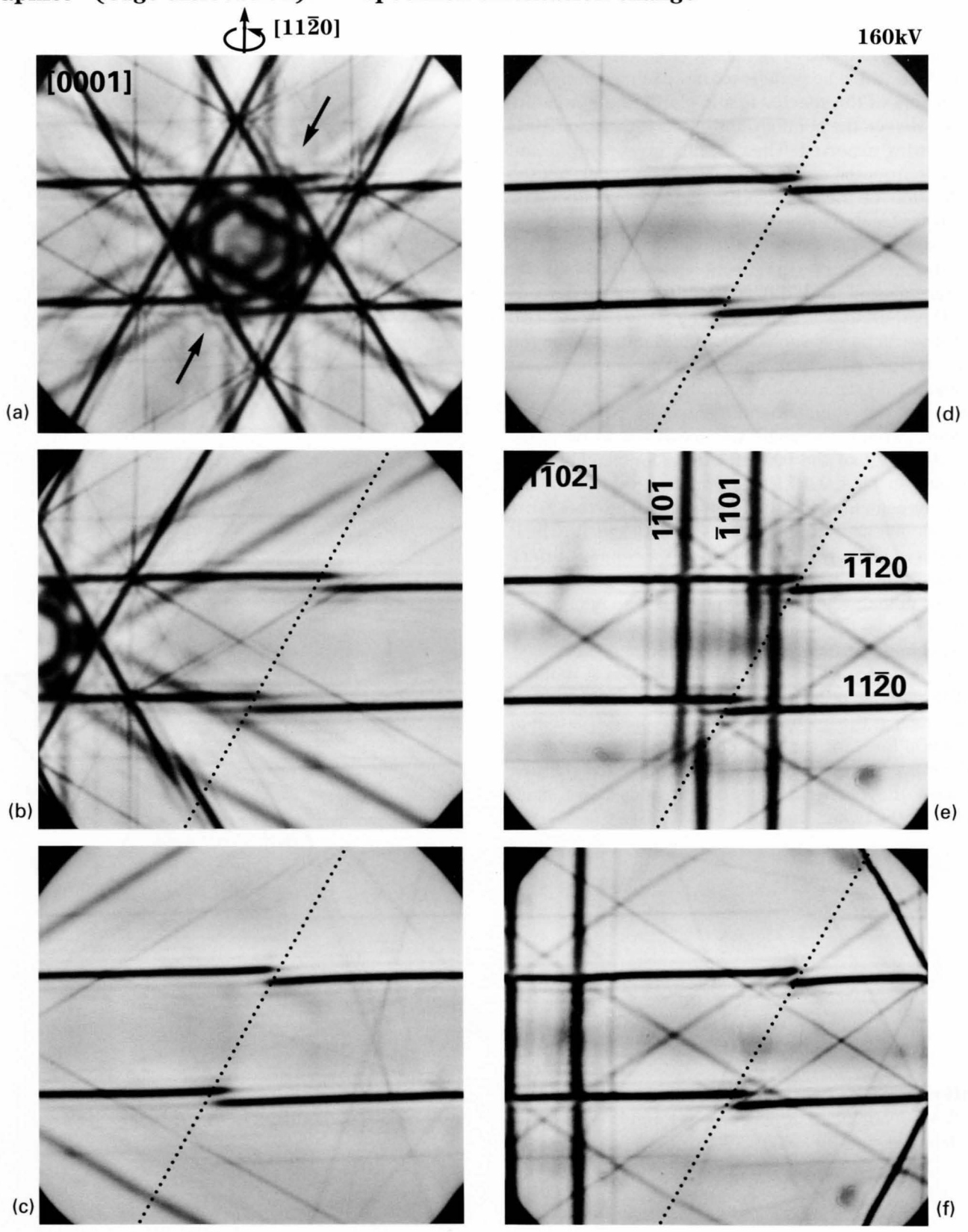

A series of LACBED patterns of an edge dislocation taken by tilting the specimen around the [11$\bar{2}$0] axis from the [0001] zone axis to the [1$\bar{1}$02] (e). Dotted lines indicate the position of the dislocation line.

Twin Boundaries

The CBED study of coherent twin boundaries (CTBs) was first carried out by Schapink *et al.* [a]. They dealt with CTBs which lie parallel to the specimen surface in the middle of the specimen, and clarified the relationships between the point groups of bicrystals and CBED symmetries expected. Their results are beautiful and valuable from the crystallographical viewpoint, but the application of their method is limited only to CTBs which are located in the middle of the specimen.

We studied CTBs inclined to the specimen surface and observed a split of a reflection line at the boundary in transmission and diffraction disks of a defocus CBED pattern. It was found that the angle between two domains can be measured with high accuracy from the split of the reflection line. Tanaka, Terauchi and Kaneyama [9] reported an example of precise determination of the rhombohedral angle of NiO using a twinned crystal. The angle was measured to be 90.07° from the shift of the $00l$ reflections for neighbouring domains in an LACBED pattern, this value showing good agreement with that determined by the X-ray method. We show here defocus CBED and LACBED patterns of CTBs lying oblique to the specimen surface and describe the method to measure the angle between the two domains adjoining at the CTB. The figure illustrates defocus illumination for a CTB lying oblique to the specimen surface and the reflection expected.

The photograph on the opposite page is a defocus CBED pattern of a twin boundary of $BaTiO_3$. Two reflections at the upper part show a typical splitting of reflection lines for the twin boundary. The systematic reflections in the lower part exhibit no splitting because the corresponding lattice planes are unaffected by the twin.

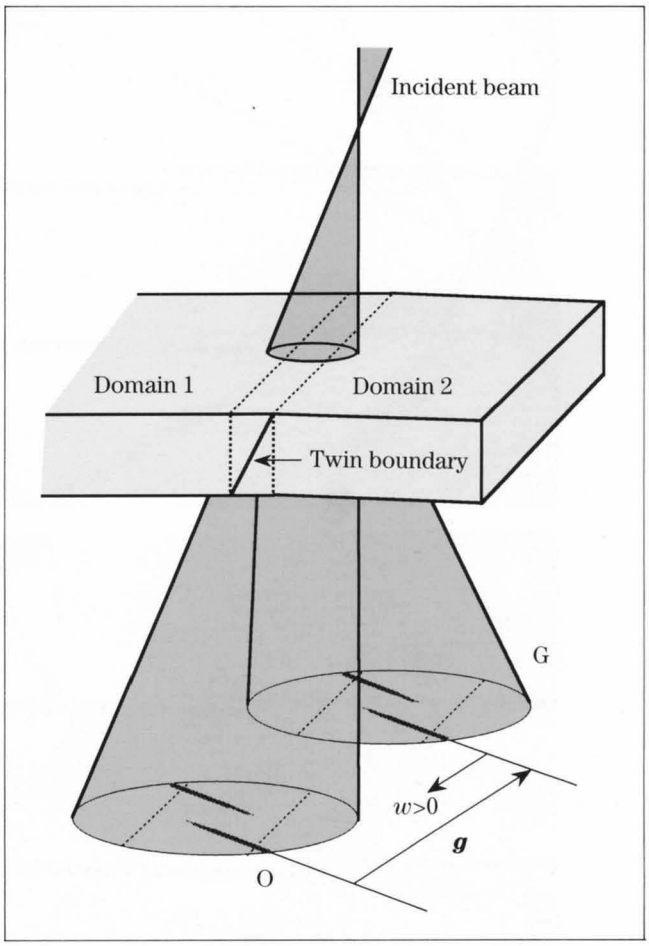

Reference

[a] F. W. Schapink, S. K. E. Forghany and B. F. Buxton: *Acta Cryst.*, **A39** (1983) 805.

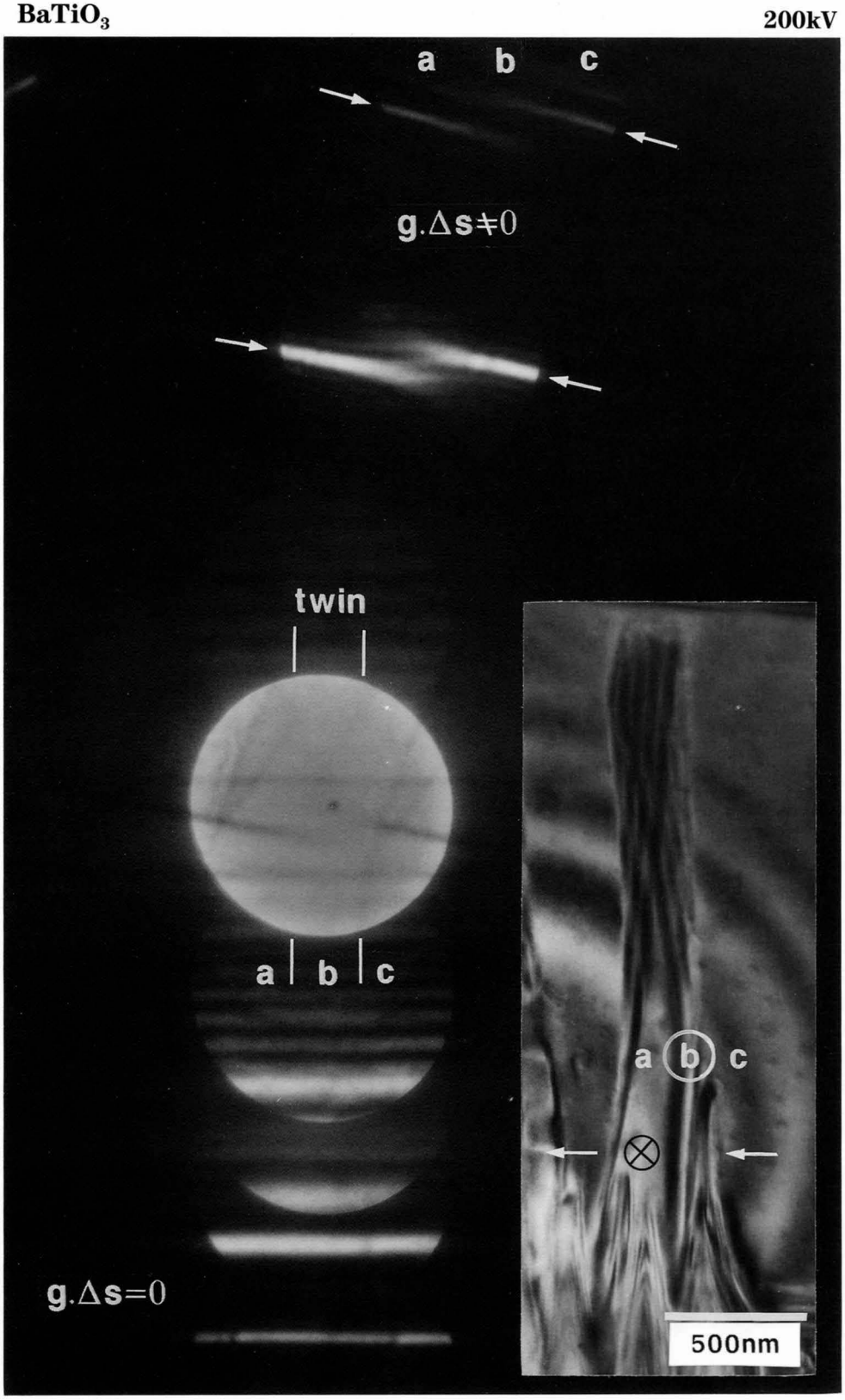
BaTiO3
200kV
a b c
g.Δs≠0
twin
a b c
g.Δs=0
a b c
500nm

Theoretical

CBED patterns from a twin boundary

Figure (a) shows diffraction vectors $\boldsymbol{g}$ and $\boldsymbol{g}'$ for two domains adjoining at a CTB. The difference $\Delta\boldsymbol{g} = \boldsymbol{g}' - \boldsymbol{g}$ is divided into three components: $\Delta\boldsymbol{g}_z$, the component parallel to the incident beam; $\Delta\boldsymbol{g}_r$, the radial component; and $\Delta\boldsymbol{g}_\phi$, the azimuthal component perpendicular to the incident beam. Defocus CBED patterns expected from the three components $\Delta\boldsymbol{g}_z$, $\Delta\boldsymbol{g}_r$ and $\Delta\boldsymbol{g}_\phi$ are schematically shown in Figs. (b), (c) and (d), respectively.

The difference $\Delta\boldsymbol{g}_z$ between $\boldsymbol{g}$ and $\boldsymbol{g}'$ (Fig. (b)) causes no difference in the magnitudes of both vectors, $|\boldsymbol{g}| = |\boldsymbol{g}'|$. Since the Bragg angles for the two reflections are the same, the two CBED disks are formed at the same position. However, the paired reflection lines at O and G′ are shifted from those at O and G by parallel translation according to the difference in the orientation between $\boldsymbol{g}$ and $\boldsymbol{g}'$, the angle between the two paired lines being $|\Delta\boldsymbol{g}_z|/|\boldsymbol{g}| = |\Delta\boldsymbol{g}_z| \cdot d$, d being the lattice spacing. $\Delta\boldsymbol{g}_z$ produces the split of a reflection line without the splitting of the reflection disk G. Since the angle is independent of the order of the reflection, the splittings of the two reflection lines are the same for the different order reflections.

The difference $\Delta\boldsymbol{g}_r$ (Fig. (c)) causes $|\boldsymbol{g}| \neq |\boldsymbol{g}'|$ and different Bragg angles for the two reflections G and G′. Thus, the reflection disks are separated by $|\Delta\boldsymbol{g}_r| \cdot \lambda$ along the direction $\boldsymbol{g}$, the quantity being derived from Bragg's law, where λ is the wavelength of the incident beam. Owing to the different Bragg angles, the distance between the paired reflection lines at O and G is different from that between the paired lines at O and G′. Therefore, $\Delta\boldsymbol{g}_r$ gives a split of reflection lines different from that for $\Delta\boldsymbol{g}_z$, and a split of reflection disks.

The difference $\Delta\boldsymbol{g}_\phi$ (Fig. (d)) produces an angular difference between the diffraction disks G and G′ with respect to the center of the disk O. The angle ϕ is given by $|\Delta\boldsymbol{g}_\phi|/|\boldsymbol{g}| = |\Delta\boldsymbol{g}_\phi| \cdot d$. The two reflection lines also make the angle ϕ.

The amounts of these splittings of the reflection lines and reflection disks are summarized in the table on the opposite page.

In general, patterns observed are explained by the superposition of these three effects. We consider a CTB intersecting the specimen surface at 45°, where $\Delta\boldsymbol{g}_z = \Delta\boldsymbol{g}_r$. The ratio between the splittings due to $\Delta\boldsymbol{g}_z$ and $\Delta\boldsymbol{g}_r$ is $d/(\lambda/2)$, resulting in 80 for d = 2nm and an accelerating voltage of 200kV. This implies that the use of the splitting of a reflection line due to $\Delta\boldsymbol{g}_z$ allows accurate determination of the angular difference between two domains.

We have thus far considered only twin boundaries. The high sensitivity of CBED to $\Delta\boldsymbol{g}_z$, however, enables precise measurement of the distances parallel to the incident beam direction in the reciprocal space. The measurement of small changes in lattice parameters of multilayer semiconductors is a good application to be conducted.

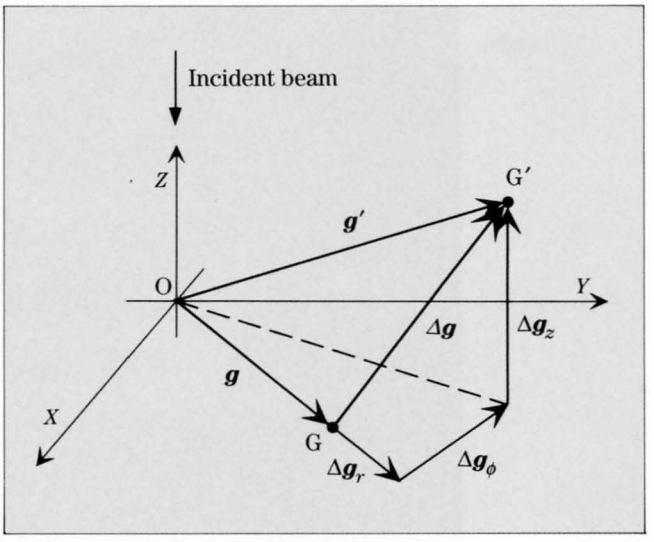

(a)

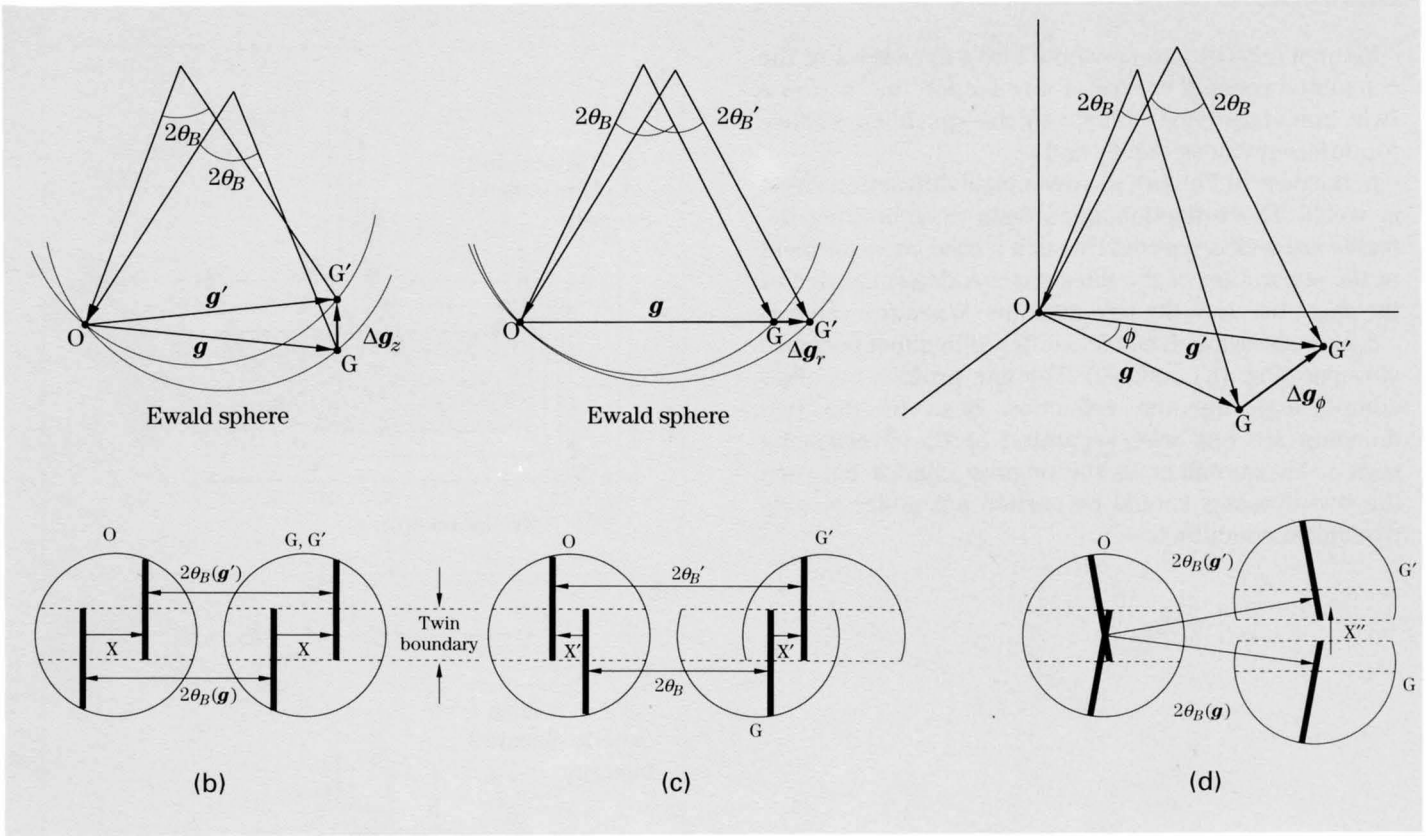

	Splitting of a reflection line	Separation of CBED disks
X ($\Delta \boldsymbol{g}_z$)	$\lvert\Delta \boldsymbol{g}_z\rvert \cdot d$	—
X′ ($\Delta \boldsymbol{g}_r$)	$\lvert\Delta \boldsymbol{g}_r\rvert \cdot \lambda/2$	$\lvert\Delta \boldsymbol{g}_r\rvert \cdot \lambda$
X″ ($\Delta \boldsymbol{g}_\phi$)	—	$\lvert\Delta \boldsymbol{g}_\phi\rvert \cdot \lambda$

Simulations

Figures (a), (b) and (c) show bird's-eye views of the calculated rocking curves of a reflection line across a twin boundary lying oblique to the specimen surface for different values of t/ξ_g and w.

In the case of Fig. (a), the dynamical diffraction effect is weak. The reflection lines from neighbouring domains are well separated. In such a case, measurement of the separation of the lines enables determination of the angle between the two domains. When the value of t/ξ_g increases, the dynamical diffraction effect becomes stronger (Fig. (b) and (c)). The line profiles becomes complicated and the reflection lines of the two domains are not well separated at the overlapping region. Measurement of the angular change between the two domains should be carried out under weakly dynamical conditions.

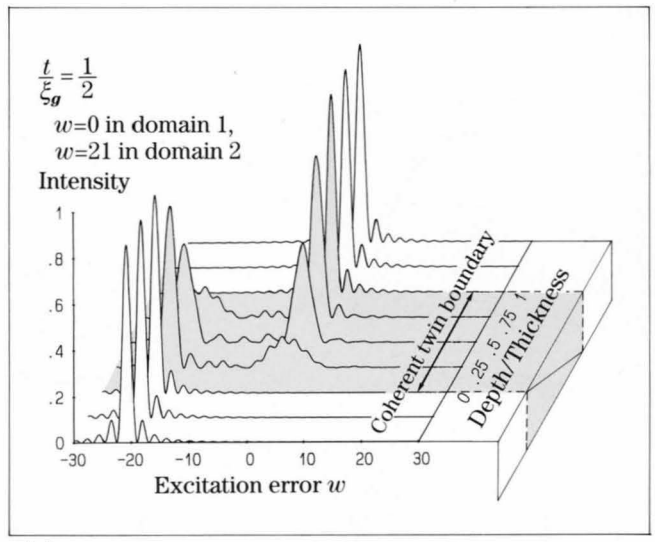

(a)

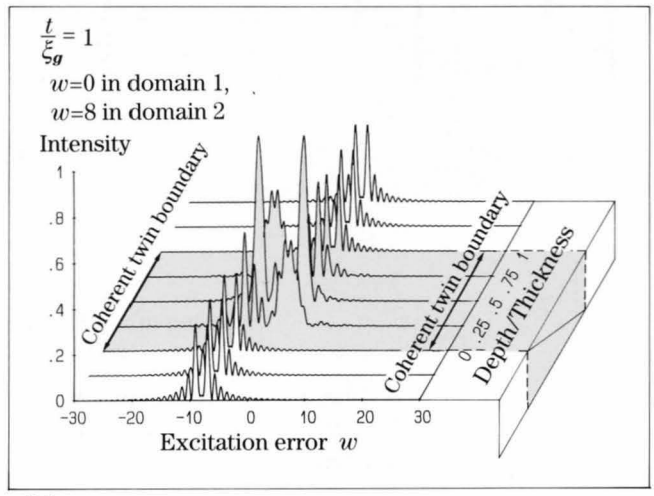

(b)

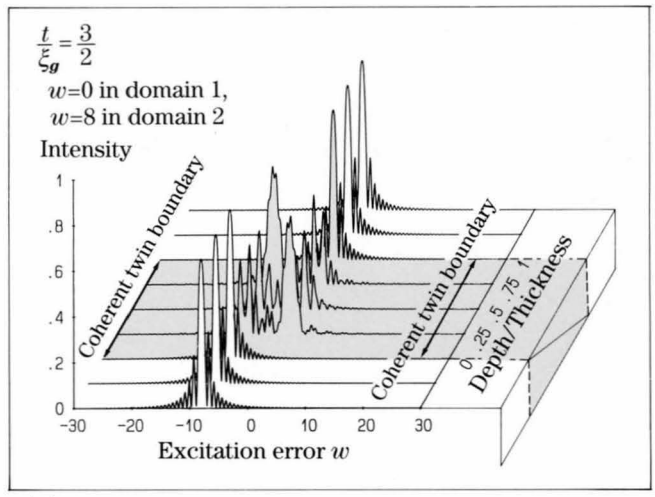

(c)

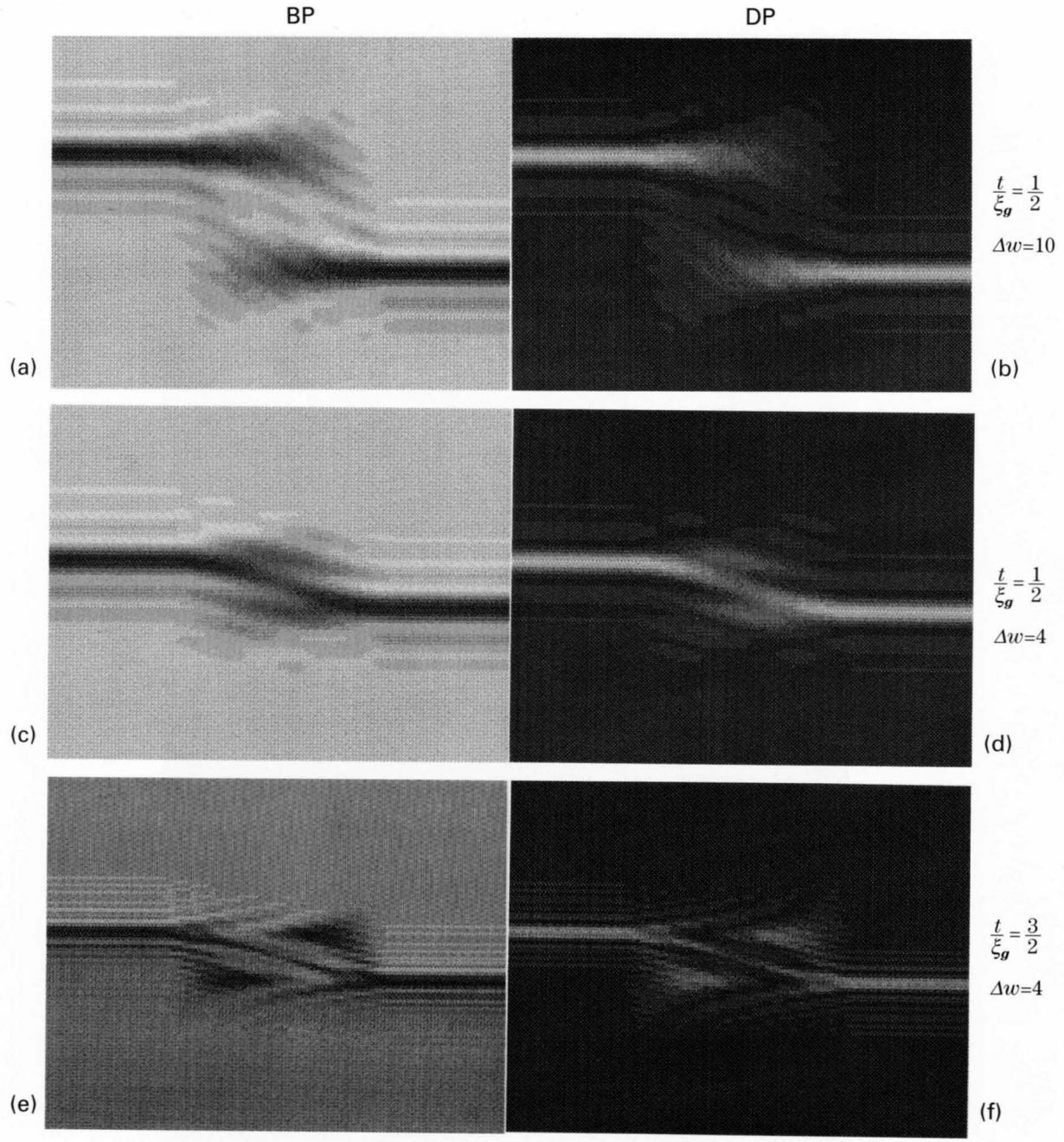

Figures on this page provide another way of presenting simulated LACBED patterns. Figures (a) and (b) show simulations of bright-field and dark-field LACBED patterns obtained from an area containing a CTB, for $t/\xi_g = 1/2$, $\Delta w = \xi_g \cdot |\Delta \boldsymbol{g}_z| = 10$ and $\xi_g/\xi_g' = 1/20$. The left and right reflection lines, which originated from domain 1 and domain 2, respectively, are well separated. The lines become weaker and broader at the overlapping region of the two domains due to the decrease of thickness of the corresponding domain.

Figures (c) and (d) show those patterns for $t/\xi_g = 1/2$ and $\Delta w = 4$. Since the misorientation between the two domains is small, the two reflection lines appear to connect continuously at the overlapping region.

Figures, (e) and (f) show those patterns for $t/\xi_g = 3/2$ and $\Delta w = 4$. A strong dynamical diffraction effect is noted.

NiO

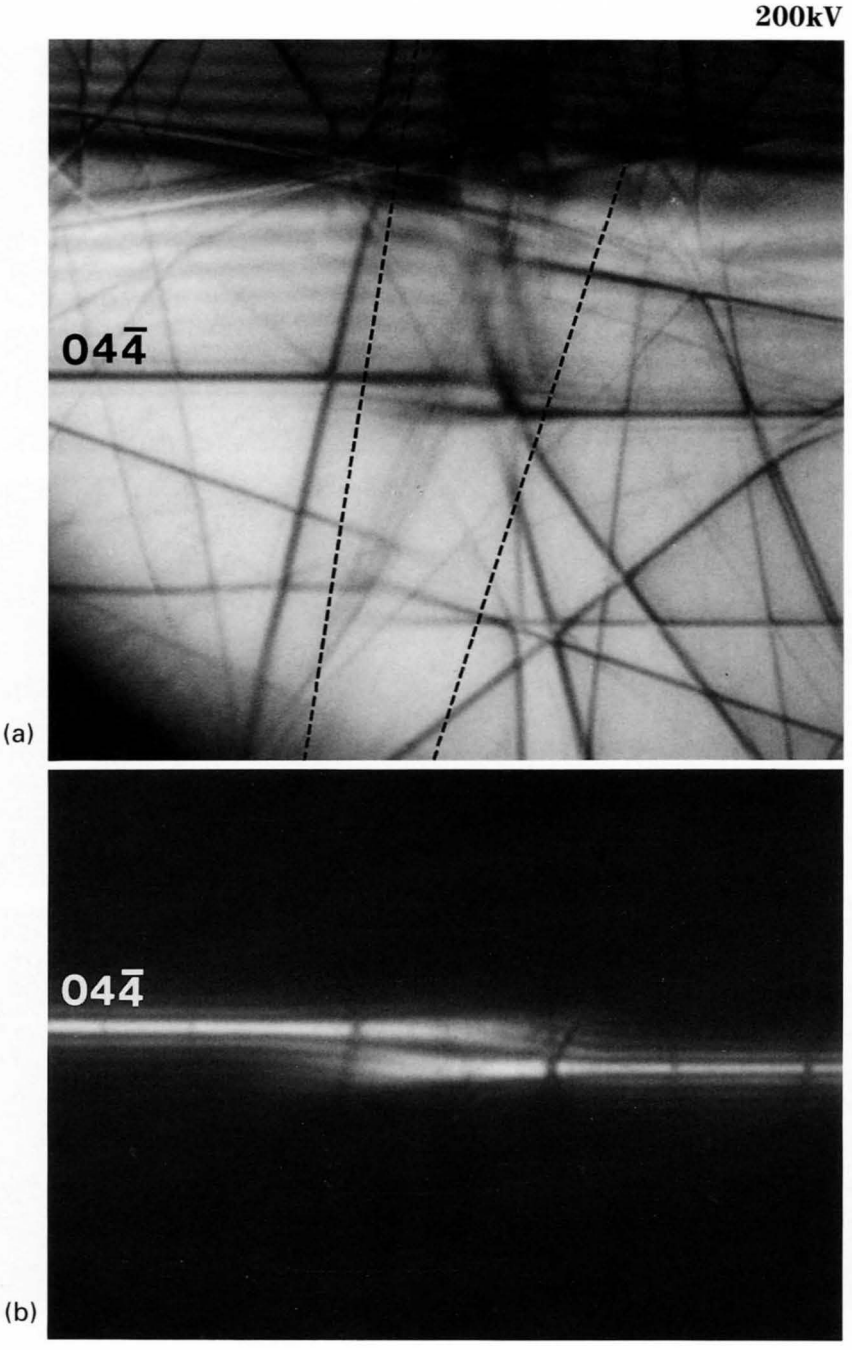

Photographs (a) and (b) demonstrate bright-field and dark-field LACBED patterns obtained from a CTB of NiO at an accelerating voltage of 200kV. The dotted lines in Photo (a) indicate the CTB. Figures (a) and (b) on the opposite page show simulations of bright- and dark-field LACBED patterns for an area containing a CTB, where the extinction distance ξ_g, specimen thickness t and $\Delta w = \xi_g \cdot |\Delta \boldsymbol{g}_z|$ were chosen to be 200nm, 100nm and 8, respectively. The simulations show good agreement with the experimental result.

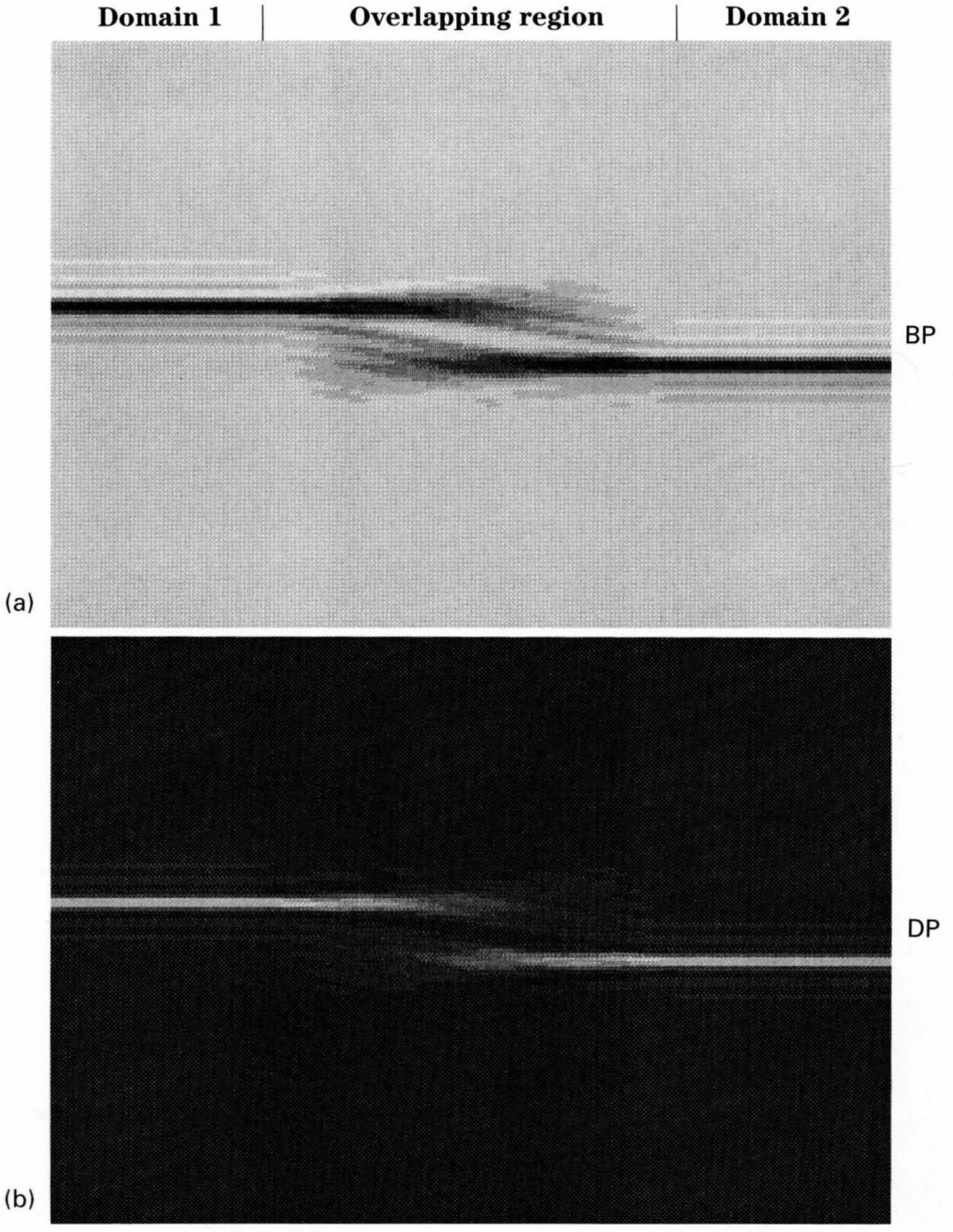

$\frac{t}{\xi_g}=\frac{1}{2}$, $\frac{\xi_g}{\xi'_g}=\frac{1}{20}$, $\Delta w=8$

NiO

Nickel oxide has a rhombohedral unit cell slightly deformed from a cubic unit cell at room temperature and has {110} CTB planes. Since the deformation is small, we use a pseudocubic or a face-centered rhombohedral unit cell.

Figure (a) shows the pseudocubic unit cell and a twin formed on the (110) plane. Figure (b) shows the relation between the reciprocal lattice vectors for the twinned cells, where $\boldsymbol{a}_2^* = \boldsymbol{a}_1^*$ and $\boldsymbol{b}_2^* = \boldsymbol{b}_1^*$. The incident beam is assumed to come parallel to the $\boldsymbol{a}^*$ direction. The relation between $\Delta\boldsymbol{g}$ and $\Delta\boldsymbol{c}^*$ is given by $\Delta\boldsymbol{g} = l \cdot \Delta\boldsymbol{c}^*$, l being the third index of a reflection and $\Delta\boldsymbol{c}^* = \boldsymbol{c}_1^* - \boldsymbol{c}_2^*$. The relation between $\Delta\boldsymbol{c}^*$ and the rhombohedral angle α of the unit cell is given in the figure. The value of α was reported to be 90.06° [a].

Reference

[a] R. W. G. Wyckoff: Crystal Structures, Vol. 1, New York, Interscience, 1963.

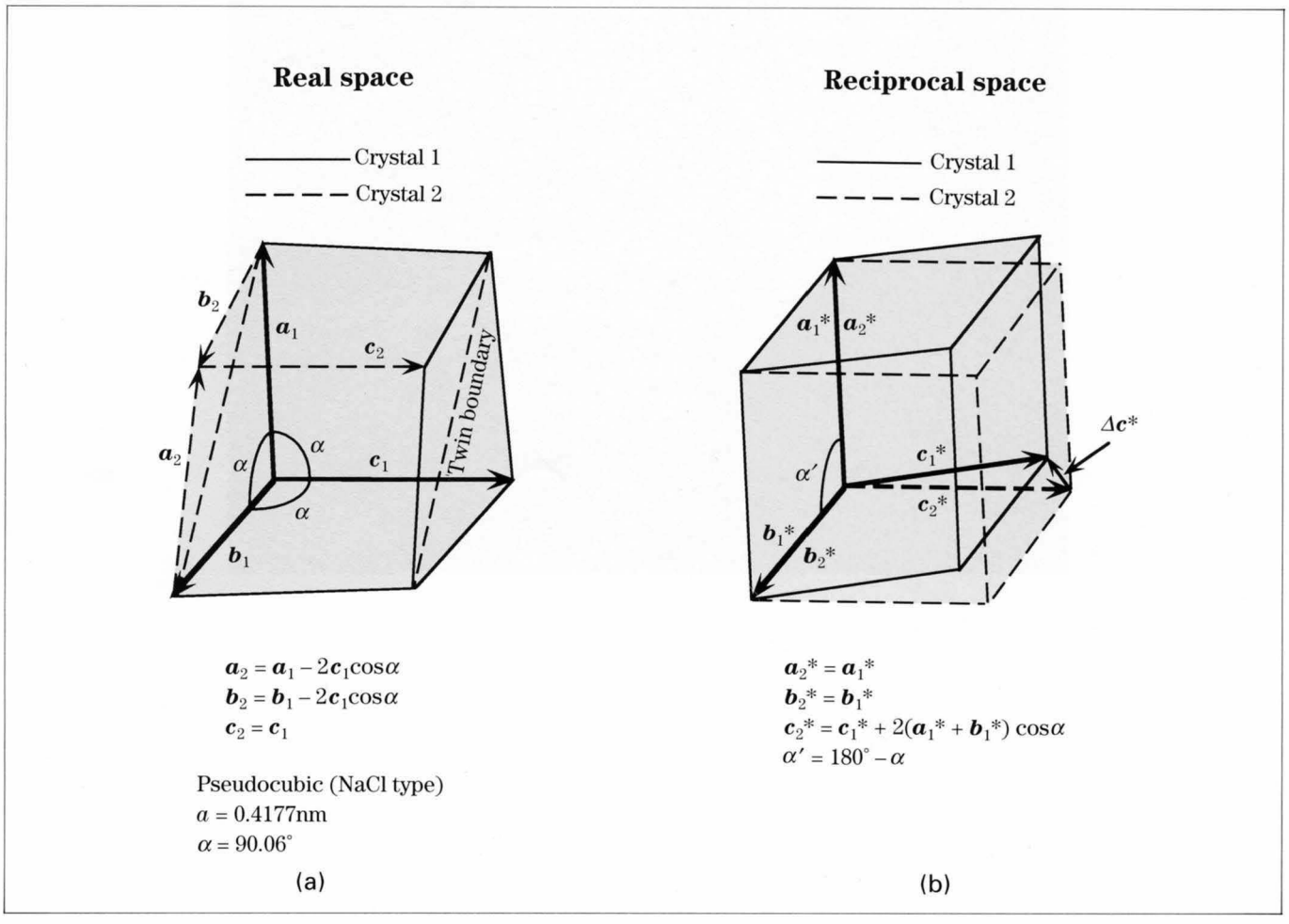

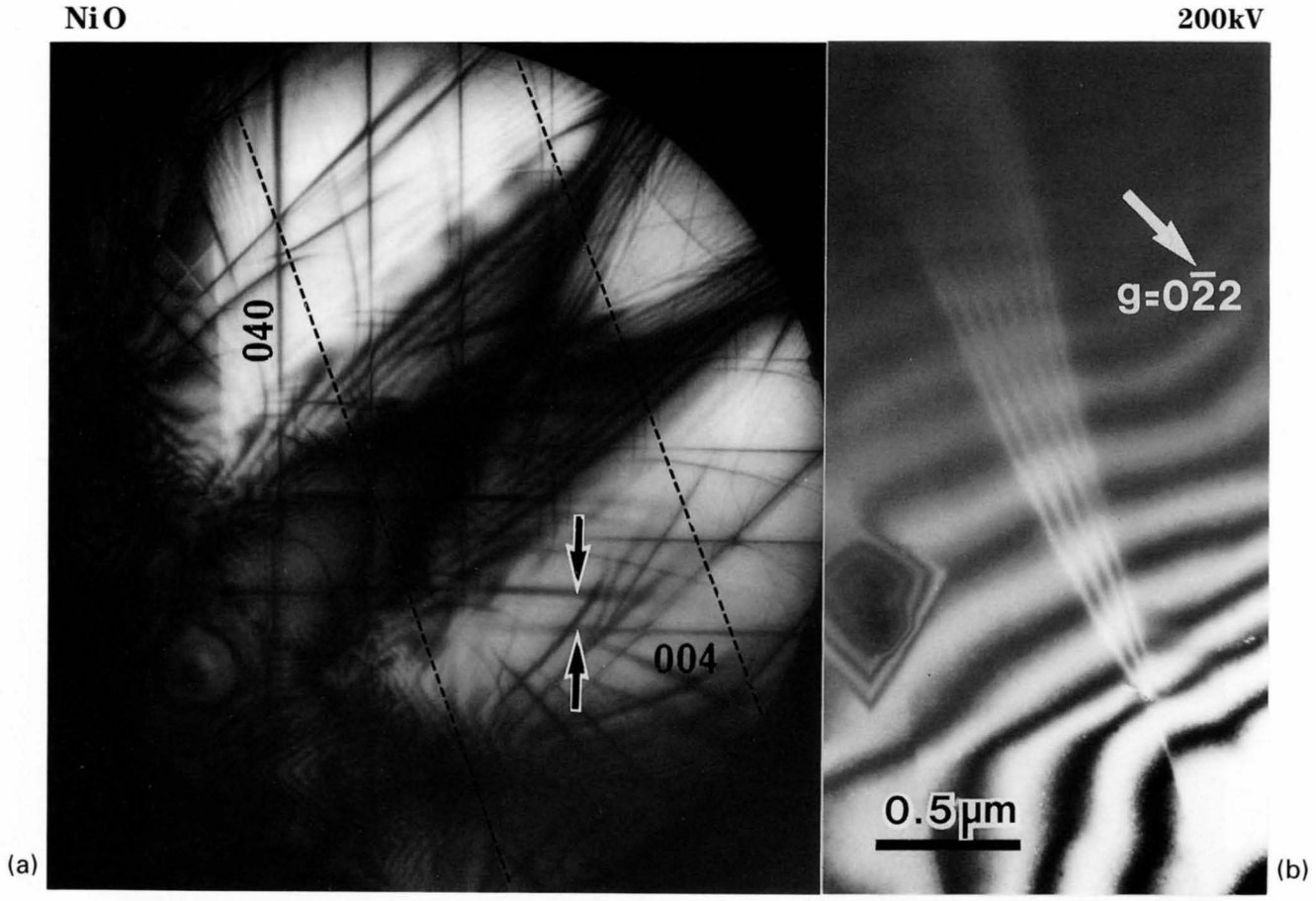

Photograph (a) is an LACBED pattern taken from an area containing a CTB of NiO at an accelerating voltage of 200kV. The area bounded by dotted lines corresponds to the CTB seen in Photo (b). All the $0k0$ reflections remain single lines, but the $00l$ reflection lines show a splitting. The separation of the 004 line pair and the distance between the 004 and 006 reflections were measured. From the ratio between these values and the lattice parameter a, the separation of the 004 line pair indicated by arrows was found to correspond to an angle of 0.13°. The rhombohedral angle α of the unit cell was calculated to be 90.07°. This value well agrees with that given in the same reference on the opposite page. It should be noted that the angular separation $\Delta \boldsymbol{g}_z$ can be measured with an accuracy of about 0.01° by CBED while conventional electron diffraction can not detect $\Delta \boldsymbol{g}_z$ but measure the angular difference $\Delta \boldsymbol{g}_\phi$ with an accuracy about 1°.

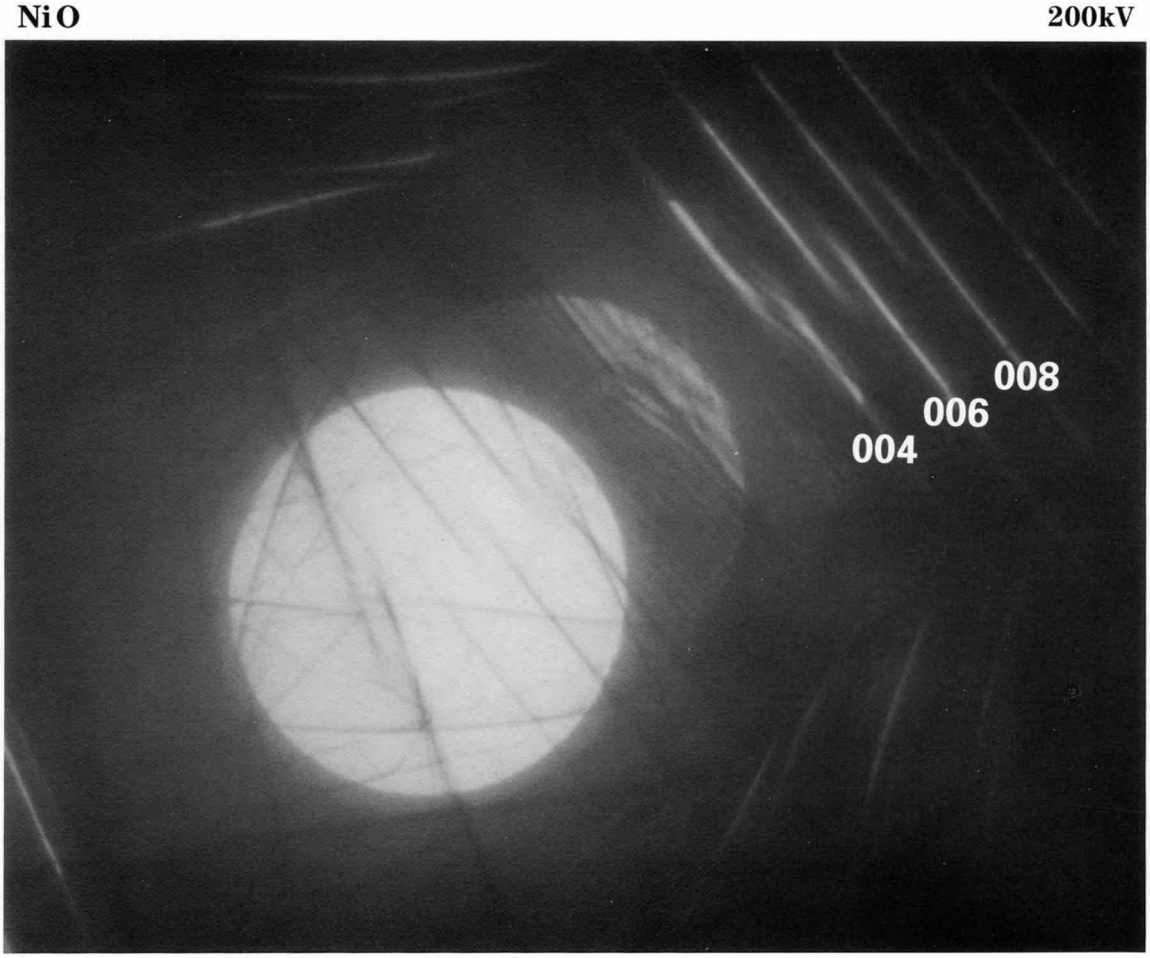

Defocus CBED pattern of a twinned crystal of NiO, showing the same amount of splitting in the different-order 00l reflections.

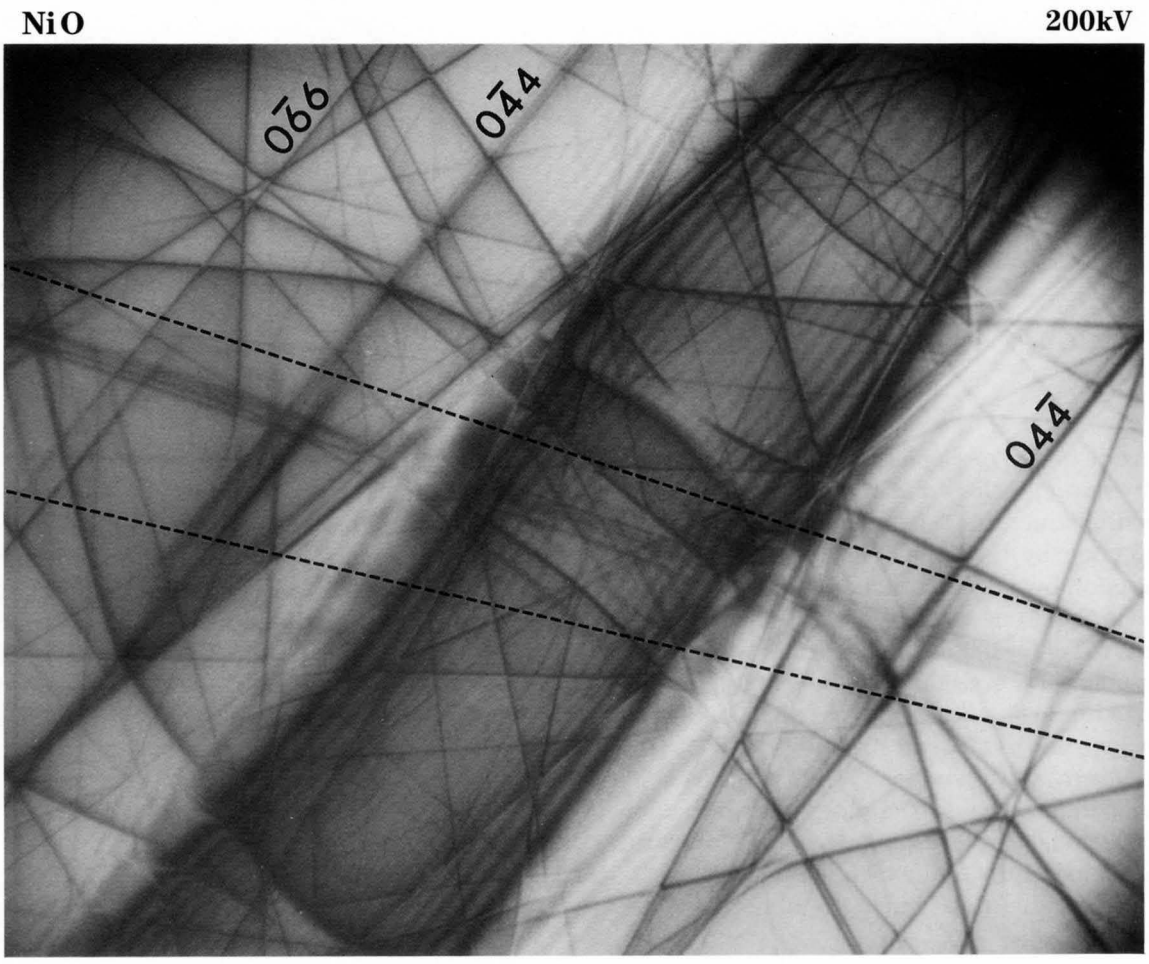

LACBED pattern of a twinned crystal of NiO. The oblique twin boundary is designated by dotted lines. The splitting of a series of the reflections $0\bar{l}l$ due to the twin is seen.

Temperature dependence

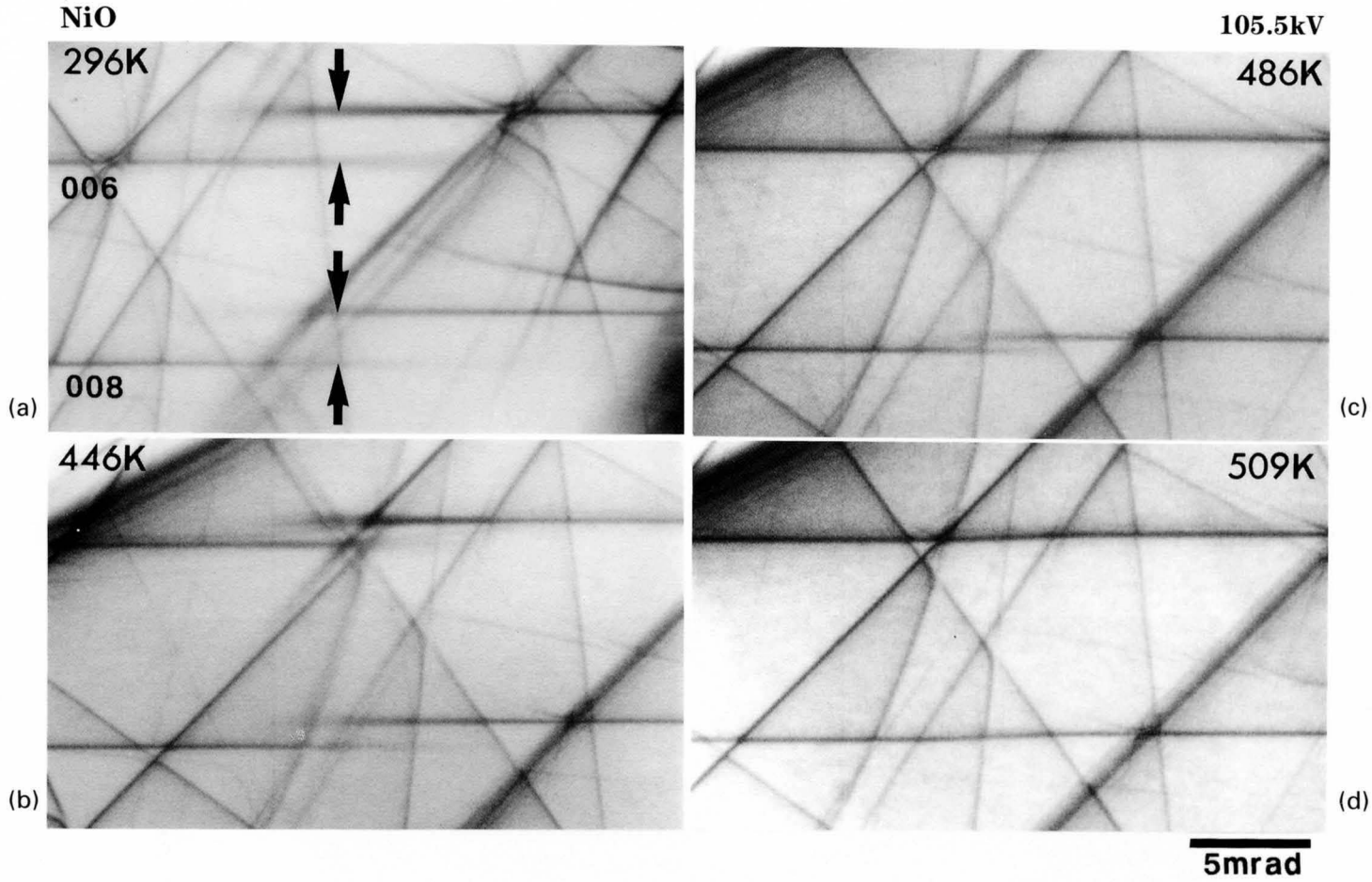

Nickel oxide undergoes a phase transformation at the Néel temperature, 520K, from a cubic structure to a rhombohedral structure. The lattice is deformed in the <111> direction by the Jahn-Teller effect and in the <100> direction by magnetostriction. Since the magnetostriction is about one tenth the Jahn-Teller distortion in this case, the deformation by the former is neglected. The latter deformation or the rhombohedral angle was measured with high accuracy from the splitting of reflection lines due to the twin structure.

Photographs (a) to (d) show LACBED patterns taken at four temperatures below the phase transformation. The split 006 and 008 reflection lines come closer with increasing temperature. At the highest temperature, the splitting is difficult to see but a continuous bend is seen.

Figure (a) on the opposite page plots the deviation angle from 90°, $\Delta\alpha$ (in degree against temperature together with three data measured by Rooksby [a]. His value at about 300K well agrees with our result but that at about 100K is largely different from the present result. From the least square fitting of the result, the angle $\Delta\alpha$ was fitted with high accuracy by a function $\Delta\alpha = 2.56 \times 10^{-3} \times (515-T)^{0.6}$ (Fig. (b)), though the data at low temperatures deviate from the function.

Reference

[a] H. P. Rooksby: *Acta Cryst.*, **1** (1948) 226.

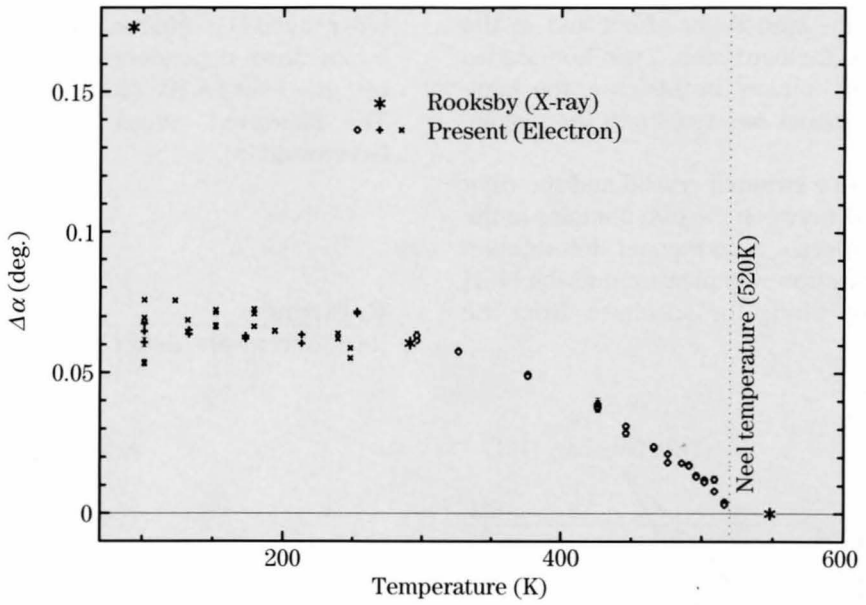
Rooksby (X-ray)
Present (Electron)
Neel temperature (520K)
Δα (deg.)
Temperature (K)
0.15
0.1
0.05
0
200
400
600

(a)

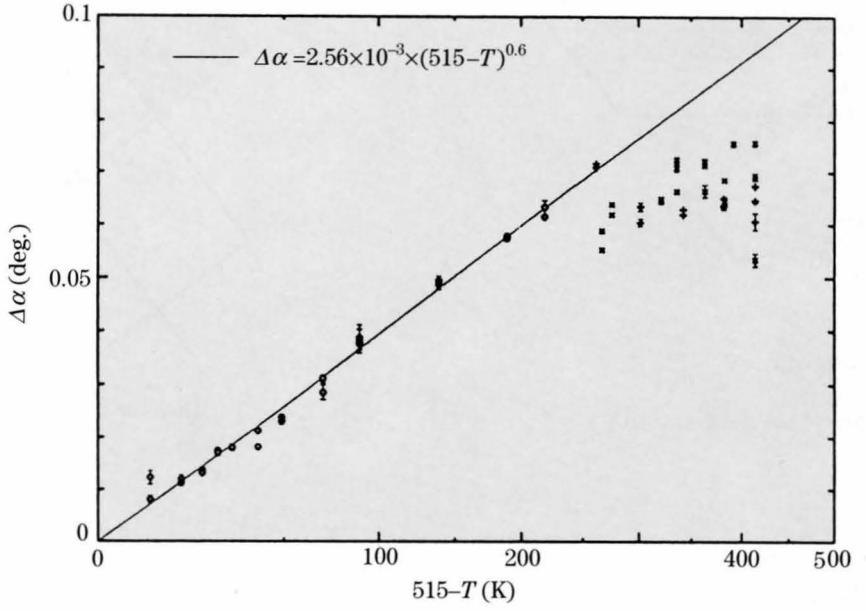
Δα =2.56×10⁻³×(515–T)^0.6
Δα (deg.)
515–T (K)
0.1
0.05
0
0
100
200
400
500

(b)

CoO

Cobalt oxide undergoes a phase transformation at the Néel temperature, 290K, from a cubic structure to a rhombohedral structure. The lattice is deformed in the <111> direction by the Jahn-Teller effect and in the <100> direction by magnetostriction. Twin boundaries are formed on the {101} planes. In this case, the Jahn-Teller deformation is about one twentieth the magnetostriction.

The left figure shows a twinned crystal and the right one the lattice relation between the two domains in the real and reciprocal spaces. A tetragonal deformation due to the magnetostriction was measured at the [161] electron incidence by tilting the specimen from the [010] zone axis.

Photographs (a) to (d) on the opposite page show the temperature dependence of the shift of the $40\bar{4}$ and $60\bar{6}$ reflection lines. The ratio between the lattice parameters c and a is plotted as a function of temperature. The temperature dependence of the ratio c/a is expressed by $c/a = 1 - 9.1 \times 10^{-5} (282 - T)^{0.93}$ as shown in the figure. The measured values well agreed with those of Greenwald [a].

Reference

[a] S. Greenwald: *Acta Cryst.*, **6** (1953) 396.

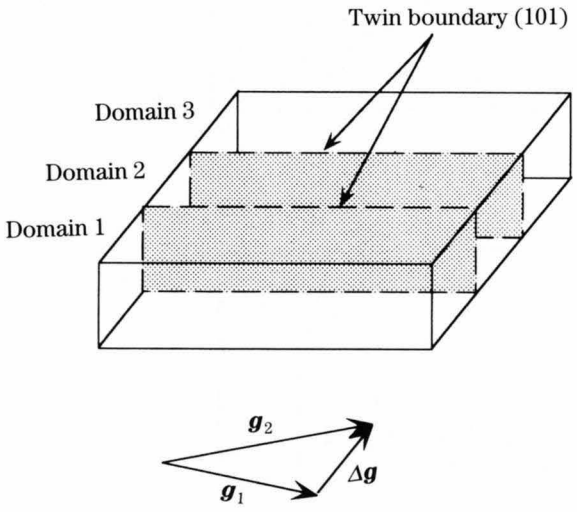

[010] incidence: $\Delta g_z = 0$

[161] incidence: $\Delta g_z = \Delta g \cdot \sin(13.3^\circ)$

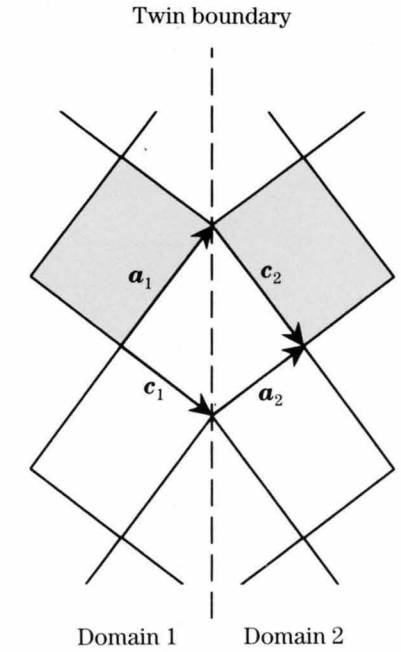

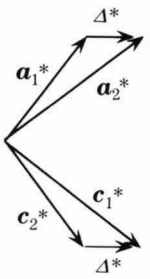

$$a_2^* = a_1^* + \Delta^*$$
$$c_2^* = c_1^* - \Delta^*$$

$$\Delta^* = \delta \cdot (a_1^* + c_1^*)$$

Relation between reciprocal lattice vectors of twin domains.

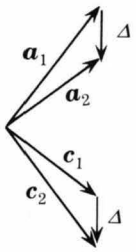

$$a_2 = a_1 + \Delta$$
$$c_2 = c_1 + \Delta$$

$$\Delta = \delta \cdot (c_1 - a_1)$$

Relation between lattice vectors of twin domains.

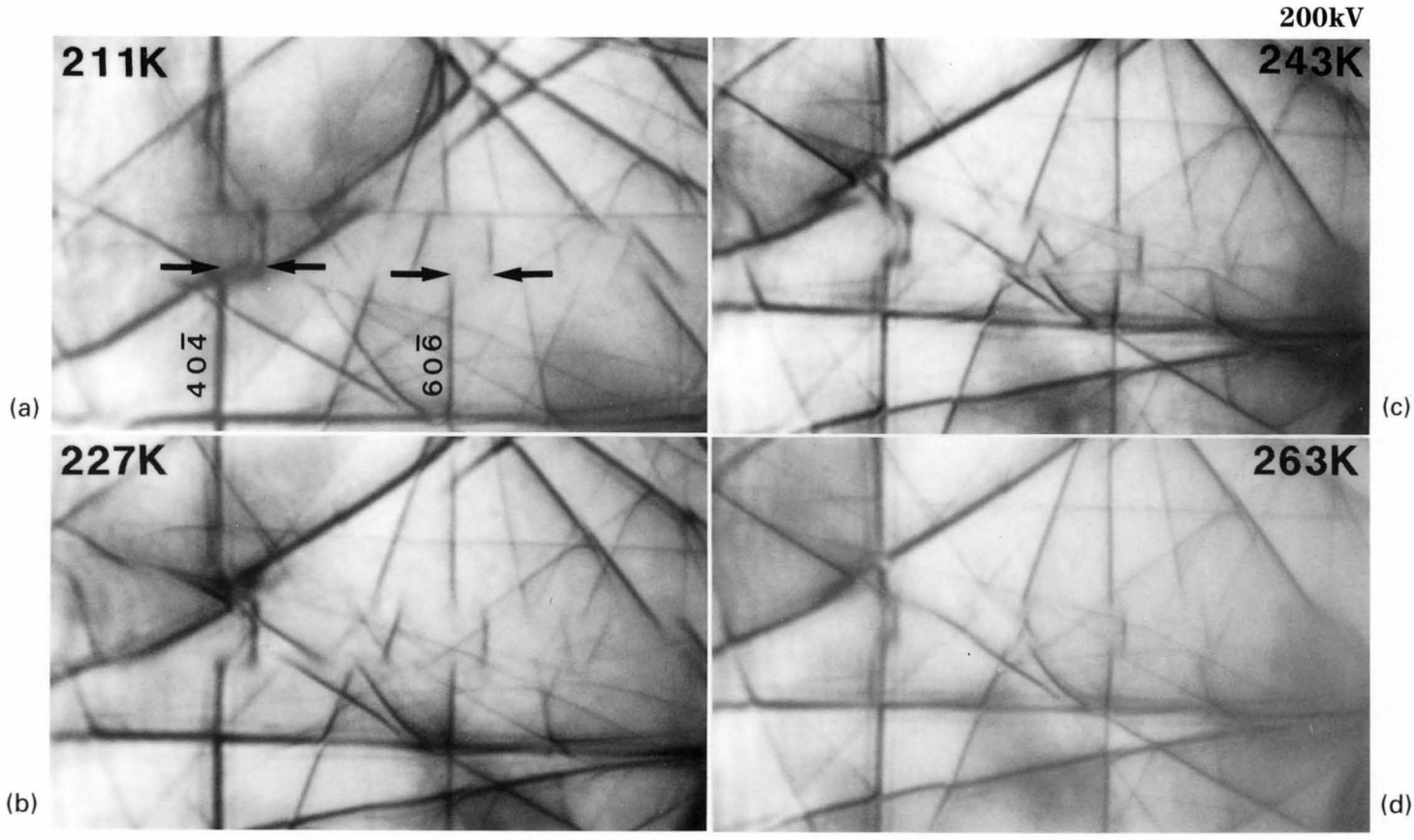
200kV
211K
243K
227K
263K
(a)
(b)
(c)
(d)
$40\bar{4}$
$60\bar{6}$

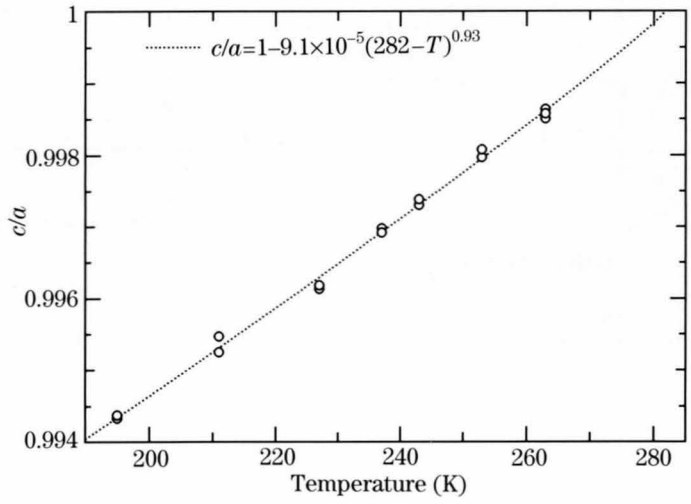
c/a=1–9.1×10^{-5}(282–T)$^{0.93}$
1
0.998
0.996
0.994
c/a
200
220
240
260
280
Temperature (K)

Kikuchi patterns

Even in the case of selected area diffraction (SADIFF) using a parallel electron beam, a divergent beam is produced by inelastic scattering. Kikuchi patterns are formed by the latter beam. Similar splitting to that observed for twins by CBED can be observed in SADIFF patterns, where reflection lines and diffraction disks for the former case are replaced by Kikuchi lines and diffraction spots for the latter case, as schematically shown in the figure. The method to use Kikuchi patterns is simple and convenient for measuring the splitting, though it is not suitable for examining thin specimens and bent ones.

Photographs (a) and (b) are SADIFF patterns of NiO taken from an area in a domain and that containing twinned domains, respectively. Doublets of Kikuchi lines are clearly seen in Photo (b), whereas all the Kikuchi lines in photo (a) are singlets.

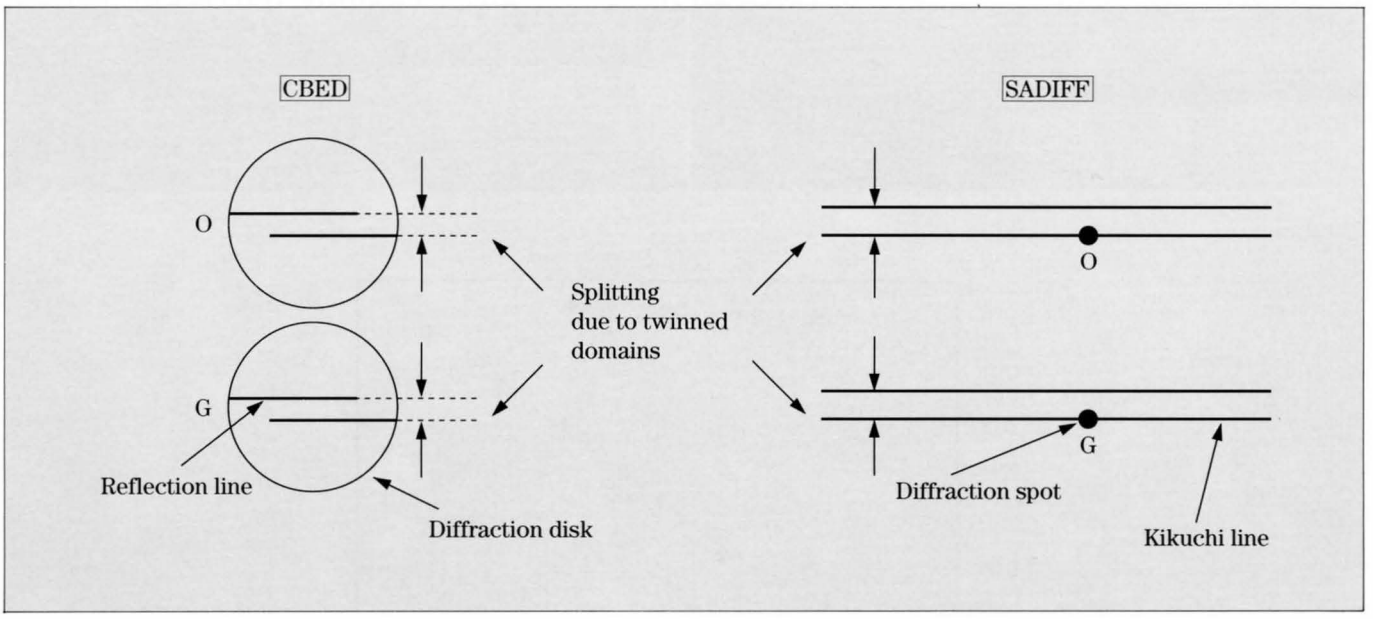

NiO **200kV**

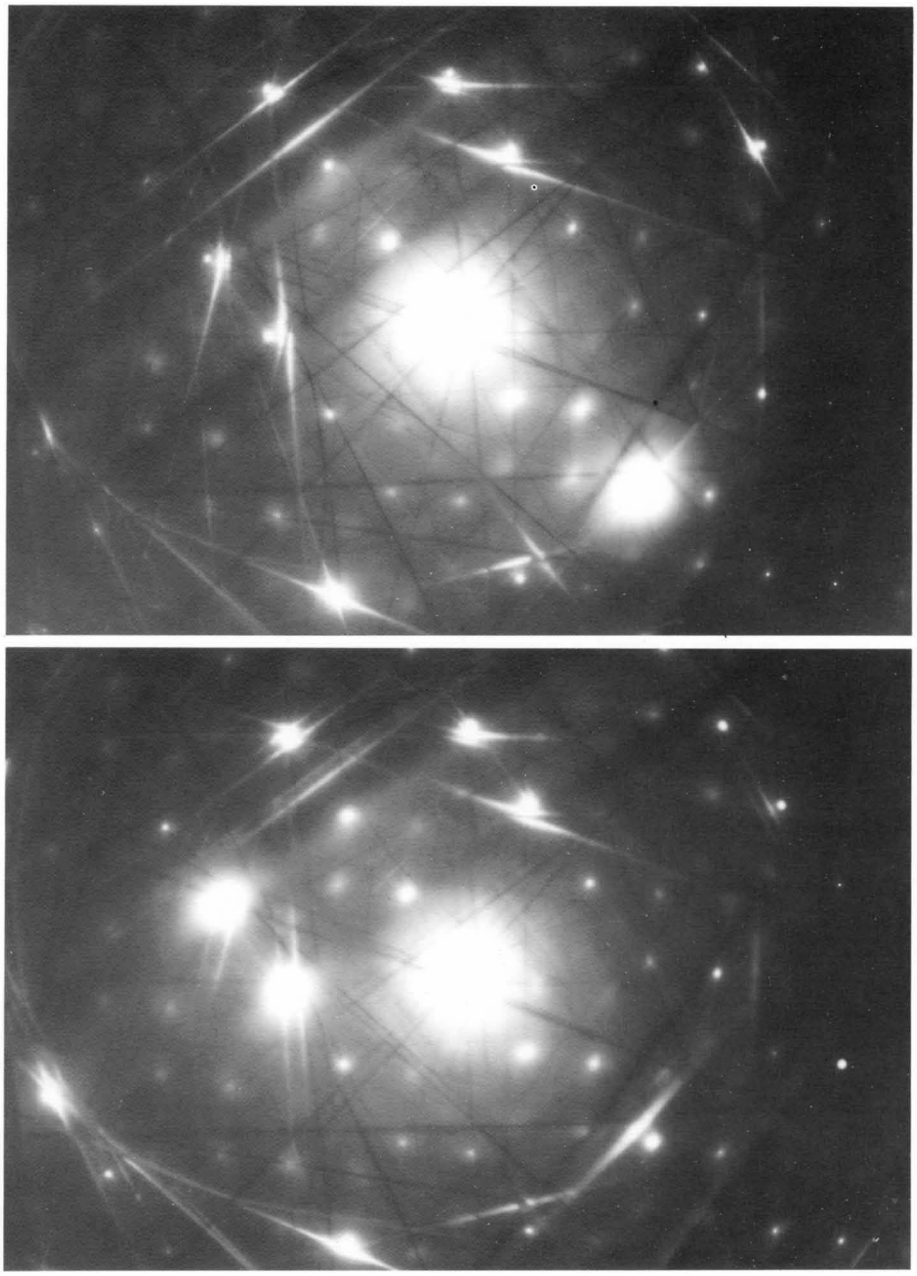

(a)

(b)

Interference Fringes

Interference fringes of a lattice spacing $d=1/|\boldsymbol{g}|$ can be observed at the overlapping region of the disks due to reflections $\boldsymbol{g}_1$ and $\boldsymbol{g}_2$, $\boldsymbol{g}=\boldsymbol{g}_1-\boldsymbol{g}_2$, when the electron probe size ΔX is smaller than the spacing d. In other words, an intensity distribution formed by coherent interference can be seen if $\Delta X<d$. For $\Delta X>d$, coherent interference is smeared out, which is said to be incoherent. Hence, coherent illumination is not determined by the absolute source size but by the relative size $\Delta X/d<1$. Using the Bragg equation $2d\theta_B \approx \lambda$, the condition $\Delta X<d$ is written as $\Delta X<\lambda/2\theta_B$ or $\Delta X\cdot\theta_B<\lambda/2$. When ΔX is regarded as the source size and θ_B as the illumination angle, the inequality is just a coherent condition in light optics.

In ordinary CBED, a specimen is illuminated with a probe about 10nm in diameter. Since the lattice spacings usually observed are less than 1nm, the lattice fringes cannot be observed even if the disks are overlapped. If the probe focused on the specimen becomes smaller than 1nm, the interference effect due to lattice planes appears at the overlapping regions. When the probe is focused below (above) the specimen with the probe size kept unchanged, the interference fringes with the spacing are observed. The photograph on the opposite page clearly shows such fringes. That the fringes are formed only at the overlapping regions vividly exhibits that they are produced by the interference of the two diffraction waves.

FeS_2 [100] **200 kV**

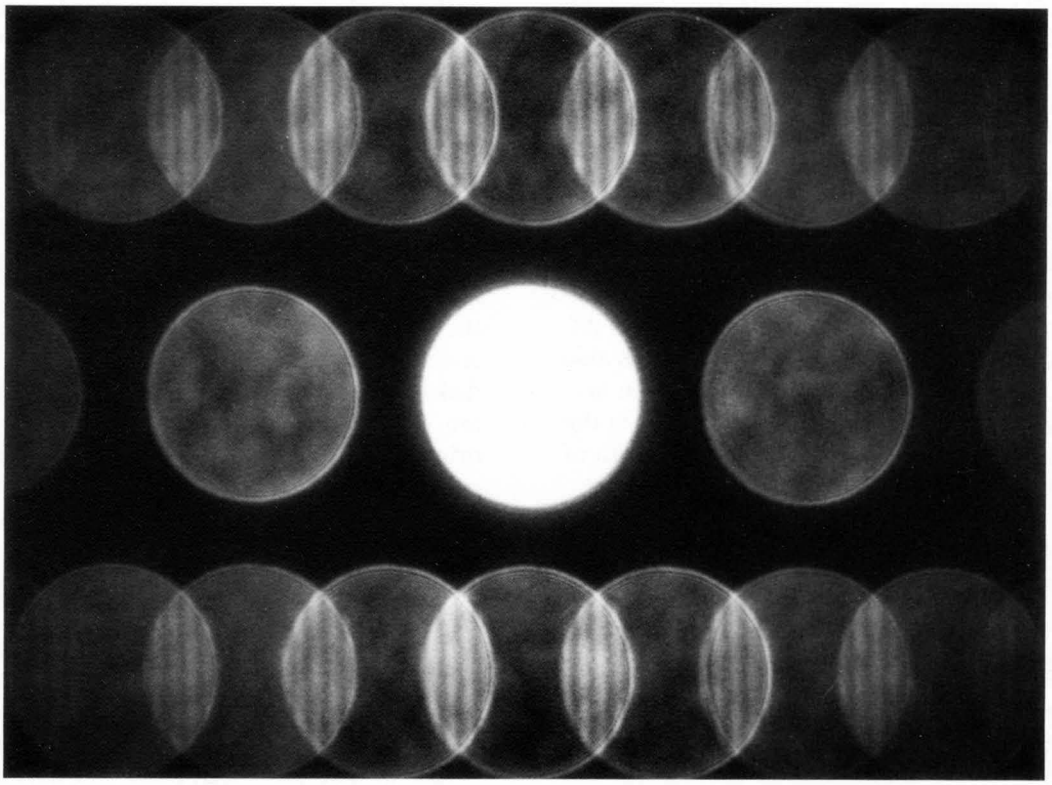

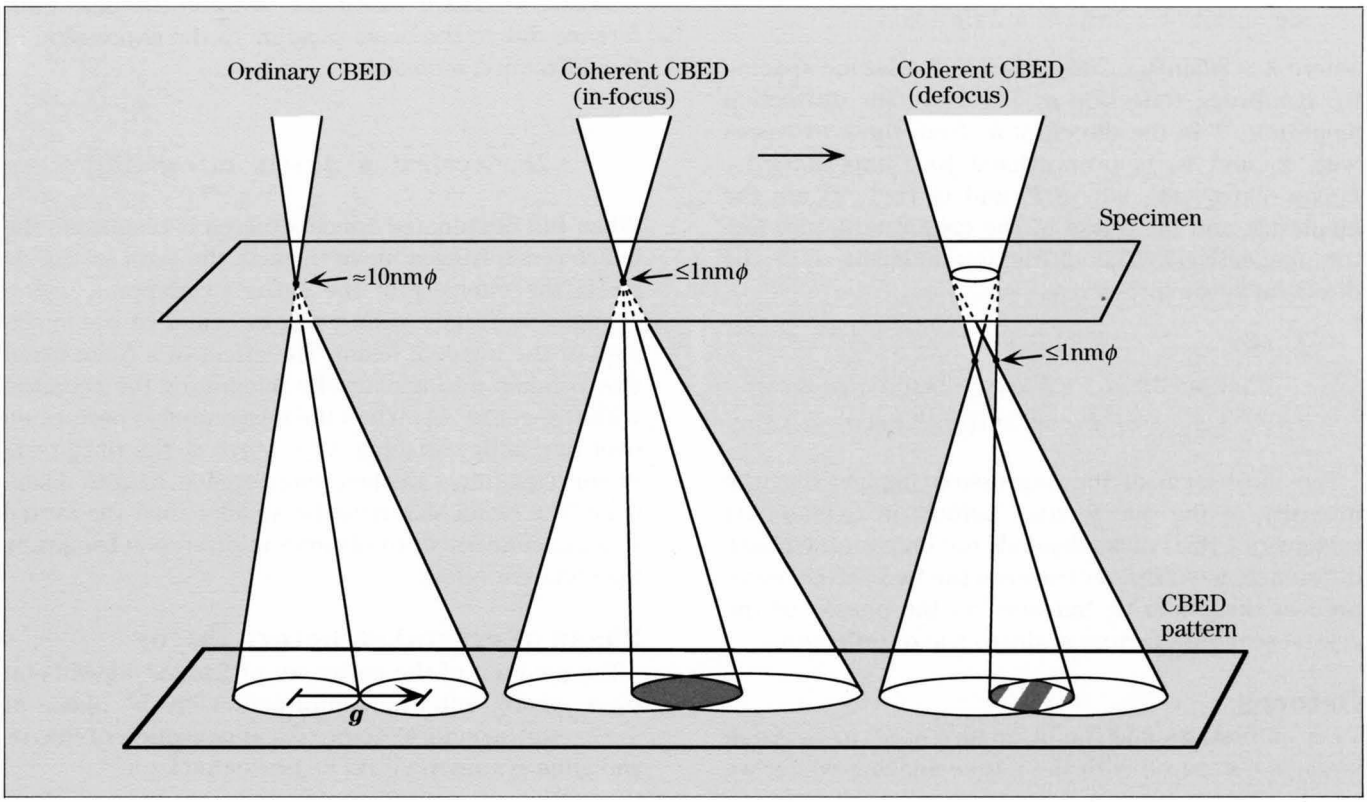

Theoretical

Formation of interference fringes in overlapping disks of CBED patterns was already explained by Cowley [16] and Vine *et al.* [18]. We provide here an alternative, probably easier, explanation about it. Figure (a) shows a schematic ray-path diagram of coherent CBED. Let the origin O of a crystal unit cell be at the cross point of the specimen and the optical axis of an electron microscope. The two incident waves with wave vectors $\boldsymbol{k}_1$ and $\boldsymbol{k}_2$ meet in phase at point O′ below the specimen. The two waves are always in phase on the bisector (dotted line) of the two directions. Let us consider that the wave $\boldsymbol{k}_1$ is diffracted in the direction $\boldsymbol{k}_3 = \boldsymbol{k}_1+\boldsymbol{g}_1$. The wave $\boldsymbol{k}_2$ is also diffracted in the same direction $\boldsymbol{k}_3 = \boldsymbol{k}_2+\boldsymbol{g}_2$ when $|\boldsymbol{g}_1-\boldsymbol{g}_2| = |\boldsymbol{g}| = 2\theta_B/\lambda$, as shown in Fig. (b), where θ_B is the Bragg angle of reflection $\boldsymbol{g}$ and λ is the wavelength of the incident electron waves.

The phase difference $\Delta\phi$ between the two waves with $\boldsymbol{k}_1$ and $\boldsymbol{k}_2$ at the origin O is given by $2\pi/\lambda$ times path difference Δl measured along the optical axis, where

$$\Delta l \approx \Delta x\cdot\tan 2\theta_B \approx \Delta x\cdot 2\theta_B,$$

Δx being the distance between the origin O and the cross point of the bisector with the specimen. The amount Δx is given by the product of defocus Δz and tilt angle of the bisector θ, $\Delta x = \Delta z\cdot\theta$. Then, $\Delta\phi$ is written as

$$\Delta\phi = 2\pi\Delta l/\lambda = 2\pi\Delta x/d = 2\pi|\boldsymbol{g}|\cdot\Delta x,$$

where $\lambda = 2d\sin\theta_B \approx 2d\theta_B$ and d is the lattice spacing for the Bragg reflection $\boldsymbol{g}$. The resultant diffraction amplitude Ψ in the direction $\boldsymbol{k}_3$ from the two waves with $\boldsymbol{k}_1$ and $\boldsymbol{k}_2$ is proportional to $F_1\exp(-2\pi i\alpha_1) + F_2\exp(-2\pi i\alpha_2-\Delta\phi)$, where F_i and α_i (i=1, 2) are the amplitude and the phase of the crystal structure factor, respectively. The diffraction intensity I in the direction $\boldsymbol{k}_3$ is expressed as

$$\begin{aligned} I &= |\Psi|^2 \\ &\propto |F_1\exp(-2\pi i\alpha_1) + F_2\exp\{-2\pi i(\alpha_2+|\boldsymbol{g}|\cdot\Delta x)\}|^2 \\ &\propto F_1^2 + F_2^2 + 2F_1F_2\cos[2\pi i\{|\boldsymbol{g}|\cdot\Delta x+(\alpha_2-\alpha_1)\}] . \end{aligned}$$

The third term of the expression implies that the intensity of the interference pattern in overlapping regions of CBED disks depends not only on the phase difference $\Delta\phi = 2\pi|\boldsymbol{g}|\cdot\Delta x$ between the two waves measured at the origin O, but also on the phases of the crystal structure factors of the $\boldsymbol{g}_1$ and $\boldsymbol{g}_2$ reflections.

Defocus

Let us first assume the beam size at O′ to be small enough, compared with the lattice spacing which we want to observe. The intensity sinusoidally changes with Δx. For a fixed amount of defocus Δz, Δx changes with θ. Thus, a sinusoidal intensity change with a period $1/|\boldsymbol{g}|$ appears in the overlapped regions of the neighbouring disks. As defocus Δz decreases, the phase change due to the change of θ decreases, the number of fringes observed being smaller. When Δz approaches zero, the phase $2\pi|\boldsymbol{g}|\cdot\Delta x$ is independent of θ, and the intensity at the overlapping region becomes uniform. It should be noted that twice the number n of fringes in the overlapping region times the spacing d equals the diameter of the illuminated specimen area, provided that the second neighbouring disks contact each other. Since the interference fringes are produced as a result of the Bragg reflection or originate in the lattice periodicity, the fringes can be called lattice fringes, though no direct correspondence exists between the positions of real lattice planes and those of the fringes.

Beam size

We consider another two incident beams with wave vectors $\boldsymbol{k}_1'$ and $\boldsymbol{k}_2'$ which meet in phase at point O″ as shown in Fig. (c). The parallel line to the optical axis through O″ crosses the specimen by ΔX right from the origin O. The path difference ΔL between the wave $\boldsymbol{k}_1$ toward O′ and $\boldsymbol{k}_1'$ toward O″ is given by $\Delta L \approx \Delta X\cdot\tan 2\theta_B \approx \Delta X\cdot 2\theta_B$, resulting in a phase difference $\Delta\phi' = 2\pi\Delta L/\lambda = 2\pi\Delta X/d = 2\pi|\boldsymbol{g}|\cdot\Delta X$. We add the phase difference due to the beam position to the expression of the diffraction intensity :

$$\begin{aligned} I \propto & F_1^2 + F_2^2 \\ & + 2F_1F_2\cos[2\pi i\{|\boldsymbol{g}|\cdot\Delta x+(\alpha_2-\alpha_1)+|\boldsymbol{g}|\cdot\Delta X\}] . \end{aligned}$$

When the illuminated specimen area is displaced, the interference fringes move through the term $|\boldsymbol{g}|\cdot\Delta X$. At Δz=0, the intensity of the entire overlapping region changes uniformly with a displacement of the specimen or the incident beam. The effect of a finite beam size is taken into account by integrating the equation with respect to ΔX. When the integration is performed over one lattice spacing $\Delta X = 1/|\boldsymbol{g}| = d$, the third term of the equation vanishes; interference fringes disappear. The beam size must be smaller than the lattice spacing concerned, to observe interference fringes or the coherent effect.

Phase of crystal structure factor

The position of the entire set of fringes depends on $\alpha_2-\alpha_1$, giving important information on the phase of the crystal structure factor. The observation of mirror and glide symmetries will be presented later.

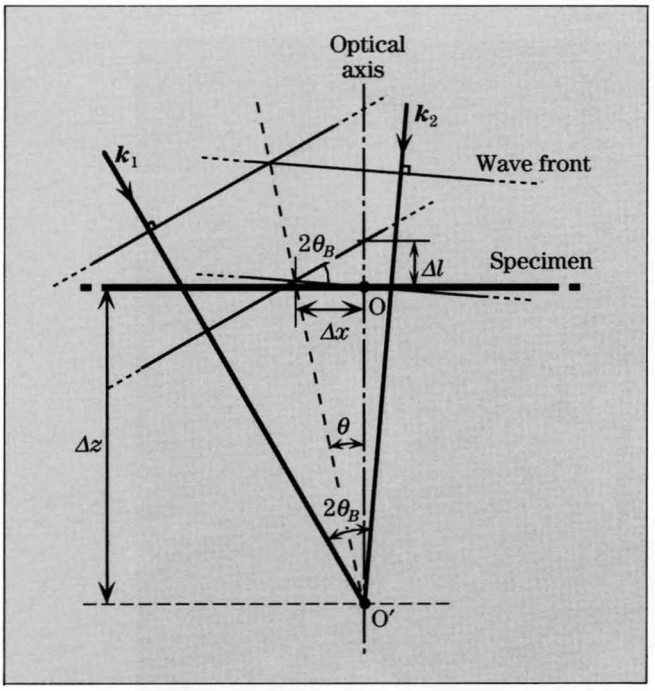
Optical
axis
k_2
k_1
Wave front
$2\theta_B$
Δl
Specimen
O
Δx
θ
Δz
$2\theta_B$
O′

(a)

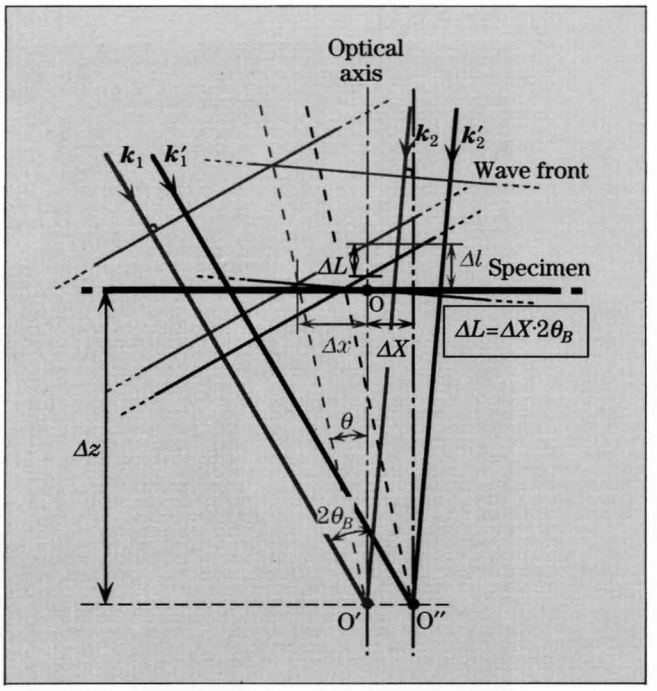
Optical
axis
k_1
k_1'
k_2
k_2'
Wave front
ΔL
Δl
Specimen
O
$\Delta L=\Delta X\cdot 2\theta_B$
Δx
ΔX
θ
Δz
$2\theta_B$
O′
O″

(c)

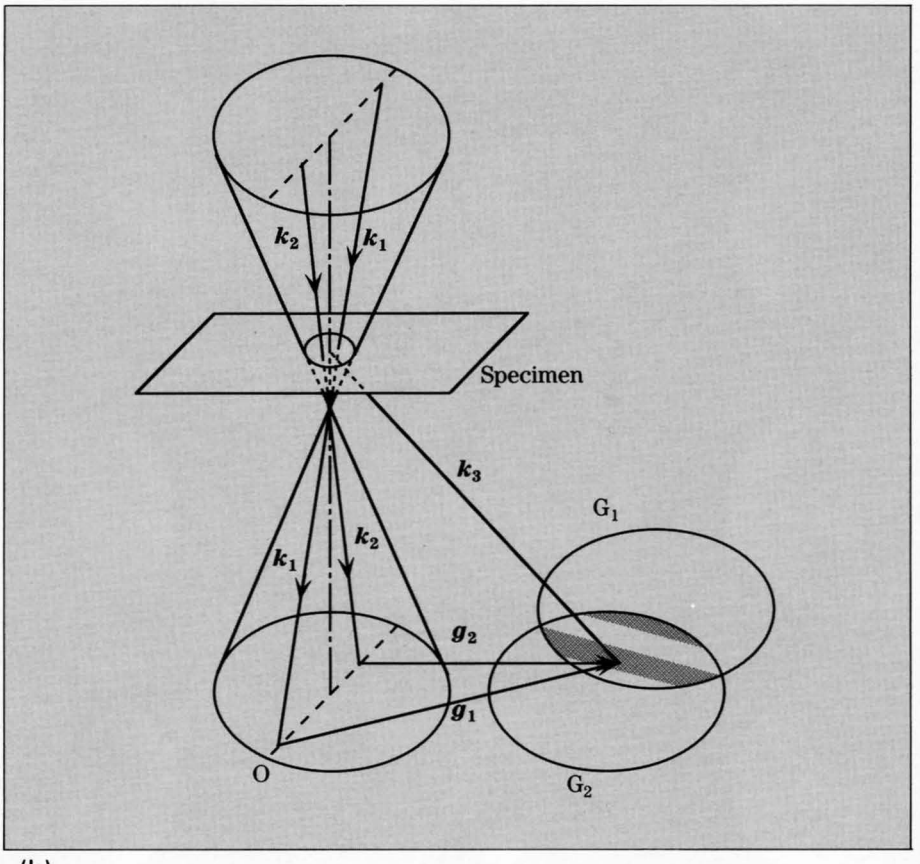
k_2
k_1
Specimen
k_3
G_1
k_1
k_2
g_2
g_1
O
G_2

(b)

Different amounts of illumination defocus

$Sr_2Nb_2O_7$ d_{020}=1.34 nm **80 kV**

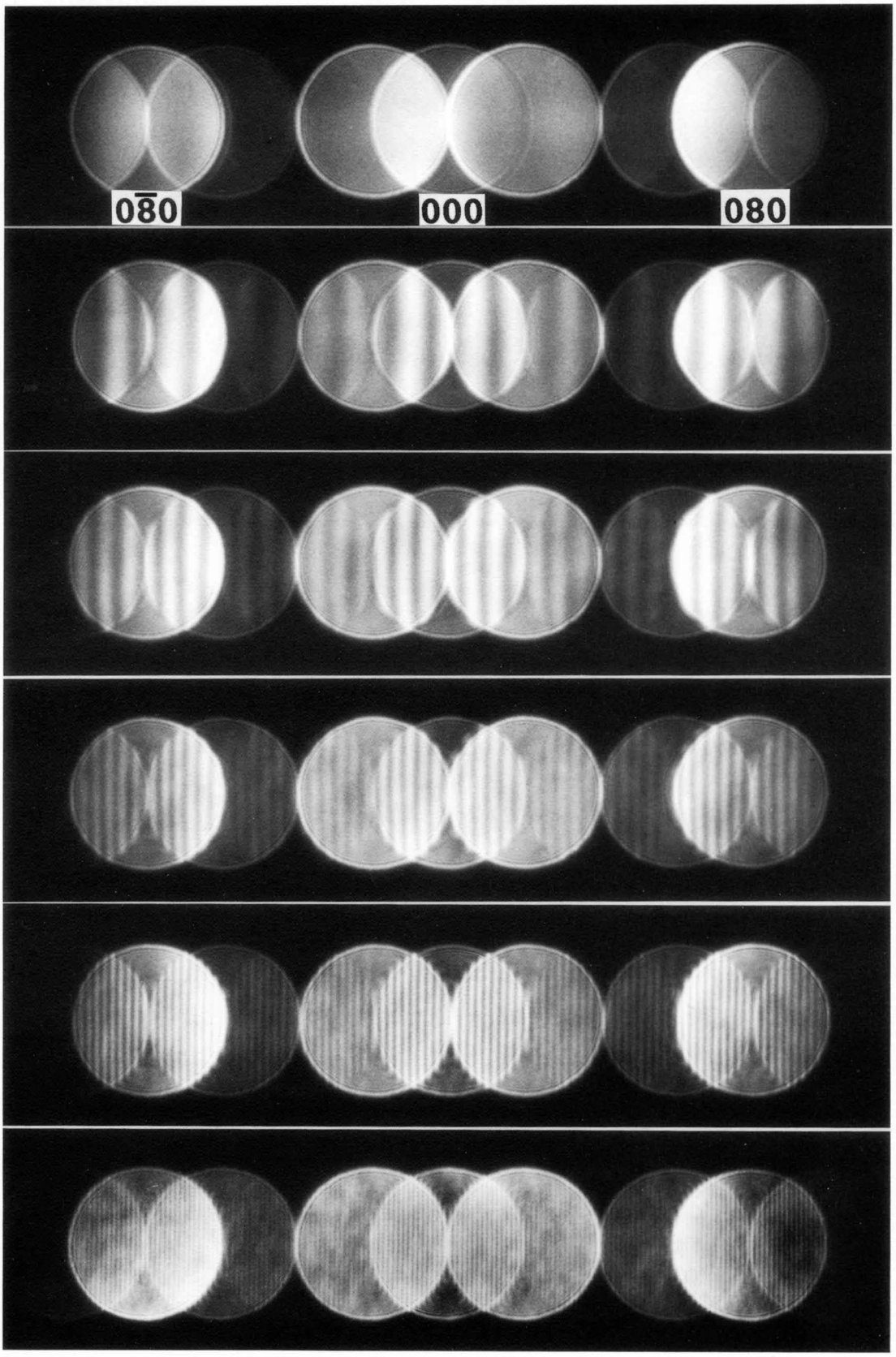

Photographs show coherent CBED patterns taken with six different amounts of illumination defocus from $Sr_2Nb_2O_7$ by exciting the $0k0$ systematic reflections at an accelerating voltage of 80kV. Fringes of a lattice spacing of 1.34nm for $\boldsymbol{g}$=020 are produced by the interference between the $0k0$ and 0, $k\pm2$, 0 ($k=2n$) reflections, where the $0k0$ ($k=2n+1$) reflections are forbidden due to the C-centered lattice type.

The uppermost photograph, which was obtained with nearly in-focus illumination, shows almost uniform intensity in the overlapping regions of the CBED disks. Five successive photographs were taken with increasing amounts of defocus. As the amount of defocus increases, a larger area is illuminated and the magnification of the shadow image is lowered, resulting in the increase of the number of fringes observed. Fifteen fringes are seen in the overlapping regions of the disks in the lowermost photograph.

Probe position

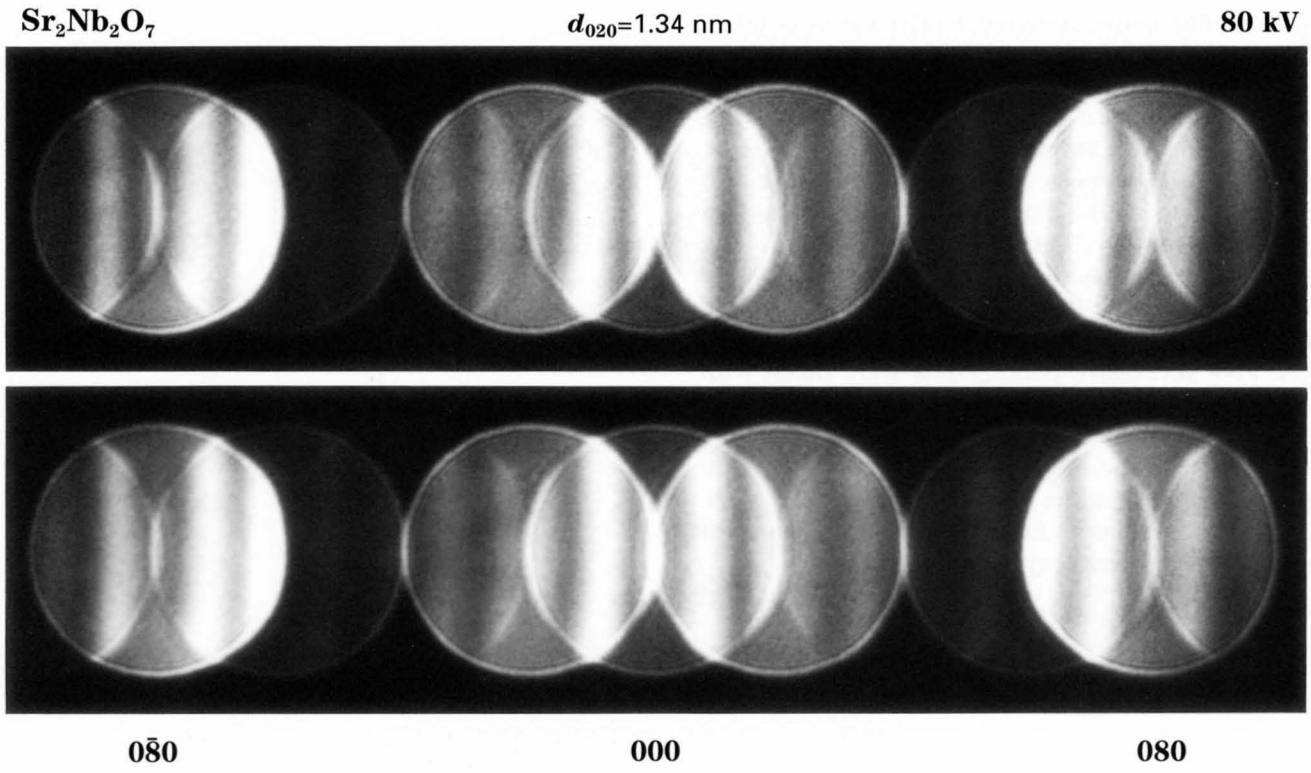

The two coherent CBED patterns were taken from two different specimen areas of $Sr_2Nb_2O_7$ by exciting the $0k0$ systematic reflections for the same amount of defocus at an accelerating voltage of 80kV. The fringe spacing is the same between the two, but the fringe positions are different because of a small displacement of the illumination probe on the specimen. Successive movements of the probe cause movements of the entire fringes. When the probe size exceeds the lattice spacing concerned, the fringes are incoherently superposed to form uniform intensity distribution (see next page).

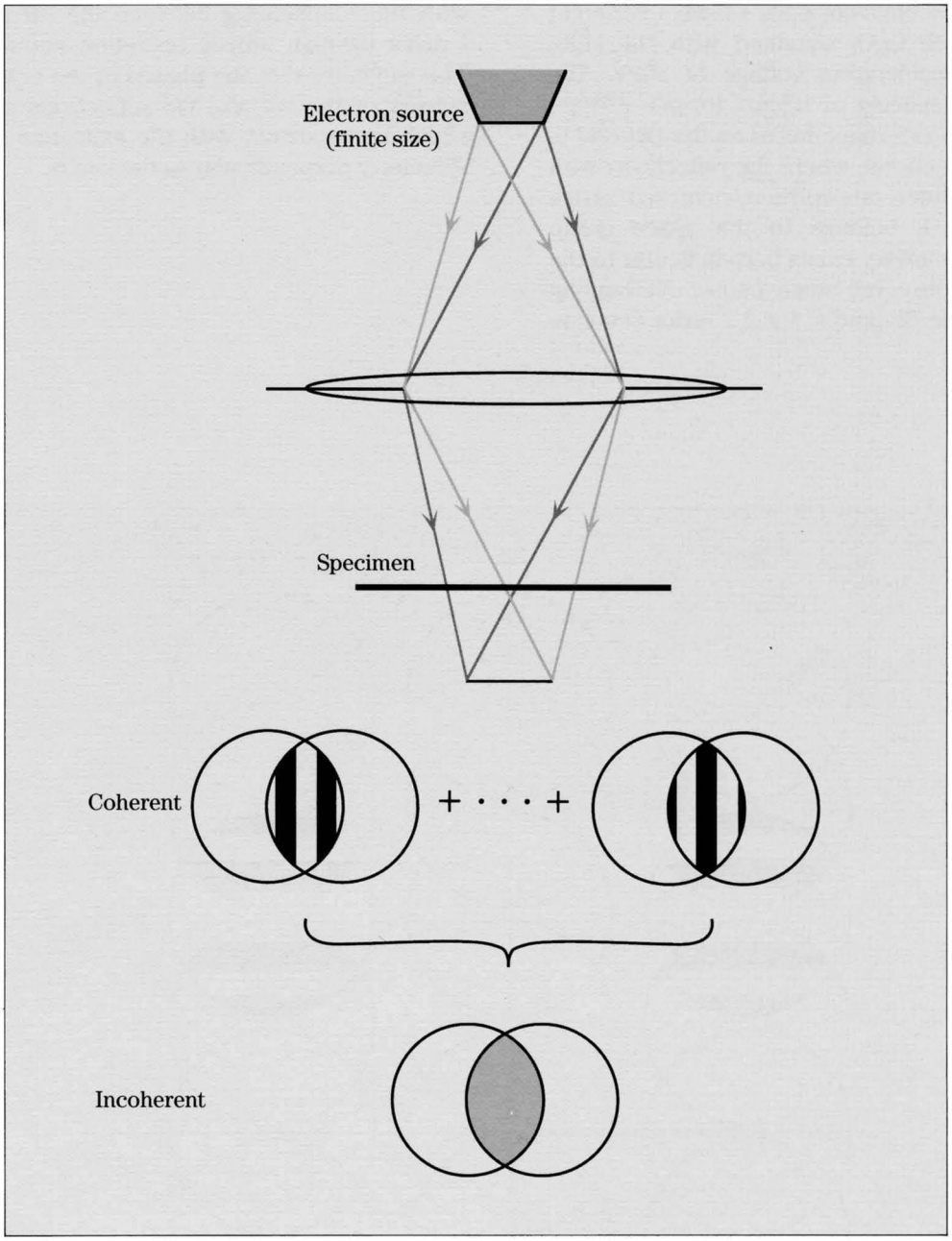
Electron source
(finite size)
Specimen
Coherent
+ · · · +
Incoherent

Mirror, Glide, and Screw Symmetries

Mirror symmetry

$Sr_2Ta_2O_7$

Photograph on the opposite page shows a coherent CBED pattern of $Sr_2Ta_2O_7$ obtained with the [100] incidence at an accelerating voltage of 80kV. The fringes of a lattice spacing of 1.36nm for $\boldsymbol{g}$ = 020 are produced by the interference between the $0kl$ and 0, $k \pm 2$, l (k=2n) reflections, where the reflections with k = 2n+1 are forbidden due to the C-centered lattice type. Since $Sr_2Ta_2O_7$ belongs to the space group $Cmcm$, a mirror symmetry exists perpendicular to the c-axis. The fringes observed in any pair of overlapping regions between the $0kl$ and 0, $k \pm 2$, l disks coincide with those appearing between the $0k\bar{l}$ and 0, $k \pm 2$, $\bar{l}$ disks through mirror operation about the b*-axis. This indicates that the phases of the crystal structure factors of the $0kl$ and $0k\bar{l}$ reflections are the same, which is consistent with the existence of the mirror symmetry perpendicular to the c-axis.

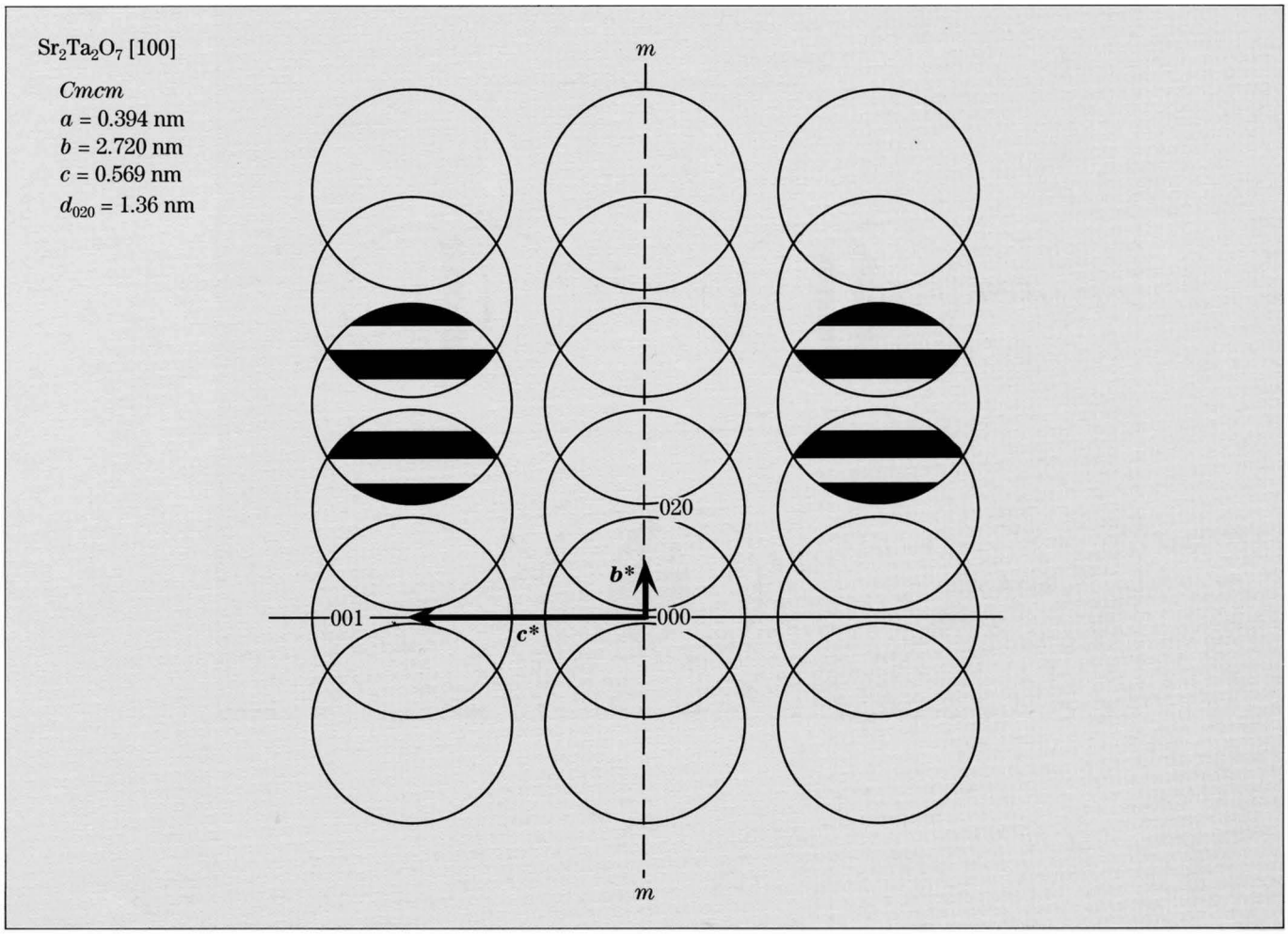

$Sr_2Ta_2O_7$ [100] | m d_{020}=1.36 nm 80 kV

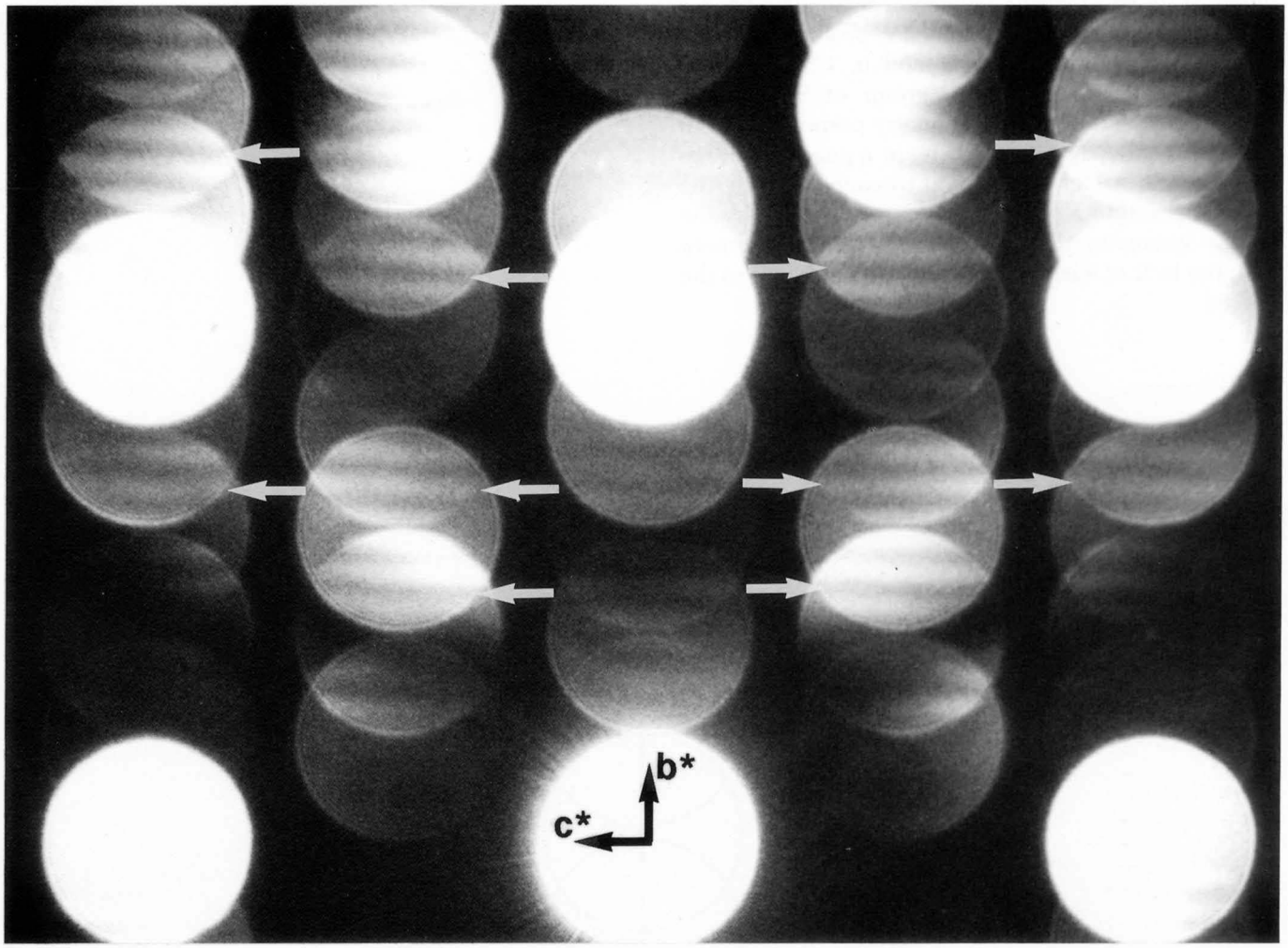

m

Nonexistence of mirror symmetry

$Sr_2Nb_2O_7$

Photograph on the opposite page shows a coherent CBED pattern of $Sr_2Nb_2O_7$ taken with the [100] incidence at an accelerating voltage of 80kV. The fringes of a lattice spacing of 1.34nm are produced by the interference between the $0kl$ and $0, k\pm2, l$ ($k=2n$) reflections. Since the space group of $Sr_2Nb_2O_7$ is $Cmc2_1$, there is no mirror symmetry perpendicular to the c-axis. The fringes appearing in a pair of overlapping regions, which are related to each other by the mirror operation about the b^*-axis, do not satisfy the mirror symmetry. This result is in good agreement with the lack of mirror symmetry perpendicular to the c-axis.

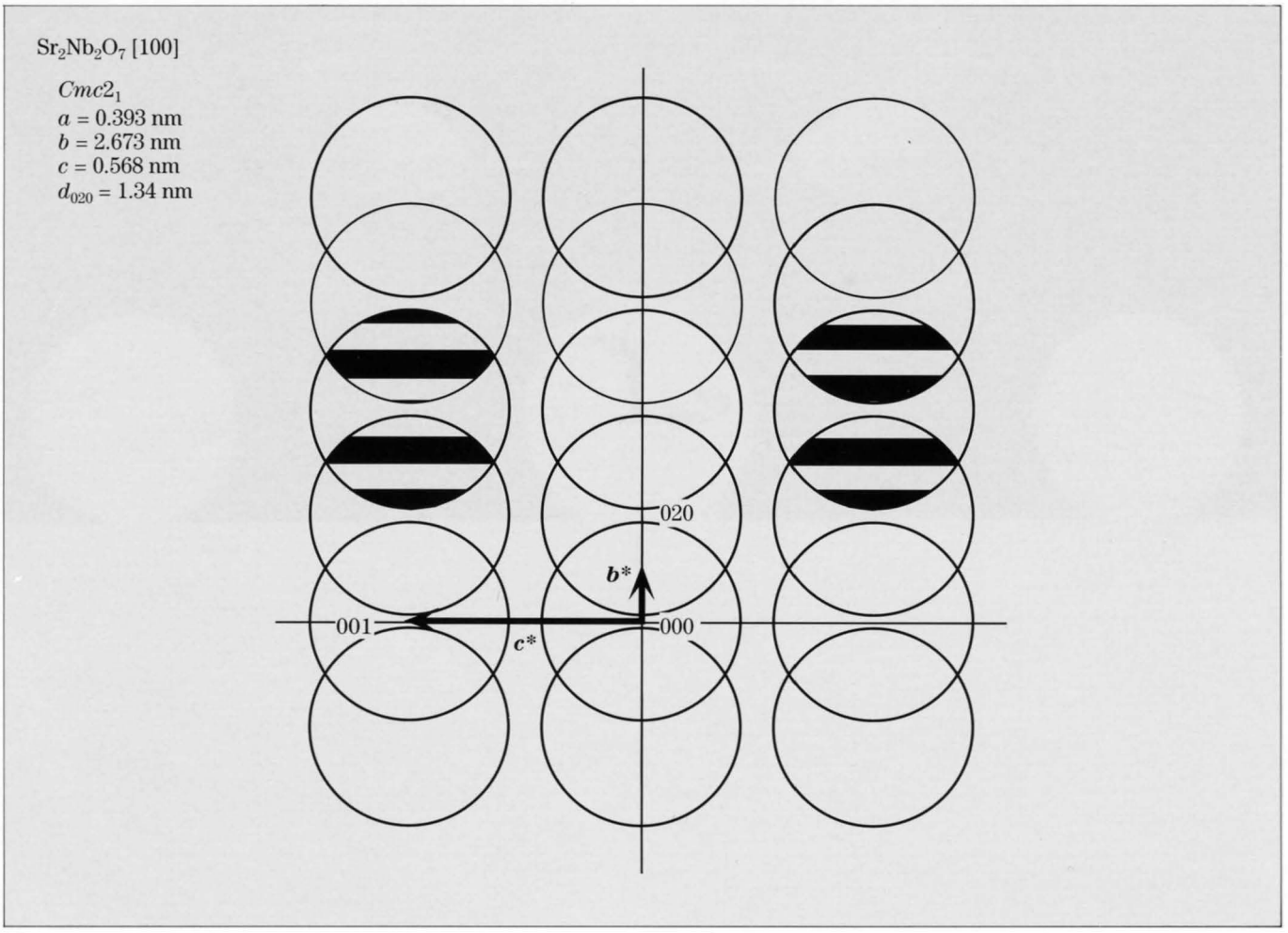

$Sr_2Nb_2O_7$ [100] d_{020}=1.34 nm **80 kV**

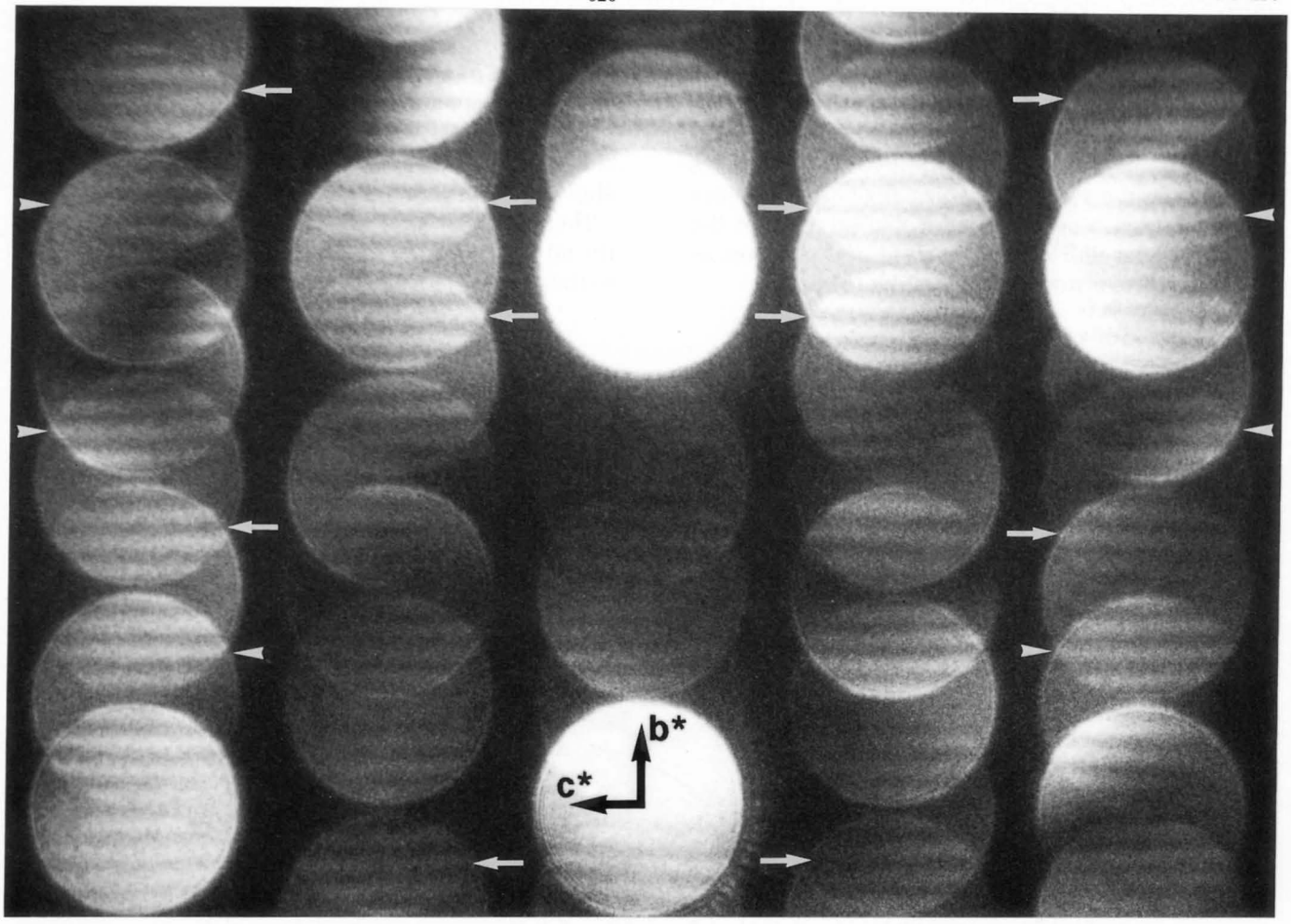

Glide and screw symmetries

Mo_8O_{23}

Photographs on the opposite page are coherent CBED patterns of Mo_8O_{23} taken with the [100] incidence at an accelerating voltage of 80kV. The fringes of a lattice spacing of 1.69nm are seen in the overlapping regions between the $0kl$ and 0, k, $l\pm1$ reflections. Since the space group of Mo_8O_{23} is $P2_1/c$, there are c-glide planes perpendicular to the b-axis. The fringes appearing in the two overlapping regions, which are related to each other by mirror operation about the c^*-axis, show a shift of a half period of the fringes as shown by white arrows in photograph (a).

The specimen in photograph (b) was sufficiently thick to show dynamical extinction due to c-glide symmetry, which is seen vertically at the middle of the $00l$ ($l=2n+1$) kinematically forbidden reflections. In the overlapping regions between neighbouring $00l$ ($l=2n$ and $2n+1$) reflection disks, the fringes at both sides of the dynamical extinction line clearly show a shift of a half period as indicated by white arrows.

These results reveal an antiphase relation between the structure factors of the $0kl$ and $0\bar{k}l$ reflections due to the c-glide plane perpendicular to the b-axis.

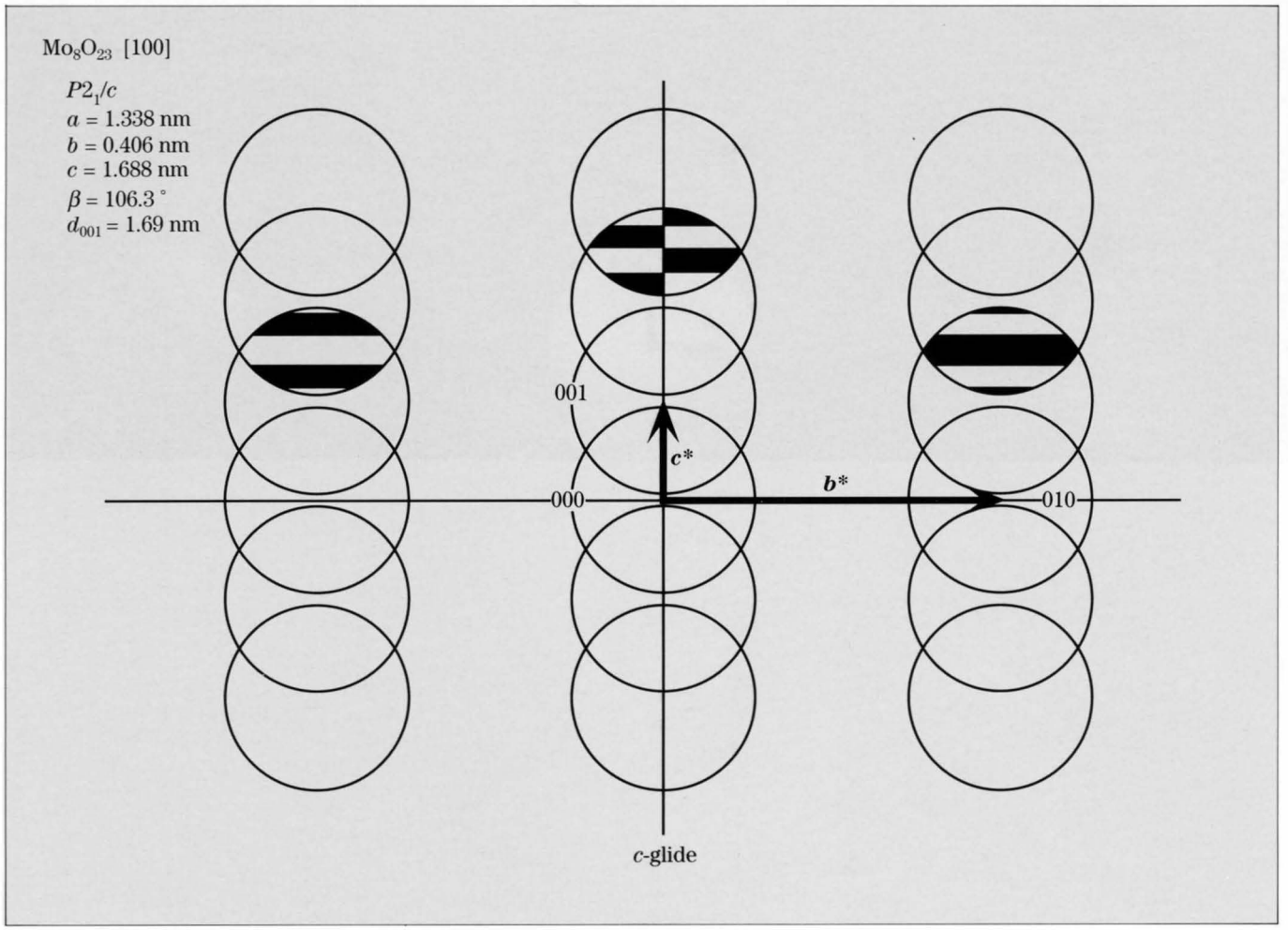

Mo_8O_{23} [100] d_{001}=1.69 nm 80 kV

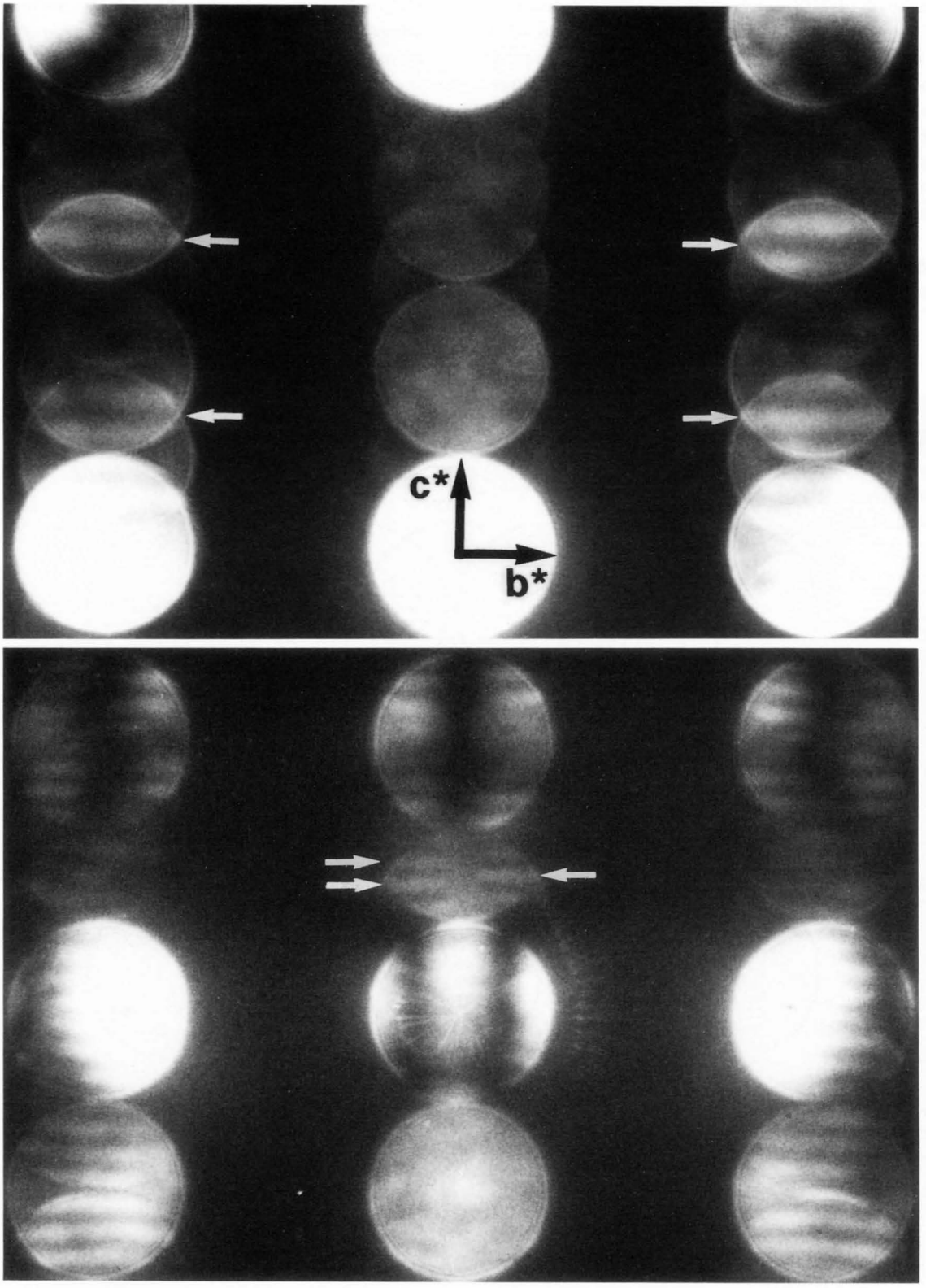

FeS_2

Photographs on the opposite page are coherent CBED patterns of FeS_2 taken with the [100] incidence at an accelerating voltage of 200kV. The fringes of a lattice spacing of 0.54nm are seen in the overlapping regions between the $0kl$ and $0, k, l\pm1$ reflections. Since the space group of FeS_2 is $Pa\bar{3}$, there are c-glide planes perpendicular to the b-axis. The fringes appearing in the two overlapping regions, which are related to each other by mirror operation about the c^*-axis, show a shift of a half period of the fringes as shown by black arrowheads in Photo (a).

The specimen for Photo (b) was sufficiently thick to show dynamical extinction due to a c-glide symmetry, which is seen horizontally at the middle of the $00l$ ($l=2n+1$) kinematically forbidden reflections. The fringes observed are not always perpendicular to the c^*-axis because of a strong dynamical diffraction effect among accidental reflections. In the overlapping regions between neighbouring $00l$ ($l=2n$ and $2n+1$) reflection disks, the fringes at both sides of the dynamical extinction line clearly show a shift of a half period as indicated by white arrowheads. Another example of FeS_2 for a large defocus is given on page 224.

These results reveal an antiphase relation between the structure factors of the $0kl$ and $0\bar{k}l$ reflections due to the c-glide plane perpendicular to the b-axis.

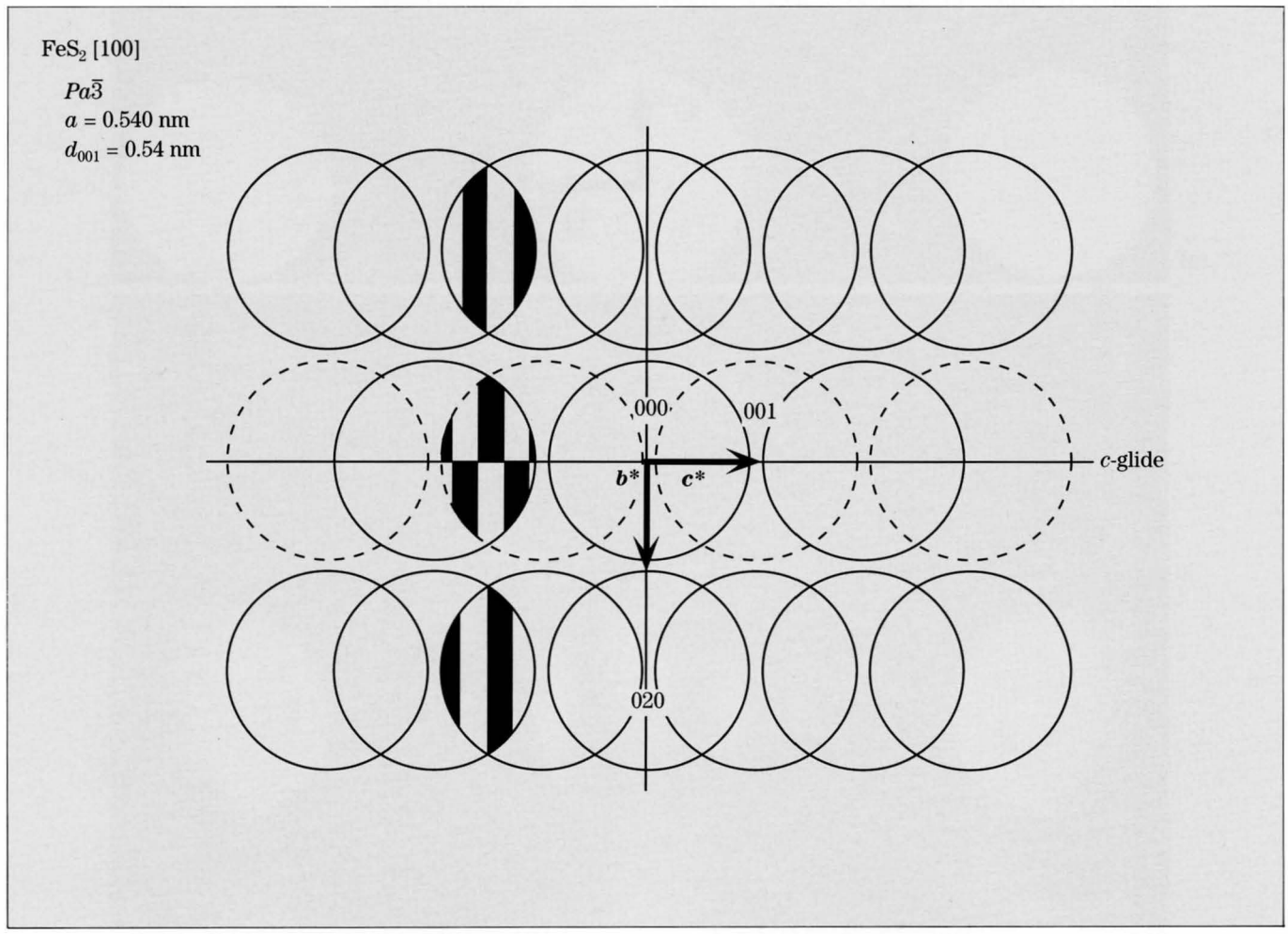

FeS_2 [100] d_{001}=0.54 nm **200 kV**

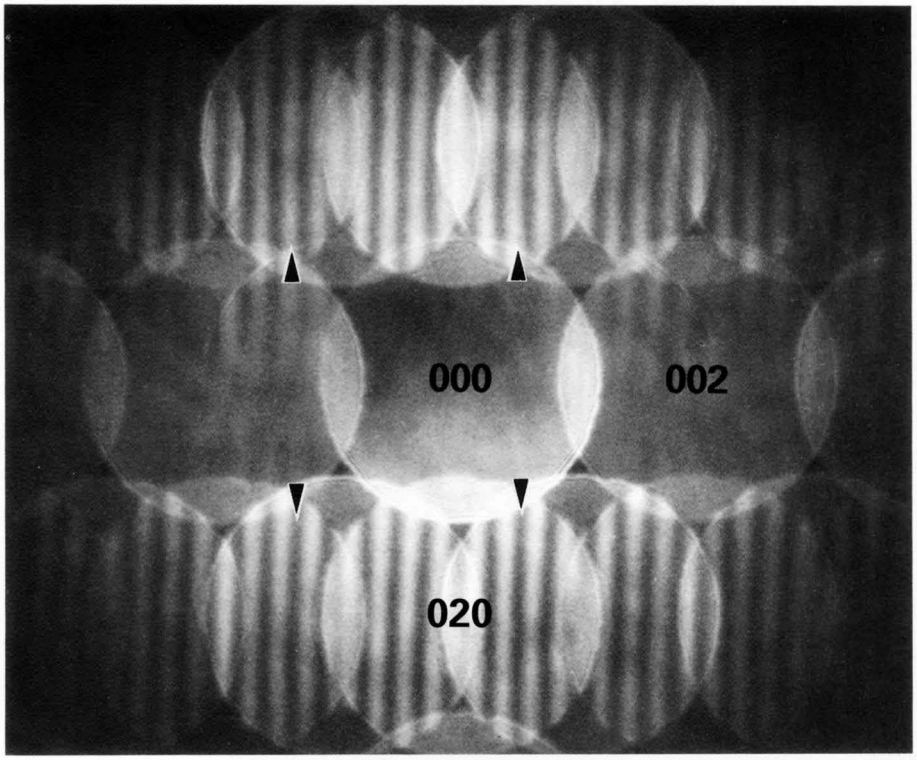

(a) Thin

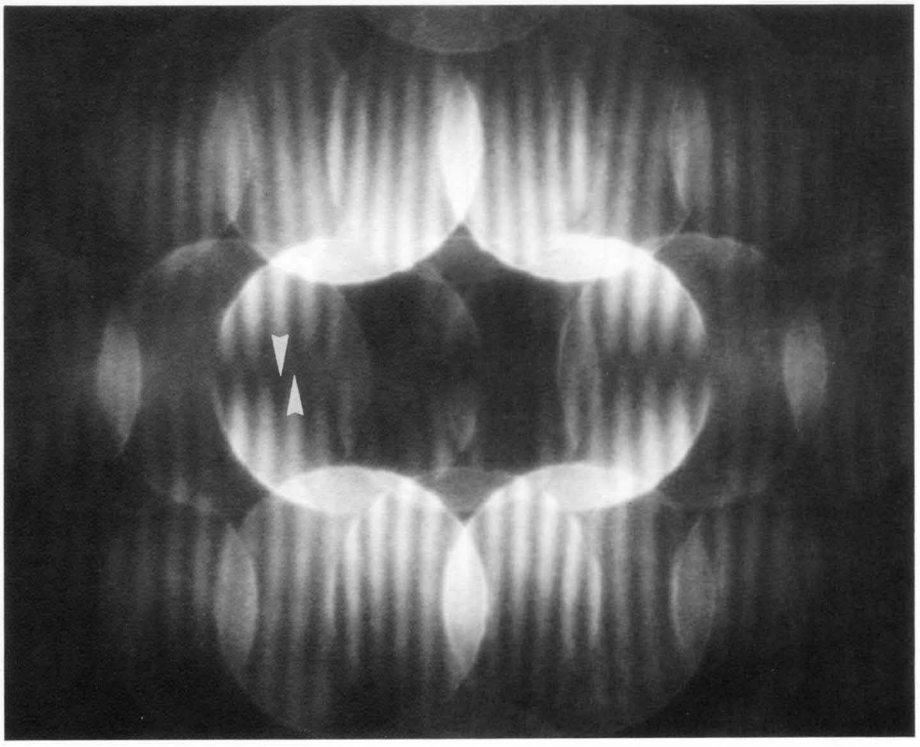

(b) Thick

FeS_2 [100] d_{001}=0.54 nm **200 kV**

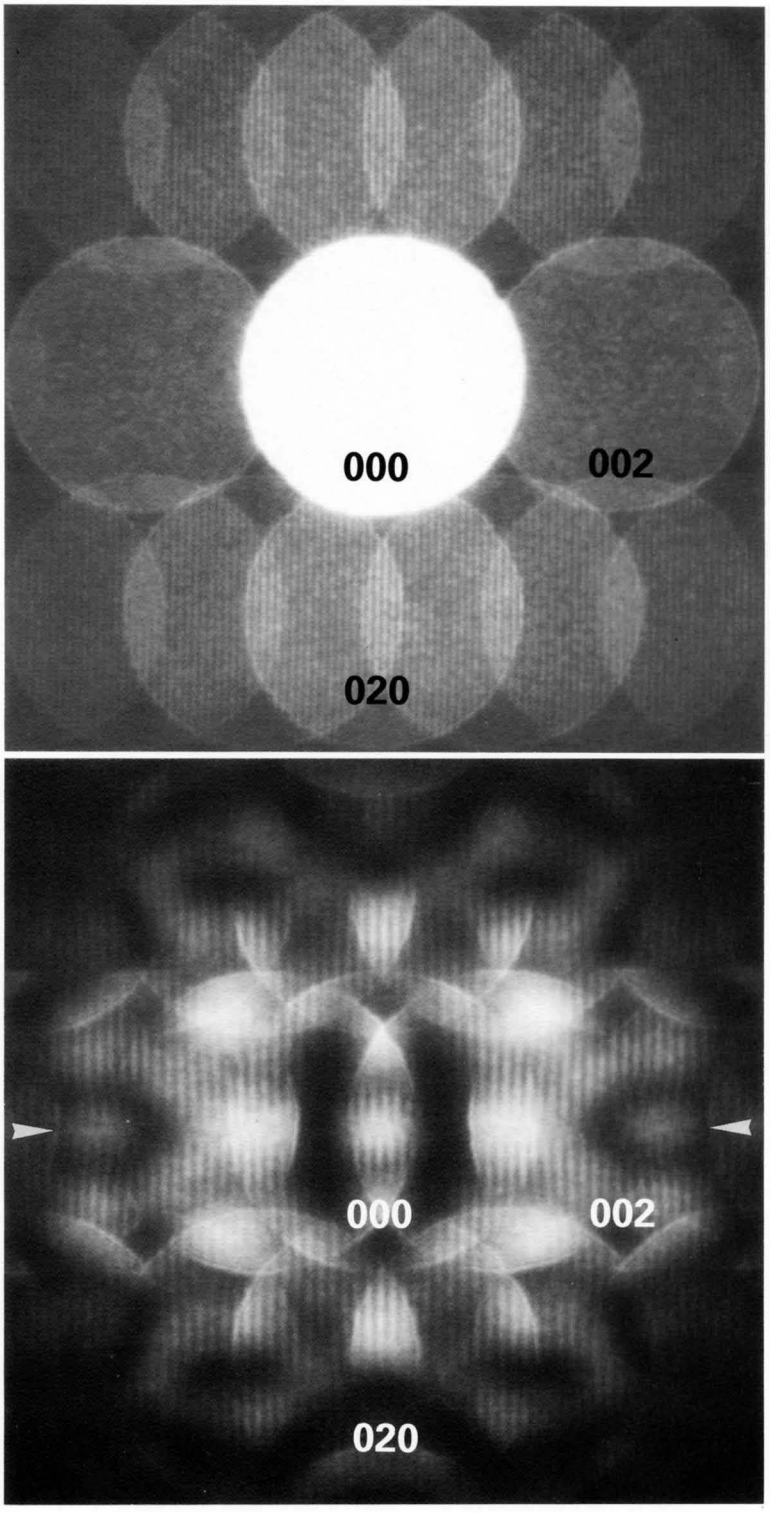

Thin

Thick

TiO_2 (rutile)

Photographs are coherent CBED patterns of TiO_2 taken with the [101] incidence at an accelerating voltage of 200kV. The fringes of a lattice spacing of 0.46nm are seen in the overlapping regions between the $\bar{h}kh$ and $\bar{h}$, $k \pm 1, h$ reflections. The fringes, which are related by mirror operation about the b^*-axis, show a half period shift as shown by black arrowheads in Photo (a). The shift is produced by a 2_1 screw axis parallel to the b-axis, which is a symmetry of the space group $P4_2/mnm$ of TiO_2. It should be noted that the projection in the [101] direction, of 2_1 screw operation parallel to the b-axis is equivalent to the b-glide plane perpendicular to the $[\bar{1}01]$ direction.

Photograph (b) was taken from a thick specimen area to show dynamical extinction due to a 2_1 screw symmetry, which is seen horizontally at the middle of the $0k0$ (k=$2n$+1) kinematically forbidden reflections.

The overlapping regions between neighbouring $0k0$ (k=$2n$ and $2n$+1) reflection disks exhibit the fringes, which clearly show a shift of a half period at both sides of the dynamical extinction line as indicated by white arrowheads.

[101] d_{010}=0.46 nm **200 kV**

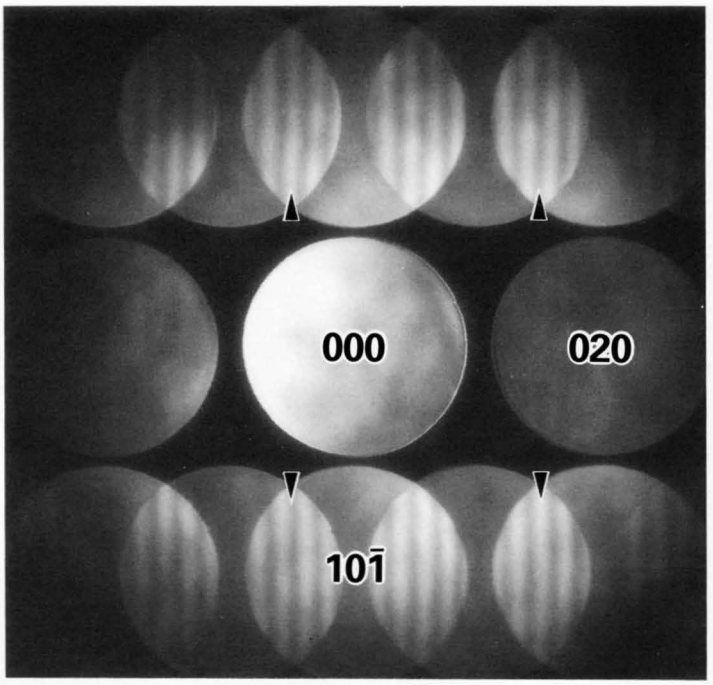

(a) Thin

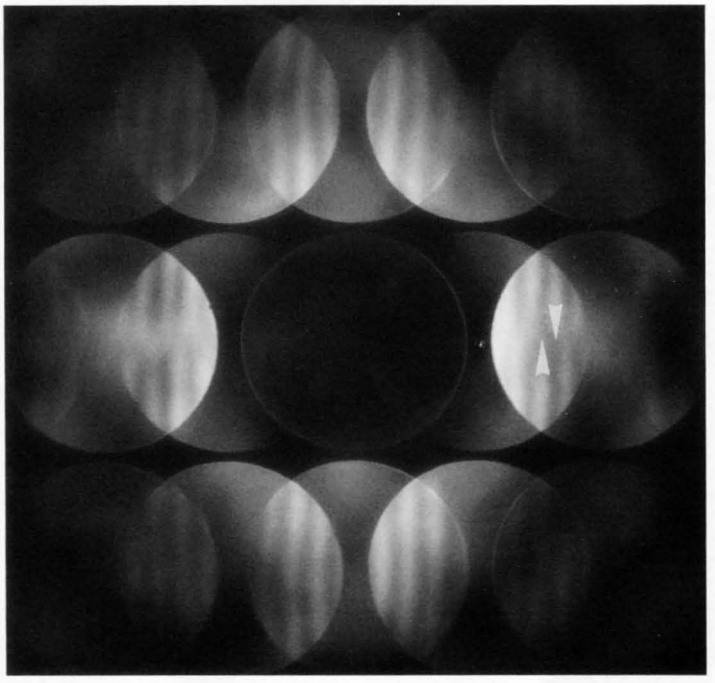

(b) Thick

$Sr_2Nb_2O_7$ [100] d_{020}=1.34 nm 80 kV

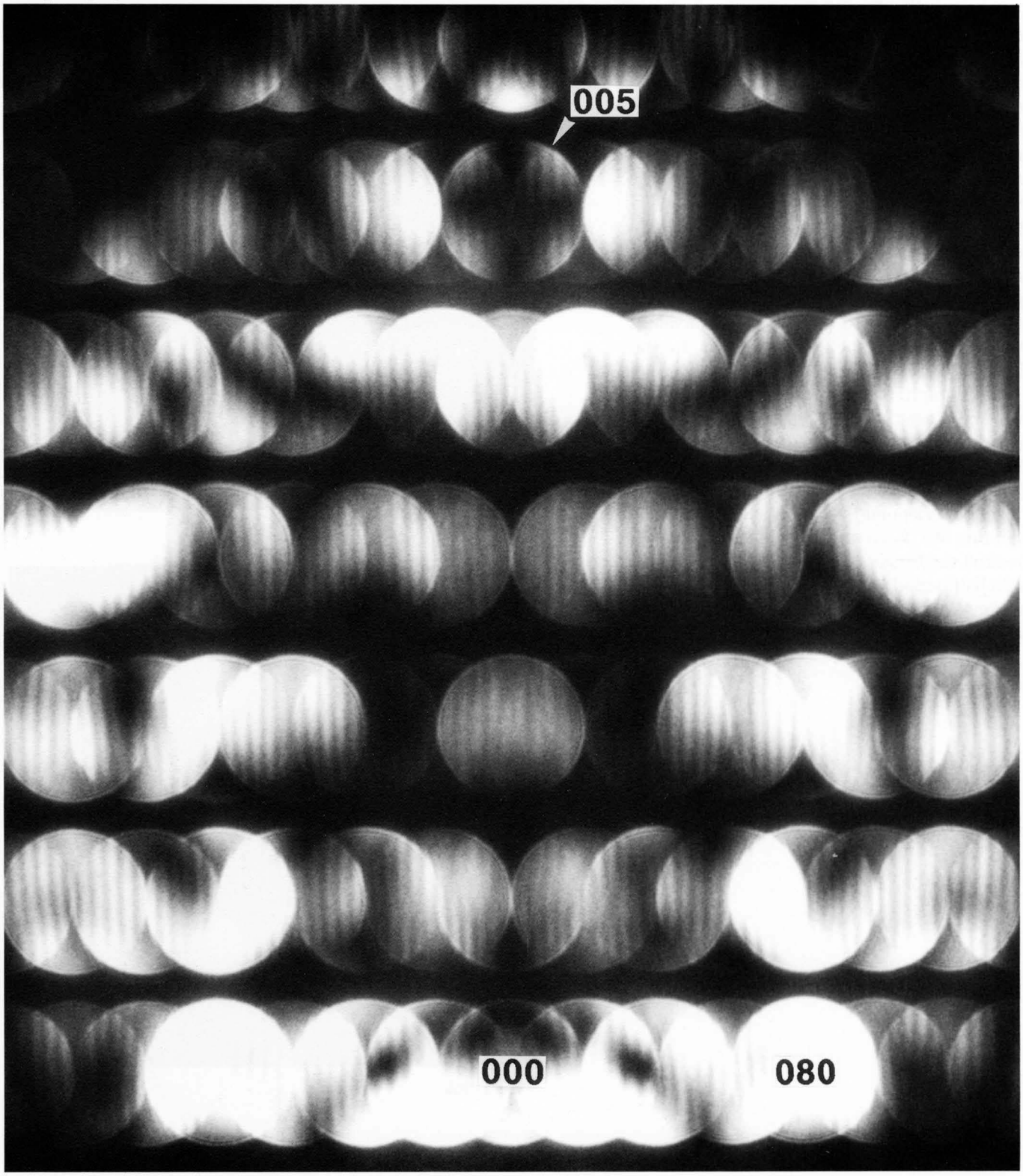

(a)

Photograph (a) on the opposite page shows a coherent CBED pattern of $Sr_2Nb_2O_7$ taken by exciting the 005 reflection with the specimen tilted from the [100] zone axis. Figure (a) explains that the fringes in a pair of overlapping regions exhibit neither mirror nor glide symmetry. We give a rule for what cases those symmetries appear between the fringes. When the sense of the difference vector $\boldsymbol{h=g-g'}$ between overlapping reflections, whose vectors are $\boldsymbol{g}$ and $\boldsymbol{g'}$, is not changed by operating a crystal symmetry, the symmetry appears at the relative positions of the fringes in the pair of overlapping regions connected by the crystal symmetry (see page 216-225).

Photograph (b) is an enlargement of the 005 reflection disk. An illustration of Photo (b) is given in Fig. (b). A cross consisting of GM lines A and B is seen in the disk. A half shift of the fringes appears across GM line B due to the c-glide plane and/or the 2_1 screw axis (projection approximation). The fringe shift (symmetry) across GM line B cannot be explained by the above rule because the symmetry is interpreted with the help of the reciprocity theorem. A shift of half the period across GM line A was seen accidentally, though no special positional relation is expected between the fringes across GM line A (as is clear from above rule).

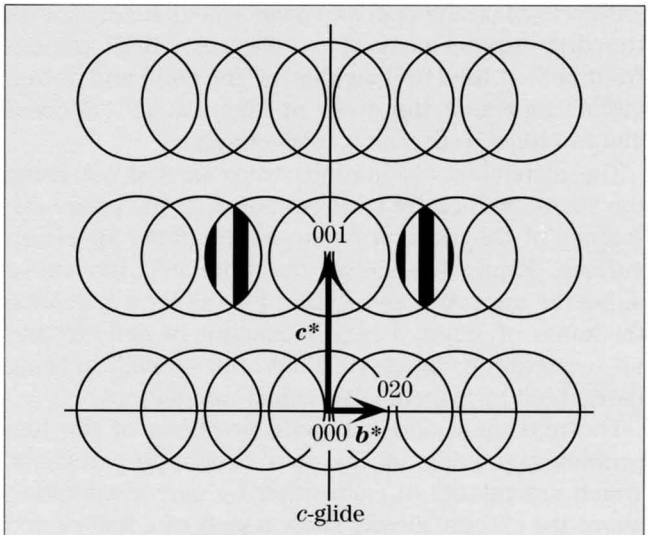

(a)

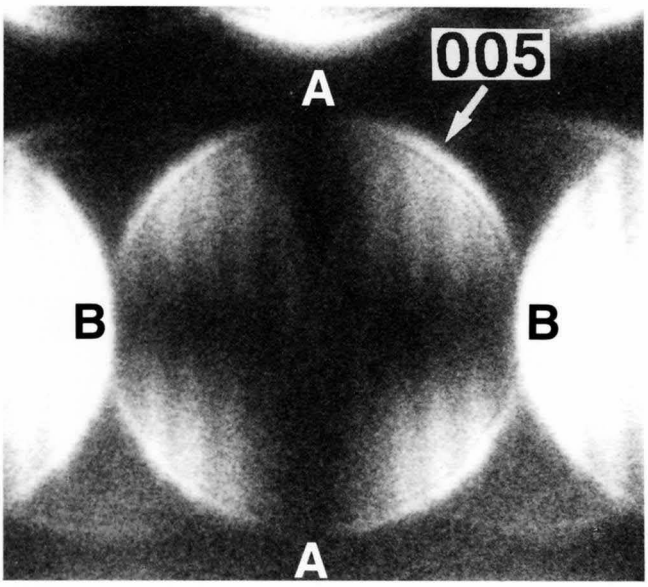

(b)

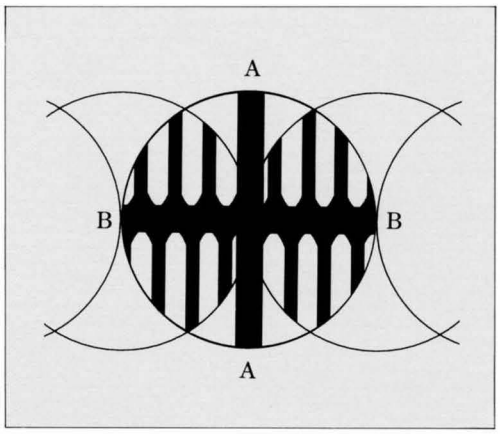

(b)

Dynamical Calculations

FeS_2

Figure (a) on the opposite page schematically shows the disk arrangement of a coherent CBED pattern from FeS_2 at the [100] incidence. The solid and dotted circles represent the disks of kinematically allowed and forbidden reflections, respectively.

The dynamical calculations were carried out using the Bethe method by taking account of the phase difference of the incident beams at the upper specimen surface. Figure (b) shows the simulated intensities along the lines A-A and B-B in Fig.(a) for a specimen thickness of 10nm, a certain amount of defocus and an accelerating voltage of 200kV, the simulation being carried out by 59-beam dynamical calculations.

The maximum and minimum positions of the line profiles appearing in the two overlapping regions, which are related to each other by mirror operation about the c^*-axis, clearly show a shift of a half period of the fringes along the c^*-axis. The shift is a result of the antiphase relation between the structure factors of $0kl$ and $0\bar{k}l$ reflections due to the c-glide symmetry in the b-plane. The peaks in an overlapping region are different in intensity, indicating an appreciable dynamical diffraction effect.

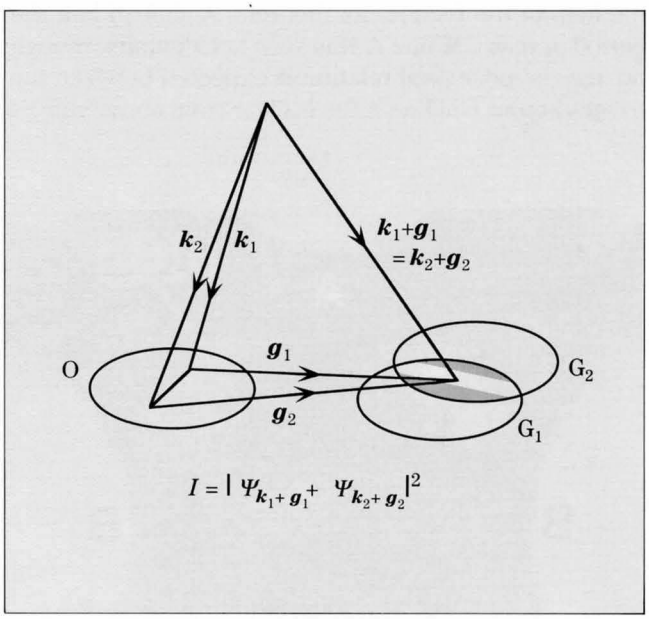

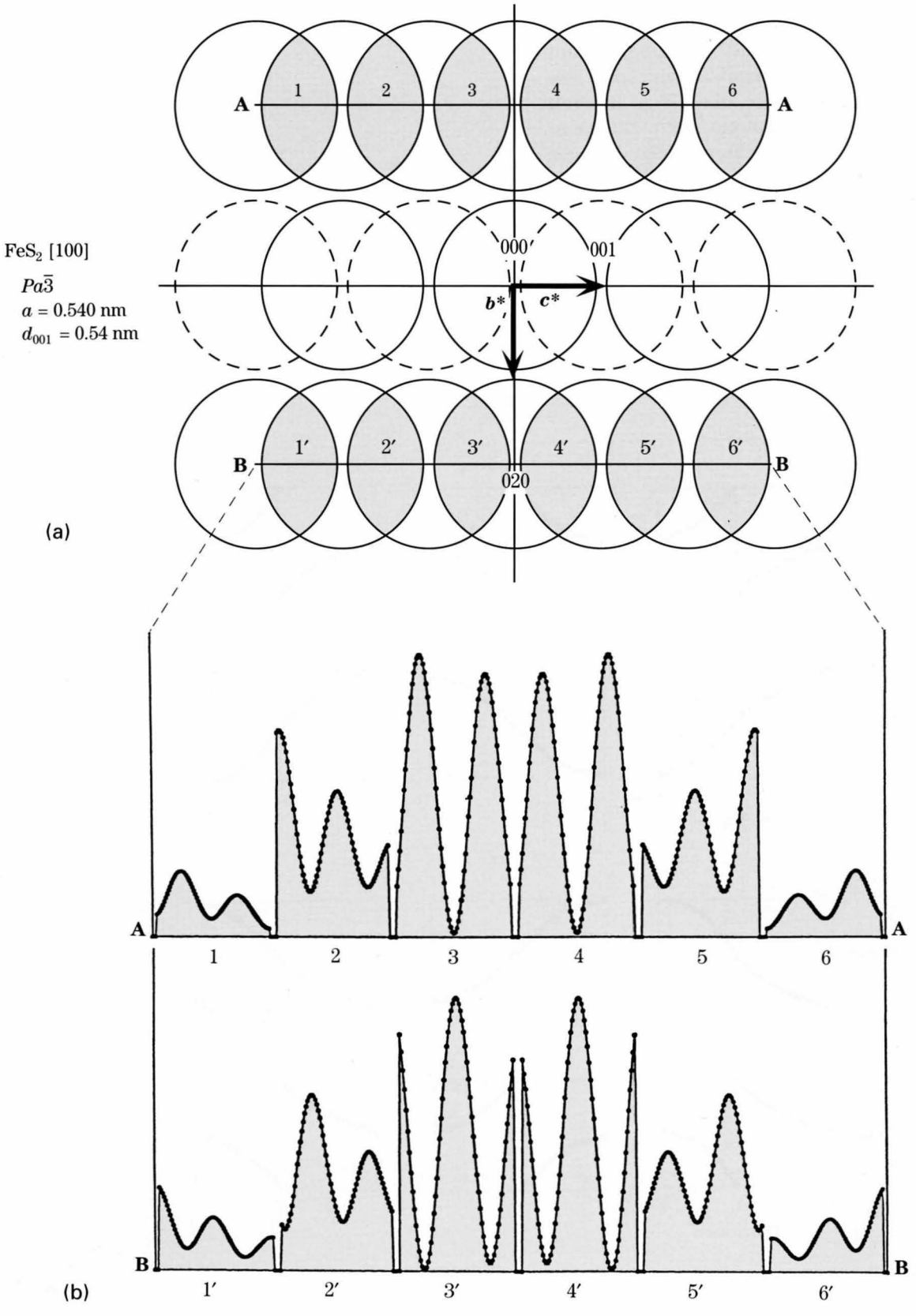
FeS2 [100]
Pa3̄
a = 0.540 nm
d001 = 0.54 nm
A
1
2
3
4
5
6
A
000′
001
b*
c*
B
1′
2′
3′
4′
5′
6′
B
020
(a)
A
1
2
3
4
5
6
A
B
1′
2′
3′
4′
5′
6′
B
(b)

FeS_2

Figure (c) shows the thickness dependence of the phase difference between neighbouring reflections. The relative phases between areas 1, 2, 3, 4, 5 & 6 and 1′, 2′, 3′, 4′, 5′ & 6′ in Fig. (a), respectively, are π irrespective of thickness. However, the phase in every overlapping area quickly changes with thickness. Even at a thickness of 10nm, the calculated fringes cannot be explained by the phase of the kinematical structure factor.

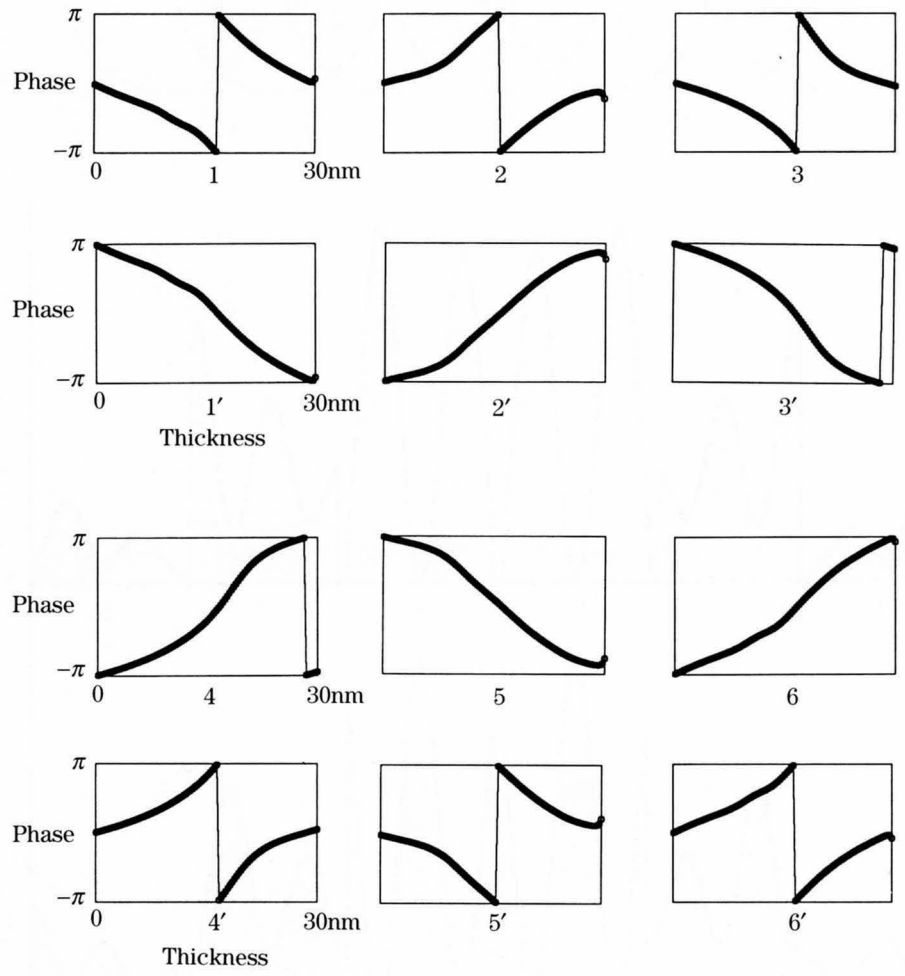

(c)

SiC

Figure (a) shows a schematic disk arrangement of a coherent CBED pattern for 6H-SiC at the [$\bar{2}$110] incidence. The solid and dotted circles represent the disks of kinematically allowed and forbidden reflections, respectively. Figure (b) shows the simulated intensities along the lines A-A and B-B in Fig. (a) for a specimen thickness of 10nm, a certain amount of defocus and an accelerating voltage of 100kV, the simulation being carried out by 31-beam dynamical calculations. The maximum and minimum positions of the line profiles shift a half period of the fringes as a result of the antiphase relation between the structure factors of $01\bar{1}l$ and $0\bar{1}1l$ reflections.

Figure (c) shows the thickness dependence of the phase difference between neighbouring reflections. The relative phases between areas 1-8 and 1′-8′, respectively, are π irrespective of thickness. It should be noted that the calculated fringes for 6H-SiC are explained by the phase of the crystal structure factor up to a thickness of about 15nm because of its small crystal potential.

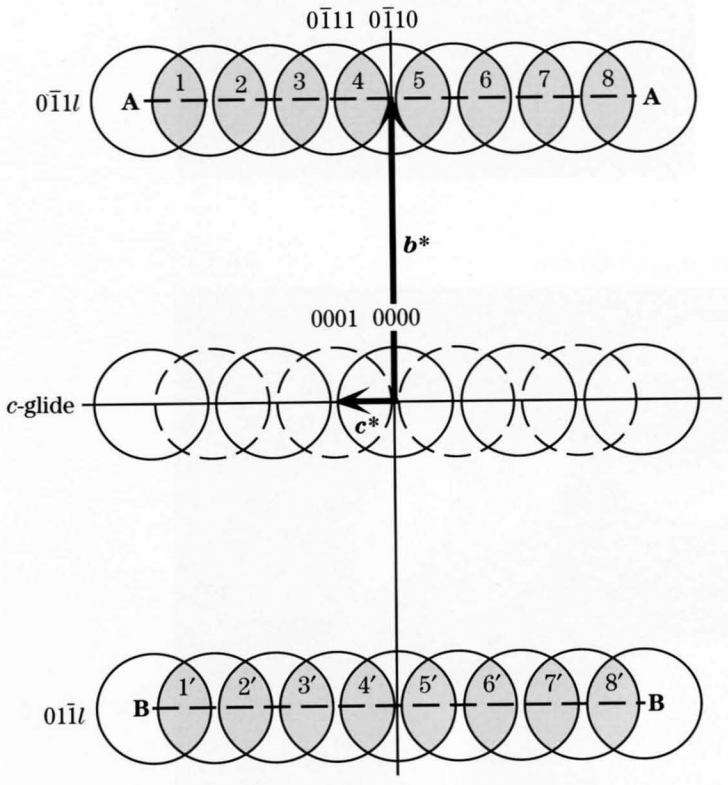

(a)

6H-SiC [2$\bar{1}\bar{1}$0]

$P6_3mc$
a = 0.308 nm
c = 1.301 nm
d_{0001} = 1.30 nm

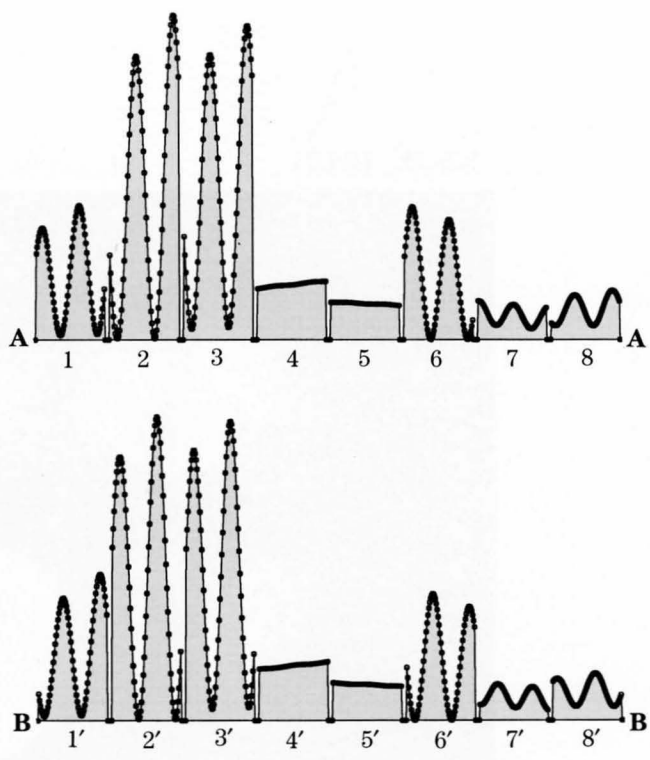

(b)

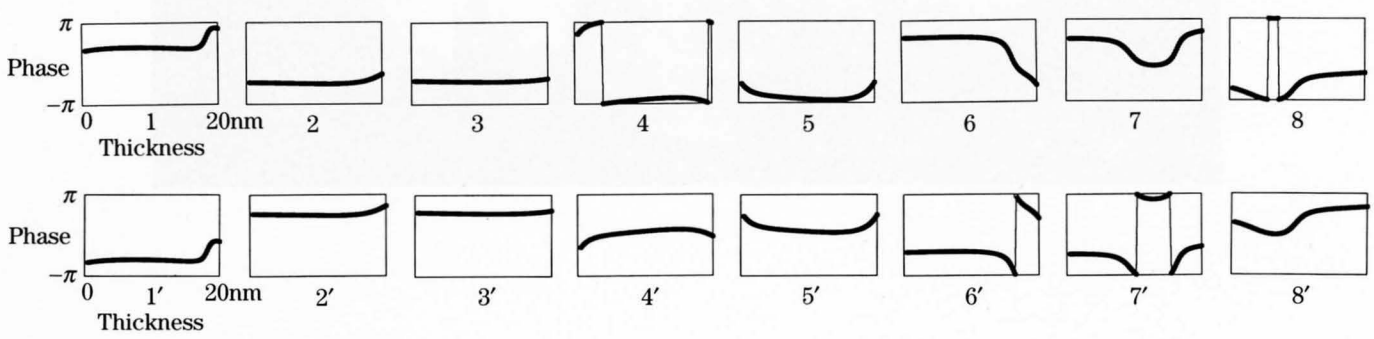

(c)

Two-Dimensional Fringes

Two-dimensional interference fringes are seen when three nonsystematic reflection disks are overlapped. Those fringes are shown for Nb_2O_5, FeS_2, TiO_2, a quasicrystal of $Al_{65}Pd_{20}Mn_{15}$ and Si.

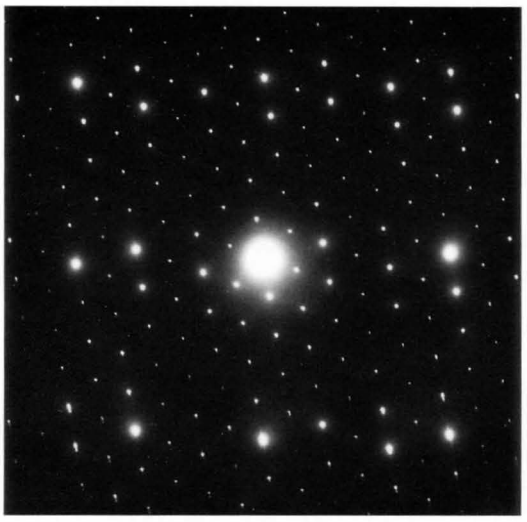

Nb_2O_5 [010] d_{100}=1.84 nm, d_{001}=1.68 nm **80 kV**

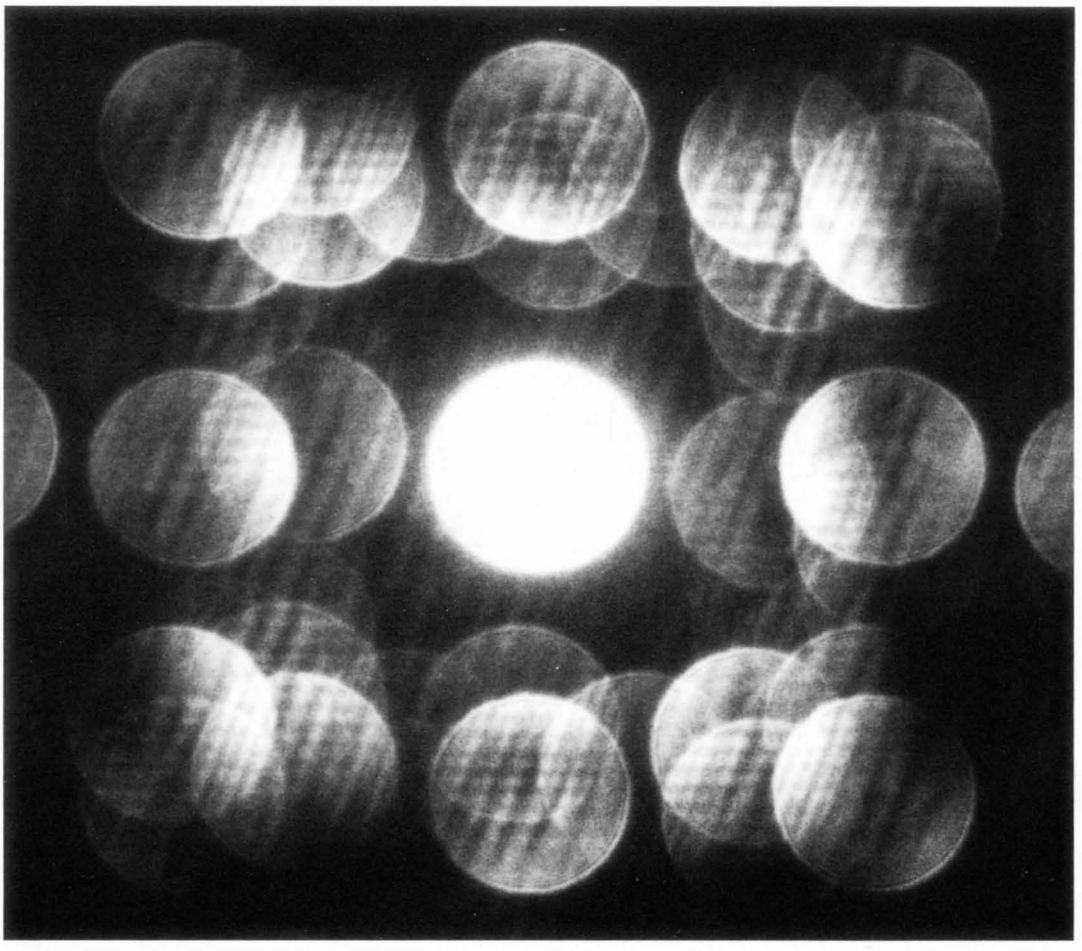

FeS_2 [111] $d_{10\bar{1}}$=0.31 nm **200 kV**

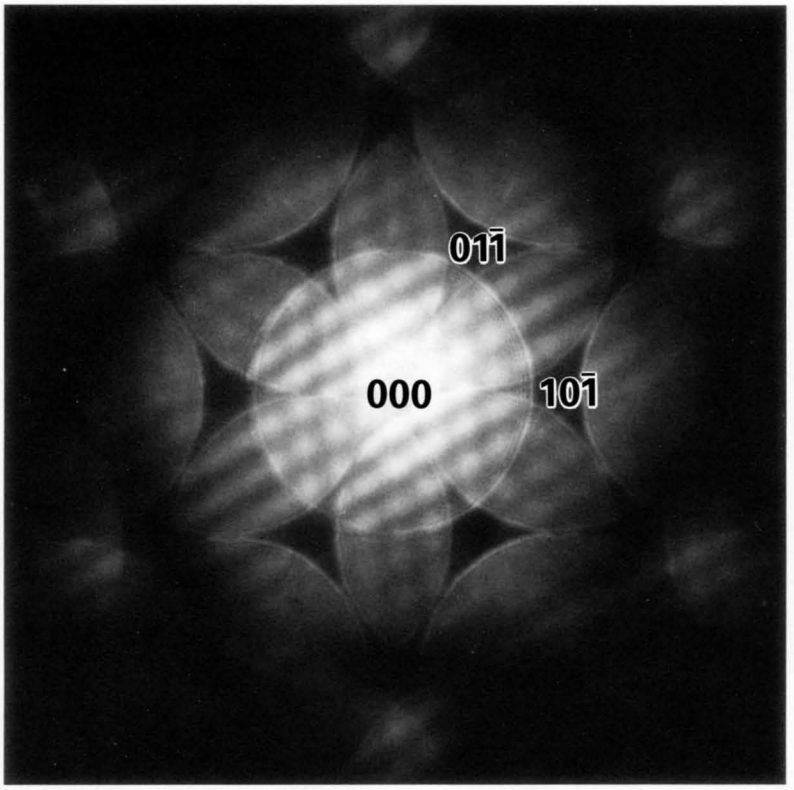

TiO_2 [111] $d_{1\bar{1}0}$=0.33 nm, $d_{10\bar{1}}$=0.25 nm **200 kV**

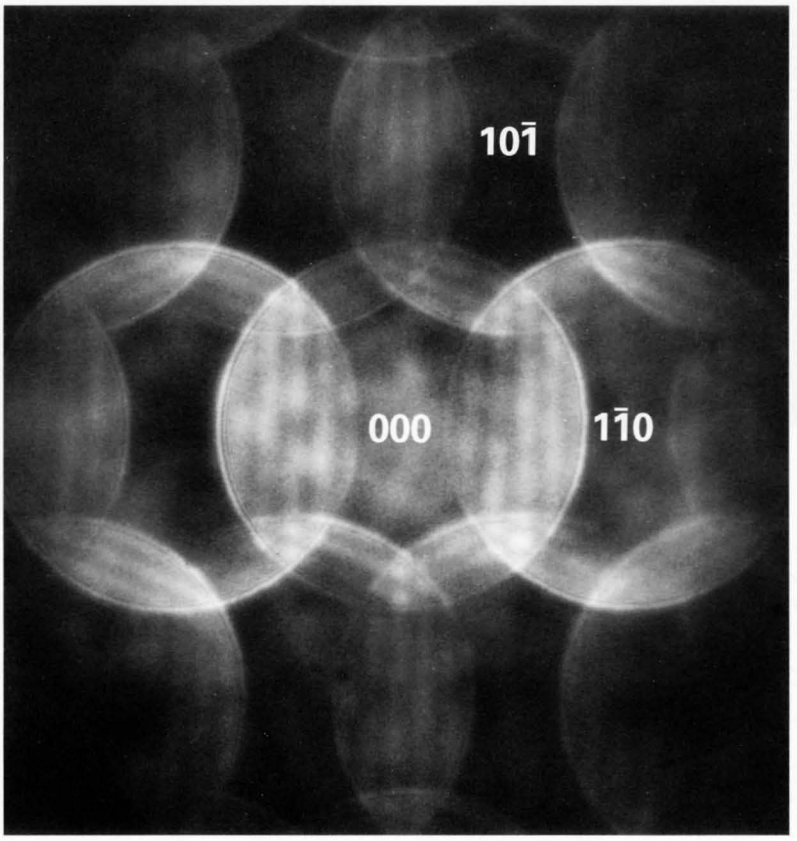

Quasicrystal — $Al_{65}Pd_{20}Mn_{15}$, fivefold axis — 100 kV

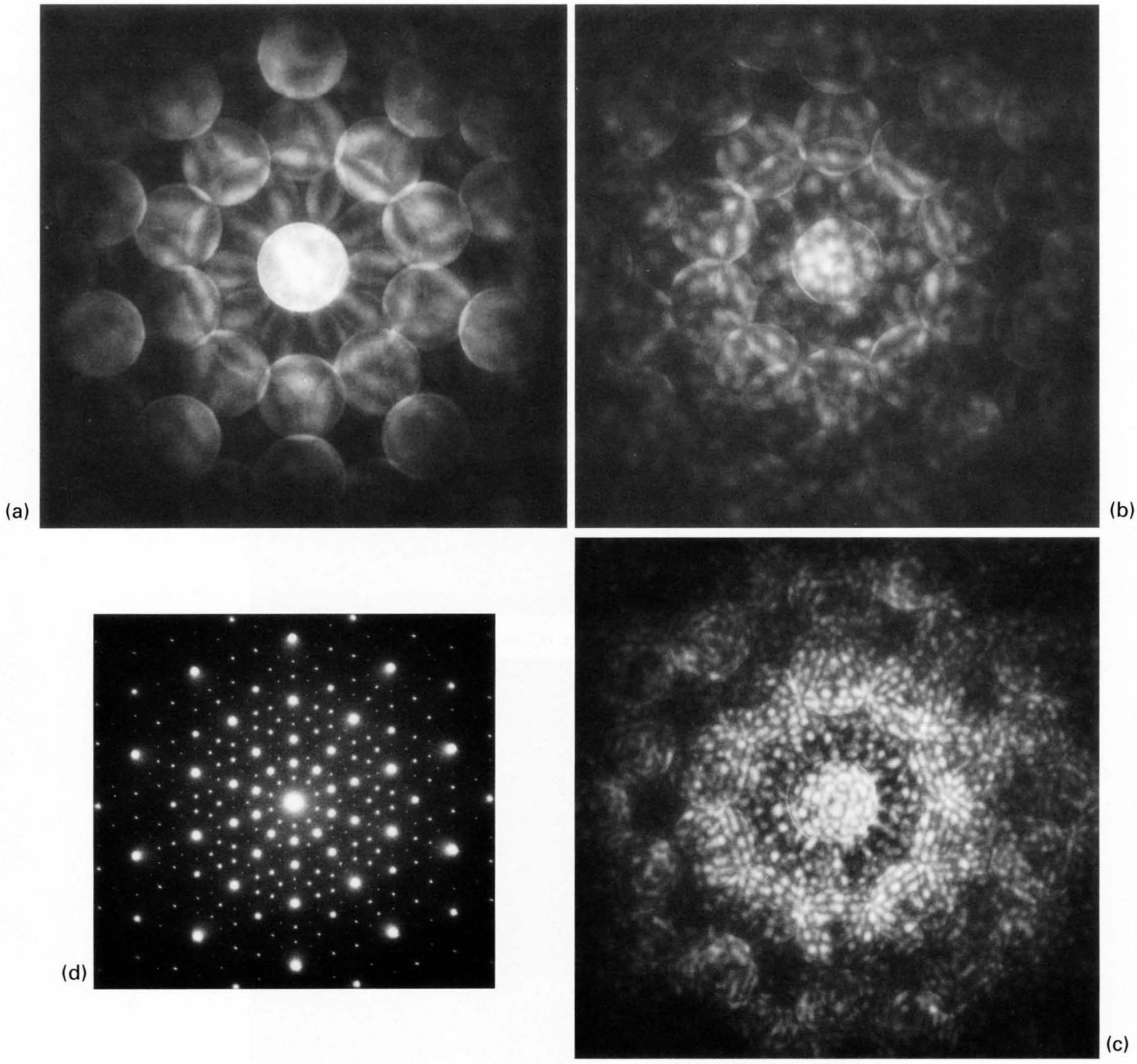

Coherent CBED patterns (a), (b) and (c) of an icosahedral quasicrystal $Al_{65}Pd_{20}Mn_{15}$ taken at an incidence along the fivefold axis with three different amounts of defocus, a selected area diffraction pattern (d) being attached.

Si [110] $d_{\bar{1}11}$=0.314 nm, d_{002}=0.271 nm **200 kV**

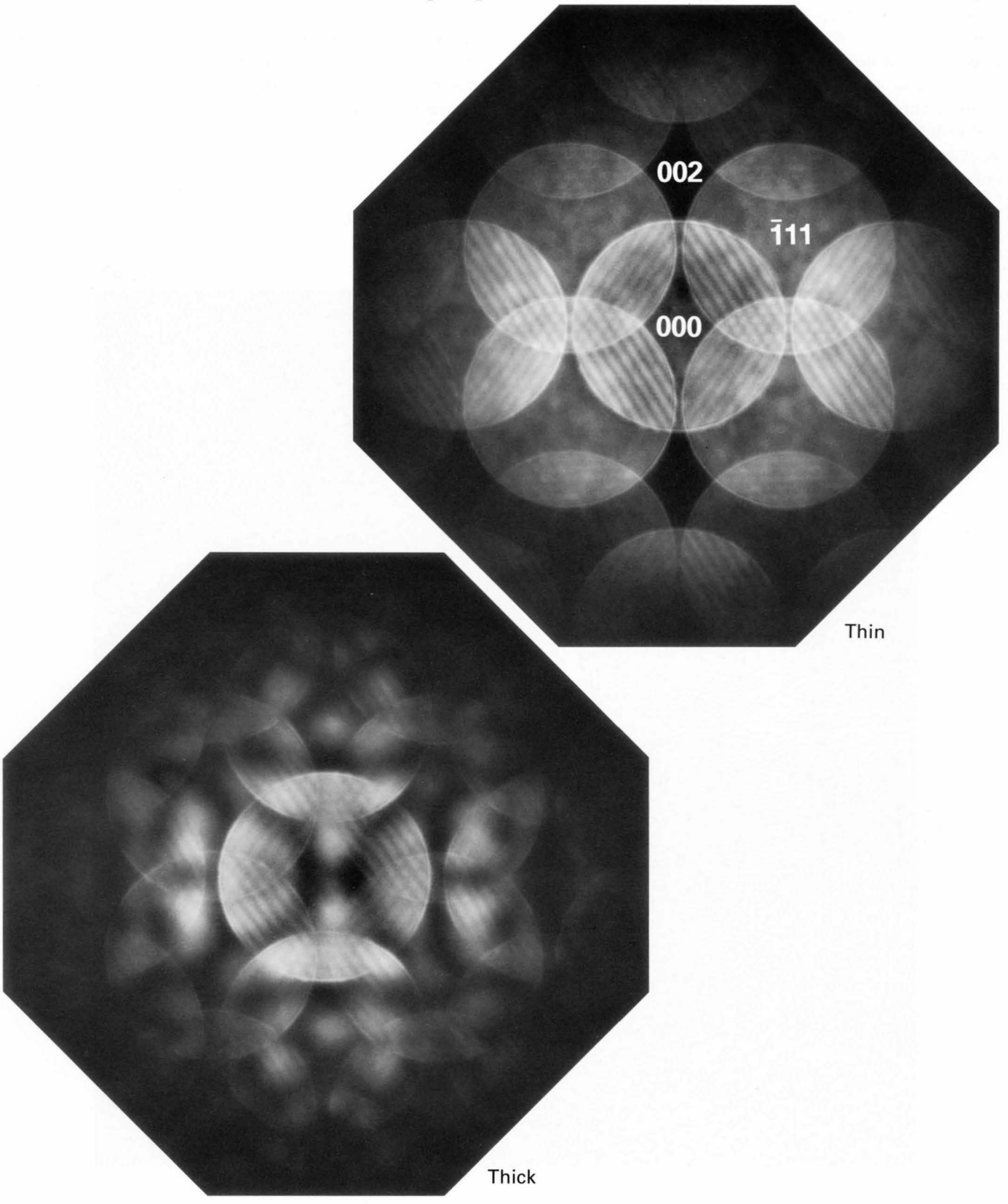

Thin

Thick

Fringes in HOLZ Reflections

Interference fringes should appear in overlapping regions of HOLZ reflections when the fringes are seen in ZOLZ reflections. The photograph is a coherent CBED pattern of $Sr_2Ta_2O_7$ taken with the [100] incidence at an accelerating voltage of 80kV. The convergence angle of the incident beam was adjusted to observe the fringes of a 1.36nm lattice spacing of the 020 reflection. The fringes clearly appear in the overlapping regions of HOLZ reflections, of which the enlargements being shown in the insets.

Simultaneous observation of the symmetries of the fringes appearing in HOLZ and ZOLZ reflections enables the distinction between a twofold axis and a mirror plane. The fringes in HOLZ reflections can give the phases of the crystal structure factors even for thicker specimens because HOLZ reflections are less dynamical than ZOLZ reflections.

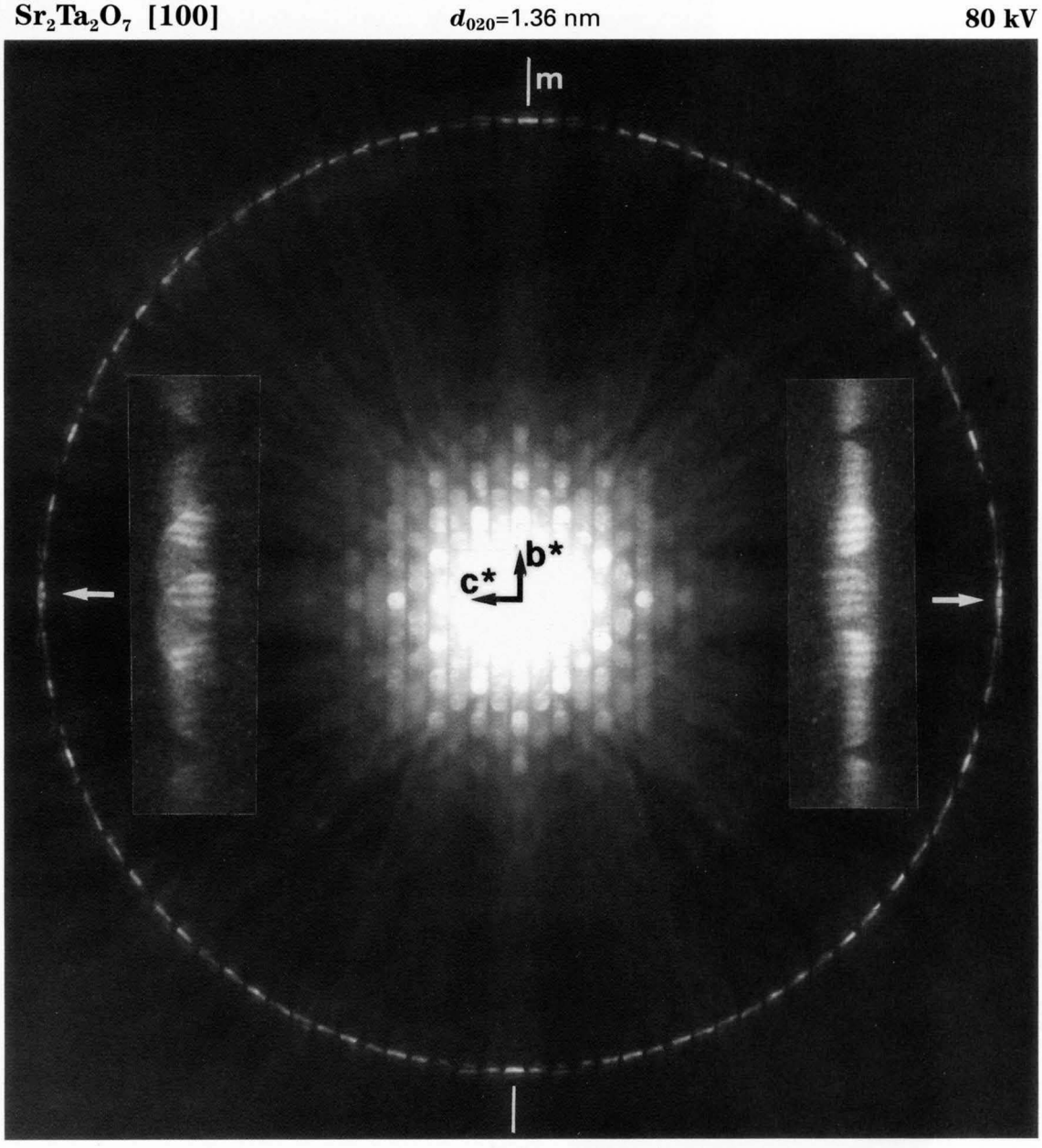

Fringes of Small Lattice Spacings

The fringes with a lattice spacing of 0.54nm appear in the overlapping regions between 0 2 l and 0, 2, $l\pm1$ reflections, which are arranged exactly perpendicular to the c^*-axis. In the overlapping regions between 0 0 l and 0 2 l ($l=2n$) reflections, the fringes (indicated by arrowheads) corresponding to a lattice spacing of 0.27nm are seen.

FeS_2 [100] d_{001}=0.54 nm, d_{020}=0.27 nm **200 kV**

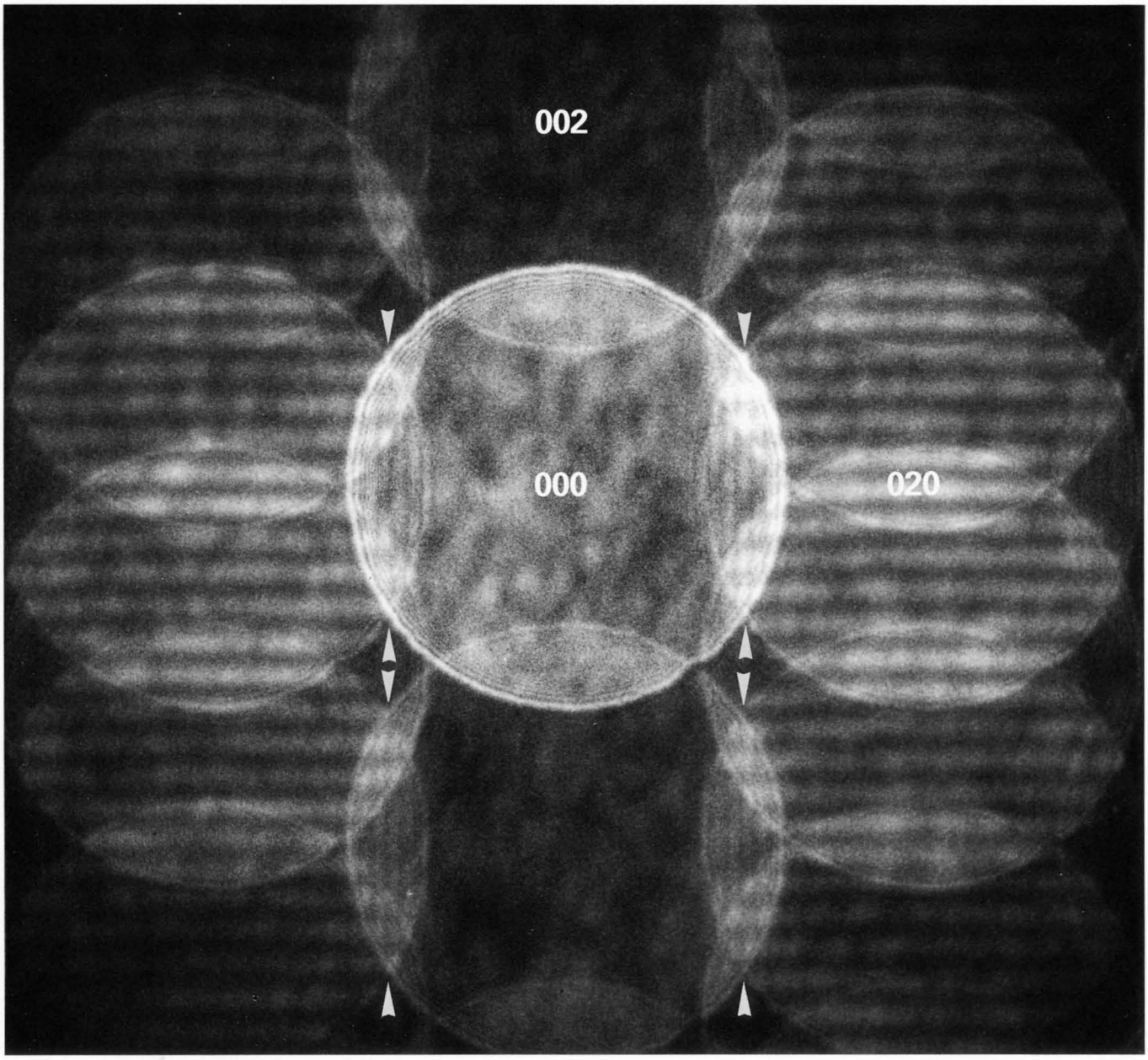

Graphite [0001] $d_{10\bar{1}0}$=0.21 nm **200 kV**

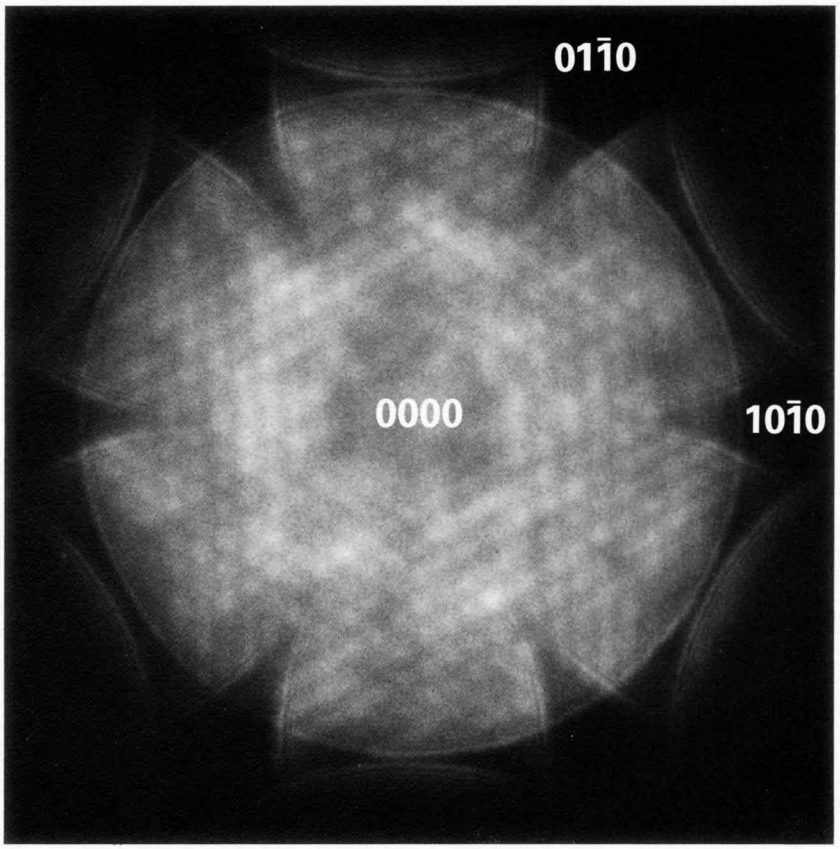

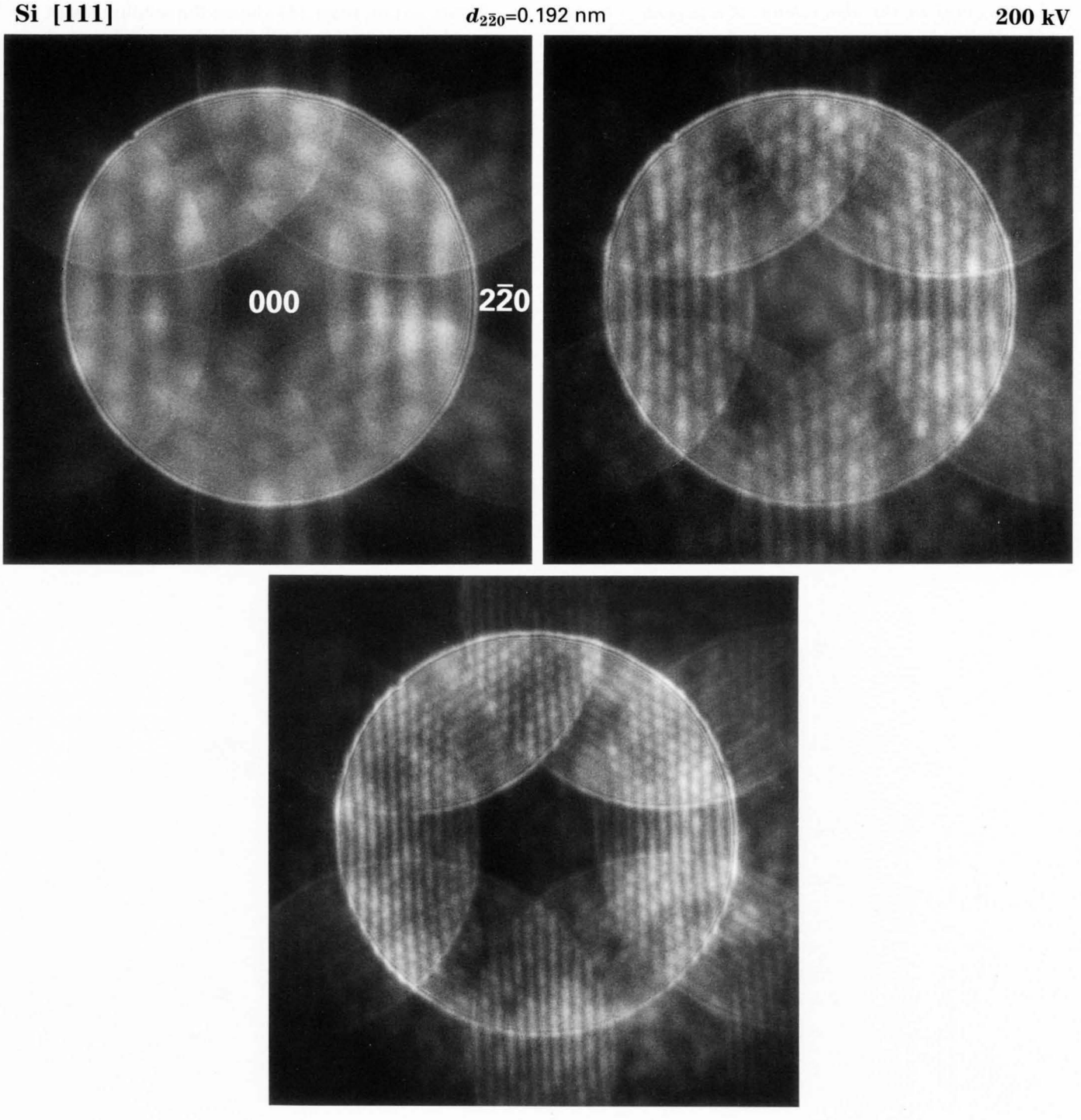

Coherent CBED patterns of Si taken with the [111] incidence at an accelerating voltage of 200kV for three different defocuses. A lattice spacing of 0.192nm is seen in the three directions. The spacing is the smallest one observed—a world record until August 1994.

Effect of Beam Size

Let us consider the observation of a periodic object using probes of different shapes and sizes. The object is expressed by a function $(\cos\pi x)^2$ as shown in Fig.(a). The probe functions are assumed to be Gaussian in shape with full widths at half maximum (FWHM) of 0.2-2.0 times the period of the object, and are normalized to 1 in their areas. Convolutions of $(\cos\pi x)^2$ and the Gaussian probes are shown in Figs. (b) to (g) on the opposite page. When the FWHM of the probe function reaches the period of the object, the amplitude of the convolution decreases rapidly.

Figures (h), (i) and (j) on page 242 show the convolutions of $(\cos\pi x)^2$ and Lorentzian (k), Gaussian (l) and rectangular probes (m) having the same FWHM of unity. The periodicity of $(\cos\pi x)^2$ is still seen for the Lorentzian probe but hardly seen for the rectangular probe.

Figure (n) on page 243 shows the amplitudes of the convolutions of $(\cos\pi x)^2$ and three different functions. The convolution with the Lorentzian probe has the smallest amplitude for FWHMs of less than unity because of a large tail of the probe, but has an absolutely small but the largest amplitude among the three probes at FWHMs larger than unity because the Lorentzian probe is the sharpest in shape of the three probes at the peak region.

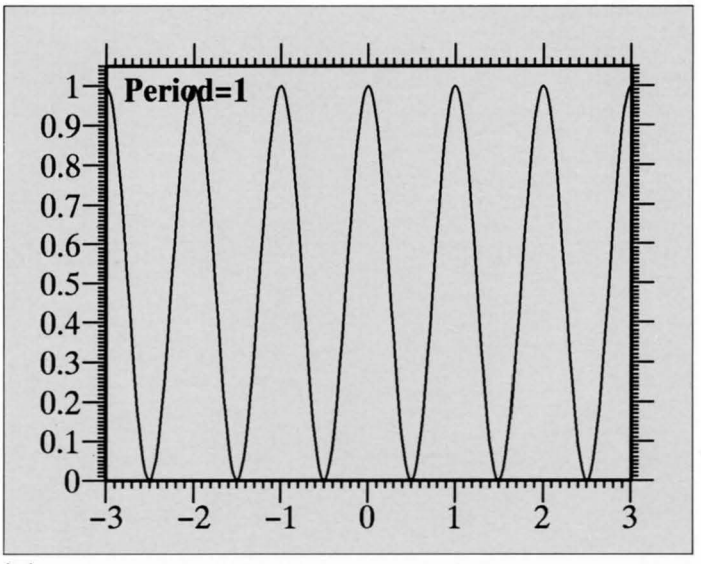

(a)

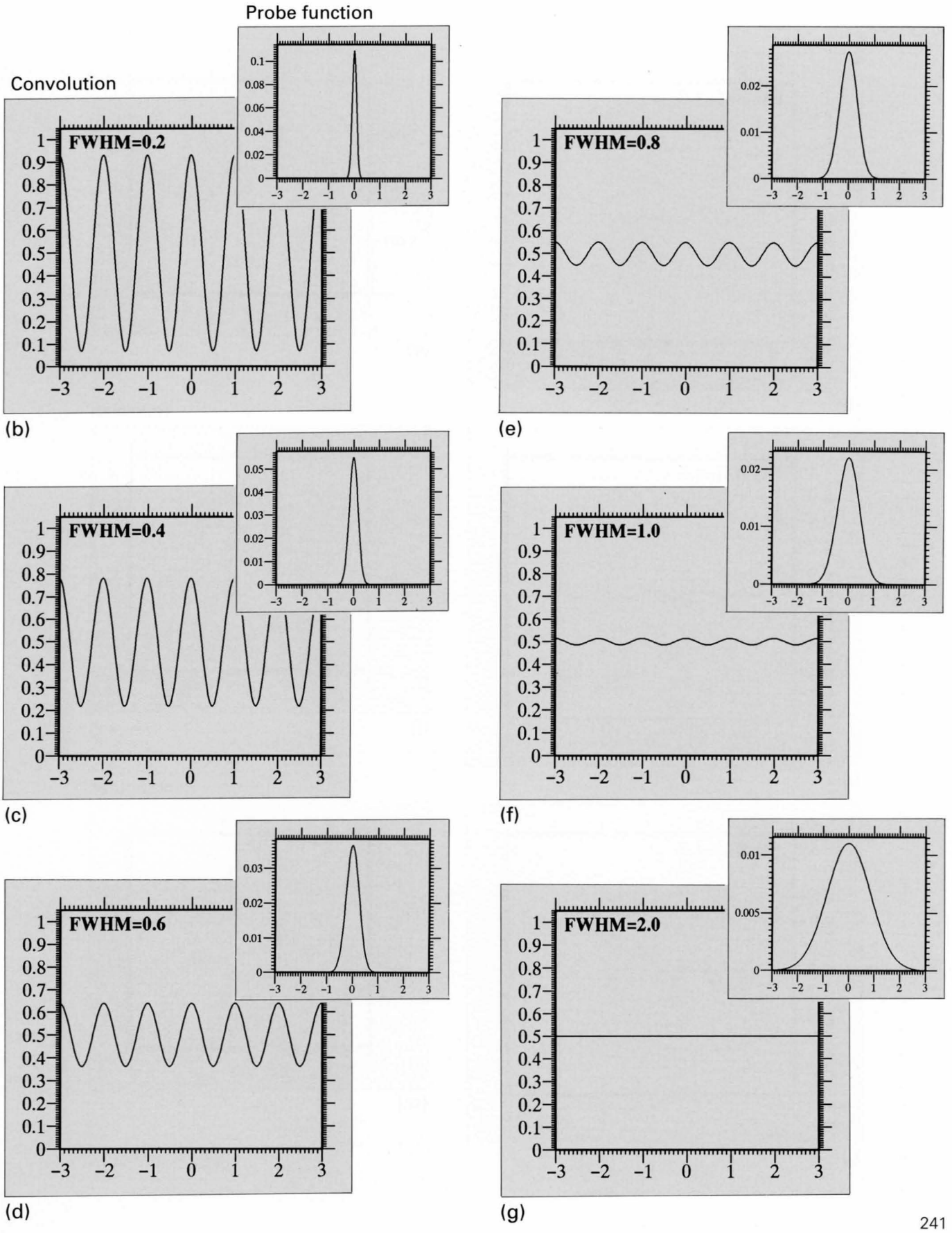
Probe function
Convolution
FWHM=0.2
(b)
FWHM=0.8
(e)
FWHM=0.4
(c)
FWHM=1.0
(f)
FWHM=0.6
(d)
FWHM=2.0
(g)

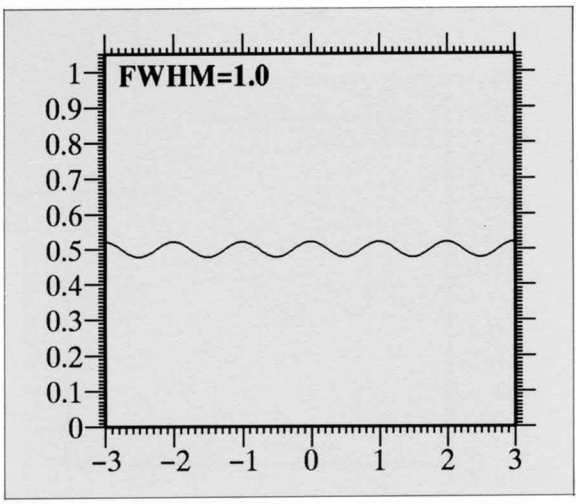

(h)

Lorentzian

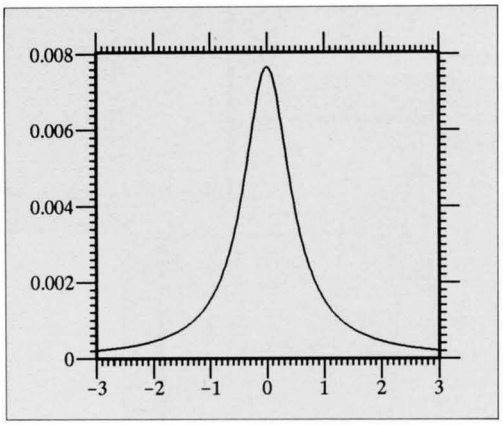

(k)

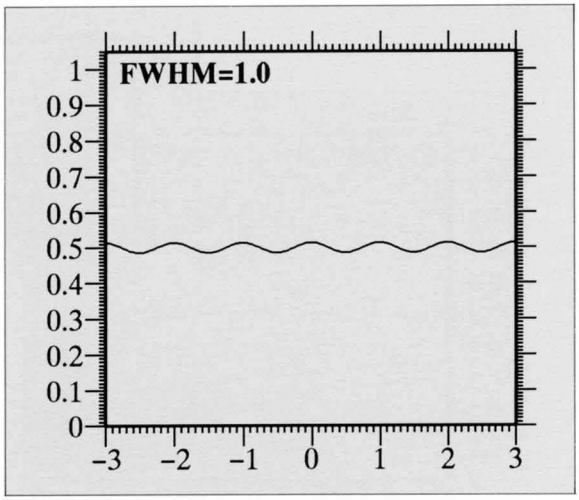

(i)

Gaussian

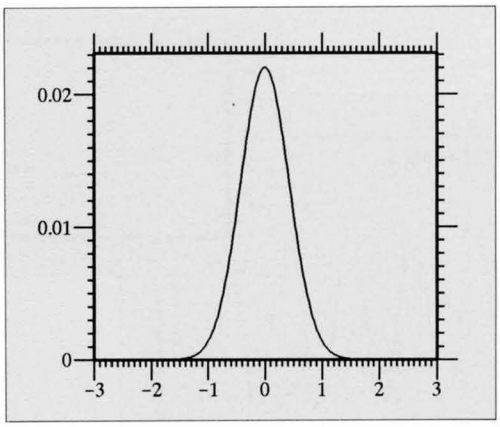

(l)

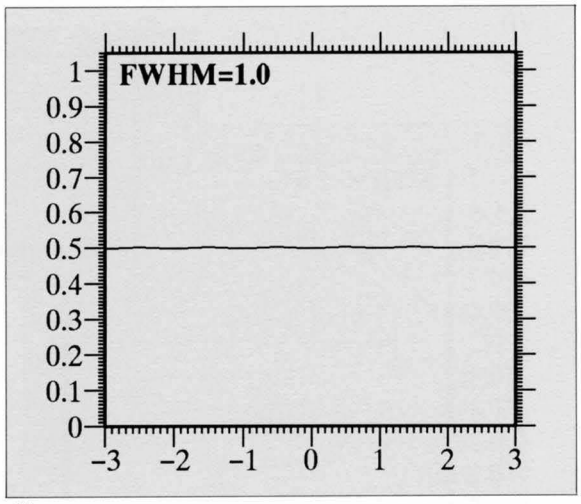

(j)

Rectangular

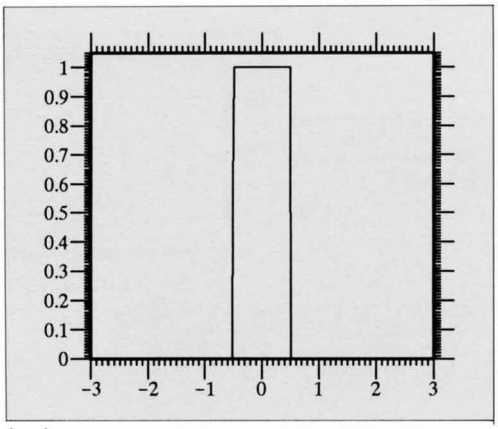

(m)

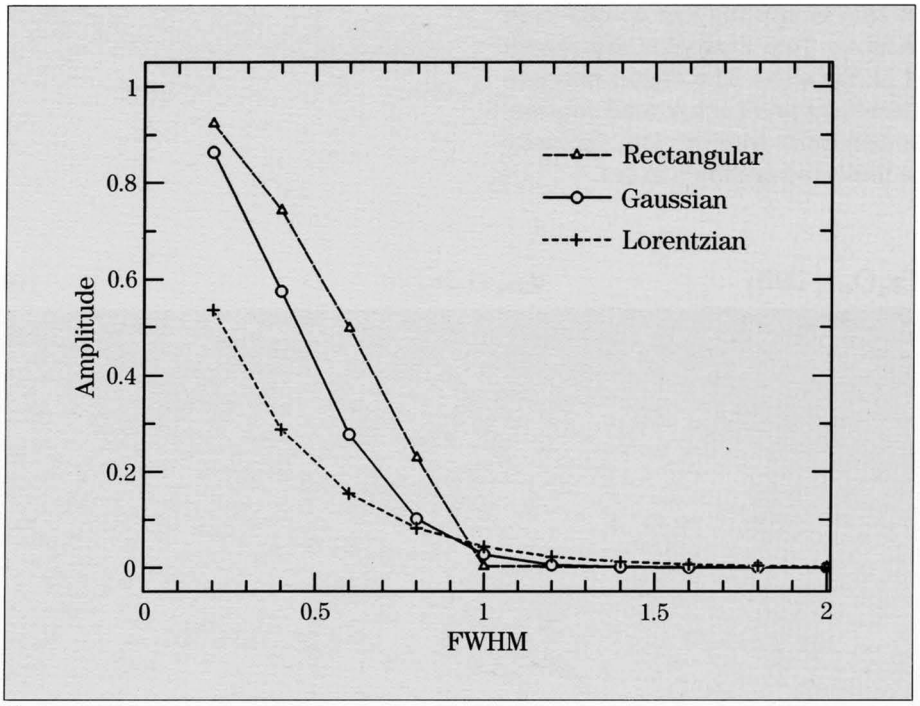
Amplitude
FWHM
Rectangular
Gaussian
Lorentzian
0
0.2
0.4
0.6
0.8
1
0
0.5
1
1.5
2

(n)

LaB_6 Source

Use of an LaB_6 electron source and a photographic film makes it difficult to take coherent CBED patterns from crystals with lattice spacings of about 1nm because of the low brightness of the source and the low sensitivity of the film. However, when the patterns are recorded on imaging plates and followed by digital image processing, the interference fringes corresponding to about 1nm in spacing can be observed by using the LaB_6 source. Two examples are shown for $Sr_2Ta_2O_7$ (a) and $La_2Ti_2O_7$ (b). Digital data processing in contrast enhancement and background subtraction elucidated the coherent fringes. The intensity profile along the line indicated is shown in (c).

$Sr_2Ta_2O_7$ [100] d_{020}=1.36 nm **100 kV**

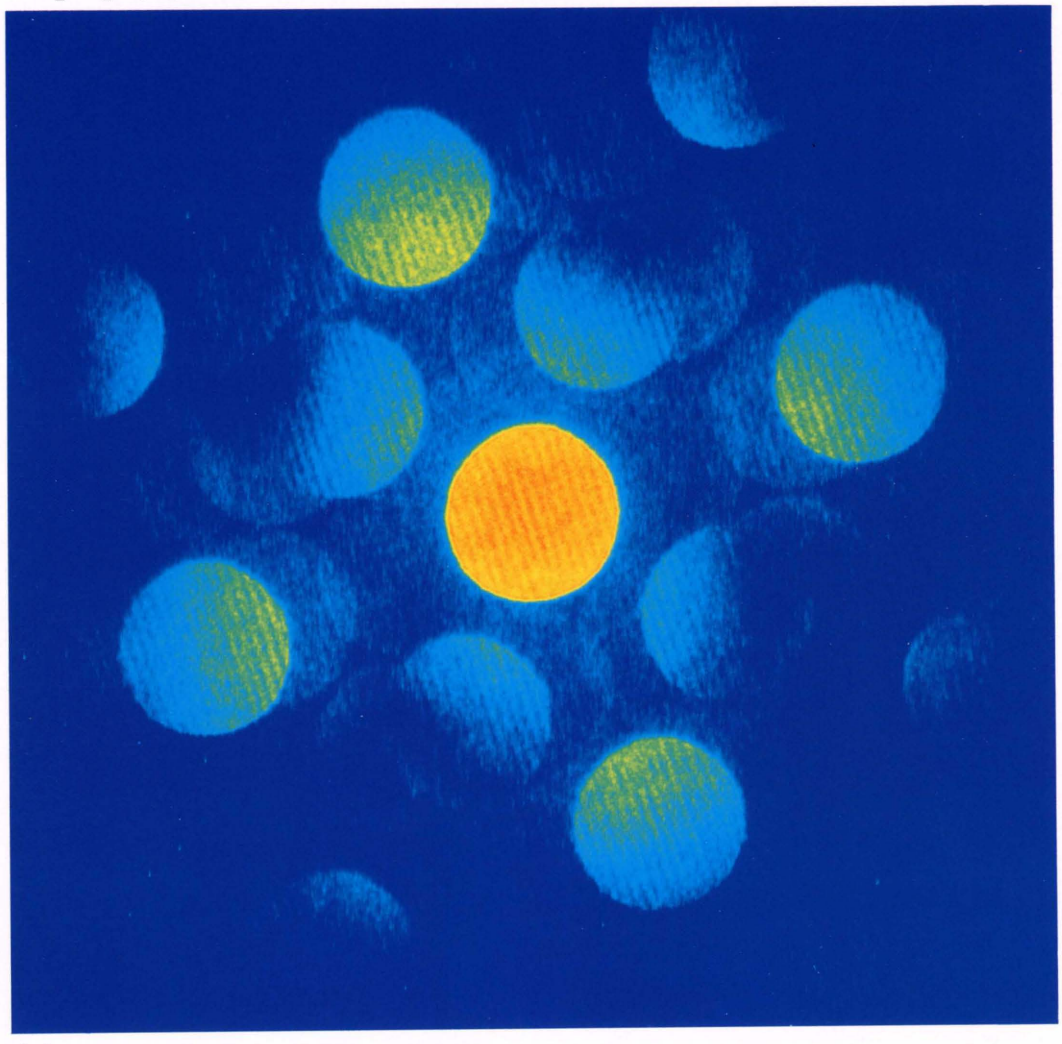

(a)

$La_2Ti_2O_7$ [100] d_{010}=1.30 nm 100 kV

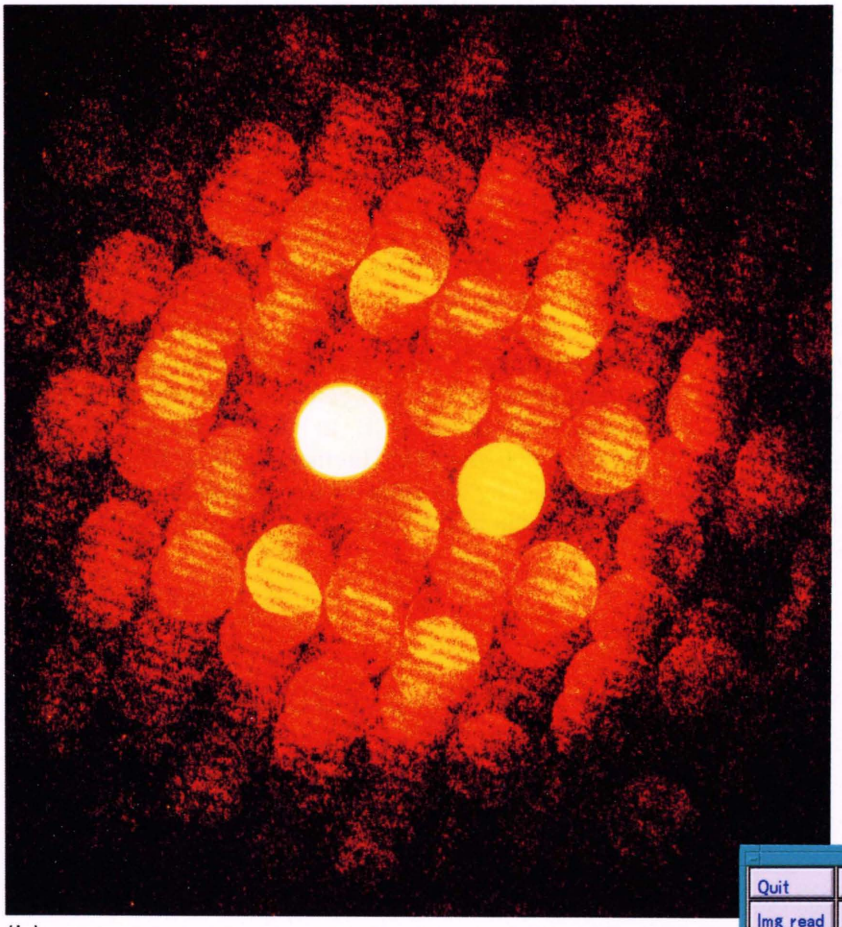

(b)

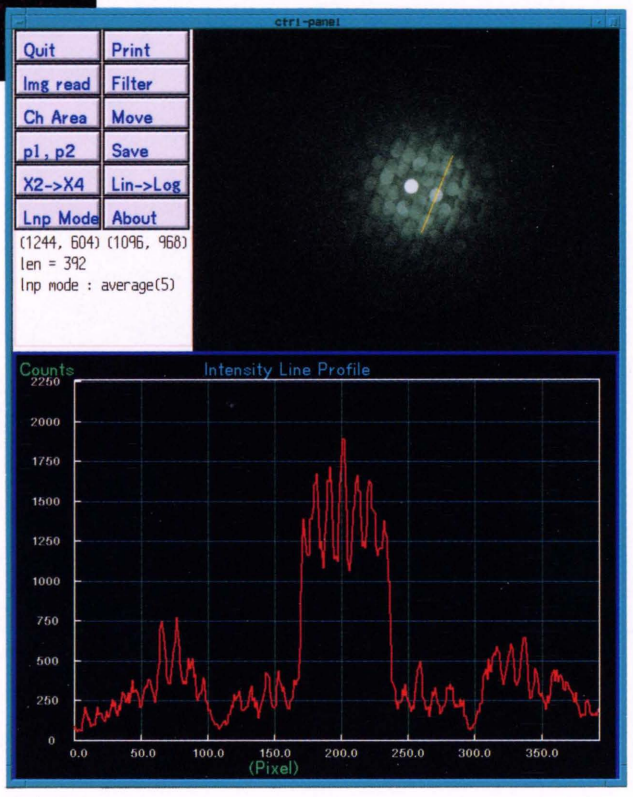

(c)

Lattice Defects

Stacking fault

Various applications of coherent CBED are possible for imperfect crystals. There are two ways of observing planar defects: plan view and side view observation. The former is the Moirè technique. We show side view observation of a stacking fault by coherent CBED.

Figure (a) shows a geometry between a defocused convergent beam and a stacking fault (S.F.) in a specimen. Shadow images of the fault are drawn by solid lines in the CBED disks. Figure (b) shows two overlapping disks, G_1 and G_2. The parts above the fault lines in the two disks (l_1 in disk G_1 and l_2 in disk G_2) are produced from the left side of the fault in the specimen and the parts below are produced from the right side. Thus, the three regions are formed in the overlapping region. That is, the first (upper: l_1+l_2) region is formed by the interference at the left crystal, the second (middle: r_1+l_2) by the interference between the left and right crystals, and the third (lower: r_1+r_2) is formed by the interference at the right crystal. It should be noted that in the middle part the interference takes place between different parts of a crystal, the part being produced when the direction of the intersection between the fault and specimen surface is oblique to the vector $\boldsymbol{g}=\boldsymbol{g}_2-\boldsymbol{g}_1$.

Photograph (a) on the opposite page shows a coherent CBED pattern of Si taken from a perfect specimen area. Photographs (b) to (f) are a defocus series of coherent CBED patterns taken from an area containing a stacking fault of the specimen, the fault plane being almost parallel to the incident electron beam. The interference fringes shift across the line A in the overlapping region between $1\bar{1}\bar{1}$ and 000 reflections and across the line B in the overlapping region between 000 and $\bar{1}11$. The magnitude of fringe shift is determined by the value of $\exp(-2\pi i\boldsymbol{g}\cdot\boldsymbol{R})$, $\boldsymbol{R}$ being the displacement at the fault.

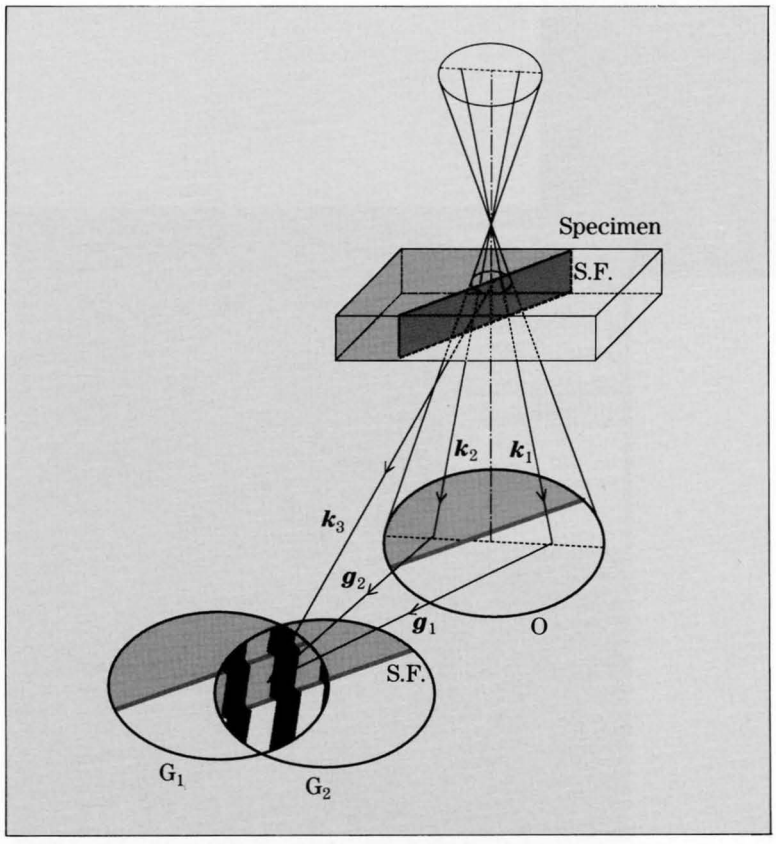

(a)

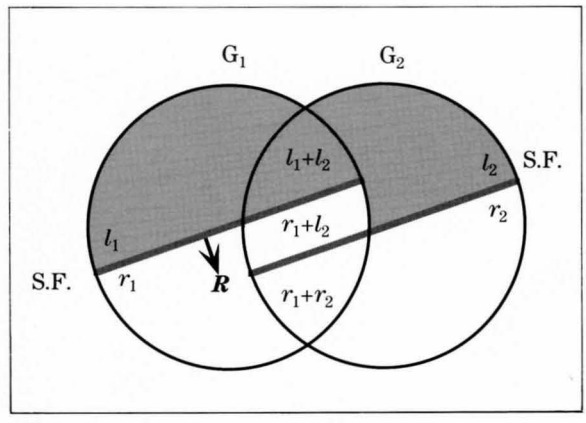

(b)

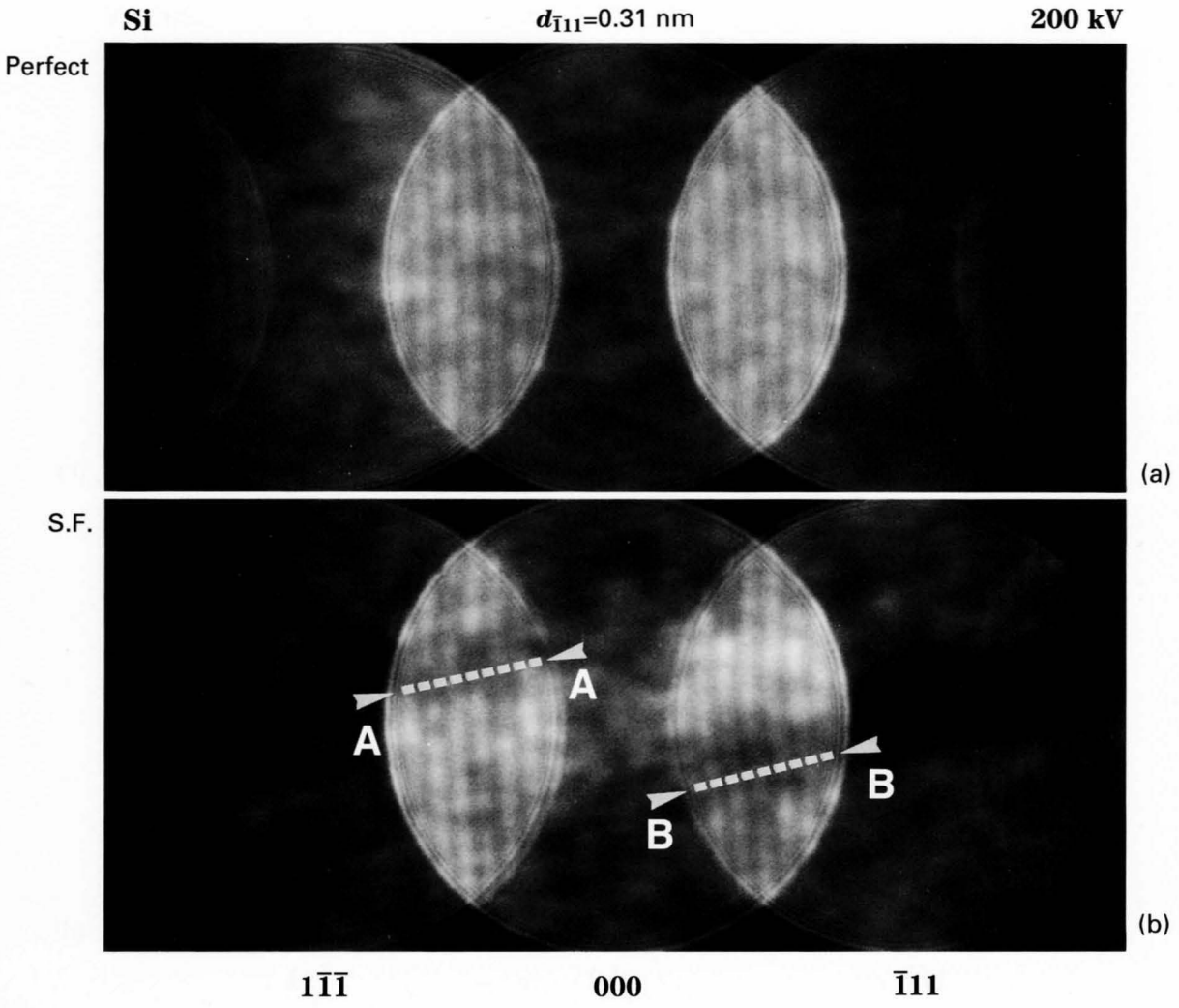
Si
$d_{\bar{1}11}$=0.31 nm
200 kV
Perfect
(a)
S.F.
A
A
B
B
(b)
$1\bar{1}\bar{1}$
000
$\bar{1}11$

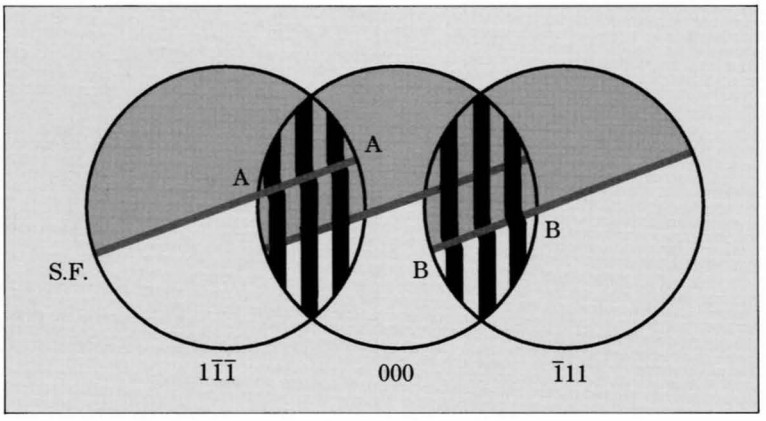
A
A
B
B
S.F.
$1\bar{1}\bar{1}$
000
$\bar{1}11$

Si — focus change —

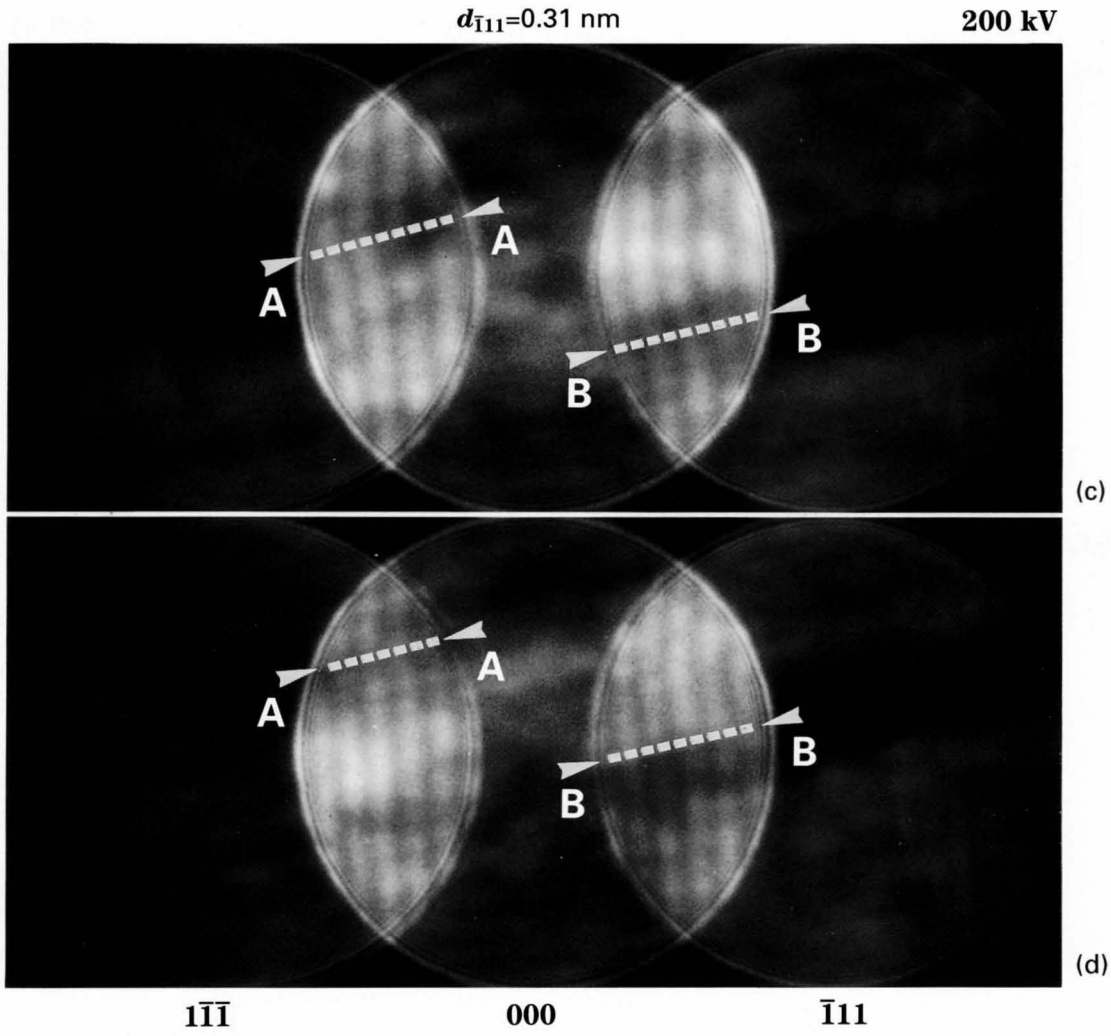

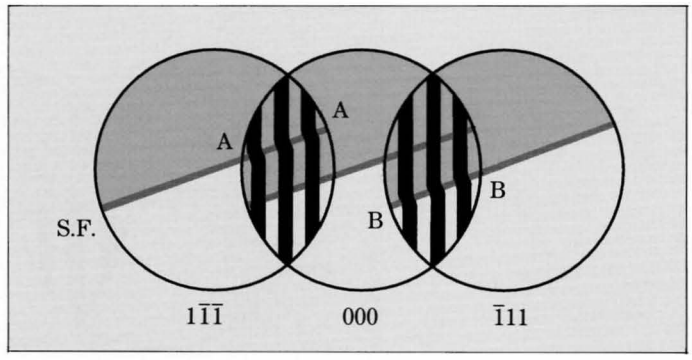

$d_{\bar{1}11}$=0.31 nm **200 kV**

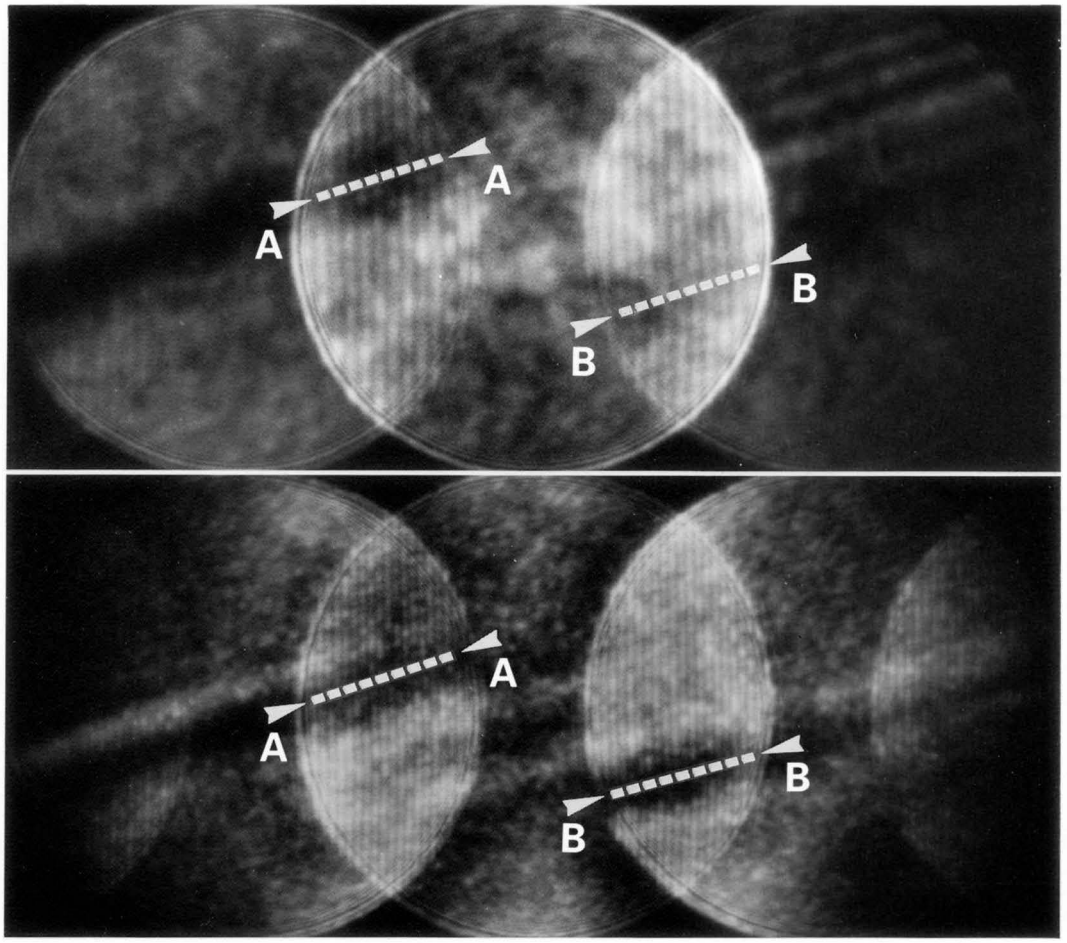

(e)

(f)

$1\bar{1}\bar{1}$ **000** **$\bar{1}11$**

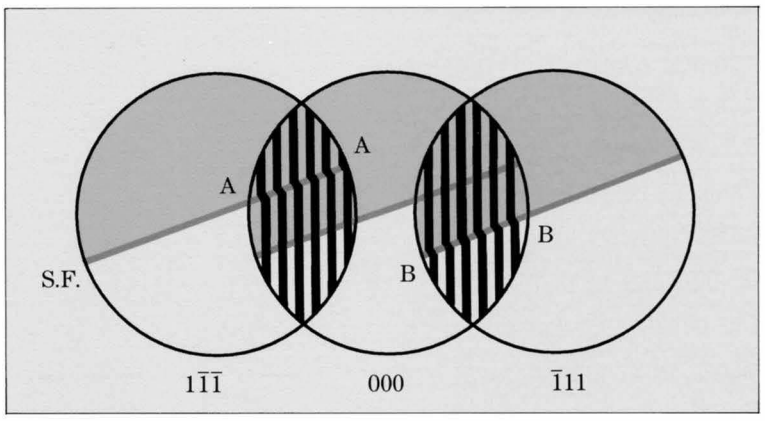

High Accelerating Voltages

The high-voltage electron microscope JEM-ARM1250 installed at the high-voltage electron microscope laboratory of Tohoku Univ. is provided with a few functions for the convenience of CBED experiments: specific presetting of the beam alignment system attached to the condenser lens, small condenser aperture diameters of 30, 60 and 120μm and short camera lengths of 23, 29 and 35cm. The objective lens can be operated approximately at the condenser objective condition when a specimen is lowered from the eucentric position. A probe size of about 10nm is attained on the specimen at an accelerating voltage of 1000kV, the size getting larger at 1250kV. The convergence angle can be varied from 0.8 to 6.0mrad., the diffraction angle of the 220 reflection of Si being 4.5mrad. at 1000kV.

We demonstrate LACBED patterns of Si, Ge, GaAs and graphite perfect crystals for different crystal orientations at different accelerating voltages. We also show LACBED patterns from dislocations and stacking faults in Si and graphite, and CBED patterns of Ge characteristic of the zone-axis critical voltage. At the end, CBED patterns taken at an accelerating voltage of 1250kV are exhibited as those obtained at the highest accelerating voltage to date.

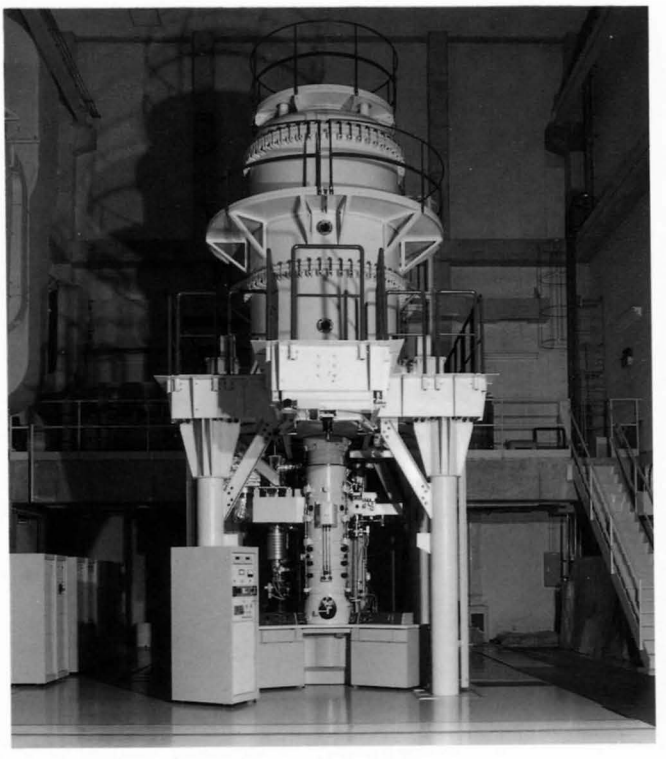

Perfect Crystals

Silicon
[111] 1000kV

Si

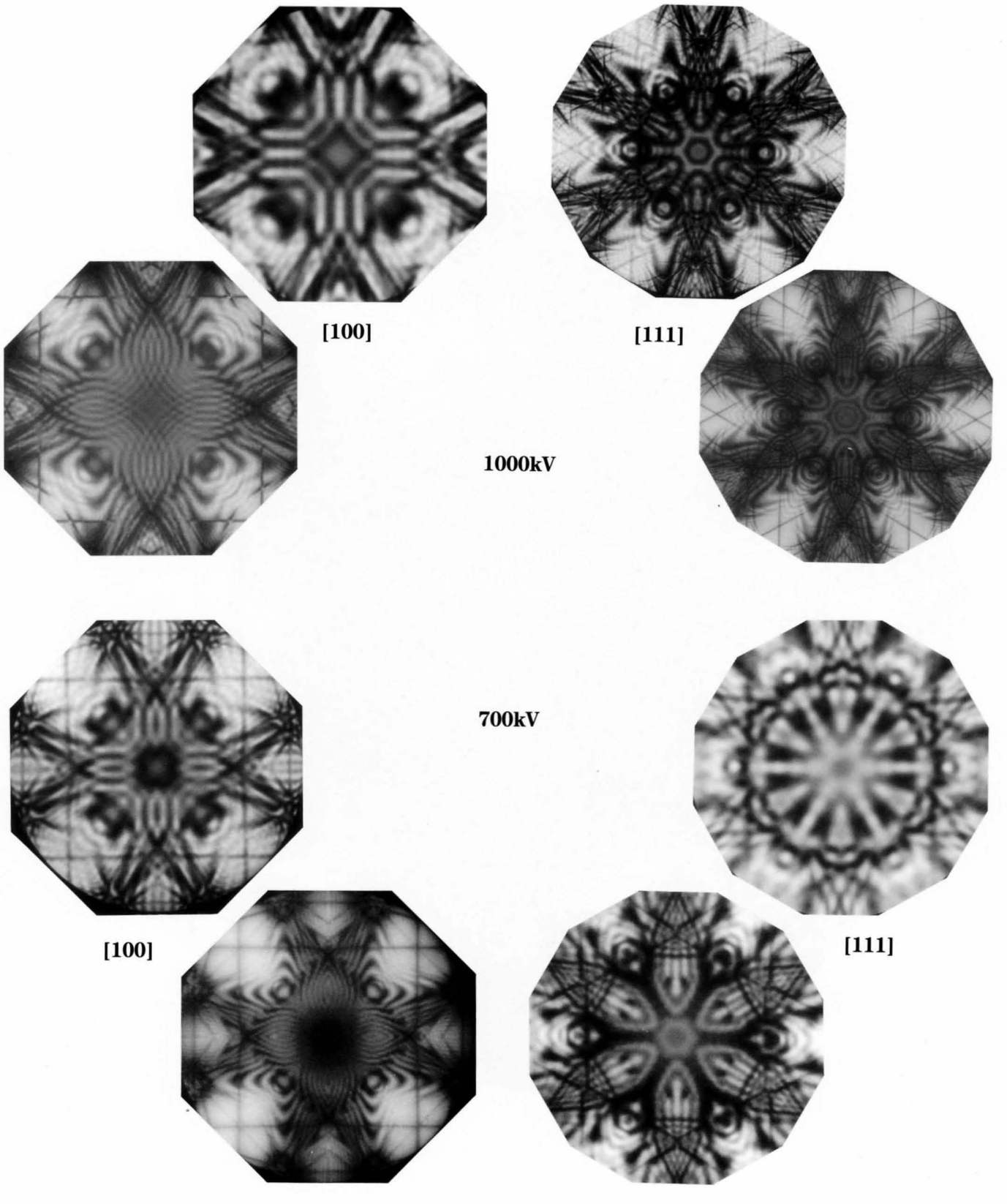

[111] 1000kV

Si [100] 1000kV

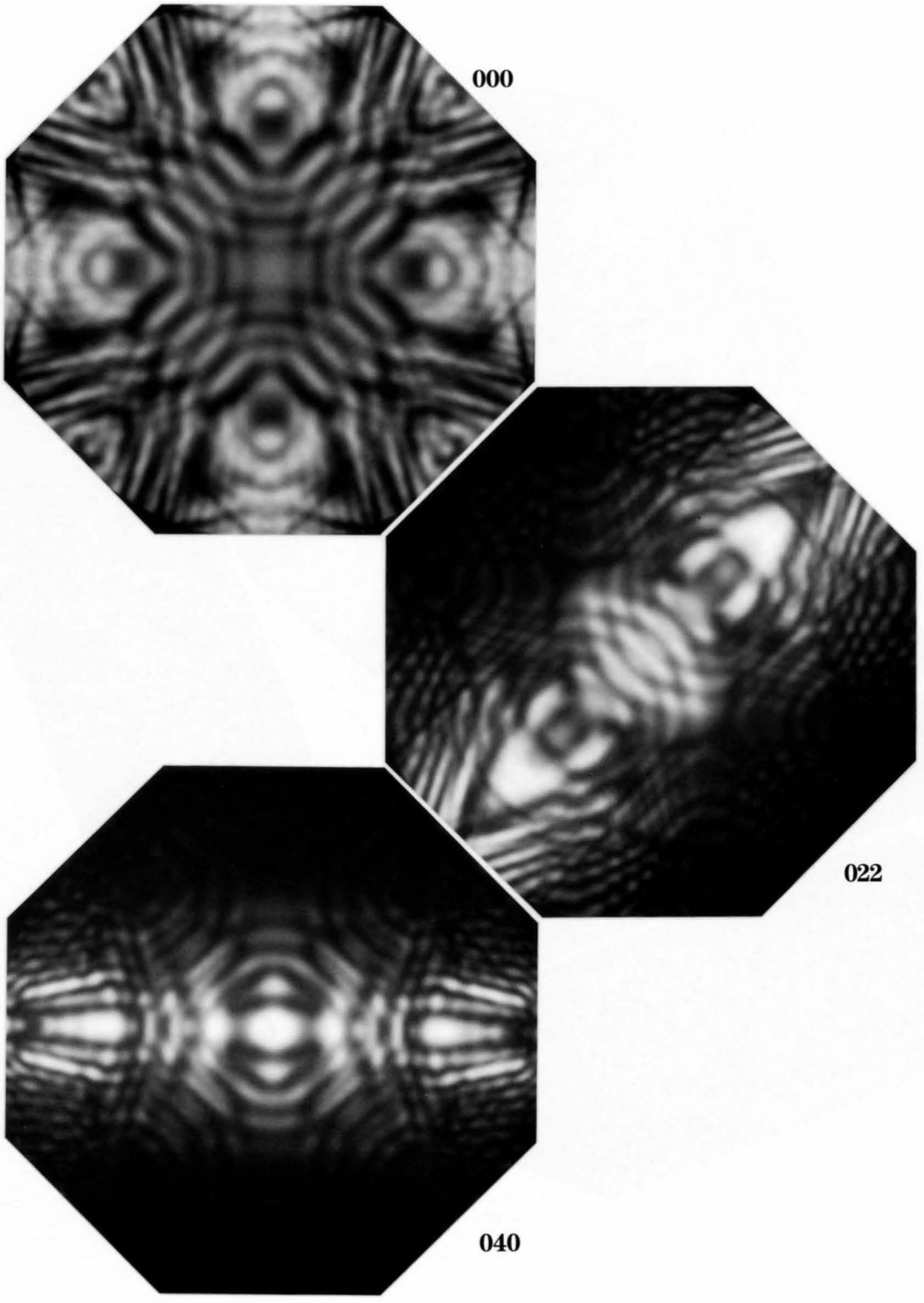

[100] 700kV

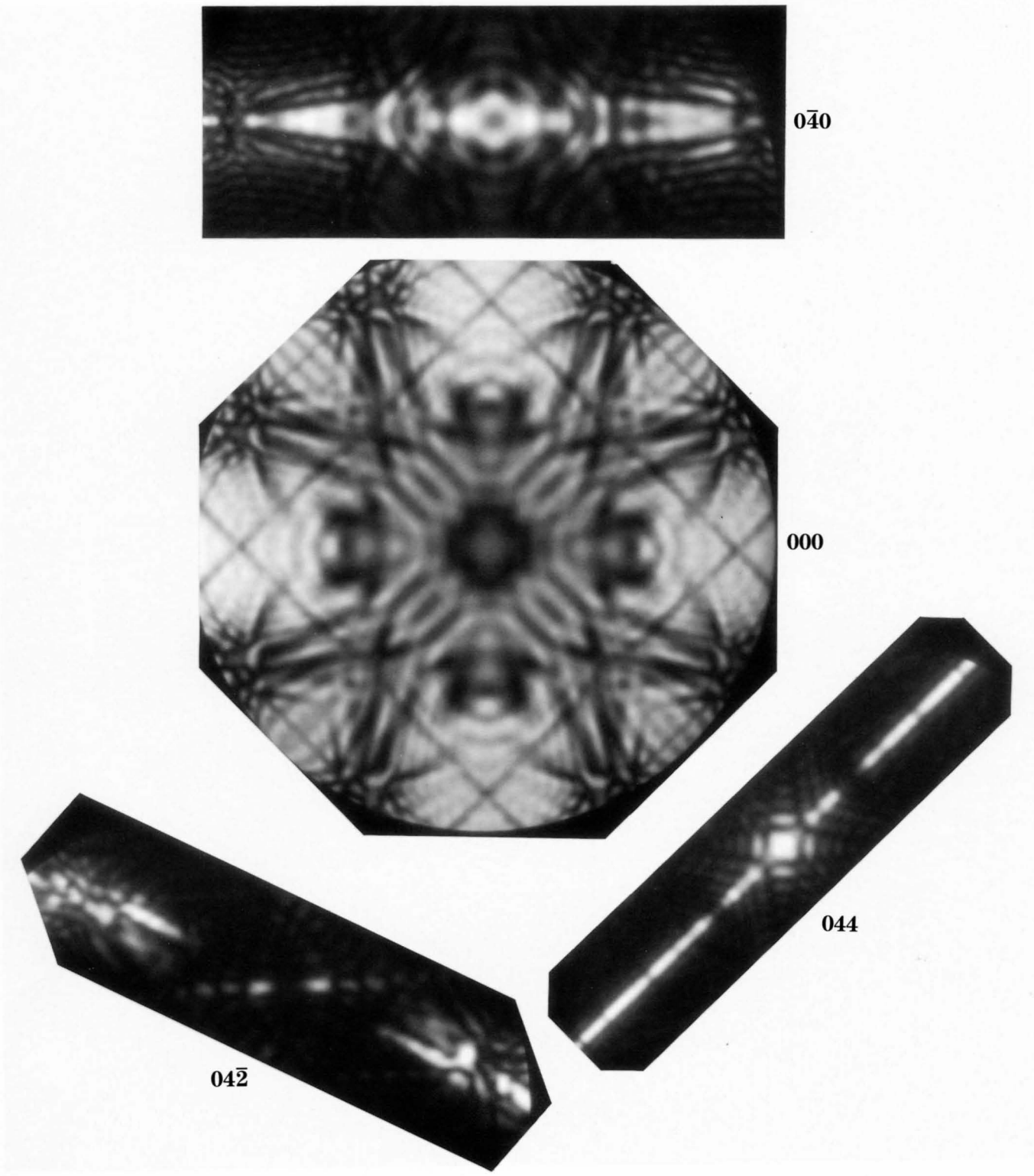

Si [100] 1000kV

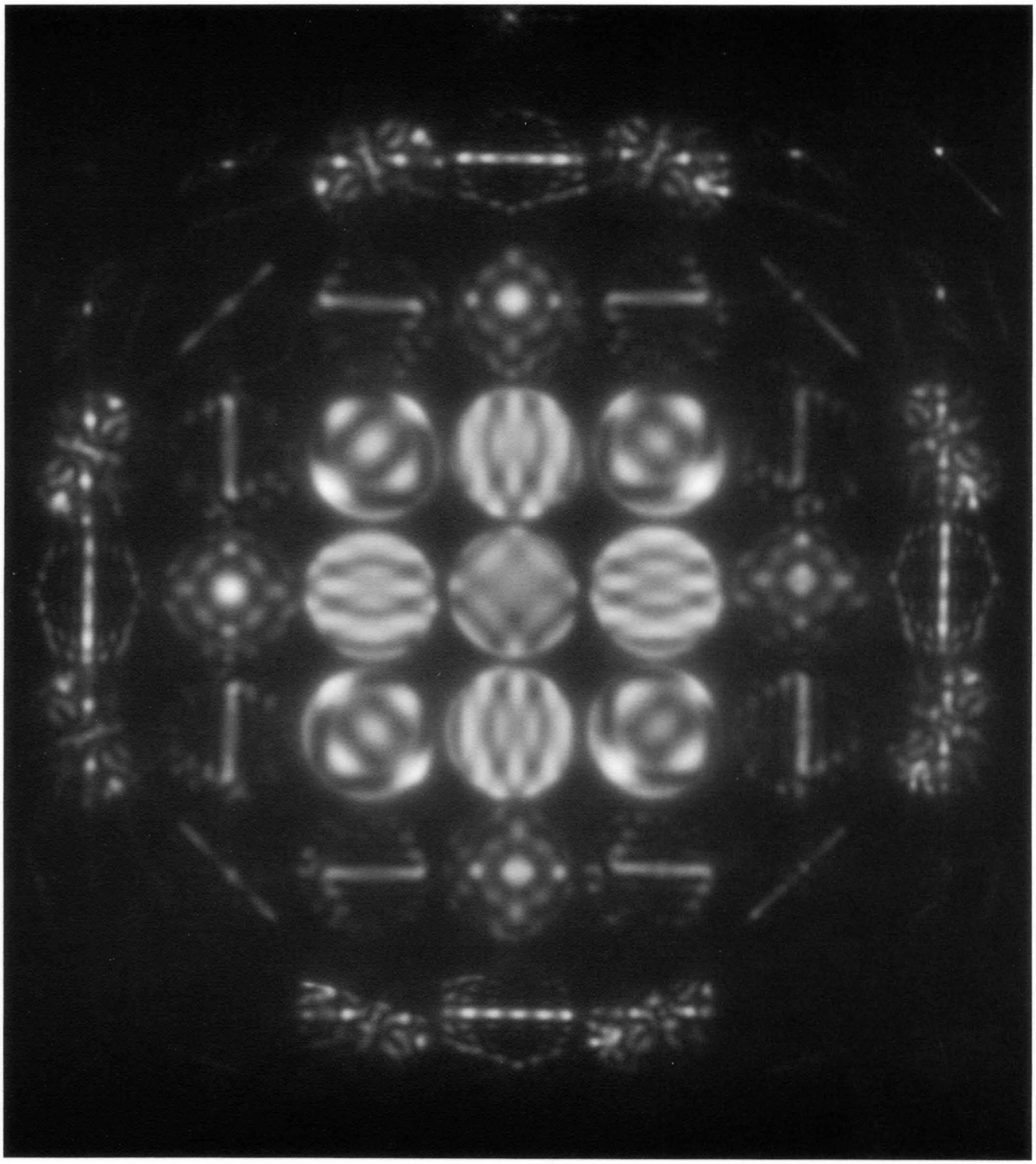

The exact Bragg positions of all the reflections are brought to the centers of the disks using the LACBED technique developed by Terauchi and Tanaka [3].

Germanium
[111] 1000kV

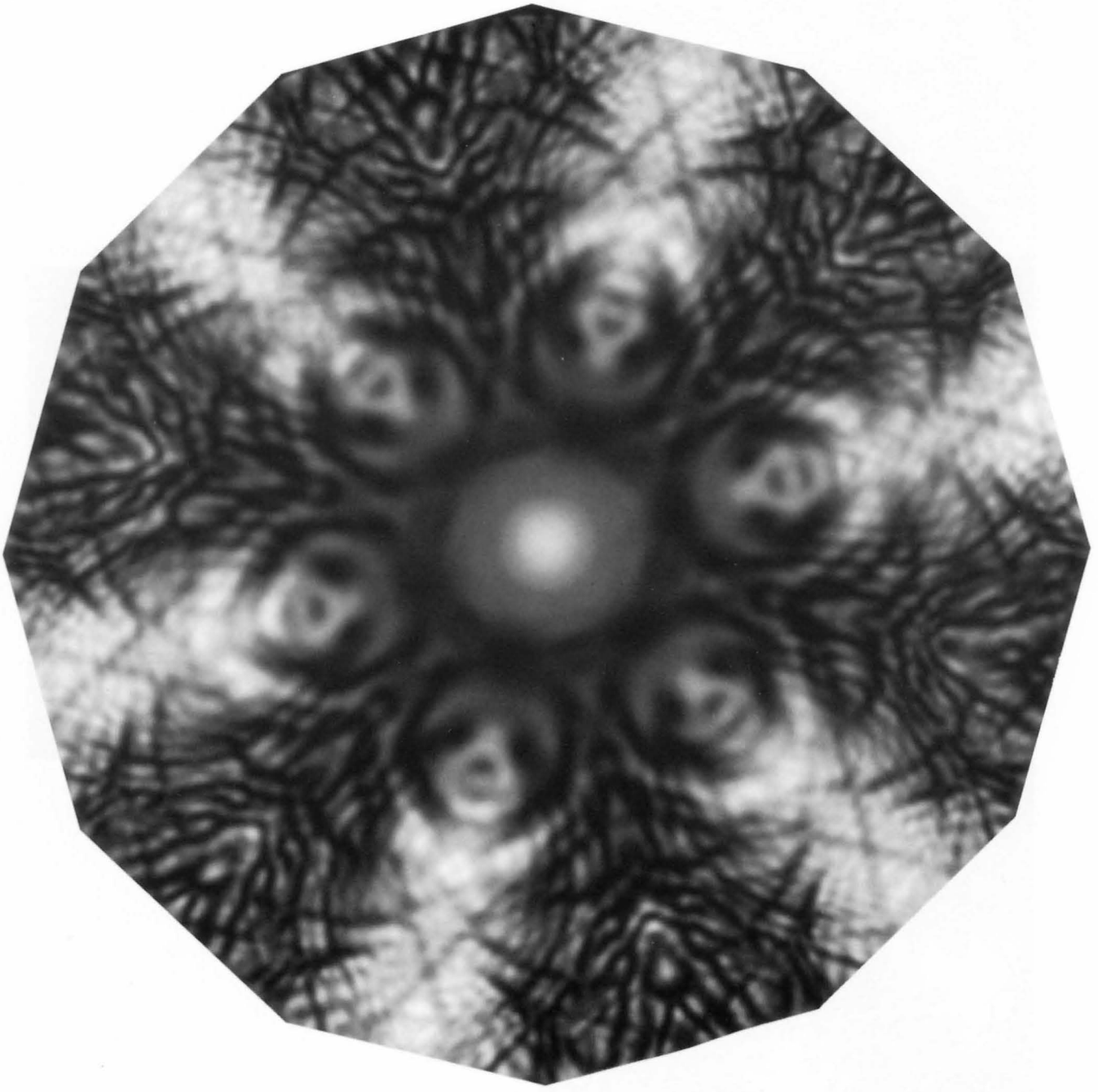

Ge [111] 1000kV

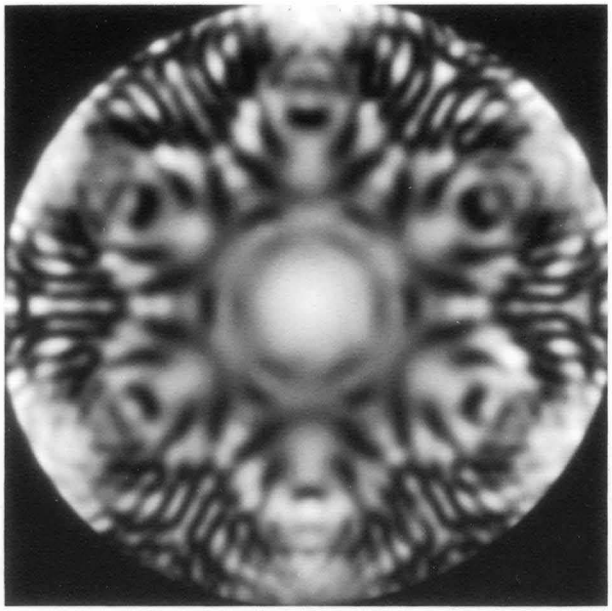

Thin

Medium

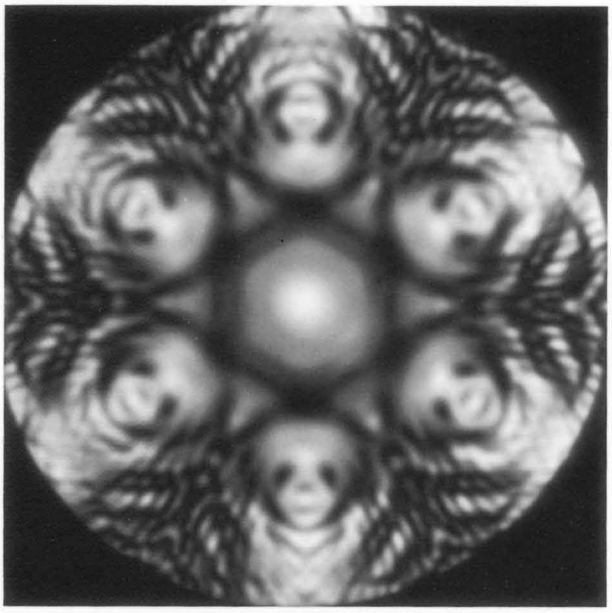

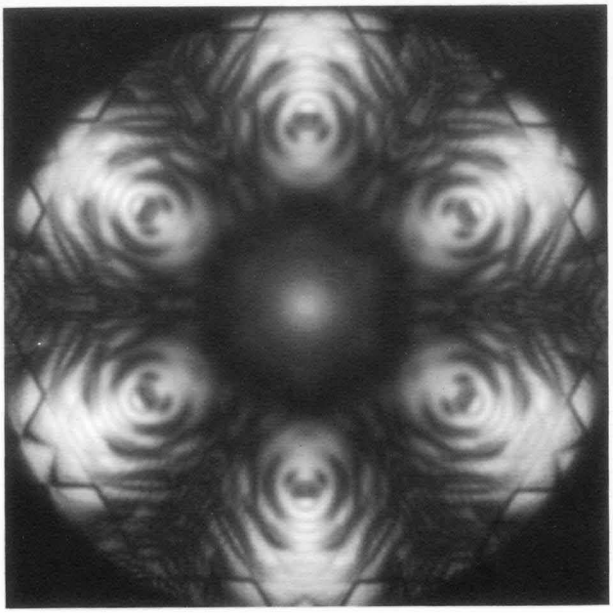

Thick

[111] 1000kV

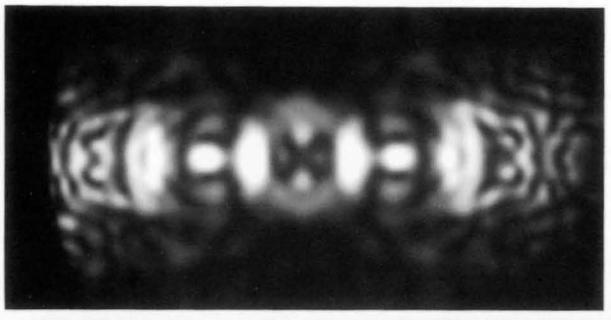

22$\bar{4}$

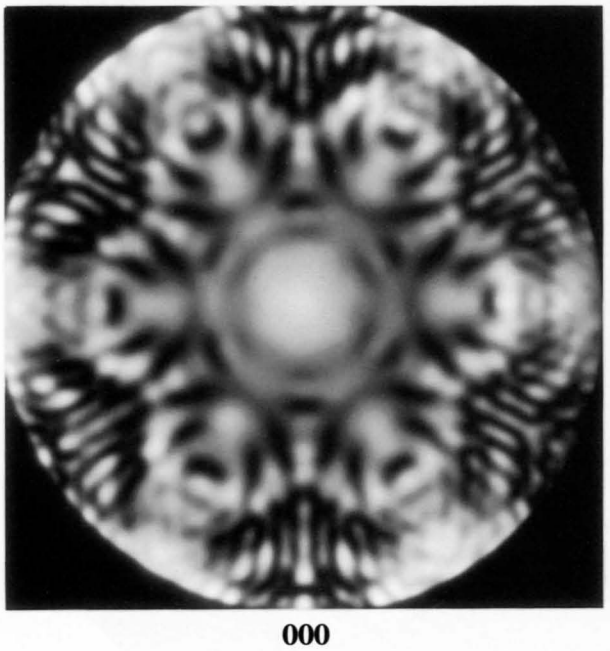

000

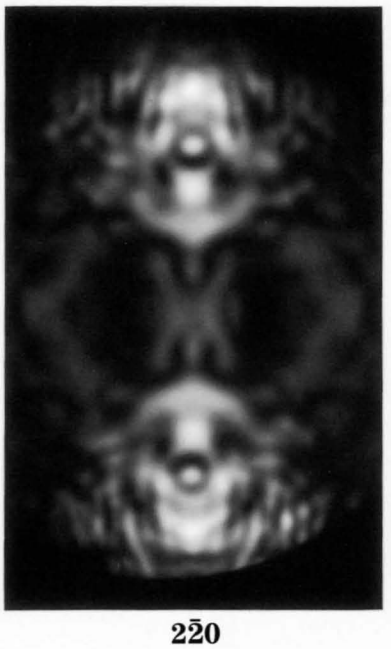

2$\bar{2}$0

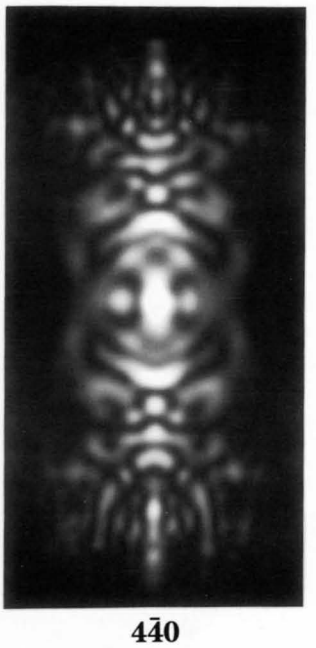

4$\bar{4}$0

GaAs

[100] 700kV

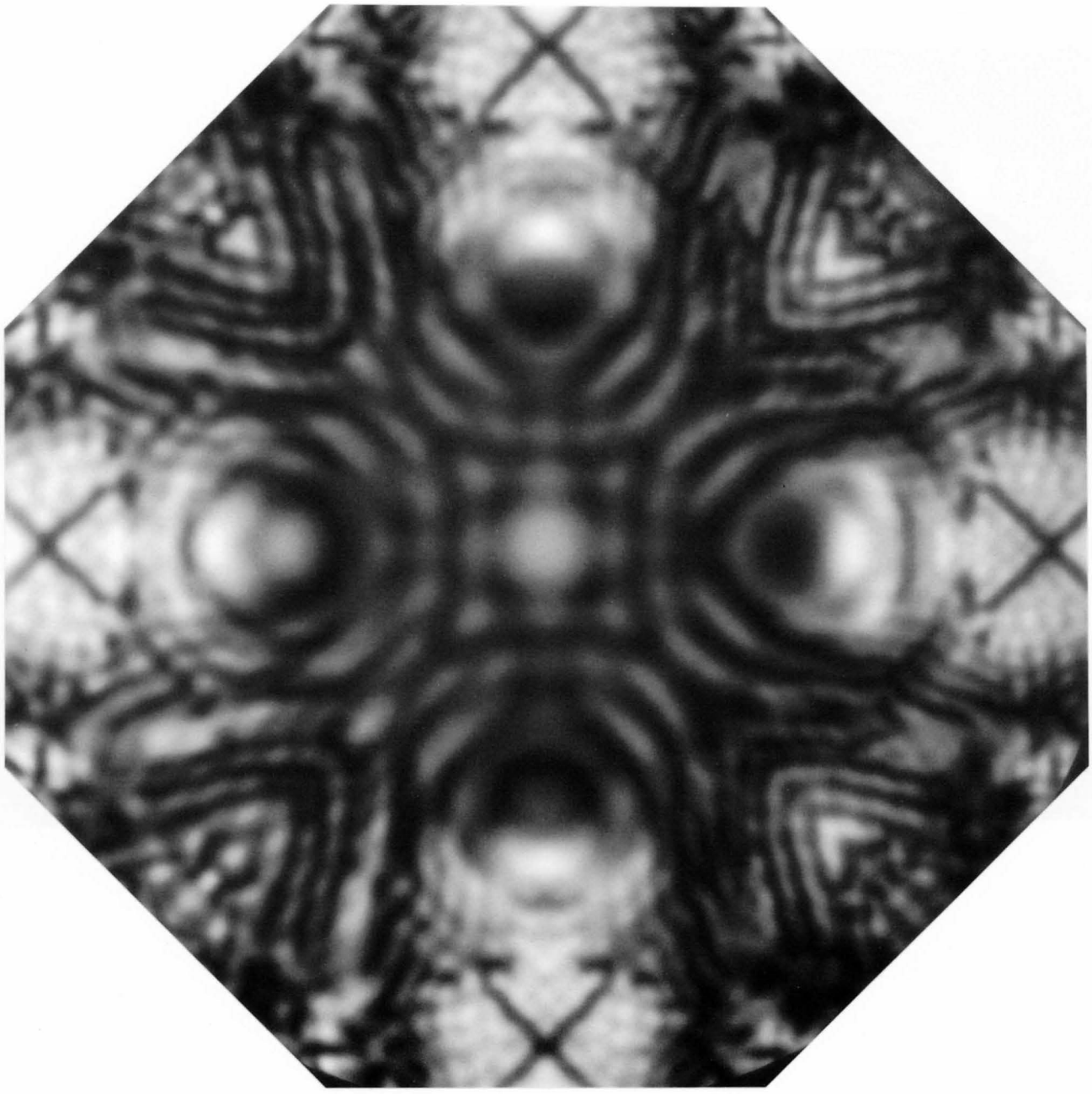

Graphite
[0001] 1000kV

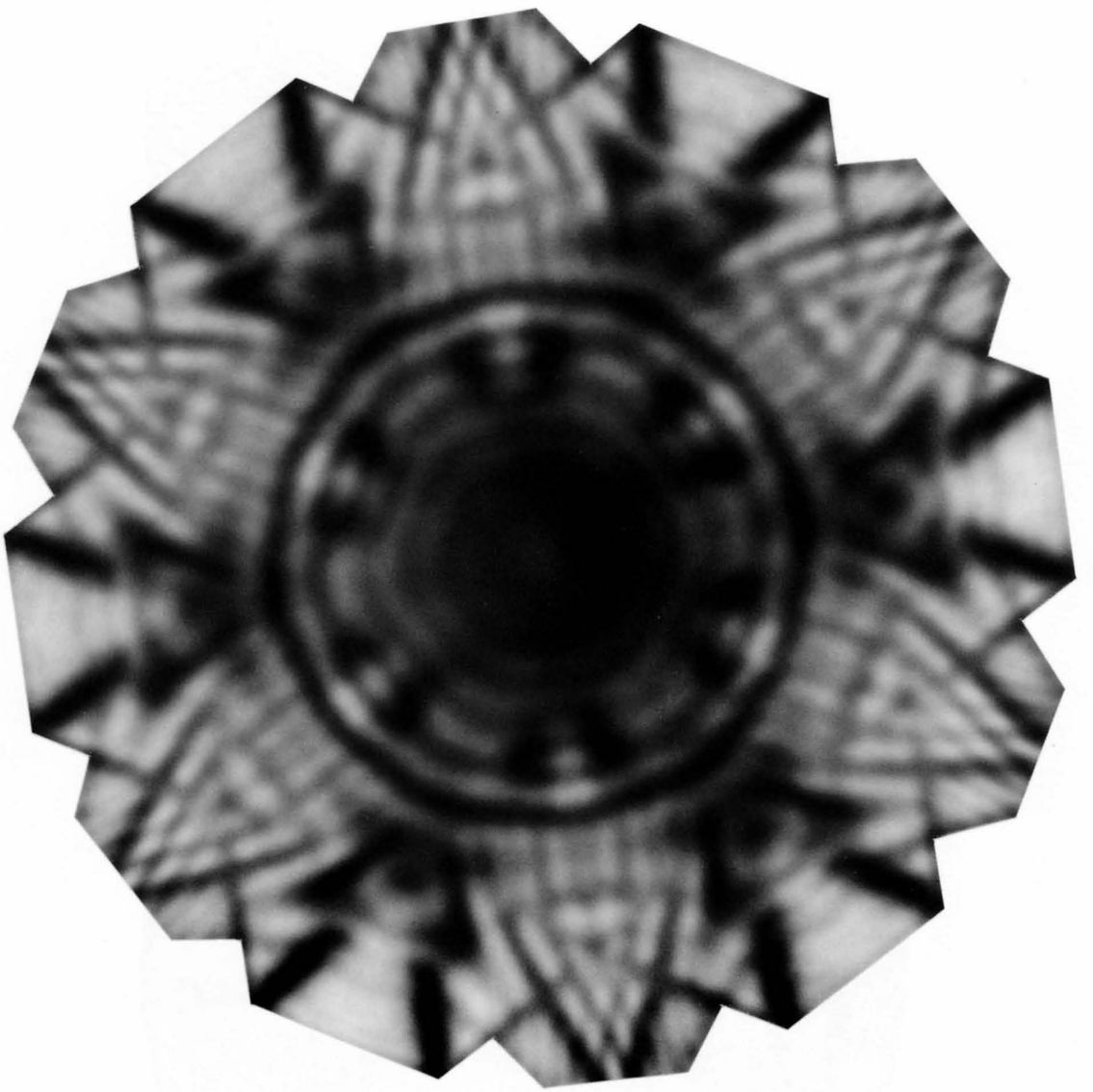

Lattice Defects

Silicon

Screw dislocation [111] 1000kV

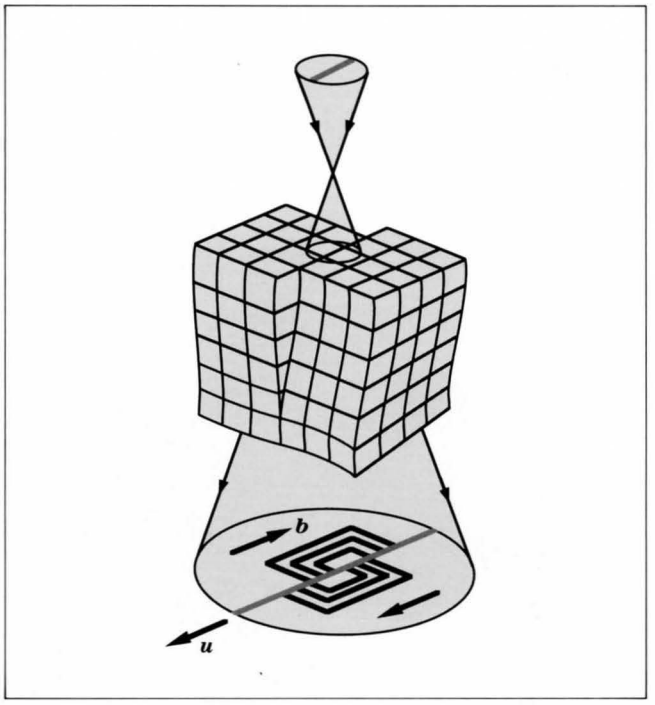

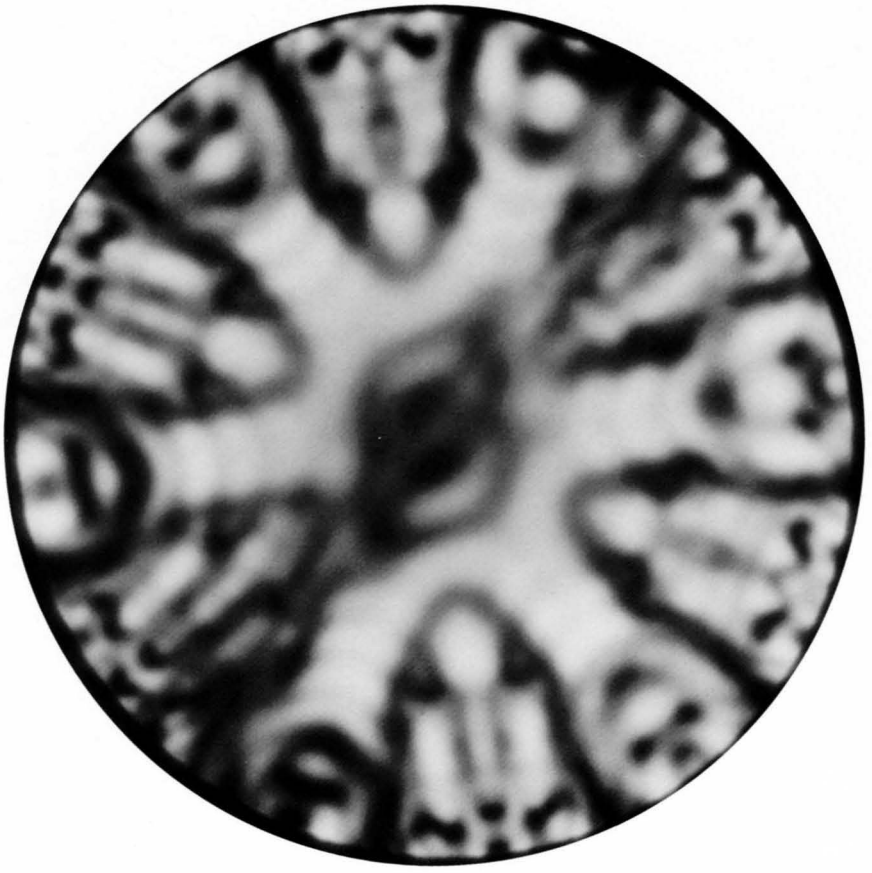

Edge dislocation [111] 1000kV

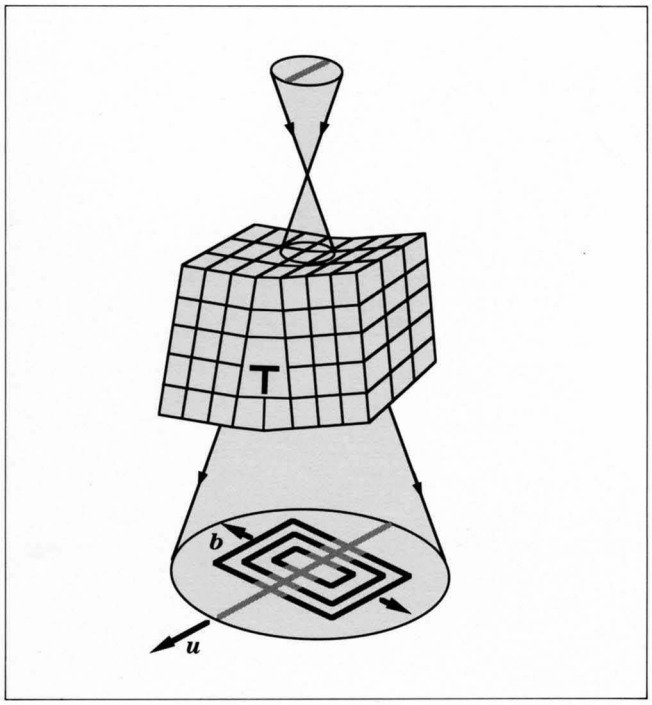

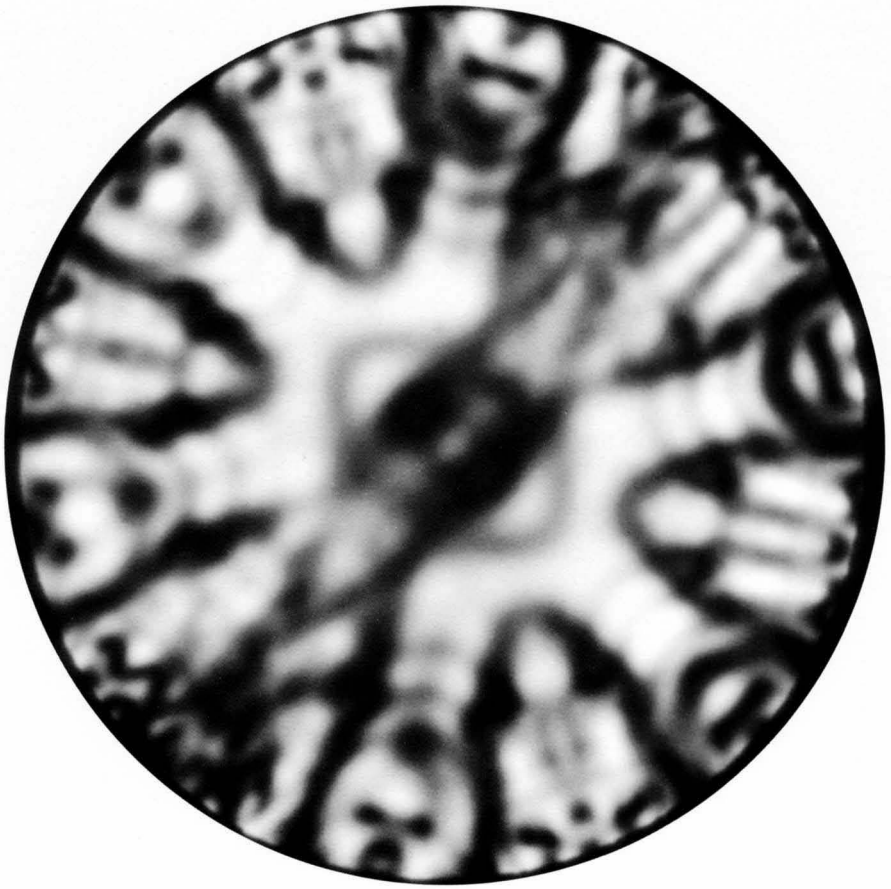

Si (stacking fault) 1000kV

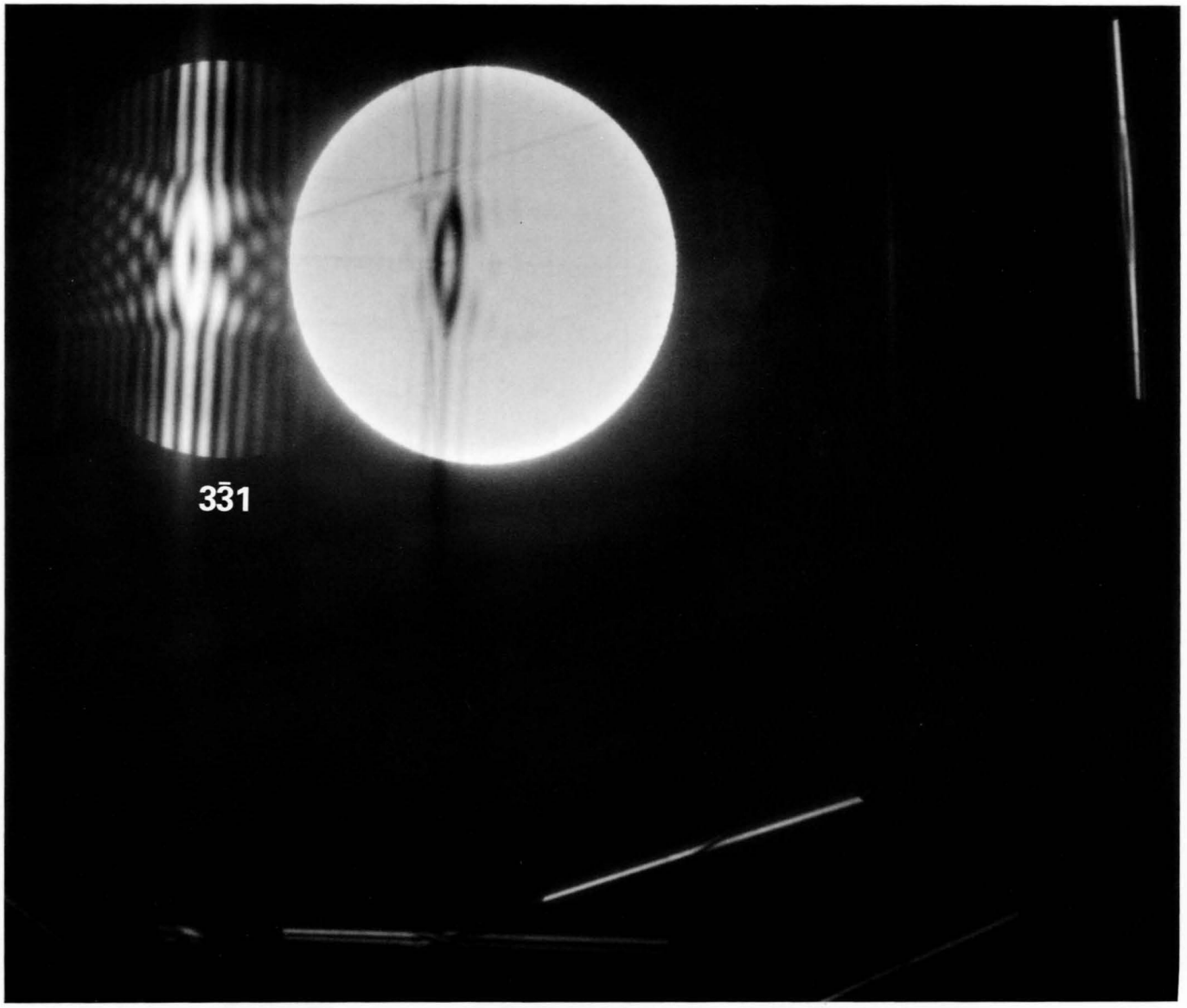

A strong dynamical diffraction effect is seen in the low-order 3$\bar{3}$1 reflection. The other two high-order reflections are weakly dynamical and appropriate for the determination of the shift vector of the fault [9].

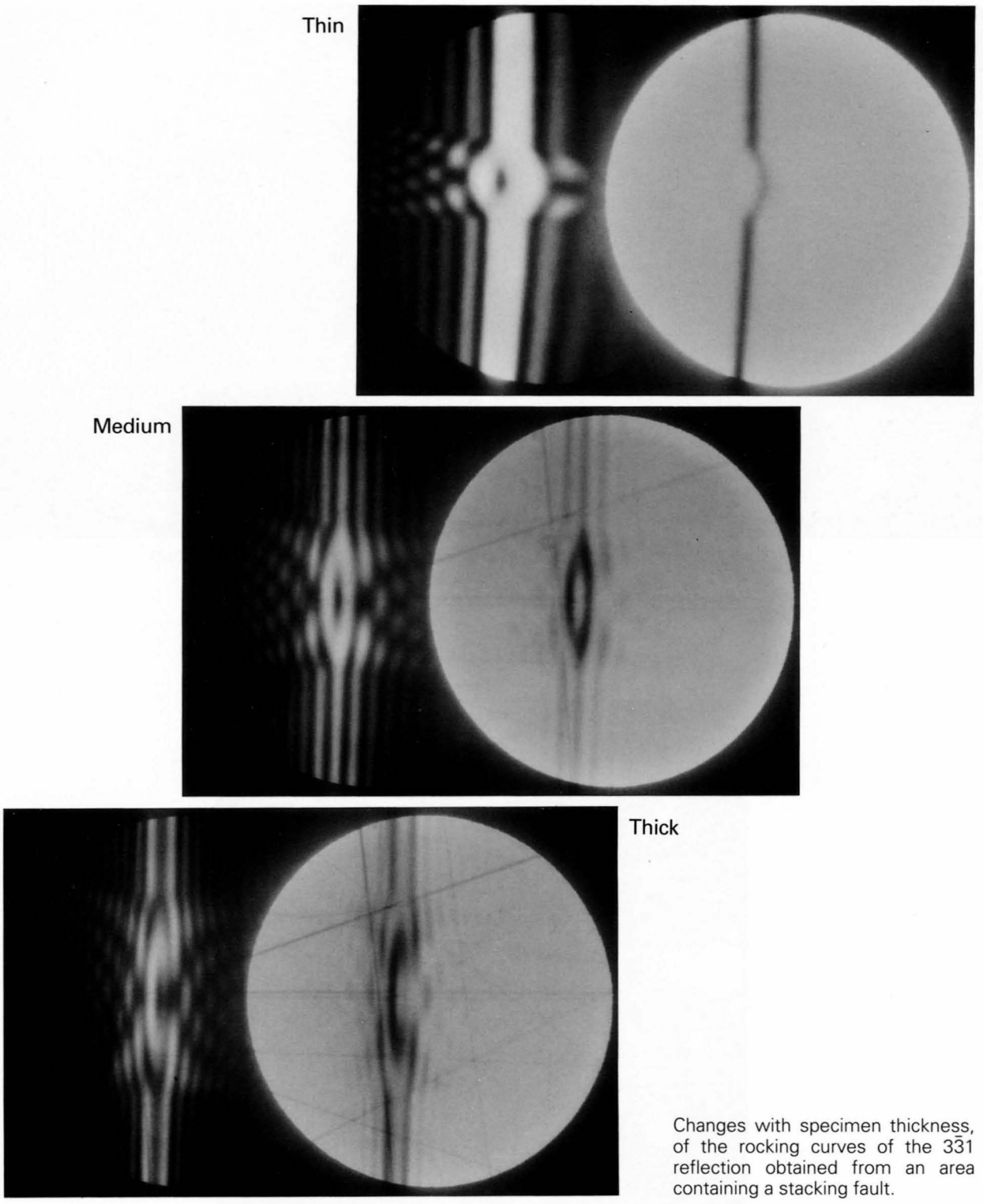

Changes with specimen thickness, of the rocking curves of the $3\bar{3}1$ reflection obtained from an area containing a stacking fault.

Graphite

[0001] 1000kV

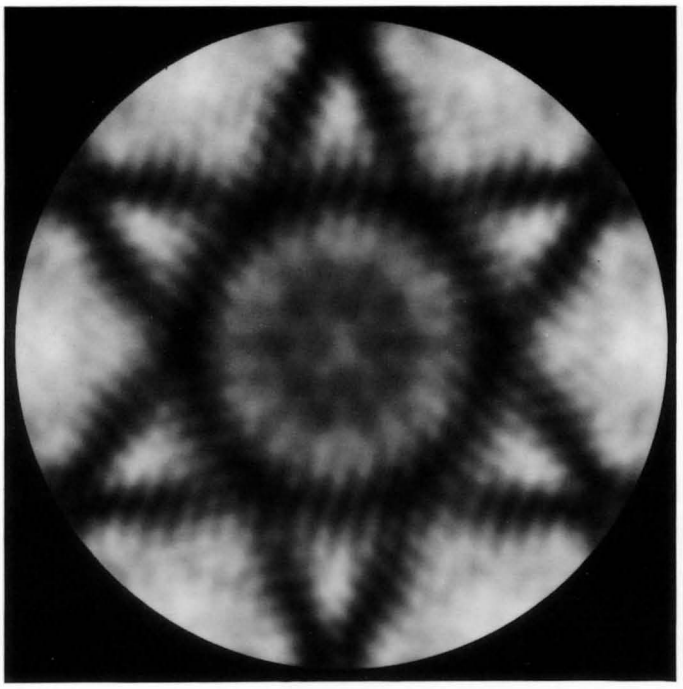

Moiré

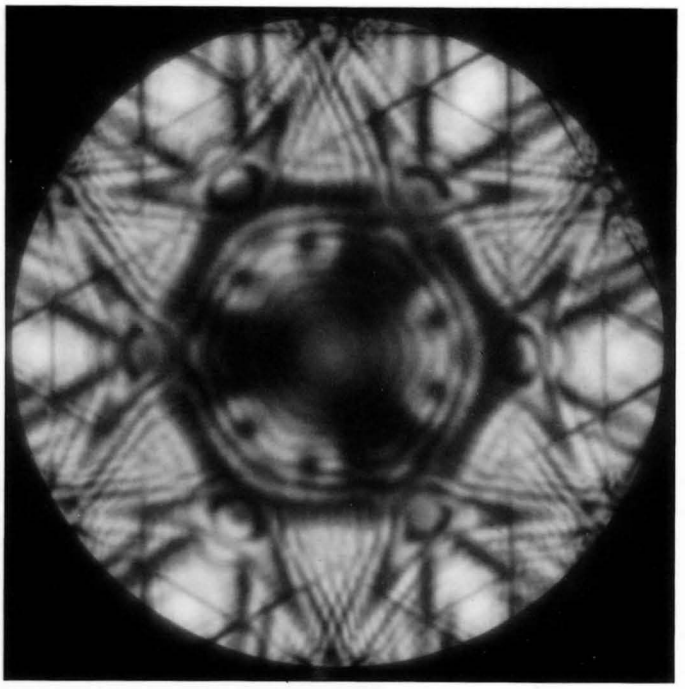

Stacking fault

Imperfect

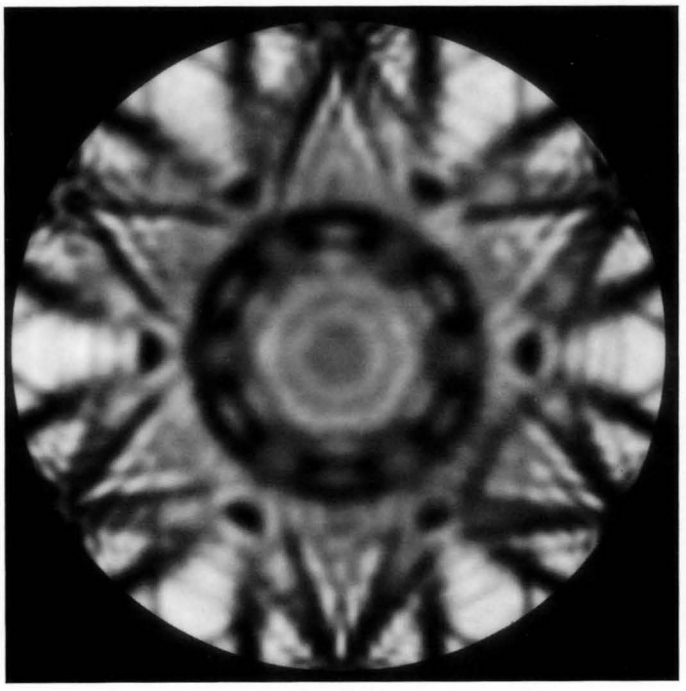

Perfect

Zone-Axis Critical Voltage

When a zone-axis critical voltage is approached, the two dispersion surfaces concerned come closer to each other and the extinction distance ξ, which is inversely proportional to the distance of the dispersion surfaces, becomes longer. At the exact critical voltage, the two dispersion surfaces degenerate and $\xi = \infty$. This phenomenon causes a specific feature in CBED patterns. That is, a bright circular area appears at the central part (the zone axis) of the bright-field pattern near the critical voltage, irrespective of the specimen thickness. The area condenses to a small spot on the zone axis at the critical voltage.

The series of photographs shows [111] zone-axis CBED patterns of Ge taken at accelerating voltages from 800 to 680kV. The critical voltage of Ge for the [111] zone axis is calculated to be 717kV [23]. The patterns show that the bright spot at the center of the bright-field disk is smallest at 700kV, indicating the real critical voltage occurring at a little lower value than the calculated one. In addition, asymmetry of the intensities at the centers of the $2\bar{2}0$ and $\bar{2}20$ reflection disks reverses its sense at the critical voltage.

Ge [111]

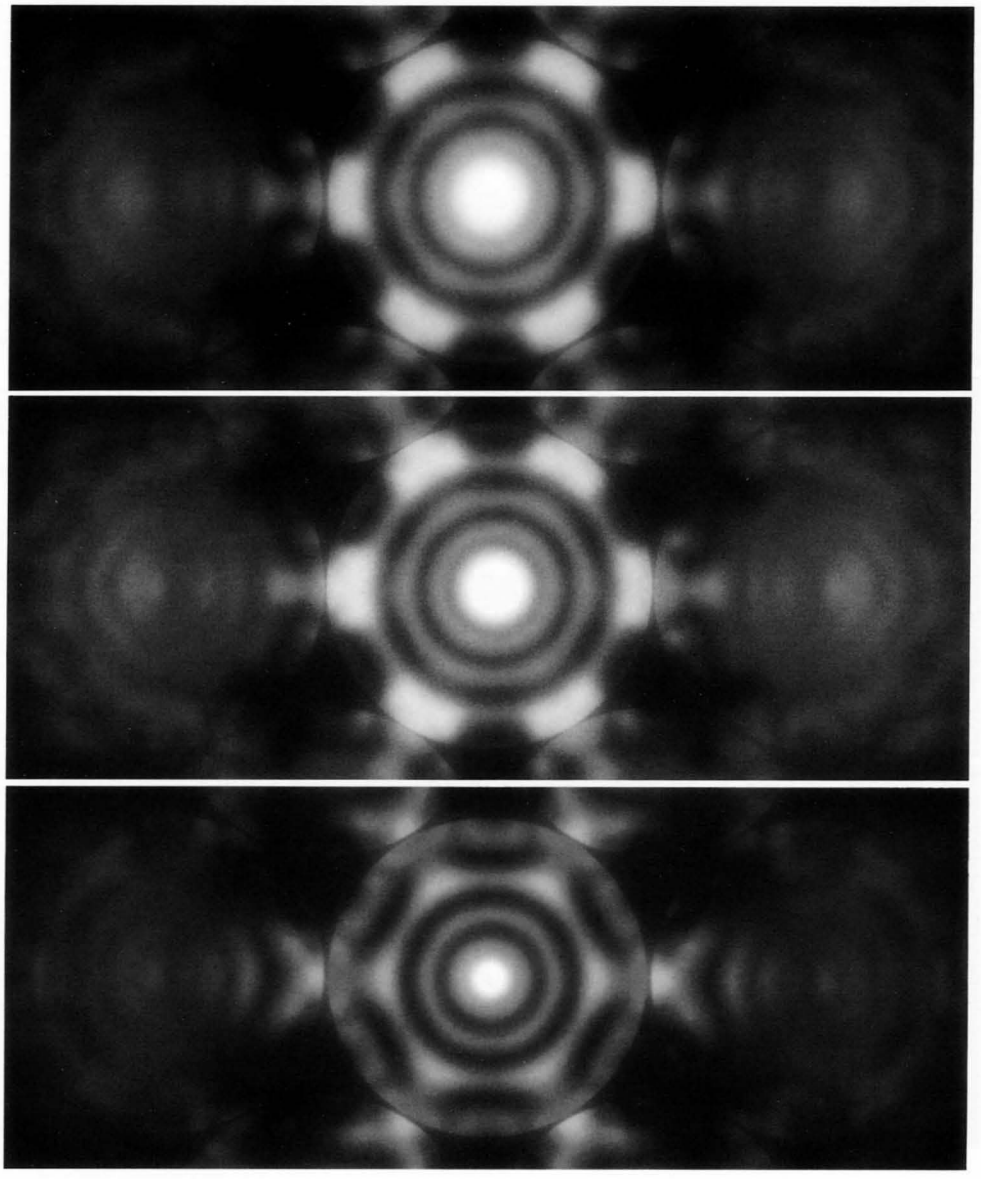

Ge [111]

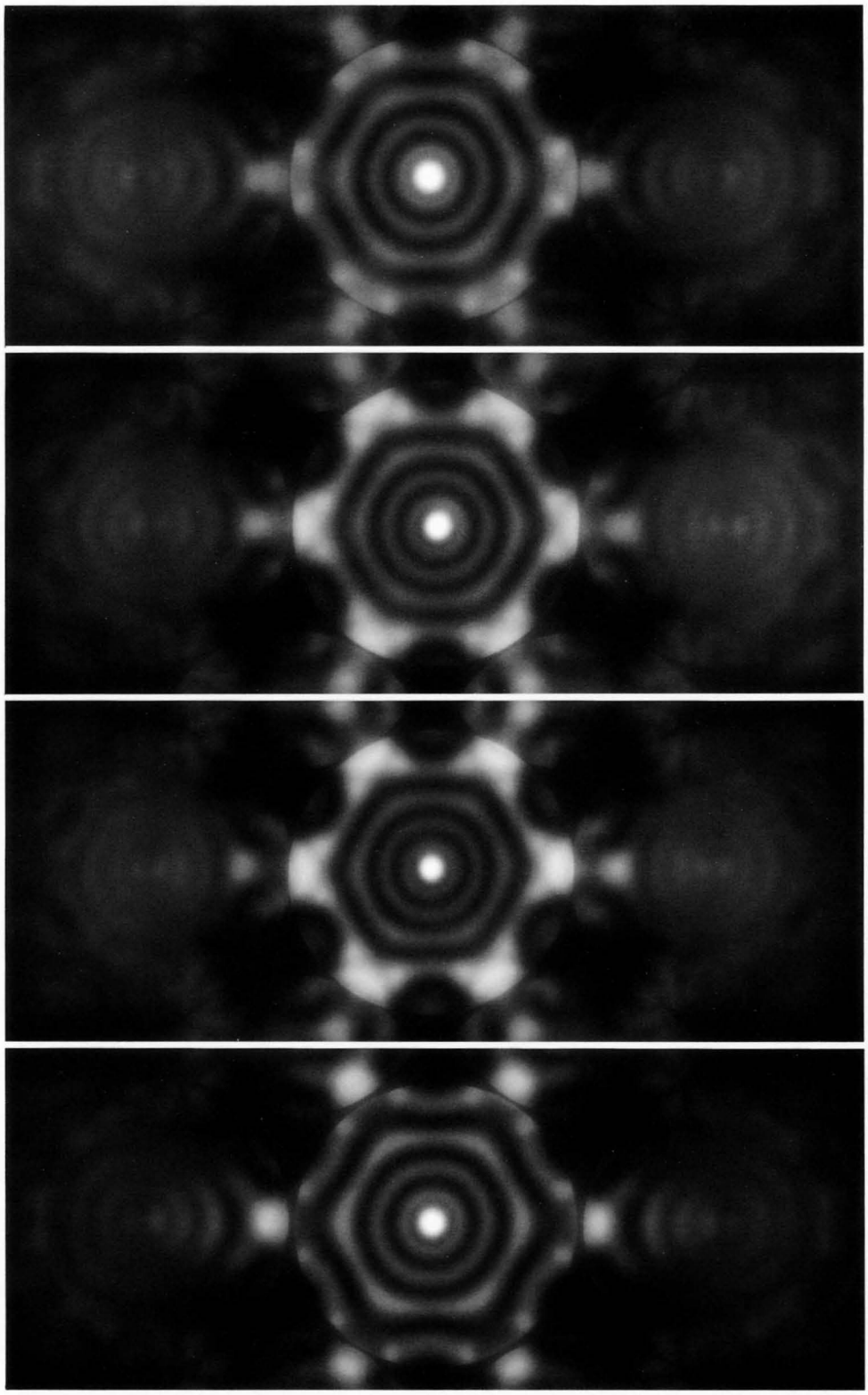

1250kV

Si [111] 1250kV

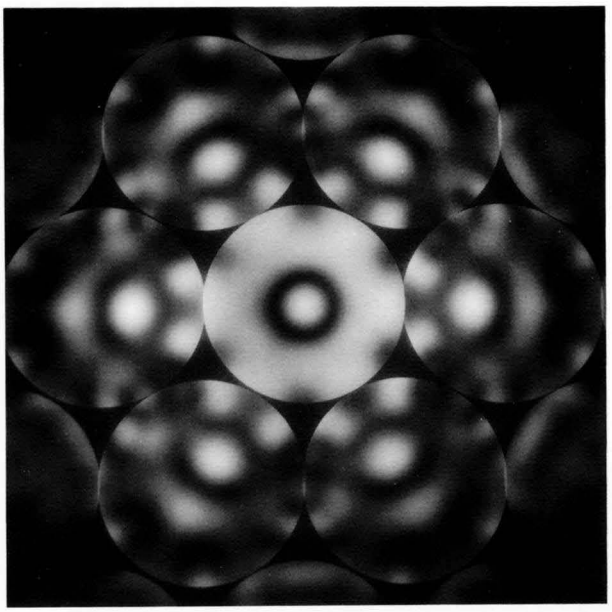

Thin

Medium

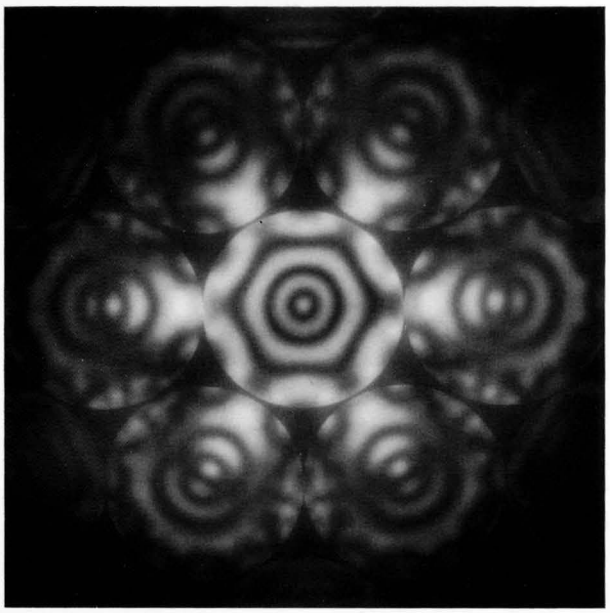

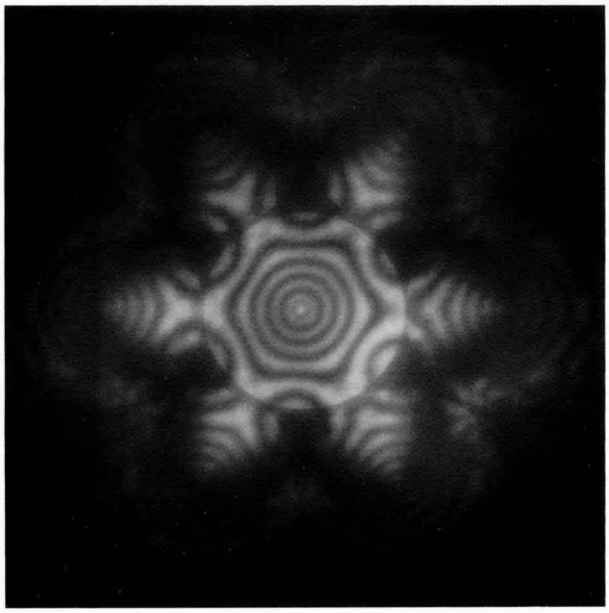

Thick

Changes with specimen thickness, of the [111] zone-axis CBED pattern. The appearance of a bright spot at the center of the bright-field pattern irrespective of the specimen thickness indicates that the operating voltage is near the critical voltage, which is calculated to be 1320kV [23].

Si [111] 1250kV

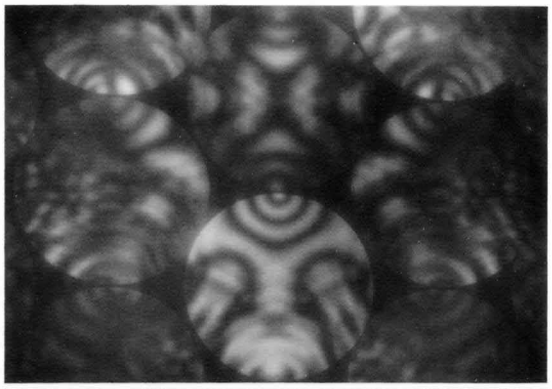

$g=2\bar{2}0$

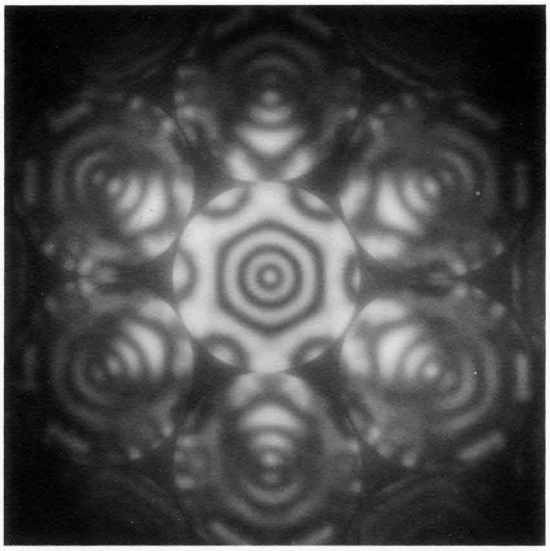

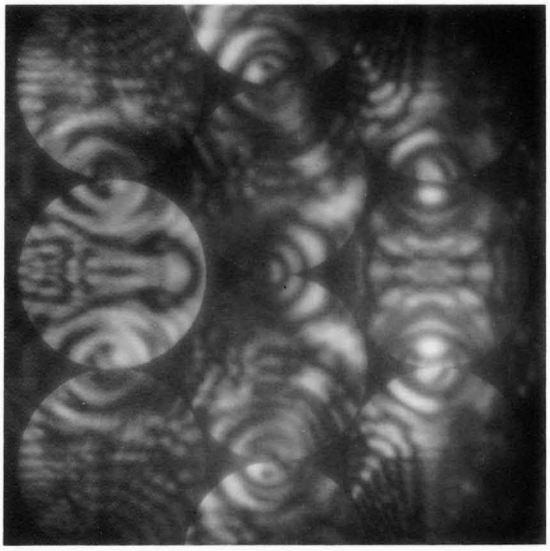

$g=\bar{2}\bar{2}4$

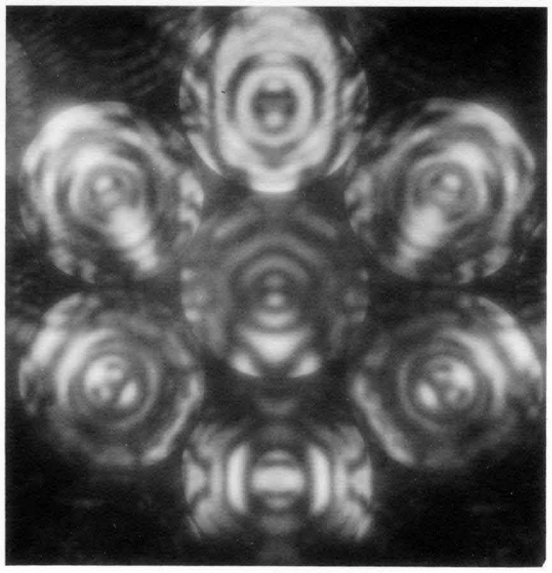

$g=\bar{4}40$

Ge [111] 1250kV

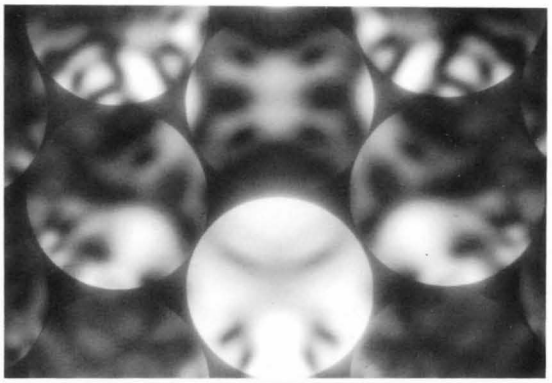

$g=2\bar{2}0$

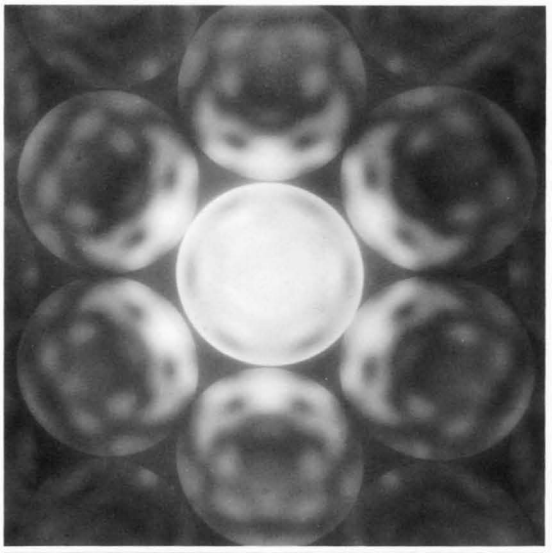

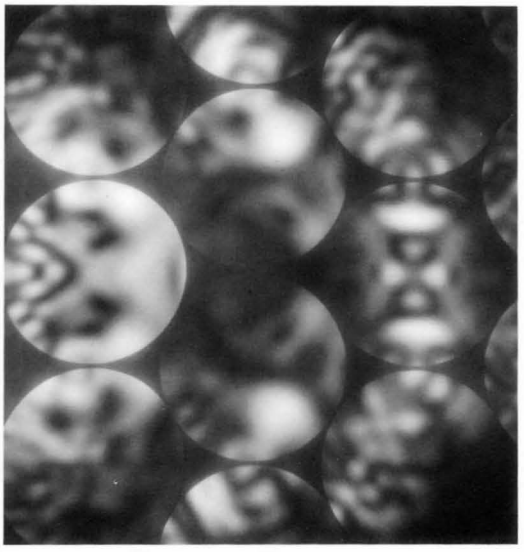

$g=\bar{2}\bar{2}4$

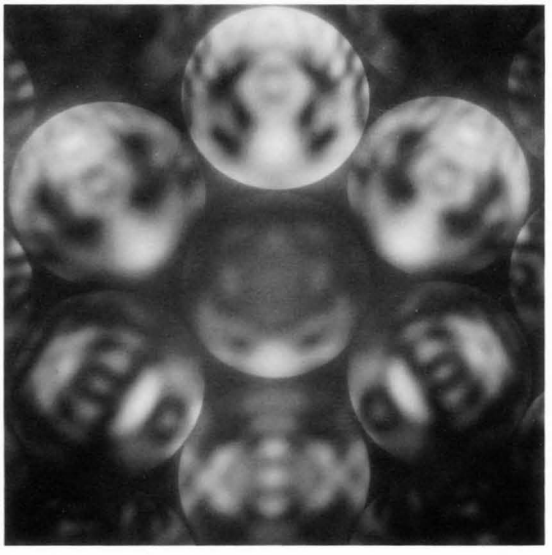

$g=\bar{4}40$

Miscellaneous

Magnetic Domains

The observation of magnetic domains by electron microscopy was originated by Hale, Fuller and Rubinstein [a]. Their method is called Lorentz microscopy. The method to use a quadrant detector in the STEM mode, which was developed by Chapman *et al.* [b], produces a differential contrast and has been applied to detailed studies of magnetic domains.

We propose a new CBED technique to observe magnetic domains. That is, the defocus CBED method can trace the change of Lorentz deflection at a domain wall as a function of the position in the wall. The method displays intensity distribution in real and reciprocal spaces for both transmission and diffraction disks simultaneously without scanning operation, which makes a great contrast to the STEM method. However, it has not ever been applied to the investigation of magnetic domain structures and domain walls. This was because the magnetic domain structure is easily destroyed by the magnetic field of the objective lens required to produce a strongly convergent beam. JEOL supplied us with a special pole-piece for the objective lens, DPC 20S, suitable for the observation.

Figures (a) and (b) show a sketch of the cross-section of the pole-piece and the distribution of the magnetic field, respectively. The specifications are given in the table. The use of the pole-piece enables us to observe CBED patterns of magnetic domains because of its weak residual magnetic field around the specimen.

We have succeeded in the first CBED observation of magnetic domains of Fe-13 at.% Si and Co. Quantitative analysis of defocus CBED patterns of magnetic domains is possible by digital signal processing techniques when the patterns are recorded on IPs. This provides valuable information on magnetic domains and domain walls. Better performance of the pole-piece with a smaller probe size, a larger convergence angle, etc., can be attained by a new design.

References

[a] M. E. Hale, H. W. Fuller and H. Rubinstein: *J. Appl. Phys.*, **30** (1959) 789.

[b] J. N. Chapman and G. R. Morrison: *J. Mag. Mag. Mat.*, **35** (1983) 254.

DPC 20S Objective Lens Pole-piece

Residual vertical magnetic field at specimen position:	1.6×10^{-2} T at 200kV 1.6×10^{-3} T at 100kV
Probe diameter on specimen:	25nm at 200kV
Convergence angle of incident beam:	5.7×10^{-3} rad.
Acceptance angle of CBED pattern:	1.7×10^{-1} rad. (9.51°)

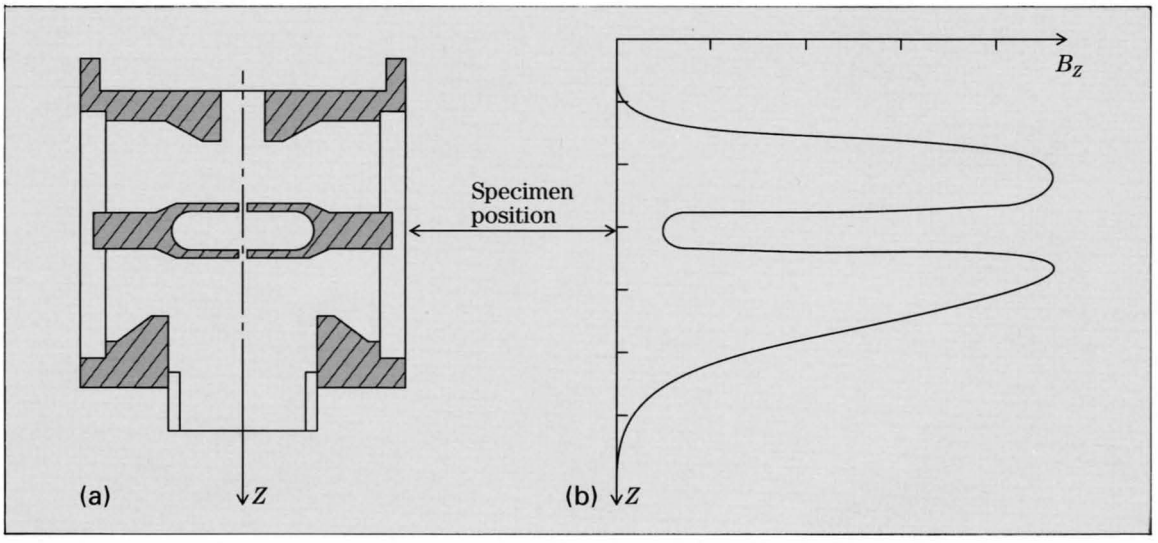

Figures (a) and (b) illustrate the observation of magnetic domains in two defocus CBED modes. In modes I(a) and II(b), the incident beam is focused above and below the specimen, respectively. The specimen has three domains, A, B and C, the direction of magnetization being indicated with the thick arrows. The regions A_1', B_1', B_2' and C_1' on the CBED patterns correspond to the regions A_1, B_1, B_2 and C_1 of the illuminated specimen area, respectively.

CBED disks are deformed by the Lorentz force acting on the electron beam. The Lorentz force is expressed as $-ev \times \boldsymbol{I}$, where $-e$ and v are the charge and velocity of an incident electron, respectively, and $\boldsymbol{I}$ is the magnetization of the substance. The sense of Lorentz deflection is opposite between the two adjacent domains because the signs of $\boldsymbol{I}$ are different.

When magnetic domains A and B are illuminated in illumination mode I, the beams passing through domains A and B are deflected to recede from the domain wall. Thus, a bright-field disk appears in an elongated form as schematically shown at the left part of Fig. (a). When magnetic domains B and C are illuminated in mode I, the beams passing through domains B and C are deflected to approach the domain wall. As a result, the disk appears in a compressed form as shown at the right part of Fig. (a).

In the case of illumination mode II, the sense of the defocus CBED pattern is opposite to the case of illumination mode I as is seen in Fig. (b). That is, the CBED disks obtained from domains A and B are compressed and those from domains B and C elongated. The deformation of the dark-field disks is the same as that of the bright-field disk. When the CBED disk is elongated/compressed, an intensity deficiency/excess occurs at the shadow image of the wall analogous to the divergent-/convergent-wall images in Lorentz microscopy.

A reflection line continuously bends at the domain wall because the magnitude of Lorentz deflection continuously changes due to a continuous rotation of the magnetization in the wall. Analysis of the bend allows us to obtain information on the wall structure.

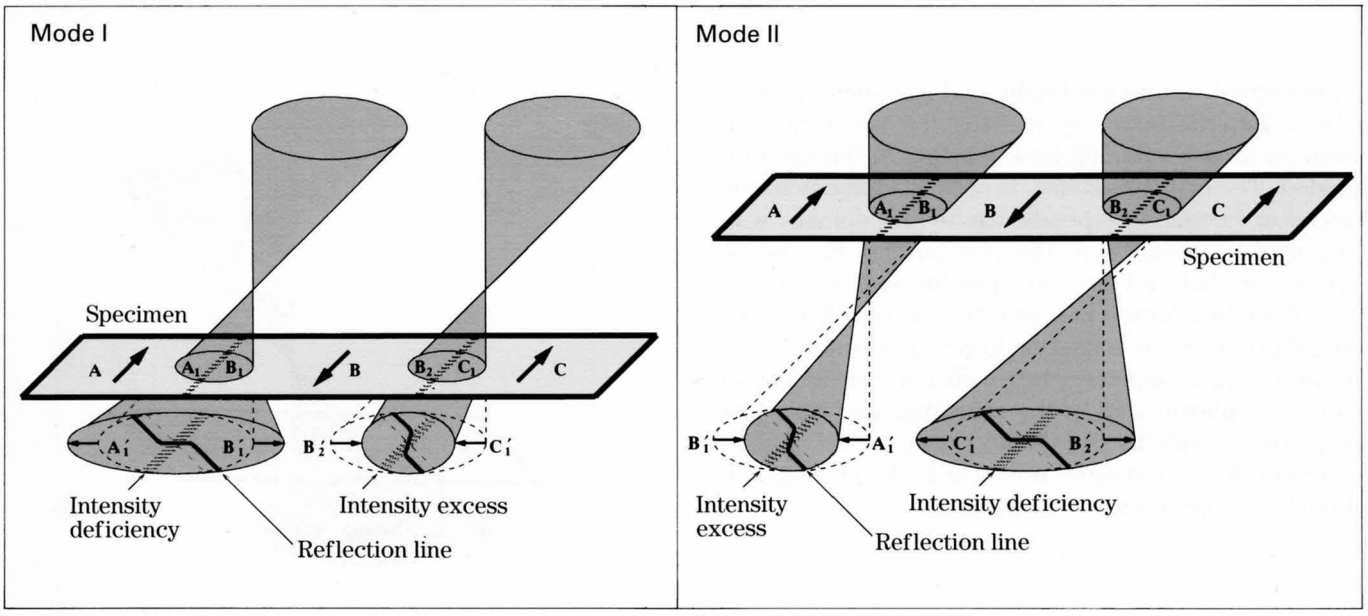

(a) (b)

Fe-13at.%Si

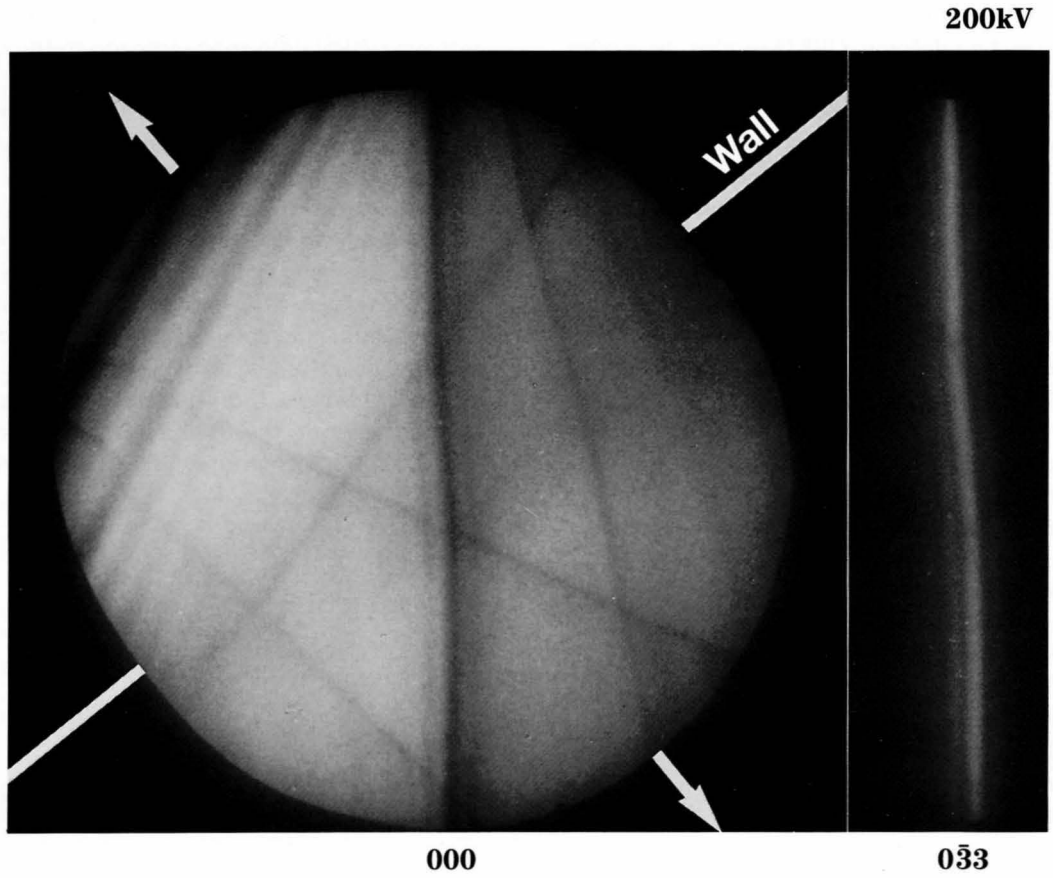

Photograph shows the bright- and dark-field defocus CBED patterns taken by exciting the 0$\bar{3}$3 reflection from an area containing two domains in illumination mode I. The bright-field disk is seen to elongate in the direction (arrows) perpendicular to the domain wall indicated by white lines. The vertical dark line in the bright-field disk and the corresponding light line in the dark-field disk form a pair of 0$\bar{3}$3 reflection lines. The straight parts of the reflection line correspond to areas in the magnetic domains, in which Lorentz deflection causes a uniform shift of the reflection line. The bent part corresponds to the domain wall. Intensity deficiency at the wall image is not clear in the photograph, though it is seen on the negative film.

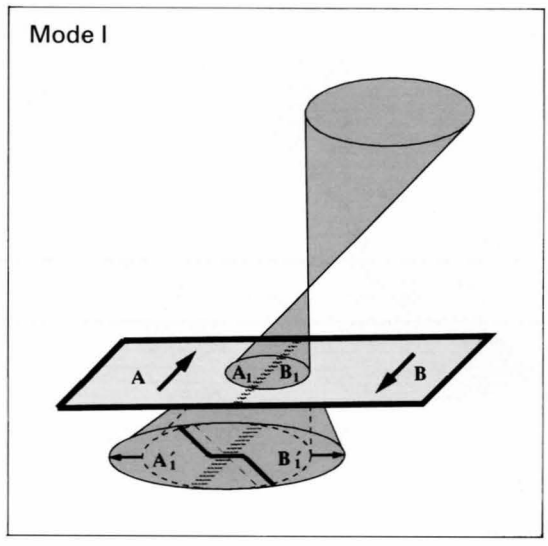

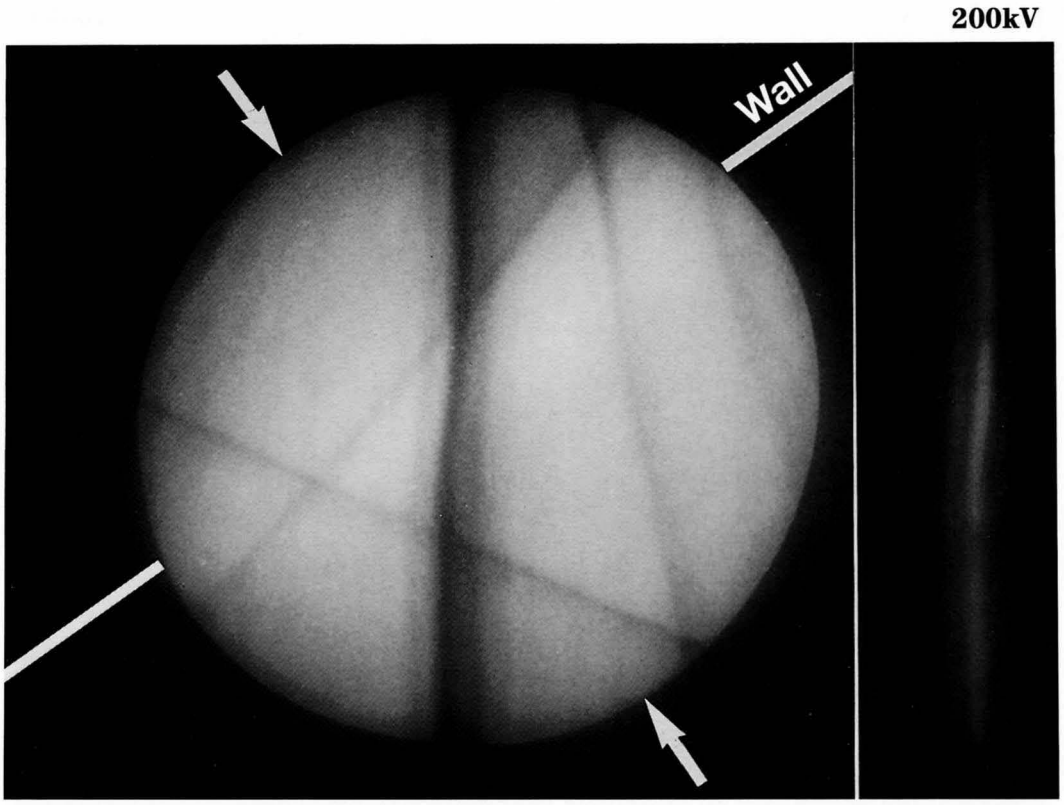

The CBED patterns were taken by exciting the same reflection from the same area as those on the opposite page but in mode II. The bright-field disk is compressed as shown by arrows. The sense of bend of the 0$\bar{3}$3 reflection lines is opposite to that on the opposite page. Intensity excess is seen at the wall.

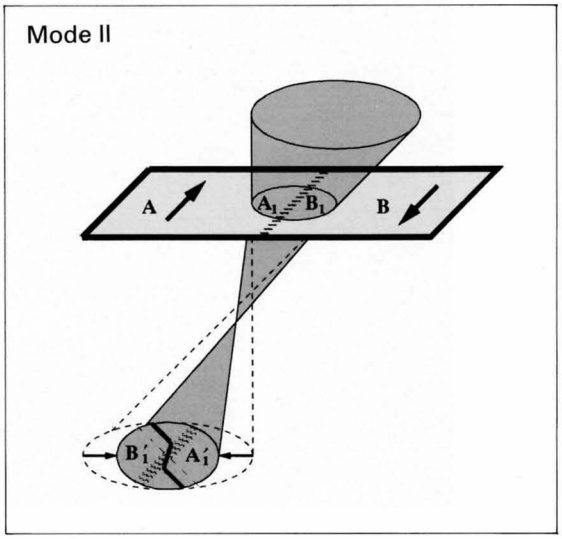

Fe-13at.%Si

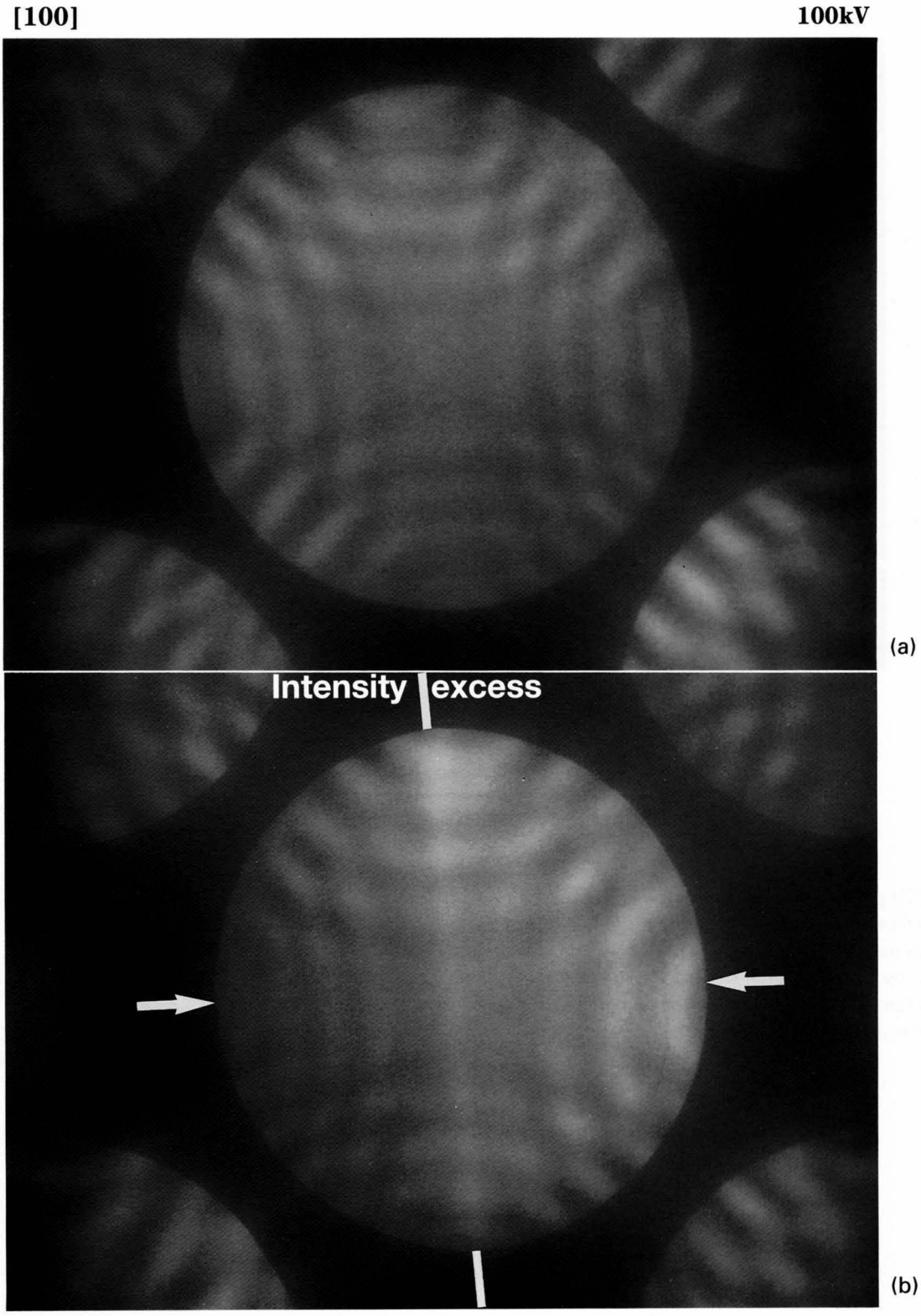

[100] zone-axis defocus bright-field CBED patterns taken from a domain (a) and from two domains (b) in mode I, the diameter of the illuminated area being 740nm. Intensity excess at the wall and the compressed disk in Photo (b) are noted.

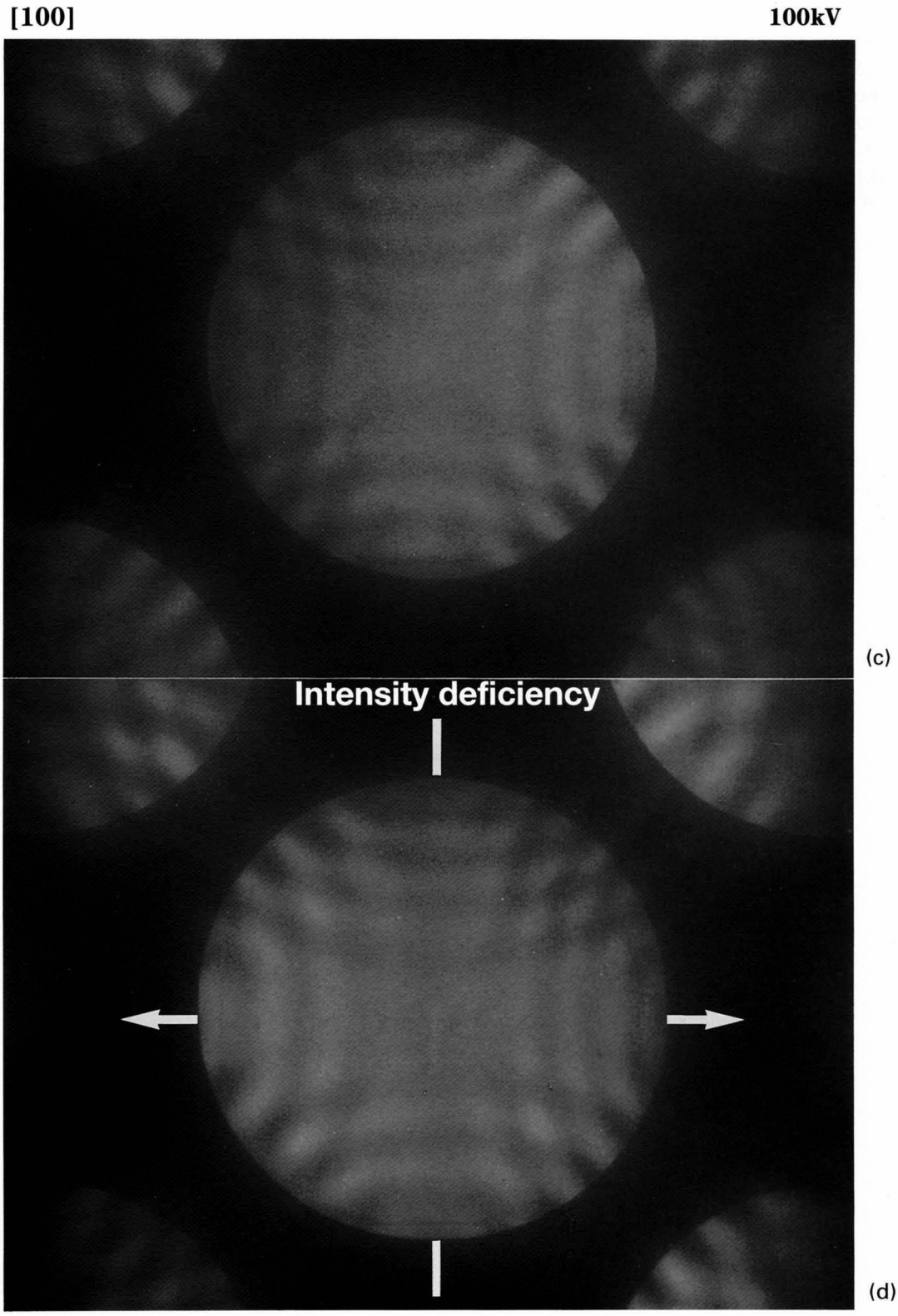

Photographs (c) and (d) were taken from the same areas as in Photos (a) and (b) respectively on the opposite page but in mode II. Intensity deficiency and the elongated disk are seen in Photo (d) instead of intensity excess and the compressed disk in Photo (b).

Fe-13at.%Si

Defocus CBED patterns taken by exciting the *hh*0 systematic reflections at different focuses of the incident beam; (a) over-focus (mode I), (b) under-focus (mode II). The bright-field disk is compressed in Photo (a) but elongated in Photo (b). The wall position and the direction of Lorentz deflection are indicated by lines and arrows, respectively. The sense of bend of the 220 reflection line is opposite between Photos (a) and (b).

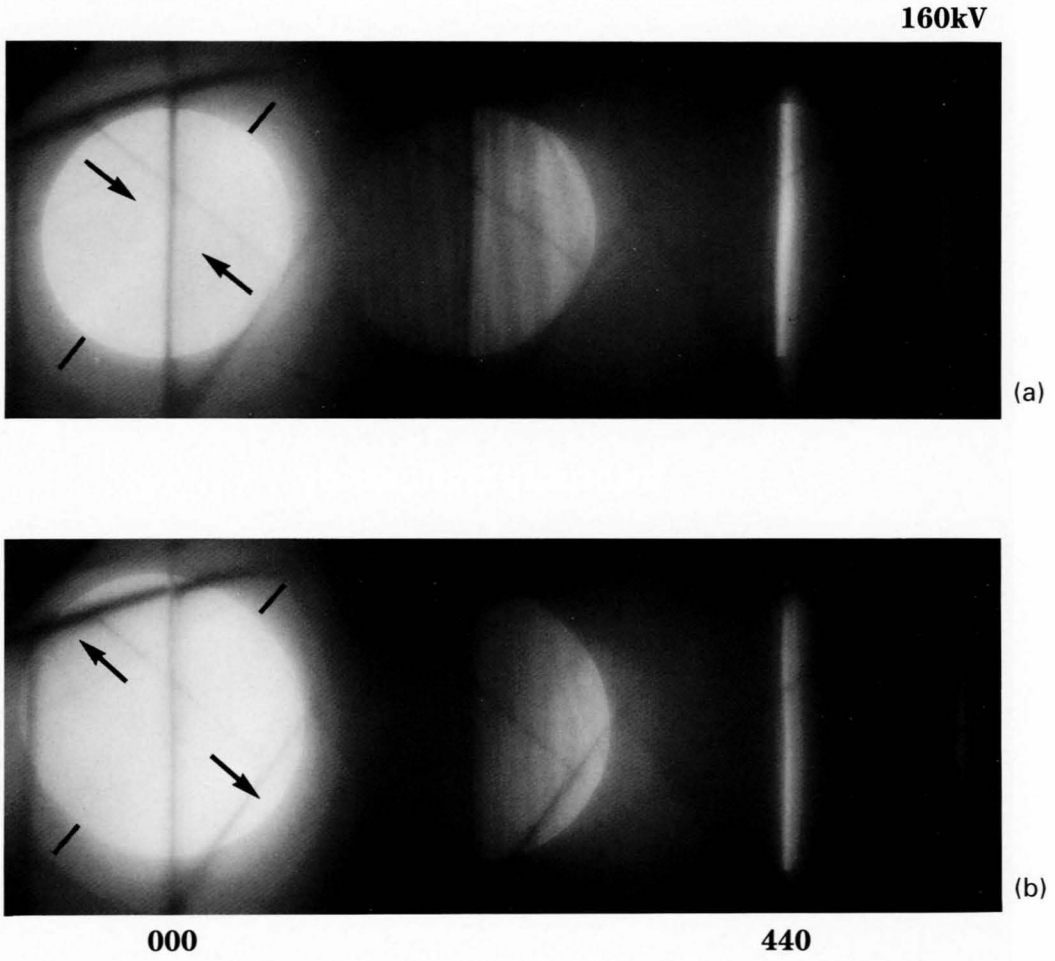

Defocus CBED pattern (a) was taken in mode I from an area containing the position at which three domains meet (Photo (b)). Three parts of the pattern (a) recede from each other to form intensity deficiency at the wall region, an illustration (c) being attached. From the result, the configuration of the magnetization was identified as indicated by arrows in Photo (b).

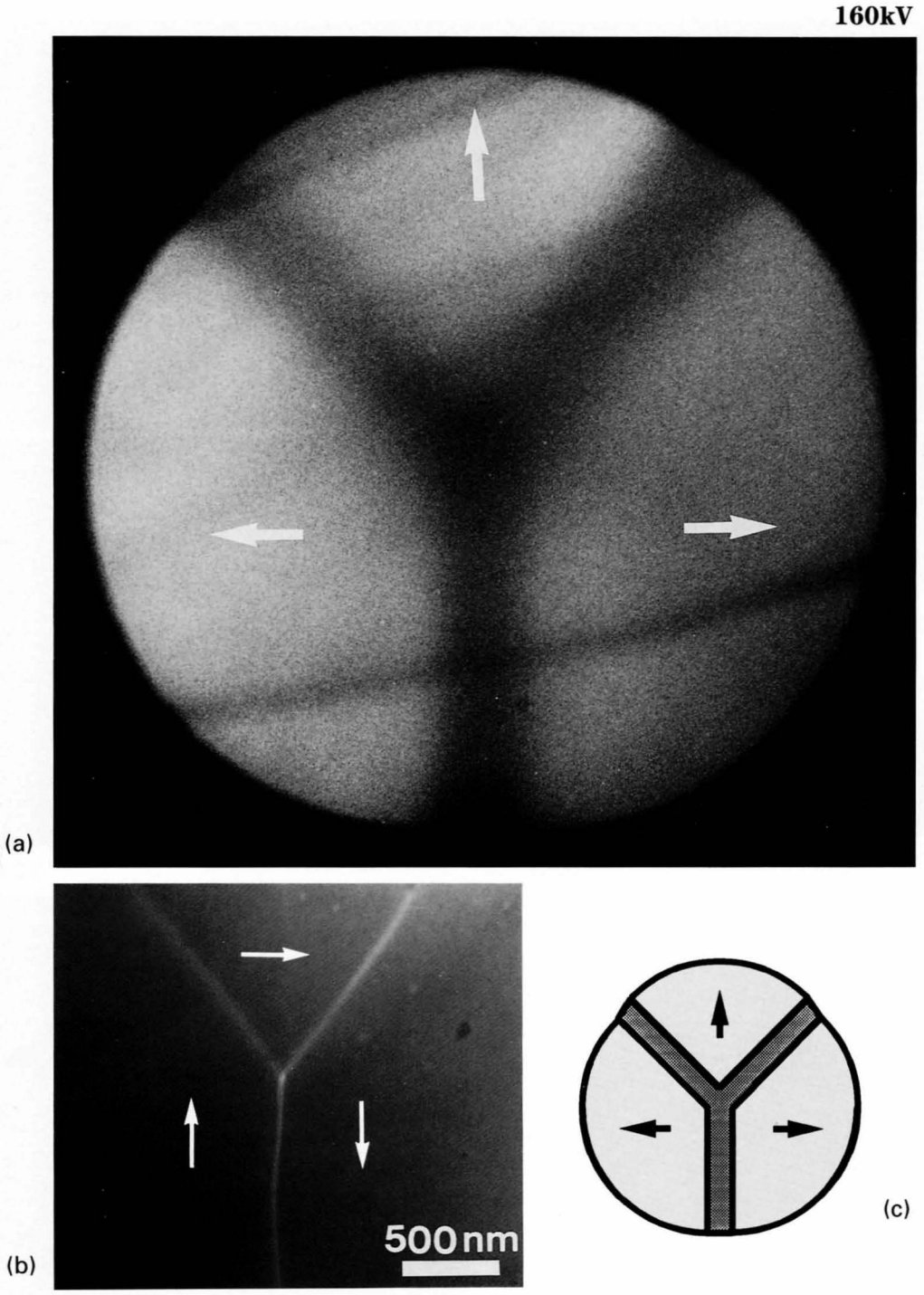

Co [0001]

Defocus CBED patterns of maze domains of cobalt (c) taken near the [0001] incidence with a large defocus (a) and a small defocus (b).

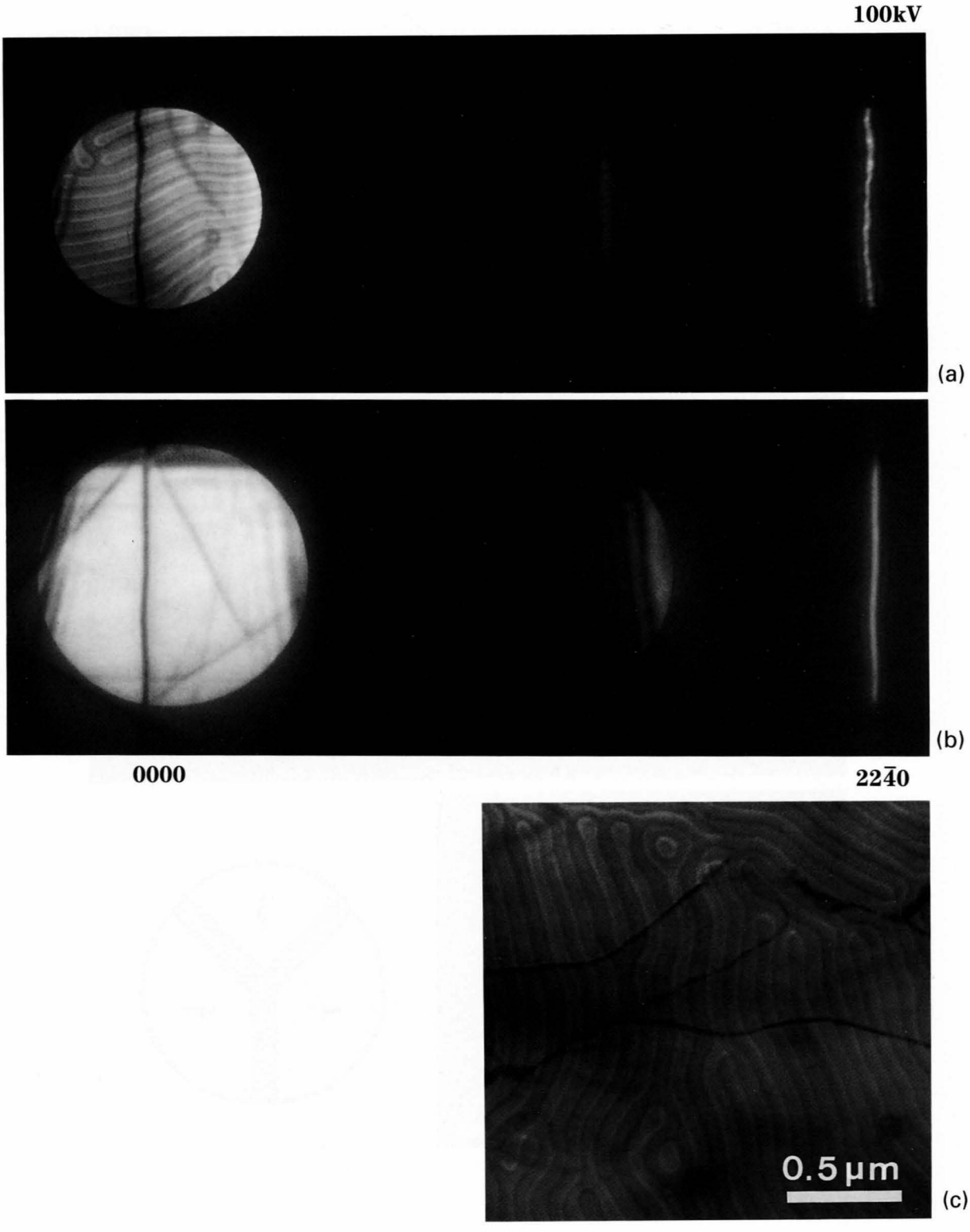

Determination of Lattice Parameters

Determination of the compositions of Fe-Ni alloys

Lattice parameters can be measured with a reasonable accuracy by using HOLZ lines. When the relation between lattice parameters and compositions is known, lattice parameter measurements enable us to determine the composition of a solid solution. As an example, calibration curves between the distances of HOLZ lines and the compositions of Fe-Ni alloys are provided for the determination of the compositions.

Figure (a) shows the phase diagram of Fe-Ni alloys. The γ - phase takes a face-centered cubic structure and a disordered state, in which atom sites are occupied by both atoms randomly at the ratio of the compositions. The relation between the lattice parameters and the compositions is given in Fig. (b). The lattice parameter a of the γ - phase of Ni is 0.3524nm at 15°C, and that of γ Fe-Ni increases monotonically with the composition of Fe up to 60 at.%. Beyond the composition, the value of the parameter decreases.

In the following pages, CBED patterns of the alloys with different compositions taken at the [441] and [631] electron incidences are shown, in which five distances A to E between intersecting points of HOLZ lines are indicated. Plots of the ratios between the distances A to E against the composition are given in the following figures. When we take CBED patterns of an Fe-Ni alloy with an unknown composition, measure those distances and refer to the figures, the composition of the alloy can be determined.

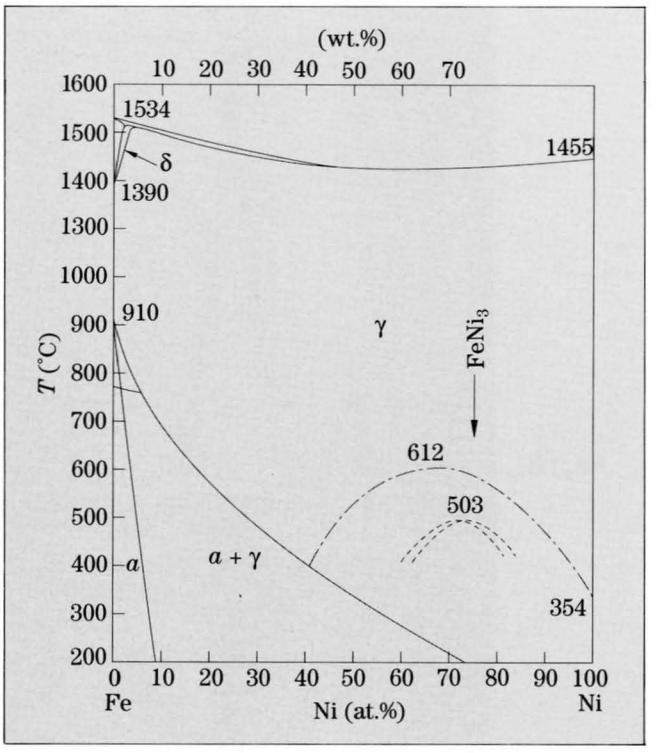

(a)

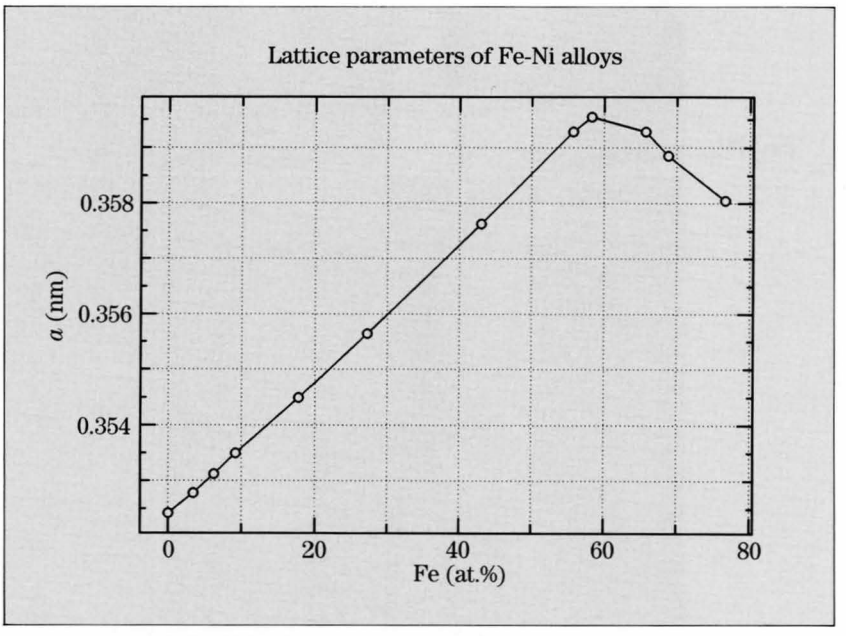

(b)

[441] 200kV

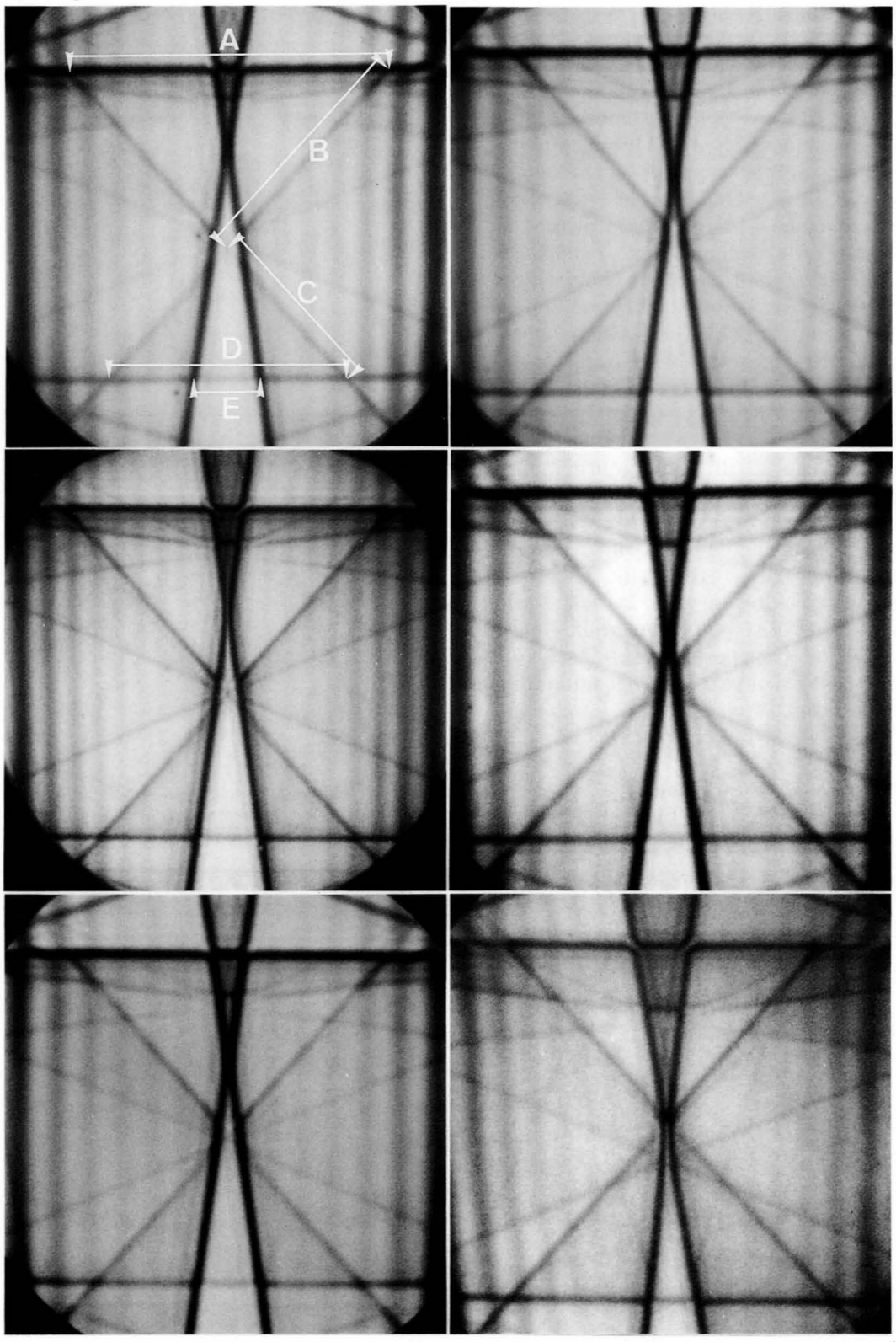

$Fe_{60}Ni_{40}$ $Fe_{30}Ni_{70}$

$Fe_{50}Ni_{50}$ $Fe_{20}Ni_{80}$

$Fe_{40}Ni_{60}$ Ni

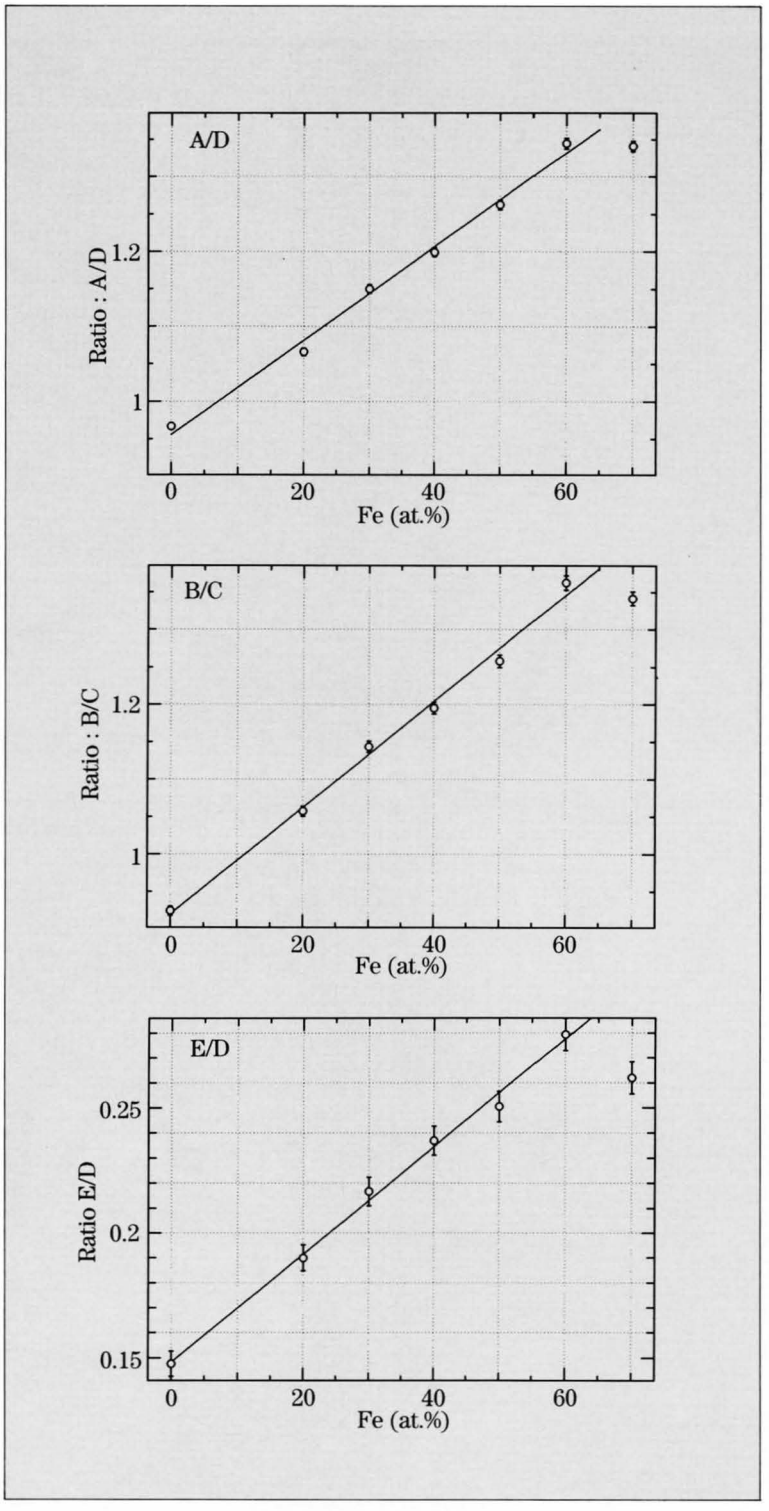
A/D
Ratio : A/D
1
1.2
0
20
40
60
Fe (at.%)
B/C
Ratio : B/C
1
1.2
0
20
40
60
Fe (at.%)
E/D
Ratio E/D
0.15
0.2
0.25
0
20
40
60
Fe (at.%)

[631] 200kV

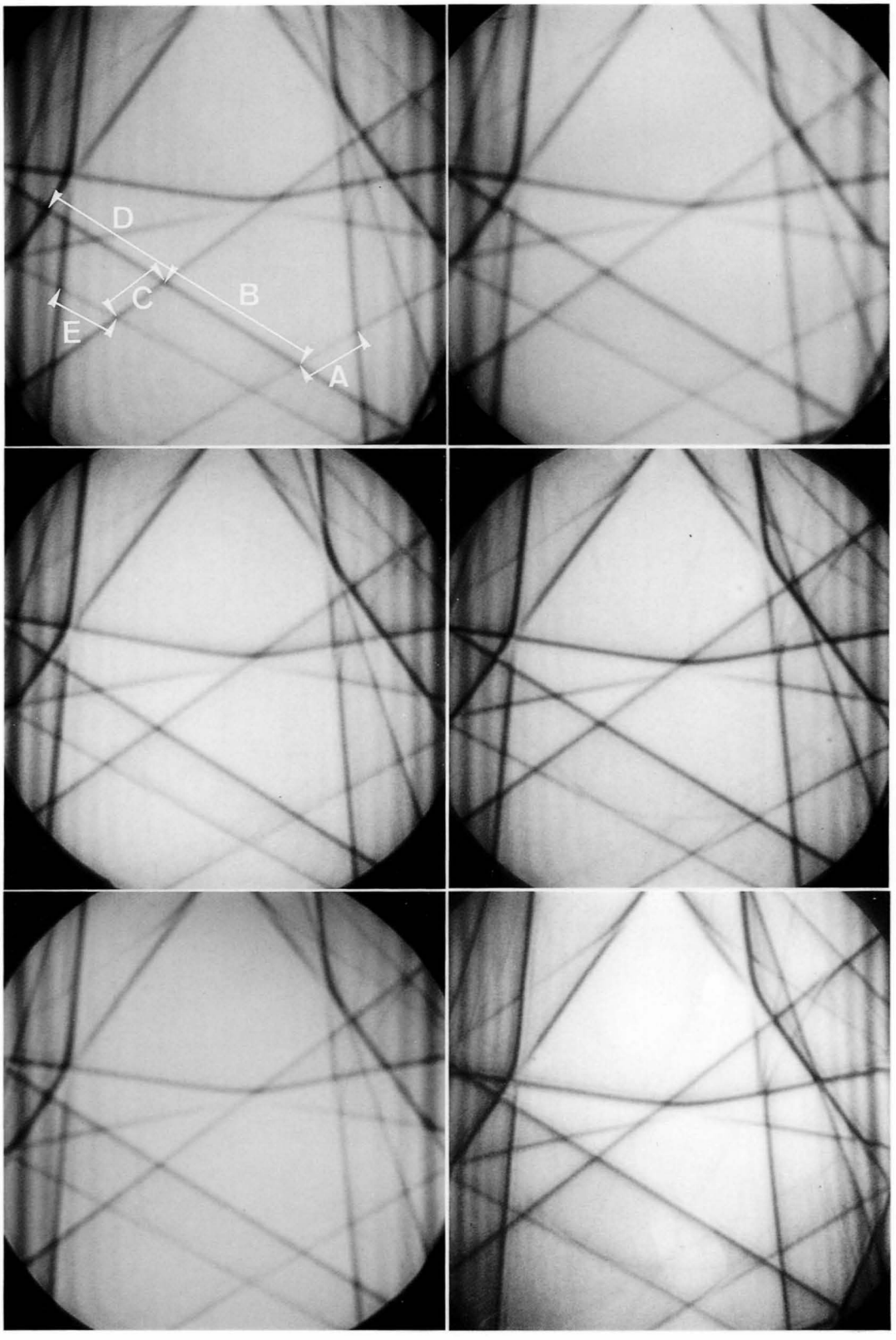

$Fe_{60}Ni_{40}$ $Fe_{30}Ni_{70}$

$Fe_{50}Ni_{50}$ $Fe_{20}Ni_{80}$

$Fe_{40}Ni_{60}$ Ni

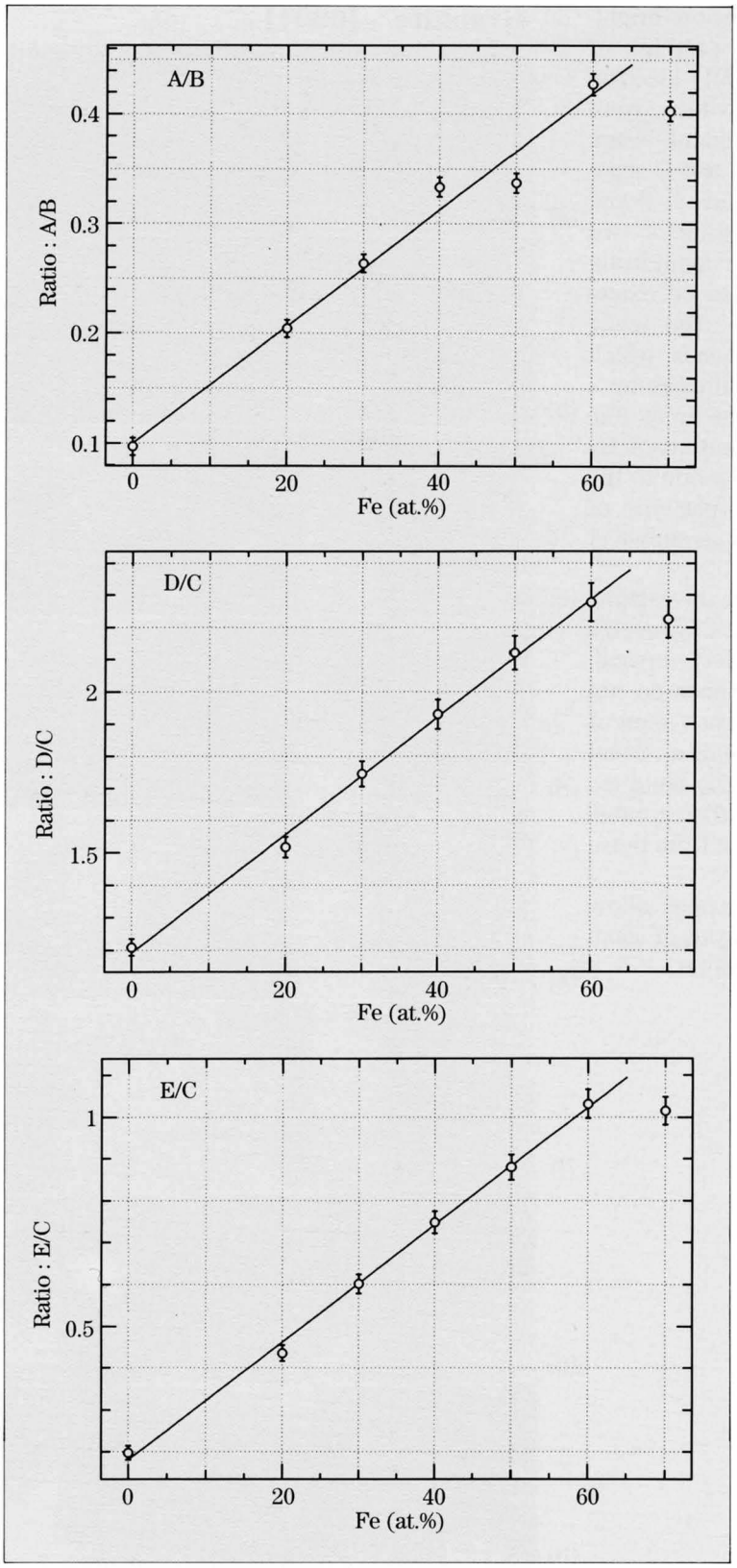
A/B
Ratio : A/B
0.1
0.2
0.3
0.4
0
20
40
60
Fe (at.%)
D/C
Ratio : D/C
1.5
2
0
20
40
60
Fe (at.%)
E/C
Ratio : E/C
0.5
1
0
20
40
60
Fe (at.%)

Selected Area CBED Patterns

Photographs (a) to (h) show bright-field images and CBED patterns of graphite taken at the [0001] electron incidence. The images, which were taken with a parallel incident beam, show four regions A, B, C and D separated by three narrow bands α, β and γ, the left band α consisting of two subbands α_1 and α_2. The incident beam was converged to areas to be examined in the image mode. The white spots indicated by arrowheads, which were superposed on the images by a double exposure, show the areas illuminated with the convergent beam. By switching from the image mode to the diffraction mode, CBED patterns of those areas were obtained, as shown at the right side.

The patterns taken from the regions A, B, C and D show a $6mm$ symmetry expected from the perfect crystal. Those from the narrow bands do not show a $6mm$ symmetry, but show a mirror symmetry at the bands α_1, β and γ, and a symmetry 1 at the band α_2. The orientation of the mirror symmetry at the band γ is different from those at the bands α_1 and β.

Recent electron microscopes allow the crystallographical analysis of small areas down to 1nm in diameter.

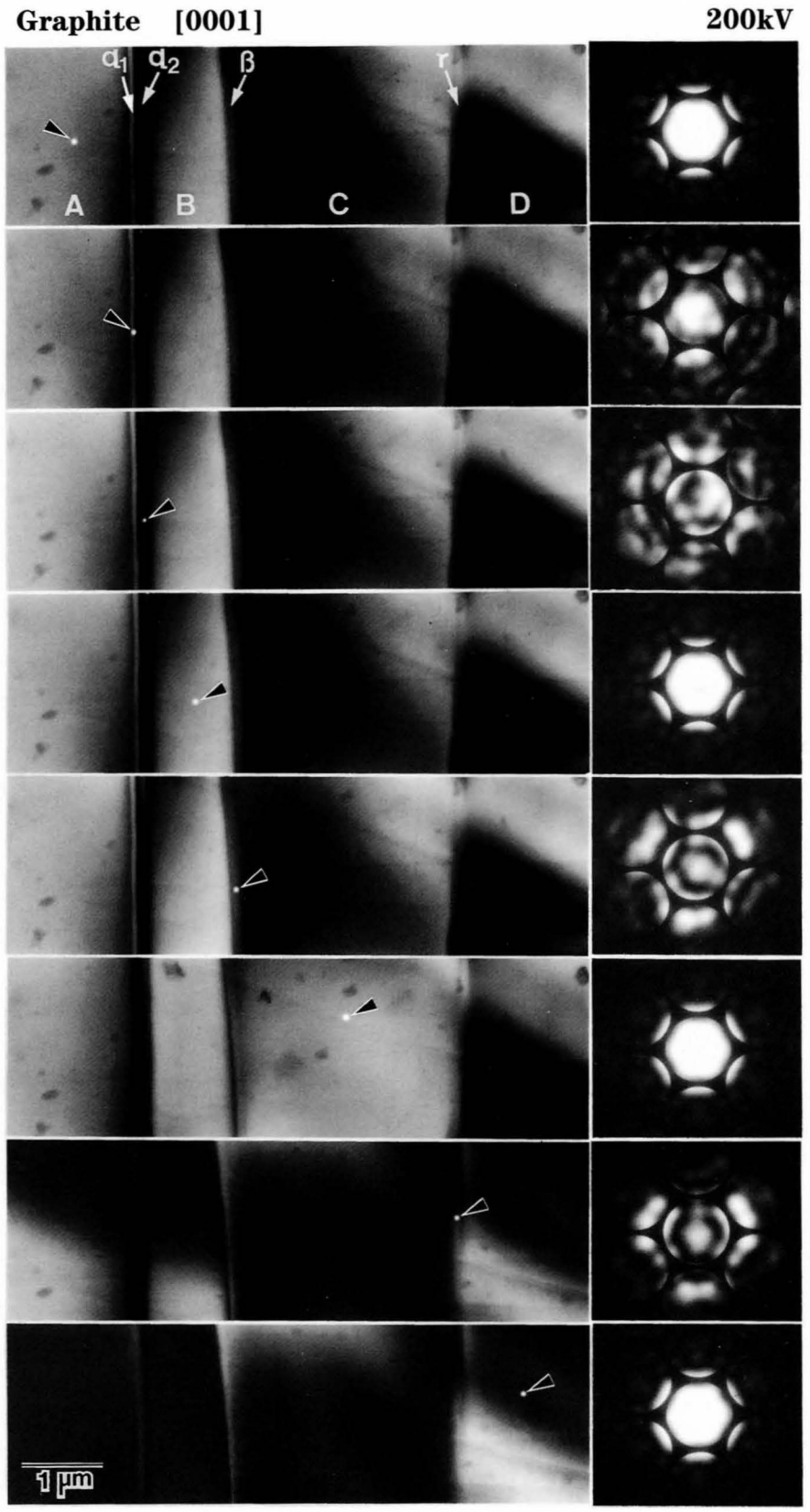

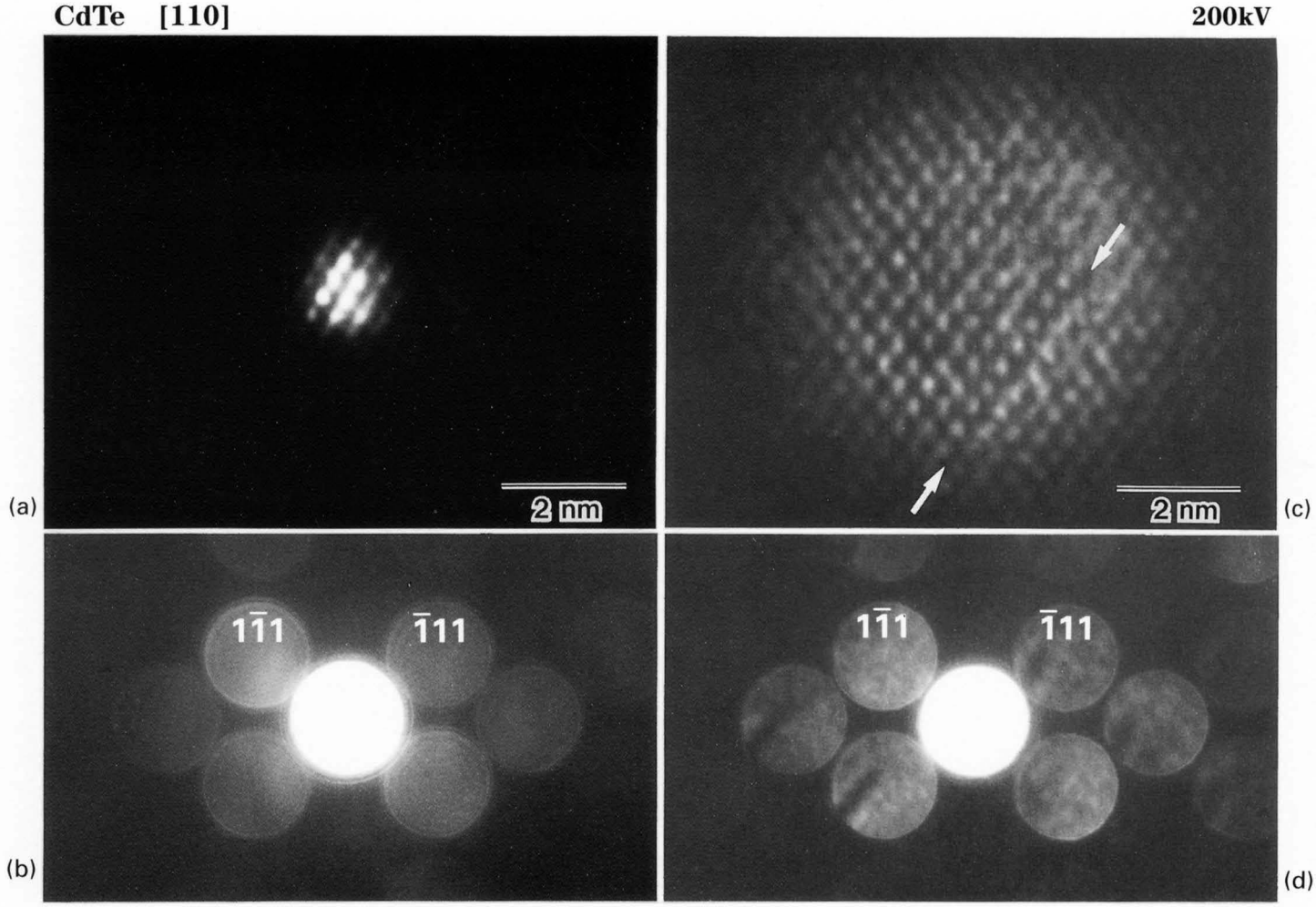

Photograph (a) shows a lattice image of a perfect area, which was taken by converging the incident beam on the specimen, the diameter of the illuminated area being about 1nm. By switching to the diffraction mode with other conditions kept unchanged, the CBED pattern of Photo (b) was obtained. Although the pattern does not exhibit a specific intensity variation in the disks because of the thin specimen, the symmetry appearing between the disks is that expected from the perfect crystal.

Photograph (c) is a lattice image of 5-nm-diameter area including a stacking fault and its edge, which was taken with a slightly defocused illumination by changing the excitation of the third condenser lens (brightness). Photograph (d) is a CBED pattern from the same area as Photo (c). The image of the fault is seen in all disks except the 1$\bar{1}$1 and $\bar{1}$1$\bar{1}$ disks, or the symmetries in the CBED disks changed except in the latter two disks. The shift vector of the fault can be identified from the CBED pattern.

The JEM-2010 electron microscope permits the simultaneous use of high-resolution imaging and CBED.

Color Presentation

Si [110]

100 kV

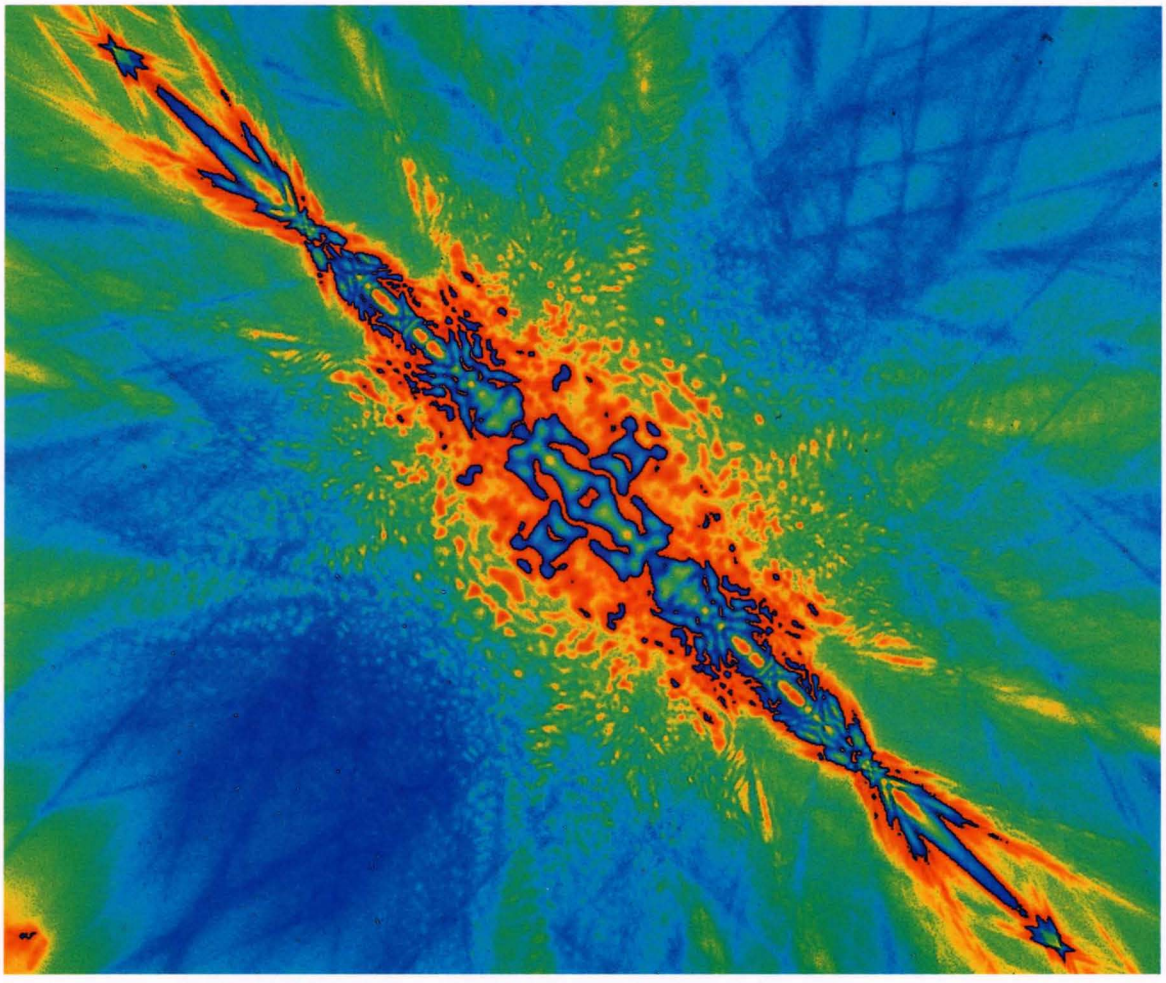

Si [111]

100 kV

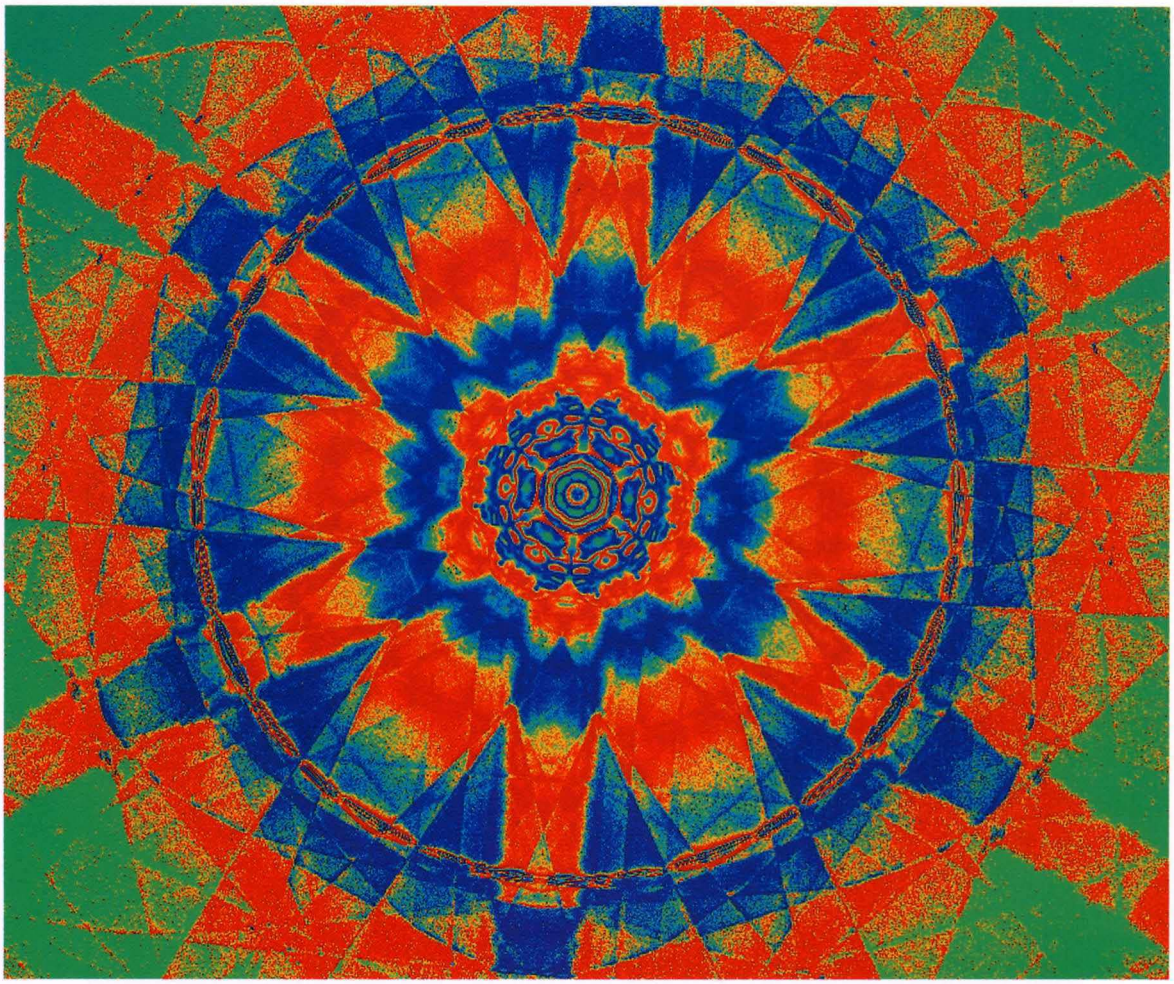

Si [111]

100 kV

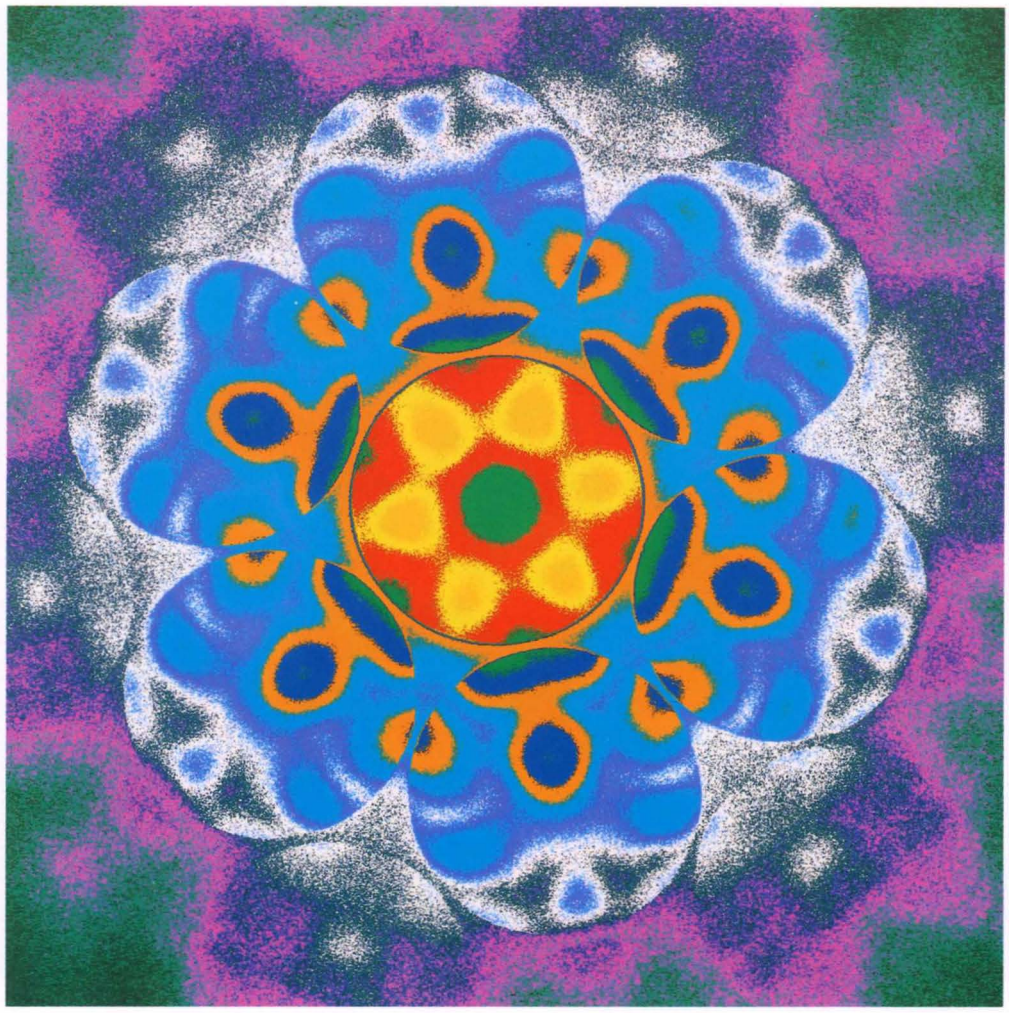

Si [111]

100 kV

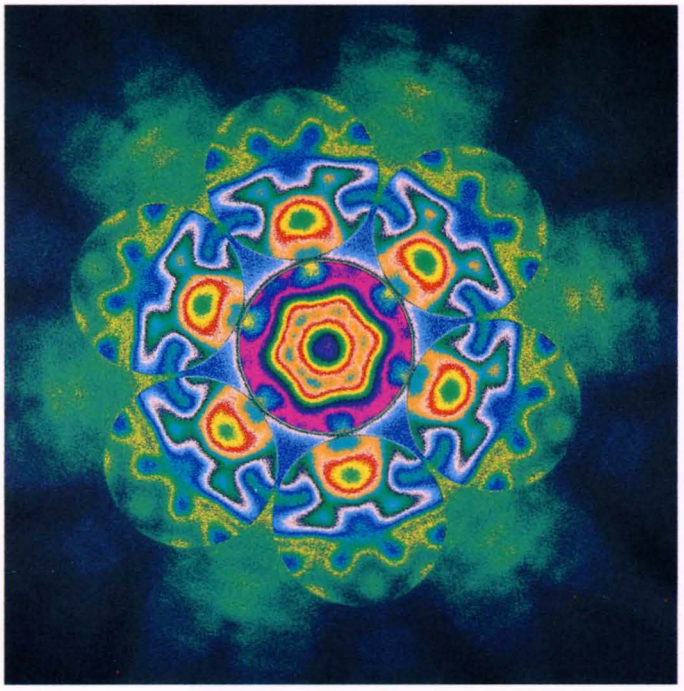

Si [111]

100 kV

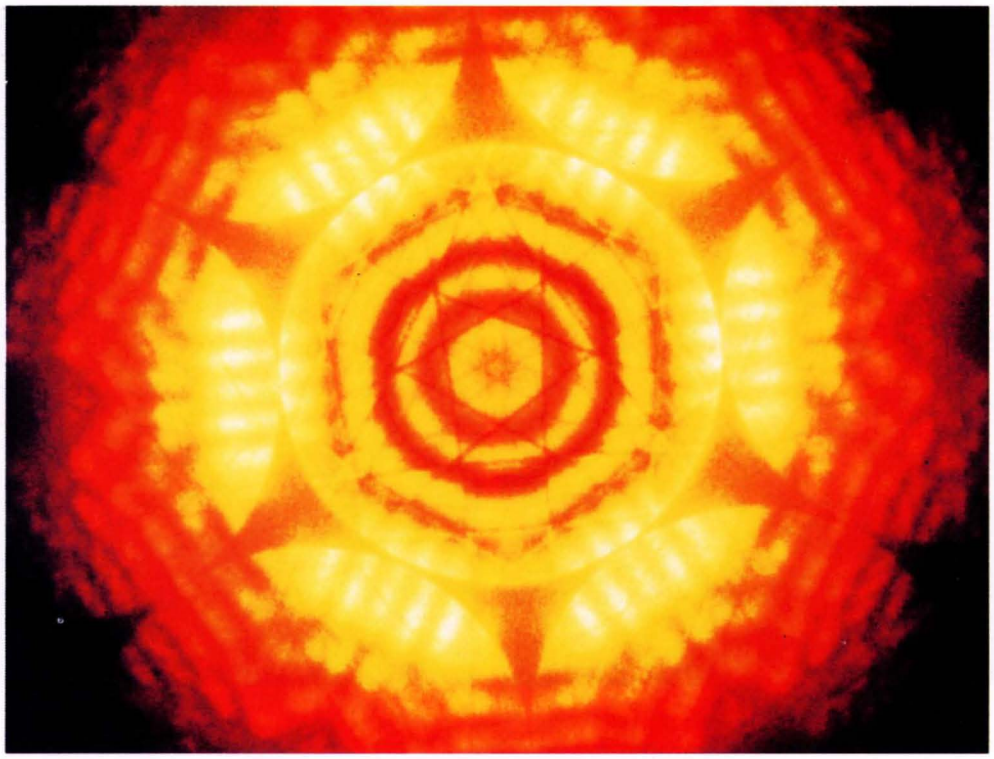

80 kV

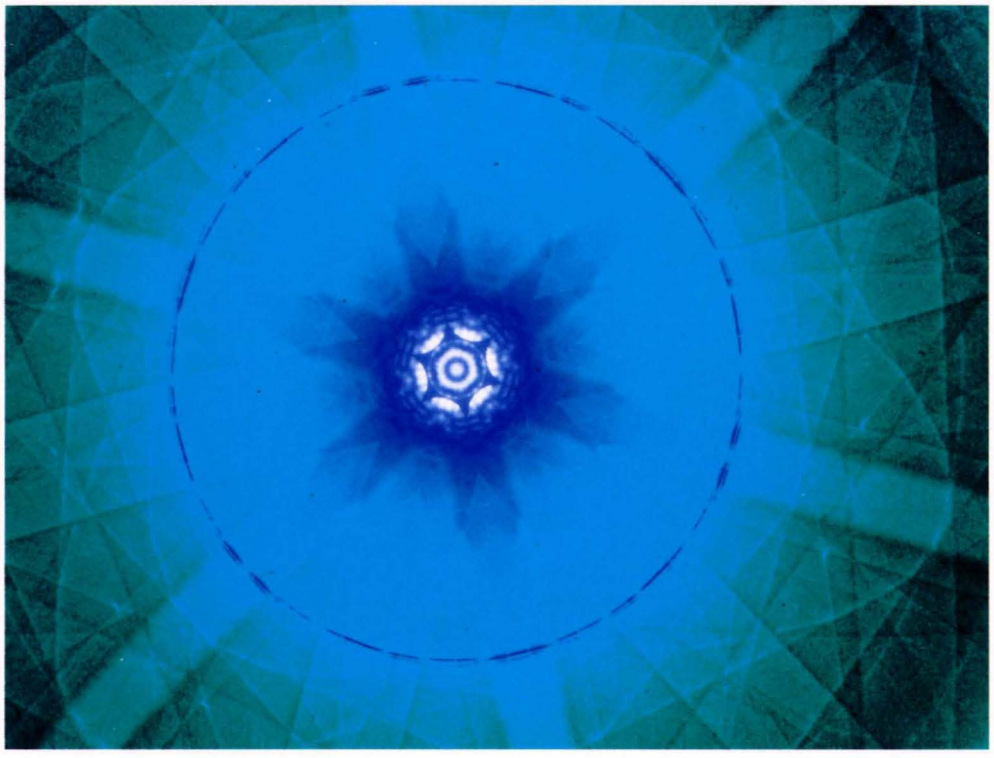

GaAs [100]

100 kV

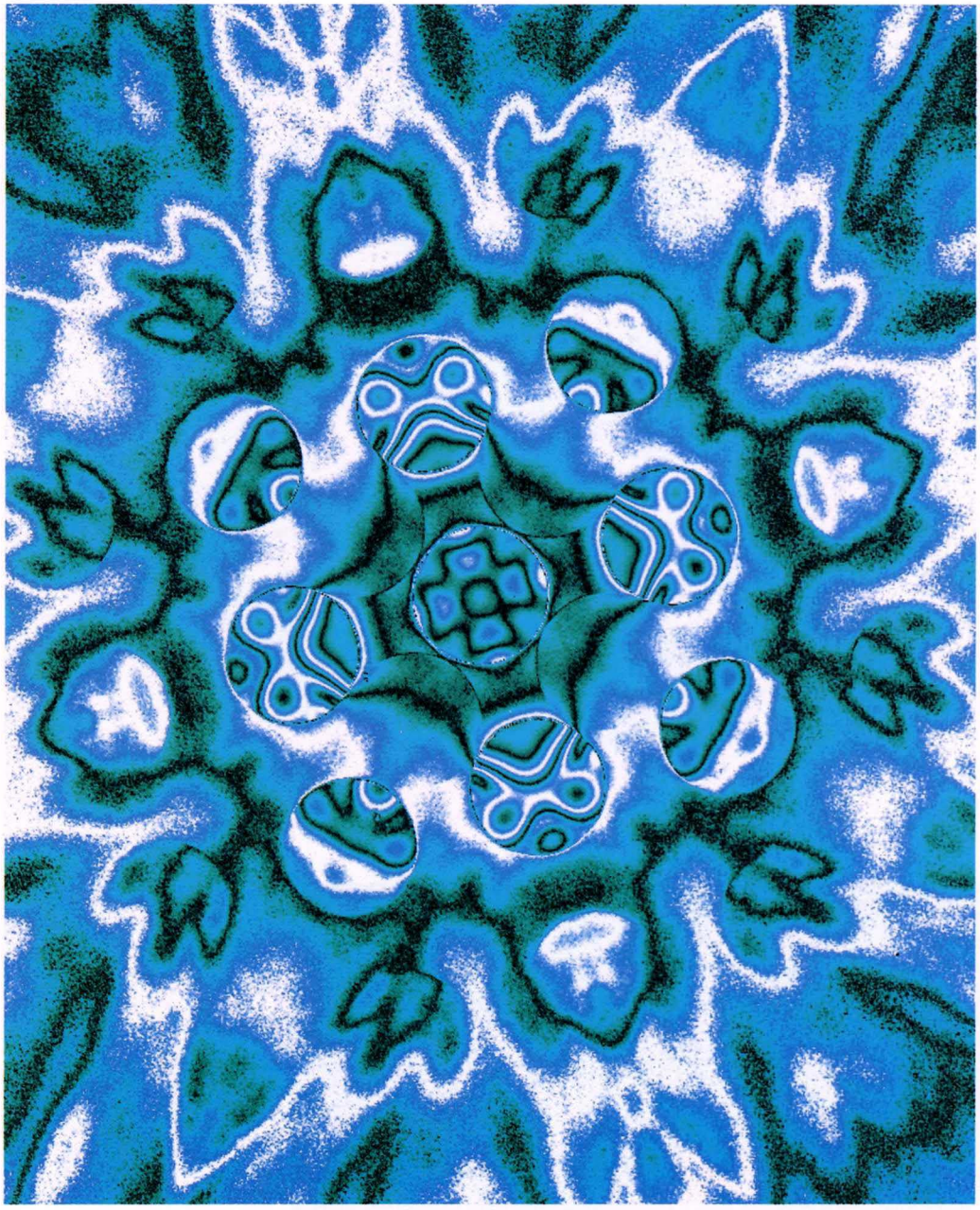

$Al_{70}Ni_{15}Fe_{15}$ –quasicrystal : De-phase–

100 kV

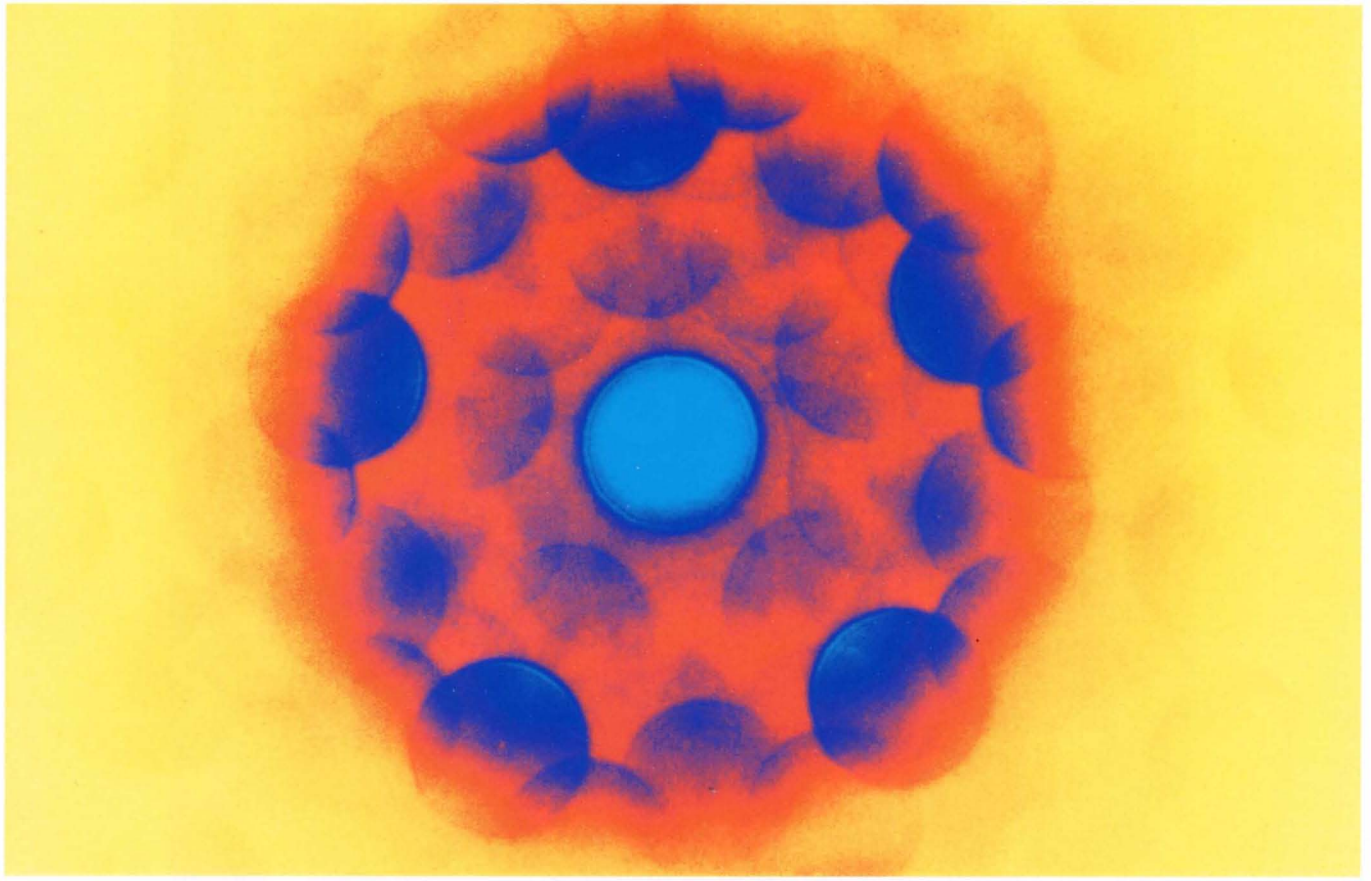

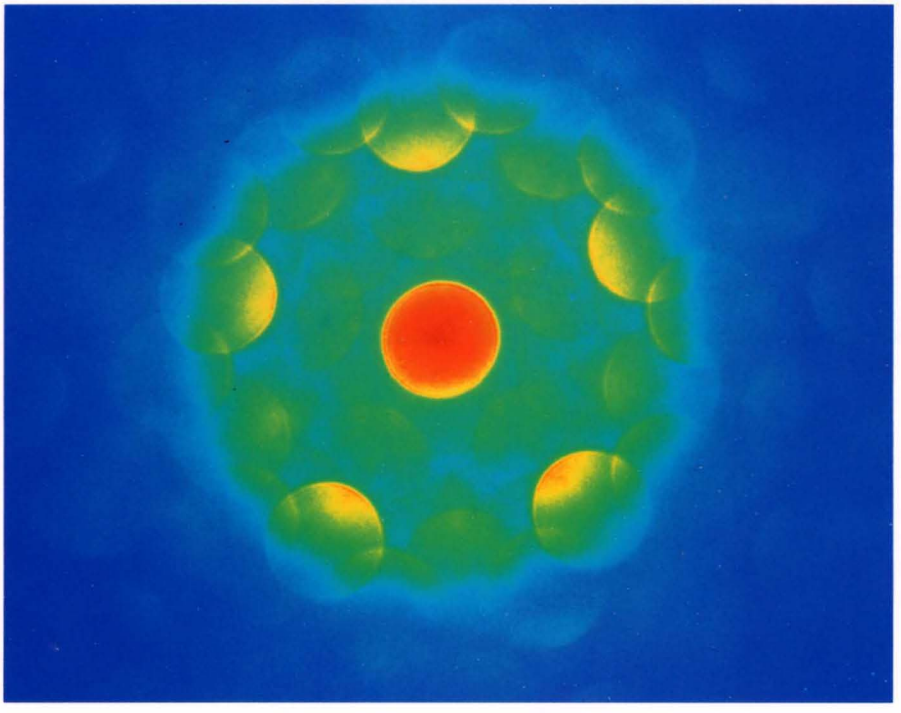

$Al_{65}Pd_{20}Mn_{15}$ –quasicrystal : I-phase–

100 kV

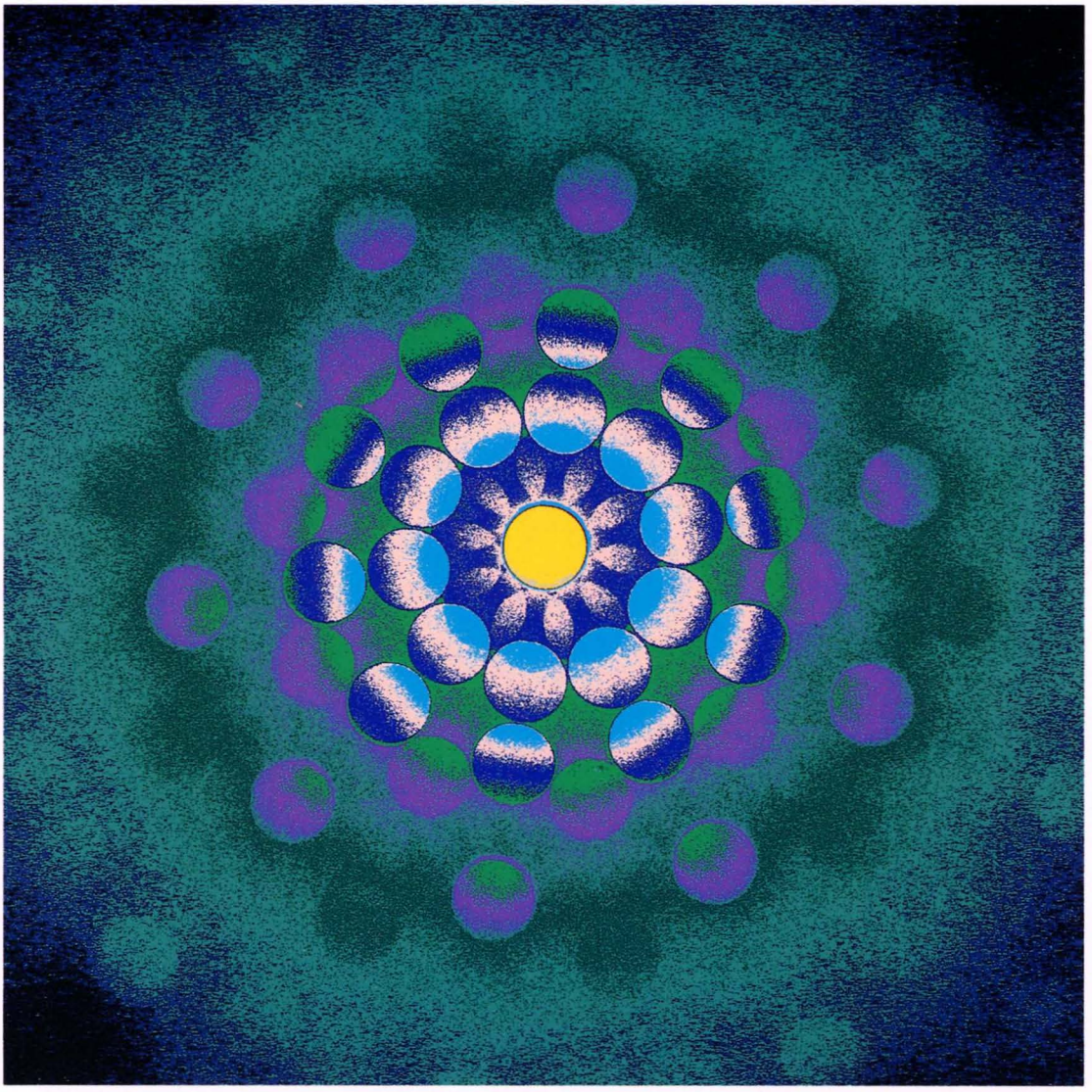

Graphite [0001] –moiré–

200 kV

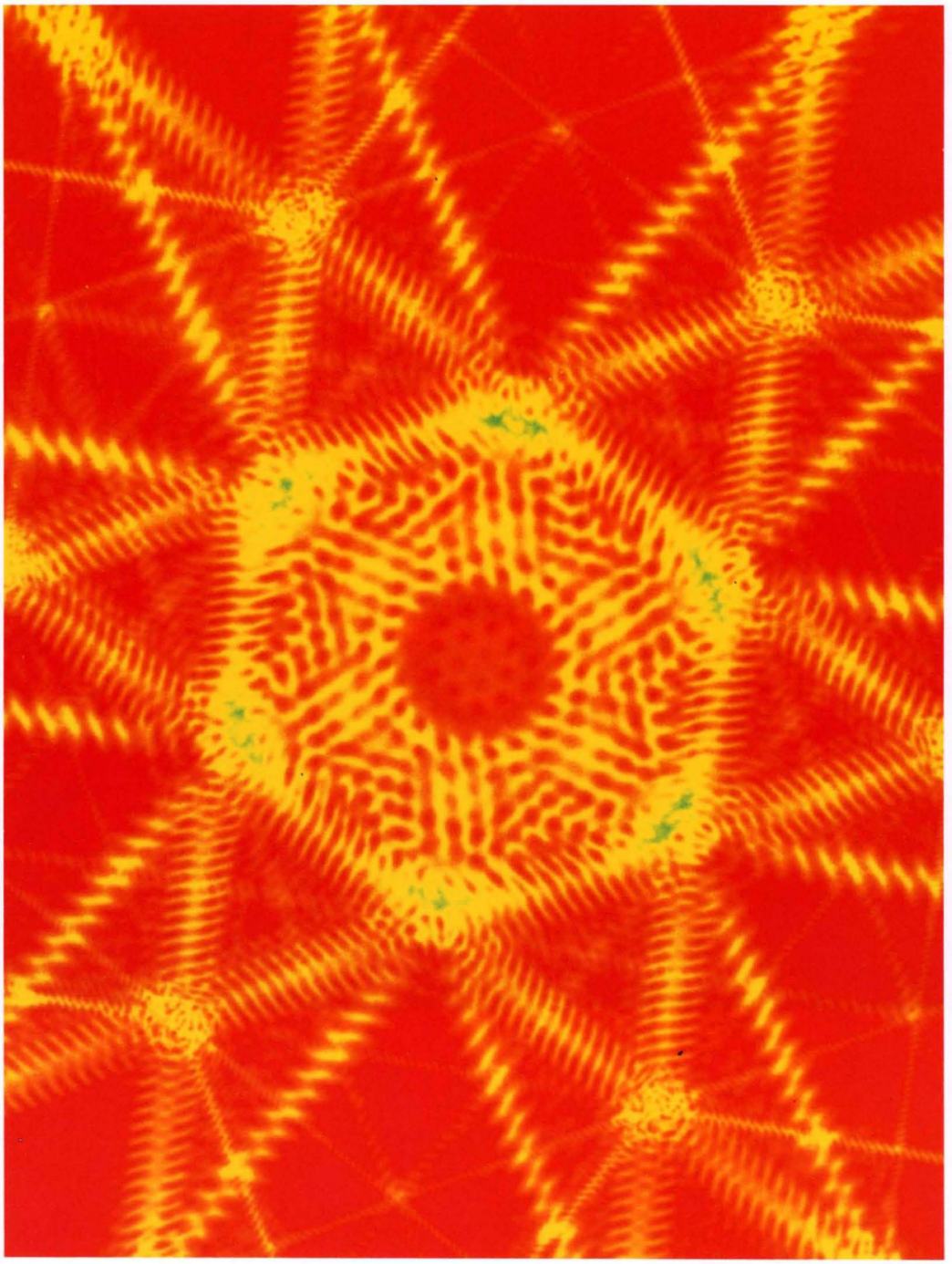

Graphite [0001] –dislocation network–

160 kV

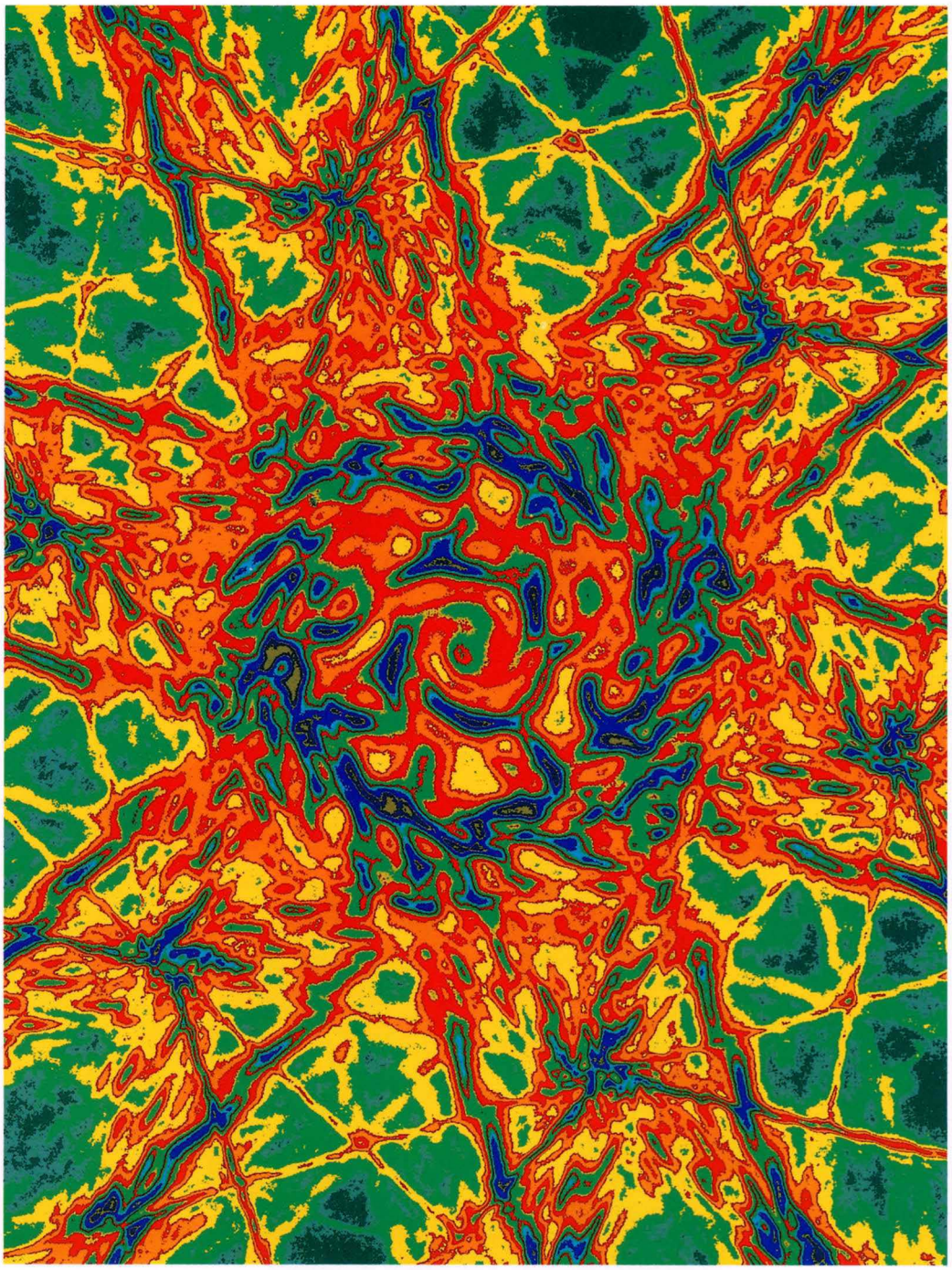

Graphite [0001]

–screw dislocation– **160 kV**

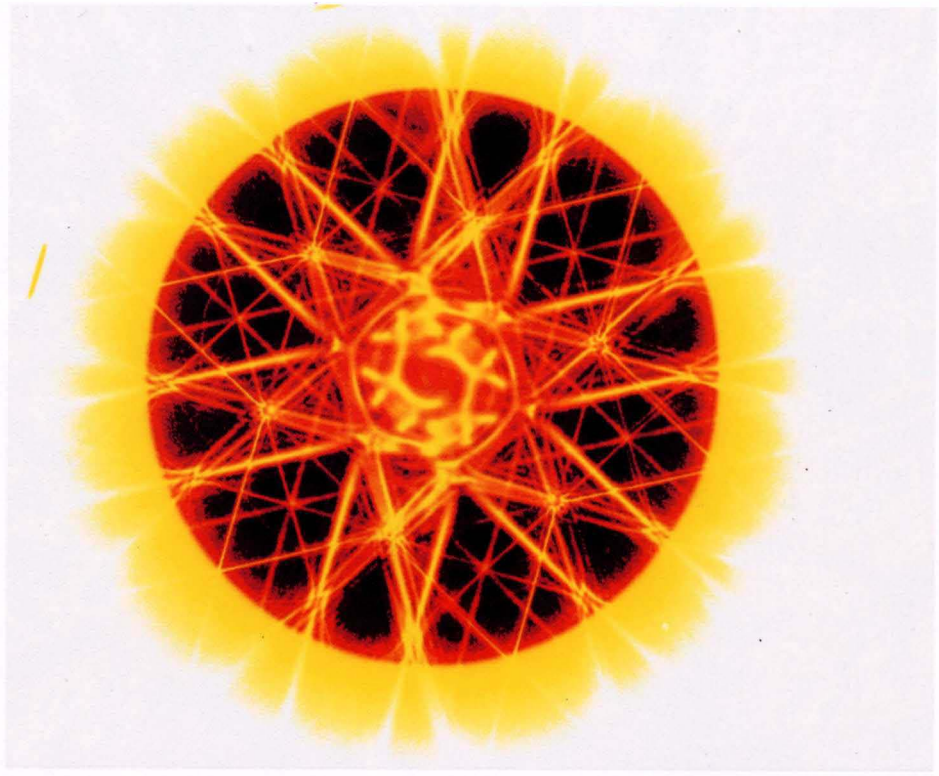

–edge dislocation–

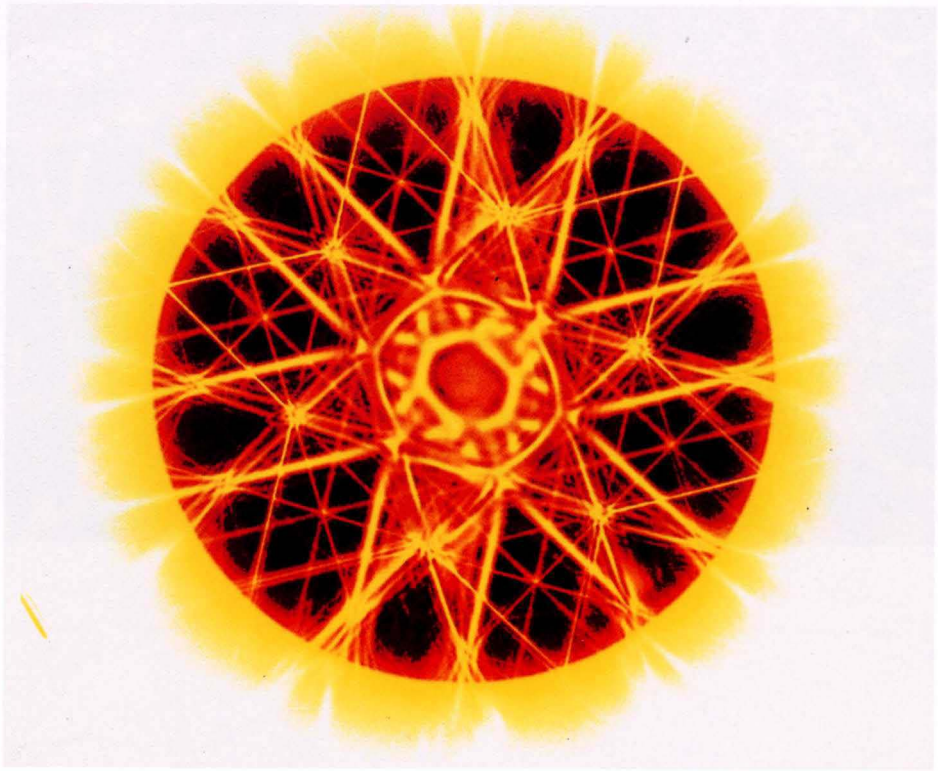

NiO **–twin boundary–** **200 kV**

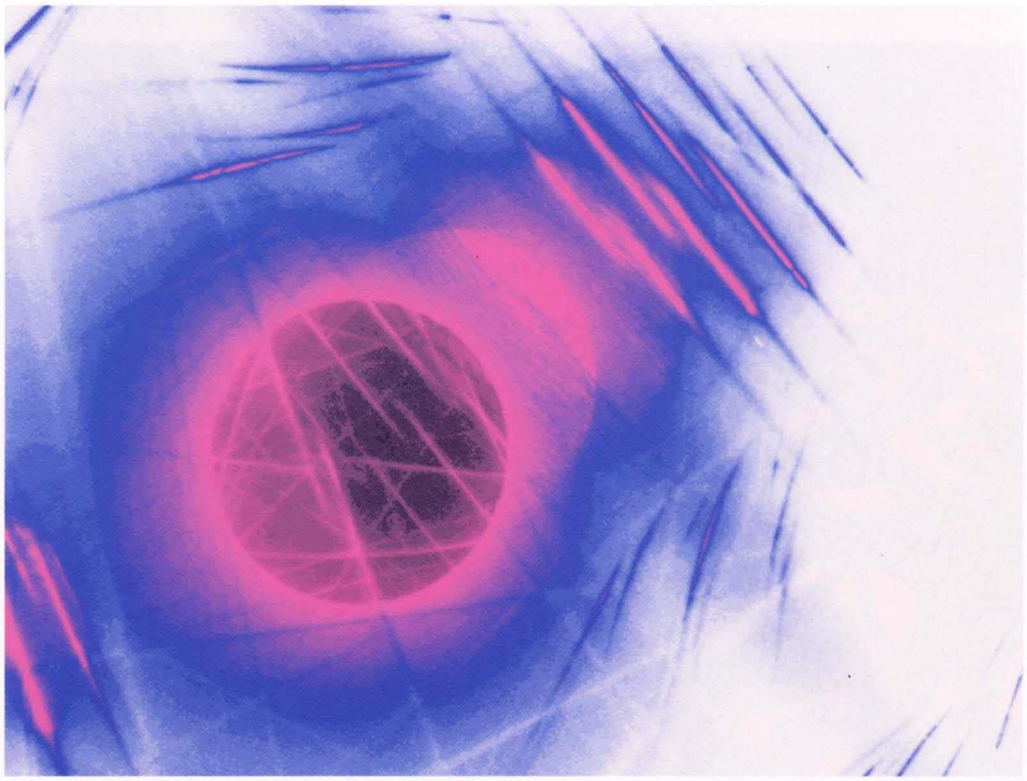

Si **–dislocation–** **200 kV**

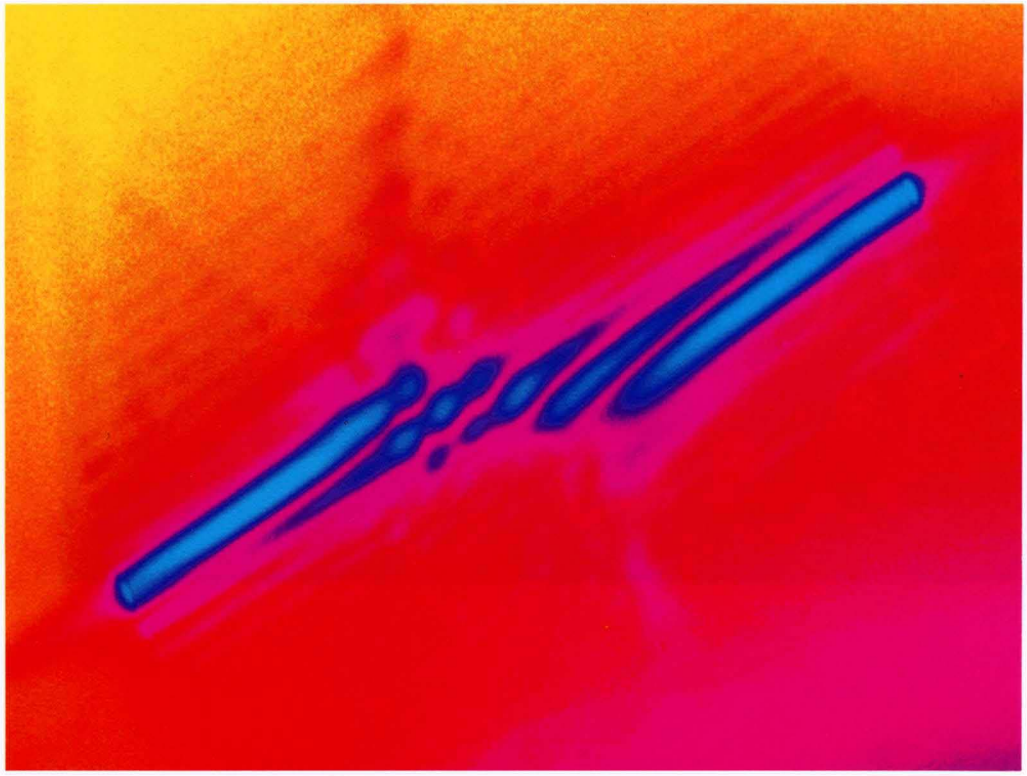

TiO_2 (rutile)

100 kV

TiO_2 (rutile)

100 kV

K. Saitoh Y. Nishida F. Sato M. Terauchi M. Tanaka K. Tsuda S. Yamada M. Kita

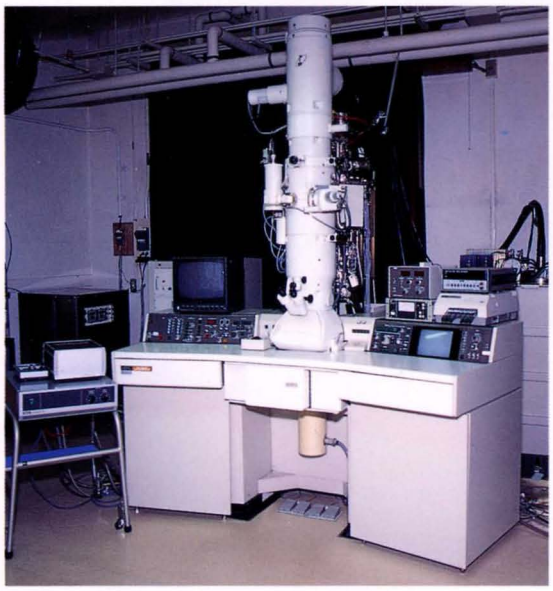

JEM-2010 with imaging plate system